Spray Dryer Modelling

Philip Nigel Threlfall-Holmes

Submitted for the degree of Doctor of Philosophy

Heriot-Watt University

School of Engineering and Physical Sciences

October 2009

ABSTRACT

Both spraying and drying are critical to spray dryer performance. Models are developed which explain the very different performance of a spray dryer when large droplets of film forming materials are created using a Rayleigh resonance atomiser. The droplet diameter distribution from this "Acoustic Atomiser" is inadequately described by previously reported spray size distribution functions, but well described by the Stable distribution. The alpha parameter of this distribution was found to tend towards the Gaussian limit for low viscosity fluids and the Lorentz limit with increasing viscosity, consistent with behaviour as a simple and damped forced harmonic oscillator respectively, and hence with the physics of the atomisation process. Droplet drying kinetics dominate model predictions. A device using an ultramicrobalance to measure droplet drying kinetics with unprecedented accuracy and range has been designed. A scaling and residence time analysis model was able to account for experimental spray dryer observations. Sprayability even of complex fluids is predicted adequately by the Ohnesorge diagram, provided that extensional rather than shear viscosity is plotted. A new determination of the transient apparent extensional viscosity from arbitrary CaBER time-diameter curves has successfully been used for fluids too complex to analyse using previously published rheological models.

DEDICATION

This thesis is dedicated to my family - Miranda, Noah, Toby and Zoë, for tolerating with good grace my disappearances into the study at weekends to write up this thesis.

ACKNOWLEDGMENTS

It is a pleasure to thank Imperial Chemical Industries PLC (now a wholly owned subsidiary of AkzoNobel) for funding this research, and colleagues at ICI who contributed to the development of the experimental apparatus and results presented in this thesis. Although many contributed to several activities within the spray drying research programme, notable specific contributions are as follows. David Prest, Carla Sanz, Mark Sains and Sian Jones ran many of the spray drying experiments; Photos Peleties and Rowan Masterson the "wire-deflection" drying kinetics apparatus experiments which results I have used. Claudia Fiannaca and Nathalie Sommier worked on spray-dried particle morphology and volatiles retention respectively, Philippe Sibomana and Roger Watson on the design of droplet drying kinetics rigs, and David Willox on the spray dryer model. Peter Saxton and Giusippina Li Puma bequethed me a half-built pilot spray dryer and a wealth of know-how. Fanny Briand captured beautiful images of Rayleigh jet breakup of non-Newtonian fluids. Richard Buscall, Anthony Stickland and Simon Davies introduced me to rheology. David Elliott and Fiona Steven measured shear viscosity data for the Chapter 9 study. I am also grateful for the practical advice, support and friendship of Owen Garrigan, John Putson, Raymond Oliver, Diego Fernandez, Stuart Trotter and David Sutton.

I would also like to thank the laboratory instrument manufacturers who made available technical details of their instruments; Jint Nijman and Kevin Barber at ThermoFisher Scientific for the Haake CaBER 1 rheometer, and Adam Bright and Peter Sieber at Mettler-Toledo for the UMX2 balance. I greatly appreciated the updates to the CaBER control software made for me by Gavin Braithwaite at Cambridge Polymer Group.

I am indebted to other workers in the field for their advice and encouragement, especially John Hecht, Tim Langrish and Gareth McKinley, and to John Nolan for making available pre-publication chapters from his forthcoming book on the Stable distribution.

Finally, I would like to thank Prof. Raffaella Ocone, my supervisor at Heriot-Watt University, for guiding me in the process of translating industrial research into an academic publication, and Drs. Richard Buscall, Anthony Stickland, Terry Threlfall and Miranda Threlfall-Holmes, for their helpful corrections and suggestions on proofreading.

DECLARATION STATEMENT

Research Thesis Submission Form in paper copies.

blank page in electronic copy: just maintains the correct pagination

TABLE OF CONTENTS

LISTS OF TABLES AND FIGURES

LIST OF PUBLICATIONS BY THE CANDIDATE

Threlfall-Holmes, P., Fiannaca, C., Oliver, R., *Jets, Drops and Powders: the basis for value enhancing materials in the 21st century*, ILASS 2004, Nottingham, UK. (Keynote lecture)

Threlfall-Holmes, P., Ocone, R., 2005, *Spray drying kinetics measurement apparatus*, 7th WCCE, 10-14 July 2005, Glasgow, UK.

Fiannaca, C., Threlfall-Holmes, P., 2005, *Particulate Materials*, Patent filing WO 2005/058473

Threlfall-Holmes, P., 2006, *Acoustic Atomisation in Spray Drying*, IN VERSCHUEREN, M. (Ed.), Designing, optimising and controlling spray drying processes. NIZO, 21-22 September 2006, Ede, The Netherlands. (Invited lecture)

Threlfall-Holmes, P., 2008, *Acoustic Atomisation in Spray drying*, Solids Drying in Theory & Practice, IChemE Particle Technology Subject Group Meeting, 2 April 2008, UCL, UK

Threlfall-Holmes, P., Ocone, R., 2008, Spray drying of large particles of film forming materials, AIChE Annual Meeting, 16-21 November 2008, Philadelphia, USA

Threlfall-Holmes, P., Ocone, R., 2008, Extensional Rheological Measurements and Sprayability, AIChE Annual Meeting, 16-21 November 2008, Philadelphia, USA

CHAPTER 1 - INTRODUCTION

The purpose of this research was to develop models of the spray drying process that could both predict performance and be used to interpret and explain observations in the case where large particles of film forming materials are being dried. This addresses a research gap identified from industrial experience during the development of a novel atomiser.

Spray dryers are extensively used, chiefly in the process, food and pharmaceutical industries, for the conversion of bulk liquid into dry powder products by evaporation of a liquid solvent. The process is straightforward to describe; referring to Figure 1, a feed liquid is atomised into small droplets, into a chamber through which hot gas is blown. The atomised droplets are dispersed across the chamber both by their initial momentum and by their interactions with the drying gas. The solvent (normally water) evaporates from the droplets. Due to their small size (typically 50-100μm mean diameter), rapid heat and mass transfer occurs, and the droplets dry in-flight, leaving solid particles which are disengaged from the gas flow and collected as product. Due to the rapid heat and mass transfer, the residence time of the process material within the chamber is in the order of seconds, which is short when compared with other convective drying processes (tray, tunnel etc.) where residence time may be minutes or hours. For this reason, spray dryers are extensively used to dry heat sensitive products, typically foods (especially dairy products) and pharmaceuticals (Masters, 1991, Oakley, 1997, van Dycke, 2006, Bartels, 2006).

Whilst spray drying itself is considered to be a mature technology (Masters, 1991), modelling of spray drying is less well developed (Verschueren, 2005, Fletcher et al., 2006). The simplicity of the outline process description above belies the complexity and interconnectedness of the underlying science. The fluid mechanics problem of the flow of and the interactions between the continuous gas and discrete droplet phases is coupled to the heat and mass transport to, from and within a droplet, where the droplets will typically have a rather wide size distribution, and may change shape and size and therefore aerodynamic drag during the drying process (Hecht, 1999, Masters, 1991). Whilst developments in computer power and accurate experimental methods for studying gas-particle flows have enabled phenomenal progress to be made in the fluid mechanics problem over the past two decades (Kievet et al., 1997, Oakley, 1997,

Fletcher et al., 2006), theory and experiment are not in close agreement even for the subsidiary problem of heat and mass transport to a drop (Kumar and Hartland, 1999) and the complexity of the process has so far eluded accessible predictive models useful for design and performance evaluation (Fletcher et al., 2006). Spray dryers are consequently designed and operated principally by experience (Bartels, 2006, Zbicinski and Li, 2002, Räderer et al., 2002), resulting in sub-optimal product quality, rate and energy usage (Baker and McKenzie, 2002, Verschueren, 2005).

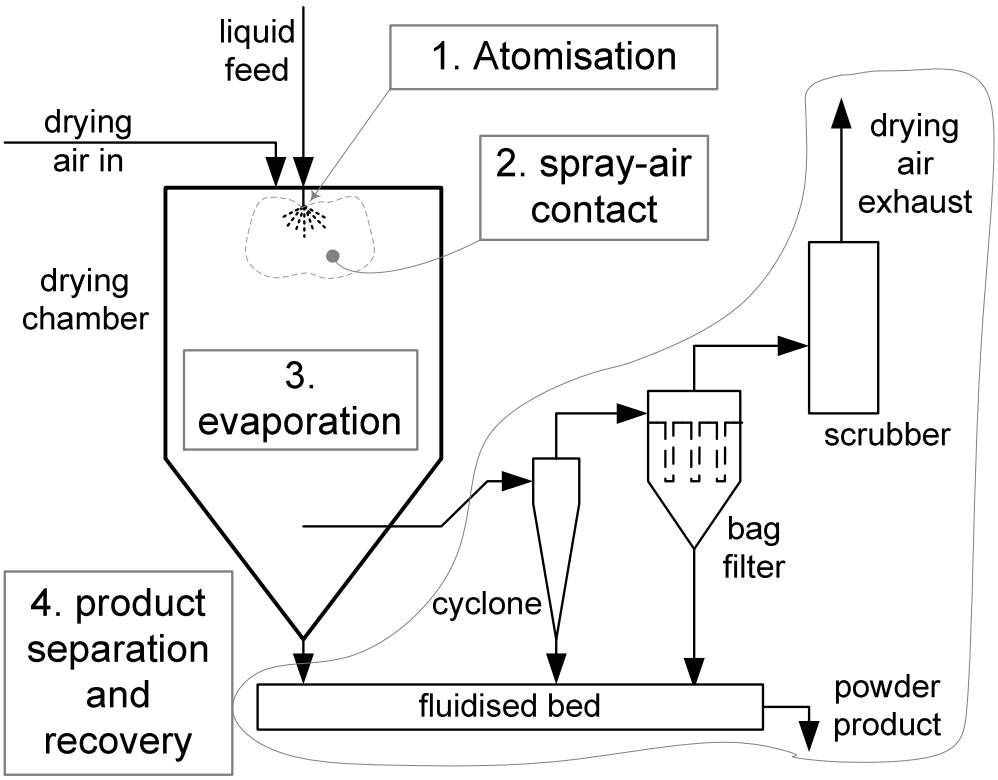

Figure 1: schematic of the spray drying process (after Masters, 1991)

Figure 2: retail coffee: a familiar example of the different product forms obtained by spray drying alone (left) as compared with spray drying followed by granulation (right)

Familiar consumer products made using spray drying are powdered milk and instant coffee, an example of which is shown in Figure 2. Spray drying typically produces a fine powder, with a mean size of order 50-100μm. Post-spray drying granulation is frequently a pragmatic necessity in order to increase the particle size to some hundreds of micrometre diameter, and hence to confer desirable properties such as flowability and re-dispersibility to the powder. The granulation step increases both the capital and operating costs of the powder production plant. It is also something of a "black-art", relying on operator experience for design and operation, rather than on robust predictive models. In consequence most spray drying operations have two series-coupled unit operations, the fundamentals of each of which are rather poorly understood.

Twenty years ago, ICI developed an atomiser for prilling (spray-solidification of melts) working on the principle of resonant breakup of laminar liquid jets. There is a brief description of the physical principle of operation of this so-called "Acoustic Atomiser" later in this introductory chapter. A prototype device was also developed for and tested in a production spray dryer as early as 1992, but due to restructuring in ICI, development ceased and the atomiser was unexploited for several years. The author was initially part of, and from 2000 supervised, a small team that resumed development of the Acoustic Atomiser for spray drying. An immediately apparent benefit of the atomiser, and the primary commercial incentive to resume development, was the ability to make large particles (hundreds of microns diameter) directly in a single step in an existing spray dryer, and hence dispense with the need for a subsequent granulation step. The commercial research project had two aspects; firstly the mechanical development of the atomiser from a chemical products prototype into production equipment for food products, and secondly the manufacture of pilot scale quantities of demonstration products. However, in both these aspects, progress was frustrated by a lack of theoretical development pertaining to the use of this atomisation technology in a spray dryer. In particular, for the film forming hydrocolloids that were the primary commercial opportunity, the existing in-house spray drying computational model was unable to predict successfully what particle size could be made in the pilot spray dryer. The development of the computational process model was beyond the scope of the commercial research project, but clearly of benefit to the commercial exploitation of the atomisation technology. Hence the project has been undertaken as a part-time doctoral research project, sponsored by ICI, the author's full-time employers.

This thesis uses results from experiments at ICI, often performed by others working under my direction. The methodology, analysis, interpretation and conclusions from these experimental results that are reported in this thesis are my own unaided work.

Whilst the particular focus of this research project was the effects on the spray drying process of employing the novel ICI design Acoustic Atomiser, the resultant discoveries are not peculiar to that special case. The use of the Stable distribution as a physically meaningful model for spray droplet size, and also the link between extensional rheology and sprayability, are both especially deserving of further studies of their wider relevance. Whilst most spray-dried products have fine particle size, large particle spray drying is especially relevant also to detergent manufacture (Huntington, 2004), and in drying of fly ash from wet scrubbers on incinerator exhausts (Tanno et al., 1988). The demand from industry for a predictive spray drying model is demonstrated not only by the sponsors of this project, but also by the funding for other spray dryer modelling programmes, for example by the European Union (Bayer AG et al.), by the Australian Dairy Research and Development Corporation (Fletcher et al., 2006), and by Unilever (Kievet et al., 1997). Other significant research programmes are in progress in Strumillo and Pakowski's group at the Technical University of Lodz, Poland (Zbicinski and Li, 2002), and in Chen's group at the University of Auckland, New Zealand (Chen, 2002).

This introductory chapter proceeds with an overview of the relevant science and process technology of spray drying, followed by an outline of this thesis and the contribution it makes to the field.

1.1 Fundamentals of drying

Drying is the partial or complete removal of a solvent from a material to give a dried product. It is differentiated from concentration or evaporation processes, which partially remove solvent to form a concentrated liquid product.

Drying is most frequently encountered as the removal of liquid solvent by volatilisation, leaving lower volatility materials as a solid phase. This is not a necessary condition. In freeze drying, the pressure and temperature are maintained below the triple point of water, and solid water is sublimed. In osmotic dehydration, liquid solvent diffuses

down a concentration gradient from the feed material discrete phase to the immiscible continuous phase. However, spray drying is an instance of convective drying, the largest class of driers (by production tonnage and research activity) (Keey, 1972, Mujumdar, 2004). These depend upon a temperature gradient to drive convective heat transfer from the gas phase to the material to be dried, which provides the energy input for a phase change of the solvent from liquid to gas, coupled to a humidity (concentration) gradient which drives the evaporation of water from the material to the continuous gas phase. Both the temperature and solvent concentration gradients are required for commercially relevant drying rates. If the gas were saturated with solvent, no drying would take place; the heat transferred to the material would cause a temperature rise (and for a finite extent of gas, cool the gas, causing supersaturation and condensation). If there were no temperature gradient, the concentration gradient would drive drying, with concurrent fall in temperature of the solid, but the rate of mass transfer would normally be uneconomically low.

Whilst there is no general constraint on the solvent that is evaporated in the spray drying process, it is generally only the pharmaceutical industry that practices organic solvent spray drying. Water is the most frequently encountered solvent (Mujumdar, 1995, Nonhebel and Moss, 1971), it has no toxicity or fire hazards associated with experimentation, and a large body of literature exists with which to compare methods and results. Hence this study is limited to water.

The progress of drying may be divided into a number of regions characterised by the mechanism by which the water is bound to the solvated material (Keey, 1972). Typically, much of the water to be removed from a material is thermodynamically 'free', i.e. no lowering of the vapour pressure above the liquid; removal of this water is normally termed 'primary drying'. Secondary drying is the removal of capillary water. Tertiary drying refers to the removal of physically bound water, for example in gels or by adsorption. Quaternary drying is the removal of chemically attached moisture – water of hydration or crystallisation. The stages of drying are characterised by increased energy for water bonding. Transitions between the stages can be observed in a sample dried in controlled conditions, as a decrease in drying rate and also in convective drying as changes in the rate of decrease of temperature difference between the sample and the drying gas.

If a dried material is allowed to equilibrate with a humid gas, the moisture content of the solid will reach an 'equilibrium moisture content'. This clearly consists of tertiary and quaternary bound water, but also of some water in very fine pores, that is, some secondary water. It is only part of the secondary water, as shown by the comparison between known porosities of materials and their equilibrium moisture content (Luikov, 1967). The concept of the equilibrium moisture content is important in dryer modelling, as during the latter stages of drying, the evaporative flux can be described as a function of the approach to the equilibrium moisture content of the moisture content in the material. The equilibrium moisture content is by definition not a fixed value but a sorption isotherm, where the equilibrium moisture content is a function of relative humidity, and a weaker function of temperature. In practice in industrial equipment, the relative humidity of the drying gas is very low, and there is typically not a close approach to equilibrium moisture content in a spray dryer due to the limited residence time. Since the equilibrium moisture content isotherm is only a weak function of temperature, the equilibrium moisture content is often measured at ambient conditions and treated as if it were a constant value.

In general, it is normal to remove only the primary and part of the secondary water in industrial drying operations. For biologically active materials, this is normally sufficient to reduce the water activity to such a low level that microbial growth is acceptably slow. Tertiary and quaternary drying would normally cause irreversible structural change to the solute, and this is frequently undesirable. Removal of tertiary and quaternary water requires both long residence times, hence increased capital cost, and high energy input, hence increased variable costs. Finally, dried materials will tend towards equilibrium moisture content on storage, so unless they are stored under dehumidified atmospheres, it would be pointless removing moisture below the equilibrium moisture content during processing.

1.2 Drying of a single droplet

1.2.1 Classical description of single droplet drying

During the drying of a single droplet clear regions can be characterised by the rate of change of moisture loss, as well as by the quantity of water loss described above. An initial constant rate period can be observed, followed by a decreasing rate (Ranz and

Marshall, 1952a). It is tempting but erroneous to equate this to the transition between the loss of primary and secondary water described previously; the distinction is between a kinetic and a thermodynamic effect. Classical drying theory is that this transition is between heat transfer limited drying and mass transfer limited drying.

In the initial, constant rate period, heat transfer to the droplet is balanced by mass transfer from the droplet. In the constant rate period, the droplet surface is saturated and the droplet remains at constant temperature: the wet bulb temperature, by definition. This gives rise to a very non-intuitive phenomenon in the spray drying process. As spray dryers are typically very thermally inefficient (Baker and McKenzie, 2005), and also because it reduces feed viscosity and atomiser blockages, it is common industrial practice to preheat the liquid feed to the spray dryer (Masters, 1991, ETSU, 1996). The degree of preheating is limited by boiling point and thermal stability of the liquid, but the liquid feed temperature will frequently be greater than the wet bulb temperature. In these cases, when the liquid feed is sprayed into the spray drying chamber, the droplet temperature initially *decreases* to the wet bulb temperature, even though the liquid droplet is in contact with air at a much higher temperature. It is well established that excessive heat can reduce product quality, for example nutritional quality of milk products (Straatsma et al., 1999b, Schuck, 2002). The initial evaporative cooling of the droplet, together with the rapid drop in the drying gas temperature with the initial surge in evaporation, help to prevent heat degradation of the particles.

As the drying progresses, the non-volatile components of the liquid droplet become more concentrated at the evaporating surface. Eventually the concentration reaches a critical threshold, the 'critical moisture content', where the limit to evaporation rate is no longer the rate at which heat can be transferred to the drop, but the rate at which solvent from the droplet interior can diffuse or convect to the droplet surface. In the classical description of the drying of an inorganic particulate slurry drop, the critical moisture content is the point at which the droplet surface has dried to a crust, following which there is a receding front of moisture into the particle. Drying proceeds at a lower rate than when the droplet surface was saturated. The rate progressively decreases as the crust thickens and the diffusion resistance increases - the ‘falling rate period’. It is only for infinitely slow drying that the transition between the constant and falling rate periods equates to the transition between primary and secondary water loss: this

condition would be physically manifest as instantaneous crust formation throughout the droplet. The critical moisture content of a droplet always occurs during primary drying.

The critical moisture content is not a constant – it will vary with the initial drying rate (air temperature and velocity) and the material thickness. When the product of the initial evaporative flux and the thickness is plotted against the ratio of the critical moisture content to the initial moisture flux a 'critical point curve' is obtained (Keey, 1972). Actual drying curves tend towards the critical point curve as a function of the mass transfer Biot number (Eqn. 1-1): the critical point curve would be the actual drying curve for an infinitely thick material. For large $Bi_m > 100$, the difference is small, and the assumption is made that the plot of the drying rate relative to that in the constant rate period against the moisture content relative to the critical moisture content is characteristic of a material – a 'characteristic drying curve', which can be used to extrapolate drying data from one set of conditions to another (Suzuki et al., 1977). It is normally a reasonable assumption in spray drying that Bi_m is large, especially in the internal mass transfer limited latter stages of drying. Hence the 'characteristic drying curve' approach is valid. Nešić and Vodnik (1991) consider the case where there is internal circulation within the droplet. This might be supposed to significantly increase the internal mass transfer, hence reduce Bi_m and jeopardise the characteristic drying curve approach. However, they decide that continued mass transfer limitation assumption is valid for a circulating drop, with estimated error no greater than 2% (although it is not clear how they quantified this estimate).

The Biot number is defined to be the ratio of either the mass or heat transfer resistance within a body to that at the surface;

Biot number (mass transfer) $$Bi_m \equiv \frac{k_m d}{D}$$ *Eqn. 1-1*

Biot number (heat transfer) $$Bi_h \equiv \frac{hd}{k}$$ *Eqn. 1-2*

after Hall (1992), where k_m and h are the surface mass and heat transfer coefficients respectively, D is the mass diffusivity at the interface, k is the thermal conductivity of the body, and d is a characteristic dimension, typically taken to be the droplet diameter in the spray drying context.

The spray drying literature infrequently explicitly states whether Bi_m or Bi_h is intended, which can lead to confusion as, in contrast to the mass transfer case it is normally a reasonable assumption that the heat transfer Biot number is small, i.e. the thermal resistance of the drop is small compared with the surrounding air. Small Bi_h is frequently used in the spray drying modelling literature as the quantitative justification for an assumption that the droplet temperature is uniform - for example $Bi_h = 0.2$ in Cheong et. al. (1986). Uniform temperature is consistent with experimental data from the earliest studies: Ranz and Marshall (1952a) checked that the position of the thermocouple junction within the drop had no effect on the indicated temperature. Strictly, small Bi_h simply quantifies that the heat transfer is externally rather than internally limited. The measure works in practice in this context as an index of homochronism because Bi_m is so much larger than Bi_h: the internal temperature equilibrates on a much faster timescale than that characterising the mass transfer. In principle, the speed with which a body responds to changes in surface temperature can be quantified directly using the Fourier number for heat transfer. This is defined (Eqn. 1-3) as the ratio of the product of the thermal diffusivity κ and a characteristic time τ to the square of a characteristic thickness d, where $\kappa = k/\rho.Cp$ and ρ and Cp are respectively the density and specific heat capacity of the body (Hall, 1992).

$$Fo_h \equiv \frac{\kappa\tau}{d^2} = \frac{k\tau}{\rho.Cp.d^2} \qquad \textit{Eqn. 1-3}$$

However, Tanno et al. (1988) is the only instance in the spray drying literature where the Fourier number is used in the experimental data analysis. Although uniform droplet temperature has normally been assumed, Patel et al. (2005) have critically reviewed the assumption, and Farid (2003) has shown that better agreement with experimental data is obtained from a droplet drying model which properly accounts for temperature gradients within the droplet.

The classical description of droplet drying has most clearly been illustrated by a five stage model (Dolinski and Ivanicki, 1984 (in Russian), cited in Nešić and Vodnik, 1991, Dolinsky, 2001). The first two stages occur during the constant-rate or low-temperature period, the latter three during the falling rate or high temperature period. In the first stage, the temperature of the droplet changes from the initial to the equilibrium temperature, close to the wet-bulb temperature. The second stage is quasi-equilibrium

evaporation, analogous to the equilibrium evaporation of a pure liquid. The droplet temperature is slightly greater than the wet bulb temperature, and increases gradually as solid accretes at the droplet surface, with commensurate reduction in surface vapour partial pressure and evaporation rate, and increase in heat transferred to droplet heating rather than evaporation. The third stage is crust formation and growth, when the surface solids concentration exceeds a critical value and the solid separates out by crystallisation or agglomeration as a crust. The resistance to mass transfer increases more than resistance to heat transfer, so proportionally greater heat is transferred into raising the droplet temperature rapidly. The evaporation rate in this third stage is primarily controlled by water permeability through the crust. The fourth stage deviates from the simplest classical descriptions. Boiling only occurs when the air temperature is greater than the solvent boiling point. The internal vapour pressure rises, and, depending on the permeability and mechanical properties of the crust, the particle may relieve the pressure by cracking, inflating, or explosion and disintegration. At the end of the fourth stage, all the free liquid has evaporated. The fifth stage, porous particle drying, is secondary drying, at ever decreasing rate and asymptotic approach of the particle to the gas temperature.

1.2.2 Deviation from the classical description

In a film forming material, as with the crust forming material, a critical moisture content can be defined at which the droplet surface de-saturates and the drying rate decreases, but in contrast to that case, the film is unlikely to be "dry". In latices, formation of a close packed array from the original colloidal suspension is followed by deformation of the particles (and hence decreasing bore of the capillaries transporting water to the droplet surface) and finally migration of polymer between particles to form the surface film (Routh and Russel, 1998). During drying, starch molecules form a three-dimensional matrix, forming cavities which trap water molecules and restrict diffusion (McMinn and Magee, 1996).

Whilst film formation undesirably inhibits the water diffusion rate to some extent, it is key to the widespread industrial use of starches in spray-dried encapsulation matrices (Ré, 1998). The well established "Selective Diffusion Theory", developed by many authors from the original work of Rulkens and Thijssen (1972), postulates that as the film dries out, the diffusion coefficients of volatile compounds reduce at a greater rate

than the diffusion coefficient of water through the film. Consequently the film becomes progressively less permeable to the encapsulated components whilst still permitting water vapour transport, albeit hindered. To ensure high total retention of the encapsulated components, the film should dry to this state of selective permeability as rapidly as possible (Kieckbusch and King, 1980, Etzel and King, 1984, Hassan and Mumford, 1996, Hecht, 1999, Flores-Martínez et al., 2004). A dispersed oil phase sequesters organic volatile compounds (Zakarian and King, 1982), and hence the archetypal industrial spray-dried encapsulation strategy is to emulsify an oil containing flavour or fragrance compounds, into an aqueous carbohydrate dispersion, where the carbohydrates have been modified in order to provide chemical functionality which both stabilises the oil emulsion drops before drying, and also promotes rapid film formation when the emulsion is sprayed into the drying chamber.

In an ideal crust forming material, the final particle diameter is set by the formation of that rigid crust, and further evaporation leads to internal voids. In contrast, due to plasticisation by moisture a hydrocolloid film may not be rigid until a very low water activity has been achieved (Roos, 2002, Vuataz, 2002). Hence the final shape and size of a film forming particle may not be set until a very late stage in the drying, and significant morphological changes can and do occur, as described in Chapter 2. Due to the morphological changes, the surface area for mass transfer will vary through the drying, and hence Perré and May (2001) propose that it would be more appropriate to term the characteristic drying periods as constant and falling flux rather than rate.

1.3 The spray drying process

Whilst the earliest detailed description of spray drying is dated 1872 (Percy, cited in Masters, 1991), there is no evidence of the process finding widespread commercial application until the 1920s. Although many modifications have been made to the implementation of the process since that time, these have been evolutionary and the process is generally considered to be mature technology (Masters, 2004). Typical modifications to the basic layout are the addition of a fluidised bed to the product stream, to increase particle residence time and energy efficiency, and various configurations of cyclones and filters for product collection, and the separation and recycling of fines (Písecký, 1983, Masters, 1991).

Co-current gas/particle contact is most frequently encountered, where both gas and liquid are introduced at the top of the chamber and exhausted at the base. Counter-current operation with liquid introduced at the top and the gas introduced at the base is less frequently encountered, as it is only suitable where the droplets are large enough not to be fluidised and the product is heat insensitive, so that the contact of the hottest gas onto the driest particles does not degrade the product. Typical applications are in the processing of detergents and ceramics. Many recent spray dryers would more accurately be called mixed flow, where either the gas is introduced co-currently with the droplets at the top of the chamber, but exhausted from various locations, or alternatively (less frequently) where the liquid is introduced upwards near the base of the chamber in a fountain. In terms of modelling, the physics of droplet drying and gas-particle interaction are the same regardless of the dryer configuration, but the airflow modelling becomes increasingly complex. This study is limited to the simplest and most widespread case, where the gas and liquid flow co-current downwards.

Spray dryers are not thermally efficient. Since they are typically employed for heat sensitive products, gas inlet temperatures are moderate, often around 200°C. In order to maintain a reasonable driving force for drying in the short residence time, a close approach to ambient temperature is not possible, and a typical gas exit temperature is in the region 80-110°C. Theoretical efficiency is thus typically only in the region 50-70%. Actual efficiencies achieved are even lower; an average of 46% thermal efficiency was reported across all dryers in a UK study (Baker and McKenzie, 2005).

Whilst liquid feed may be a solution, suspension, dispersion, emulsion, slurry or paste, the limitations are that it must be both pumpable and dispersible into small droplets by some form of atomisation process.

1.4 Atomisers for spray dryers and droplet size distributions

Atomisers in spray dryers are normally either pressure nozzles, two-fluid nozzles, or rotary atomisers (Masters, 1991). The descriptions given below are précis of a variety of sources, principally Lefebvre (1989) and Bayvel and Orzechowski (1993).

If a liquid is sprayed sufficiently fast through a nozzle into a gas, turbulent eddies in the liquid, and turbulence generated by the friction at the interface between the liquid and

the gas, quickly lead to the disintegration of the liquid into droplets. This effect is exploited in pressure nozzle atomisers.

In two-fluid (or air-blast) nozzle atomisers, an additional stream of high velocity gas is used to enhance the atomisation effect; the shear at the liquid-gas interface generates surface instabilities on the liquid that tear it apart. This means that the liquid can be atomised at a lower pressure drop across the nozzle than using liquid pressure alone, and a finer dispersion can be created. The atomisation air is normally unheated, so two-fluid nozzles reduce the efficiency of the spray dryer.

In both pressure and two-fluid nozzles, fluid pressure is the energy source to create the surface energy of the droplets. In rotary atomisers, mechanical energy is used to rotate a disc at high speed (10,000 - 30,000 rpm), creating a very high shear rate at the periphery of the disc and hence liquid surface instabilities that cause the liquid to disintegrate into droplets. Rotary atomisers are the most common type in spray dryers, because they are hard to block up, require low feed pressure, and the mean size can be readily controlled by varying the rotation speed. However, they have the complexity, hazards, and relatively high cost that are associated with high speed rotary machinery.

In all these atomisers that are conventionally used in spray dryers, a wide distribution of droplet sizes are created. It is not yet possible to calculate the droplet size distribution explicitly from first principles (Mandal et al., 2008), but indicatively, the two fluid nozzle is likely to give the widest distribution and the pressure nozzle the least wide (Walzel, 1990). This is so much determined by the geometry of the nozzle and operating parameters (pressure, feed rate, feed viscosity, etc.) that it would be unwise to draw this as a firm general conclusion, however.

1.4.1 The impact on the spray drying process of droplet size distribution

The smallest drops in the size distribution form dust, which must be separated from the spray dryer airflow before the air can be exhausted to atmosphere. In extreme cases, the dust must be discarded as waste, but it is normal to try to recover it in some way. Sometimes the dust is directly harvested as product. This tends to reduce flowability, and dust around or below 10μm is respirable, so the personal protection equipment required - especially with the encapsulation of biologically active materials - makes the

powder more difficult to handle. The dust may be recycled back into the feedstock, or into the atomisation zone, as nuclei to promote agglomeration within the spray dryer. Dust increases the explosion risk; the finest dusts are the most sensitive to ignition due to their very high specific surface area. When dust explosions occur in spray drying plant, they are most frequently initiated in the dust collection systems (bag filters and cyclones), where the dust is both most concentrated, and also driest, due to long residence time in contact with hot gas.

The largest droplets in the size distribution have the largest terminal velocity, so have the least residence time in the spray dryer. However, the largest droplets also require the longest residence time to dry or solidify. A spray dryer must be made sufficiently large to have residence time large enough to solidify these largest drops, otherwise they will be deposited on the inside surfaces of the chamber, especially at the base. Not only are chamber deposits inefficient loss of product, they also increase fire and explosion risk, limit the on-line time between cleanouts, and make cleaning more arduous. Since the spray dryer must be sized to solidify the largest droplets, the majority of droplets have a residence time much larger than is required for solidification. In spray drying, the sensible heat of the dry particle is normally tiny compared with the latent heat of the evaporation of water, so the effect of increased residence time is to heat up the dry particle significantly, risking the very heat degradation which is intended to be avoided by the short spray dryer residence time. In practice, a balance is struck (even if it is not articulated explicitly by plant operators), averaging out the final moisture content and heat degradation across the size distribution. Whilst acceptable products have been made for many years in this way, there is potential for improved products and enhanced process efficiency.

1.4.2 The Acoustic Atomiser

The ICI Acoustic Atomiser exploits the Raleigh jet instability in order to produce a stream of droplets which are all of substantially the same size. The jet instability is named after the physicist Lord Rayleigh, who laid the theoretical foundations of the phenomena (Rayleigh, 1878, 1879).

A jet of liquid in air is always unstable. It is easy to imagine how turbulent eddies in high velocity liquid jets lead to instability, but breakup to droplets occurs even when a

jet of liquid is run sufficiently slowly that it is in varicose laminar flow, and the jet remains initially coherent, as a smooth parallel sided cylinder of liquid. The interaction of gravitational forces on the jet and interfacial tension of the liquid jet with the air eventually leads to its disintegration into droplets, with non-uniform sizes (although the size distribution from this uncontrolled laminar jet breakup is still narrower than from nozzle or rotary atomisers).

If the varicose jet is vibrated at its natural (resonant) frequency, surface waves at this frequency are propagated along the jet, increasing in amplitude until they neck off uniform sized droplets from the jet. The principle is shown in Figure 3, together with an image taken using strobe lighting of the shower of uniform droplets created from an array of multiple jets.

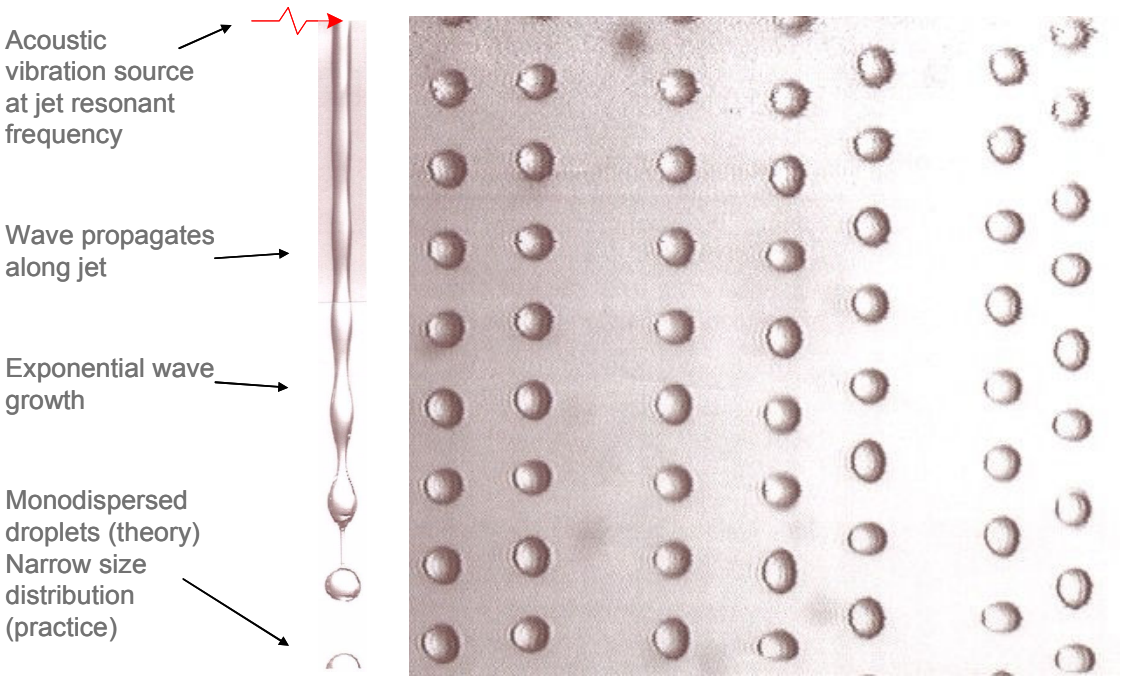

Figure 3: resonant breakup of laminar jets (Fanny Briand, ICI)

The acoustic wave is not the energy source for atomisation. The energy source is pressure - the Acoustic Atomiser is by category a type of pressure atomiser, albeit with a multiple orifice sprayplate rather than a single nozzle orifice. The acoustic wave is simply conditioning the size distribution of the atomisation. Because it is a resonance phenomenon, the natural amplification inherent to the system is exploited, and only a small initial perturbation is required.

This resonant effect can only be seen for relatively low velocity jets. At higher velocity, turbulent eddies in the liquid damp out the resonance effect. This has the unfortunate consequence that the flowrate of a single jet must be rather low, and many jets are required in order to obtain commercially useful flowrates - from a few hundred to a few thousand. Additionally, vibration is normally undesirable in mechanical equipment: it can lead to premature failure, e.g. by shaking apart fixings such as screws. The oscillator electronics are destroyed by high temperatures, so in spray drying, they must be protected from the hot drying air. The sprayplate orifices must be no greater than half the desired droplet diameter - and this diameter ratio increases as the feed viscosity increases. Hence in the spray drying case, the orifices are rather small, typically 120 - 200μm diameter in experiments at ICI Wilton, and must be protected from blockage by guard filters. The many practical complexities have limited the use of this atomiser type to academic investigations and niche applications. However, the difficulties were overcome in two ICI designs for large scale spray processing (Oliver and Lloyd-Jones, 1993, Oliver et al., 1994). Although patented and hence notionally in the public domain, these devices were not publicised. When ICI were operating the atomiser in a number of spray-cooling plants at between 60 and 80 te/hr, and running trials in a 1 te/hr evaporative capacity spray dryer, a paper in a mainstream journal claimed to have overcome some of the practical limitations of size and production rate with a 27 litres/hour device (Hunik and Tramper, 1993). A few years' later it was still claimed that industrial scale rates (by which was meant just 10 - 1000 kg/hr) had not been reached (Brenn et al., 1997). Even a recent paper discusses issues thought still to be overcome before drop generator atomisers could be scaled up to order litres per hour flowrate in a spray dryer, although this was for very small droplets, where the difficulties of small orifice size and low flowrate per nozzle are most severe (Wu et al., 2007).

Atomisers using the Rayleigh jet instability principle to produce narrow droplet size distributions were used in some of the studies described in Chapter 3 where free-falling droplets were used to measure drying kinetics. However, narrow "drop tubes" were used, rather than conventional spray dryers, and the atomiser was used simply as a stratagem to remove the complication of droplet size distribution from the experiments.

Since the atomisation method has not been used for larger scale spray drying outside ICI, it is unsurprising that the effects of using a Rayleigh jet instability atomiser on the

process and products of spray drying has not been systematically studied and reported in the literature. Fiannaca and Threlfall-Holmes (2005) and Threlfall-Holmes (2008) contain phenomenological reports of the differences in powder product made using the Acoustic Atomiser. The research reported in this thesis provided the models which were used both to predict process performance and also to gain a theoretical understanding of how and why the powder product obtained with the Acoustic Atomiser was so different to conventional spray-dried powder.

1.5 Outline of this thesis

The structure of the argument in this thesis is depicted in Figure 4 and described below.

The field of spray dryer modelling is reviewed in Chapter 2. Computational Fluid Dynamics (CFD) models have been demonstrated to be an exceedingly useful tool for analysing and predicting spray dryer performance, at least for typical spray dryers with small droplets in the range 50 - 100μm mean diameter, where the air residence time distribution and temperature distribution are more significant than the drying kinetics. Indeed, Zbicinski and Li (2002) claim to have experimentally validated that droplet drying kinetics are irrelevant. The wider literature shows that in contrast to this claim, droplet drying kinetics are expected to be not only significant, but dominant when drying large droplets of film forming materials.

The corollaries of that conclusion are first a significant and welcome simplification that a process model need not be overly concerned with the complexities of the air flow, but unfortunately also that the error in model predictions is dominated by the error in the droplet drying kinetics. These could not be measured with sufficient accuracy by an existing device. Methods for determining droplet drying kinetics are reviewed in Chapter 3, in order to identify the most satisfactory technique for an improved device.

In Chapter 4, the design is described of a droplet drying kinetics measurement apparatus using an electronic ultramicrobalance to determine rate of weight loss of a single droplet. The combination of operating range, precision and accuracy of the apparatus design would greatly exceed other devices reported in the literature.

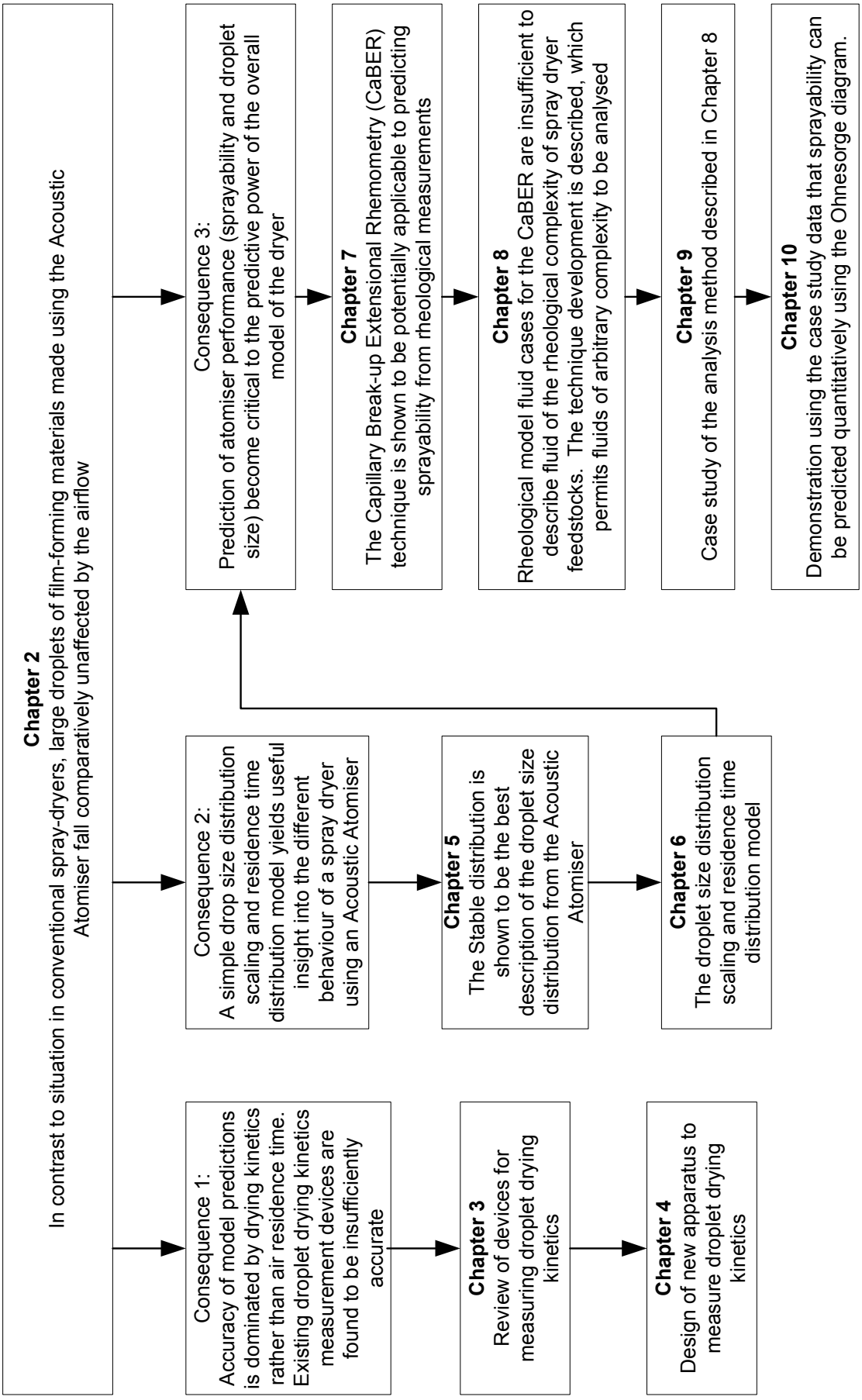

Figure 4: flow diagram of the structure of the thesis

Pending completion of the new droplet drying kinetics apparatus, it was necessary to find an alternative modelling strategy in order to predict spray drying performance when using the Acoustic Atomiser. The inspiration for a suitable alternative was the experimental observation that the large droplets from the Acoustic Atomiser appeared to be falling in plug flow. In Chapter 6 it is shown that simple manipulation of droplet size distributions is a powerful model to predict the change in performance of a spray dryer when an Acoustic Atomiser is used in place of a rotary atomiser. The analysis has not been reported by others.

The analysis in Chapter 6 relies upon the manipulation of atomiser droplet size distribution functions. However, the Acoustic Atomiser is novel, and there are no independent published sources of its droplet size distribution. In Chapter 5, the droplet size distribution is established, using the 40 size distributions from the 180 experiments conducted in the pilot spray dryer at ICI Wilton over the duration of the project, together with historical data from production scale prilling and a selection of laboratory liquid jet experiments. Surprisingly, it was found that the distribution functions commonly used for sprays are not a good representation of the droplet size distribution from the Acoustic Atomiser. The novel findings reported are not only that the Stable distribution appears to be numerically a good model for the droplet size data from the Acoustic Atomiser, but unusually for a sprays size distribution function, there are indications of some underlying scientific rationale to the values of the parameters of the distribution.

Despite the indications that the Stable distribution is in some sense the correct model for the size distribution from the Acoustic Atomiser, care has been taken to ensure that the results of the analysis in Chapter 6 are not contingent upon that novel choice of distribution function. It is shown that the conclusions are substantially unaltered when the log-normal distribution is used instead.

The analysis in Chapter 6 demonstrates that the atomiser performance is critical to the spray drying process. However, the vast majority of the modelling effort in the literature reviewed in Chapter 2 is devoted to the fluid flows and heat and mass transfer within the spray drying chamber. The atomisation is normally excluded from spray dryer models. An assumption of sprayability is made, with point sources of liquid droplets appearing as an input to the model. In operational practice, however, liquid

feedstocks are often dewatered to the rheological limit of sprayability, both to minimise energy consumption and to ensure that an encapsulation film forms most rapidly on the droplet surface. The limit is empirically determined by spray trials; there are currently no robust predictive rules to determine sprayability from rheological measurements. The review in Chapter 7 identifies that the Capillary Breakup Extensional Rheometry (CaBER) technique is potentially applicable to this problem.

The CaBER technique is not yet mature, and only a handful of rheological model fluid cases with which to interpret the instrument data have so far been reported. The consequence of dewatering so close to the limit of sprayability is that commercial spray dryer liquid feedstocks exhibit rheology of greater complexity than can well be represented by model fluids. Chapter 8 describes the analysis technique development that has been undertaken in order to analyse fluids of arbitrary complexity. Stepwise differentiation of the CaBER instrument data has been used to make a transformation of the raw data into a measure of transient apparent extensional viscosity.

The analysis methodology developed in Chapter 8 is novel. The method is exemplified by an experimental study which is reported in Chapter 9. The fluids used for the study are used commercially for flat-fan coatings sprays, rather than spray dryer feedstocks, but this is unimportant to the demonstration of the method. It matters only that the studied fluids exhibited a rheological response in the CaBER experiment that is sufficiently complex that it could not be interpreted using the rheological model fluid cases which have previously been published.

Finally in Chapter 10 it is demonstrated how the measure of transient apparent extensional viscosity obtained from the developed CaBER technique can be used to predict quantitatively, sprayability from the Ohnesorge diagram. This is a dimensionless chart which characterises regions of spray behaviour. Two causes are expounded for why the Ohnesorge diagram has been neglected as a useful quantitative tool in sprays research. Firstly, most references reproduce an incorrect transcription of the original diagram, so the regions of spray behaviour are incorrectly delineated. Secondly, shear viscosity data have previously been used in the dimensionless groups which plot onto the diagram, whereas extensional viscosity is shown using the data obtained from the study reported in Chapter 9 to be a more appropriate choice of parameter.

Chapter 11 provides a summary of the significant results obtained in this study. Recommendations are made in Chapter 12 for studies that would extend these findings.

1.6 Important notes about treatment of sources

It is customary in a doctoral thesis to place the entire literature review within a single chapter. Such a structure is not well suited to this research, however. Workers in the spray drying field have often turned their attention to a selection of aspects of the spray drying problem (e.g. evaporation rate, morphological development, retention of volatiles, droplet drag and trajectory, modelling, experiment) and their interconnection. In contrast, there is rather little intersection between rheologists and spray scientists, and even less between these and drying specialists. Insightful studies are often found in related fields, for example in combustion or atmospheric science (vaporisation of fuel and water droplets respectively). Furthermore, to review the breadth of subject matter at an appropriate depth, the number of literature sources reviewed would entail an excessively long single chapter. A structure has instead been chosen so that the review follows thematically through the developing argument, avoiding apparently capricious jumps between threads of thought that could occur were the material forced into a monolithic literature review into a single chapter. The literature review has been split into thematic sections, principally spread between Chapters 2, 3 and 7. In those cases where authors have considered a number of relevant aspects of the problem in a single paper, it has been deconvoluted, and each aspect is reviewed separately in the relevant sections of the literature review.

As in any human endeavour, progress has not necessarily been neatly chronological. Hence in each thematic sub-section of literature review, sources are normally ordered chronologically, but not strictly so to the detriment of obvious clustering by thematic concepts, or to the developing understanding generated by a progression of papers from a prolific research group.

CHAPTER 2 - REVIEW OF SPRAY DRYER MODELLING

In this chapter, an overview of the spray dryer modelling literature is presented, and an assessment is made of the key factors to consider for the subject of the present study, large droplets of film forming materials.

A pragmatic simplification of the physical reality in the overwhelming majority of the spray dryer models reported in the literature is to confine the model to the spray drying chamber itself. Whilst the spray drying unit operation frequently has a fluidised bed coupled to the drying chamber outlet to remove residual moisture, and may have product or recycle streams of fines from cyclones, the whole system is simply too complex to model in detail as a whole. Atomisation is normally considered to be a separate model. A source of pre-formed droplets, potentially with diameter and/or momentum distributions, is a inlet boundary condition to the spray dryer model.

Even when the model is confined to the spray drying chamber, there are a daunting number of physical processes occurring simultaneously in a real spray dryer. There is a continuous phase gas flow and a discrete phase droplet/particle flow. There is heat transfer from the gas to the droplets, and there is moisture transport both within the droplet, and from the droplet to the gas. These processes all interact: single phase gas flow is different from two-phase flow of gas with inert particles, and different again when the gas is cooled and humidified by evaporating droplets. The particles initially have a distribution of diameters, but as the drying progresses they develop additional distributions of moisture content and shape, and may also change size due to coalescence or breakage. Sticky particles may form deposits on the chamber wall. A comprehensive spray dryer computational model would require; equations of motion for both phases; energy balance equations accounting for interphase heat transfer and heat transfer from the gas to the environment through the chamber wall; moisture transport equations both within and external to the droplets, including some form of boundary layer concentration and temperature gradients model; a solid phase mechanical properties sub-model to account for developing drying stresses and hence morphological changes; and a phase equilibrium sub-model to determine stickiness and hence probability of wall or interparticle impacts leading to rebound or adhesion.

In practice it can be seen in the literature that no model presented is entirely comprehensive by the above definition. However, it is possible to identify a trend towards more comprehensive models in the historical development of spray dryer modelling. There is an association between model complexity and available computer power. The complexity of description of the flows in the chamber progresses from simple one-dimensional steady plug flow, through two-dimensional axisymmetry to full three-dimensional, transient simulations. There is also a trend in the number of processes considered, for example, it is only in recent years that wall deposition modelling has been reported (Fletcher et al., 2006). These are only broad trends, however. Contemporaneously with three-dimensional simulations are studies implementing steady-state one-dimensional models (Negiz et al., 1995, Meerdink and van't Riet, 1995, Garcia and Ragazzo, 2000, cited in Palencia et al., 2002, Truong et al., 2005, Chiou and Langrish, 2008) as well as studies considering the gas flow field as well-mixed (Birchal and Passos, 2005) and a series of well-mixed dryers (Palencia et al., 2002).

2.1 Early spray dryer models

Gluckert (1962) assumed that since the largest particles take the longest to dry, they limit the chamber performance, hence a calculation of the heat transfer rate to the largest particles would define the dryer limiting heat transfer rate. The simple model showed good agreement with overall heat transfer rates measured in pilot spray dryer experiments. Sjenitzer (1962) presented a simple graphical solution, although with oversimplistic assumptions of axial motion from rest, of monodisperse droplets which do not coalesce or break, in a co-current gas of constant velocity, with constant gas and liquid phase properties, at constant temperature difference between the gas and droplet. Dickinson and Marshall (1968) appears to be the first numerical solution with a droplet size distribution. Hortig (1970) presents a method for approximate spray dryer sizing for particles greater than 100μm diameter, with a spread of trajectories based on the spray angle, using nomographs. Miura and Ohtani (1980) assumed a 1-D model of the gas phase (no radial temperature or humidity gradients), but 2-D particle trajectories. Stein (1973) and Katta and Gauvin (1975, 1976) independently showed that simple differential equations of motion can be used successfully to calculate helical particle motion, a quarter of a century earlier than swirl was incorporated into CFD models. Truong et al. (1983) accounted for the effect of the jet of atomising air from a two-fluid

nozzle on the mixing of the spray with the drying air. Flick et al. (1988) develop an explicit equation for the drying rate, using a series of assumptions to reduce differential equations to algebraic equations. The model was not experimentally validated. Some of the assumptions are only valid for the specific case studied, of milk in the early stages of drying.

2.2 Spray dryer modelling using Computational Fluid Dynamics (CFD)

The limited number of reported studies in spray dryer modelling in the last fifteen years have primarily focused on the implementation of CFD. Whilst there is a sense in which any numerical model of a spray dryer is by definition computational fluid dynamics, the term CFD has come to mean specifically the technique whereby a complex physical volume - for example a spray drying chamber - is divided into a very large number of polyhedral cells. The equations of motion are then solved numerically within each cell, and the model is iterated until the boundary conditions of each cell converge to within acceptance criteria. Brief discussions of turbulence models and the treatment of the particle phase are pertinent to the comprehension of the literature.

Turbulence occurs on a range of length scales, so either it must be solved on all length scales, a technique known as Direct Numerical Simulation, which is computationally exorbitantly expensive, or more normally a turbulence model is introduced as a closure for the Navier-Stokes equations of motion. Large Eddy Simulation is one approach, where eddies large enough to be dependent on the flow geometry are explicitly simulated, but smaller scale eddies are considered to have a universal, self-similar characteristic, captured by an "eddy viscosity". However, the turbulence model most frequently cited in spray dryer CFD models is the Reynolds-averaged Navier-Stokes equations. This introduces "Reynolds-stress" terms, the equations for which must then be closed by some model. Again the most frequently cited in spray dryer modelling is the k - ε closure for turbulent kinetic energy and dissipation, but there is an alternative Reynolds Stress Model where the transport equations for the Reynolds stresses are directly solved. In general there is a trade-off in turbulence modelling between the speed of calculation and the accuracy of flow resolution. Even using the k - ε model, weeks of CPU time may be required to converge spray dryer CFD models (see later), hence the predominance of this turbulence model in the literature over others which are even more computationally expensive.

The finite volume CFD method is most naturally a Eulerian reference frame for the continuous gas phase, that is, the grid of cells is a fixed reference frame through which the fluid flows. The treatment of the discrete droplet/particle phase is a less clear cut choice. The most intuitive and prevalent approach has been developed from Crowe's "particle-source-in-cell" model (Crowe et al., 1977), where the interactions between "packets" of droplets and the gas are solved in each individual cell, and the path of those packets is tracked through the dryer. This is a Lagrangian reference frame: the volume mesh moves relative to the particle packet "observer". Hence most spray dryer CFD models are described as Eulerian-Lagrangian in the literature. However, Eulerian-Eulerian models have also been explored and will be discussed later. A single paper has proposed a Lagrangian-Lagrangian formulation (Salman and Soteriou, 2004), but this approach has not been adopted by others in the field.

The reason for the timing of the introduction of CFD into spray dryer modelling is the increased capability of commercial CFD packages, initially in the ability to include dispersed phases into the models, which opened up the interest in their use in the spray drying field and led to the sort of results reported by Oakley (1997), and then within the last few years, the capability of modelling unsteady flows using transient three dimensional cases with very fine grids and Lagrangian tracking of large numbers of particles (Fletcher et al., 2006).

The results from CFD studies have been exceedingly useful, in particular; confirmation of empirical dryer design rules for the importance of air swirl in promoting flow stability in spray dryers (Southwell and Langrish, 2000, 2001, Harvie et al., 2001), the confirmation of experimental evidence of unsteady flows, especially the precession of the axis of the core vortex induced by the inlet air swirl (Langrish et al., 1993, Stafford et al., 1997, Moor and King, 1998, Lebarbier et al., 2001), the design of the inlet air plenum (Southwell et al., 2001), the position and severity of wall deposition (Fletcher et al., 2006), and the prediction of agglomeration in the dryer (Verdurmen et al., 2004). CFD has been used to improve both the design of new spray dryers (Schwartzbach, 2000) and also the performance of existing dryers (Straatsma et al., 1999a). Some counter-intuitive phenomena have been first predicted by CFD and subsequently experimentally validated. Papadakis and King (1988a, b) reported that since the largest droplets were transported further radially, they experienced higher temperatures and dried in a shorter time than intermediate-sized droplets. Nijdam et al. (2006) reported

that the smallest droplets evaporated even faster than expected, because they were found to disperse to the boundaries of the spray cloud where lower humidity air was drawn in, which increased the local driving force for evaporation.

2.2.1 Limitations of CFD as a tool for modelling spray dryers

The most significant disadvantage of the CFD approach to spray dryer modelling is the enormous computational effort involved in Lagrangian tracking of the tens of thousands of drops required to achieve adequate resolution of features. In a case study of a CFD model of a real industrial dryer, two days of CPU time was required for each second of real time (Fletcher et al., 2006). Total CPU time per run was six weeks, as such transient simulations must be run for some period of time for the droplets to have moved through the dryer and achieved some approach to a quasi-steady state. Several runs were required for each optimisation. It was estimated that computational speed would need to improve by five orders of magnitude for real-time simulations as on-line optimisers. The extended run times are a direct consequence of the large number of particles tracked: the gas model uses a k - ε closure for turbulence, and even with a transient three dimensional simulation on a very fine grid that is stated to be required for resolution, a couple of days CPU time was sufficient to converge a "gas only" case. Elsewhere in their paper, Fletcher et al. (2006) question why drying simulation is not more used by industry, but they have already provided sufficient explanation. Full 3-D transient CFD modelling using domain decomposition to permit parallel computation schemes is simply beyond the budget and patience if not the capability of operators. Schuck (2002) says that the spray dryer mathematical models reported in the literature have become too complex for manufacturers to put into use. Langrish (2007) states that CFD modelling of spray dryers is sufficiently complex to require post-graduate training. Of course, provided that Moore's "law" continues to hold, and computer speed roughly doubles every eighteen months, the five orders of magnitude increase in speed will be achieved within a quarter of a century. Until then, it would be useful to have an alternative modelling strategy.

The alternative Eulerian-Eulerian approach where the gas and particle phases are treated as interpenetrating continua within the CFD model removes the requirement to keep track of tens of thousands of droplets. However, this approach has its own difficulties – not least the problem of modelling collision and coalescence of droplets (Nijdam et al.,

2004). The issue in essence is this. An Eulerian phase is assigned to a droplet size range. Collisions between droplets can be modelled by code controlling the interaction between two different phases - for example assigning some fraction of the mass of two interacting phases to third and fourth phases representing larger and smaller droplet sizes, and hence the fraction of collisions that result in coalescence and breakage events. However, collisions between identical sized particles cannot be modelled successfully. The result of interaction of two fluid Eulerian phases is simply more of that phase. The physical interpretation of such model behaviour is that a collision between two identically sized particles always results in a rebound rather than a coalescence or breakage event. If a square matrix were to be written of the possible two-particle interactions between the droplet phases, the diagonal would be the like-sized particle interactions. With two assumptions, the chance of any interaction in the matrix is equally probable. The first assumption is that the phases (size classes) have been chosen so that the number of particles is evenly distributed between the phases, which is a reasonable choice for a modeller to make. The second assumption is that the gas flow has not resulted in droplet size segregation between cells. This is not true, but is good enough for this estimate. Given that the chance of any interaction in the matrix is equally probable, the fraction of incorrectly modelled interaction events is simply the ratio of the length of the diagonal of the matrix to the total number of possible interaction, or $n/n^2 = 1/n$ for n phases. So if there are 10 phases representing the size distribution, 10% of collisions are like-sized particle interactions which are incorrectly modelled, if there are 100 phases, a more acceptable 1% of collisions are incorrectly modelled. Whilst this is still two orders of magnitude less phases to deal with than the tens of thousands of particles required for Lagrangian tracking, each additional Eulerian phase adds a complete set of momentum, mass and energy balance equations, so the reduction in computational load is not as great as might be anticipated.

A further disadvantage of the Eulerian approach to modelling the droplets is that the tracking of the residence time history of individual particles is lost, so spatial averages only are considered (Fletcher et al., 2006). This somewhat dilutes an important claimed advantage for the CFD models over simpler non-transient approaches which implicitly if not explicitly consider averages over time, and frequently averages over space also.

2.2.2 Drying kinetics in CFD models

A final and important issue with the CFD studies published so far, is that a great deal more computational effort is expended in simulation of the air flow than in modelling the droplet drying kinetics. In the majority of spray drying applications this is not an entirely unreasonable focus. In the dairy industry, for example, small droplets typically in the range 50 - 100μm mean diameter are produced using a rotary atomiser. The terminal velocity of such droplets is order 0.1m/s; of the same or lesser order than the superficial gas velocity of between 0.1 and 1 m/s in the drying chamber of typical industrial spray dryers. Therefore it is a reasonable assumption that the droplets are fully relaxed to the air flow (i.e. they follow the air flow streamlines). In this case the air residence time distribution and temperature distribution will be critical to the drying performance, and since the air flow is typically designed to promote recirculation zones (Schwartzbach, 2000), the airflow pattern may be exceedingly complex. In such circumstances, CFD models have been demonstrated to be an exceedingly useful tool for analysing and predicting spray dryer performance. It appears that the determination of residence time and temperature history of the droplets is more significant than the drying kinetics. Indeed, Zbicinski and Li (2002) claim that they have experimentally validated that droplet drying kinetics are irrelevant in CFD spray dryer models. On closer examination this result is only obtained because the liquid feed was very dilute (13% solutions of yeast) – for which case one would expect a material to dry very much as a water droplet and the drying kinetics not to have a measurable effect. The claim is surprising not least because the same authors in a contemporaneous paper state that determination of drying kinetics is the key unsolved problem in spray drying (Zbicinski et al., 2002), and in a later paper that drying kinetics do matter in CFD models (Li and Zbicinski, 2005). The claim is not supported by other literature: to take as example, *"to improve the spray drying process one must examine drying kinetics"* (Dolinsky, 2001). A more nuanced response is obtained from Fletcher et al. (2006). With fine particles fully relaxed to the flow streamlines, and with unhindered or only moderately retarded drying rate by crust formation, most dryers can be considered to be effectively equilibrium limited devices, where the equilibrium is moisture and temperature between the exit gas and droplet phases (Ozmen and Langrish, 2003). Where drying kinetics are significant, as in this study (see later) and also rare literature references (Ozman et al., 1998, cited in Fletcher et al., 2006, Hecht and King, 2000b, Langrish et al., 2006, Langrish, 2007), the spray dryer is better considered as a rate limited device.

Langrish and Kockel (2001) demonstrated that the simple characteristic drying curve (CDC) model for drying kinetics worked acceptably in CFD models for the typical case of a dairy dryer producing small particles. The CDC concept was introduced in section 1.2.1. It is an empirical concept which lumps together all drying phenomena without attempting to physically describe what is occurring. Langrish et al. (1991) compared the CDC with a receding interface model, which is a physically based model of one mechanism of moisture transport. The CDC was found to be more successful, which was hypothesised to be because a number of transport mechanisms operate simultaneously. Fyhr and Kemp (1998) compared the CDC with a rigorous diffusion model. They found that in most cases, the simple lumped CDC model gave as good predictions as the rigorous model. The exception was the effect of humidity on the drying rate.

Lin and Chen (2005, 2007) describe an alternative "reaction engineering approach" (REA), where it is assumed that evaporation has to overcome an activation energy barrier. The new approach has been compared to the CDC (Chen and Lin, 2005, Patel and Chen, 2005). The REA method has been devised to reduce computational complexity in CFD models, as it removes the need to calculate spatial concentration gradients within a droplet. The REA method has most recently been extended to binary mixtures of non-volatile components, each of which has a different moisture desorption energy (Patel et al., 2009).

Handscomb et al. (2009) comment that both the CDC and REA methods return only particle averaged properties, and more sophisticated droplet drying models are required to obtain spatially resolved information such as morphological changes that may occur as a result of drying. The proposed alternative population balance sub-model for the droplet drying kinetics is discussed later. Kraft (2007) has presented work in progress on incorporating this meso-scale model within an overall macro scale CFD model of spray dryer.

2.3 The effect on drying rate of morphological development in droplets during spray drying

In the classic description of the drying of a single droplet, during the constant rate period, the droplet shrinks as mass is lost at close to constant liquid density. When the

crust forms at the critical moisture content, the particle diameter is fixed. Since solvent continues to vaporise out of the particle, a void is formed at the core of the particle. Thus arises the archetypal cenospherical spray-dried particle.

In practice, significant deviations from this ideal behaviour are normally observed. Walton (2004) recorded non-sphericity during drying even of a pure water drop, and even for materials which form classical capillary porous crusts, the crust may crack, giving a much lower resistance route for solvent evaporation than diffusion through the crust (Tanno et al., 1988). For materials which form elastic films rather than capillary porous crusts, some very curious behaviour has been reported in the literature. Once a surface film is formed, the rate of heat input to the droplet exceeds the rate at which solvent can be lost by vaporisation, so the droplet temperature rises. It is then possible for the droplet internal vapour pressure to deform the surface film – giving rise to 'blowholes' where a section of the film has ruptured, inflated droplets where the film has expanded and then dried through the glass transition temperature and solidified, and 'popcorn' where weak sections of the film have inflated and solidified. In addition, the film may remain elastic to very low moisture contents, resulting in 'deflated soccer balls' or 'dried peas' where the particle has collapsed on the internal void, or in some instances, a series of inflation-deflation cycles. As Oteng-Attakora and Mumford (1994a) say with formidable understatement "*depending on porosity of skin and or the rheological properties of the crust, subsequent evaporation may cause the particle to assume one of several forms*".

The morphological changes may be droplet size dependent. The driving force for distortion is the internal vapour pressure, which is driven by heat transfer to the droplet through the surface, and hence increases with the square of the diameter. The hoop stress of the surface crust or film resists distortion, but increases only linearly with the thickness of the layer and hence the particle diameter.

There are various practical implications of the morphological developments of droplets during spray drying. Of primary concern to this study is that the evaporation rate can be significantly altered, either due to change in surface area caused by droplet inflation and shrivelling, or because interior liquid becomes exposed. However, product quality can also be affected. Retention of volatile components may be reduced, especially if interior liquid is ejected through the particle shell (Verderber and King, 1992, Sunkel

and King, 1993, Hecht, 1999). Variability in particle morphology has been reported even under tightly controlled processing conditions (Sunkel and King, 1993). The physical properties of the bulk powder (bulk density, flowability, friability) are affected by the shape and size of the final particles. Hence there is a spread of particle properties in a typical spray-dried powder product (Wu et al., 2007).

It is well substantiated from careful reading of the literature that droplets of film forming materials are prone to extreme morphological changes during spray drying, that particle morphology is droplet size-dependent, and also that the droplet drying rate is greatly affected by various morphological developments. Only a selection of particularly relevant studies is presented here. Handscomb (2009) and Hecht (1999) both present good summaries of the field.

Duffie and Marshall (1953a, b) appears to be the first systematic study of process variables on droplet morphology in spray-dried product. Four mechanisms of hollow particle formation were postulated;

1. formation of film causing puffing or ballooning of the particle
2. rate of evaporation exceeding diffusion rate of salts back into the particle
3. capillary action of the material on the drop surface drawing liquid and solids to the surface and creating sub-atmospheric pressure within the particle
4. expansion of entrained air in the liquid feed

The classic early treatise on spray-dried droplet morphology is Charlesworth and Marshall (1960). Morphological changes were rationalised in terms of the relationship between the mechanical properties and porosity of the shell, and the internal vapour pressure. It was noted that the changes in morphology could expose interior liquid.

Trommelen and Crosby (1970) observed that droplets of various foodstuffs which were dried in air at or above 150°C did not exhibit any constant temperature period, and some were prone to undergo one or more cycles of inflation, rupture and collapse. They also noticed that when milk droplets were dried in superheated steam, the skins were more elastic and pliable, and the degree of inflation was greater.

Büttiker (1981) found that drops of pure chalk dried to dense solid spheres, but increasing concentration of dissolved polymer changed the morphology progressively through "mushroom cap", cenospheres with opening, intact cenospheres, shrunken cenosphere, and burst cenosphere. Progressive indentation to form mushroom caps was observed to occur slowly compared with the rapid collapse of the hollow spheres. Although he does not make this connection, the rate and shape transition from intact to shrunken (and then burst) cenospheres at high concentrations of polymer, is consistent with a transition from a rigid to a plastic shell. Büttiker observed that the polymer concentration required for the transitions between the morphologies depended on the particle size: higher concentrations were required for any given transition for smaller particles. He hypothesised that the indentation seen in the "mushroom cap" morphology was at the low pressure region in the wake of the free-falling particle - all the particles collected in oil were observed to have the indentation in the upper surface (it must be assumed that the oil was sufficiently viscous to prevent the particles rotating between impact and observation). The distribution of the polymer in these dried "mushroom cap" particles was inferred from the extent of agglomeration of the chalk. From the anisotropy in polymer distribution, he concluded that after the concave surface formed it was no longer involved in mass transfer, postulated to be due to inadequate convection in the indentation, so that the local atmosphere in the indentation became saturated. Such chemical imaging results have not been presented by others, but they are more than intriguing. From Charlesworth and Marshall onwards, a common assumption of authors appears to be that when particles rupture the inner surface becomes active in mass transfer. Büttiker's observation suggests that the assumption is erroneous, and Hecht and King (2000a) showed quantitatively that water vaporisation into the internal void was an insignificant fraction of the total evaporation rate.

Greenwald and King (1981, 1982) observed that both the fraction of particles showing expansion and the amount of expansion increased with the air temperature. At the highest temperature, some samples collected during drying had blowholes. Ejection of droplet interior liquid from these blowholes was presumed to account for a similar fraction of contracted particles at the base of the dryer. There was a clear droplet size dependence: smaller droplets expanded earlier, but in a lesser fraction of the particles. Considering a variety of possible mechanisms, they concluded that a two-stage mechanism for expansion is operative. Voids did not occur if the feeds were degassed and the atomiser blanketed with steam, hence a single step nucleation of steam is not

credible. In the first stage of expansion, air which has been absorbed either into the feed liquid or into the droplet immediately below the atomiser, is desorbed into a bubble. This desorption is triggered either by temperature increase (oxygen tension of water decreases with increasing temperature) or by the increased solids concentration in the droplet liquor. In the second stage, water vapour accumulates within the air bubble. Particles are more likely to expand if the droplet temperature approaches the liquid boiling point after the surface has begun to solidify, but whilst there is still a large amount of water in the core. The observation that only a fraction of particles expanded was explained by the stochastic nature of bubble nucleation and the limited availability of heterogeneous nucleation sites. This explanation is not entirely convincing: there should have been a plethora of heterogeneous nucleation sites in every drying particle, if not from the crust, from colloidal dispersions in the case of the maltodextrin, coffee and milk studied.

El-Sayed et al. (1990) described a period of rapid inflation-deflation cycling during boiling of suspended drops drying above the solvent boiling point. It was observed that bubbles breaching the surface of drying coffee droplets pushed wet core fluid onto the surface, and occasionally ejected a satellite droplet. The observed inability of many of the blowholes to seal subsequently, was rationalised by the balance between surface tension forces trying to seal the hole and viscous forces resisting the flow. Studies with sparged and degassed droplets reinforced the Greenwald and King (1981, 1982) conclusion of the importance of gas bubble nucleation to the developing droplet morphology.

Tanno et al. (1988) observed differences in morphological development depending on initial droplet size in their single droplet drying experiments. After the temperature of calcium chloride solution droplets had approached the air temperature, crust break-up occurred, and the larger droplets ceased to change, whereas the smaller droplets continued to decrease in size. In the case of ammonium sulphate solutions, the crust breakage occurred during the region of rapid rise of droplet temperature. Once the drop temperature had approached the air temperature, the larger droplet inflated and then remained at constant diameter, whilst the smaller droplet underwent a number of inflation-deflation cycles.

Experiments conducted on the pilot spray dryer at ICI Wilton also indicate some droplet size dependence of morphology (Fiannaca and Threlfall-Holmes, 2005). Morphologies were observed in the large particles made using the Acoustic Atomiser that were not seen in the fine particle product made using conventional rotary or nozzle atomisers. Where multiple spray-dried particle morphologies were possible, particles predominantly of a single morphology could be made by the selection of processing conditions using the Acoustic Atomiser (Threlfall-Holmes, 2008). This is depicted in the cartoon, Figure 5. The thick grey lines indicate regions where the morphology is not stable, and a mixed morphology will always be obtained.

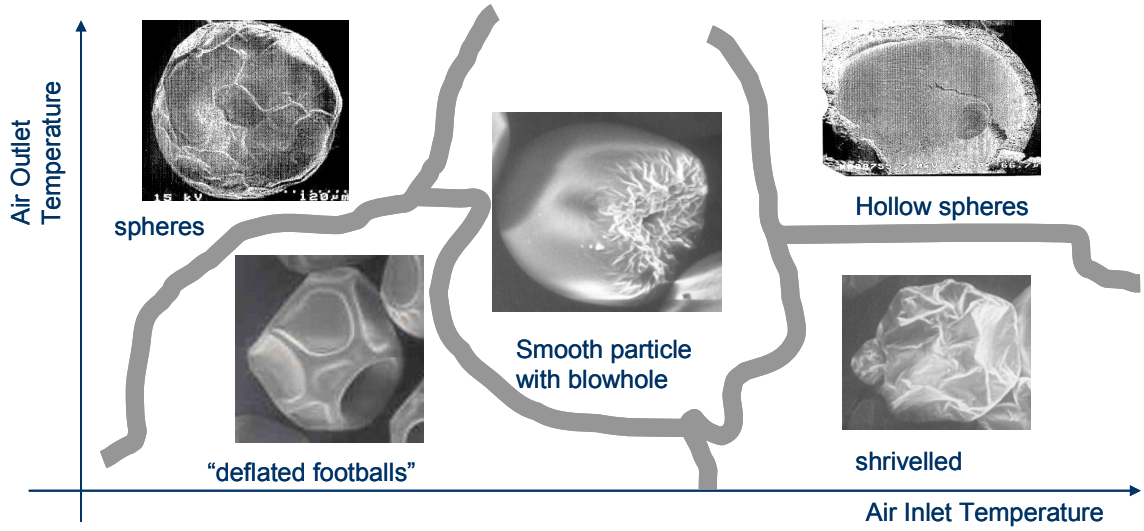

Figure 5: cartoon of regions of single predominant spray-dried particle morphology (Threlfall-Holmes, 2008).

2.3.1 Modelling morphological development

Räderer et al. (2002) hypothesised that since the limit to droplet drying rate in a spray dryer was known to be internal mass transfer, which was limited by diffusion, then a measurement of the diffusion coefficient could be used to determine the limiting drying rate of a droplet. In thin layer drying experiments, they used agar to viscosify some samples in order to suppress internal circulation. In critiquing alternative experimental methods, they refer to "*the presence of undesired phenomena affecting the results*". The flaw in the argument is that the phenomena may be undesirable, but they occur in reality to the droplets in the spray drying process, just as they do in the single droplet drying experiments. The internal circulation and morphological changes occur and they change the drying rate. The real drying rate will not be well estimated if the diffusion

coefficient is accurate to within a percent, but 20% of the contents of each droplet are ejected through a blowhole. A robust fundamental model of single droplet drying must account for morphological development. In principle this might be predicted from constitutive equations for strain and stress in a drying material (Hasatani and Itaya, 1996), but it is only the most recent work that even approaches this ideal.

Alexander and King (1985) examined tendencies for formation of surface folds as drops dry. They concluded that the higher viscosity associated with solutes of higher molecular weight resist flow sufficiently to preclude smoothing of surface irregularities under the surface tension driving force. The mechanistic model gave partially quantitative agreement with observations.

Lin and Gentry (1999a, b, Lin et al., 2000) have attempted to model the conditions under which a cenosphere rather than a dense particle is produced, although apparently without good agreement with experiments, judging by the lack of cross references between the experimental and modelling papers published from the study.

Sano and Keey (1982) noted that there could be multiple cycles of inflation, rupture and shrinkage, but their model was restricted to a single such cycle. Hecht (1999, Hecht and King, 2000a, b) was also able to obtain stable inflation-deflation cycles in his experiments. Modelling work confirmed that this was due to vapour formation driving inflation, but then the larger surface area resulted in cooling and consequent condensation of the vapour, resulting in collapse. This cycle could be repeated a number of times until the film hardened.

Tsapsis et al. (2005) showed good agreement between a drying stress model and experiments using the Leidenfrost effect to levitate droplets of colloidal suspensions in their own vapour. Buckling of the shell was found to occur when the stress accumulated sufficiently for attractive capillary forces to overcome repulsive electrostatic forces that had provided colloidal stability. This was coincident with a transition from fluid-like to solid-like behaviour in the particle layer at the drop surface.

Most recently, Werner et al. (2008) have demonstrated that a wide range of morphological developments in polymer solutions can be modelled with a combination of an effective diffusion model with a receding interface model. The proximity of the droplet surface temperature to the glass transition temperature is used to indicate the

plasticity and mechanical stress of the developing polymer film and hence to predict the path of morphological development. Excellent agreement is obtained with the experimental data shown.

2.4 Considerations when drying large droplets of film forming materials

It was observed in experiments using the Acoustic Atomiser on the pilot spray dryer at ICI Wilton, UK, that drying kinetics are not only significant, but dominant, when drying large droplets of film forming materials. By varying the composition of the liquid feed under otherwise identical drying conditions, the maximum mean droplet diameter that could be dried varied from 250μm to 450μm. The feed liquids were dispersions of starch in water, sometimes with an emulsified flavour or fragrance oil. The dryer was a 1.6m diameter Niro P-6,3 that had been specially manufactured with the cylindrical section extended from 0.8 to 7.8m fall height in order to mimic the fall height available in large production dryers. The airflow was co-current. A total of around 180 experiments were conducted over a period of several years.

It is the confluence of several factors that ensures that drying kinetics dominate the spray drying of large droplets of film forming materials. Considering first the film forming characteristic, it was previously noted that spray dryers are thermodynamically inefficient, and it is desirable for encapsulation matrices to form a film as soon as possible after atomisation into the dryer. Hence it is normal industrial practice to remove as much water as possible from the liquid feed, constrained only by limits of product quality, and rheology for pumping and spraying. To take an example, the hydrocolloid based industrial formulations used in the ICI Wilton experiments are often used close to the limit of dilatency in the liquid feed, at between 30 and 50% solids. Measured drying curves frequently show little or no initial constant flux period (Figure 6 for example), that is, the drying rate is limited by mass transfer through the film for almost the entire drying time. The combination of constrained evaporation rate and a flexible film gives rise to morphological variability, which further influences the evaporation rate.

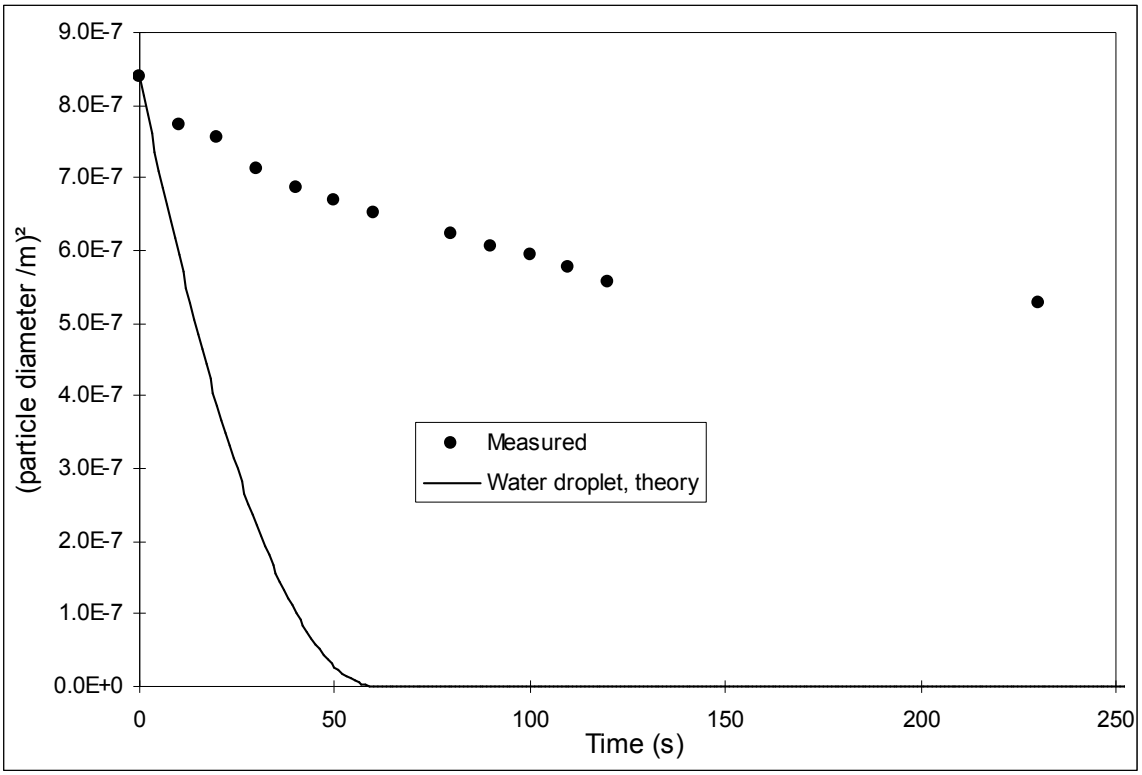

Figure 6: measured drying rate of 1mm diameter droplet of 50% starch and encapsulated oil dispersion in water, at 101.2°C, 3m/s air velocity, compared with the theoretical water droplet evaporation curve (ICI - Photos Peleties)

Considering the droplet size, it will be seen later in Chapters 5 and 6 that the Acoustic Atomiser produced droplets with characteristic diameter around 300µm. These would have a terminal velocity of order 1m/s. In contrast to the small droplets considered earlier, this is of the same or greater order than the superficial gas velocity in the dryer, hence the expectation is that the trajectories of the larger droplets are much less affected by the gas flow. This is consistent with observations through the sight glasses fitted to the ICI Wilton pilot dryer, with ~0.1m/s superficial gas velocity. When using a rotary atomiser, the particles appear to be tracers for the air flow. They are seen to be flying around in the bulk circulation of the air flow at the length scale of metres, and on the decimetres length scale they are observed to blow around in chaotic eddies. Such behaviour has also been observed through the sight glasses of production spray dryers. In contrast, it was observed that the spray shower from the Acoustic Atomiser was coherent, simply diverging in a cone of size and shape consistent with predictions from a simple trajectory calculation from droplet momentum. That is to say, to the level of detail observable with naked eye observation, the spray shower was entirely unaffected by the bulk rotation of the air, let alone the vagaries of turbulent eddies in the airflow.

This would suggest that plug flow droplet residence time would be an adequate approximation. This is supported by Fiannaca and Threlfall-Holmes (2005), where it is reported that in contrast to the normal expectation with a spray-dried powder, when using the Acoustic Atomiser it is possible to make all the particles with substantially the same morphology, a very exciting result which strongly suggests that all the particles had very similar residence time-temperature histories.

The partial decoupling of the gas and particle flows has been found to have advantages in consistency of residence time and hence product properties, but it is no longer the gas holdup that primarily determines the droplet holdup. Increasing the co-current gas flowrate will speed the droplets and decrease the particle residence time, but given the magnitude of the droplet terminal velocity relative to the gas velocity, this is a relatively minor effect, and there is little scope to increase the particle residence time by entrainment of particles in large recirculation zones. To a first approximation, large droplets can be considered to fall vertically at their terminal velocity, with maximum particle residence time determined by the freefall height available. The dryness of the particles at the spray drying chamber exit is determined primarily by the droplet drying rate compared to that relatively immutable particle residence time.

2.5 Selection of an appropriate modelling strategy for drying large droplets of film forming materials

CFD has become the predominantly reported technique for spray dryer modelling in the recent literature. However, an early advocate of the use of CFD for spray dryer modelling has cautioned that a modelling strategy should be selected to give the most appropriate level of detail for the practical situation, whilst not imposing excessive run times and complexity (Oakley, 2004). The most-published advocate of 3-D transient CFD simulations of spray dryers selected a steady state 1-D model to be fit-for-purpose in his most recent paper (Chiou and Langrish, 2008). It has been established that for the object of the present study, drying kinetics dominate and plug flow of the particles is a reasonable first approximation. Hence the precise simulation of the gas flow, and the Lagrangian tracking of tens of thousands of particles, is unnecessary and unproductive computational effort in the present case.

It will be shown in Chapter 6 that a simple scaling model yielded surprisingly good predictions for the largest dryable droplet diameter. However, this model requires performance data for a given product in an existing process from which to base the scaling. As future work, it would be desirable to have a more fundamental model in order to make predictions when the existing process data is not available. Regardless of the degree of complexity of such a computational model, the accuracy to which the droplet drying kinetics are established determines the overall accuracy of the predictions of the spray dryer model. This was most clearly demonstrated in an unpublished internal ICI study (Watson, 2001) which was one of the stimuli to undertake the present study. The effect was studied of the measurement errors from an existing in-house 'wire-deflection' apparatus for measuring droplet drying kinetics (described later), on the range of predictions from the in-house 1-D computational drying model. The results from this study have been re-plotted in Figure 7. It will be seen that the effect of measurement errors is so large that the model predictions are frequently no better than a guess. The test material is commercially confidential, but the specific formulation is immaterial. The important details are that the product variants were similar, changing only in concentrations of various constituents which affected the rapidity of formation of a surface film and the porosity and mechanical properties of that film.

It was clear that the droplet drying kinetics measuring apparatus would need to be either modified or replaced in order to reduce the range of uncertainty in the predictions to an acceptable level. A literature search was conducted in order to identify potential solutions. This review is reported in the following chapter.

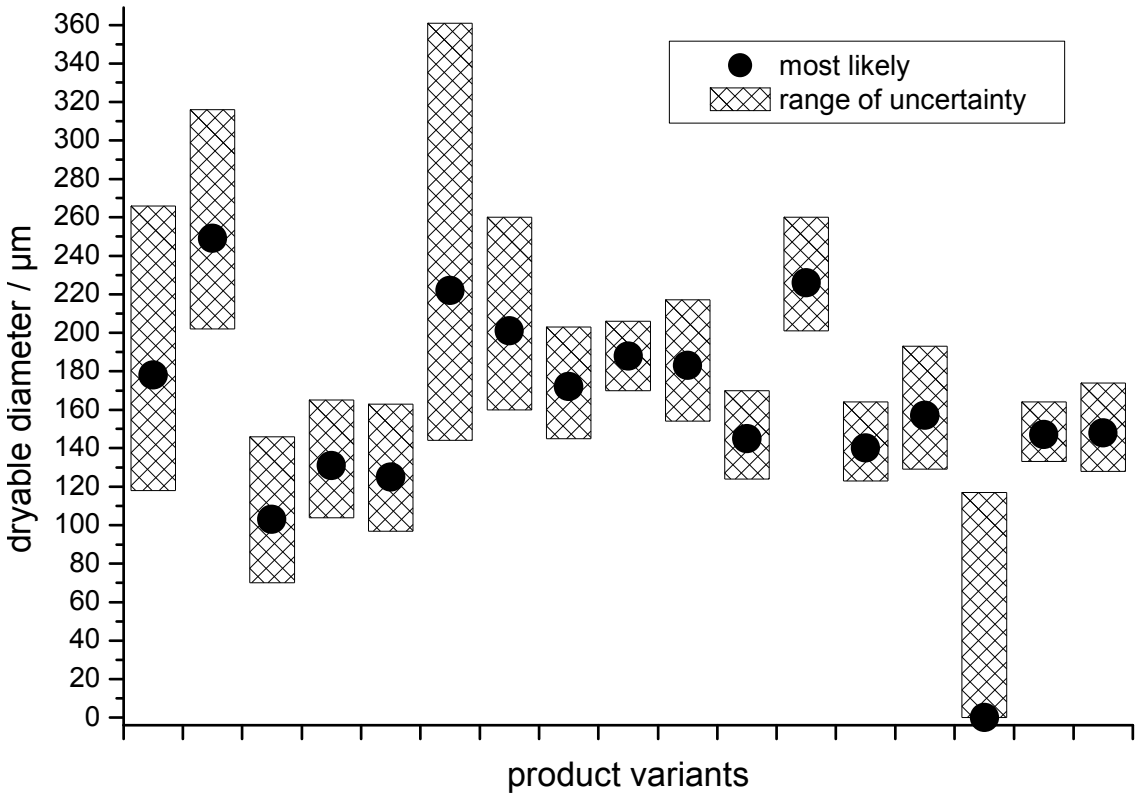

Figure 7: predictions of maximum dryable size for a selection of variants of an industrial product (after Watson, 2001).

CHAPTER 3 - REVIEW OF METHODS FOR THE DETERMINATION OF DROPLET DRYING KINETICS

It will be clear from the discussion in the preceding chapter that an adequate model of spray drying for film forming materials must contain rather more droplet drying physics than the simple classical crust formation model. It would be most desirable for this to be based on sound theory. However, as is discussed in the first subsection of this chapter, this problem has eluded satisfactory theoretical approaches to date. Hence most researchers in the spray drying field have resorted to experimental determination of droplet drying kinetics. The classic study to which all others are referenced is Ranz and Marshall (1952a, b), although there were many earlier studies: 70 of 88 citations in Fuchs' (1959) review predate Ranz and Marshall's study. The literature contains a wide variety of experimental techniques, which have here been categorised as firstly *thin layer studies*, then *free falling droplets*, *free droplets held stationary to observer*, and finally *droplets constrained on supports*. The category 'free droplets held stationary to observer' naturally subdivides into 'aerodynamic' and 'acoustic' levitators. There are a variety of approaches to constraining a droplet on a support, but the 'rotating capillary', 'cantilever' and 'microbalance' methods have each attracted sufficient studies to merit separating them out into separate sub-sections.

The literature reports of the various methods have been reviewed to determine an appropriate methodology and important construction details for new apparatus. All the methods involve some compromises between precision and/or simplicity of measurement and close approximation to the conditions experienced by a droplet in a real spray dryer.

ICI had previously constructed and tested a number of droplet drying kinetics measurement apparatus using a variety of the techniques described in the literature. Although reports of these apparatus were not published in the open literature, the knowledge gained from using them did inform the design of the new apparatus, hence relevant details of previously unreported ICI in-house apparatus are reported here.

Apart from the range of basic techniques reported in the literature, there are wide variations in what variables are measured, how they are measured, and the ranges of droplet size and air temperature, humidity and velocity accessible to the instruments that

are described. Hecht (1999) usefully compiled a summary table with 26 references in chronological order, indicating the method of determining drying rate, loss of volatile component, drop temperature and morphology. Table 1 at the end of this chapter is an extension of that concept, including details of the materials and range of experimental conditions studied. The loss in volatile component column in Hecht's table has not been included: it was a particular focus of his study, but not of this. A few of the references in Hecht's table were not obtainable to check details. These are asterisked in Table 1.

3.1 Theoretical solutions to droplet heat and mass transfer

Although droplet heat and mass transfer is a complex problem, there has been some progress in theoretical solutions. There are two aspects to the problem, firstly the external heat and mass transfer between the droplet and the air through which it flows, and secondly the heat and mass transfer within the droplet. Most authors are concerned with a single isolated particle, although the heat and mass transfer is altered by an array of particles (Ocone and Astarita, 1991). Single isolated particles is an acceptable assumption in the body of the spray drying chamber. Simple flux calculations using data from a few ICI dryers indicates that the inter-particle separation is between ten and one hundred particle diameters. The assumption will, however, break down at some point close to the atomiser, where the droplets are sufficiently close to each other that there is mutual interdependence of the heat and mass transfer.

Han et al. (1996) use potential flow theory to reduce the partial differential equations for mass transfer to tractable ordinary differential equations. However, to do this they needed to assume steady vortex formation in the droplet wake, which is invalid for droplet Reynolds numbers greater than 130 (Clift et al., 1978). The result is valid for small particles in the main body of the spray dryer, but most heat and mass transfer occurs in the region close to the atomiser and air inlet, where air velocity may be as high as 40 m/s, with droplet Reynolds numbers in the order of 300, so the result has limited practical application. The result has not been verified experimentally.

There is good agreement between theory and experiment for a drying slurry droplet in Liang et al. (2001), for very high solids contents ceramics slurry feeds, where it is a good approximation to assume that the slurry particles are discrete, non-interacting and not drawn to the surface by capillary action. These are not good assumptions for the

case of film forming materials that are the key concern of this study. Jørgensen et al. (2006) have subsequently shown that the boundary condition was chosen incorrectly, and the method cannot predict the formation of the hollow particle morphology that is most frequently found from spray drying. The latter conclusion is disputed by an author of the original study (Minoshima, 2006).

Alassar and Badr (2007) reports a theoretical study of droplet heat transfer under forced and free convection, including the effect of airflow oscillation. A full solution of the Navier-Stokes equation was computed, for the case of droplet Reynolds number up to 200, which is of relevant magnitude. For computational tractability, sinusoidal fluctuations were assumed, but it would appear possible to extend the solution strategy to some simplified model of turbulent eddies, and perhaps to a generalised stochastic fluctuation model. Heat transfer only was considered, but the solution is clearly extensible to mass transfer. However, the solution is sufficiently complex that such extensions would be studies in their own right. It remains to be experimentally validated.

Seydel et al. (2006) describe a new approach, where the solid particle formation is modelled by a population balance model. Handscomb et al. (2009) model nucleation and growth of the solid phase from an ideal binary solution. A companion paper is cited, as yet unpublished, where the model is extended to shell and internal void formation. The model is claimed to predict the microstructure of the shell formed, and hence provide a basis for predicting both the drying rate and the overall morphology of the particle. This is a rational sequence to predict overall particle behaviour, but many more extension studies would be required in order to achieve this aim. The model actually presented in this paper predicts the microstructure of the shell formed from precipitation from ideal binary inorganic solutions: simulations of colloidal silica and also of sodium sulphate solutions are presented as exemplars. Overall droplet spherical symmetry and crust formation to cenospherical final particle form are assumed. From previous discussion it will be clear that inorganic crust forming materials are most unlikely to exhibit the reported range of morphological variation in film forming materials, and most morphological variants do not show spherical symmetry. No experimental validation of the model is presented, and it is not made clear whether any such validation studies are or have been in progress.

Štěpánek (2008, Kohout et al., 2006) has shown good agreement with experiments with an alternative approach to modelling the porous microstructure during drying. In a unit calculation cell, the ballistic deposition of particles was modelled in order to obtain a random structure, then a "Volume of Fluid" method was used to determine the equilibrium spreading of interstitial fluid. A stochastic method was used to determine the effective thermal conductivity for the unit cell, using a transient hot wire probe for experimental validation. A similar calculation method was used to determine permeability, with a capillary pressure saturation evaporation/re-condensation hysteresis curve for pore transport. The structure during and at the end of drying were visually similar between the model and validation experiments using X-ray computed micro-tomography scanning. Quantitatively the x-y plane averaged liquid phase volume fraction predicted by the model closely matched the experiment. Although the study was directed towards contact drying of inorganic particles, the underlying science of the method is in principle portable. The 40μm resolution of the validation technique may be insufficient for the scale of the relevant microstructure of a spray drying droplet, however.

3.2 Thin layer studies

The key advantage of drying a thin layer and correcting the measurement for geometry is that the planar extent of the layer can be large enough for a readily measurable mass rate of vapour to be generated, whilst maintaining one dimension with particle-appropriate length scale. An additional practical advantage is that sample preparation does not require the same precision of micromanipulation as the dispensing of small droplets required in many other methods.

In a device built at AEA Technology, a flow of dried air was passed through a relatively thin bed (2-7mm) of moist particles (Langrish et al., 1991, Fyhr and Kemp, 1998, Hirschmann et al., 1998). The drying rate was determined from the humidity of the exhaust air, measured by an infra-red gas analyser. The technique is unsuitable for use in this study, as it requires moist particles as starting materials, rather than droplets of bulk liquid. Morphological changes on drying are not expected to be reversible, so drying of re-wetted spray-dried powder product is not expected to yield a meaningful measurement of the drying rate during the original drying.

Räderer et al., (2002) used a thin film device to determine water diffusion coefficient. Unfortunately for the purposes of this review, only sketchy details of the apparatus are reported. The air was recirculated by a fan. Test chamber velocity was in the range 0.5 - 1.0 m/s. Humidity was controlled in the range 4 - 22 % RH by passing the airflow through a cold trap. The air was subsequently heated to between 40 and 70°C. The airflow was then passed through "several" (sic) meshes in order to achieve uniform flow over the sample. The actual number, type and spacing of the screens are unreported. It is reported that the efficacy of the flow conditioning was checked by CFD and measurements, but neither method nor results are presented. Mass loss and sample temperature are stated simply to have been measured, without elaboration. From the sketch flowsheet in the paper, it seems most probable that the sample holder was connected to an electronic balance outside the chamber, but this is inference, and the precision of the device is unknown. The initial thickness of the liquid film was between 0.6 and 2.0mm, but neither the planar extent of the layer not the chamber dimensions are reported.

A significant disadvantage of the thin liquid layer method for this study, is that it is entirely dependent on the validity of the geometrical correction, and it has been previously noted that the geometry of a droplet may alter during the course of the drying. When a liquid layer is dried, formation of vapour pockets will cause inflation of the layer as with droplets, but the relative change of surface area (and therefore overall heat transfer) will be much less - there is a vapour bubble on some fraction of only the upper free surface of the film, compared to the expansion of the entire droplet. A further disadvantage of the thin layer drying method is a practical one. The liquid layer must be of sufficiently large planar extent that edge effects are negligible. Since the airflow must be parallel to the surface of a liquid layer, then the leading edge of the layer is preferentially dried. If the airflow were perpendicular to the film, it would distort the layer, thinning in the centre and creating radial ripples. The surface temperature of the liquid layer and the temperature of the gas boundary layer will vary across the film. It is average moisture loss over the whole surface of the layer that is measured.

3.3 Free falling droplets

Some studies have used free falling droplets in order to avoid potential artefacts introduced by droplet tethers in other methods. Rather than a normal spray dryer, where the gas flow patterns are highly complex with significant effect on the particle residence time, these studies typically use 'drop tubes' which are narrow, with the airflow arranged to be as uniform and parallel as could be established, sometimes with a special type of atomiser in order to produce a low flux of relatively uniform particles.

Duffie and Marshall (1953a, b) built a drop tube 0.2m diameter and 6m high, using a Rayleigh resonant jet break-up nozzle in order to obtain a stream of droplets of controlled size. They could not make this atomiser work with drops less than 150μm, and found that they normally had to use inlet air temperatures in excess of 300°C in order to obtain dry product. Crosby and Marshall (1957) modified the drop tube with a wider upper section to minimise wall deposition so that they could use a conventional pressure nozzle and thus circumvent the drop size and atomiser blockage issues encountered in the earlier study.

In order to measure the humidity of the air in their drop tube with high precision, Dlouhy and Gauvin (1960) employed a sampling technique which has not been reported by other workers in the field: the volume change in magnesium perchlorate as it absorbed water from the air drawn into a sampling burette.

Büttiker (1981) used a Rayleigh resonance jet breakup nozzle in a drop tube. There are few experimental details and no data on the drop tube conditions, but drying rate was determined from measurements of the moisture content and estimates of the surface area from microscopy on particles samples at varying points in the drying, as well as diameters from photographs of the droplets in flight. Initial droplet diameters varied from 0.27 to 0.84 mm.

Etzel, Frey and King (Etzel and King, 1984, Frey and King, 1986a, Frey and King, 1986b) used a device more akin to a pilot spray dryer than a drop tube. Swirl cone and flat-fan nozzles were used in a 57cm diameter tower. Total available fall height was 2.6m, but samples were only taken in the first 30cm of fall height, as the purpose of the studies was primarily to measure volatiles loss in the atomisation zone. Air temperature was 243°C max. An air velocity range of 0.03 - 0.06 m/s can be calculated from quoted

flowrate and temperature data (Etzel and King, 1984). This extremely low velocity explains the reported problem of recirculating air flows. The sampler described would have collected all droplets impinging onto it, so the measurements are an average over all the drop sizes. The drop size distributions are not reported, but Frey and King (1986a) report a final dry particle Sauter mean diameter of 400μm: astoundingly large in the available fall height. This may be due to additional residence time in the cyclone collectors that Frey added to the exhaust, but it is still surprising that moist sugar and coffee particles did not stick to the tower base before reaching the cyclones.

Greenwald and King (1981, 1982) used a drop tube 7.62cm in diameter and 2.28m in length, with a vibrating reed device to produce a stream of uniform droplets. A packed bed of 2mm spherical molecular sieve beads was used to create a uniform air velocity profile across the tube. A combination of inlet air and wall heating was used to create a temperature profile. They appear to be the first authors to report this, as opposed to either a controlled uniform temperature or an uncontrolled profile. Particles were sampled on a microscope slide spread with a layer of neutrally buoyant high viscosity silicon oil. Maximum droplet size was limited to 250μm by the fall height: surprisingly large for coffee even in dilute solution in 2.3m fall height. It was reported, however, that skimmed milk drops were hard to dry in the apparatus.

Alexander and King (1985) replaced the vibrating reed device in the Greenwald and King (1981, 1982) drop tube with a Rayleigh jet resonance instability monodisperse generator together with an electrostatic droplet dispersion device. The same drop tube was used by Wallack et al. (1990), with a solvent sampler as used by Etzel and King (1984). To determine the water content, HPLC was used where sugars were the dissolved solid, mass loss after freeze-drying for coffee, and Karl-Fischer titration when the droplets had been sampled into DMSO.

Morimoto et al. (1985) measured drop size, temperature, velocity and drag coefficients of an evaporating drop falling freely in air. A droplet generator was used to feed droplets down a 100mm diameter tube. The test section was a 900mm long PVC tube, with light sources and optical sensors at 100mm axial separation. The falling droplet triggered the optical sensors. Measurements for ~100 drops were averaged to determine the velocity. A spacer tube of length varying from 0.1 to 2.2 m was inserted between the droplet generator and the test section, so the total fall height from the droplet

generator to the final sensor position varied from 0.9 to 3 m. No airflow is described in the text, and the data presented suggests that the droplets were falling through stagnant ambient air. Droplet temperature was measured periodically by inserting a thermocouple into the droplet stream. Droplets were periodically sampled, weighed and the droplet diameter inferred by assuming all droplets collected in the sample were spherical and of the same size. Taniguchi et al. (1991) use the same apparatus. Although once again no airflow is described in the text, a table lists air velocity as 0.11 - 0.83 m/s. Electric heaters were used to heat the air, but only for small deviations from ambient temperature, up to 31°C.

The drop tube of Flick et al. (1988) was 0.16m diameter and 2m high. The air temperature varied between 80 and 180°C. The mass rate of air was constant, so the co-current air velocity must have varied from 0.41 to 0.53m/s over the temperature range. The air temperature in the drop tube was kept constant by the ingenious solution of introducing the air from the heater into the base of a jacket around the drop tube. This hot air stream then flowed up the jacket before flowing into the top of the drop tube (with a diffuser to even out the flow). A vibrating reed droplet generator based on Greenwald and King (1981) was used. Droplet diameter was 200 -500µm. The sampling method is not reported elsewhere. A roll of aluminium paper was wound from reel to reel, so that droplets fell from the open base of the tower onto the strip of aluminium paper between the reels. The droplets were caught on the strip which was then wound up quickly, confining the droplets away from the airflow and cooling them on contact with the aluminium, and hence arresting evaporation. The mass loss after oven drying was used to determine moisture content, with error estimated to be +5/-10%. They present only a little data, but it does appear to be good, correlating well with model predicted values. However, on close inspection, the residual moisture contents are very high: the particles can barely have formed crusts, and the micrographs of the material are still very spherical. It would have been interesting to see how the sampling technique worked with a longer column, drying to more realistic product final moisture contents, and with a film forming material that showed more interesting morphological changes during drying.

Meerdink and van't Riet (1995) used a drop tube 0.63m in diameter, 6m fall height, with single fixed rate 0.2m/s co-current air. A Rayleigh jet resonant breakup device was used to generate a dilute stream of monosized droplets, with an electrostatic dispersion

ring to prevent droplet coalescence. Drying rate was determined by collecting samples through ports spaced down the dryer. The sampler was water cooled and contained paraffin oil, in order to minimise evaporation during sampling. Moisture content was determined by weight after vacuum drying, and particle diameter was measured under a microscope. An earlier report from the study contains further details that the drop tube air temperature was in the range 80 - 150°C and the droplet diameter was 160 or 200µm (Meerdink and van't Riet, 1994).

Sommerfeld and Qiu (1998) determined vaporisation rate from rate of change of the diameter distribution measured with a Phase Doppler Anemometer (PDA).

Zbicinski et al. (2002) constructed a drop tube equipped with a PDA on a traversing mechanism, so the droplet size and velocity distributions and phase concentration could be measured at any point within a 5.5m height range. The paper lacks many specific details of the experiments, but it can be inferred from the diagrams that the tower diameter was at least 0.36m, with total freefall height around 7.5m: the PDA traverse did not reach either quite up to the atomiser or right down to the base of the tower. The air velocity calculated from the quoted mass flowrate and operating temperature is a factor of ½ - $^1/_3$ lower than the stated velocity. It is not clear which figures are erroneous. Very dilute maltodextrin dispersions were sprayed with a pressure atomiser. No comment is made regarding wall deposition relative to product recovery. Droplet samples were collected at several heights and analysed by an unspecified method for moisture content. Similarly air temperature was measured at several heights. The authors state that the air temperature drop is mainly due to the drying, with only small losses to atmosphere. It is unclear how the tower and especially the numerous observation windows were so well insulated. Drying rate was determined from the moisture content measurements together with the average velocity data obtained from the PDA measurement.

Vehring et al. (2007) used a drop-on-demand monodispersion generator, similar to ink-jet printer heads, so that the droplets could be much wider spaced than from a Rayleigh jet instability monodispersion generator, and hence avoid droplet interaction effects. The droplets were sized at various heights by what appears from the description to be a home-made Laser Doppler Anemometry, and the droplet velocity was determined with a laser strobe. The dry particles were shown by SEM to be only slightly non-spherical,

so the determination of an equivalent spherical diameter by image analysis was acceptable.

In summary, the advantages of the 'free falling droplet' approach is that it is possible to set up a gas temperature profile and velocity similar to that obtained in a real spray dryer, and that the droplets can freely rotate, unlike devices where the droplet is constrained on a support.

A disadvantage of this approach is that examination of anything other than the dried particle requires sampling at intermediate points. Feasibility of equipment design and safe practical operation limits the number of possible sampling points, and the samples are always time and droplet size averaged to some extent.

The greatest disadvantage of the 'drop tube' methods, however, is the assumption that the gas and particles flows can really be maintained parallel down a height which is sufficient to achieve drying. The open literature sources largely avoid explicit discussion of this aspect, although experimental details such as droplet generators or widened sections around the atomiser suggest that the researchers were well acquainted with the issue. In unpublished experiments on a 0.3m diameter x 6m high drop tube at ICI Wilton (Nawaz, 1997), significant wall deposition was normally observed, typically far in excess of the product recovery. The atomiser in this drop tube was a Rayleigh resonance jet breakup atomiser, with typically seven jets, all of which were aligned vertically, no more than 1cm away from the centre line of the tower. In some cases, the required atomisation condition meant that jet velocity was significantly greater than particle terminal velocity, and the "slipstreaming" of the particles gave rise to coalescence. In these cases an electrostatic dispersion ring was sometimes used, but only to knock particles slightly off course. This electrostatic dispersion method has also been reported in a far narrower drop tube at Judson King's group at the University of California, Berkeley (Alexander and King, 1985, El-Sayed et al., 1990). That wall deposition overwhelmed product recovery in the ICI Wilton drop tube indicates that significant deviation from the predicted trajectories must not only have occurred, but was the norm. Hence significant deviation should be expected from the plug flow residence time that is assumed in the drop tube methods for determining droplet drying kinetics. Together with concerns about the sampling, it is difficult to remain confident about the accuracy of the drying data.

These doubts seem to be confirmed in Meerdink and van't Riet (1995), both by the limited range of experimental conditions reported and by the adjustments required in their model to match experimental data. Sunkel and King (1993) further back up this conclusion, summarising King's studies over the previous decade (Greenwald and King, 1981, 1982, Alexander and King, 1985, Wallack et al., 1990), that even a single stream of uniform drops through a controlled temperature field develops a range of substantially different morphologies and degrees of expansion, although they rationalised this as the difference in number and effectiveness of bubble nucleation sites within droplets.

3.4 Free droplets held stationary relative to observer

In order to maintain free rotation of the droplet for similarity with real spray-dried droplets, whilst overcoming the limitations of free falling droplet methods, in some studies a droplet has been levitated in such a way that it remains stationary relative to the observer. The studies can be subdivided into aerodynamic and acoustic levitators. It has also been reported (Dransfield and Davis, 1985) that if a drum with a heel of liquid is rapidly rotated so that an annular liquid film is formed around the inside of the drum, then a drop from a syringe of the same liquid will not merge into the spinning film, but float just above it, adopting an equilibrium position that is stationary relative to the observer. However, there are no known studies of droplet drying which exploit this phenomenon.

3.4.1 Aerodynamic levitators

Jones and Smith (1962) measured the mass transfer from particles suspended in a vertical airflow in a rotameter tube. Since a rotameter tube bore gradually increases along its length, the air velocity fell as the air rose. The evaporating particles migrated up the tube as they became progressively lighter and hence a diminishing air velocity was required to suspend them. No active control of the air rate was required in order to keep the particle suspended. The spheres were rather larger than those in other studies, ranging from 2.3 to 19mm in diameter, and were slowly subliming solid organic chemicals; hence the rate of migration was sufficiently slow to follow the particles with a camera on a manual traverse. Measurements were made both with single particles and ensembles of up to fifty particles, always in dilute phase. Particles were periodically

removed, weighed, and the diameter measured with a micrometer in order to determine the interfacial area and mean diameter. A number of observations are made that are relevant to this study. Even though stroboscope measurements showed that the particles spun at up to 300 Hz, the data indicated no measurable enhancement in mass transfer rate for free floating particles over control experiments, either with tethered particles or with free floating particles made with an internal off-centre ball bearing in order to damp motion. This suggests that data from drying tethered droplets is relevant to the real spray dryer free falling case. The data also confirmed the expectation that there was no change in mass transfer rate between single particles and dilute phase ensembles of particles. This is also an important assumption when using single droplet drying data in a spray dryer model. Finally, the data was found to vary with the *tube airflow* Reynolds number, where the tube diameter is used in the dimensionless group, as well as the *droplet* Reynolds number, using the droplet diameter. This had not been reported by others: Jones and Smith (1962) note that in most experiments, tube Reynolds number is correlated with droplet Reynolds number, so no separable effect can be observed. There is no evidence in the literature to suggest that others have subsequently considered or investigated the influence of drying tube Reynolds number.

An aerodynamic levitator was used to study the rate of evaporation in ambient temperature (22 - 24°C) air of water drops of between 27 and 375µm diameter (Beard and Pruppacher, 1971). Unusually, the relative humidity was varied, between 27 and 65%. An air flowrate control valve was adjusted to keep the droplet stationary. The valve position had previously been calibrated to the flowrate, so together with a drag correlation and the assumption that the droplet was always at its terminal velocity, the droplet diameter was inferred. The drop surface temperature (required to calculate the diffusivity and density at boundary layer conditions) was calculated iteratively from a heat balance.

It may be the same levitator in a later study by Pruppacher (Mitra et al., 1992). The stated air velocity control range is very large, from a few cm/s to 30m/s. This is claimed to be capable of suspending particles from 50µm to 4mm, although the actual range of dried particle sizes reported in the study is 40 to 300µm. A slight convergence upstream from the test section helped to stabilise the levitated particle. Flow conditioning screens and a honeycomb together reduced the turbulence to 0.3%. The airflow control was via a variable throat sonic contraction with downstream vacuum

pumps. This gave control sufficiently fine to suspend the studied particle at any height within the 25cm observation section, and also to be able to maintain the levitation even whilst the droplet became progressively lighter during the drying. Relative humidity was controlled between 5 and 60%. The field of the study was meteorology rather than spray drying, so elevated temperatures were not used. The focus of the study was the crystal structure and robustness of the dried particles: the only observation of drying rate is that the droplets were dry generally within ten minutes.

Miura et.al. (1977) and Akbar (1988) also report devices which used an ascending air current to keep a single droplet stationary by matching the air current velocity with the terminal velocity of the droplet. Oteng-Attakora and Mumford (1994a) used a water cooled catchment device to sample individual droplets from the tunnel for weighing.

One intuitively apparent issue with aerodynamic levitation is positional stability of the droplet. Jones and Smith (1962) used the simple but crude technique of a long straight section of tube to steady the flow before the test section. They observed that the particles always moved close to the wall. The rotameter tube used as the test section had a narrow divergence and hence the velocity changes very gradually up the tube, and they chose to experiment with very slowly evaporating particles, both of which would contribute to short term positional stability. It is not clear that the method would be so satisfactory with rapidly evaporating aqueous droplets of relevant size to spray drying. The rapid rate of mass loss and the shape change of the droplet alter the buoyancy and drag force of the droplet respectively and hence modify the equilibrium position in the levitator. There is also the constraint of the limited field of view and depth of focus of the macro or microscope lenses required to image the small droplets. For a practical device to study spray drying droplets, the position of the droplet should be well constrained. Winborne et al. (1976) report designs of levitator nozzles to achieve this, where the particle is suspended close to the nozzle on an air jet that emerges from a central orifice, surrounded by a curtain of air jets from a ring of peripheral orifices, in order to prevent radial migration. Experiments are reported using a selection of metals, introduced as cold solid particles, levitated and then induction heated to melt them to droplets before starting the experiment, a neat trick which is unfortunately not transferable to spray drying. The analogy would be to suspend particles harvested from a spray-dried powder, then rewet them in a saturated air stream before re-drying them. This would be a useful technique only for a material that dried reversibly, which as

previously discussed, is not a supportable assumption for the objects of this study. The concept of levitation in an air jet shaped by air nozzle geometry is understood to have been used in one spray drying droplet kinetics study, although known only by citation, as the conference paper was not available (Furuta et al., 1983, cited in El-Sayed et al., 1990).

The great strength of the aerodynamic levitation technique is the potential for correspondence to conditions in a real spray dryer. The droplet is unconstrained, and the air temperature, velocity and humidity and the droplet diameter can all be of the appropriate magnitude. In order to achieve this ideal, there is a severe specification on the air flow control. It must be both precise and stable, but also have an exceedingly fast acting feed back loop to be able to rapidly respond to changes in particle shape and mass if the correct magnitude of all the variables are observed. A serious drawback of the technique is that the "just suspended" criterion must always be maintained. This limits the parameter space that can be probed. It also complicates the experimental design and data analysis, as it is not possible to alter a single independent variable over a sequence of experiments: for example, to hold constant all of the air velocity, temperature and humidity, and vary only the droplet diameter between experiments.

For droplets that remain spherical, drying rate can be estimated by measuring the evolution of diameter and air velocity. This approach fails when there are gross morphological changes, as are expected for the materials that are the object of this study. It would be more appropriate to measure the humidity change in the airstream, by some sensitive and rapidly responding technique. In other single droplet drying measurement devices in this review, gas thermal conductivity detectors and infra-red gas analysers have been used to answer this purpose. However, these methods have not been reported in conjunction with an aerodynamic levitator.

3.4.2 Acoustic levitators

The earliest known report of a droplet acoustic levitator device is a citation to a NewScientist news article (Anon, Jan 9, 1975, p74, cited in Winborne et al., 1976), but Toei and Furuta (1982) are the first workers to report a drying study of droplets suspended in a sound field. Later authors elegantly describe these devices as "acoustic levitators", but it is not clear who first coined this term. The basic principle is that the

droplet is held in the acoustic potential well at the nodes of standing waves (Ohsaka and Trinh, 1989). The key advantage of the acoustic over the aerodynamic levitator is that droplet size is no longer coupled to air flow velocity.

In Toei and Furuta's study (1982), the ultrasonic transducer was a cylindrical tube. The frequency was controlled in order to hold the droplet stationary. The frequency had to be adjusted during the drying as the air around the droplet heated up. A drop was introduced on the tip of a filament, from where it was "grasped" (sic) by the sound pressure well. The droplet was observed to rotate with frequency around 10 Hz. The range of drop sizes is unstated, although 1.5mm diameter is quoted on one diagram. The droplet was heated with a carbon dioxide laser. The apparatus was then measuring primarily radiative heat transfer, when the aim is to assess drying rate under primarily conductive heat transfer. The choice of laser heating is not discussed, but inferring from other later reports of acoustic levitators, it is assumed that the sound field was either insufficiently strong and/or well controlled to maintain a droplet stationary in a flowing air stream. The air temperature was measured by a thermocouple, the droplet temperature by an infrared thermometer. It was thus measuring droplet *surface* temperature. Even though the sight line of the IR thermometer was placed perpendicular to the laser beam, it was found that reflections of the laser beam from the drop surface interfered with the temperature measurement, and a filter was placed in front of the IR thermometer objective in order to minimise this error. Toei and Furuta (1982) were aware that the vibration of the air would increase the heat transfer coefficient. In the absence of valid correlations to predict this increase, the heat transfer coefficient of the device was calibrated by heating PMMA or glass spheres to around 90°C with the laser, then measuring the cooling curve when the laser was turned off. This calibration indicated that the heat transfer coefficient was enhanced approximately threefold by the ultrasonic sound field. The impedance of the drop surface is stated to be a thousand times that of the air, so the sound wave would be reflected from the surface and would not be expected to enhance the liquid-side heat transfer, only the gas film heat transfer. It is not made explicit, but this is a key assumption, as in the initial stage of drying with a saturated drop the heat and mass transfer analogy should hold. If the liquid-side heat transfer were enhanced, it seems probable that the mass transfer would also be enhanced, and since the purpose of the experiment is to determine mass transfer, large uncorrected artefacts in the mass transfer measurement would seriously undermine the conclusions. The drying rate was estimated by a heat balance, using the

measurements of the air and droplet temperature, together with the photographic record of the experiment to determine the droplet area exposed to the laser heater. There is thus an implicit assumption that the droplet temperature is uniform, so the surface temperature measurement is representative of the whole. There is also a second implicit assumption, of spherical symmetry, so that the area exposed to the laser beam can be determined from a photograph taken at 90° to the laser beam. The sequences of photographs shown in the paper indicate some deviation from sphericity.

Ohsaka and Trinh (1989) measured melting and solidification of droplets. The whole of the acoustic levitator was enclosed within a domed heated water jacket, which heated the air within the dome, and hence heated the droplet by natural convection. Sloth et al. (2006) appears to be the only study in the drying literature to have used the concept. They do not make this attribution, however, but rather describe the device as being similar to Toei and Furuta (1982) and Groenewold et al., (2002), which is correct in virtually no other respect than it was an acoustic levitator for studying droplet drying. The drying chamber was controlled between 25 and 80°C and 0 - 80 % relative humidity. They observed that the droplet became elliptical in the acoustic field, but then in order to determine the drying rate by filming the droplet diameter, they explicitly assumed that the droplet was spherically symmetrical and shrunk during evaporation to a dense particle.

Groenewold et al. (2000, 2002) overcame the limitations of radiative heat transfer in Toei and Furuta's (1982) work using an acoustic field sufficiently powerful to hold the droplet in place while air was blown over the droplet. However, this was only achieved with the highly undesirable side effect of significant corrections to the data for the droplet distortion and the approximately 30% enhancement to the heat transfer rate that were due to the acoustic field (Yarin et al., 1999). The airflow was cool (24.4°C), dried to 2 - 4 % RH, and slow (0.02 - 0.09 m/s). The acoustic field was so strong it locally heated the air by about 4°C. Droplets were around 1.8mm diameter. The drying rate was determined from the humidity change of the airstream blown over the droplet, measured by a high accuracy dew-point hygrometer. Attention was drawn to the smooth drying curves obtained, but there is no discussion of whether this is potentially simply an artefact of implicit averaging, either in the numerical correction method, or due to the slow response time obtained from high accuracy dew-point hygrometers.

The droplet distortion can be very severe in a high intensity acoustic levitator. It has been deliberately exploited as a moulding technology (Venturelli and Culick, 2003). Lee et al. (1991) found that droplets first flattened to dimpled discs (resembling a "Werthers Original" toffee to judge by the photographs in the paper), then surface ripples appeared, before the droplet buckled, ballooned and finally shattered. Large "disk-like" distortions were also reported in an acoustic levitator constructed by ICI to measure solidification rate for fertiliser prills (Haire and Kaldas, 1989). They also found that due to manufacturing tolerances, the resonant frequency of the transducers drifted apart as they warmed up, so the phase interlocking and hence the low pressure well drifted, and the particle levitation became unstable. It was concluded that the device was better as a qualitative screening tool than a quantitative measuring instrument.

The object of the present study are droplets which are expected to change shape during drying, and numerous authors report that such morphology changes are associated with changes in heat and mass transfer rates. The droplet distortion induced by the acoustic levitator would obscure the features that are the object of the study. Hence this type of device does not answer the design brief.

3.5 Droplets constrained on supports

The most reported method for measuring droplet drying kinetics is to suspend the droplet upon a support – a thin wire, a thermocouple, or a syringe. Evaporation rate has been determined by measuring outlet air humidity (Audu and Jeffreys, 1975, Hecht, 1999) and by diameter, either by recording the rate of water addition required to maintain constant diameter (Ranz and Marshall, 1952a, b, Chuchottaworn et al., 1984), or from the rate of change in droplet diameter (Walton, 2004). This inference from diameter can only be valid for a material which shrinks predictably as a function of its moisture content. This is not a good assumption for the objects of this study. The largest group of studies follow the drying rate by loss in weight of the droplet. The two principle approaches are by deflection of a wire cantilever and by suspending the droplet and wire from an electronic microbalance.

The classic droplet drying study is Ranz and Marshall (1952a, b), who measured the evaporation of a droplet in the constant rate period of drying, both by keeping the

droplet at constant diameter by feeding from a microburette, and also by suspending the droplet on a thermocouple. Fairly small drops (600 - 1100μm diameter) were measured, over a wide air temperature range from ambient to 220°C, and from still to 2.9 m/s air velocity. Droplet Reynolds numbers were in the range 0 to 200. The data were found to conform to the Colburn heat and mass transfer analogy, and were also found to correlate according to theoretically derived dimensionality, which correlations have become eponymous. Ranz and Marshall also ran experiments during the later periods of drying of crust-forming droplets, where they noted that the temperature and/or the diameter could to an extent be used as surrogate methods for determining the changing moisture content of the droplet, and a plot of the square of the droplet diameter against time should be straight for a uniformly evaporating water drop. They made quantitative measurements in this later period of drying only in still air, but identified the step change in evaporation rate at the point of crust formation by the step change in the slopes of the plots of both d^2 and Δt with time.

Pei et al. (1962) also measured the drying rate by the rate of water addition to the drying particle, but using a hollow sphere of porous diatomaceous earth in order to maintain the diameter, fixed to the end of a microburette through which a stream of water was introduced into the centre of the particle. The water flowrate was adjusted to maintain the surface just saturated (although it is not explained how the surface was judged to be just saturated). There are a number of unusual features reported. Superheated steam was used as the drying medium, and measurements were made to very high temperatures, in the range 150 - 750°C. The experimental rig design is also novel: the wind tunnel test section in which the particle was suspended, was open between the divergent inlet and exhaust nozzles, with the whole being encased within a stainless steel sphere. Schlieren flow visualisation was used to determine flow patterns around the particle. The flow could be varied from forced convection to buoyancy (natural convection) dominated. In intermediate flow regions, the data indicated that heat transfer was depressed as the natural convection opposed the forced convective flow.

Yuen and Chen (1978) also used steady state forced liquid feed from a microburette to saturate a porous sphere (sintered bronze in this case) in order to measure drying rate. However, in contrast to Pei et al. (1962), they deliberately operated at high enough Reynolds numbers to avoid the effects of natural convection. A vertical wind tunnel was constructed with 7.6cm square cross section, and data is presented from 150°C to

960°C and 2.5 to 11.4m/s - although the claimed maximum capability of the tunnel was an even more astonishing 1000°C and 20m/s. This wind tunnel is in size, temperature range and air velocity, dramatically more ambitious than any other reviewed here. The porous sphere was 6.35mm diameter, and the internal liquid temperature was measured with a thermocouple. The liquid feed line was cooled, except the final connection to the particle, which length was carefully chosen so that it neither overheated the introduced liquid nor interfered with heat transfer to the particle. The feed rate was adjusted manually to maintain the sphere surface just saturated, which was judged to be when neither dry spots nor drips were observed. Radiative heat transfer was significant and was corrected for.

3.5.1 Rotating capillary

The most intuitively obvious potential weakness of methods where the droplet is constrained on a support, is that the droplet dries preferentially on the leading edge. In the early stage of drying, this is not an acute issue, as Charlesworth and Marshall (1960) and many subsequent authors have noted that the droplets internally circulate. But after crust formation, the surface is constrained from rotation, and there arises the potential for artefacts, both from preferential drying on the leading edge and also (in a plastic filmed droplet) from distortion from the low pressure zone in the droplet wake as reported by Büttiker (1981). In order to try to avoid this potential source of artefacts, researchers at Aston University constructed a device which rotated the suspension capillary and hence the droplet. This device was used in a number of studies over three decades, but the technique was not adopted by other academic research groups.

The original device (Audu and Jeffreys, 1975) was a wind tunnel with a 1" diameter Perspex test section. Temperature range was 26.5 to 121.5°C, limited at the upper end by the Perspex. Hemispherical drops 1 to 5mm in diameter were created on the tip of a capillary, which capillary was rotated, typically at 20 rpm. The evaporation rate of pure water droplets was measured by constant feeding. The droplet size was maintained constant by pressure head, and checked at intervals by measurement with a cathetometer. Crust forming materials were also studied, without constant feeding of water during the drying. In all cases, the air flowrate, temperature and humidity were measured at intervals, both upstream and downstream from the drop. From the conclusions in the paper, droplet temperature measurements must also have been made,

at least for the water droplets, but it is not described in the text, although a likely thermocouple position can be inferred from the rig diagram in the paper. The range of air velocity is also not explicit in the text, but 0.4 to 2.5m/s can be estimated from data in the figures. It may have been as high as 3.3m/s if coincident maximum air flowrate and temperature were possible. In the crust formation studies, a series of droplets were dried for a sequence of increasing times and then sliced off the tip of the capillary. In this way a series of crusts were collected for thickness measurements (mean of numerous points over the crust) and structural analysis by SEM. In another series of experiments, drying drops together with the attached nozzle were removed at intervals for weighing. In separate experiments, the air flowrate and pressure drop were measured through a series of crusts, again removed at different times during the drying. A diagram in the paper suggests that the crust was maintained attached to the nozzle, and inverted, so residual liquid may simply have drained under the joint effects of gravity and the air being blown through the crust during the porosity measurement, although this is not explicitly described. Porosity was estimated from the air pressure and flow data, assuming (in order to obtain pore surface area) an equal probability of pores being at all inclinations from normal to the crust, an estimate of the number and mean radius of the pores from SEM, and a textbook value for pore tortuosity. From these measurements, Audu and Jeffreys derived an estimate of the crust mass transfer coefficient. There is no discussion of the potential error from heat conduction from the large circumferential contact between the capillary to the hemispherical drop, other than a mention that PTFE capillaries were sometimes used instead of stainless steel, although from the context it is unclear whether this was simply to make guillotining off the crusts simpler.

The range of the Aston rotating nozzle device was extended to 20 - 200°C in Ali et al. (1988). A copy of this modified device was installed at the ICI Specialties Research Centre in Blackley (Hull, n.d.; 1988?). It is reported for this latter device that 3m/s was the highest speed at which the droplet was not deformed by the airflow.

Modifications to the Aston device were made for later studies. The capillary was replaced first by a rotating thermocouple (Sayed et al., 1996, Hassan et al., 1996a, b) and then by a rotating glass filament (Walton and Mumford, 1999, Walton, 2000, 2004).

3.5.2 Wire deflection

If a droplet is placed upon the free end of a thin and flexible wire which is cantilevered from the other end, the weight of the drop causes the wire to droop. By Hooke's spring law, the deflection of the wire is proportional to the mass of the droplet, so as the droplet dries in an air stream, the wire rises. A key experimental difficulty is the selection of the wire, to get an acceptable precision. If the wire is too rigid, it will not deflect very much, and the precision will be limited by the discrimination of very small deflections. If the wire is too flexible, the tip will move wildly in the air flow, and the precision is limited by the noise in the droplet position measurement. Some researchers, especially the earlier studies, have used a combination of stagnant or very slow moving air, and interrupted air flow, to minimise the droplet oscillation and remove the contribution to deflection given by the drag on the drop and wire. More recent studies have made continuous measurements, calibrating the deflection due to drag with non-evaporating droplets as a function of air velocity, and estimating a central tendency of the noise in tip position with the aid of video recordings of the experiment.

The wire deflection method is very old: Morse (1910) reports the evaporation rate of a sphere of iodine on a fibre of quartz or glass, and casually claims that "there is no difficulty in detecting and measuring changes of weight of 0.001 milligram or less". However, the method is even older; Morse refers to it as "the micro-balance of Salvioni and Nernst", without further bibliographic reference, so presumably he expected the method to be already well known.

The first application of the wire deflection balance to measuring evaporation rates specifically with reference to spray drying is the study of Charlesworth and Marshall (1960). The droplet was suspended from a 43cm long glass capillary, which tapered from 425μm diameter at the fixed end to 210μm at the free end. The fixed end was inclined up at 45°, but it bent along the length until the tip was almost horizontal. From this free horizontal end, a second glass capillary 3cm long was hung vertically downwards, with a tip flamed to a bulb around 200μm diameter, from which the pendant droplet hung. The arrangement must have looked something like a fishing rod. Although not mentioned in the text, from the photographs in the paper and a later publication describing the same apparatus (Trommelen and Crosby, 1970), the wire was enclosed within a box in order to minimise artefacts from laboratory draughts. The airflow was from below, so that the suspension wire was vertically in the wake of the

droplet, to minimise interference with the airflow around the droplet. The air jet was generated using the same rig as Marshall's earlier study (Ranz and Marshall, 1952a, b), except that the exit air flow distributor gauze was removed, as it quickly became fouled by droplets falling onto it. The consequence must have been that the airflow was less uniform, but no measurements are reported, so it is not possible to confirm this. Rather than the conceptually simplest scheme, of measuring the deflection of the free end of the droplet, instead at each measurement time the fixed end was moved until the droplet was back in its original position. Presumably this was in order to maintain the droplet within a limited field of view of the microscope camera with which the droplet appearance was studied. The deflection was calibrated to weight, with a maximum capacity of 4mg, equivalent to a water droplet of just under 2mm diameter, and an accuracy of 0.01mg (around 1% of the mass of the smallest droplet tested - range 1.3 - 1.8mm). The air velocity and temperature were 0.4 - 1.6m/s and 30 - 160°C respectively. The airflow was interrupted for around 10 seconds in order to make the measurements of wire deflection on a 1 minute period. Whilst intuitively such interruption is undesirable, it does not appear to have given rise to measurable error in the determination of the drying rate: it is stated that changing the frequency of weighings did not noticeably affect the results. Furthermore, in separate experiments, droplets were suspended from a thermocouple junction, and the temperature during drying was recorded continuously. No gross mismatch in drying time between the continuous and the interrupted experiments was reported. It is honestly stated that there could be great variation in drying time between droplets dried under notionally identical conditions. Apart from the novelty of the method at the time, this study is notable for the huge range of materials studied.

Trommelen and Crosby (1970) used a development of the Charlesworth and Marshall (1960) apparatus. The short vertical glass capillary was replaced by a thermocouple junction, so the temperature and mass loss could be obtained from the same experiment. The purpose was to study drying in superheated vapours. In order to prevent condensation, the jet of gas or superheated vapour was enclosed within a heated air jacketed glass drying chamber, rather than being a free jet as in the earlier study. The drying chamber was fitted with optical glass windows for observations, a slot for the cantilever balance wire to enter, and an access port through which to place droplets on the wire. Measurements were again made by stopping the air (or vapour) flow, but due to the higher temperatures and velocities in this study, drying could be too rapid for

sequential measurements on the same drop to be accurate, and instead each drying curve was constructed from a series of droplets, each one dried for a different length of time.

Cheong et al. (1986) used a glass tube as their capillary (drawn so that it was thin enough to be flexible), with a nickel wire passed down the centre of the tube and the outside of the tube vacuum coated with a copper film. In this fashion, the tip of the wire from whence the droplet was suspended formed a thermocouple junction, and droplet temperature could be measured simultaneously with mass loss. By varying the length of exposed wire, either the core or an average temperature could be measured. This detail is interesting, as the standard assumption in the literature is that the droplet temperature is uniform, but no internal and external temperature data are presented to confirm or confound that assumption. Slurry droplets between 1 and 1.5 mm in diameter were dried in a stream of dehumidified air with temperature controlled in the range 20 - 78°C. The air flowrate is unspecified. At one point a typical experimental condition is given as 0.3m/s air velocity, although the thermocouple calibration velocity is stated to be rather higher (2m/s). The weight-deflection was calculated from a calibration curve. It is stated that the deflection was corrected for drag force on a spherical droplet and the cylindrical wire, but it is not made clear how the spherical drop size was determined during the course of the experiment, or whether the assumption of sphericity remained valid through the experiment. It is possible that only the initial drop diameter was used, determined from volume dispensed. Photographs of droplets are shown in the paper, so the drop diameter may have been measured directly from these photographs. After drying, the thickness of the crust and porosity were estimated by SEM. The porosity was also measured using the apparatus described by Audu and Jeffreys (1975).

Tanno et al. (1988) used an apparatus which diagram looks similar in outline if not in precise detail to Charlesworth and Marshall (1960). Variable ranges are unstated, but all results shown are for 1m/s air velocity, with temperature varying from 128 - 226°C. The major interest of this paper is that the droplets were as small as 200 - 300µm. Although not highlighted in the paper, it is the earliest literature report of measurement of such small droplets on a tether. The droplets were made by dipping the tips of two 5µm quartz filaments into the test liquid, withdrawing the filaments at a spacing of around 2mm so that a liquid film bridged between them, pricking the film, then transferring the resultant small droplet from the end of one of the filaments, to the

measurement apparatus filament. For droplets above 1mm, the displacement of the droplet was measured with callipers, but for the smaller droplets it was measured from video footage, averaged over three successive video frames, as the vibration was severe.

The wire deflection method has recently been considerably advanced by Chen's group at The University of Auckland, New Zealand (Chen, 2002, Lin and Chen, 2002, 2007). Great care has been exercised in order to quantify, control and minimise sources of error. Glass filaments have been drawn to very fine diameters (30 - 70μm) to minimise heat conduction to the drop and disturbance to the airflow. A 13μm diameter thermocouple was also inserted into the droplet so that temperature could be recorded simultaneously. Droplets as small as 400μm have been measured. The method of droplet formation and wire attachment was reproducible to within ±0.03mg: 100% of the smallest droplet, but just 0.3% of the largest. Two air heaters in series, with both PID and fuzzy-logic control are used to ensure precise temperature control, within ±0.3°C. Ten layers of 24-mesh screen are used to reduce air velocity fluctuation to less than 4% of minimum drying air velocity, and hence minimise droplet bounce. As with most of these devices, the body of the cantilever is contained within a box to minimise disturbance due to external draughts, but in this device the air within the box is heated to the same temperature as the main drying chamber. This removes vibration from temperature gradient induced draughts through the entry slit of the cantilever into the drying chamber. The deflection of the wire was recorded by analogue video and digital image analysis. Resolution was 0.007mg, and calibrated accuracy within 0.05mg. Hysteresis was excluded by a repeatability check that the wire returned to the calibrated position for the weight after repeated manual displacements. Repeatability was found to be better than resolution when there was no airflow, and at 0.01mg, only just greater than resolution when there was airflow. Droplet drag force was corrected for by calibration with non-volatile spherical droplets. Where the droplet shape deviated from spherical during drying, it was assumed that the drag force was equal to that of a spherical drop of the same weight. This explanation is not entirely coherent, as the weight and the drag are not separately measured. However, the authors state that they checked the assumption was valid by spot checks in various experiments, halting the airflow to determine the weight without conflation of drag. It is claimed that the average error in the spot checks were within 0.02mg, less than the balance accuracy.

In Threlfall-Holmes and Ocone (2005), results were reported from a wire deflection device at ICI Wilton, constructed by Keith Appleby in 1993. In using the apparatus, a number of limitations of the method became apparent. Especially at higher velocities, the droplet vibrated in the airstream, with magnitude of oscillation between 10 - 100% of reading. This vibration was corrected for, in as much as was possible, by manually analysing the video recording of the experiment frame by frame to determine an average position at a particular time. This vibration is expected, due to wake vortex shedding for droplet Reynolds numbers $130 < Re_d < 400$ (Clift et al., 1978, p103); Re_d varied between 130 and 350 in the experiments shown in the paper. The vibration could be minimised by using a shorter or more rigid wire, but at the expense of precision; initial (maximum) deflection of the wire might only be 8mm, compared with the vertical position resolution, estimated at about 0.4mm. However, this wire vibration limitation is now much less constraining than when the experiments were performed, as high speed digital cameras and motion tracking software have since become affordable. Certain materials appeared to dry more quickly than an equivalent water droplet. This was shown to be neither a calibration nor a vibration induced error. It is possible that the apparent anomaly was the effect of changes in droplet drag due to the morphological changes during drying. An inflated droplet presents greater surface area for mass transfer, which genuinely enhances the mass transfer rate, but an inflated droplet will also present a greater cross sectional area in the flow, hence have greater flow resistance and therefore apparent mass loss on the wire deflection device. The wire deflection device conflates the real enhancement in mass transfer rate with the artefact. The only method reported that would deconvolute the effects on the data is intermittent measurements with the airflow removed. Shape and size changes were certainly observed in some experiments, and reasonably accounts for some of the curious data reported, however, it is not clear that was the case in all instances, as the departure from expected behaviour could be immediate, whereas if caused by inflation of the droplet during drying, some delay would be expected whilst any such expansion developed.

The details of several other wire deflection devices are included in Table 1 (Sano and Keey, 1982, Nešić and Vodnik, 1991, Yamamoto and Sano, 1992, 1995). These have no unusual features described that merit further discussion in the text.

3.5.3 Electronic microbalance

There are a few reports of a droplet suspended on a wire attached to an electronic microbalance (Kwapinski and Tsotsas, 2004, Taniguchi et al., 1999, Hirschmann et al., 1998, Furuta et al., 1984, cited in Hecht, 1999). This has the advantage that the droplet mass is measured directly, without calibration. Also, the air flow can be horizontal, so that drag on the particle causes minimal mass loss and mass errors from flow induced vibrations, although both Kwapinski and Tsotsas (2004) and Taniguchi et.al. (1999) use vertical air flow, causing the same problem with apparent loss of mass as the wire deflection method. This may explain why these studies were limited to around 1m/s maximum air velocity.

The apparatus of Taniguchi and Asano (1994) simultaneously measured droplet weight and temperature. The device was subsequently modified to also simultaneously measure projected surface area (Taniguchi et al., 1999). The air was dehumidified and the dry air humidity measured. The flowrate was controlled coarsely using a spill valve just after the inlet fan, and finely with an in-line needle valve. A large and small heater in series were used, presumably intended for precise control over a wide temperature and flowrate range, although this is not explicit in the paper. The air entered the test section through a convergent-divergent nozzle with a flow straightener. The test section was 70mm square by 166mm long, with a window for a digital video microscope. The droplet surface area was calculated by image analysis software, calibrated to within 1% accuracy by stainless steel spheres of known diameter. The droplet was hung at the tip of a 50µm thermocouple connected to a datalogger. The thermocouple was attached to the end of a 150mm long by 6mm diameter glass tube which was hung from an electronic balance. The droplet was placed on the end of the thermocouple via a feed syringe and a traversing mechanism for aligning the feed tube and suspension wire. The data acquisition was continuous, with a sampling interval of two to five seconds. The balance precision was 0.2mg. Maximum air velocity was 0.72m/s, and maximum temperature was 120°C. Droplets were 2mm diameter.

The droplet suspension method of Hirschmann et al. (1998) used fifty rather large (1.1mm) particles held on a wire lattice, to achieve measurable mass changes on drying with the 0.1mg resolution balance. Hence average drying rates were measured, with a

mathematical correction applied from ensemble to single particle drying kinetics. Very low air velocities were required in order to avoid balance error.

McMinn and Magee (1996) describe apparatus to measure the drying curve of starch gels using a microbalance. They cleverly use a recirculating wind tunnel, which permits a large air velocity without a large heating element. It is not clear whether the inventory of air within the tunnel was sufficient that the humidity did not vary much during the drying, or whether the tunnel purge flow and measured humidity were used to minimised and/or correct for humidity accumulation. Unfortunately it was large cylinders of starch gel rather than single small droplets that were being dried, so the details of the experimental design are not portable to the current application.

Kwapinski and Tsotsas (2004) describe an apparatus where the sample holder was connected to a 1µg resolution electronic microbalance by a magnetic coupling. This avoided direct contact, so air temperatures up to 350°C were possible. It also acted to absorb the vibration of the droplet and suspension wire that were induced by the airflow. It was reported that this reduced noise in the drying curve sufficiently that no data smoothing was required until the air velocity exceeded 1m/s. The device was only capable of drying wet particles, not droplets, for reasons that are not explained. A dry particle of molecular sieve was glued to the tip of the wire, and then moistened.

3.6 Summary

The various literature reports of devices are summarised in Table 1. The selection of a method that is appropriate to the objects of the current study is made in the following chapter.

A3 landscape in paper copy:

this page in electronic copy just maintains the correct pagination and cross references to the table

Table 1: summary of experimental methods for measuring droplet drying kinetics. Asterisks indicate references from Hecht's table (1999) which it has not been possible to obtain to check details.

CHAPTER 4 - DESIGN OF A NEW APPARATUS TO MEASURE DROPLET DRYING KINETICS

The confluence of the droplet size effect on morphology, and the effect of morphology on drying rate, requires that droplets of the correct order of size must be measured in order to obtain representative drying rate data. This is not a new observation: Alexander and King (1985) comment on the need to measure droplets of correct size to obtain the correct morphology. It is an exceedingly challenging measurement task, however. A typical 50µm diameter spray-dried droplet has a volume of 65 picolitres. In industrial practice, feed solids concentration is typically high, and water may account for only half the initial mass of the droplet; 30 ng of water. It will be shown later that the Acoustic Atomiser produced particles around 300µm diameter, but even these large droplets contain no more than 14µg of water.

Measuring droplets as small as are found in a spray dryer presents challenges other than the sensitivity of the mass loss measurement. At 200°C typical, 300°C maximum inlet temperature in a spray dryer with the materials of interest to this study, the timescale for drying is very short, just a few seconds. To obtain equivalent droplet Reynolds numbers, the flow velocity must match that found in industrial dryers. Whilst the superficial velocity in the main body of the dryer is typically in the region of 0.1 - 1m/s, the greatest drying rate is where the hot gas is introduced into the chamber at the same point as the atomiser, where gas velocity is typically 25 - 30 m/s (Schwartzbach, 2000).

The majority of the apparatus described in the literature rely on scaling by dimensional analysis, so large droplets in slow airflow can be measured whilst maintaining the droplet Reynolds number of the small droplets in fast airflow encountered in the spray dryer. The benefits of this approach are manifest: less absolute mass loss precision is required, larger droplets are easier to create and to manipulate, and slower airflows are cheaper to engineer, and easier and safer to work with. In contrast, the device required for this study must be capable of making measurements of small droplets in hot, fast airflows. It is apparent that under such extreme conditions, it will never be possible to obtain good data: indeed, one would be well content with *any* data. Table 1 shows that in most of the devices reported in the literature, the ranges of airflow temperature, velocity and humidity are all less than the ranges of those operating variables in a spray dryer. Hence the devices were almost always extrapolating from the measured values to

some extent. The approach adopted in this new design is an apparatus that will operate over a wide range of droplet diameters and air velocity, temperature and humidity. This can be used to make series of measurements from mild conditions where high accuracy can be obtained, (and comparison with literature data made), through to extreme, high error conditions where the measurements provide a reality check for the extrapolations. Additionally, size dependent morphology effects can potentially be characterised from discontinuities in trends over the range of a variable, especially if there is simultaneous imaging of the drying droplet experiments with which to cross-correlate the data.

A final criterion, which arises from the high air velocity, is that any direct measurement of mass loss from the droplet must be perpendicular to the flow velocity, so that vibration induced by wake vortex shedding is orthogonal to the plane of the mass measurement.

4.1 Selection of appropriate measurement technique

The literature contains many ingenious methods for elucidating droplet drying kinetics. No single method is perfect, but the review indicated that the thin-layer and acoustic levitation techniques were not suitable for this study, and ICI had previously tested acoustic levitation, rotating capillary, free-falling droplets and wire-deflection devices. Even the most carefully constructed cantilever device reported so far (Lin and Chen, 2002) has a resolution of 7μg, equivalent to the total mass of a 240μm diameter water droplet, and an accuracy of 0.05mg, equivalent to the mass of a 460μm diameter water droplet. It is not until 2mm diameter that the accuracy is a negligible 1% of a water droplet mass. These devices also measure mass loss in the direction of the air flow, and hence conflate mass loss and drag, and become noisy at high droplet Reynolds number due to wake vortex shedding.

The aerodynamic levitation technique has many appealing features. However, it is cumbersome to vary operating parameters over a range of conditions, due to the need to maintain the just-suspended criterion. The deciding factor disqualifying it from this study, however, was that at the early stage of the project when the apparatus design was conceived, a safe, available and affordable technique could not be found that was capable of measuring the mass loss by humidity difference. The extreme sensitivity required from such a humidity instrument can be appreciated by considering the air flow

in a 25mm diameter duct, which will be shown later to be a sensible size for a single droplet drying wind tunnel. Taking a moderate air velocity of 1m/s in this duct, there is 4µg/s water flowrate, even when the air has been dried to -40°C dewpoint; and 20mg/s at temperature and humidity conditions equivalent to a typical spray dryer outlet condition. This is to be compared with the total mass of 70ng in a 50µm droplet, and 14µg in a 500µm water drop. The thermal conductivity detector used by Hecht (1999) was reported to be extremely sensitive, but required nitrogen rather than air flow, as the elements were destroyed by exposure to oxygen when hot. In that study, a very low flowrate purge of nitrogen was used. In this study, where it is intended to produce blasts of drying gas, and the operator will require access to the test chamber to place and remove droplets, nitrogen flow is unacceptably hazardous. Groenwald et al. (2000, 2002) report the use of a high accuracy dew-point hygrometer to measure humidity change, but on investigation the commercially available devices were all limited to 180°C maximum operating temperature by solder joints in the sensor, and had long integration times, so were unsuited to the measurement of small droplets, where the drying may be completed in just a few seconds. An IR gas analyser (Langrish et al., 1991) was too expensive for this study.

Should a suitably sensitive and rapid humidity instrument become available, the aerodynamic levitation technique is worthy of further investigation. It could be used to compare results with the device described here, to check for artefacts from tethering. It would not require a second apparatus to be built from scratch: the air flow control, conditioning and flow calming stages could be re-used. Such re-use is seen in the literature, for example the electronic microbalance device described in Taniguchi et al. (1999) is an extension of the device used by Chuchottaworn et al. (1984) to infer evaporation from droplet diameter.

The remaining droplet drying measurement technique is where the droplet is suspended from an electronic balance. The major disadvantage of this method was that until very recently, microbalances of sufficient accuracy to measure the drying rate of a single droplet were exceedingly costly, very susceptible to random error from external vibration, draughts, etc., and not designed for hanging a wire underneath the balance pan. Hence the recourse to experimental ingenuity such as that demonstrated in Hirschmann et al. (1998), where a fifty particle array was assembled on a wire lattice, in

order to provide sufficiently large overall mass for the mass loss on drying to be measurable.

Further disadvantages are common to all wire suspension devices.

It is exceedingly hard to make a simultaneous temperature measurement without affecting the primary mass loss reading. If the suspension wire is a thermocouple, then the torsion in the electrical connection leads will affect the load on the balance cell. If a second, independent, very fine thermocouple is inserted into the droplet (in the trailing edge to minimise disruption to airflow), more heat is conducted into the droplet, and also surface tension forces will tend to pull the tips of the two wires together, leading to artefacts in the balance trace.

A practical difficulty is the droplet dispensing and placement upon the wire tip. Hecht (2002) has estimated that perhaps one in ten droplets of about the desired size were successfully placed. Such a high success rate demonstrates considerable experimental technique.

The final disadvantage common to all wire-suspension techniques is that drying occurs preferentially on the leading edge, whereas a droplet in a spray dryer is free to rotate in the airflow. Although it appears intuitively obvious that the constraint from rotation would lead to artefacts, and many authors express this concern, it is not actually clear that the published data supports the concern. Mitra et al. (1992) and Büttiker (1981) both observed that untethered droplets remain in the same orientation once surface solidification had begun. Hull (n.d.; 1988?) reported that differences observed by scanning electron microscopy between particles of the same product dried on the rotating capillary device and a production dryer as were much less than between different products. Walton (2000) reports "strong similarity" between industrial spray-dried powder and that obtained from tethered single drop drying experiments. There are few comparative studies of the different single droplet drying methods, but Jones and Smith (1962) reported that the mass transfer measurement was unaffected between aerodynamic levitated and tethered particles. El-Sayed et al. (1990) reported qualitative agreement in the sequence of morphological development between suspended and free-falling droplets.

Considering all the alternatives, it is believed that developments in the capabilities of ultramicrobalances make the droplet suspended from a balance method the best available compromise to tackle the particular constraints of this application. A device with the accuracy of the one proposed here has not previously been reported. A particular aspect of the design which is novel and key to attaining the target precision, is a pressure balancing concept described later, that avoids artefacts from frictional forces from the air flow on the wire connecting the droplet to the balance.

The device has largely been constructed, but the remaining work of completion, commissioning, beneficial operation and validation of results in a spray dryer computational model would form at least one additional doctoral research project.

4.2 Description of the new apparatus

The new apparatus is shown as a schematic flowsheet in Figure 8, in detail in the line diagram Figure 9 and in the annotated photographs Figure 10. A highly sensitive ultramicrobalance (UMX2, Mettler-Toledo) (WE901 in Figure 9) with 10^{-7}g precision is used, which is sufficient to obtain a drying curve down to about 300μm droplet diameter. In practice, this has been found by others to be about the lower limit of size at which a droplet can be placed upon a wire, and even then with considerable ingenuity and skill (Lin and Chen, 2002, Hecht, 2002). The update rate is eight readings per second, which is sufficiently rapid to obtain at least a few data points with which to construct a drying curve for even the smallest droplets in the hottest, fastest air. The balance is provided with an underpan hook from which the droplet suspension wire can be slung, although there is a severe constraint that the suspension assembly must weigh less than the 2g maximum load capacity of the balance. The key problem, is to devise a means of blowing an air stream over the droplet, suspended from the balance, without introducing so many sources of error in the balance reading that the signal is swamped by the noise.

It is desirable to make the measurement chamber the smallest possible diameter. This minimises the volume flowrate of air, the heater duty, and the cantilevered length of the suspension wire in the flow (and therefore the axial deflection due to drag). However, the minimum chamber diameter is limited by empirically established guidelines of 5% of area and 1/5th diameter for the maximum size of obstruction that can be placed in a

wind tunnel airflow without wall effects changing the airflow pattern around the droplet (Barlow et al., 1999, EIA/JEDEC, 1999). The wind tunnel internal diameter has been chosen to be 22.1mm to match a standard tube bore. This permits droplets up to around 4.5mm diameter to be measured, which as discussed later is about the largest size that has been found not to distort excessively under self-weight.

A supply of compressed air, dried to -40°C dewpoint, is heated in the apparatus to a controlled temperature using a custom made 4kW helical annular electrical heater (Rapid Response Heat Exchanger, Watlow Inc.) (B101 in Figure 9), and precisely rehumidified with demineralised water fed by a metering pump (Encynova Travelcyl) (J701 in Figure 9). The air flowrate is measured cold using a high and low ranged pair of thermal mass flowmeters (Brooks) (FT101 and FCT102 respectively in Figure 9). The lower ranged meter has an integral flow controller, with a 1s response to step change. Higher flowrates are controlled with an air regulator (PRV21 in Figure 9). The air velocity around the droplet is calculated from the density at the temperature in the droplet measurement chamber. In consequence, the accuracy to which the air velocity around the droplet can be established is limited by the accuracy of the temperature measurement, rather than the flowmeter. It would be desirable to measure the air flowrate directly at the potentially high temperature in the measurement chamber, but at the time the apparatus was specified, no instruments were available that were fit for this arduous duty.

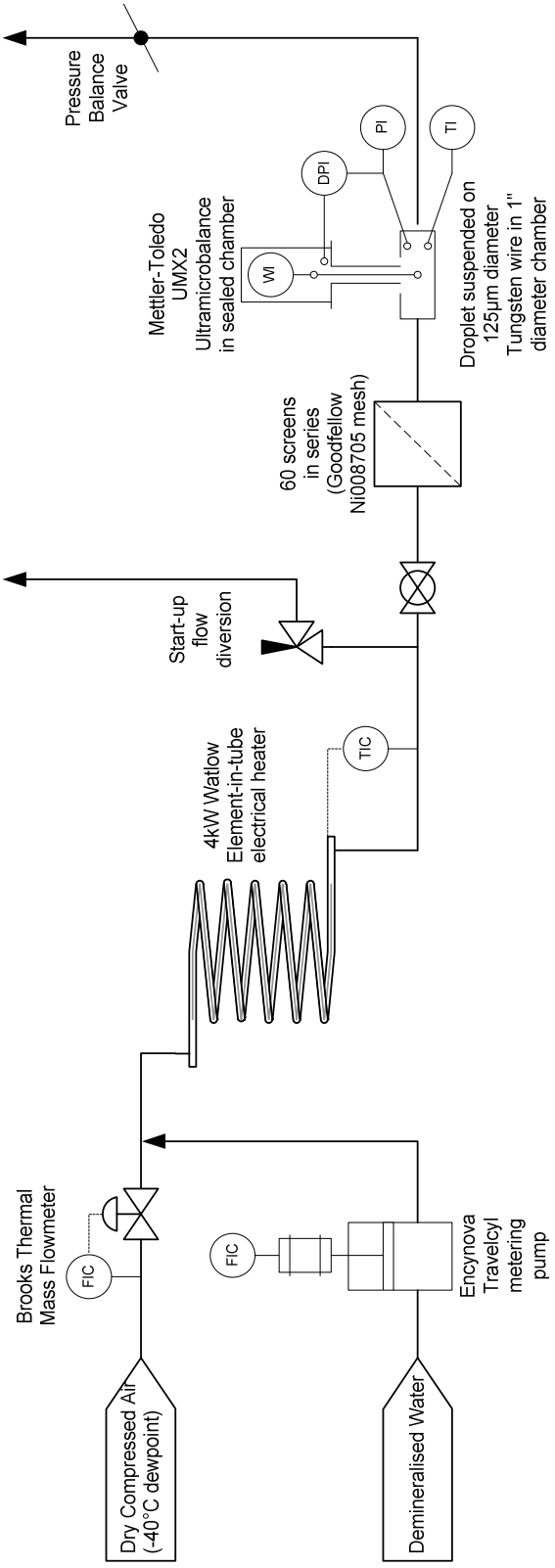

Figure 8: schematic flowsheet of the new droplet drying measurement apparatus

A3 landscape in paper copy:

this page in electronic copy just maintains the correct pagination and cross references to the figure

Figure 9: line diagram of the new droplet drying measurement apparatus

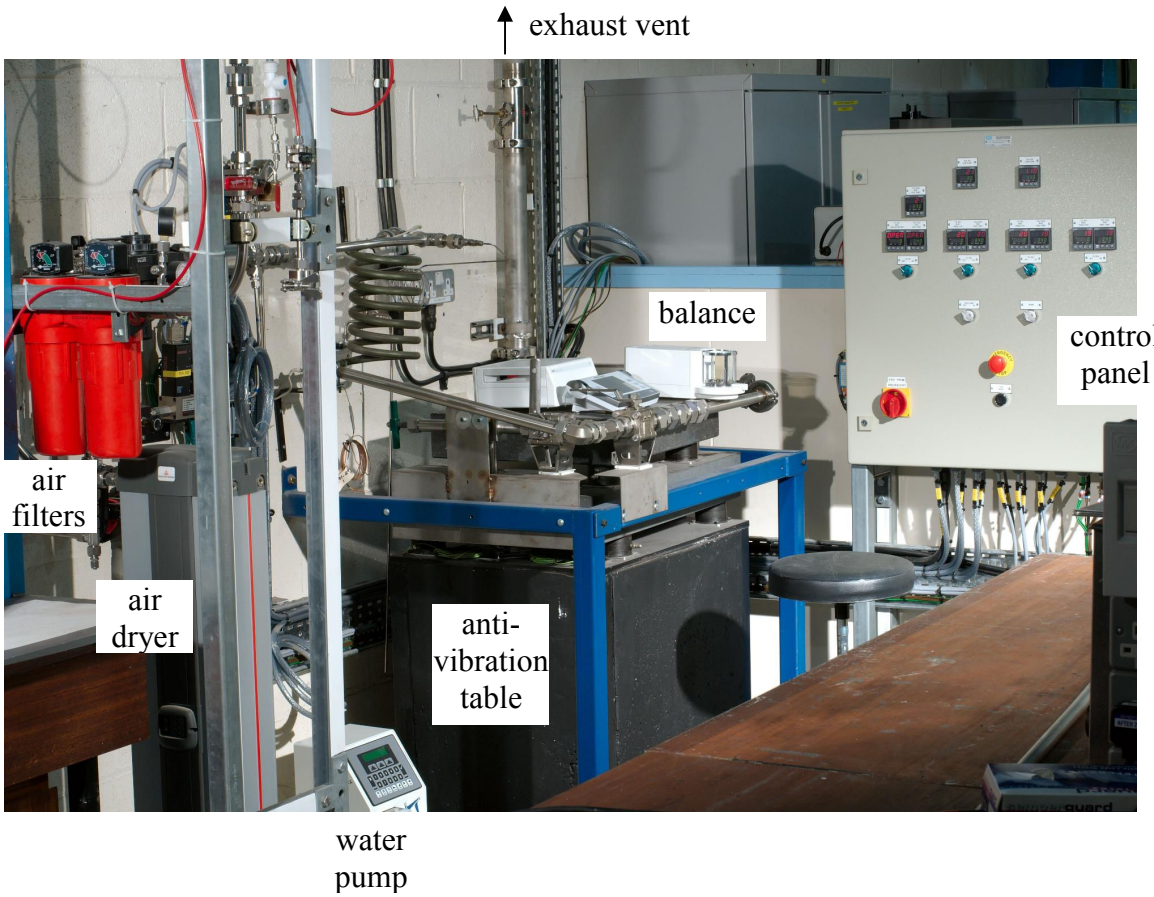

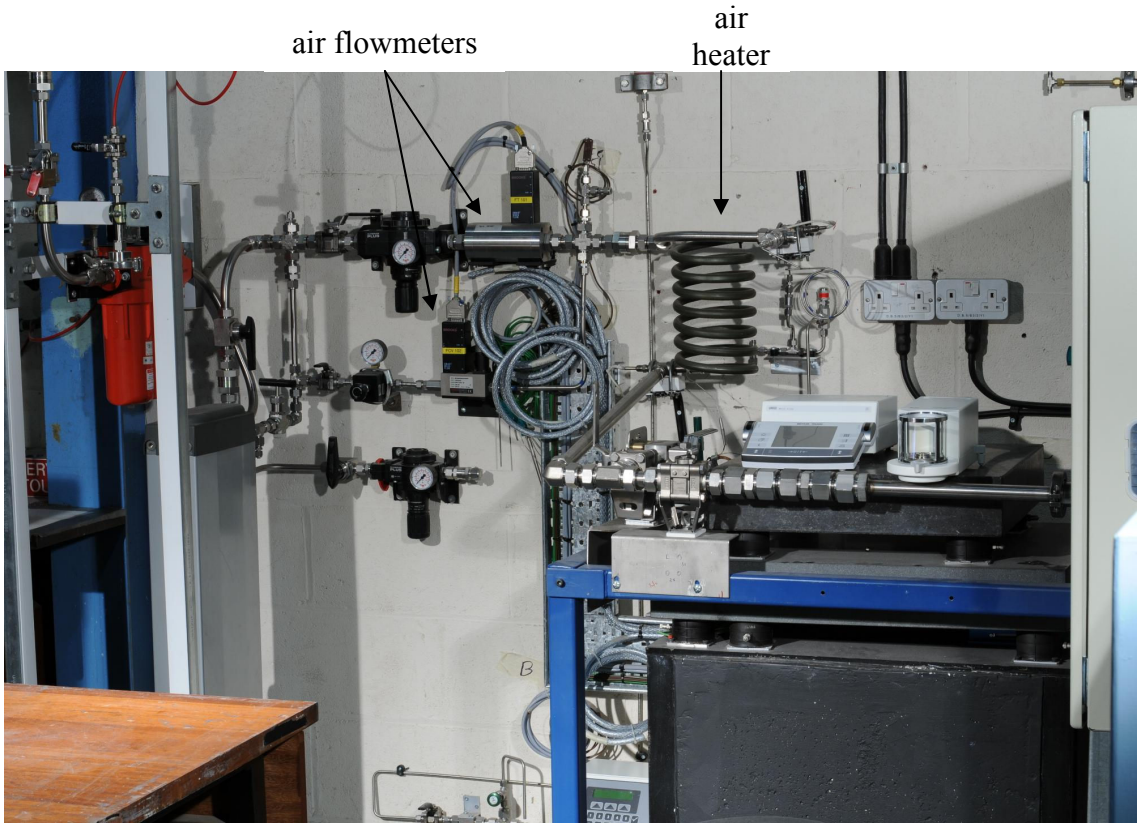

Figure 10: photographs from two angles of the new droplet drying measurement apparatus

4.3 Minimising sources of error

As a key feature of the design brief was improved accuracy, it was particularly noticeable when reviewing the literature that only Lin and Chen (2002) devote concerted attention to identifying and evaluating sources of error in their device. Elsewhere in the literature there are only occasional remarks to indicate that error sources have even been considered let alone quantified. A couple of studies note that there could be great variation in drying time between droplets dried under notionally identical conditions (Charlesworth and Marshall, 1960, Sano and Keey, 1982). A working assumption is that it will be necessary to generate ensemble average drying curves from a large number of repeat experiments, but most authors show drying curves obtained from only a single droplet experiment, and only Nešić and Vodnik (1991) explicitly say that they performed 10-20 repeats to generate each evaporation curve.

Similarly, surprisingly little attention is devoted to the processing of the data obtained. This has also been observed by Kemp et al. (2001), who reviewed methods for processing the data from drying kinetics rigs, concluding that a cubic spline curve fit to the data gave least smoothing artefacts.

In this design, a careful error analysis was conducted in order to determine the required precision and accuracy of all aspects of the instrumentation, from the primary sensing elements to the analogue/digital converters.

The need to correct the air flowrate measured at ambient temperature for the temperature and pressure in the measurement chamber is shared with most of the devices reported in the literature. The intent is that the measurement chamber is cool whilst the droplet is placed, and then the hot airflow is introduced, so the temperature measurement must also have a very fast response. It is not possible to achieve both the required speed and accuracy with a single element, so there are two measurements of the chamber temperature, one with a Class 1 Type T thermocouple, in the smallest available size for minimum thermal lag, and the other a 3mm diameter PT100 element (both sensors TC Thermocouples) (TE205/1 and /2 respectively in Figure 9). The chamber absolute pressure is determined from a micromanometer (Furness Controls FCO12/332) (PDIT306 in Figure 9) for gauge pressure together with a barometer for atmospheric pressure (Druck RPT) (PI390 in Figure 9).

4.3.1 Balance artefacts

Although the balance is supplied with noise filtering algorithms good enough to obtain stable readings to the balance precision on a normal laboratory bench, these algorithms are designed for variation around a constant weight, for the normal use of this instrument. To avoid introducing damping artefacts into the reading, it is necessary to disable the internal damping algorithms, to draught screen the balance carefully (not shown in photographs Figure 10), and to insulate it from structure-borne vibration with an isolation table. The isolation table consists of a block of approximately one tonne of concrete, on top of which are two stages of marble slabs supported on pneumatic isolation mounts (Fabreeka).

The loadcell of the balance is sensitive to draughts and can only withstand a maximum temperature of 40ºC, very much lower than the 300ºC maximum temperature in the measuring chamber, so it has been necessary to isolate the balance thermally from the measurement chamber. The wire on which the droplet is suspended from the balance must therefore necessarily enter the drying chamber through a hole. The dynamic pressure of the airflow through the drying chamber will give a pressure differential between the drying chamber and the balance, and drive an air flow through the annular gap between the wire and its entry hole, which will exert a vertical drag force on the wire, resulting in a balance error which is considerably greater than the balance resolution, so cannot be ignored. It has been found impractical to completely eliminate this source of error. However, by encasing the balance in a sealed chamber (Figure 11), and by careful design of exhaust diffuser (Figure 12), the dynamic pressure in the measurement chamber can be recovered, and by adjustment with a balance valve (V12 in Figure 9), trimmed so that the pressure differential between the measurement and balance chambers is minimised and the equalisation time is of the shortest practicable duration - calculated to be no more than 0.5s in the worst case. The differential pressures are determined by the aforementioned micromanometer, with two sensors, one between the measurement and balance chambers, and one between the measurement chamber and atmosphere.

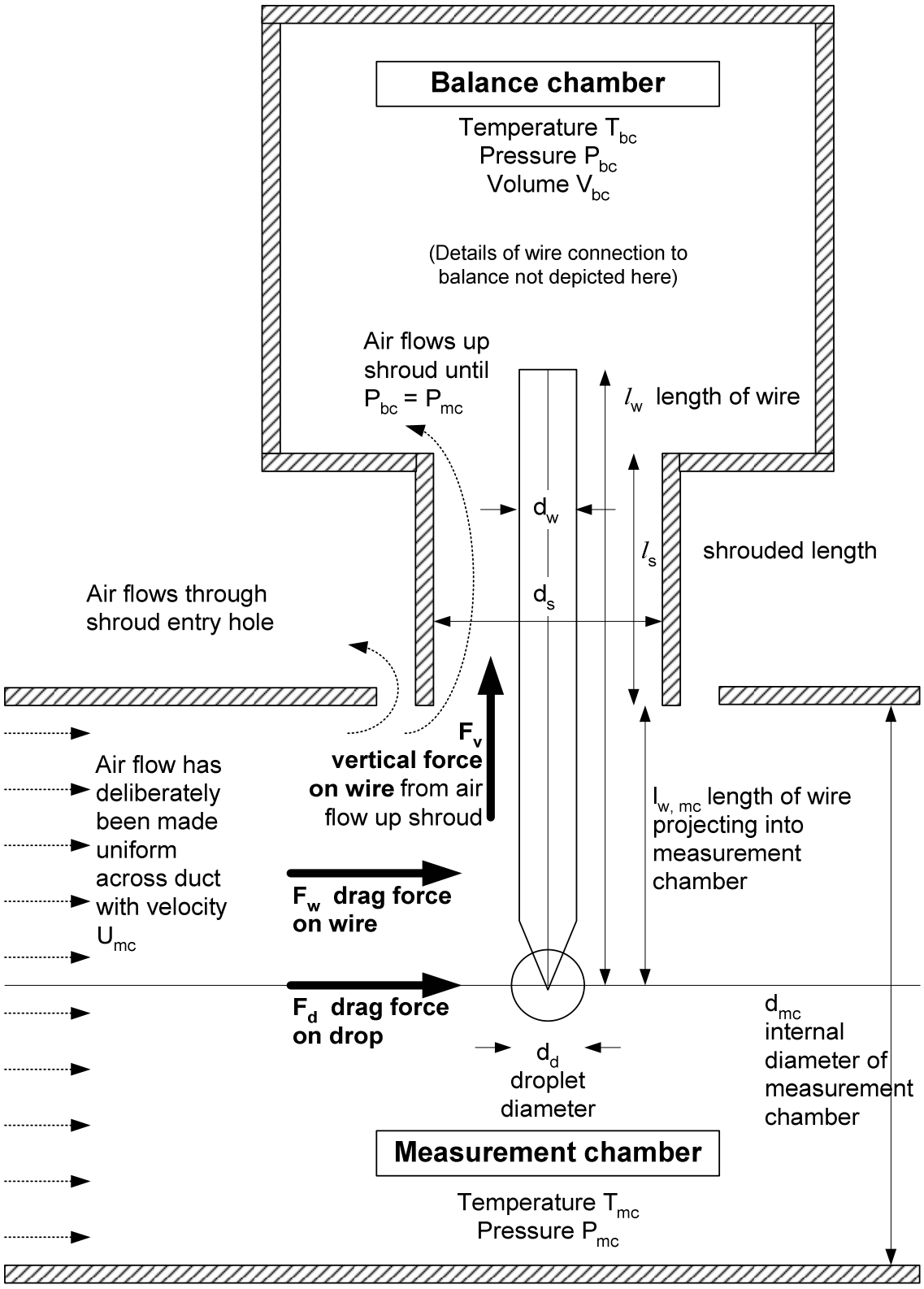

Figure 11: sketch of balance and measurement chambers

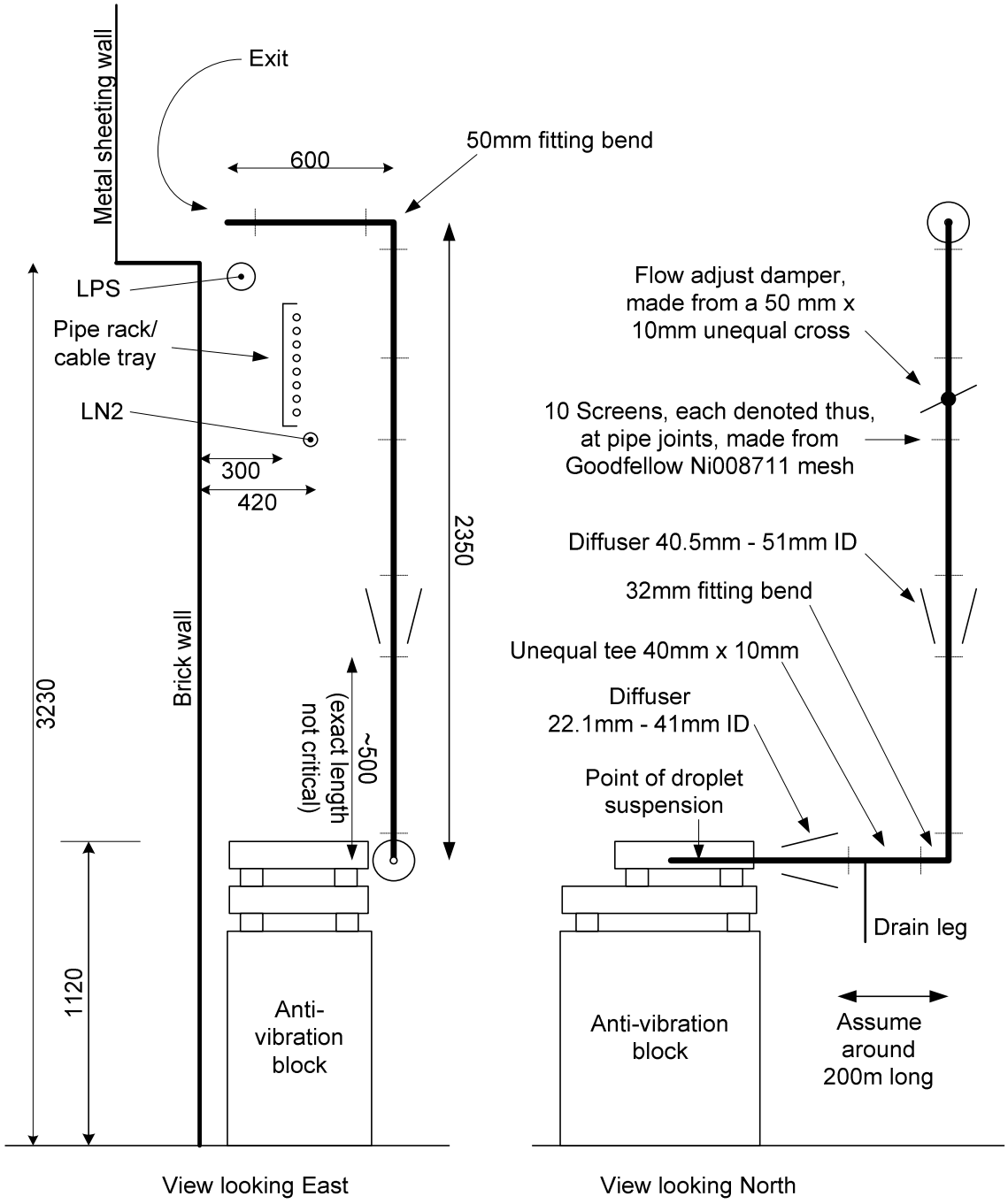

Figure 12: plans of exhaust diffuser

4.3.2 Axial deflection of droplet and wire

It is essential to ensure that the force of the airstream does not deflect the droplet sufficiently far from the vertical that the suspension wire chafes against its entry hole into the measurement chamber. In addition, if the wire is deflected from the vertical, then a resolved component of the axial drag force on the droplet is balanced by tension in the suspension wire. This tension will be detected as apparent mass gain by the balance Figure 13. The greater the angle of deflection, the greater the fraction of the

drag force that is seen as a balance artefact. Thus it is desirable to maximise the stiffness of the suspension wire in order to minimise deflection.

The deflection of the droplet has been estimated by a force balance, where the drag force on the wire and droplet were estimated from correlations for drag force on an isolated sphere and long wire respectively. This assumes that the droplet suspension wire is sufficiently thin that it does not noticeably alter the streamlines around the droplet, and therefore the drag on the droplet, and correspondingly that the droplet is sufficiently small when compared to the length of the wire exposed to the flow, that the streamlines around the wire, and therefore the drag upon the wire, are not noticeably affected by the droplet.

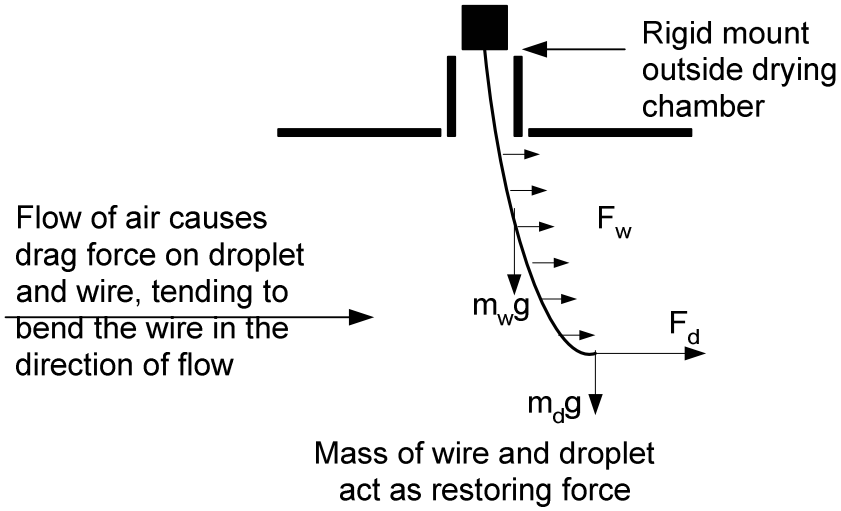

Figure 13: sketch of force balance on droplet suspension wire

The conclusion of this analysis was that, especially for larger droplets and at high air velocities, the high and temperature insensitive Young's Modulus of tungsten is required. 125µm diameter Tungsten wires have been obtained (Goodfellow). It was subsequently found that there is a previous citation of the use of Tungsten suspension wires (Tanno et al., 1988), although they do not explain why they selected this material. They do note that heat transfer rate from the air to the wire to the droplet needs to be compensated for, and provide a calculation method for doing so. They also tested quartz fibres, and found that there was then no need to correct for heat transfer. The most satisfactory solution, at least at moderate drying air temperature, is probably to coat a Tungsten wire core with a thin layer of PTFE, which would also reduce the tendency of the droplet to climb the wire. The very tip would need to be uncoated to ensure droplet adhesion.

4.3.3 Droplet distortion

Two effects contribute to droplet distortion. Initial distortion of the liquid droplet on the wire is an artefact of the measurement technique and should be minimised. Shape and size changes during drying are neither practicable nor desirable to suppress, however.

It is readily observed, and noted by many authors in this field, that a droplet suspended on a wire has a tendency to adopt a slightly pendant shape (Figure 14a), so characteristically indeed that Hecht (1999) refers to it as "the pendant drop method". This shape is of course not representative of a droplet in free flight. There are actually two related effects at work in distorting the drop. The first is capillary creep up the wire, a function of the interfacial tension between the liquid drop and the solid surface of the wire. The second is the force balance between the gravitational attraction of the mass of the droplet and the interfacial tension between the liquid and the air. Correct solution of the force balance is exceedingly complex (O'Brien, 1991), but a simple force balance is sufficient to place a theoretical upper bound of just under 7mm diameter for a spherical water drop, rather less for materials of industrial interest which often exhibit air-liquid surface tension in the range 35 - 45 mN/m. It was found that near spherical water droplets could be created when the diameter was 2 - 3mm (Figure 14b), but the upper limit on droplet diameter was much less than the theoretical prediction. This may reflect trace impurities in the water lowering the surface tension.

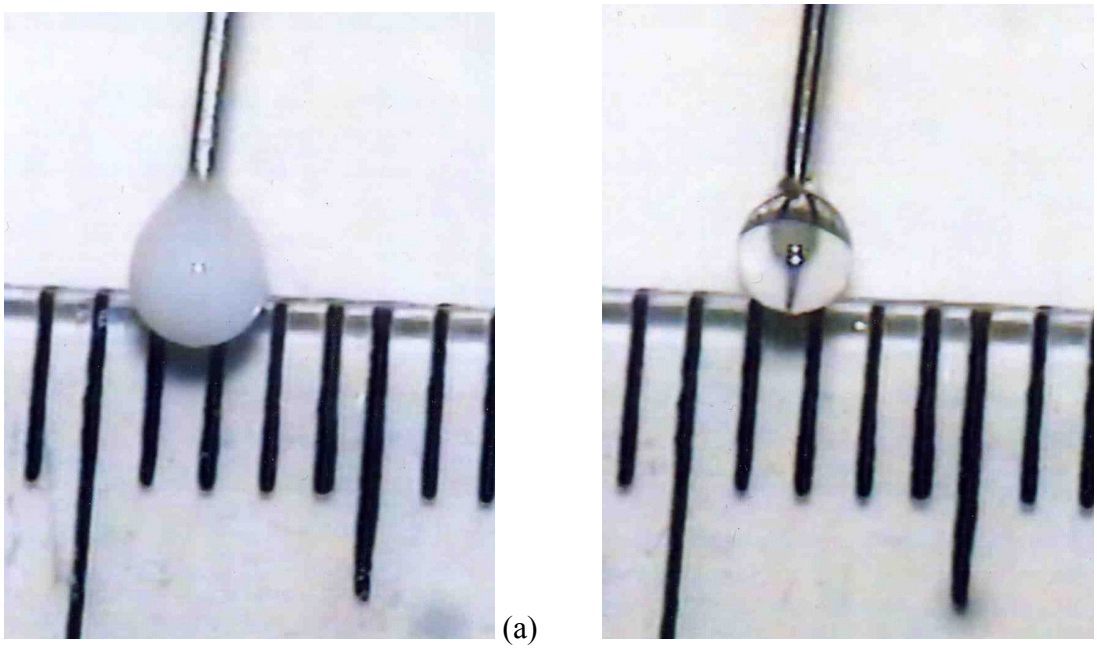

(a) (b)

Figure 14: droplets on a wire. (a) 30% starch dispersion in water, (b) water. Scale graduations are mm. (ICI - David Willox/Roger Watson)

4.3.4 Droplet oscillation

Several authors have noted that droplet oscillation enhances the evaporation rate (Yao and Schrock, 1976, cited in Nešić and Vodnik, 1991, Oteng-Attakora and Mumford, 1994b). Oteng-Attakora and Mumford hypothesised that the stretching of the droplet surface film or crust during oscillation increased porosity. Walton (2004) reports droplet oscillation in all experimental conditions in his single droplet drying experiments. This in itself will not necessarily give rise to an artefact in measurement, however. It is consistent with the observed behaviour of droplets in sprays, as seen in Figure 15.

Figure 15: droplet oscillation; droplet stream from breakup of a single jet of 40% solution of glycerol in water, captured under strobe lighting. (ICI - Fanny Briand)

4.3.5 Premature evaporation

Experience gained with the wire deflection apparatus previously described showed that even with skill, it is tedious and slow to place a droplet accurately upon the tip of the wire. Even if the flow over the droplet has been stopped, radiation from the preheated chamber walls causes evaporation during the placing of the droplet and the commencement of the experiment. It has been reported that radiation accounts for a large fraction of the overall heat transfer at or above 200°C (Yuen and Chen, 1978, Walton, 2004).

Therefore it is desirable if the measurement chamber can be kept cool and draught free during the placement of the droplet, so the apparatus has been provided with a hot-air diversion, so that the flow and temperature controls can be stabilised on start up, without heating the chamber.

Also to minimise radiative heat transfer, the glass measurement chamber is externally silvered except where a direct view on the droplet is required. This also provides a

means to dissipate any accumulated static charge. This is helpful to avoid small droplets adhering to the chamber walls in preference to the wire tip.

4.3.6 Radial deflection of the droplet

By far the most troublesome aspect of the design of the apparatus was found to be the minimisation of radial deflection of the droplet, which is manifest directly as balance error. The velocity profile of the air must be flat, so that there is no lift on the drop from differential velocity over the top and bottom surfaces, which are manifest as a systematic error in balance reading. Also, turbulent velocity fluctuations must be minimised, again to suppress lift from differential velocity, but manifest as random error in the balance reading.

Uniform, parallel and low turbulent airflows are also the specification for wind tunnels, so wind tunnel design methodology was employed, especially Barlow et al. (1999), the standard reference work. Additional references have been used both for clarification and also to inform design decisions where alternatives are presented (Mehta and Bradshaw, 1979, Bradshaw and Pankhurst, 1964, Eckert et al., 1976). Both flow uniformity and reduction in the magnitude of turbulent velocity fluctuations are achieved by passing the airflow through a series of fine gauzes, where non-uniformities are reduced by that for a single screen raised to the power of the number of screens (Barlow et al., 1999). Goodfellow Ni008705 is the commercially available mesh which best meets the criteria of temperature and corrosion resistance, small mesh size relative to the droplets, and maximum pressure drop coefficient whilst having sufficient open area to avoid a known flow instability (Mehta and Bradshaw, 1979, Barlow et al., 1999). However, even with this screen, theory suggests that between fifty and one hundred screens in series are required to sufficiently damp out turbulence. In order to perform their job as intended, these screens must be held taught to prevent "flapping" instabilities, and parallel to each other, perpendicular to the direction of air flow. Clearly this is exceedingly difficult to construct. The solution arrived at, in collaboration with Mr. John Putson of Cordell Fine Mechanics, is shown diagrammatically in Figure 16 and in the photograph Figure 17. The outer pressure shell is one and a half inch outside diameter stainless steel tube, with a rather thin wall. This outer tube was filled with annular aluminium split rings, with inner diameter equal to 22.1mm wind tunnel test section, and with outer diameter just fractionally less than

the inner diameter of the housing tube. These aluminium rings were made 6mm thick, dictated by a rule-of-thumb that minimum inter-screen separation should be 500 gauze wire diameters (Barlow et al., 1999), and also by the requirement that the ring must be pushed square down the tube without rotating and jamming against the tube wall. A circle of screen was punched out from a sheet, and wrapped around the aluminium ring, so that the action of pushing the screen and ring together down the tube acted both to tauten the screen and to hold it in place. This required several iterations in order to get a reasonable degree of restraint of the screen by the close fit, without tearing the screen in the process. Finally, the stack of discs and screens was compressed as the Swagelok compression joints were pulled up. This ensured that the screens were tightly retained. The shortest possible sections of tube were required, to minimise the length that the rings had to be slid down the tube. The minimum length of tube between two Swagelok joints is available as a special "port connector" fitting. This has the particular advantage for this purpose that it is a machined part, with a much closer tolerance on circularity and inner diameter than a drawn tube. However, at one end these port connector fittings do not draw up against the tube stop. A custom tube stop insert was constructed, and is shown in Figure 17, to compress the disc stack whilst ensuring that the pressure seal was maintained.

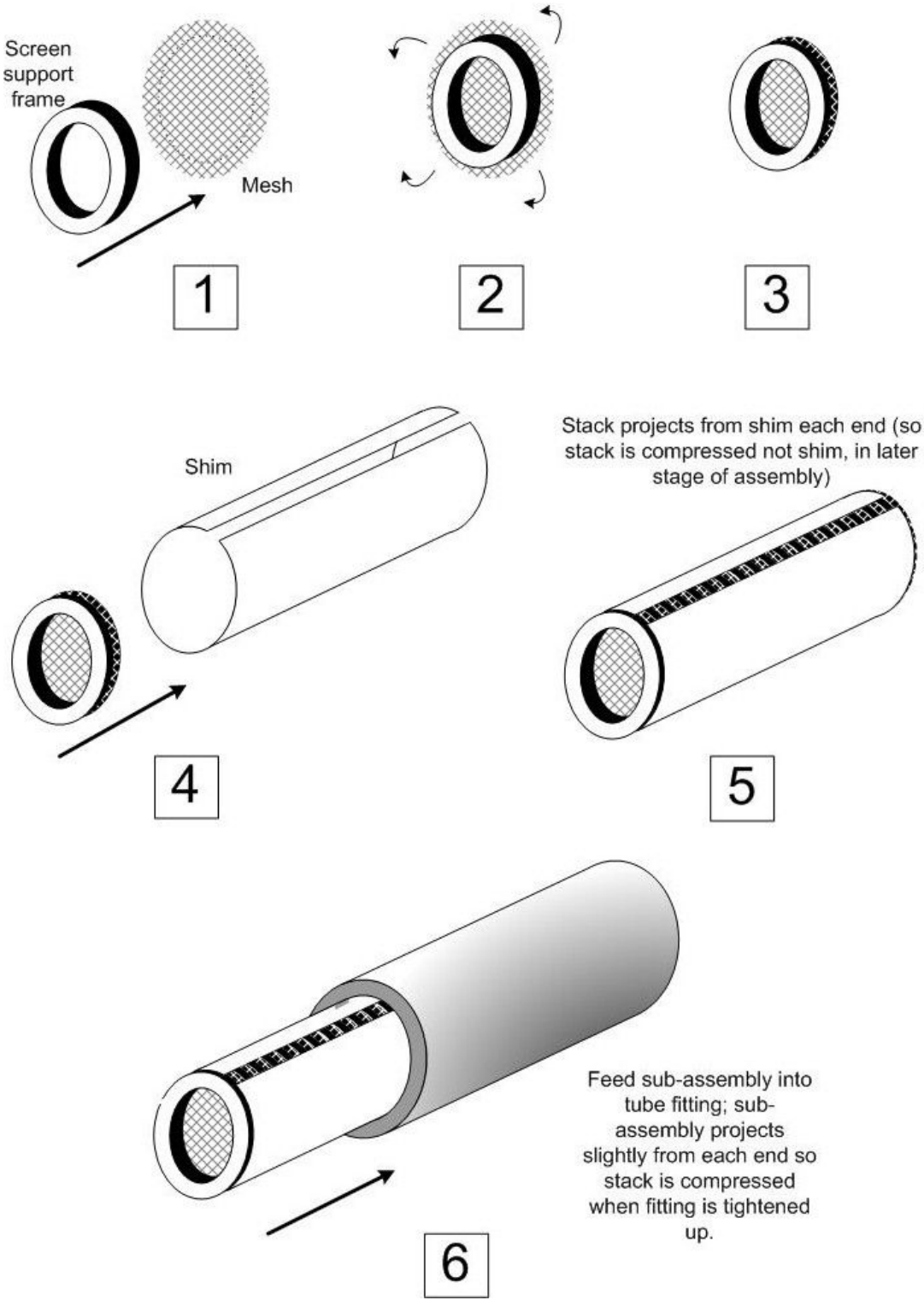

Figure 16: sketch of assembly method for retaining the series of flow conditioning screens into the wind tunnel

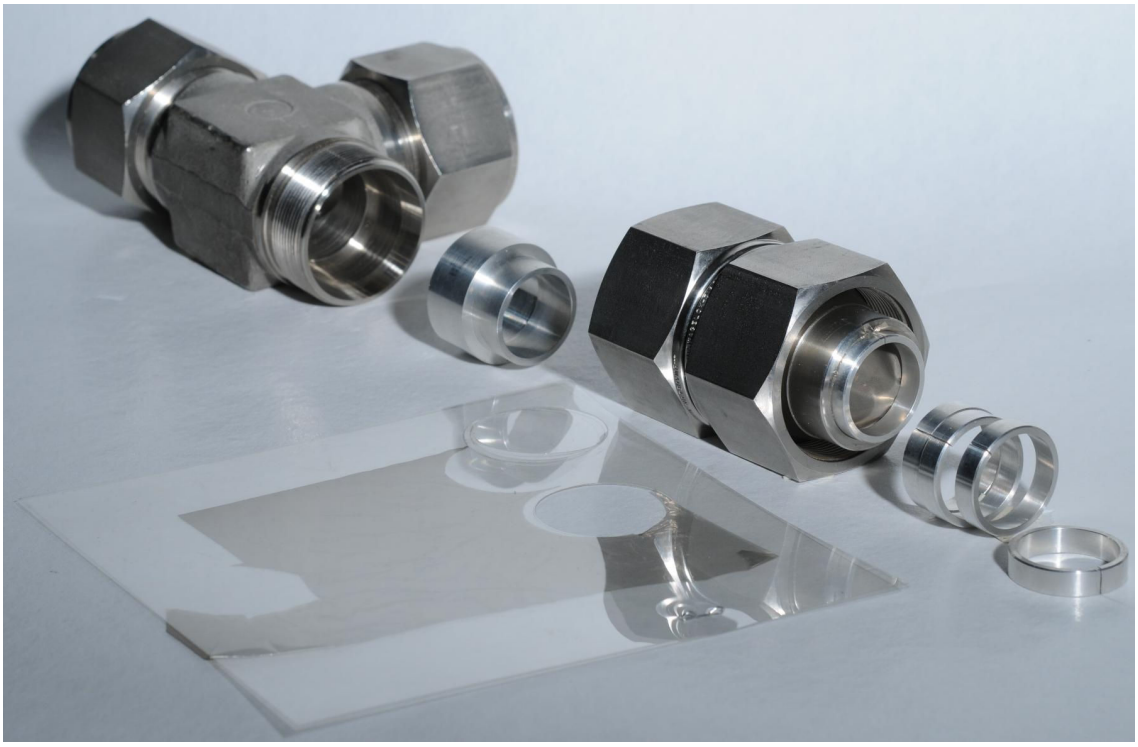

Figure 17: photograph showing an exploded view of the first wind tunnel section with flow conditioning screens. Four of the retaining split rings are shown bottom right. Behind and above them in the mouth of the adjacent wind tunnel section, a partially inserted ring and its screen can be seen. Behind the wind tunnel section is the back retaining stop, and then the tee-piece inlet junction to the flow diversion. The sheet of screen from which the section have been cut is shown in the foreground. In order to cut the circles from the sheet neatly without tearing the delicate screen, they were punched straight through the plastic envelope in which the screen was supplied.

4.4 Conclusion

An apparatus based on an ultramicrobalance has been designed to address limitations with other techniques used to measure the drying rates of droplets of film forming materials.

CHAPTER 5 - DROPLET SIZE DISTRIBUTION FOR THE ACOUSTIC ATOMISER

In a preliminary version of the analysis which follows in Chapter 6, a log-normal distribution was used as a model for the droplet size distribution from the Acoustic Atomiser. It had previously been established that a log-normal distribution appeared to be an acceptable fit to sieve-sizing data for a material made using the Acoustic Atomiser (Dataset B shown Figure 25). However, the log-normal spread parameter σ_g, (the geometric standard deviation) was not estimated from that set of sieve-sizing data alone, but from two metrics used in ICI, which were based on both research and production plant experience. The first metric was a historical rule-of-thumb that 95% of the weight distribution of spray-cooled product ("*Material A*") from the Acoustic Atomiser was less than 4/3 of the mode size. The second metric was polydispersity index (PDI) = 0.4 , where the PDI is defined as $(dv_{90}-dv_{10})/dv_{50}$ by percentiles of the weight distribution. The PDI value was established as the smallest spread that was obtained for experimental spray-dried powder ("*Materials D*"), when all the powder dried to a single morphology (Fiannaca and Threlfall-Holmes, 2005). PDI = 0.4 is thus a measure of inherent atomisation spread, as little as possible conflated by spread due to morphology changes on drying. The two metrics both gave 1.17 as the fitted value for σ_g. Such agreement is most satisfactory, and was sufficient to demonstrate the principle of the analysis method in Chapter 6, as presented in a conference paper (Threlfall-Holmes, 2008).

As the Acoustic Atomiser is novel, there are no independent published sources of its droplet size distribution and the metrics described above for the spread of the particle size distribution lack authentication. In this chapter a more rigorous fit to a range of experimental size data will be substantiated, before proceeding to the analysis in the next chapter. Since the physics of atomisation are not completely understood, it is not the normal expectation to be able to select an appropriate function *a priori*, and a selection of likely candidates are tested. It is found that the best fits are obtained with the Stable distribution. This has not previously been reported to be applicable to spray size distributions. Surprisingly, there appears to be some scientific rational for the values of the Stable parameters, tending towards the Gaussian limit for inviscid fluids, and moving towards the Lorentz limit as the viscosity increases. This is consistent with behaviour as a simple or damped forced resonator respectively.

5.1 Droplet size distribution data sources

There are a variety of data sources for the droplet size distribution from the Acoustic Atomiser. The sources are described in the following sub-sections: tabular and graphical data are in Appendix A. The data sources cover a variety of materials, spray-dried and spray-cooled, with mean sizes varying over two orders of magnitude and flowrate ranging over four orders of magnitude. The data have been measured by a selection of techniques. A few datasets are measurements of liquid droplet size, but most are measurements of solid particle product, i.e. incorporating dispersion in particle size due to morphology and size changes during solidification, as well as due to variations in droplet size from the atomiser. Whilst the datasets are thus individually rather noisy, we can be confident in the robustness of a fit to such a range of data.

5.1.1 Water

A single laminar jet of water was measured by Phase Doppler Anemometry (AEA Technology PD Lisatek). The PDA technique is considered the reference standard in sprays sizing, as it measures size and velocity simultaneously from first principles of optics, and hence requires no calibration. It measures droplets passing through the intersection of four laser beams. This point is rather small - around 1mm³ in our instrument. Hence the measurement in this case is naturally of droplets in the stream issuing from a single jet. To obtain the size distribution from a whole sprayhead, would require traversing the head so that each jet in turn was in the probed volume.

The PDA instrument measures a number distribution, in discrete diameter bins rather than continuous. The droplet size distribution peaks from a single resonant nozzle are very sharp, and this PDA is an old design, so the bins are not as finely spaced as would be ideal for resolution of the shape of the peak. However, the spacing of the bins is sufficiently fine that there is little error in the instrument's conversion to volume distribution using the upper limit diameter of the bin, and it is this data which is quoted in Appendix A.1. Volume distribution data have been chosen, as this is the natural representation of data from sieve sizing, which is not only the most abundant source of size data for the Acoustic Atomiser, but also is discretised rather coarsely, so the alternative strategy of conversion of sieve sizing data to a number distribution for comparison with PDA data would create serious error.

5.1.2 Spray-cooled materials A and B

Datasets A (Appendix A.2) are sieve size data for a spray-cooled product Material A made in production plants operating at between 60 and 80 te/hr. Dataset A1 is from samples collected at approximately half-hourly intervals during a commissioning trial of the Acoustic Atomiser. Datasets A2 and A3 are daily production logs from two different plants, each covering a month of operation.

Datasets B (Appendix A.3) are sieve size data for spray-cooled product Material B, made in a 2 kg/hr pilot tower at ICI Wilton.

5.1.3 Spray-dried material C

Material C was a spray-dried product, but the size distribution data are of the liquid droplets in the spray using PDA (Appendix A.4). Datasets C1 and C2 are measurements made on single nozzles. Dataset C3 is the cumulative droplet volume distribution curves from a 1 te/hr Acoustic Atomiser, compared with the rotary atomiser that it replaced. The original PDA frequency data tables are not available for this dataset, and the data have been digitised from the secondary source of the plotted graph.

5.1.4 Spray-dried materials D

Materials D are a range of spray-dried powder products made in a pilot spray dryer at ICI Wilton at 1 - 5 kg/hr. Powder product size distribution was measured for some samples by sieve sizing (Appendix A.5), and for others by image analysis (Oxford Lasers Visisize) (Appendix A.6).

In the Visisize image analysis sizing, the powder was fed from a hopper using a vibrated feeder, with the vibration amplitude carefully adjusted so that the flow of powder through the field of view of the instrument was maintained sufficiently dilute that individual particles could be properly resolved. The image analysis algorithm in the instrument software determines an area and a perimeter of the objects passing through the field of view, with corrections and rejections for various artefacts such as out of focus objects and dust spots on the lens. The diameter of an equivalent circle is calculated from the area. The area and the perimeter together can be used to test the

assumption of sphericity, in a shape factor which is the ratio of the perimeter of an area-equivalent circle to the measured perimeter;

$$\text{circularity} = \frac{2\sqrt{\pi.\text{Area}}}{\text{Perimeter}} \qquad \textit{Eqn. 5-1}$$

Most of the datasets in Appendix A.6 were filtered for gross non-circularity during acquisition. A further analysis of non-circularity has been carried out, see section 5.2.2.

The Visisize instrument creates a count of particles as a function of their area. As with the PDA data, this number distribution has been transformed into a volume distribution. The original datafiles were available electronically, so the conversion to volume could be made directly on the 0.1µm precision to which the diameter data was computed by the instrument. Hence there is negligible loss in precision through the transform. With the lens and camera used for these measurements, the calibrated resolution is 7µm/pixel, with a minimum resolvable diameter of 30µm. The loss in precision in the transform from a number to a volume distribution is an order of magnitude less than the inherent resolution accuracy of the data even in the fine droplet tail, where the quantisation by pixilation of area and perimeter measurements is most severe.

It can be seen in Figure 18 that the number distribution is quantised by discrete number counts at a diameter increment. These horizontal bands in the number distribution become cubic curved bands in the volume distribution: these are not a reprographic artefact. Each point on these frequency plots represents the frequency at a 0.1µm diameter increment. There may be many empty size bins between each plotted point, as shown on the inset graphs: this is not apparent on the full range axes due to finite printable and visible line width compared with bin width. The empty bins need not confound numerical fitting algorithms, hence numerical fits have been made to this unprocessed data. However, the visual impression of the frequency spectra is erroneous. Hence to depict the goodness-of-fit of theoretical distribution curves to these data, they have also been plotted as histograms, where the bin size was manually iterated until it was sufficiently large that spurious peaks of noise disappeared but the underlying shape of the distribution was not lost. Bins were typically a fixed width of a few µm, up to typically 120% of the fiftieth percentile of the volume distribution (dv_{50}), and thereafter the bins were linearly increased in bin width, typically to 10 - 20µm width at maximum diameter. It is emphasised that this is purely to aid visual evaluation of fit curves, and the arbitrary histogram bin size is hence defensible.

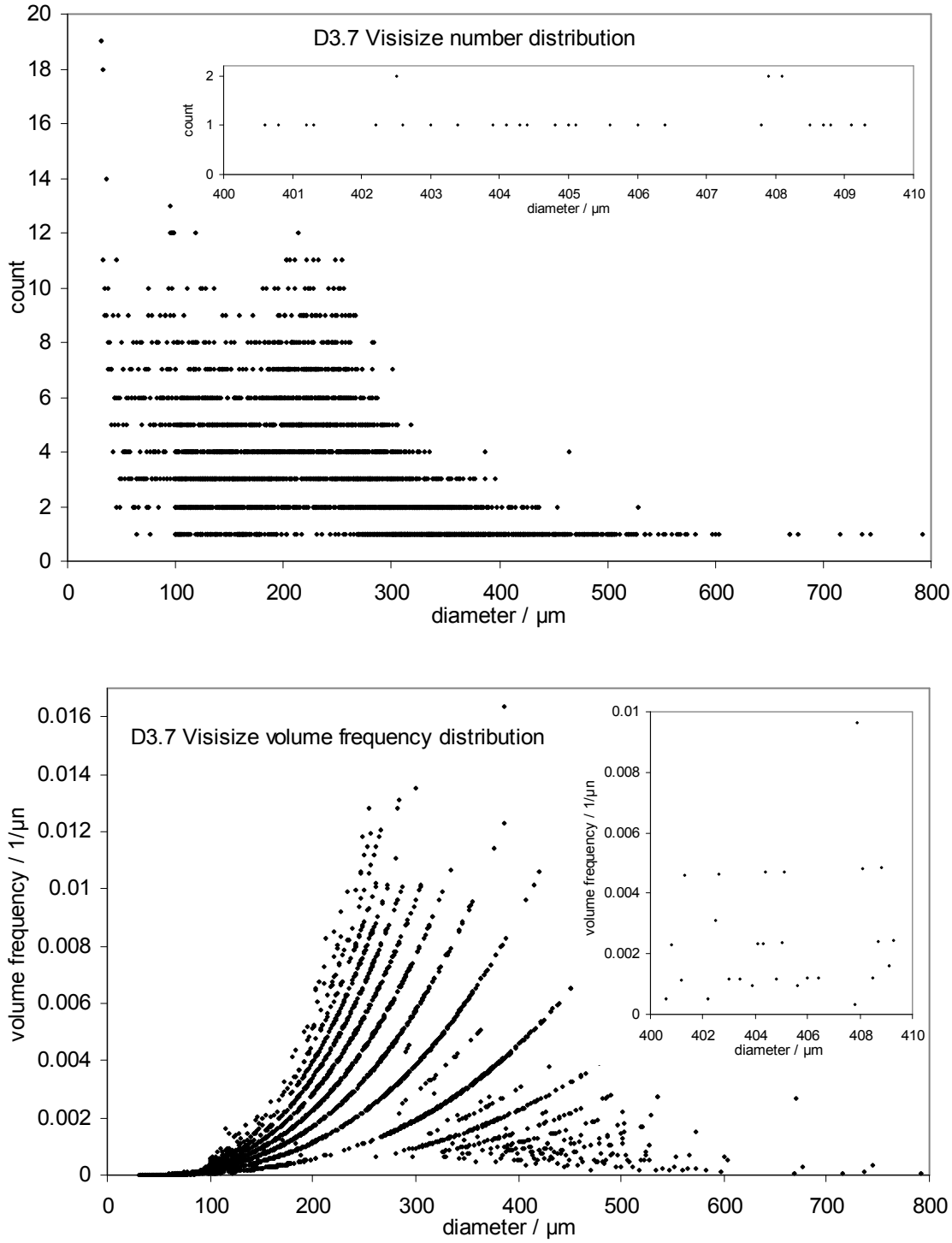

Figure 18: effect of count quantisation in the Visisize data

5.2 Droplet size distribution artefacts

5.2.1 Steady satellite droplet formation

When the driving frequency for jet break-up is not quite at resonance a small satellite droplet can form between each main droplet (Bousfield et al., 1986) (Figure 19). The breakup still appears to be uniform under strobe lighting. The satellite droplets are small. In the materials D spray drying experiments, the jets were imaged with a low resolution CCD camera, through a sight glass and across the body of the spray dryer. Hence it is understandable that the operator did not always observe the satellite droplet formation and tune them out. However, the consequence of steady satellite formation is that some of the particle size distributions are bimodal (e.g. Figure 27). Satellite droplets can also occur by a different mechanism, for non-Newtonian jet rheology from the collapse of "beads-on-a-string" formations (Figure 20) (Clasen et al., 2006a). Such "beads-on-a-string" structures would have been visible to the operator, so are a less credible explanation for the bimodal product size distributions in these experiments.

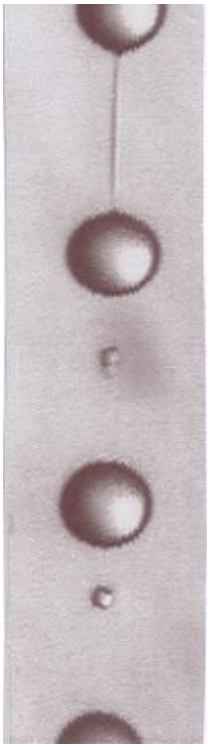

Figure 19: steady satellite droplet formation from a vibrated laminar jet 80% glycerol, 500µm nozzle, 4.3m/s jet velocity, 2.3kHz driving frequency. Fanny Briand, 1999, ICI Wilton.

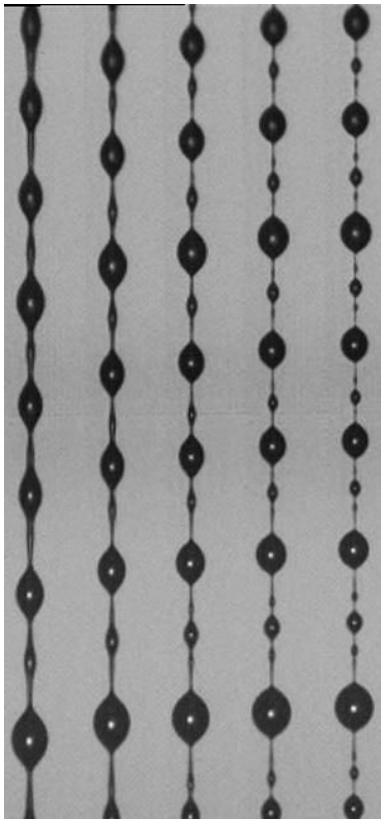

Figure 20: sequence of evolution of iterated beads-on-a-string structure (Oliveira and McKinley, 2005).

5.2.2 Orifice size variation

Multiple peaks that are too similar in peak location and volume fraction to be satisfactorily explained as satellite droplet peaks can be observed in a number of the materials D datasets. A particularly clear example is Dataset D7.9 (Figure 21). The Acoustic Atomiser used in these experiments had orifices in removable inserts, so that the diameter, number and patternation of the orifices could be varied between experiments. Inconsistency in the orifice diameters fitted to the atomiser is the most likely explanation for the multiple peaks. The manufacturing tolerance on the diameter of the orifice in the inserts was not always as tight as would be desirable. Great care was taken to segregate orifices of different diameters, but it is also possible that sets of orifices were mixed up.

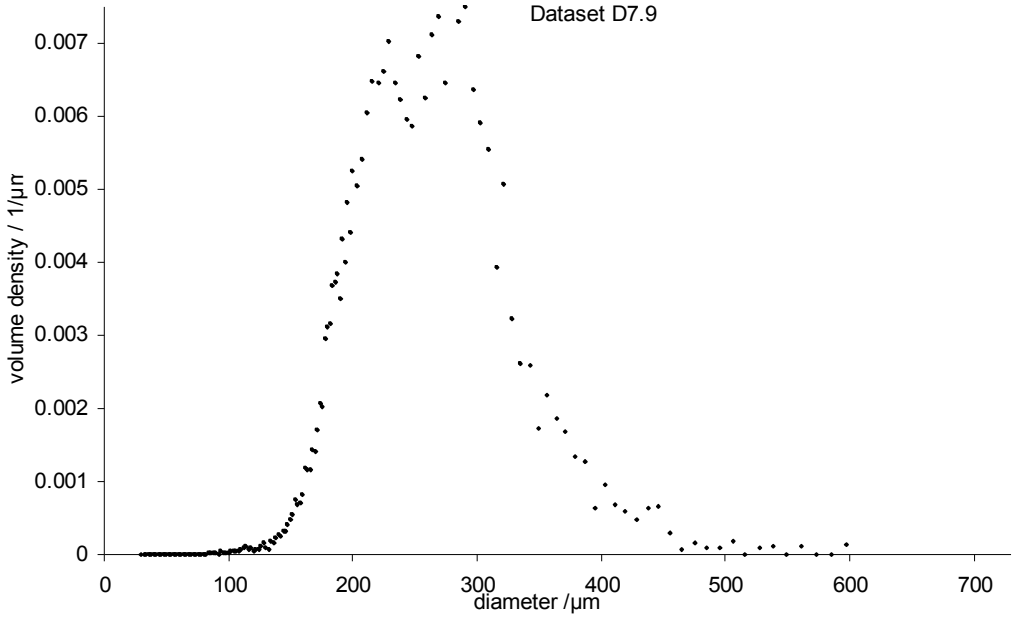

Figure 21: example of multiple peaks, best explained as error in orifice diameters

5.2.3 Agglomeration

Some agglomeration was observed in some of the spray-dried materials D, either by visual examination of the product in the powder collection bucket or by examination under a microscope. These agglomerates appeared to be composed of discrete particles stuck together, rather than a fused mass. This strongly suggests that agglomerates formed during the late stages of drying from solid but still sticky particles rather than wet liquid droplets. The presence of agglomerates indicates that the powder may not have been fully dry. The result of agglomerates in the product is noisy scattered tertiary

peaks in the droplet size distribution at large sizes (e.g. Figure 27). As it occurs at large sizes, the data scatter from agglomeration may appear to be large in a volume distribution, even when the number of agglomerates in the sample was small.

A check has been made on the Visisize datasets for diameter dependent asphericity (e.g. agglomerates or aspherical morphologies in the spray-dried powder). For each individual particle count recorded in the instrumental output data file (i.e. data prior to binning), the circularity parameter has been calculated, and plotted as a function of diameter. An example is shown Figure 22, plots for other datasets can be found in Appendix A.6.

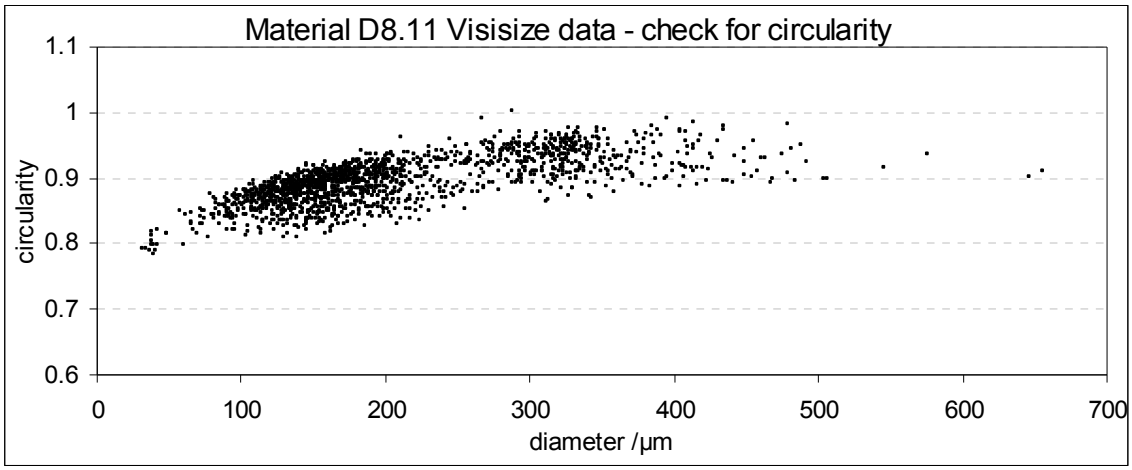

Figure 22: example of diameter-circularity plot check for diameter dependent asphericity in Visisize datasets

In all cases, these plots show that whilst the range of asphericity varied between samples, in any one sample the range of particle asphericity was almost independent of diameter, even when the presence of agglomerates was recorded in the experimental log. That is, for each sample, the primary particles cover as great a range of asymmetry as do the agglomerates, and the shape factor cannot be used to filter out secondary peaks in the size distribution caused by agglomerates. The observable trend in all datasets to reduced asphericity with increasing particle diameter is most credibly an artefact of quantisation due to pixilation in the measurement.

5.3 Droplet size distribution function

A log-normal distribution was assumed in the first instance. The physics of atomisation have not been sufficiently well understood for functional forms to be selected *a priori*,

but the log-normal distribution has been found to fit a number of naturally occurring particle size distributions and is widely used in sprays analyses (Lefebvre, 1989). It has already been noted that the log-normal distribution had previously been considered to be a satisfactory model for particle size data of material made using the Acoustic Atomiser (Dataset B shown Figure 25). Particular mathematical attractions of the log-normal distribution are the ease of transformation from number to weight distributions, the known and mathematically relatively straightforward forms of frequency and cumulative distributions, and that the probability density function is normalised and goes to zero at zero diameter.

However, it has been found that the log-normal distribution is not a satisfactory fit to all the data. In particular, the tails are not well fitted: using statistical tools the tail behaviour is shown to be deviant even for the fit to the Material B data which were the original reference. Fitting the tails is crucial to the credible validity of the analysis performed with the fitted distribution, which relies on comparison of the large diameter tails between distributions. A better fit function has been sought.

5.3.1 Alternative fitting functions

The distributions selected for testing include those used for sprays analysis in the literature, either commonly (log-normal and Rosin-Rammler), or rarely (hyperbolic), and also others selected from statistical literature sources which appeared to have a potentially appropriate peak shape (Laplace, Lorentz/Stable). McLaughlin (1999) was found to be an especially useful source, as not only are an unusually large range of distribution functions described, they are expressed in parameterisations which are conducive to data fitting. The log-logistic and its extension, the Burr distribution, were selected from that source as showing potentially the right sort of peak shape. However, when tested against the data neither was found to be any more satisfactory than the log-normal distribution, and they will not be considered further.

To fit the size distribution data to theoretical distributions, in most cases the Non-Linear Curve Fitting tool (NLFit) in Origin 8 (OriginLab Corp.) was used. This relies on the Levenberg-Marquardt algorithm to minimise the chi-squared deviations of the fit curve from the experimental points. Functions definitions in the tool library were used where available, but in many cases it was necessary to code a function definition. The Stable

distribution function would have been excessively complex to code into NLFit, and in this case an alternative strategy was employed, using a Visual Basic macro behind an Excel spreadsheet to call a third party program to generate the Stable distribution datapoints. This is further described in section 5.3.8.

An Excel spreadsheet was also used for the bimodal fits. Multimodal fitting is possible for many of the NLFit library functions, but excessively complex to code for novel functions used just once as a screening test.

The selection of an appropriate fit function for the Acoustic Atomiser size distribution is made more complex by the variable quality of the experimental data. The high resolution of the image analysis datasets (D4, D7, D8) most clearly shows the shape of the primary peak (Figure 27 for example), but in all these datasets there are secondary peaks which mask the tails of the primary distribution. The sieve sizing data for materials A and B are unimodal, but the diameter resolution is low, so the peak shape and kurtosis are not well defined. The PDA data for water and material C have such sharp peaks that the diameter resolution is low, even though the bin size is fine. To be sure that a distribution function is satisfactory, it must be tested in parallel between the various datasets, in order to check goodness-of-fit to both peak and tails. However, it is impractical and unnecessary to test every possible distribution function against every dataset. To screen the fit functions, datasets A1, B, C, D4.15 and D7.3 were chosen as representative of the range of sources. These show the features of the primary peak at as high a resolution as the measurement technique permitted, with as small secondary peaks as possible. Most of the functions were clearly inappropriate when tested against any one of these datasets and so were rejected without testing them against even the remaining screening datasets. Only the theoretical distributions which performed satisfactorily in screening tests were fitted to other datasets.

The variable quality of the data also explains why a fit function is required at all. We could calculate moments of the raw data without an assumed distribution, but especially the higher moments that would be required for the analysis in Chapter 6 would be unusably variable due to the coarseness of the sieve fraction data and the secondary peaks in the Visisize data. The fit function acts as a filter for the data artefacts.

In the initial screening, volume distributions normalised by the total volume were used, i.e. including any secondary peaks where present. This is ultimately inadequate: a good

fit to the primary peak is impossible if both data and fit are normalised, but there is an appreciable volume fraction of the data in secondary peaks. With distribution functions which appeared on preliminary screening to be about the right shape, the volume fraction in the primary peak of the data was corrected by an iterative procedure using the fit function. The procedure is described in Appendix B. Confining the fit to just the primary peak data is based on the assumption that the secondary peaks arise from ascribable physical phenomena and are not part of the primary atomisation distribution. The validity of this assumption has been tested by performing multimodal fitting (section 5.4).

5.3.2 Determining goodness-of-fit

The goodness-of-fit has been tested by visual comparison on the volume density, the cumulative volume, and a delta stabilised probability (DSP) plot. This latter presentation is derived from the stabilised probability (SP) plot of the cumulative data against the value for corresponding diameter predicted by the cumulative fit function. Figure 23 is an example of the SP plot. Both the data and fit probabilities are scaled by;

$$sp = \frac{2}{\pi}\sin^{-1}\left(\sqrt{p}\right) \qquad \textit{Eqn. 5-2}$$

where p is the probability value and sp the scaled value. This transformation makes the variance more uniform across the distribution, and hence is a much more sensitive test of fit to the tails than a standard probability-probability (p-p) plot (Michael, 1983, Nolan, 2009). If the theoretical distribution tested were a perfect model for the data, the plotted points would all lie on the x = y line. Thus it is straightforward to evaluate goodness-of-fit visually from the SP plot. In addition, a goodness-of-fit statistic D_{SP} has been defined (Michael, 1983): analogous to the Kolmogorov-Smirnov statistic for a standard p-p plot, it is the maximum deviation of the data from the theoretical fit. This statistic can be tested against confidence limits, which depend only on the sample size, not upon the form of the distribution being tested (Lloyd, 1984). This has the huge advantage that the goodness-of-fit statistic can directly be compared between fits of different theoretical distributions to the same dataset. The 95% confidence limits have also been plotted, to further facilitate the visual evaluation of goodness-of-fit.

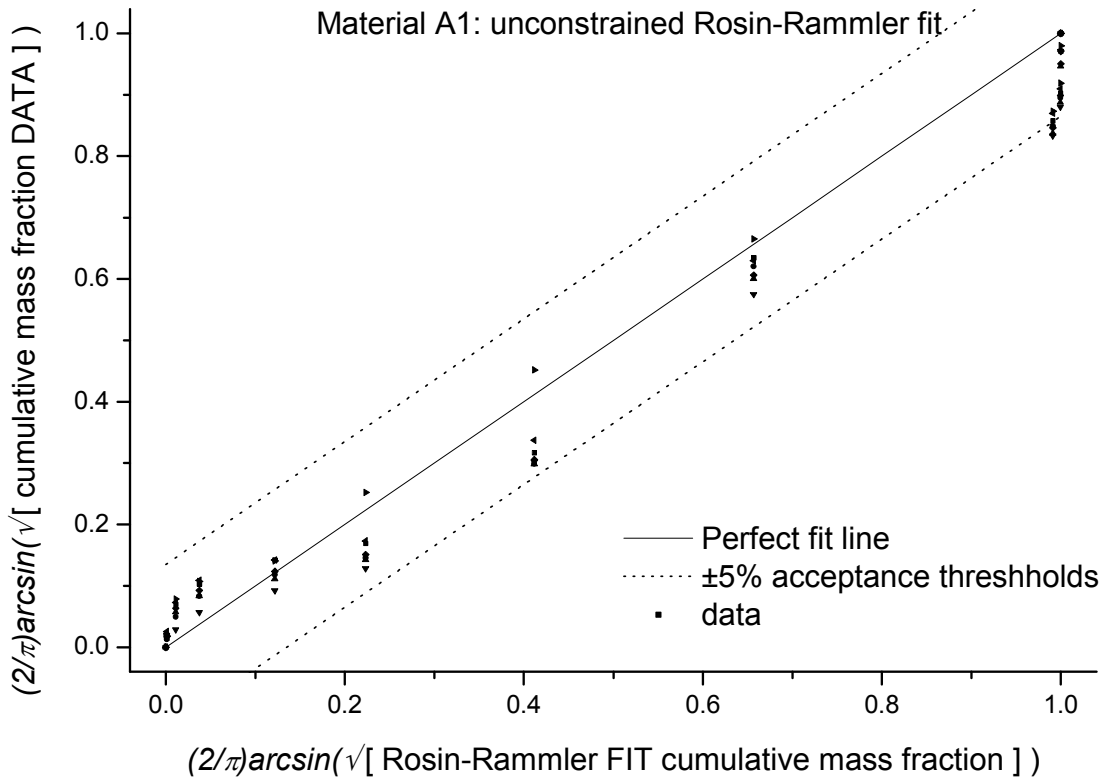

Figure 23: example of the stabilised probability (SP) plot

Michael (1983) only computes the confidence limits up to a sample size of 100, whilst the Visisize data have thousands of discrete diameters. There are no literature tabulations of the limits for large samples, and the method Michael describes for the computation of the confidence intervals is daunting. The pragmatic approach of extrapolating from a curve fit to Michael's tabulated values has been adopted (Appendix C). Even though the extrapolation curve fit is very near perfect to the precision of Michael's tabulated data, such gross extrapolation is of course conjecture, and it incorrectly asymptotes to $D_{sp} = 0.0548$ rather than zero as $n \to \infty$. It is fit for the purpose of discriminating between the various theoretical distributions tested, but it is wise to be especially cautious when the test statistic for the Visisize datasets is close to the confidence limit. Such caution is anyway recommended for the Kolmogorov-Smirnov test on which the D_{SP} test is based (Pollard, 1977).

Most of the area in the SP plot is unused, and it is hard to magnify the area of interest around the perfect fit line. Visual assessment of goodness-of-fit is further enhanced in the delta stabilised probability (DSP) plot, where the deviation of the data from the theoretical fit is plotted against the theoretical fit. In the DSP plot the perfect fit line is $y = 0$ and the acceptance bounds become horizontal (e.g. Figure 24),

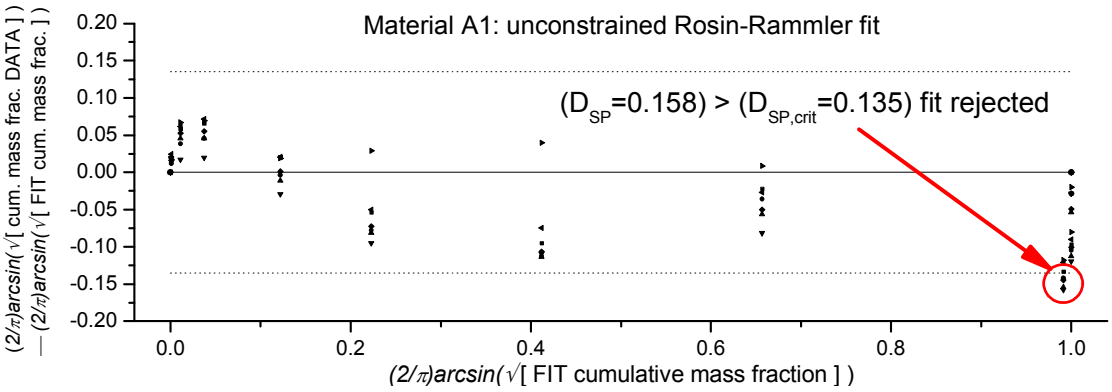

Figure 24: example of the delta stabilised probability (DSP) plot

When performing the fits, from the available sources only the data from where it was indicated that the Acoustic Atomiser was running normally in steady state has been selected. Each dataset is a group of one or more individual determinations of size distribution at a given operating condition. If the sprayhead was truly in steady state, each individual determination of size distribution in any dataset would be a sample of the same time-invariant population. Hence the fit has been performed on the combined data in each dataset. Especially for the larger datasets, fitting to each and every determination would be computationally intensive. It would also detract from the purpose, which is to clarify from the mass of experimental size distribution data, a single fit curve which is characteristic of this type of atomiser. It can be seen in Figure 25 that the expectation of time invariance appears reasonable: the fits to each dataset and the fit to the combined data are only trivially different to each other. In principle it would be possible to demonstrate quantitatively the time invariance of the realisations within the dataset using the 2-sample Kolmogorov-Smirnov test (Lloyd, 1984) to test for confidence that two fitted sample size distributions came from the same population. In practice in this instance it would not improve the reliability of the inference about time invariance. The datasets with multiple realisations are all by sieve-sizing or PDA, with only a small number of datapoints in each realisation, and hence large acceptance bands on the 2-sample Kolmogorov-Smirnov statistic. In this circumstance, the visual check of similarity of the distribution fits between realisations in a dataset (as depicted in Figure 25) is just as precise.

5.3.3 Log-normal distribution

The definition of the log-normal distribution in the Origin NLFit tool library is a generalised form, with a y-offset parameter y_0 and an area parameter A. These were set to fixed values of 0 and 1 respectively in order to obtain the zero baseline normalised log-normal distribution required for this analysis.

in Origin's notation; $$y = y_0 + \frac{A}{\sqrt{2\pi}wx}\exp^{-\left(\frac{[\ln(x/x_c)]^2}{2w^2}\right)} \qquad \textit{Eqn. 5-3}$$

and in the more normal notation used for sprays, for the weight density distribution w(d), with parameters geometric mean and standard deviation, d_g and σ_g respectively;

$$w(d) = \frac{1}{d\sqrt{2\pi}\ln(\sigma_g)}\exp^{-\left(\frac{\ln(d/d_g)}{\sqrt{2}\ln(\sigma_g)}\right)^2} \qquad \textit{Eqn. 5-4}$$

Material B appears to be a reasonable fit to the log-normal distribution Figure 25, with $w = \ln(\sigma_g) = 0.148 \pm 0.002 \Rightarrow \sigma_g = 1.160 \pm 0.003$ from the combined data, which is only trivially narrower than the value of 1.17 derived from the rule of thumb in the original analysis. However the DSP plot reveals deviation in the tails.

The log-normal distribution is not a good fit to Material A data (Figure 26), especially in the large diameter tail. It is possible to force a better fit to the large diameter data (by setting a minimum constraint on parameter w in the solver), but only at the expense of underestimating the peak magnitude by ~50%, which is highly undesirable.

The log-normal distribution fails to capture the peak shape correctly for the Visisize data (Figure 27), and both tails are too narrow. As described in section 5.1.4, the numerical fitting has been made to unbinned data (top plot), but the fits are also shown on binned data (middle plot) for convenient visual assessment of the fit. In the middle plot, two fit curves have been plotted: with parameters fitted to the entire range of data, and with parameters fitted only to the primary peak. It is observed that the fit curves are almost coincident. This was observed to be the case with other distribution functions. Both for brevity, and also to make it clear that it is the quality of fit to the primary peak that is of most interest, only the data match for the primary peak is shown for the other distributions functions in the following sub-sections, and the goodness-of-fit statistic D_{SP} is taken as the maximum deviation in the fitted range of the primary peak.

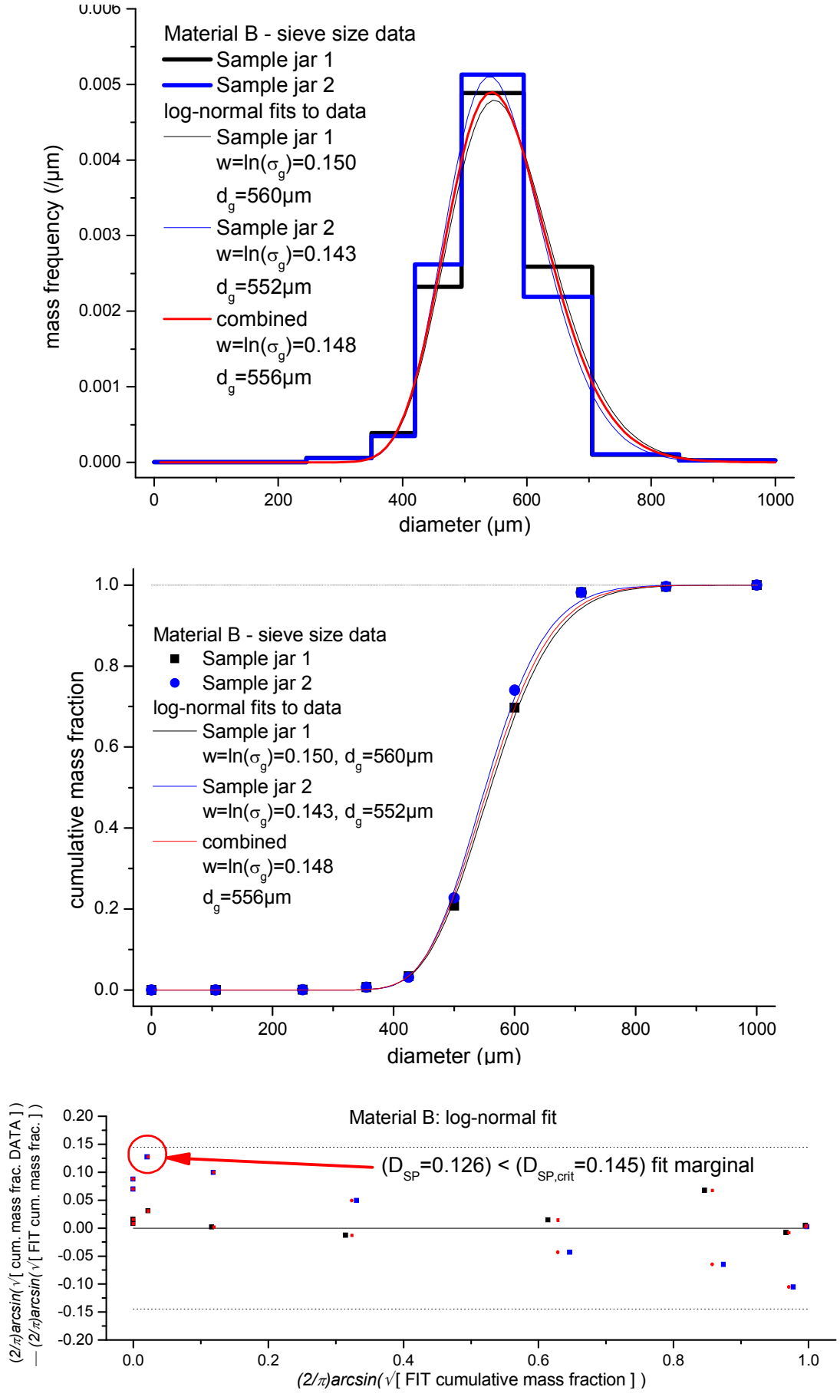

Figure 25: log-normal fits to material B sieve size distribution data

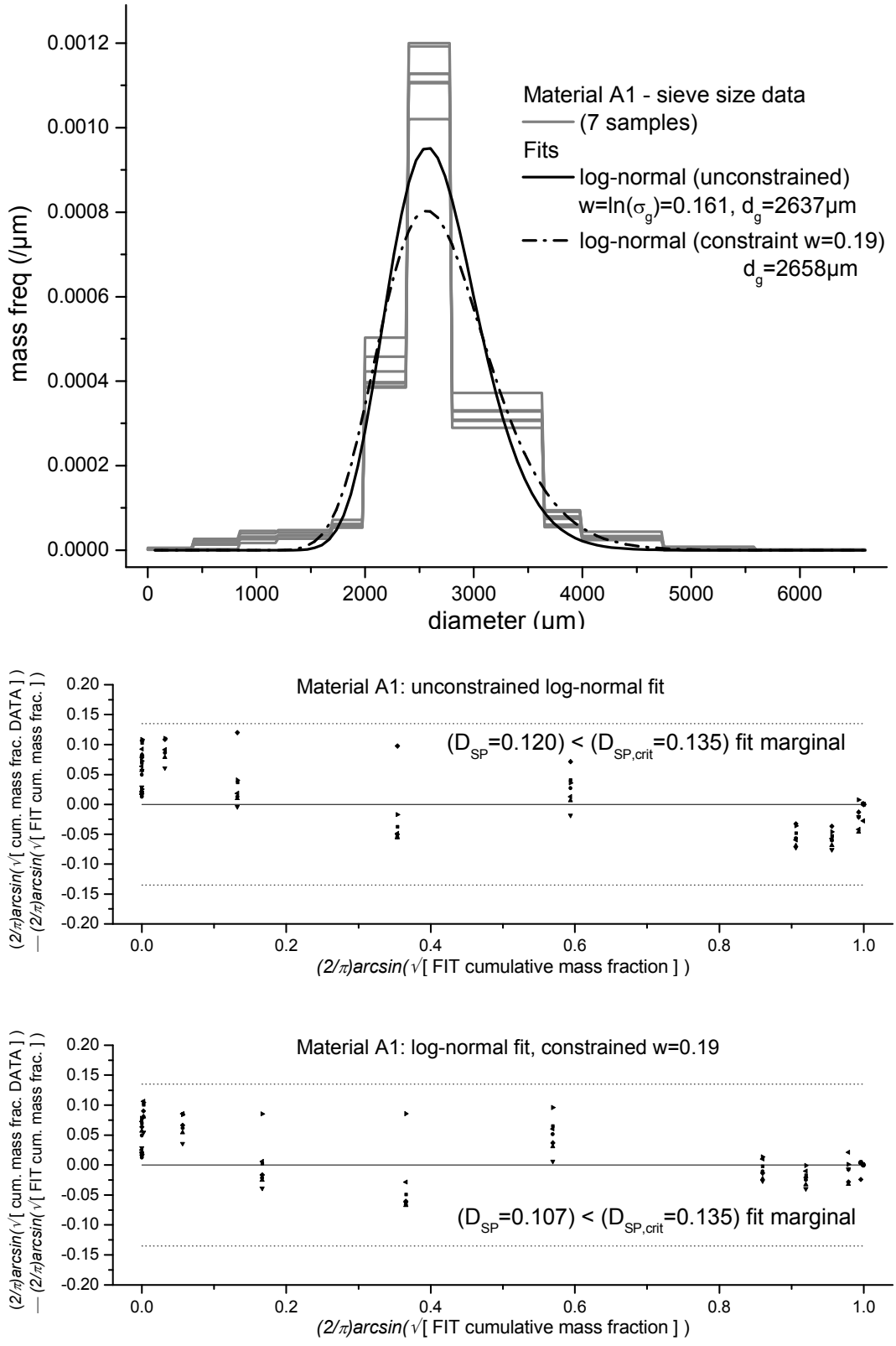

Figure 26: log-normal fits to dataset A1 sieve size distribution

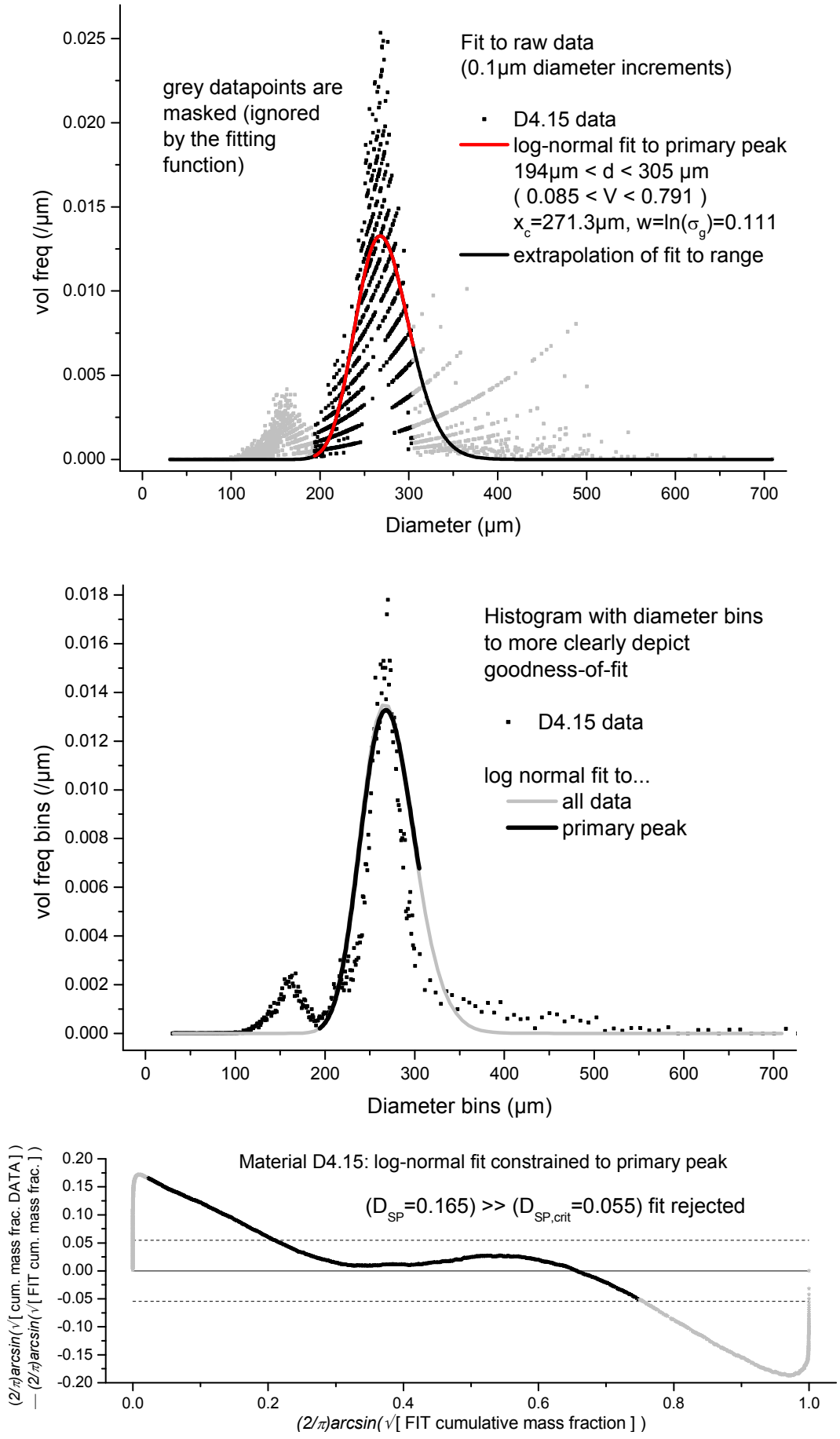

Figure 27: log-normal fits to Visisize dataset D4.15

5.3.4 Rosin-Rammler distribution

The Rosin-Rammler distribution (Eqn. 5-5) is the most widely used sprays distribution, largely because of its mathematical simplicity (Lefebvre, 1989). The function is not in the Origin NLFit library, so Eqn. 5-6 was coded as a user function, with initialisation for the fit parameters for test dataset A1 from Microsoft Excel linear regression of ensemble averaged data (Figure 29). To linearise the data, double logs are taken: this will tend to smooth any dataset considerably, yet in Figure 29 it is already obvious that the fit will be poor. The Rosin-Rammler is often poor at fitting the large and small diameter tails of size distributions (*ibid.*, and personal industrial experience), and it can be seen in Figure 28 that this expectation was realised, the fit to the large diameter tail data is worse than the log-normal.

R-R cumulative mass $$W(d) = 1 - e^{-\left(\frac{d}{d_{RR}}\right)^q}$$ *Eqn. 5-5*

R-R mass frequency $$w(d) = q\frac{d^{q-1}}{d_{RR}^q} \cdot e^{-\left(\frac{d}{d_{RR}}\right)^q}$$ *Eqn. 5-6*

Where d_{RR} is a characteristic diameter and q is a width parameter.

Rizk and Lefebvre have proposed a modification to the Rosin-Rammler which is asserted to be better fit to the large size tail (Eqn. 5-7) (Lefebvre, 1989). The mass frequency distribution was again coded as a user function in Origin NLfit, with initialisation parameters from Microsoft Excel linear regression of ensemble averaged data. Despite the originators' assertion, the best fit (Figure 30) is virtually identical to the parent distribution (Figure 28).

$$W(d) = 1 - e^{-\left[\frac{\ln(d)}{\ln(d_{RLRR})}\right]^q}$$

$$w(d) = q\frac{\left[\ln(d)\right]^{q-1}}{d.\left[\ln(d_{RLRR})\right]^q} \cdot e^{-\left[\frac{\ln(d)}{\ln(d_{RLRR})}\right]^q}$$ *Eqn. 5-7*

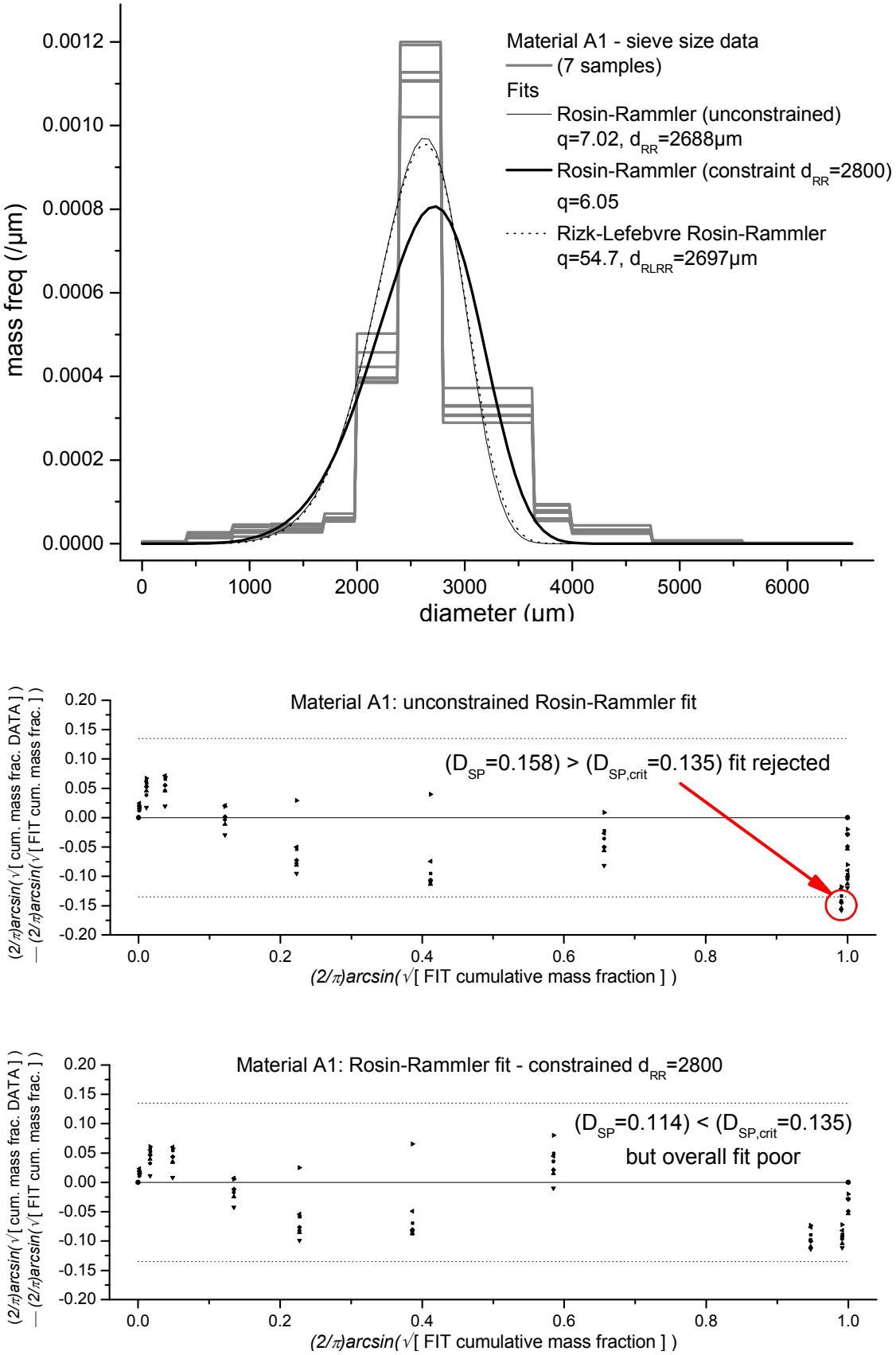

Figure 28: Rosin-Rammler fits to sieve sizing dataset A1

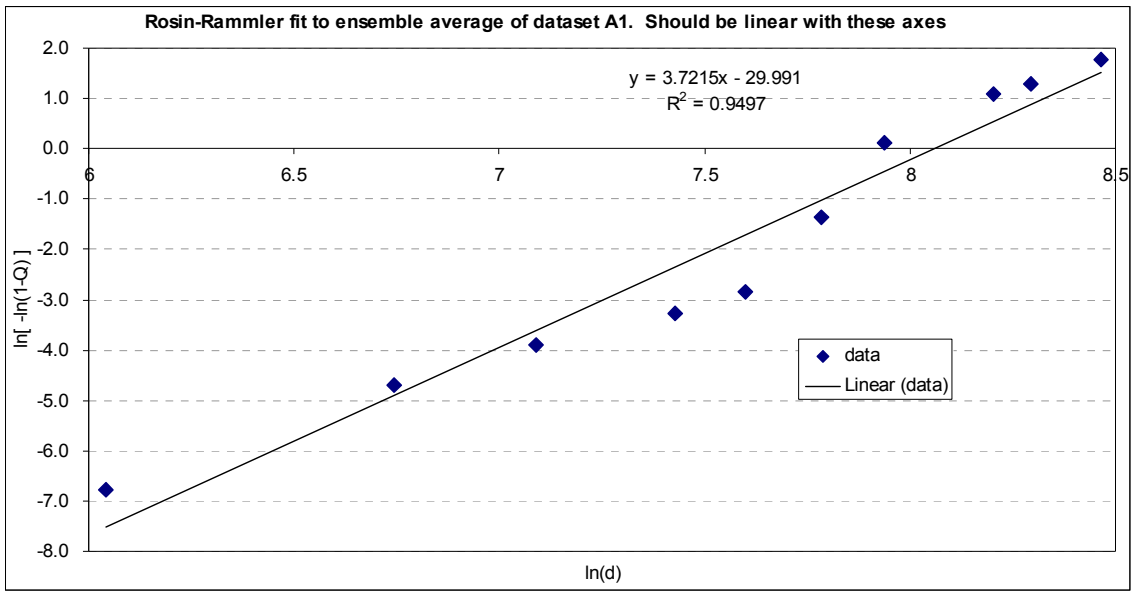

Figure 29: linear regression to obtain initialisation values for Rosin-Rammler fit to dataset A1

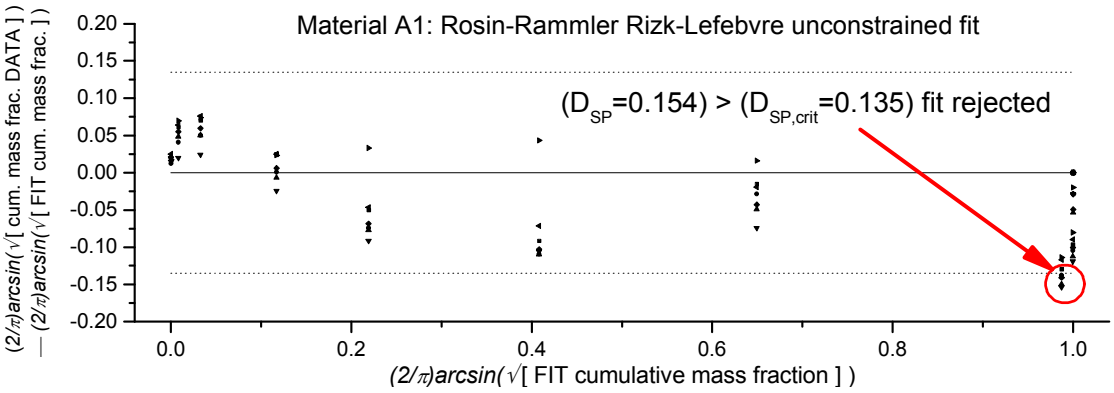

Figure 30: Rosin-Rammler Rizk-Lefebvre fit to dataset A1

5.3.5 Laplace distribution

The Laplace distribution (Eqn. 5-8) is symmetrical about the mean, and hence unlikely to ultimately be the best fit to the right skewed size distribution data. However, not only is the peak shape more credible as a model than the distribution functions tested thus far, the hyperbolic distribution is a superclass which includes the Laplace distribution as an instance. The promising fit of the Laplace distribution to the data indicates that it is worth tackling the complexities of the hyperbolic distribution.

$$w(d) = \frac{1}{2w} \cdot e^{\frac{-|d-d_m|}{w}}$$

$$W(d) = \begin{cases} 0.5e^{\frac{-|d-d_m|}{w}} & d \le d_m \\ 1 - 0.5e^{\frac{-|d-d_m|}{w}} & d > d_m \end{cases}$$

Eqn. 5-8

where d_m is the mean, mode and median, and w is a width parameter.

It can be seen in Figure 31 that the peak shape shows much better concordance with the data than seen thus far, as evidenced by the approximately horizontal central portion of the DSP plot, although the sides of the base of the peak are overpredicted, and the fit is rejected by the D_{sp} parameter. When the peak area is corrected (according to the method described in section 5.3.1 and Appendix B), the fit is numerically acceptable (Figure 32), although it can be seen from the ripple around the baseline in the DSP plot that it is qualitatively not quite the correct description. Note that for the peak area corrections for dataset D4.15 (here for the Laplace fit and subsequently), the estimate of the lower limit of the base of the peak was adjusted from 194µm to 210µm. This was to ensure discrimination of the primary peak from the secondary peak that arises from satellite droplet formation.

The fit to the example sieve dataset A1 (Figure 33) qualitatively shows more clearly than for dataset D4.15 (Figure 31) that a skewed version of the Laplace function would be required for good agreement, but it is again quantitatively accepted by the D_{sp} parameter (the acceptance band is considerably wider for the n = 13 sieve data than for the n ~ 3000 Visisize data).

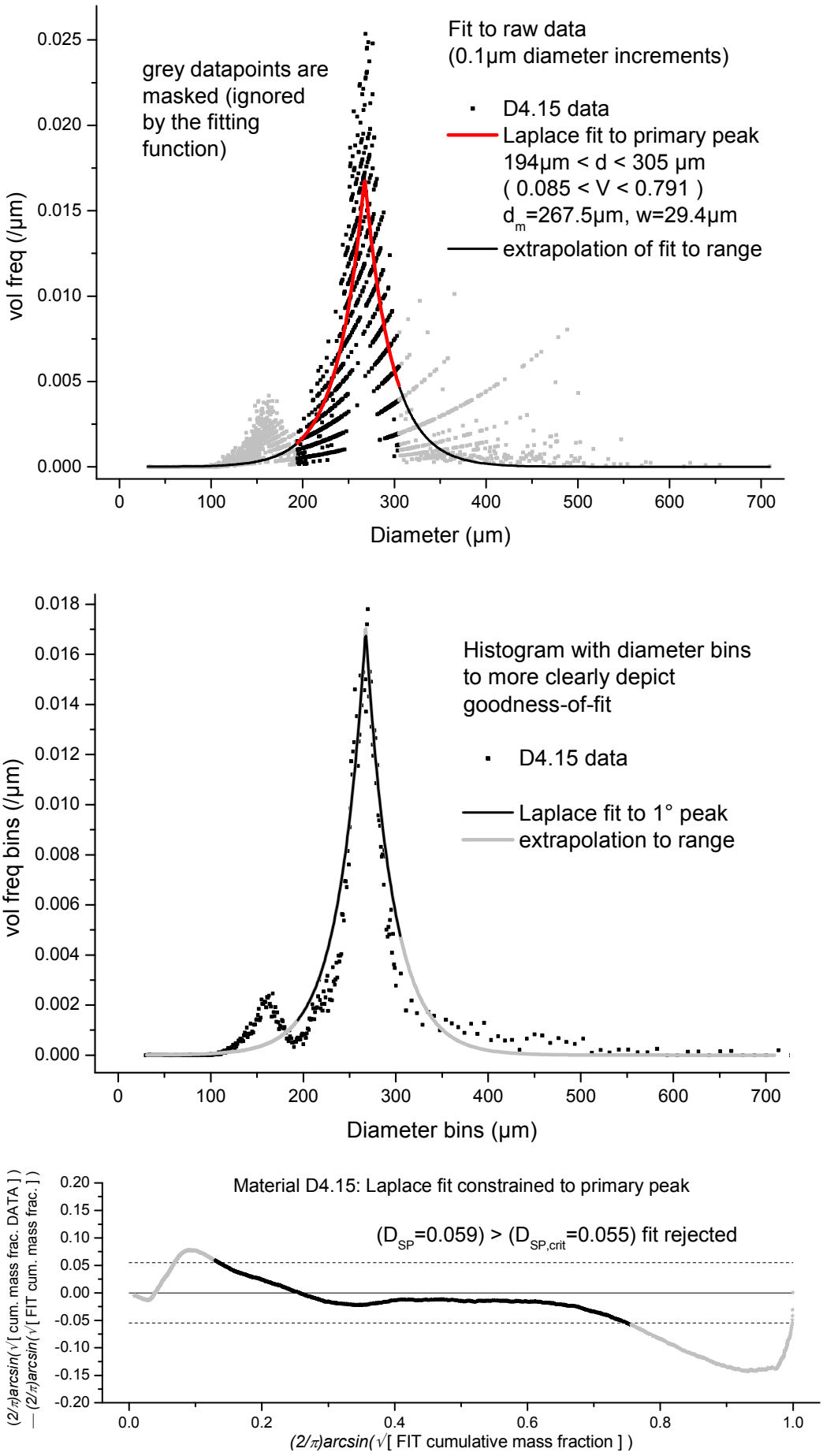

Figure 31: Laplace fit to primary peak of Visisize dataset D4.15

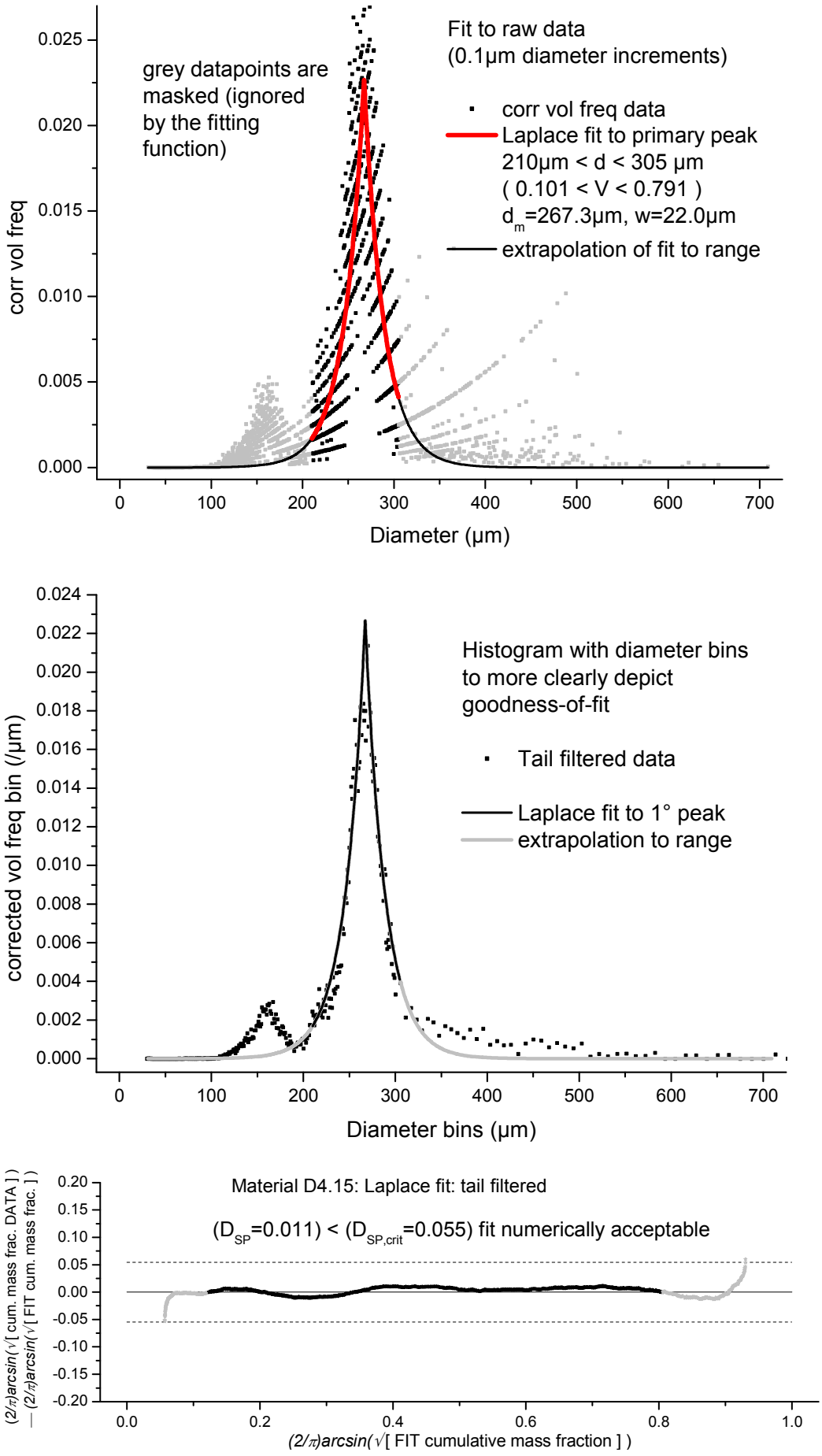

Figure 32: Laplace fit to area-corrected primary peak of dataset D4.15

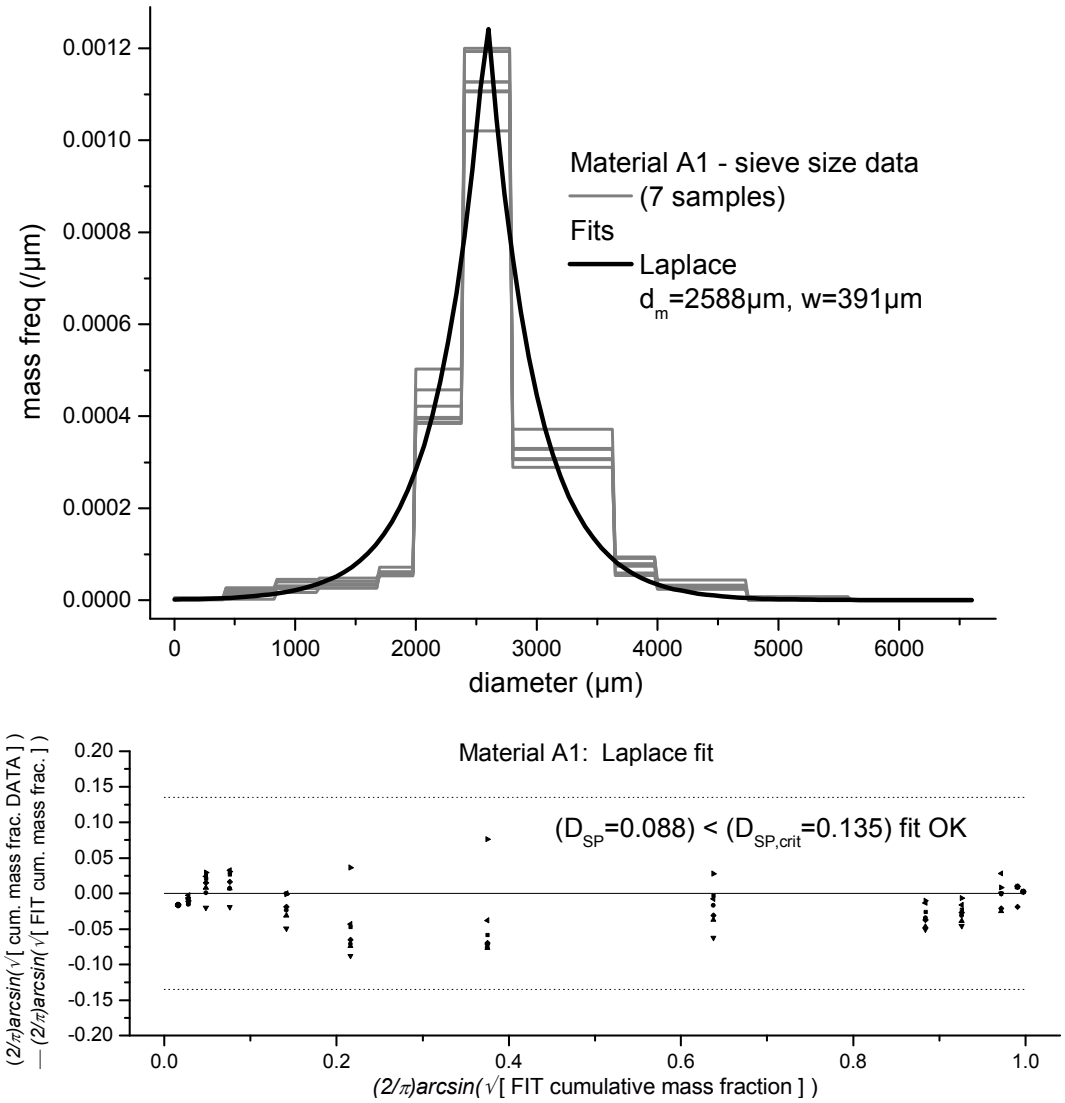

Figure 33: Laplace fit to dataset A1

5.3.6 Hyperbolic distribution

The three and four parameter log-hyperbolic distributions have been shown to be a good fit to spray size distributions (Stanton et al., 1998, Xu et al., 1993), although they appear not to be widely used. This is probably due to a combination of the mathematical complexity and the difficulties and instability of fitting. Xu et al. (1993) have shown that for the 4-parameter log-hyperbolic (4P-LH) distribution, with the likely accuracy of spray size data, the δ scale parameter is so dominant at the distribution tails that the distribution can be well fitted with arbitrary combinations of the α parameter and the β asymmetry parameter. Although this does not allow for easy comparison of parameters between fits to different datasets, it is an inconvenience rather than a fatal weakness. If the fit is good, either it can be visually compared, or some statistics of the distributions,

for example the moments, can be computed and compared between datasets as proxies for the distribution parameters.

The 4P-LH distribution is given by;

$$w(d) = \frac{\sqrt{\alpha^2 - \beta^2}}{2\alpha\delta K_1\left(\delta\sqrt{\alpha^2 - \beta^2}\right)} \exp\left[-\alpha\sqrt{\delta^2 + (d-\mu)^2} + \beta(x-\mu)\right] \qquad \textit{Eqn. 5-9}$$

with parameters α, β (asymmetry), δ (scale) and μ (location), and K_1 is a modified Bessel function of the second kind, first order. The function has again been coded into the Origin NLFit non-linear least squares fitting tool, using the routine s18adc() from the NAG function library for C to calculate K_1.

The cumulative function is undefined. The cumulative volume fraction has been calculated by numerical integration of the density function.

Stanton et al. (1998) recommend plotting the hyperbolic shape triangle (Figure 34) to check that the dataset lies within the parameter space of the distribution. The bounds are given by Eqn. 5-10, and the letters on the bounds in Figure 34 indicate limiting distributions, N = normal, L = Laplace, E = exponential, H = hyperbolic.

$$\xi = \pm\chi \qquad \xi = 1 \qquad \textit{Eqn. 5-10}$$

Values of parameters χ and ξ for the dataset are calculated from the skewness γ_1 and kurtosis γ_2 which are themselves determined from moments m_n about the mean of the distribution of the raw data, where the mean $\bar{d}$ can be found from the ratio of the zeroth and first moment about the origin;

$$\chi = \frac{\gamma_1}{3} \qquad \xi = \sqrt{\frac{\gamma_2}{3}}$$

$$\gamma_1 = \frac{m_3}{(m_2)^{1.5}} \qquad \gamma_2 = \frac{m_4}{(m_2)^2} - 3$$

$$m_n = \sum_0^\infty \left(d - \bar{d}\right)^n .w(d).\Delta d \qquad \textit{Eqn. 5-11}$$

$$\bar{d} = \frac{m_1'}{m_0'} = \frac{\sum_0^\infty d.w(d).\Delta d}{\sum_0^\infty w(d).\Delta d}$$

A practical difficulty is immediately apparent: as noted earlier the higher moments of the distribution are sensitive to the large diameter noise caused by agglomerates. For the example dataset D4.15 (which was selected as a test dataset precisely because the tertiary agglomeration peak is *least* significant), $\gamma_1 = 1.7$ and $\gamma_2 = 4.9$ when all the data are used, and $(\chi, \xi) = (0.6, 1.3)$ plots outside the hyperbolic shape triangle. When only the primary peak data are used to calculate the moments, $\gamma_1 = -0.75$ and $\gamma_2 = 1.8$ and $(\chi, \xi) = (-0.25, 0.77)$ plots within the hyperbolic shape triangle, although the negative skew indicates a *left* skewed distribution. This arises from the choice of truncation of the primary peak.

A three parameter log-hyperbolic distribution has been proposed, which does not exhibit the parameter instability (Xu et al., 1993). The reduced parameter space of the 3P-LH distribution is shown shaded in grey in Figure 34. It can be seen that the example dataset does not lie within these bounds. Hence the 3P-LH distribution will not be considered.

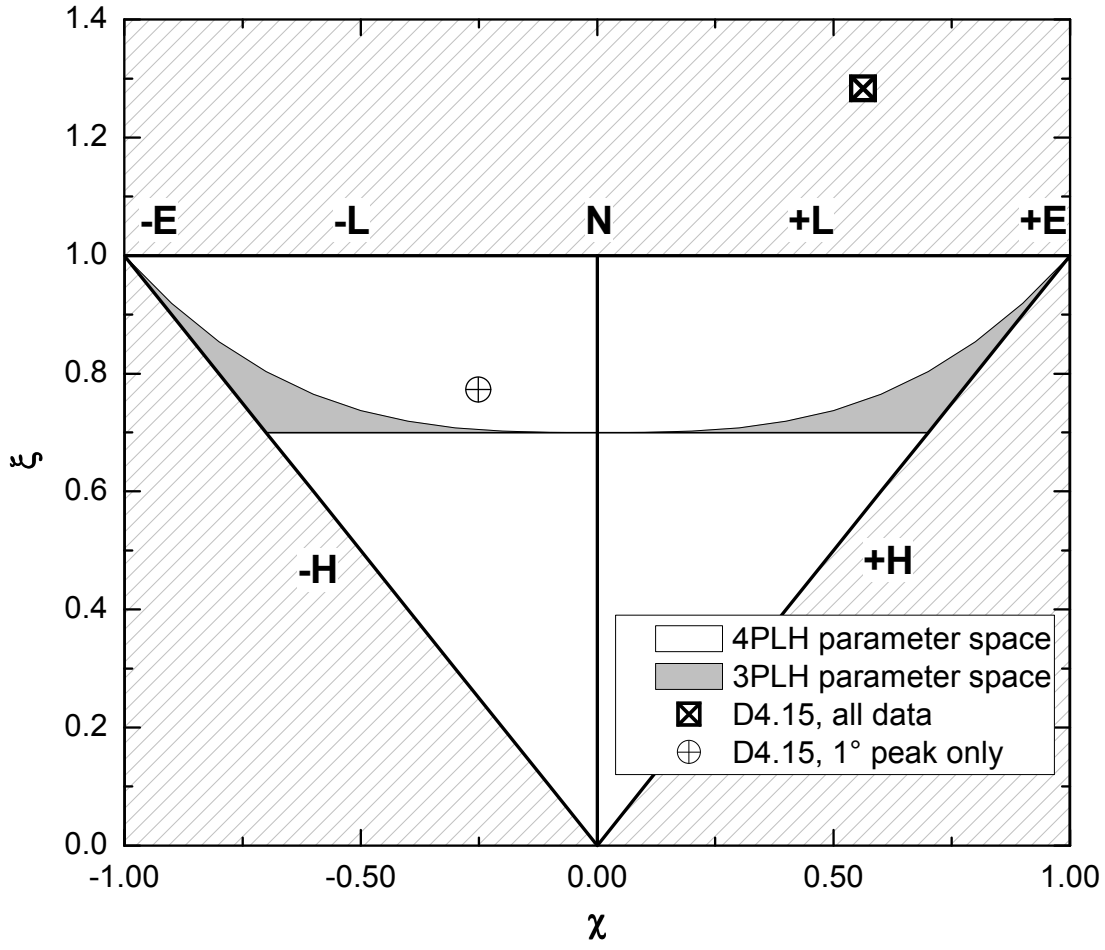

Figure 34: 4P-LH distribution hyperbolic shape triangle for dataset D4.15

In principle initial estimates of the (α, β, δ, μ) parameter set can be obtained from the (χ, ξ) co-ordinates, but it would be unwise given the known instability of the solution and the observed variation in the (χ, ξ) co-ordinate depending on the choice of peak data truncation. An alternative graphical method is recommended to determine initial parameters (Stanton et al., 1998). This was found to not only to give inconsistent estimates for the parameters, but at least for the tested data, the location parameter μ is simply and well estimated as the mode diameter by inspection of the frequency plot of the data. Convergence was stable for any reasonable initial guess for α, β and δ, provided that μ was initially held fixed at this estimated mode diameter whilst good estimates for α, β and δ were computed by the NLFit least squares fit algorithm. The solver could then be re-run with all four parameters free. The laborious graphical estimation of input parameters could be entirely dispensed with.

The fitting was found to be more stable than the literature would suggest, repeatably converging to the same parameters for a given input dataset. However, in contrast to the distribution functions tested so far, the fit to the whole dataset was clearly different to the fit to just the primary peak, both in the shape and the values of the parameters: the fit is undesirably sensitive to the selection of the data range. The fit to the whole dataset was so poor it is not shown.

The distribution function parameters on all plots are quoted rounded to the significant digits of the least squares calculated error in that parameter reported by NLFit. Considering Figures 35, 36 and 37, the fractional error in the α, β and μ parameters was satisfactory, but the error in δ was found to be up to 2δ. This is far from satisfactory.

The fit to the primary peak of dataset D4.15 with all parameters free is shown in Figure 35. The agreement is worse than for the Laplace distribution (Figure 31). The DSP plot is above the perfect fit line, which indicates that the fit is right-skewed relative to the data: this can be seen in the middle plot by the divergence of the fit from the data at the right hand base of the peak. A better fit is obtained (Figure 36) by fixing μ at a visual estimate of the peak diameter, although this fit is still qualitatively and quantitatively unsatisfactory and no better than the mathematically simpler Laplace distribution.

The calculated curve has approximately the right shape peak, so the lack of numerical fit may be due to the uncorrected peak area. It can be seen in Figure 37 that the fit is

much improved when the peak area has been corrected according to the procedure described in section 5.3.1 and Appendix B. However, it is still by the measure of the D_{sp} parameter, quantitatively a less good match than that obtained for the Laplace distribution with the same peak area correction (Figure 32), although qualitatively the ripple around the baseline is reduced with the 4P-LH distribution fit, apart from the divergence near the lower bound of the peak which gives rise to the large value of D_{sp}.

There is a concern about the large fractional uncertainty in one of the estimated parameters. Whilst the fit repeatedly converges to the same parameters for the same dataset, there is no apparent pattern to the values of the parameters between datasets. The agreement was only achieved with considerable computational effort. There is no explicit cumulative distribution. Despite these concerns, the fit in Figure 37 is too good to reject the 4PLH distribution without further testing.

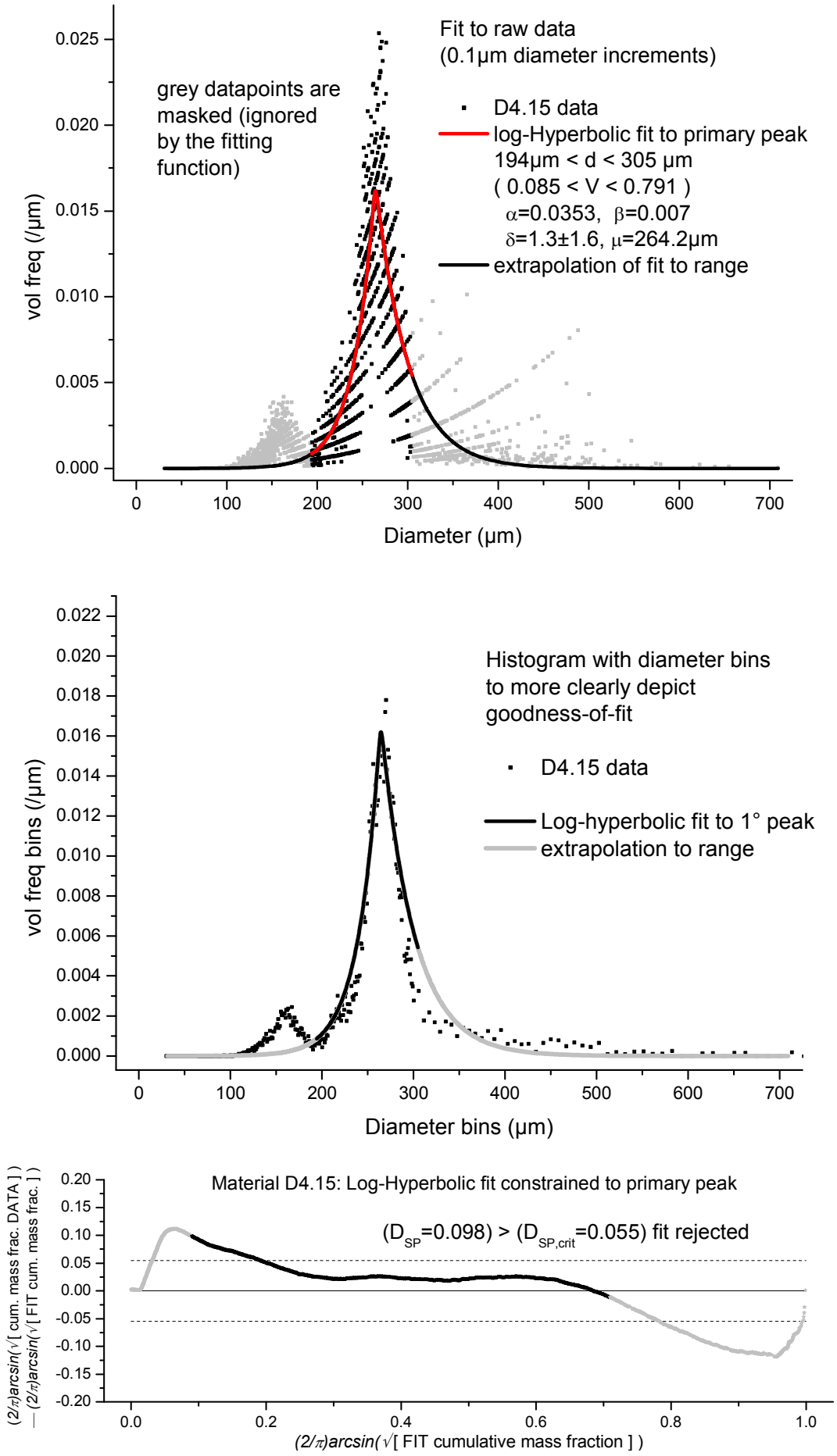

Figure 35: unconstrained 4-parameter log-hyperbolic fit to 1° peak, dataset D4.15

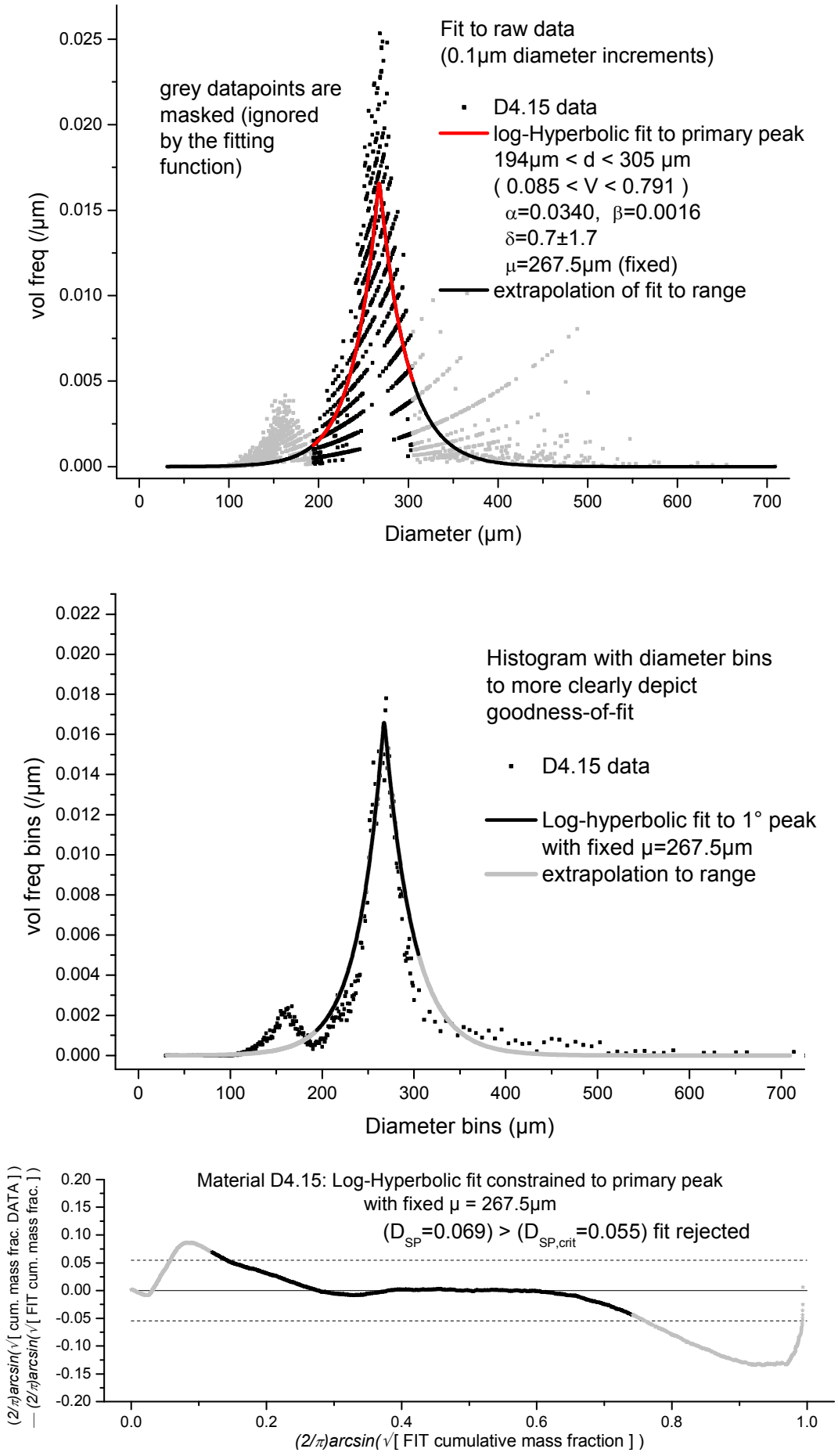

Figure 36: fixed µ, 4-parameter log-hyperbolic fit to 1° peak, dataset D4.15

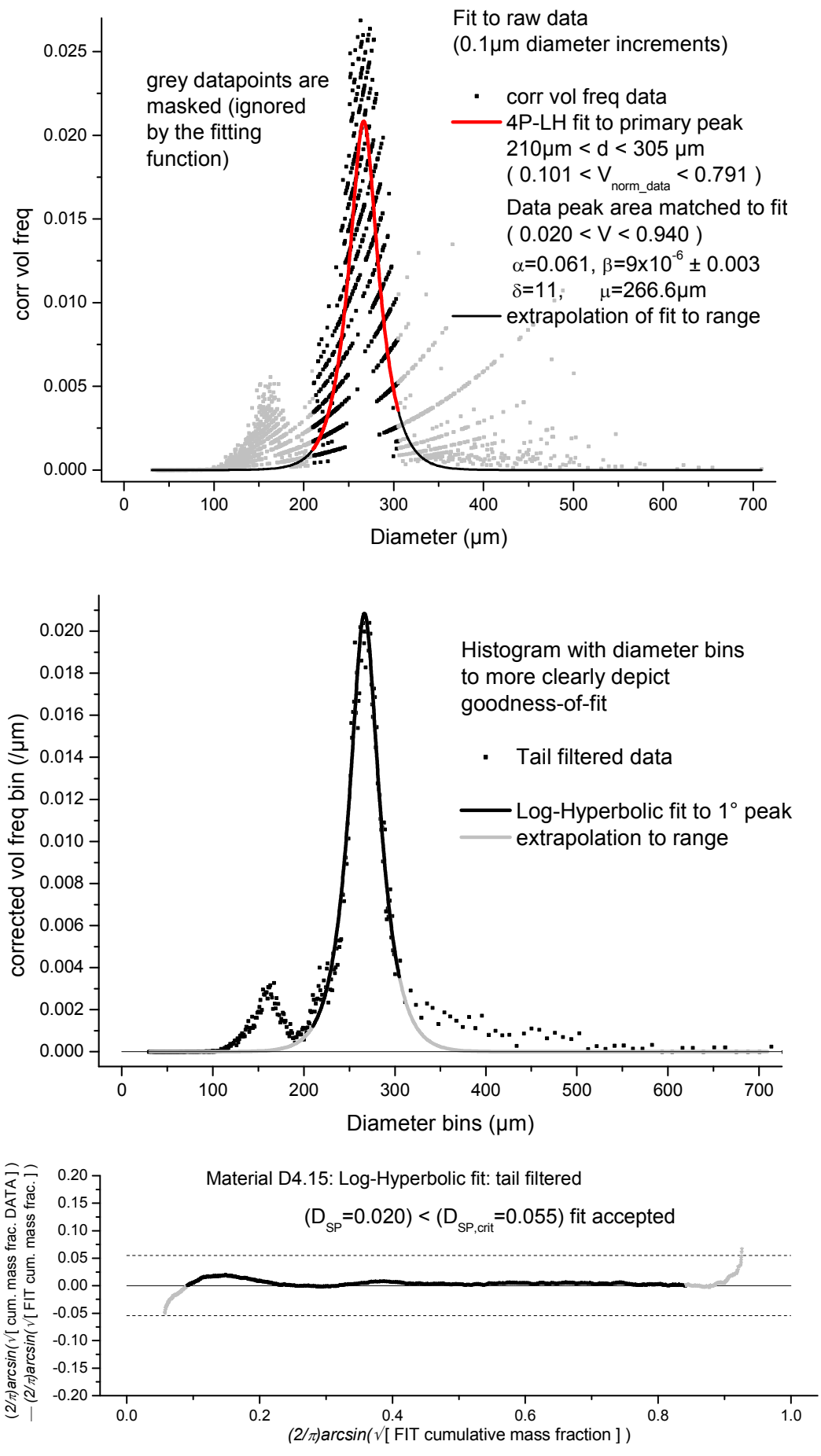

Figure 37: 4P-LH fit to area-corrected primary peak of datset D4.15

5.3.7 Lorentz distribution

In the same way as the Laplace distribution was considered before the hyperbolic distribution, the simple symmetrical Lorentz distribution will now be considered before tackling the complexities of its generalised form, the Stable distribution.

A physical justification might be made for the Lorentz distribution (Eqn. 5-12, with width parameter w and characteristic diameter d_c) for the droplet size distribution from these resonance jet break-up nozzles with viscous fluids, as the distribution arises in physics from the solution for a damped harmonic oscillator excited by a resonant sinusoidal fluctuation. In which case, intuitively the best fit would be expected to the PDA droplet data, the sizes of which are distributed only by the resonant nozzle, without conflation of size changes during solidification. In fact it is seen in Figure 38 and Figure 39 that the Lorentz distribution is not a good fit to the PDA data, whilst the log-normal is good or excellent. Unusually for a spray size distribution, which are normally right skewed, these figures also show that the normal distribution is a good fit:- typically almost indistinguishable from the log-normal.

$$w(d) = \frac{2w}{\pi\left[4(d-d_c)^2 + w^2\right]}$$

$$W(d) = \frac{1}{2} + \frac{1}{\pi}\tan^{-1}\left(\frac{2(d-d_c)}{w}\right) \qquad \textit{Eqn. 5-12}$$

However, it can be seen in Figure 40 that the Lorentz distribution is the best match yet to dataset D4.15, with only a little ripple around the baseline of the DSP plot. Note that the distribution tracks the baseline for a short distance into the masked tail data. The peak boundaries for area adjustment were set very conservatively, so this quantitatively correct extrapolation is indicative that the fit really is a good model of the data.

When fitting the PDA datasets, the obvious outlier datapoints have been excluded, for example the blips at 210 and 260μm in water nozzle A (see table Appendix A.1) which are from inspection almost certainly spurious single particle counts. Origin NLFit has been used as a first estimate of parameters, which were then adjusted where necessary to obtain the best fit on the DSP plot, in order to obtain the fairest comparison between fit functions. For Material C2, where there are four datasets, only the combined data is shown on the frequency plot, as it otherwise becomes too confused: the individual datasets and the combined data are shown on the cumulative and DSP plots.

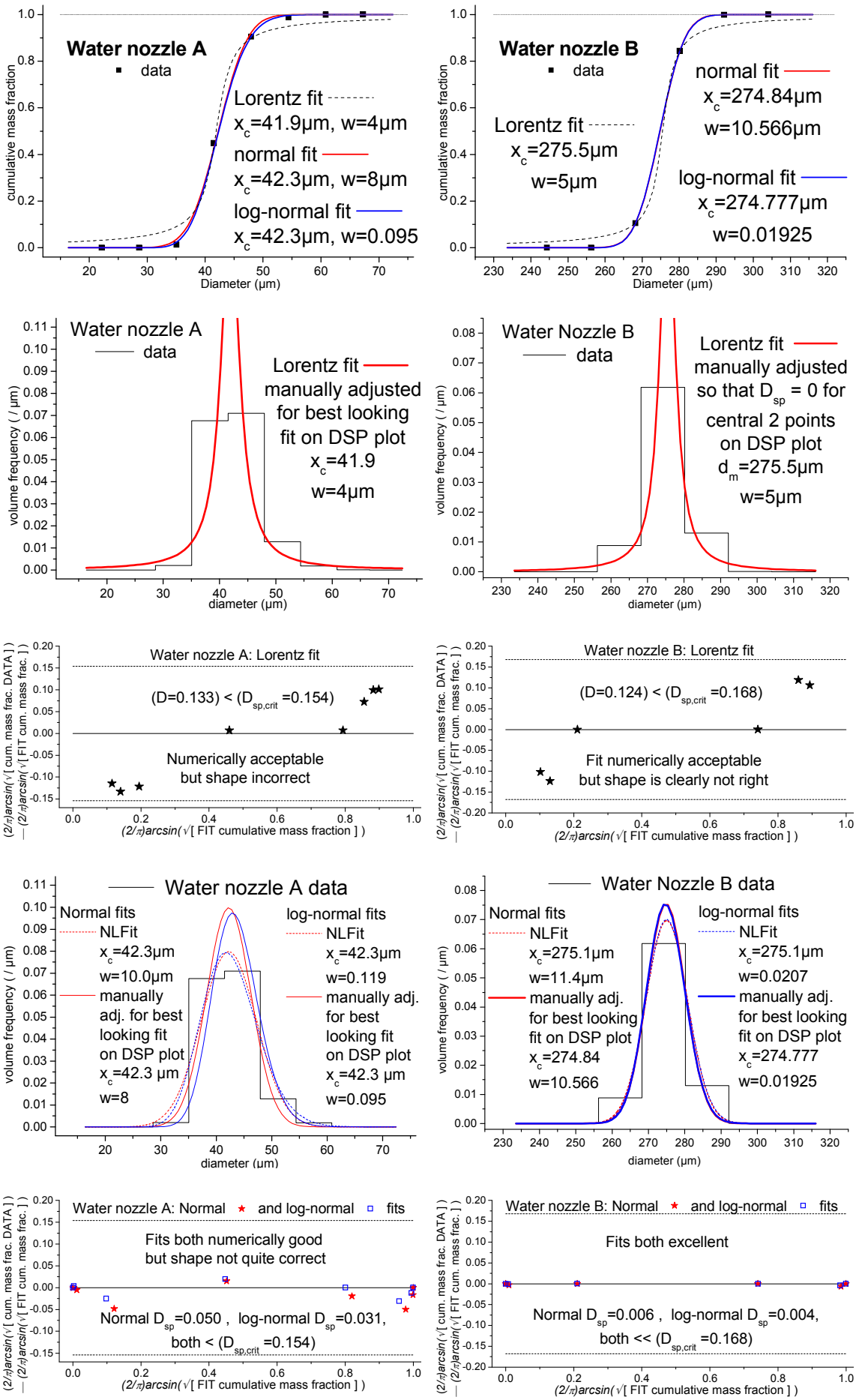

Figure 38: Lorentz, normal, and log-normal fits to PDA water data

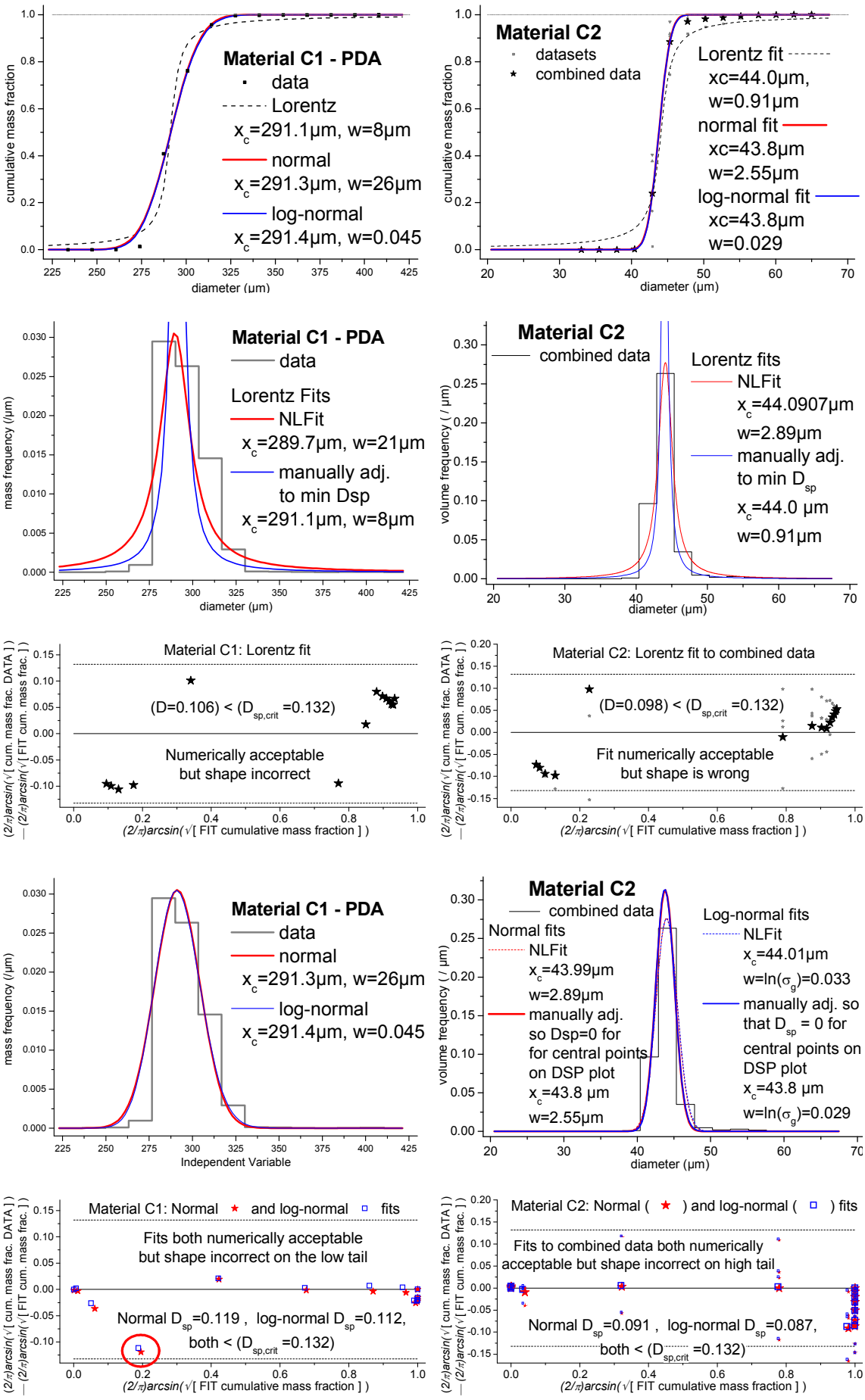

Figure 39: Lorentz, normal and log-normal fits to PDA data, Material C

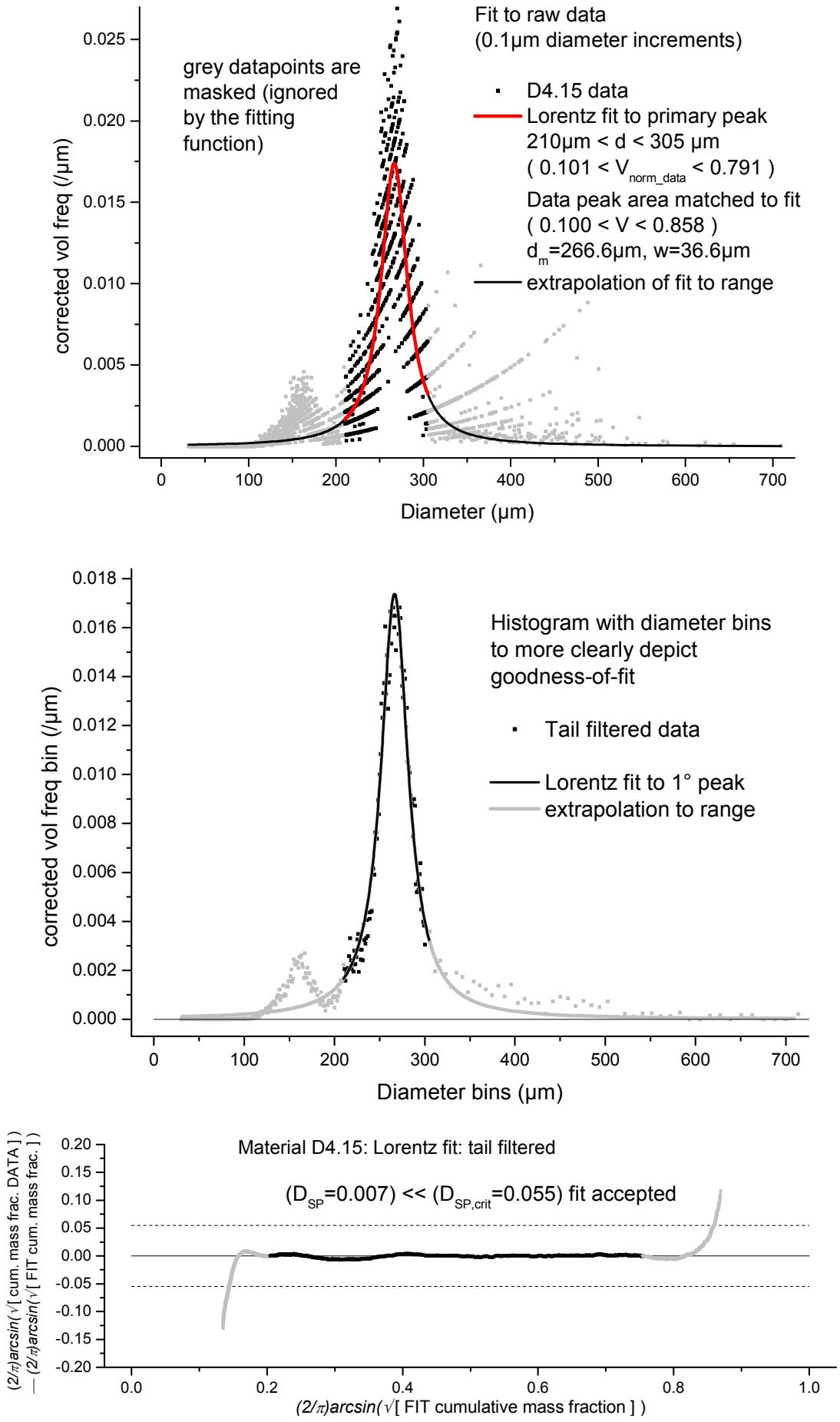

Figure 40: Lorentz fit to area-corrected primary peak of dataset D4.15

5.3.8 Stable distribution

The Stable distributions are a class of wide-tailed distributions whose instances include the Gaussian and Lorentz distributions (Nolan, 2009). They are also known as Levy skew alpha stable distributions after Paul Lévy who was the first to characterise them. There are four parameters: an index of stability $0 < \alpha < 2$, skewness $-1 < \beta < 1$, scale $\gamma > 0$ and location δ. Alpha is two for a Gaussian and one for the Lorentz distribution. As alpha tends to zero the Stable distribution tends towards the Dirac delta function.

The Stable distribution is defined by a Fourier transform of its characteristic function (Eqn. 5-13). There are a variety of parameterisations (Eqn. 5-14 - Eqn. 5-16). Index α and skewness β are the same in all of them, but definitions of the scale γ and location δ parameters differ. The most frequently quoted is the 1-parameterisation (Eqn. 5-14), which is favoured for demonstrating mathematical properties of the distribution, for example asymptotic behaviour. Nolan (2009) recommends that the 0-parameterisation (Eqn. 5-15), which is everywhere continuous, should be favoured for numerical fitting and statistical inference. However, the analysis in Chapter 6 uses distributions where the diameter is non-dimensionalised around the mode, hence for the current purpose the 2-parameterisation (Eqn. 5-16) is preferred, as δ is defined to be the mode, in contrast to the 0 and 1 parameterisations where δ is less intuitively defined. As they are unfamiliar, the mathematical definitions of the parameterisations are included, but in practice Nolan's "STABLE" FORTRAN program (Nolan, 1997) has been used to perform the Fourier transform computations, and the mechanics of the solution of these equations need not be considered any more than would the mechanics of the calculation of the error function when fitting a Gaussian or log-normal distribution. The equations have been rearranged from those given in Nolan (1998, 2009) in order to more clearly show the family resemblances and differences between the parameterisations.

$$w(d) = \int_{-\infty}^{\infty} \varphi(t) e^{-itd} dd \qquad \textit{Eqn. 5-13}$$

1-parameterisation $$\varphi(t) = \exp\left\{ it\delta - \gamma^{\alpha}|t|^{\alpha}\left[1 - i\beta.\mathrm{sign}(t).\Phi\right]\right\} \qquad \textit{Eqn. 5-14}$$

$$\left.\begin{aligned} \Phi &= \tan\left(\frac{\pi\alpha}{2}\right) && \alpha \neq 1 \\ \Phi &= -\frac{2}{\pi}\ln|t| && \alpha = 1 \end{aligned}\right\}$$

0-parameterisation $\varphi(t) = \exp\left\{ it\delta - \gamma^{\alpha}|t|^{\alpha}\left[1 - i\beta.\mathrm{sign}(t).\Phi\right]\right\}$ *Eqn. 5-15*

$$\left.\begin{aligned} \Phi &= \tan\left(\frac{\pi\alpha}{2}\right).\left[1 - \gamma^{1-\alpha}|t|^{1-\alpha}\right] && \alpha \neq 1 \\ \Phi &= -\frac{2}{\pi}\left(\ln|t| + \ln\gamma\right) && \alpha = 1 \end{aligned}\right\}$$

2-parameterisation $\varphi(t) = \exp\left\{ it(\delta - \alpha^{-1/\alpha}\gamma\Psi) - \gamma^{\alpha}|t|^{\alpha}\frac{1}{\alpha}\left[1 - i\beta.\mathrm{sign}(t).\Phi\right]\right\}$ *Eqn. 5-16*

$$\left.\begin{aligned} \Phi &= \tan\left(\frac{\pi\alpha}{2}\right) && \alpha \neq 1 \\ \Phi &= -\frac{2}{\pi}\ln|t| && \alpha = 1 \end{aligned}\right\}$$

$$\left.\begin{aligned} \Psi &= \beta\tan\left(\frac{\pi\alpha}{2}\right) + m(\alpha,\beta) && \alpha \neq 1 \\ \Psi &= \beta\frac{2}{\pi}\ln\gamma + m(\alpha,\beta) && \alpha = 1 \end{aligned}\right\}$$

Where $m(\alpha,\beta)$ is the mode of the standardised 0-parameterised distribution $S(\alpha, \beta, \gamma, \delta : 0) = S(\alpha, \beta, 1, 0 : 0)$ which is found numerically.

The 0-parameterised Maximum Likelihood solver in Nolan's "Stable" FORTRAN program fails against the droplet size distribution datasets in this research, probably due to the secondary peaks in the tails, whether the secondary peak data is left in or elided as with the Origin NLFit solver. The "Stable" solver is also a number distribution solver only: it takes a single column of data and calculates the number frequency from this.

However, the "Stable" program will also generate tabular density and cumulative functions from input parameters. An Excel macro was written (Appendix D) to generate the Stable input files, run the command line executable version "Stablec.exe", and read the "Stable.out" results file back into Excel to calculate D_{sp}. The Excel Solver cannot be programmatically interrupted, so it was instead necessary to explicitly code a optimisation routine. The inelegant approach of sequential direct substitution of parameters has been used. The limited number of datasets required to be fitted does not justify the programming effort required to code a more elegant maximum gradient solver routine for example. A large degree of manual intervention was required, with intelligent selection of input parameters, to avoid mathematical artefacts of shallow local minima far from a visually acceptable fit. The parameter chosen to be minimised was normally D_{sp}, but in cases where there was a single "wiggle" away from an

otherwise excellent fit, attempting to minimise D_{sp} simply resulted in the whole curve being vertically translated on the DSP plot and the resultant agreement was much worse overall. In these cases minimisation of the sum of the absolute deviations of all the datapoints away from the perfect fit line [notation $\Sigma(\Delta sp)$] was used instead. The Excel macro method was crude but fit-for-purpose. A more elegant solution should be considered for future studies.

Initially the Origin NLFit Lorentz fit to the data was used to generate iteration initialisation values for the parameters, where Lorentz d_m and w are Stable δ and 2γ respectively in the 2-parameterisation and $(\alpha, \beta) = (1, 0)$ by definition in a Lorentz distribution. However, this gave rise to an additional computation step. It was subsequently found that adequate parameter estimates could be made by inspection. A more serious weakness of using the best Lorentz curves as the initial estimates is assuming symmetry around the mode as the starting point. The normal expectation for a sprays droplet size distribution would be positive skew. Except at the Gaussian limit ($\alpha = 2$), Stable distributions are wide tailed. The exclusion of the secondary peak data leads to the undesirable situation where a wide-tailed distribution is fitted to data where the tails have been truncated. At least for moderate skew, the effect of skew on the shape of the distribution is seen most clearly at the tails. It was found that when the truncated peak was considered in isolation, that a visually and numerically acceptable fit was obtained for $\beta = 0$. It was only when a wider range of the datasets and especially the bimodal distributions were fitted (see following section) that a skewed distribution was found to be a better fit to the data. Figure 41 is the original symmetrical best fit: it has not been post-rationalised and re-plotted skewed. Although the consequence of this decision is that the quoted values of the Stable distribution parameters vary between the monomodal and bimodal fits to the same data, the impact is insignificant upon the derived parameter of interest - the d_v95 relative to the mode.

The sensitivity of the DSP plot shows that the Stable distribution is in the small diameter limit not quite the correct description of the data. However, the plot also very clearly indicates that the Stable distribution is an exceptionally good model over the vast majority of the range of the data.

It can be seen in Figure 41 that the fit to dataset D4.15 is numerically slightly better than the Lorentz fit, although the slight ripple around the baseline is still present.

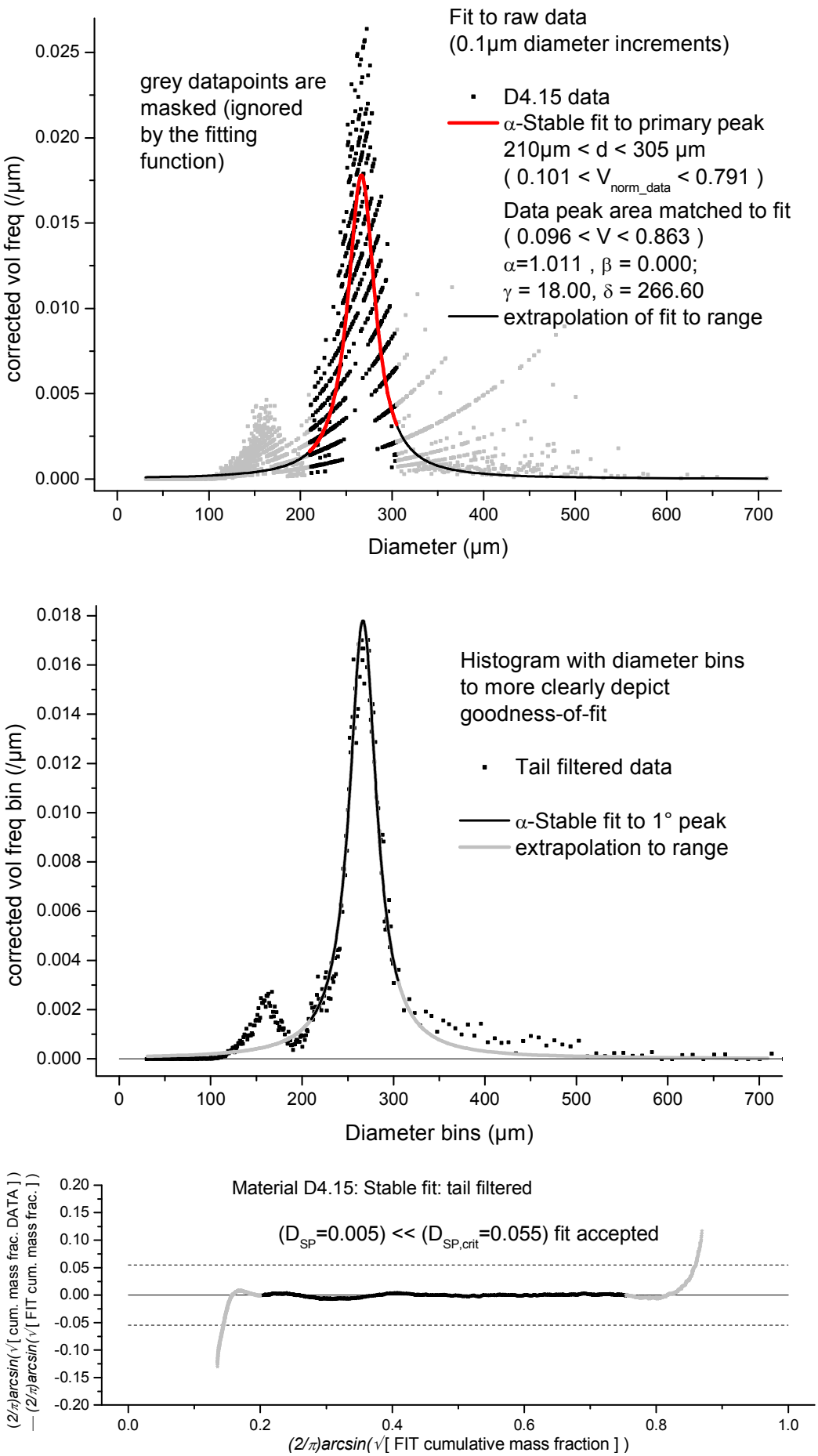

Figure 41: Stable fit to area-corrected primary peak of dataset D4.15

5.4 Testing fit functions against the multimodal distributions

If the observed secondary peaks at small sizes were truly solely due to either satellite droplet formation or orifice size variation, then they arise from the same physical mechanism as the primary peak, and a good fit function should be able to account for both primary atomisation and secondary satellite droplet peaks with meaningfully related parameters. Two distribution functions have been shown to be plausible fits to the Acoustic Atomiser droplet size distribution data: the 4-parameter log-hyperbolic distribution (4P-LH), which has previously been applied to sprays size distributions, and the Stable distribution, which is novel in this application. Fitting to the bimodal data has been used as a demanding test to resolve which distribution function is the best model for the data.

An important property of the Stable distribution is self-similarity. If the Stable distribution really were a good description of the underlying physical phenomena, then the secondary peak should come from the same (α, β) family and vary only in the location parameter delta. Mathematically self-similarity would be satisfied if the scale parameter γ varied also, but on an intuitive argument the width parameter γ should be the same for the primary atomisation and secondary satellite droplet peak as they arise from the same atomisation event. As there is no previous reference to the use of the Stable distribution to describe the droplet size distribution of a spray, there is no evidence to support this postulate of constant γ between the peaks. However, from consideration of the physical process, it appears to be a reasonable assumption to be tested against the data. Hence in performing the bimodal fits α, β and γ have been constrained to be the same between primary and secondary peaks, and it is only the location parameter delta that has been permitted to differ. Again intuitively it is expected that γ would widen with increasing number of nozzles, and also that for a given fluid with constant number and detailed mechanical construction of the nozzles, that the ratio of γ/δ should be constant as nozzle size (and hence δ) were varied. However, there are insufficient appropriately sequenced datasets available in this study to test these further postulates about γ.

In contrast to the Stable distribution, it is unclear how the parameters of the 4-parameter log-hyperbolic distribution should be related between the primary and secondary peaks, as the parameters have less intuitive physical meanings.

Tertiary peaks at large diameter have been postulated to be artefacts due to agglomeration. The agglomeration process is independent from the atomisation. Hence it is not expected that the tertiary peaks should be exhibit self-similarity with the primary atomisation peak, or even that they should follow the same type of distribution. Thus the multi-peak analysis has been confined to bimodal primary mode atomisation and secondary mode at smaller diameter.

The Excel worksheet and macro method described in the previous section has been extended to cover bimodal fits for the Stable distributions. Each peak has been fitted separately, and then a linear combination of these curves has been applied to the combined data. The volume ratio between the two peaks was first estimated by inspection, and subsequently adjusted if necessary. A similar Excel spreadsheet was constructed to calculate the bimodal fits for the 4-parameter log-hyperbolic distribution, although in this case the distribution function can be calculated explicitly, within the worksheet cells, and the Excel Solver used to vary the parameters to minimise D_{sp}. Although the 4P-LH distribution fit to each individual peak was more convenient with the Origin least-square non-linear curve fit used earlier for the monomodal fits to the 4P-LH distribution, the iteration required for the bimodal fitting would be excessively tedious to construct in Origin and hence a modified form of the Excel worksheet used for the bimodal Stable fits was a more efficient tool.

If the secondary peak were truly only satellite droplets, regardless of how many jets there are in total in the sprayhead, there should not be more than one satellite droplet per primary droplet. This sets an upper limit on the volume fraction of the secondary peak relative to the primary peak, if the physical mechanism were satellite droplet formation;

$$\frac{\frac{\pi}{6}d_2^{\,3}}{\frac{\pi}{6}d_1^{\,3}+\frac{\pi}{6}d_2^{\,3}} = \frac{d_2^{\,3}}{d_1^{\,3}+d_2^{\,3}} \qquad \textit{Eqn. 5-17}$$

where d_1 and d_2 are the mode diameters of the primary and secondary atomisation peaks respectively. In practice it was found that the ratio was much less than this limit for most datasets, consistent only a small fraction of the total number of jets forming satellites. This is credibly due to nozzle manufacturing tolerance limitation combined with the narrow frequency window for resonant break-up of non-Newtonian fluid jets: the spray dryer operator observed controlled break-up in those jets in the camera view, but some out-of-field or out-of-focus jets were just out of tune and forming satellites.

The small secondary peak size relative to the main peak is also consistent with scanning electron micrographs and mechanical attrition tests that were performed on the products. These showed that the particles were robust, with only a small quantity of broken particle fragments. Hence there is no separately observable contribution to the size distribution from fragments as there is from agglomerates. However, such fragments are still credible sources of some of the variation observed of the droplet size data from the fits, even were the calculated curves a perfect description of the atomisation physics.

Some datasets were found to have a secondary peak that was both too large in volume fraction and too close in diameter to the main peak to be convincingly attributed to satellite droplet formation, but was better described as variation between orifice sizes in the sprayplate. It is less defensible in this case that the Stable width parameter γ should be the same for each peak. One of the nozzle diameters will give a jet that is excited at resonance from the driving frequency, and will have the value of γ characteristic of the resonant jet breakup. Another jet emerging from the same sprayplate, driven at the same frequency, but from an orifice of different diameter, is unlikely to also be at resonance, and thus γ might be expected to be larger. The assumption made here is that the operator would have tuned the driving frequency so that the largest number of jets appeared to be breaking up at resonance, i.e. the primary peak is the one expected to be at resonance. Thus γ has been adjusted to fit the primary peak best. The same γ was used to fit the secondary peak. It is not often an excellent fit to the secondary peak - as anticipated by the discussion in this paragraph - but in only one case (dataset D7.7) was the value of γ fitted to the primary peak not an acceptable fit against the secondary peak. It was, however, acceptable for $\gamma_2/\gamma_1 = \delta_2/\delta_1$.

5.4.1 Discussion of multimodal fits to test datasets

Comparing Figure 42 for the 4-parameter log-hyperbolic distribution fit and Figure 43 for the Stable fit to dataset D4.15, both appear on inspection to fit the data reasonably, although both show some ripple around the baseline in the DSP plot, indicating that neither fit is perfect. The 4-parameter log-hyperbolic distribution produces numerically the better fit, but the Stable distribution is more compelling in the maintenance of self-similarity in the values of the parameters between the peaks: a better agreement than that shown in Figure 43 could be obtained by the artifice of letting the α,β,γ parameters float between peaks as was permitted for α, β, δ in the 4P-LH fit shown in Figure 42.

Neither distribution function bottoms the trough around 200μm between the peaks. The Stable distribution underestimates significantly the cluster of datapoints just greater than 200μm. When compared to the rest of the data range, there is rather more noise or spread in this cluster, which suggests that there may be an additional physical explanation behind this feature other than simply points mapping the locus of the primary atomisation curve. A similar pattern of overestimation followed by under-estimation can be observed at the lower-diameter base of the secondary satellite droplet curve in Figure 44. Furthermore, the shape of this secondary atomisation peak is rather similar to the primary atomisation peak of a dataset not examined up to now, D7.3a shown in Figure 45. The simplest explanation is that the Stable distribution fails to describe some feature of the physics. However, it was considered interesting to explore whether the step around 200μm in dataset D7.3a could be described as a secondary peak merged into the base of the primary atomisation peak. The unimodal Stable distribution fit is shown in Figure 46, the bimodal fit in Figure 47. When these two figures are compared, it can be observed that the bimodal Stable distribution fit shows very good agreement with the data right down to the minimum resolvable size of the Visisize instrument. In contrast in Figure 48, a bimodal 4-parameter log-hyperbolic distribution fit deviates from these data more than the monomodal Stable fit in Figure 46. In the 4-parametrer log-hyperbolic case the Excel solver failed to fit the secondary peak parameters entirely, so β_2 and δ_2 were constrained to match the primary peak, and α_2 only was solved to minimise D_{sp}.

In principle, dataset D4.15 could similarly by fitted exceedingly closely by a quaternary-modal Stable distribution, but it would be complex to compute, and whilst mathematically it may be satisfying to obtain ever closer statistical descriptions of the data, it is less easily physically justifiable than the bimodal fits. It is plausible that jets from out-of-spec nozzles were producing droplets with a second primary peak diameter, and all nozzles were not quite at resonance and forming satellite droplets, hence producing a quaternary modal distribution. However, it is less credible that the same conditions pertained to both experiments D4.15 and D7.3. Simpler and more plausible explanations are that either the Stable distribution fails to capture something of the underlying atomisation process, and/or that the atomisation size distribution peak has been distorted by morphological changes during drying.

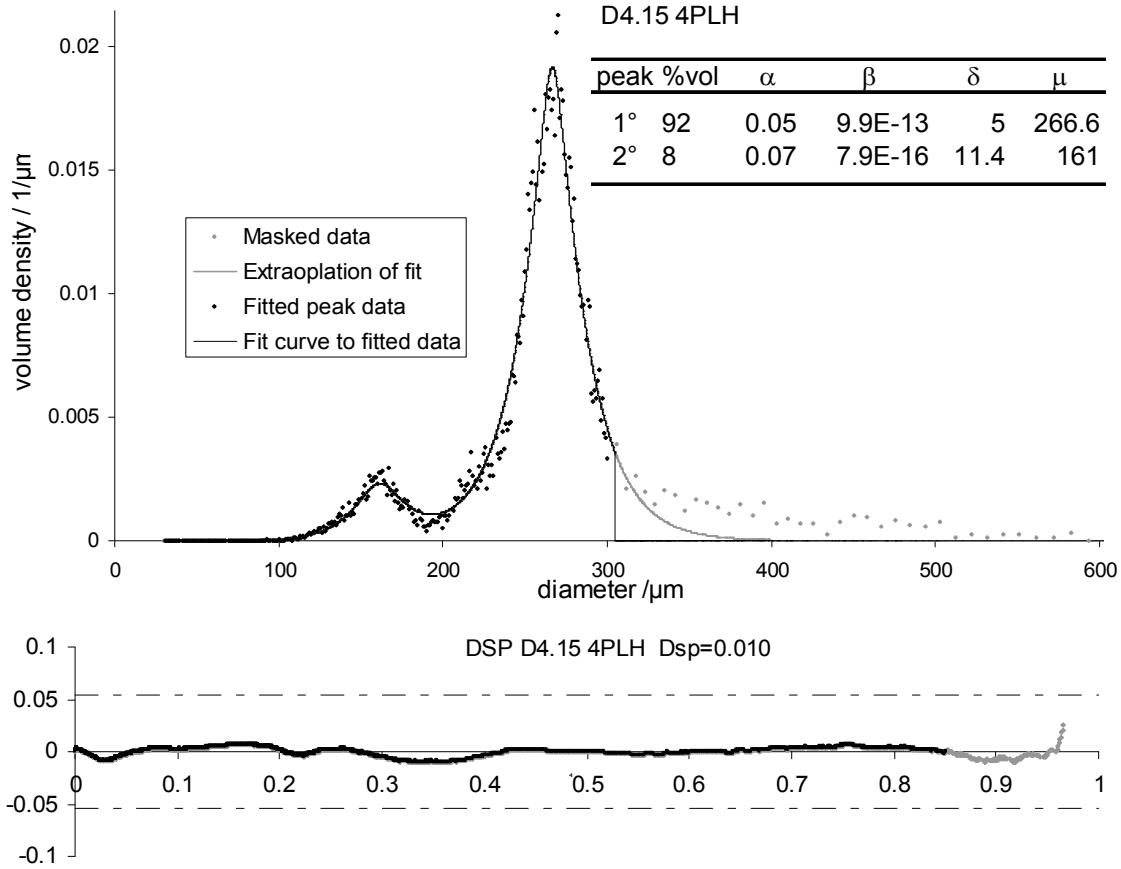

Figure 42: bimodal 4-parameter log-hyperbolic fit to dataset D4.15

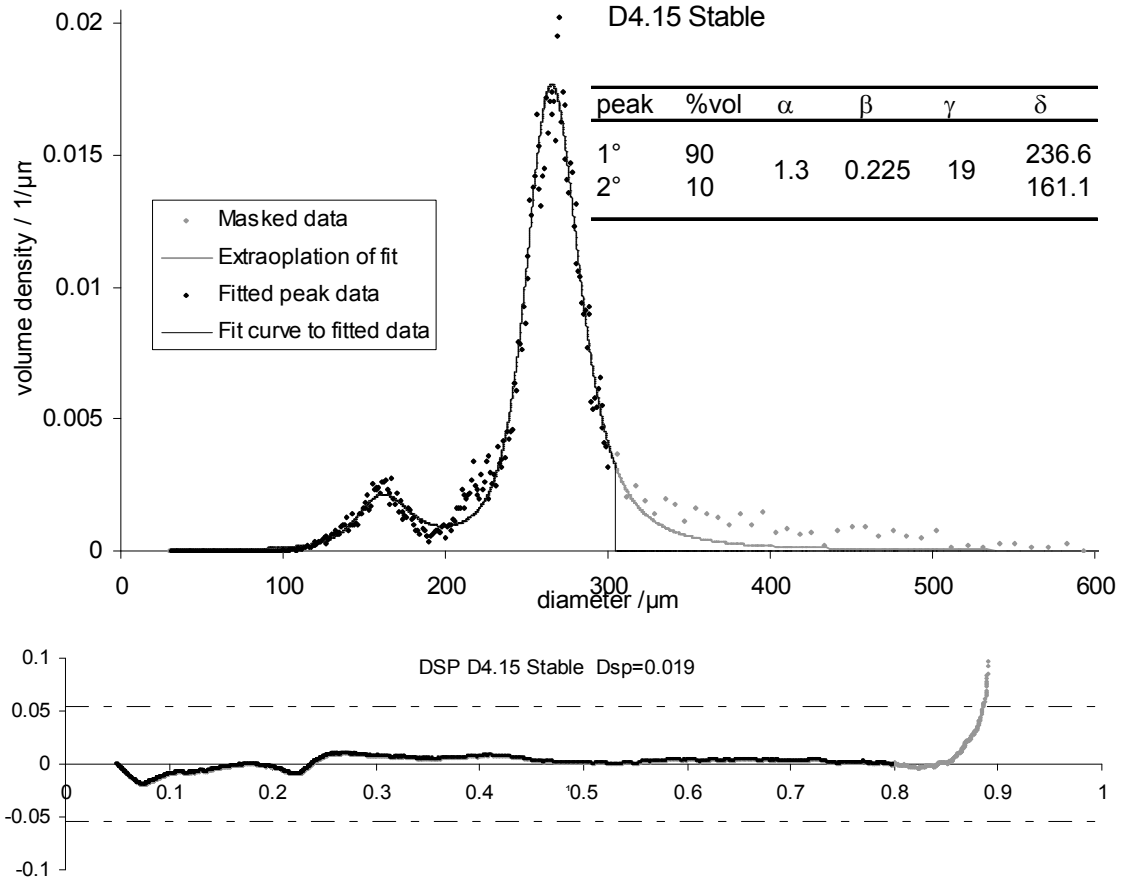

Figure 43: bimodal Stable fit to dataset D4.15

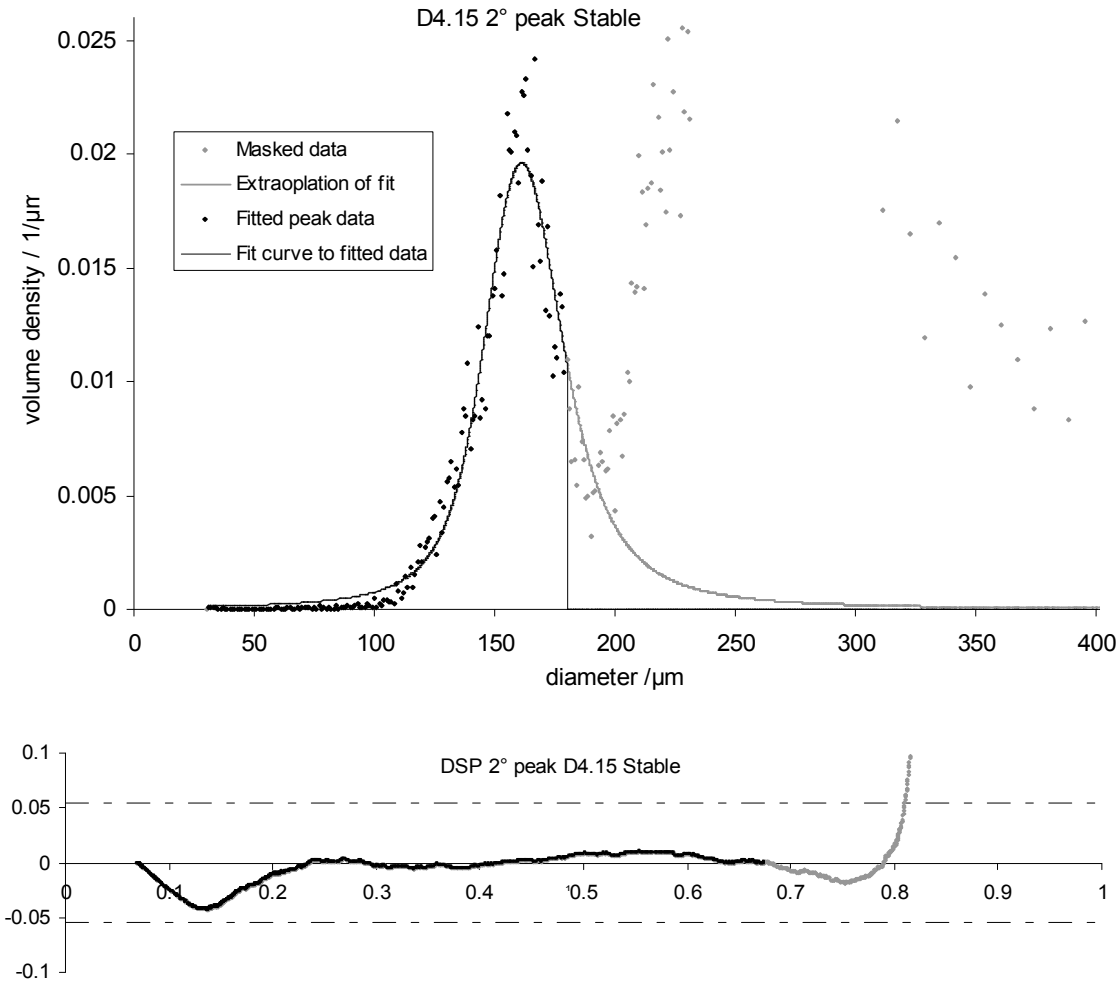

Figure 44: Stable fit to secondary satellite droplet peak, dataset D4.15

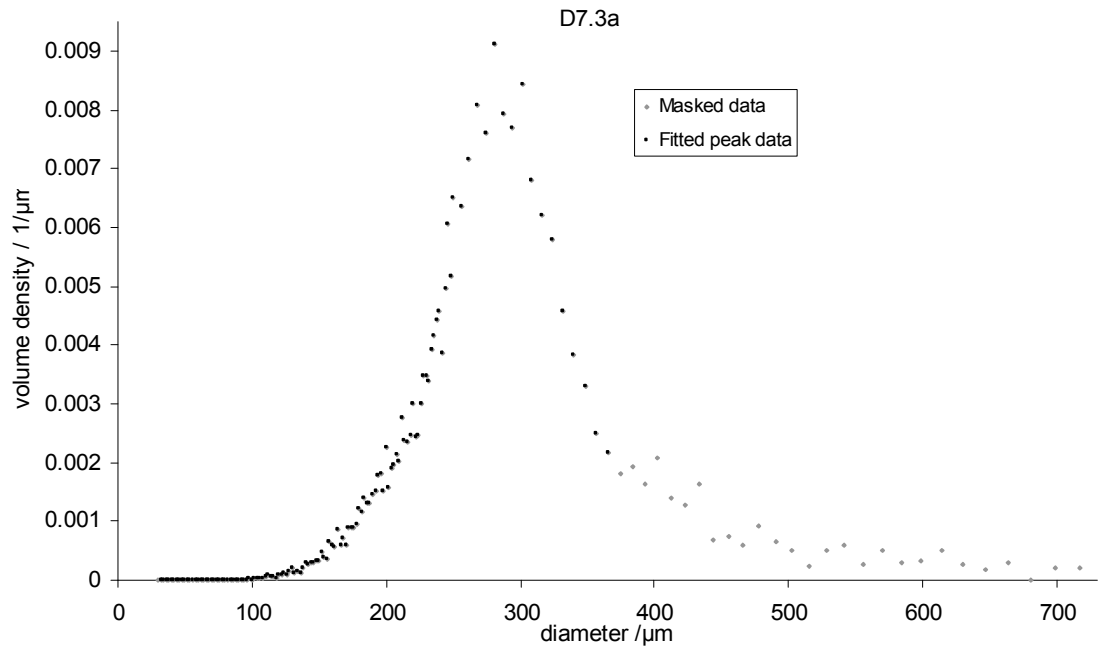

Figure 45: dataset D7.3a

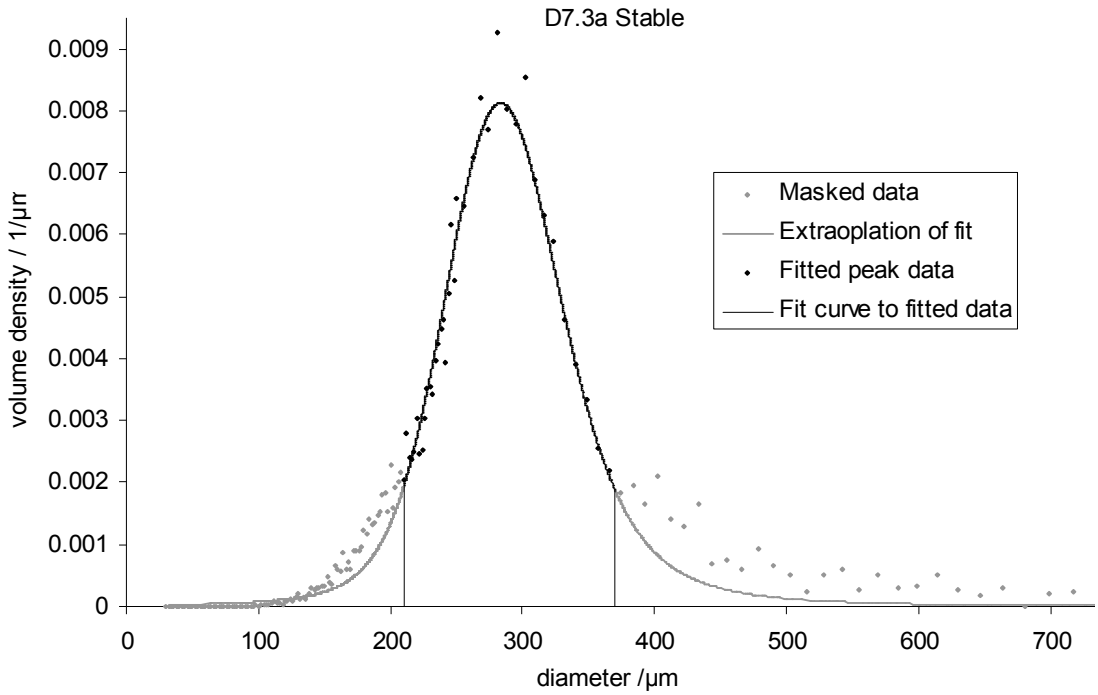

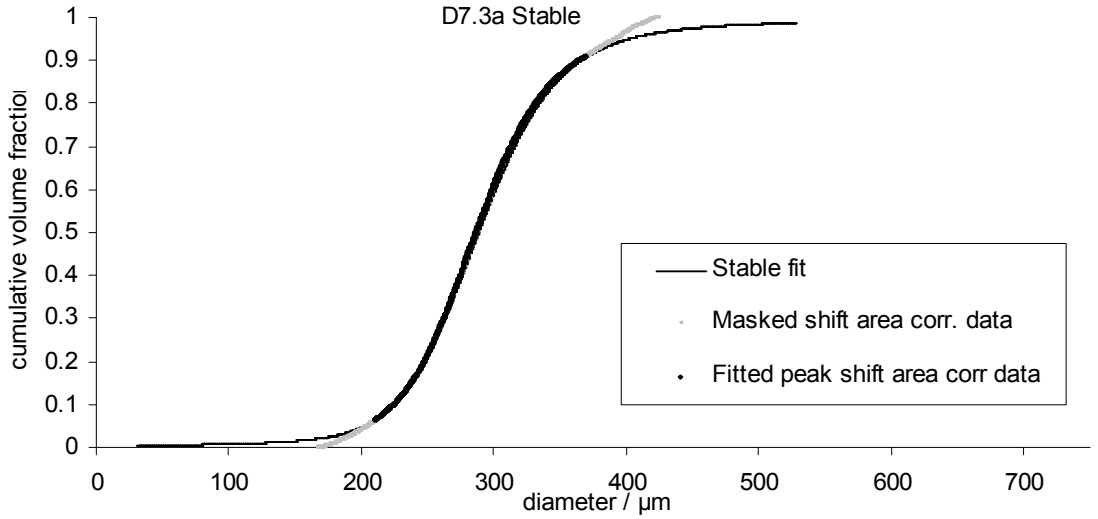

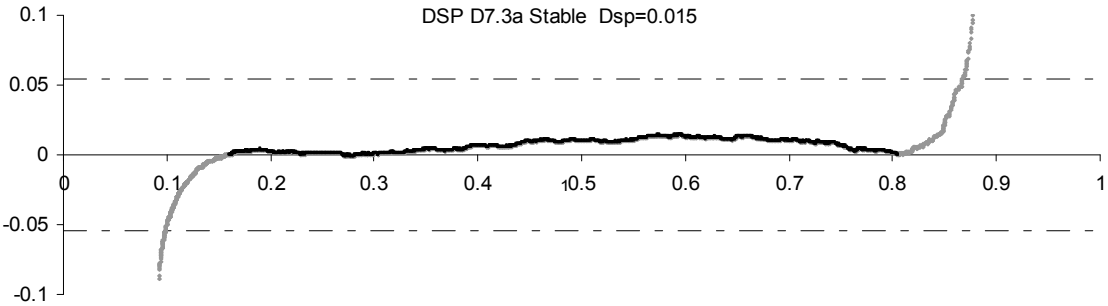

	Parameters of the Stable distribution			
	α	β	γ	δ
D7.3a	1.6	0.4	47	283.1

Figure 46: unimodal Stable fit to dataset D7.3a

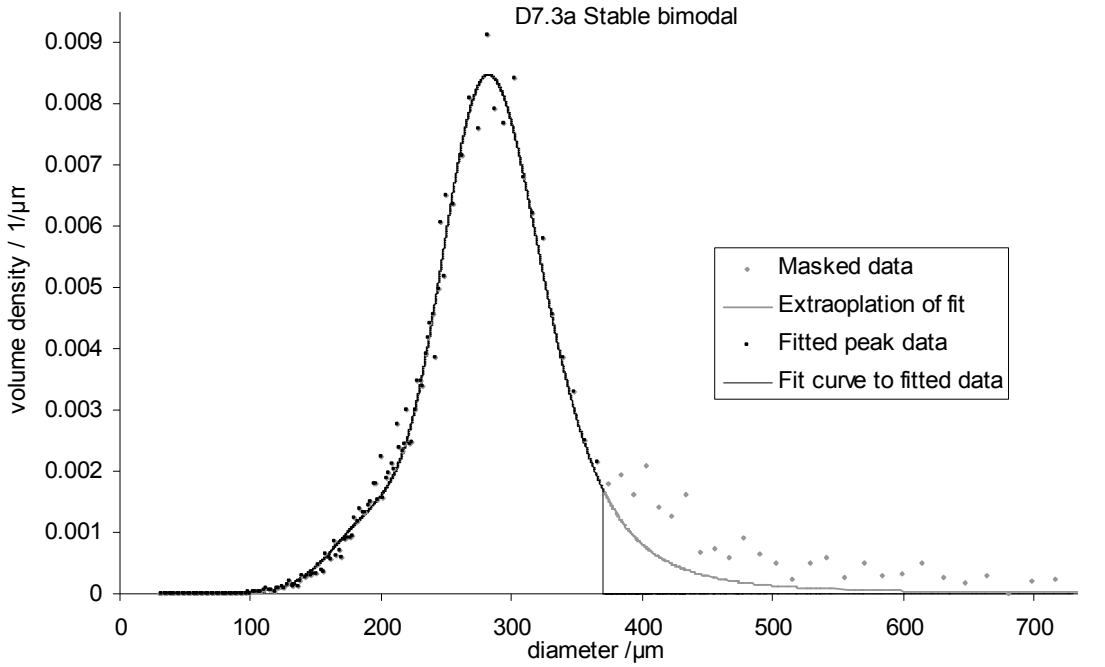

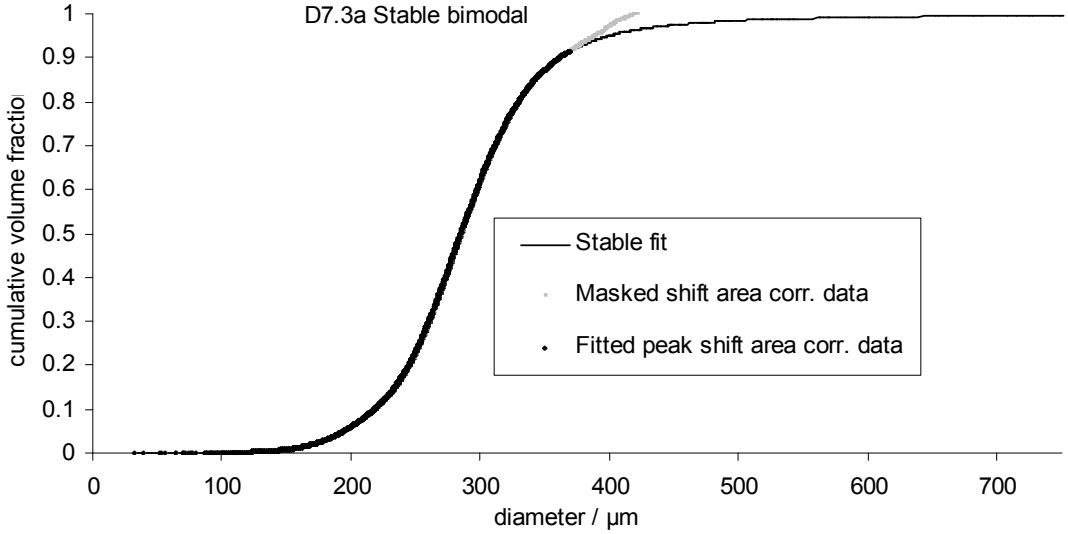

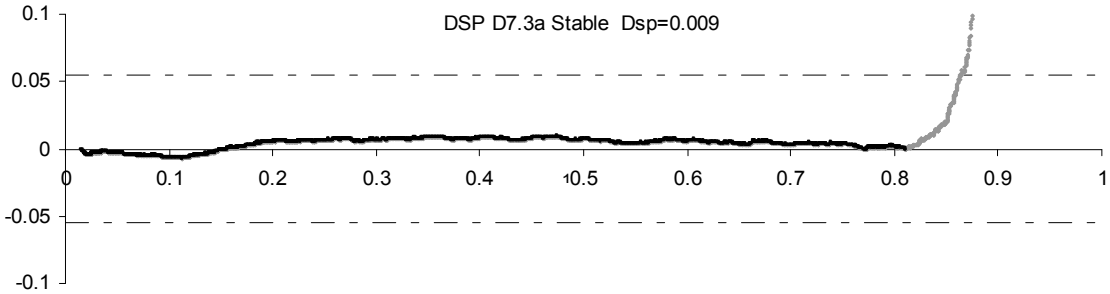

peak		Parameters of the Stable distribution			
D7.3a	%vol	α	β	γ	δ
1°	87	1.6	0.9	40	283.1
2°	13				200

Figure 47: bimodal Stable fit to dataset D7.3a

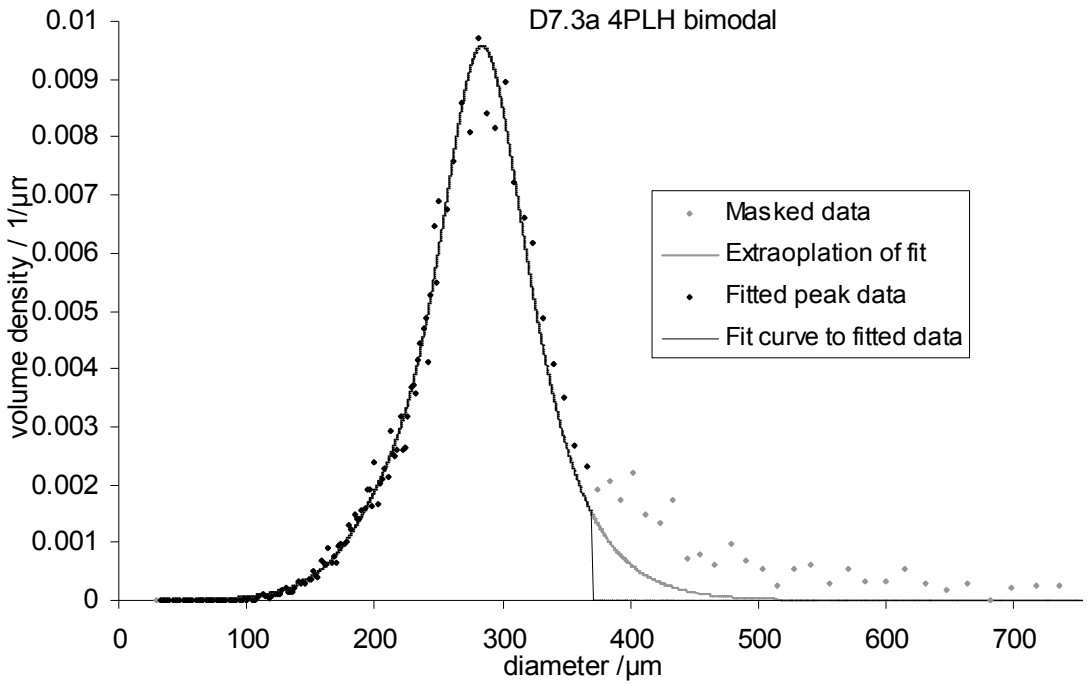

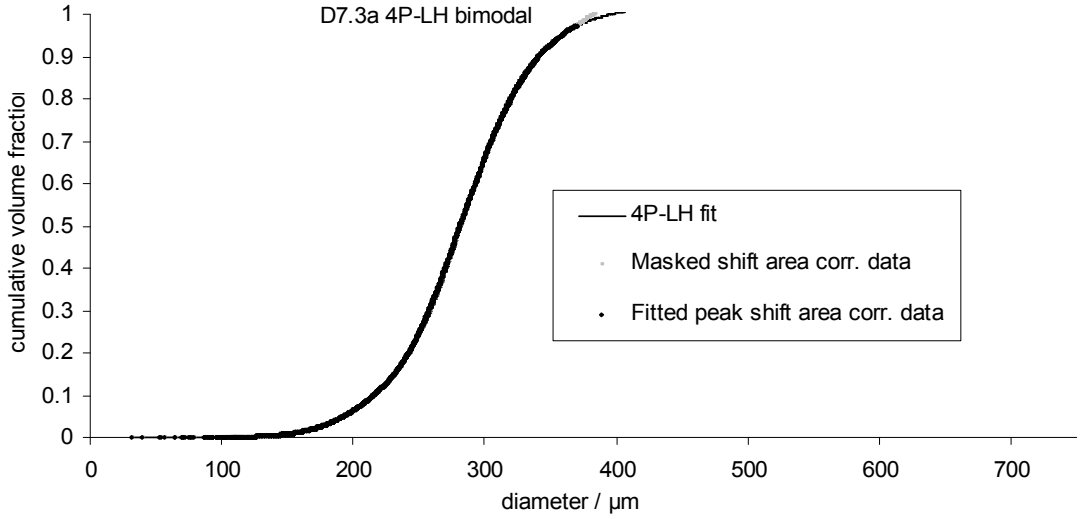

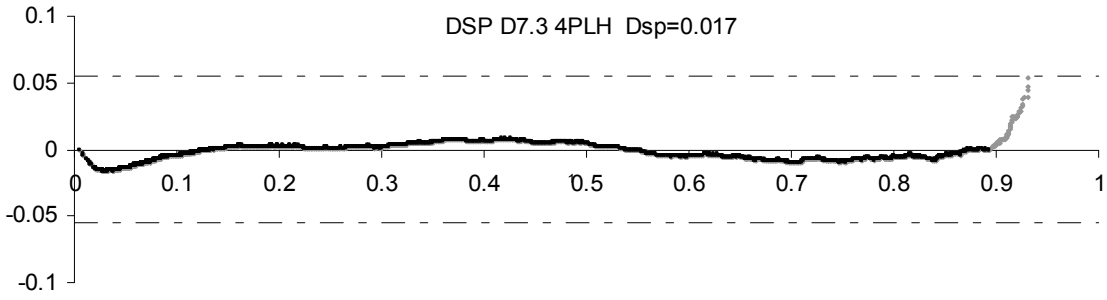

peak		parameters of the 4P-LH distribution			
D7.3a	%vol	α	β	δ	µ
1°	99	0.032	7.9E-4	32.6	283.1
2°	1	0.055			200

Figure 48: bimodal 4P-LH fit to dataset D7.3a

5.5 Stable distribution fits to all datasets

The Stable distribution performed better in the tests than the 4-parameter log-hyperbolic distribution. The fits are almost always both qualitatively and quantitatively better, and the fit parameters are always less arbitrary, especially when applied to the bimodal distribution case, when the assumption of self-similarity of the distribution between the primary atomisation and secondary satellite droplet peaks works consistently for the Stable distribution, but erratically for the 4-parameter log-hyperbolic distribution.

Stable distribution fits have been performed on all size distribution datasets. Appendix A contains the plots. The fit parameters, the D_{sp} goodness-of-fit statistic and the comparison with the 95% confidence level limiting value are summarised in Table 2. With bimodal fits, only parameters that differ for the secondary peak are tabulated. The D_{sp} statistic is tabulated for both peaks individually, and also for the combined fit to both peaks. Peak upper and lower limits are explicit where the fit is to a subset of the data. The lower bound of the secondary peak is normally the dataset minimum, in which case the value appears in brackets. In five cases, however, the smallest diameter data was discordant even with a bimodal fit, and the secondary peak lower bound was chosen to be greater than the dataset minimum. In these cases, the D_{sp} statistic is shown for both the fit within the selected limits, and also from the dataset minimum.

In all cases the agreement of the Stable distribution model with the data is acceptable at the 95% confidence level, and in most cases it is a comfortably small fraction of the limit. The borderline fit of datasets D10.6 and D11.4 is attributed in Appendix A.5 to agglomeration: as indicated by the values in Table 2, when the largest sieve data are excluded (10 and 20% of the total volume for each dataset respectively), the concordance is comfortably within the confidence limits in both cases. For the bimodal fits, the D_{sp} statistic for each peak in isolation is often relatively poor compared to the D_{sp} value for the fit to the combined peaks. This is an artefact of the selection of the bounds. The assumption was made that bounds could be chosen by inspection such that the contribution from other peaks was trivial. In many cases, the peaks are too closely spaced for this assumption to be valid, unless the bounds are set so conservatively that there are too few data to be fitted to each peak to be able to meaningfully gauge the quality of the fit. Hence the bounds have been chosen to be sufficiently wide to enable the fit to be judged, and in consequence there may be significant contributions from other peaks. Thus the D_{sp} statistic for each peak in isolation looks poor relative to the

overall peak fit. It should be noted, however, that even if poor by comparison, the D_{sp} statistic is still always within the 95% confidence limits, even for the peaks in isolation.

Also shown in Table 2 are the polydispersity index of the volume distribution (PDI_v) and the ratio of the ninety-fifth percentile to the mode of the volume distribution for the Stable distribution fits. The average PDI_v over all datasets is 0.4, and the average $D_{v,95} / d_m$ ratio over all datasets is 1.33. These are the same as the ICI metrics introduced at the beginning of this chapter. The metrics were previously obtained, independently from the fitting that has been discussed in this chapter.

5.6 Trend in Stable alpha parameter with feed liquor viscosity

In section 5.3.7 it was hypothesised that the PDA data, for water and Materials C, should be the best fit to the Lorentz distribution. In fact they were found to be good fits to the Normal distribution, which can be described as a Stable distribution with parameter $\alpha = 2$. Water and Materials C have rather low viscosity. The liquid feed to the atomiser for Materials D had higher viscosity, and the alpha parameter is smaller. Surprisingly, it can be seen from Figure 49 that the Stable alpha parameter is roughly correlated with the viscosity of the liquid feed to the Acoustic Atomiser. A linear regression line has been plotted, not because the trend is necessarily supposed to be linear, but because there are many coincident datapoints, which lessen the visual impression of the trend. The linear regression excludes the outlier data discussed in the following paragraph. The viscosity data are the shear viscosity at the nozzle wall shear rate. At the time the measurements were made, the CaBER instrument for measuring extensional viscosity that is described later was not available, and the conclusion of Chapter 10 that atomisation behaviour was best mapped by extensional viscosity had not yet been made. Materials D have the greatest range of viscosity in Figure 49. These materials were all aqueous carbohydrate dispersions, sometimes with an emulsified oil phase. Starch molecules in solution were the only species that might give rise to strain hardening, and thus an extensional viscosity greater than would be predicted from a shear viscosity measurement. Since the occurrence of starch molecules in solution was broadly similar between Materials D, it is a defensible assumption that the extent of strain hardening would be similar for all materials. Thus the use of shear viscosity data in Figure 49 instead of extensional viscosity data should not alter the validity of the conclusion.

A3 landscape in paper copy:

this page in electronic copy just maintains the correct pagination and cross references to the table

Table 2: summary of Stable distribution fit parameters for all datasets

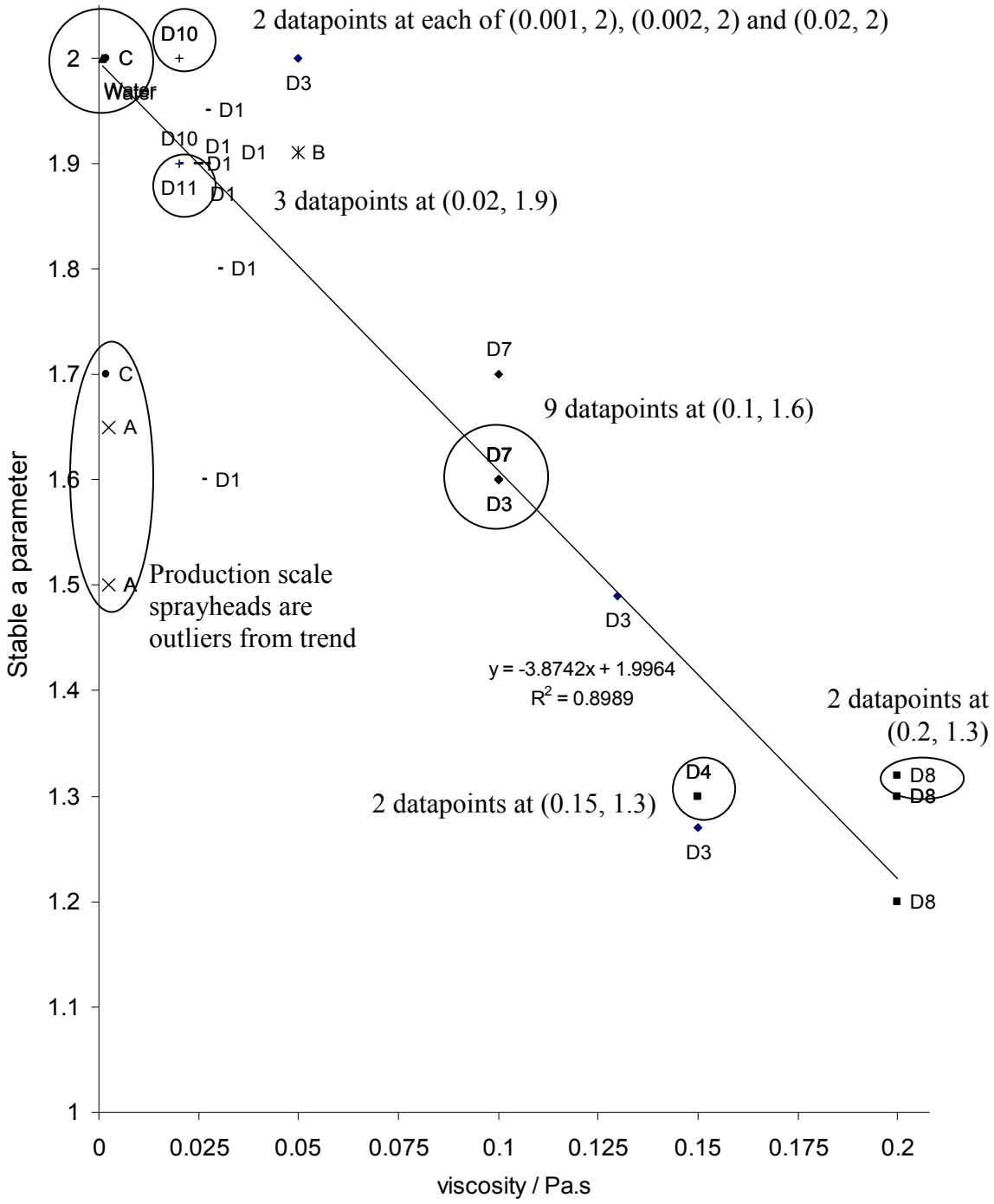

Figure 49: trend in Stable distribution α parameter with atomiser liquid feed viscosity

Outliers from the trend of decreasing alpha with increasing viscosity are the Material A and dataset C3 production plant data. This is not a difference between spray-solidification and spray drying; Material B was spray-solidified as was Material A, but fits well to the trend, and C3 was spray-dried. Material A was made using an earlier mechanically vibrated atomiser design, which may have given less uniform jet breakup, with more dispersion in the size distribution and hence larger tails. However, the atomiser used for dataset C3 was the same type as used for C1, C2 and Materials D.

The most satisfactory explanation for the outliers is increased dispersion in the size distribution from production scale atomisers, as the result of manufacturing tolerance in size of holes, where the overall size distribution is an ensemble of several hundred individual nozzle size distributions, each with a slightly different mean and width. Intriguingly and somewhat counter-intuitively, although α decreases for the production scale atomisers, the ratio of the 95th percentile to the mode of the volume distribution does not increase. The analysis in Chapter 6 relies on the ratio of the large size tail diameter to the mode. The data in Table 2 indicate that the analysis in Chapter 6 will be valid for production scale as well as pilot scale Acoustic Atomisers.

5.7 Conclusions

A selection of distribution functions has been tested against various Acoustic Atomiser droplet and particle size distribution datasets. Although it has not previously been reported for use in droplet size distributions, the Stable distribution has been found in this research to be a better fit to the Acoustic Atomiser size distribution data than any of the fit functions commonly reported in the sprays literature.

It is proposed that the Stable distribution is not only a good numerical fit to the data, but furthermore that it is in some way descriptive of the physics of atomisation. The trend in alpha towards the Gaussian limit $\alpha = 2$ for inviscid liquids and towards the Lorentz limit of $\alpha = 1$ as the feed viscosity increases, is consistent with the physical description as a simple or damped forced resonator respectively.

CHAPTER 6 - ANALYSIS OF THE EFFECTS ON SPRAY DRYING OF NARROWER DROPLET SIZE DISTRIBUTION

In this chapter it will be shown that a drop size distribution and residence time analysis gives insight into why large droplets behave so differently from small droplets in a spray dryer. Although this analysis is straightforward and powerful, it has not been previously reported.

The experimental observations and reasoning that led to the conclusion that plug flow residence time was a reasonable approximation for large droplets in a spray dryer was described in section 2.4. It was observable because all the droplets from the Acoustic Atomiser had similar size and trajectory. Other than initial velocity, the droplets have no "memory" of the type of atomisation. The fraction of droplets with the same large size from conventional atomisers should be as comparatively unaffected by the vagaries of the gas flow. This is not directly observable because the trajectories of the few large particles are hidden by the many smaller particles swirling around in the air eddies. However, existing spray dryers must have sufficient plug flow residence time to be capable of drying the large droplets, regardless of the method of atomisation. Since the Acoustic Atomiser size distribution is considerably narrower than that from conventional atomisers, the mean droplet size should be greater. It is established in this chapter that the increase in mean size is at least a factor of two.

It will be shown that the corollary of the increase and narrowing in droplet size distribution is that the droplet residence time is shortened and narrowed. A seven-fold decrease in the spread of droplet residence times is predicted.

6.1 Largest dryable size

The size distribution is rather broad from a conventional rotary or 2-fluid atomiser used in a spray dryer. For a material behaving according to the classic crust formation model, the drying time is expected to increase with the square of the droplet diameter. It will be immediately apparent that it will be uneconomic to provide sufficient residence time to dry the tiny fraction of, say 1000µm diameter droplets when the mode diameter is 50-100µm. Apart from the unfavourable economics of the enormously oversized drying chamber (expensive to construct, and with greater heat loss from the

greater surface), the sensible heat of the dry particles is tiny compared to the heat of vaporisation of the water: dry particles rapidly relax to the drying gas temperature. In a dryer constructed to dry even the very largest droplets, most of the rest of the particles would be dry from an early stage, and would spend excessive time at high temperature. Designing to dry too large a fraction of the droplet size distribution is expensive and reduces product quality.

Conversely, if the chamber residence time is insufficient, too many droplets will still be wet and sticky when they strike the walls or outlet cone of the dryer. At best, there is the unnecessary cost of recycling or disposing of the excessive quantity of agglomerates and sloughed-off wall deposits that are caught on screens. At worst, the wall deposits will char and could ignite a dust explosion.

In any spray drying operation there will be some optimum cut fraction of the size distribution, the largest dryable size. This is not normally made explicit by spray dryer operators, but it is possible to estimate it from the material efficiency of the dryer. This estimate is based on the assumptions that oversize droplets always end up as wall deposits rather than product powder, and also that the oversize are the only droplets to deposit upon the walls. Whilst this is evidently a simplification of the physical reality, empirically it accords to a first approximation with spray dryer operating practice. When wall build-up is excessive, a standard control action would be to increase the driving force for atomisation (increase rotation speed or atomisation air pressure for example) and hence shift the droplet size distribution to smaller sizes. The problem of estimating the largest dryable size is then reduced to estimating the acceptable material efficiency of a spray drying operation, together with a droplet size distribution.

The acceptable material efficiency will vary somewhat; between operators, depending on the value of the material being processed, potential safety hazards from charring of deposits and hence dust explosion initiation, and finally the mode of operation - a high wall deposition rate might give acceptable total accumulation over an eight hour batch operation, but not on a continuous plant. The estimates here have been combined from personal communications from ICI plants, a non-ICI operator and also a spray dryer manufacturer. In a well run, high quality continuous spray drying operation, material efficiency could be 99%, i.e. only 1% of the feed builds up on the wall. Most operations are in the range 95 - 98 % material efficiency. Rarely, batch operations only reach 85 - 90 % material efficiency. In apparently the sole open literature source,

Pemberton and Keey (1980) estimate 92 - 98 % over all dryers in their survey of New Zealand dairy dryers.

In this work the 95th, 98th and 99th percentage points of the droplet size distribution will be used as the range of cut points of the largest dryable size. The size distribution for the Acoustic Atomiser was established in the previous chapter. A representative size distribution for conventional spray dryer atomisers is also required for comparison

6.2 Droplet size distribution for the Acoustic Atomisers

It was established in the previous chapter that the Acoustic Atomiser droplet size distribution was most accurately represented by the Stable distribution. A range of sets of distribution parameters were obtained. However, a representative distribution can be created by the observations from Table 2 and Figure 49 that the central tendency of the alpha and beta parameters is 1.6 and 0.3 respectively, and the mean value of the ratio of the diameter of the 95th percentile of the volume distribution to the mode diameter was 1.33. Hence a representative 2-parameterisation Stable distribution, non-dimensionalised around the mode, can be generated using the parameter set $S(\alpha, \beta, \gamma, \delta ; 2) = S(1.6, 0.3, 0.137, 1 ; 2)$. This is plotted in Figure 50.

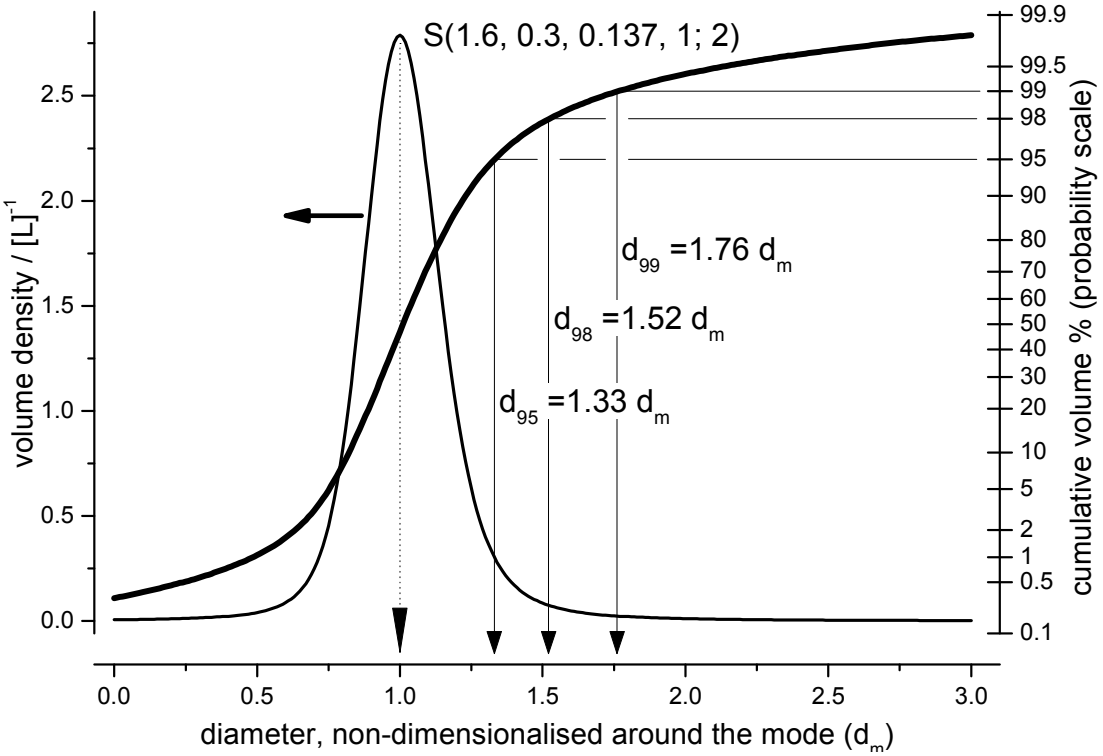

Figure 50: generic Acoustic Atomiser 2-parameter Stable distribution, non-dimensionalised around the mode

The conclusions of the analysis presented below are not dependent upon the selection of the Stable distribution as the model of the Acoustic Atomiser size distribution, but rather upon the experimental observation that the d_{95} is 4/3 the mode diameter d_m. Indeed, the analysis was originally undertaken with the log-normal distribution: the Stable distribution model was a later refinement. In order to demonstrate that the analysis is independent from the specific droplet size distribution model function, it will be worked through with both the log-normal and the Stable distributions. It can be calculated from standard results for the log-normal distribution that a geometric standard deviation $\sigma_g = 1.17$ gives the required width such that $d_{95} = 4/3 d_m$. Table 3 is a summary of the log-normal σ_g parameter from fits to a selection of droplet sizing datasets for the Acoustic Atomiser. It should be recalled from the earlier discussion that the log-normal distribution was found not to be a good fit to the data, hence there is no purpose in fitting all the datasets. However, the selection of datasets that have been fitted are sufficient to confirm that $\sigma_g = 1.17$ is a reasonable choice for the log-normal width parameter. This distribution is plotted in Figure 51.

Material	sizing method	Unconstrained fit to all data			
		σ_g	$w=\ln(\sigma_g)$	PDI	d95/dm
Water nozzle A	PDA	1.131	0.123	0.3	1.24
Water nozzle B	PDA	1.021	0.0207	0.05	1.04
A1	sieve	1.175	0.161	0.4	1.34
A2	sieve	1.1194	0.1128	0.3	1.22
A2	sieve	1.1471	0.1372	0.4	1.28
B	sieve	1.160	0.148	0.4	1.30
C1	PDA	1.05	0.045	0.1	1.08
C2	PDA	1.0317	0.0312	0.08	1.05
D4.15	Visisize	1.115	0.109	0.3	1.21

Table 3: summary of log-normal distribution parameters for fits to Acoustic Atomiser droplet size distribution data

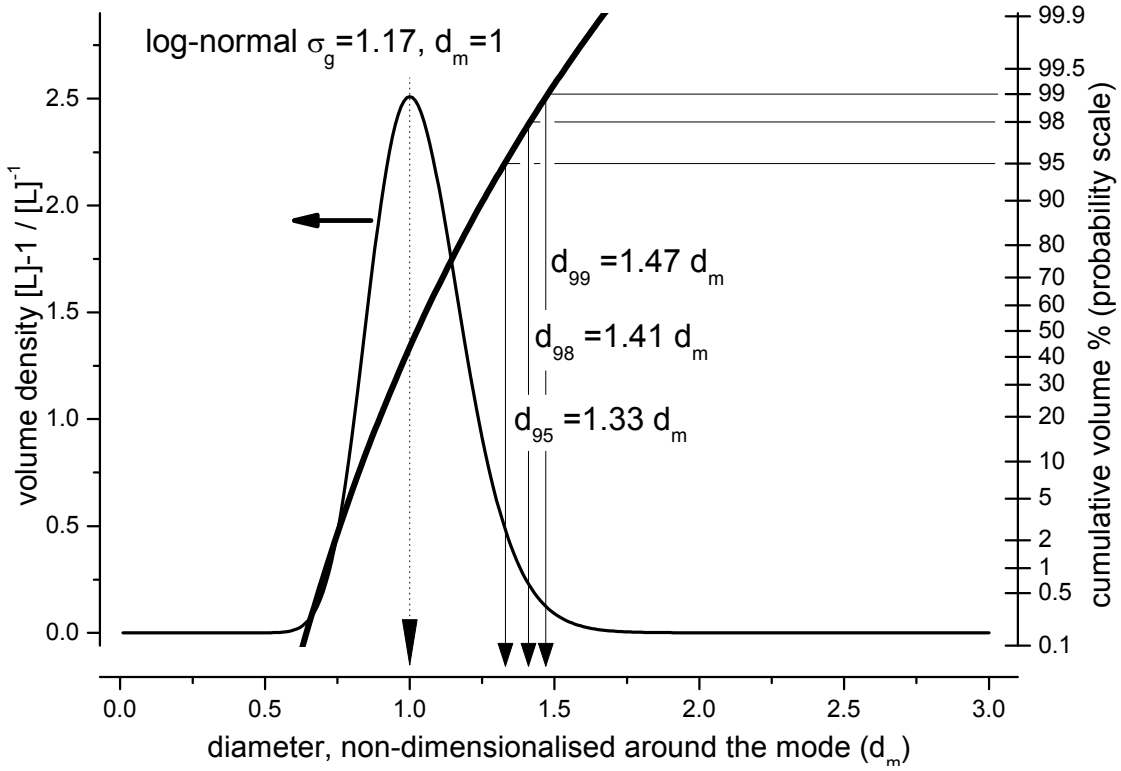

Figure 51: generic Acoustic Atomiser log-normal distribution, non-dimensionalised around the mode

6.3 Droplet size distribution for conventional spray dryer atomisers

It is remarkably difficult to find reliable literature data for the droplet size distribution for conventional spray dryer atomisers. The primary literature sources used even in recent spray dryer models all pre-date modern sizing instruments, so should be used with caution (Welander and Vincent, 2001). To take as an example, in their otherwise detailed overview of the state-of-the-art in CFD modelling of spray dryers, Fletcher et al. (2006) cite a 1981 paper as the source of the atomiser droplet size distribution experimental data.

In common with numerous authors in the sprays literature, Lefebvre (1989) is more concerned with expressions for the estimation of mean diameters from atomisation parameters. The width of the distribution is quantified only in a single paragraph, and then only as a range of 1.5 - 4 for the width parameter of a Rosin-Rammler distribution. Huang et al. (2003, 2004) use a Rosin-Rammler spread parameter of 2.05. This is referenced to a PhD thesis (Kievet, 1997) which it has not been possible to obtain. The published work from the doctorate (Kievet et al., 1997) does not refer to the spray, so it is unclear whether the droplet size was measured, or referenced from other earlier

investigations. Schröder and Walzel (1998) quote values of three to five for the Rosin-Rammler spread parameter, depending on detail of mechanical design for a modified narrow size distribution rotary atomiser, but no reference for a standard rotary atomiser. Despite Mugale and Evans (1951) demonstrating over fifty years ago that the Rosin-Rammler distribution was not a good model for spray droplet sizes, it continues to be used to the present day. The analysis in this chapter is reasonably independent of the detail of the fit function, but the chosen distribution must be at least a passable representation of the large size tail of the droplet size distribution data, so the Rosin-Rammler distribution is not fit for purpose. The problem is that the pertinent large size tail of the distribution is so severely underestimated, that without the original sizing data for spray drying atomisers used in the literature, it is not possible to reliably translate the quoted Rosin-Rammler width parameters into log-normal width parameters.

Both Matsumoto et al. (1985) and Masters (1991) note that there is considerable discrepancy between literature reported distributions. Matsumoto et al. (1985) reference ten studies of rotary atomiser size distributions, although they only include the data from the oldest work (Herring and Marshall, 1955). This data plots as a straight line on log-probability axes, so a log-normal distribution is the appropriate fit function. Values for d_{16}, d_{50} and d_{84} have been read from this chart. Using the standard results for the log-normal distribution (Irani and Callis, 1963) that the geometric mean is the d_{50} and the geometric standard deviation $\sigma_g = d_{84} / d_{50} = d_{50} / d_{16} = \sqrt{(d_{84} / d_{16})}$, a value of around $\sigma_g = 1.6$ is obtained. Similarly, values for σ_g between 1.34 and 1.46 can be obtained from measuring of percentile points on the chart reported by Masters (1991). This is not only incredibly narrow, it is narrower than a rule-of-thumb quoted earlier in the same work (Masters, 1991);

$$d_{95} = \begin{matrix} 2d_{m,} ; & d_{mean} < 60\mu m \\ 2.5d_m ; & 60\mu m < d_{mean} < 120\mu m \end{matrix} \qquad \textit{Eqn. 6-1}$$

It can be calculated that these correspond to log-normal σ_g of 1.42 and 1.55 respectively. Even the $d_{95} = 2d_m$ rule-of-thumb is surprisingly narrow. The $d_{95} = 4/3\ d_m$ historical rule-of-thumb for the width of the Acoustic Atomiser droplet size distribution was introduced in the previous chapter. There was a similar $d_{95} = 2d_m$ rule-of-thumb for the size distribution of unvibrated laminar jets. Although there are no droplet size distribution data to validate this second rule, the validation of the first against forty sets of droplet size distribution data gives some confidence that the $d_{95} = 2d_m$ metric for

unvibrated laminar jets is also valid. Without detailed substantiation, consideration of atomiser physics as well as experience would suggest that the chaotic break-up of liquid from a rotary atomiser would lead to a wider droplet size distribution than that obtained from the breakup of a laminar jet. Masters does not show the data from which his distribution parameters were obtained. The graph axis is labelled as particle size rather than droplet size, and it may be that these are data for screened product. Overall, the narrower widths presented by Masters are considered unreliable, but the $d_{95} = 2.5\ d_m$ or equivalently $\sigma_g = 1.55$ is sufficiently similar to the value of $\sigma_g = 1.6$ from the data of Herring and Marshall (1955) for these to be taken as reasonable literature estimates of the expected width for a log-normal distribution from a rotary atomiser.

There are a few experimental rotary atomiser droplet size data from the research programme at ICI. Datasets C3 and C4 are direct comparisons of a production rotary and an Acoustic Atomiser (Figure 52). The rotary atomiser dataset C4 is an acceptable fit to a log-normal distribution with $\sigma_g = 1.8$ (Appendix A.4), rather wider than the literature data. Dataset D7.17 is a Visisize measurement, and Dataset D8.14 is sieve sizing data, from powder made on the Wilton pilot spray dryer using a rotary atomiser, as comparison data for the Acoustic Atomiser experiments. D7.17 fits well to a log-normal distribution with $\sigma_g = 1.61 - 1.63$, depending on whether the slightly agglomerated tail is included or excluded from the fit (Appendix A.6.3). Dataset D8.14 fits acceptably with $\sigma_g = 1.52$ (Appendix A.5.2).

Between the literature and experimental data, a log-normal distribution with $\sigma_g = 1.6$ is considered to be a reasonable estimate of the width of a typical rotary atomiser size distribution (Figure 53).

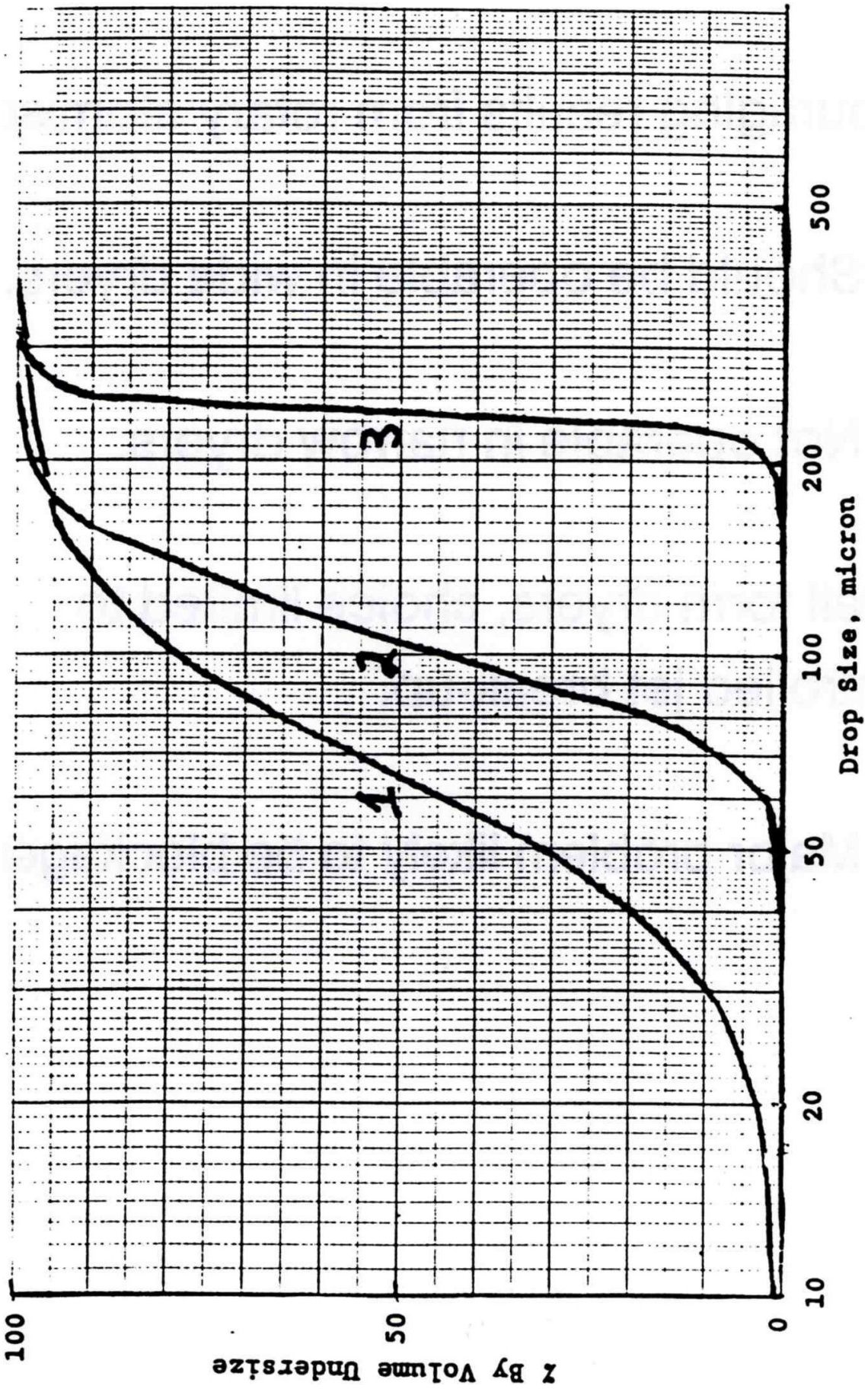

Figure 52: chart comparing drop size distribution of a production Acoustic Atomiser (line 3) to the rotary atomiser that it replaced (line 1). Image courtesy of ICI.

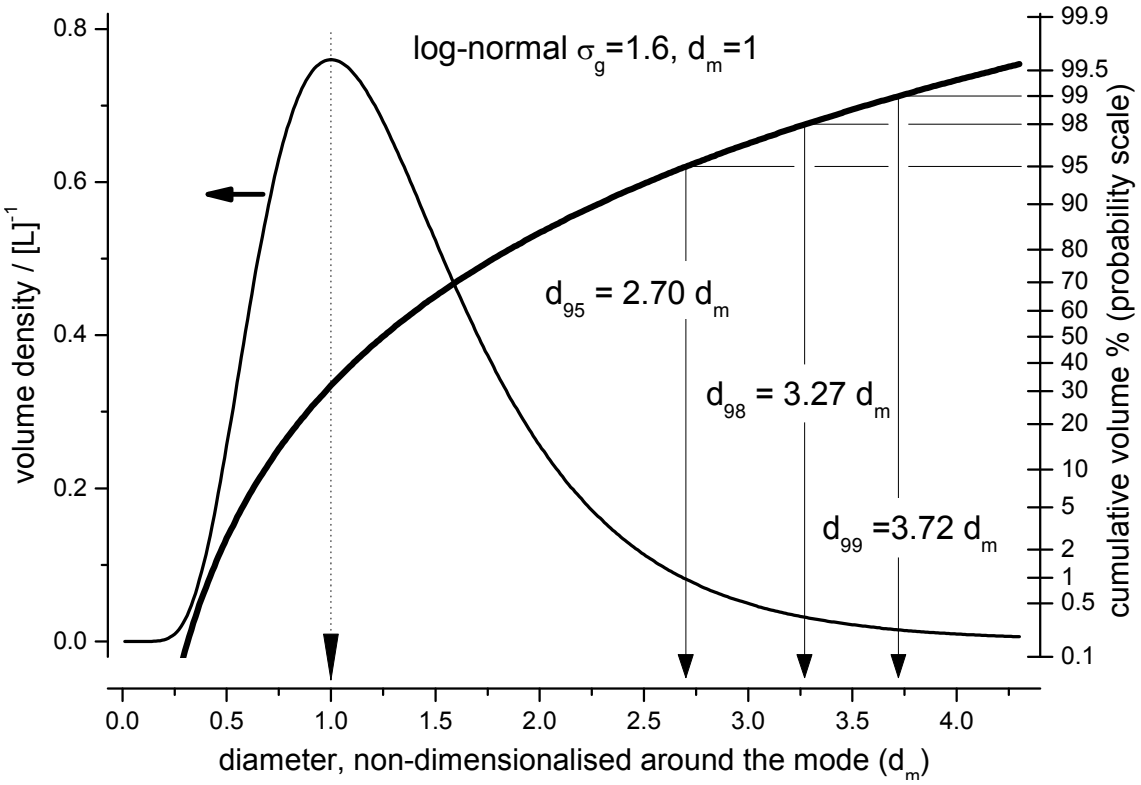

Figure 53: generic rotary atomiser log-normal distribution, non-dimensionalised around the mode

6.4 Potential increase in droplet size using the Acoustic Atomiser

The distributions for the conventional and the Acoustic Atomiser are matched at the cut point chosen as the largest dryable size $d_{XX} = \{d_{95}, d_{98}, d_{99}\}$. To take as example, if d_{95} is considered as the largest dryable size, the cumulative volume fraction V is 0.95 regardless of the distribution model chosen. Diameters are chosen to be non-dimensionalised around the mode of the conventional atomiser distribution. To be found are the non-dimensionalised location parameters of the Acoustic Atomiser distribution with matching d_{XX}.

The log-normal distribution is considered first as it can be solved analytically. From inspection of the standard definition of the cumulative distribution (Eqn. 6-2), equality in the value of the cumulative volume fraction requires equality in the parameter z also (Eqn. 6-3), where subscripts a and c refer to parameters for the Acoustic and conventional atomisers respectively. A substitution (Eqn. 6-5) can be made using the relationship (Eqn. 6-4) between the mode d_m and the geometric mean $\overline{d_g}$. $d_{m,c} = 1$ and $d_{xx} = d_{xx,c}$ by definition of the chosen non-dimensionalisation. The solution is given algebraically in Eqn. 6-6, numerically in Table 4, and plotted in Figure 54.

$$V(z) \equiv 0.5\left[1 + \mathrm{erf}(z)\right]$$

$$z \equiv \frac{\ln(d/\overline{d_g})}{\sqrt{2}\ln(\sigma_g)} \qquad \textit{Eqn. 6-2}$$

$$\frac{\ln(d_{XX,c}/\overline{d_{g,a}})}{\ln(\sigma_{g,a})} = \frac{\ln(d_{XX,c}/\overline{d_{g,c}})}{\ln(\sigma_{g,c})} \qquad \textit{Eqn. 6-3}$$

$$d_m = \overline{d_g}\exp\left[-\ln^2(\sigma_g)\right] \qquad \textit{Eqn. 6-4}$$

$$\frac{\ln\left(\frac{d_{XX,c}}{d_{m,a}}\exp\left[-\ln^2(\sigma_{g,a})\right]\right)}{\ln(\sigma_{g,a})} = \frac{\ln\left(\frac{d_{XX,c}}{d_{m,c}}\exp\left[-\ln^2(\sigma_{g,c})\right]\right)}{\ln(\sigma_{g,c})}$$

$$\frac{\ln\left(\frac{d_{XX,c}}{d_{m,a}}\right) + \ln\left\{\exp\left[-\ln^2(\sigma_{g,a})\right]\right\}}{\ln(\sigma_{g,a})} = \frac{\ln\left(\frac{d_{XX,c}}{d_{m,c}}\right) - \ln^2(\sigma_{g,c})}{\ln(\sigma_{g,c})} \qquad \textit{Eqn. 6-5}$$

$$\ln\left(\frac{d_{XX,c}}{d_{m,a}}\right) = \left[\ln\left(\frac{d_{XX,c}}{d_{m,c}}\right) - \ln^2(\sigma_{g,c})\right]\frac{\ln(\sigma_{g,a})}{\ln(\sigma_{g,c})} + \ln^2(\sigma_{g,a})$$

$$d_{m,a} = d_{XX,c}\exp\left\{\left[\ln^2(\sigma_{g,c}) - \ln\left(\frac{d_{XX,c}}{d_{m,c}}\right)\right]\frac{\ln(\sigma_{g,a})}{\ln(\sigma_{g,c})} - \ln^2(\sigma_{g,a})\right\} \qquad \textit{Eqn. 6-6}$$

A numerical solution is required for the Stable distribution. A modified version of the spreadsheet previously described for the experimental data fitting was used. The parameter delta has been iterated, with gamma maintained at 0.137 δ, until the diameter cut point of the Stable distribution matched that of the rotary atomiser log-normal distribution. The solution is given numerically in Table 4, and plotted in Figure 55.

Location parameters of Acoustic Atomiser drop size distribution relative to rotary atomiser log-normal drop size distribution, $\sigma_{g,c}$=1.6 & non-dimensionalised around the mode			matched at cut-point XX % of the cumulative volume distribution		
			95	98	99
log-normal model	$\sigma_{g,a}$ = 1.17	$d_{m,a}$	2.04	2.31	2.52
		$d_{g,a}$	2.09	2.37	2.58
Stable distribution model	S(1.6, 0.3, γ, δ;2)	δ	2.03	2.15	2.13
		γ	0.278	0.295	0.292

Table 4: increase in droplet size distribution using the Acoustic Atomiser

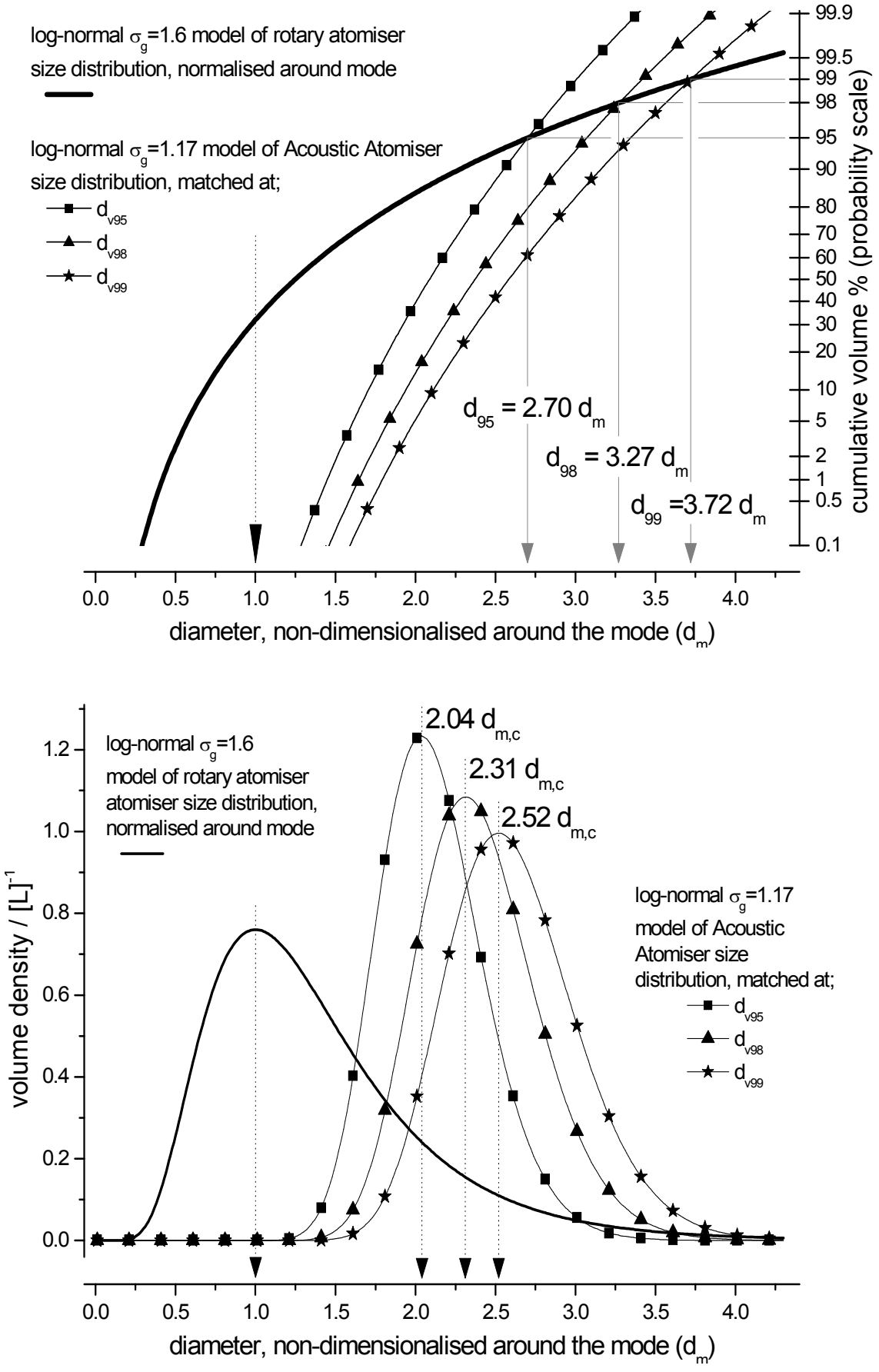

Figure 54: increase in droplet size distribution using the Acoustic Atomiser: log-normal model

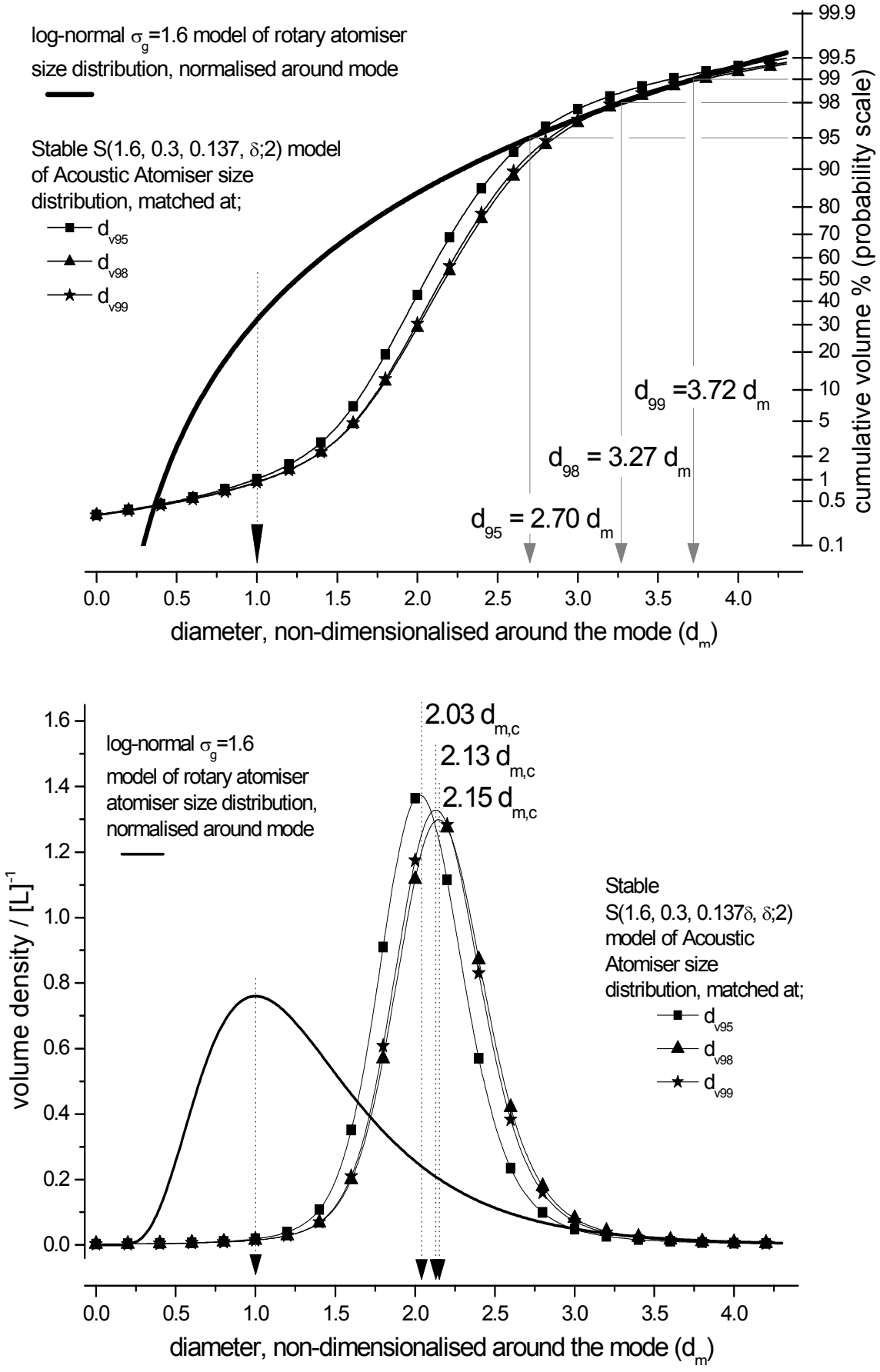

Figure 55: increase in droplet size distribution using the Acoustic Atomiser: Stable distribution model

It can be seen between Figures 54 and 55 that doubling the mode droplet size is predicted when an Acoustic Atomiser is used in a spray dryer in place of a rotary atomiser. If the log-normal model is assumed, the factor of increase may be as great as 2.5 if the cut point is taken as d_{v99} rather than d_{v95}. The Stable distribution has been shown in this research to be a better model of the droplet size distribution from the Acoustic Atomiser. If the Stable distribution is used in the analysis, only modest further increases in the droplet size distribution are predicted when cut point diameters greater than d_{v95} are chosen. Indeed, due to a numerical peculiarity of the differing rates of tail decay of the Stable distribution and the matched log-normal distribution, the match at d_{v99} is predicted to be at fractionally *lower* mode size than that at d_{v98} (it is not a typographical error in Table 4).

The predicted droplet size distribution increase when the Acoustic Atomiser is used in place of a rotary atomiser accords well with informal observations made during the ICI in-house development programme. Indeed, a factor of 2.5 increase in mode size result from the original log-normal model analysis was subsequently used as a rule-of-thumb in experimental design by the research team. At 7.8m, the ICI Wilton pilot spray dryer is unusually tall, so that the droplet residence time is similar to typical production spray dryers. When a research programme with a new material was commenced, data for the mode size in the existing production plant was obtained. This diameter was increased by a factor of 2.5 as an estimate of the expected dryable size in the Wilton pilot facility, and the atomiser parameters for experiments chosen accordingly. Prior to this research, a 1-D computational model was used to make the estimate of dryable size, with experimental drying kinetics data from a wire deflection device that has previously been described (section 3.5.2). The new method was not only a cost-effective saving in research time, but was found to give more reliable predictions. However, the more recent refinement of the analysis with the Stable distribution suggests that the factor of 2.5 was ambitious. A more conservative estimate using a factor of 2 increase in mode size may have given fewer problems with agglomeration. The ubiquity of agglomeration seen in the Visisize datasets suggests that too large a fraction of the droplets were not quite dry.

The magnitude of the predicted droplet size distribution increase is less well substantiated with the very few instances where there are comparable rotary and Acoustic Atomiser droplet size data. Taking the fit parameters from Appendix A.4, a

mode diameter of 47µm can be calculated using Eqn. 6-4 for rotary atomiser dataset C4, compared to 238µm for the Acoustic Atomiser dataset C3. This is a factor of 5 increase. However, it was previously noted that rotary atomiser dataset C4 was unusually wide compared to literature and other experimental data, and dataset C3 is unusually narrow. In contrast to this larger than expected increase, a mode diameter of 220µm can be calculated from the fit parameters for dataset D7.17 in Appendix A.6.3. The 280 - 305µm mode diameters for the comparable Material D7 Acoustic Atomiser datasets are only a factor of 1.3 - 1.4 increased. However, the mode diameter of 169µm calculated for the D8.14 rotary atomiser dataset is almost perfectly a factor of two less than 330µm mode diameter of the primary atomisation peak of the Stable fits to datasets 8.9a - 8.12a shown in Appendix A.6.4.

As the Acoustic Atomiser is novel there are no independent validation data, but the predicted increase in size is not inconsistent with data from a survey of production spray dryers with conventional atomisers (Pemberton and Keey, 1980). This was the first report that most of the drying occurs within a short distance of the atomiser. It was concluded that manufacturers' scale-up rule-of-thumb was that the air residence time should be held constant for a given height to diameter ratio. Consequently the designs were very sub-optimal. Chamber volume was ineffectively utilised: all the dryers studied had surplus drying capacity. Dryers with product mean diameter from 25-55µm had air residence time sufficient to dry particles of order 250µm diameter. However, between 92 and 98% of product was found to be below this maximum size.

Whilst the model qualitatively demonstrated its practical worth, there are insufficient size distribution measurement validation data from rotary atomiser comparative experiments to be able to demonstrate quantitatively the correctness of the analysis.

6.5 Comparison of droplet residence time in a spray dryer

Personal industrial experience is that a widespread myth amongst spray dryer operators is that the spray drying chamber residence time is only a few seconds. This is perpetuated by, for example, a statement in the sales literature of the market leading spray dryer manufacturer that the whole process generally takes no more than a few seconds (Niro, 1999). The standard textbook gives a more nuanced view (Masters, 1991). Chamber residence time may be as short as 5s, but 20 - 40s is typical. Schuck

(2002) quotes 20 - 60s from his experience of dairy spray dryers. These are gas mean residence times, but the standard assumption described earlier has been made, that the particles are sufficiently fine to be fully relaxed to the flow streamlines, so the air residence time and the particle residence time are the same. Pemberton and Keey (1980) distinguish between the two, reporting gas residence time from 7 to 30s and shorter particle residence times from 6 to 17s in their survey of production spray dryers.

Experimental data for droplet residence time distribution in a spray dryer are scarce. There are only two known reports in the literature, both of studies in pilot dryers.

Kröger and Schulte (2000) reported a radiotracer study of residence time distribution in a pilot spray dryer 1.5m in diameter and 2.7m total height, of which the upper 1.7m was cylindrical and the lower metre was conical. Air flowrate was 210 Nm^3/hr. Water with 70μm mode droplet size was sprayed. A tracer pulse was injected into the liquid feed to the atomiser, and the radiation intensity emitted from the product stream was measured. The intensity was converted into a mass concentration of tracer, and this mass concentration against time data was presented graphically in the paper.

Taking Kröger and Schulte's (2000) data, it has been calculated that the chamber volume was $3.6m^3$, the gas mean residence time was 62s and the gas superficial velocity in the upper cylindrical portion was just 0.03m/s. The tracer concentration data has been read from the graph, and normalised. The concentration had not fallen to zero by the end of the recording period. By extrapolating the decay curve (Figure 56), it has been estimated that 87% of the tracer was recorded, so the data has been normalised to 0.87 rather than 1. This is a refinement: the conclusion is not sensitive to the accuracy of the estimate. The data has been re-plotted in Figure 57 as cumulative mass fraction of tracer in the product as a function of time. Also plotted are hypothetical limiting cases. Plug flow gives the theoretical minimum droplet residence time, whilst the plug flow dead time and stirred tank model gives the maximum. The plug flow curve has been calculated assuming that droplets fall vertically at steady terminal velocity, without evaporation. A log-normal droplet size distribution with $\sigma_g = 1.6$ has been assumed. It is apparent that the actual median residence time of the droplets is roughly double the theoretical minimum. This is consistent with the reports of numerous authors, as previously reviewed, that many droplets become entrained in large recirculation zones in a spray drying chamber.

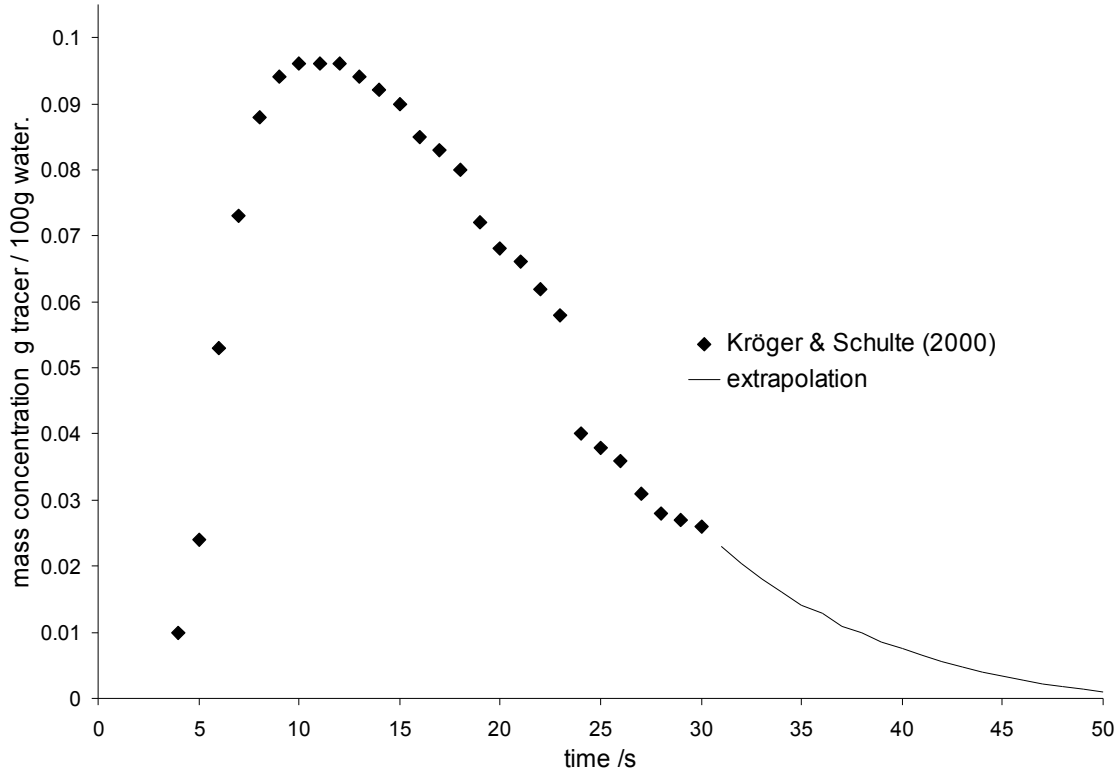

Figure 56: mass concentration of radiotracer in powder product as a function of time, after Kröger and Schulte (2000).

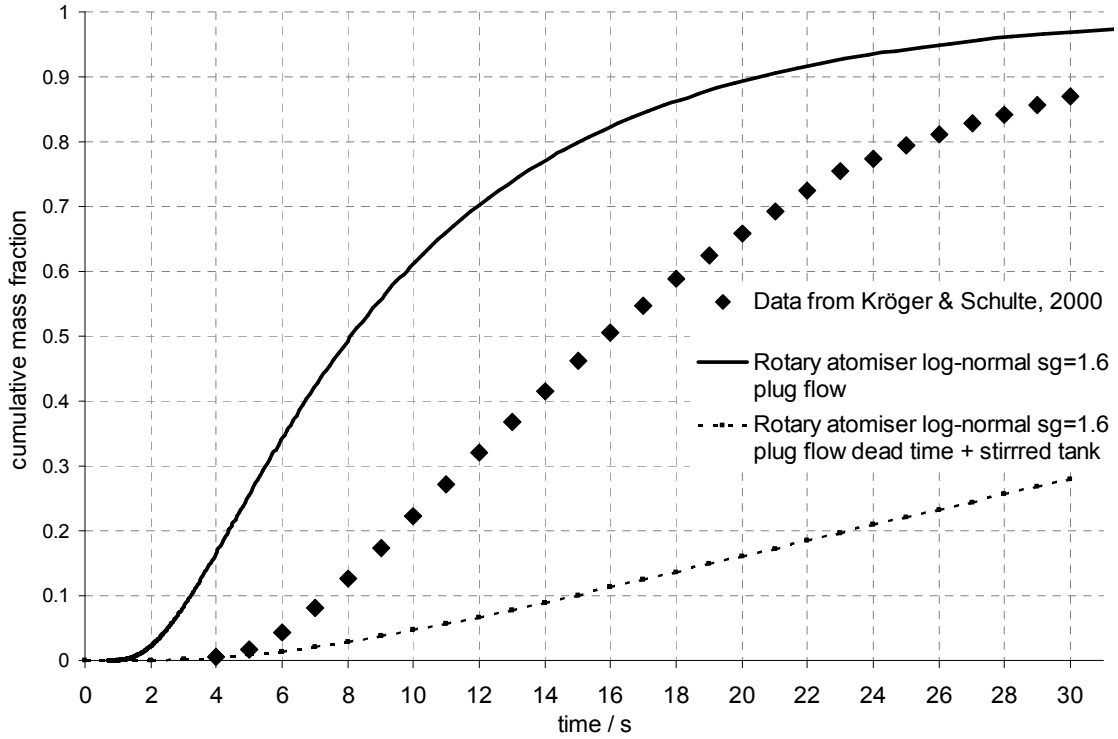

Figure 57: residence time analysis using data from Kröger and Schulte (2000) radiotracer study.

If spray drying has been selected over a cheaper drying process, it is normally because the material is temperature sensitive and will be degraded by long residence times. If the particles actually dry in just a few seconds, holding them at high temperature for a further half minute is not an obvious strategy to minimise thermal degradation. It would also be preferable for any unavoidable thermal degradation to be distributed throughout the sample, especially if the material is used in extremely small doses, as sometimes occurs with flavour ingredients or pharmaceuticals for example. Instead, the most heat degradation is expected to occur in the smallest particles which both dry most rapidly and also are most prone to being entrained in recirculation zones.

The effect on the residence time distribution (RTD) of the narrower size distribution from the Acoustic Atomiser has been calculated and then plotted (Figure 58). The black points and line are as in Figure 57, respectively the data from Kröger and Schulte (2000) and the theoretical plug flow RTD for a log-normal distribution with 70μm mode diameter and $\sigma_g = 1.6$. The red lines are the plug flow RTD for an Acoustic Atomiser droplet size distribution, with 70μm mode diameter, matched to the conventional atomiser. The solid red line is the log-normal $\sigma_g = 1.17$ model, the red dashed line is the Stable distribution $S(\alpha, \beta, \gamma, \delta ; 2) = S(1.6, 0.3, 0.137*\delta, 70 ; 2)$ model. There is little difference between the two models. It can be seen that the prediction is that the narrower size distribution from the Acoustic Atomiser gives a massive decrease in the spread of the residence time distribution. The blue line with circle symbols is the plug flow RTD for a Stable distribution model of the Acoustic Atomiser size distribution, matched to the log-normal distribution for a conventional atomiser at d_v95. From the previous section, this is $S(1.6, 0.3, 0.137*\delta, 2.03*70 ; 2)$. Taking this effect of larger mean size into account as well as the narrower size distribution, the predicted spread of the RTD becomes extremely narrow, far more so than might have been anticipated from inspection of the comparative size distributions plotted in Figure 55.

In an attempt to quantify the narrowing in the spread of the RTD, the residence time between the 5^{th} and 95^{th} percentiles of the cumulative mass fraction has been selected as a arbitrary baseline for comparison. From inspection of the data in Table 5, a seven-fold reduction in the spread of the RTD is predicted when an Acoustic Atomiser is used in place of the rotary atomiser. Of course, these are only the predictions from the hypothetical ideal case of plug flow. It is clearly seen in Figure 58 that the experimental RTD is significantly wider than plug flow, which widening has been rationalised as the

effect of the entrainment of droplets in the air recirculation zones in the spray dryer chamber. There is no experimental data for the residence time distribution of a spray dryer using an Acoustic Atomiser. However, as previously discussed, the larger droplet sizes will have greater momentum and thus be less likely to be entrained by the airflow. Hence the RTD when an Acoustic Atomiser is used is expected to deviate less from plug flow than the experimental RTD data for the conventional atomiser. Thus the surprising expectation is that the calculated seven-fold decrease in the spread of the RTD would be a conservative estimate in practice.

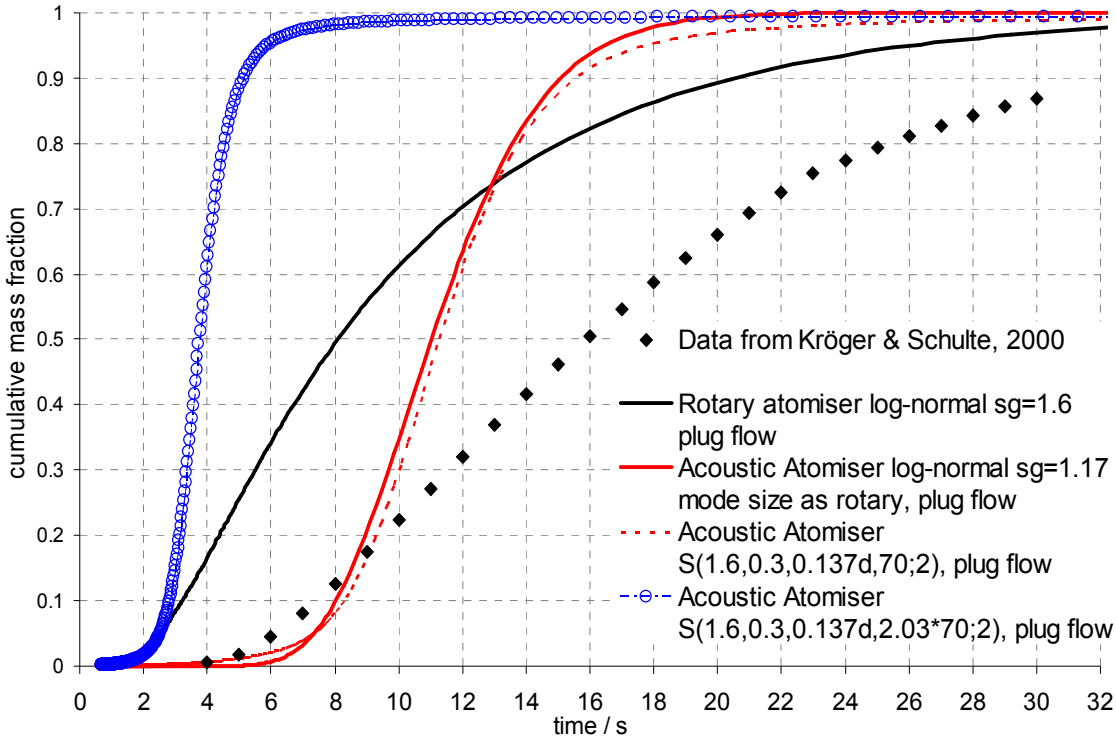

Figure 58: theoretical Acoustic Atomiser RTD compared with data from Kröger and Schulte (2000) radiotracer study.

		residence time /s at cumulative mass faction cutpoints		
		5%	95%	t_5-t_{95}
Conventional atomiser	log-normal, d_m=70μm, σ_g=1.6	26.3	2.5	**23.8**
Acoustic atomiser	log-normal, d_m=70μm, σ_g=1.17	16.7	7.5	**9.2**
	S(1.6, 0.3, 9.6, 70; 2)	18.1	7.3	**10.8**
	S(1.6, 0.3, 19.5, 141.2; 2)	5.9	2.5	**3.4**

Table 5: reduction in spread of theoretical plug flow RTD with the Acoustic Atomiser

In the other RTD study reported in the literature, a maltodextrin dispersion in water was dried in a pilot spray dryer 2.215m diameter, 3.73m total height, of which the upper 2m was cylindrical and the lower 1.73m was conical (Kievet and Kerkhof, 1995). The drying air was again at very low flowrate, 1040 m^3/hr, with inlet temperature 195°C and outlet 105°C. A pressure nozzle atomiser was used. Sieve sizing data of the dry product from both the spray dryer and the cyclone are presented, together with Rosin-Rammler fits.

From the published data (Kievet and Kerkhof, 1995) the gas mean residence time has been calculated to be 34s. The size distribution data has been re-fitted by a log-normal distribution with $\sigma_g = 1.65$, $d_g = 125\mu m$, $d_m = 97\mu m$, which is a more satisfactory agreement to the data in the tails of the distribution (Figure 59). The tabular data for the residence time distribution which can be plotted without further processing (Figure 60).

The recorded times are astoundingly long, much greater than can be accounted for by particle entrainment in the airflow. Kievet and Kerkhof (1995) note that a large fraction of the product was deposited on the walls. They ascribe the extended particle residence times to particles slowly sliding down the walls and cone of the drying chamber. Since this effect dominates the particle residence time distribution, the data presented in the paper is not useful for substantiating a model of how a typical spray dryer would be expected to perform.

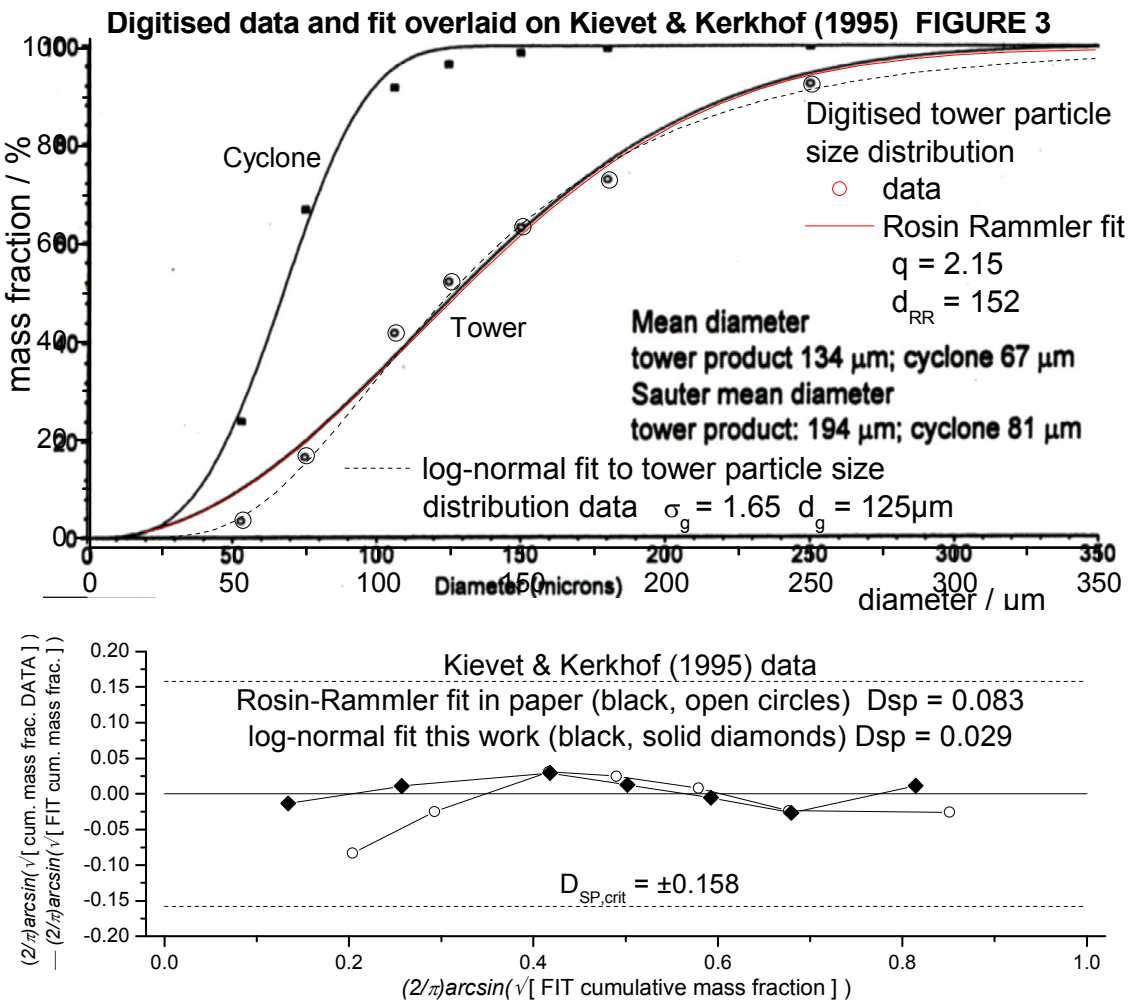

Figure 59: particle size distribution after Kievet and Kerkhof (1995)

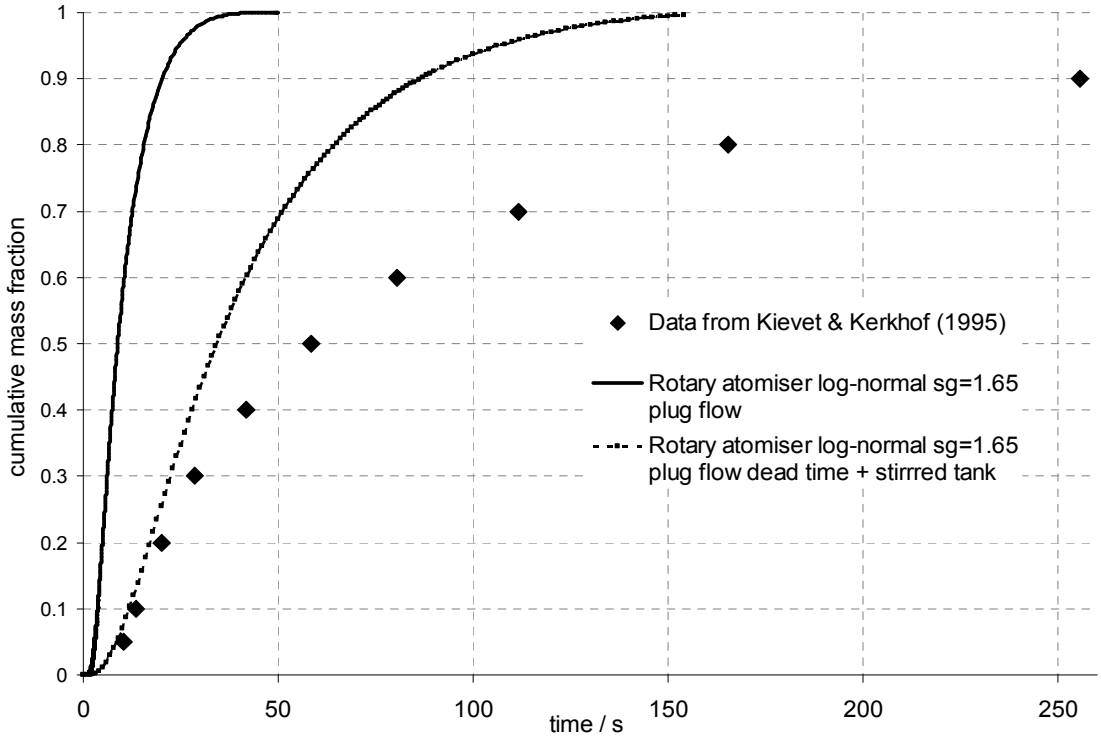

Figure 60: particle residence time distribution after Kievet and Kerkhof (1995)

6.6 Conclusions

In this chapter it was shown that simple manipulation of droplet size distributions is a powerful model to predict the performance of a spray dryer when an Acoustic Atomiser is used in place of a rotary atomiser.

A factor of two increase in mode size is predicted, which accords well with experimental observations, although there are insufficient rotary atomiser comparative experimental data to robustly quantitatively validate the conclusion.

The predicted effect on droplet residence time when using the Acoustic Atomiser is even more dramatic than the increase in size. If the mode size is kept constant between rotary and Acoustic atomisers, then the effect of reducing the fine and oversize tails of the droplet size distribution is alone sufficient to more than halve the spread of the droplet residence time distribution (RTD). If the mode size is increased by a factor of two, then a seven-fold decrease in the spread of the particle RTD is conservatively estimated. There is no experimental RTD study for the Acoustic Atomiser to directly validate this prediction. However, the large decrease in spread is consistent with and explains the finding in Fiannaca and Threlfall-Holmes (2005), reviewed earlier, that where multiple spray-dried particle morphologies were possible, particles predominantly of a single morphology could be made using an Acoustic Atomiser. This strongly indicates that the particles each had very similar time-temperature histories during the drying.

The potential decrease in the spread of droplet residence times may not always be practically realisable. Langrish (2007) hypothesised that residence time grossly in excess of that required for drying alone may for some materials be required for phase transformation from amorphous to crystalline. He also noted, however, that fluidised beds on the dryer outlet perform the function of extended residence time at lower temperature. It remains for further work to confirm the expectation that even if extended residence times were required for phase transformation, it would still be more thermally efficient and produce the most consistent product, to minimise the residence time in the spray drying chamber to that required for drying.

This chapter has underlined the importance of atomisation in the spray drying process. However, there are currently no robust predictive rules to determine sprayability. The remainder of this thesis describes how sprayability can be predicted.

CHAPTER 7 - REVIEW OF EXTENSIONAL RHEOLOGY, THE CaBER TECHNIQUE AND THE RELEVANCE TO SPRAYABILITY

Extensional rheology is the study and behaviour of fluids under an extensional deformation. The most widely known examples of where elongational flows are encountered are polymer melt processing operations such as extrusion, fibre spinning and film blowing, but elongational flows are also important in such applications as roller application of coatings and glues, various jet dispensing techniques such as ink-jet printing, as well as in sprays (Petrie, 1978, McKinley, 2005, Chan et al., 2007). The behaviour of Newtonian fluids in elongational flows can be predicted from their behaviour under shearing deformations. In contrast, the rheological behaviour of complex fluids may differ markedly between extensional and shear deformations. The deviations from ideality may be so extreme, that even allowing for the complex combination of shear and extensional flows in real processing equipment, extensional rheology may dominate the overall behaviour of the flow. Industrial spray dryer feedstocks are expected to exhibit complex fluid rheology, as they are commonly extensively dewatered and may contain dispersed polymer, as has previously been noted.

The importance of extensional deformations to spray droplet formation is readily appreciated from a description of the process. In most atomiser types, liquid leaving the nozzle orifice initially diverges into a sheet. The friction at the interface between the sheet and the air drives instabilities at the interface, forming waves and perforations, which grow until ligaments are formed, which are themselves unstable, and break-up into droplets (Figures 61 and 62). The diagram and image are for a fan shaped sheet, as this is the configuration in the study reported in Chapter 9, but the description is extendable to other atomisers: for example a pressure swirl nozzle with a circular orifice will form a cone shaped sheet, and a rotary atomiser an annular sheet. As liquid velocity increases, the sheet becomes shorter lived until eventually atomisation occurs immediately at the nozzle. There is also no sheet formation at very low nozzle exit velocities: in the atomisation mode exploited by the Acoustic Atomiser the droplets are formed from a varicose laminar jet which emerges directly from the nozzle, as depicted in Figure 3 in the Introduction. Common to all of these atomisation mechanisms is the final droplet formation from the stretching of a ligament. This ligament breakup is a

uniaxial extension at very large strains and strain rates, and explains why extensional rather than shear viscosity is expected to dominate atomisation behaviour.

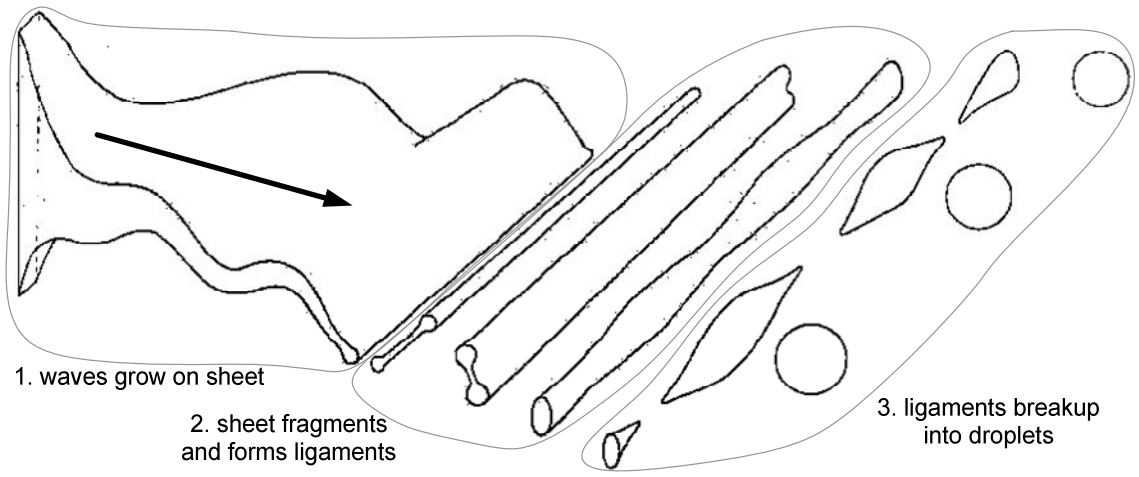

Figure 61: idealised sketch of wavy sheet breakup (after Dombrowski and Johns, 1963)

Figure 62: example of flat-fan spray. Cuprinol Sprayable Timbercare. Image captured under laser strobe sheet illumination. Greyscales inverted to more clearly show features of spray. Scale is approx. 8cm from top to bottom of image. (Tony Flounders and Phil Threlfall-Holmes- ICI)

Petrie (2006b) has described the historical development of understanding of extensional viscosity, from Trouton's description of the "coefficient of viscous traction" (Trouton, 1906) and Fano's of *corpi filanti* (thread forming materials) 100 years ago (Fano, 1908). The importance of extensional rheology in the types of industrial application noted in the introductory paragraph has long been recognised and acknowledged in the academic literature, if not so widely in the applicable industries. Measurement methods for characterising the extensional rheological response of high viscosity melts have been developed and applied to problems such as polymer fibre spinning. Strain hardening of dilute solutions of high molecular weight polymers has also received significant research attention; the effect is very extreme and amenable to quantitative explanation from simple models of molecular structure. However, in the absence of a commercially available measurement technique, or indeed any technique which gave consistent results (Combloux, 1990, James and Walters, 1994), studies of the extensional rheology of other complex fluids and especially low viscosity solutions have been sparse. The practical difficulty is in obtaining a steady flow at constant extension rate. Generally the best that can be obtained from real apparatus are measures of a tensile stress growth function (most frequently termed as a "transient apparent extensional viscosity", despite the confusion this term is reported to cause (Petrie, 2006a)), which requires specification of the details of the flow geometry employed.

The importance of extensional rheology has been acknowledged in the sprays literature (e.g. Xing et al., 1999, Dexter, 1996), but the context of such acknowledgements make clear that it is not common practice within the sprays community to utilise the concept.

In the following chapters of this thesis it will be demonstrated that the prognosis has been improved by the commercial availability of the Capillary Breakup Extensional Rheometer or CaBER technique, implemented in the Haake CaBER 1 instrument from ThermoFisher Scientific. Whilst the CaBER 1 as supplied is best considered as a "commercial prototype", technique and analysis method development has been found to be sufficient to utilise it to gain useful insight into the problem of sprayability. The CaBER technique still only yields a measure of transient apparent extensional viscosity at best, but it has been found that the flow geometry is sufficiently similar to the ligament breakup occurring in sprays processes for the transient apparent extensional viscosity coefficient to be a useful measurement parameter to predict sprayability.

7.1 The capillary thinning and breakup principle

Jetting and dripping from a nozzle both exhibit a region of uniaxial extensional deformation in the fluid neck between droplets, but this region moves rapidly relative to the observer and so is hard to instrument. If a disc of fluid held between two plates is stretched by the separation of the plates, however, then the thinning ligament can be constrained to be in a stationary reference frame to the observer and hence can form the basis of a rheometer. The CaBER technique is an implementation of this flow configuration. In the experiment, a disc of fluid is introduced into the gap between parallel co-axial cylindrical plates typically 6mm in diameter [Figure 63(a)]. The upper plate is raised [Figure 63(b)] as rapidly as possible, from the initial height L_0 which is typically half the plate diameter, to a predetermined final height [Figure 63(c)], typically set in the range 8-20mm, thus stretching and imparting a step strain upon the fluid. The fluid ligament then thins down under the action of gravitational and surface tension forces, resisted by the elasticity and viscosity of the fluid [Figure 63(c)]. Finally, the fluid thread snaps [Figure 63(e)].

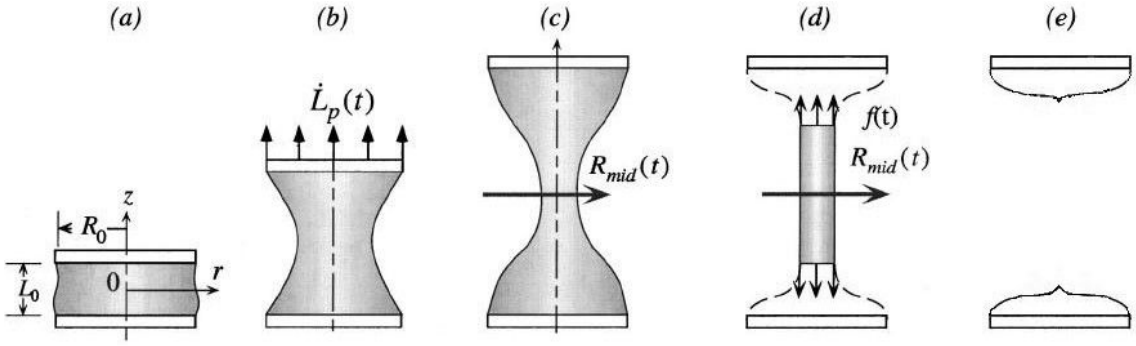

Figure 63: schematic of the course of a CaBER experiment (after McKinley and Tripathi, 2000)

As the fluid thread becomes very thin, gravitational drainage becomes negligible, and the rate of thinning is determined by the visco-elasto-capillary balance. The capillarity is separable (and can be characterised by independent measurement of the static surface tension), provided that two key assumptions are satisfied; that the tensile stress developed by the initial strike has relaxed away before capillary thinning takes over and also that the surface tension is constant. Separating out the capillarity permits analysis of the visco-elastic response of the fluid. The behaviour of the thread is dominated by the visco-elastic response at the thinnest point, where the strain rate is greatest. It is typically a reasonable approximation that the thread is thinnest at the mid-point between

the plates, thus measurement of this mid-point diameter as a function of time as indicated in Figure 63(c) can be analysed to yield information about the visco-elasticity of the fluid in uniaxial extension. Since the thread is thin compared with the plate separation, it is normally also a reasonable assumption that the thread is sufficiently close to cylindrical local to the mid-point, that the flow is entirely axial, as illustrated in Figure 63(d). This significantly decreases the mathematical complexity so that it is possible to reduce the force balance to (Anna and McKinley, 2001) ;

$$\bar{\eta}_{app}(t) = \frac{\sigma}{2dR_{mid}(t)/dt} \qquad \textit{Eqn. 7-1}$$

where σ is the static surface tension, dR/dt the rate of thinning and $\bar{\eta}_{app}(t)$ the transient apparent extensional viscosity. It is important to appreciate that the strain and strain rate vary throughout the thinning, and are not controlled by the experimenter but rather by the physical properties of the fluid. Thus the force balance is a pseudo-equilibrium for a differential timestep, and the parameter obtained is a transient apparent extensional viscosity not *the* extensional viscosity (i.e. in the widespread casual usage of the term to mean a steady state viscosity coefficient), except under certain special conditions (McKinley, 2005).

7.2 Implementation of the CaBER technique

The principle of optical measurement of capillary thinning and breakup as the basis for a rheometer was first described by Entov and co-workers (Bazilevsky et al., 1990a). This filament thinning rheometer was developed through the 1990's, notably by Prof. Gareth McKinley's group at MIT. It is a version of the MIT CaBER that has been commercialised as the ThermoHaake CaBER 1. In this instrument, the mid-point diameter is determined by a laser micrometer. The obscuration by the filament of a UV laser sheet generated by a laser diode is measured by voltage drop on a detector, which voltage drop is then calibrated to filament diameter. Due to refraction in the thin filaments of interest, the filament shadows the detector regardless of the transparency of the samples (Thermohaake, 2003). However, the beam is not infinitesimally thick as is implied by the mid-point arrow in Figure 63(c), but rather is 1mm thick. Thus the assumption of cylindricity of the filament around the mid-point is required not just for the mathematical simplifications outlined above, but also for practical accuracy of determination of the mid-point diameter.

The viscosity limits of the CaBER are not well defined, as they are dependent on the surface tension and elasticity of the fluid, together with the actual performance of the instrument as against published specification. Rodd et al. (2005) have estimated the lower limit of viscosity for an inelastic fluid to be around 70mPa.s, but conservative assumptions of the surface tension and instrument performance were made, and lower viscosities can be measured when there is elasticity. Personal industrial experience would suggest that 20-30mPa.s may be achievable in some cases, although this has yet to be formally substantiated. The vendor documentation (Thermohaake, 2003) claims the upper limit to be around 10^5 - 10^6 Pa.s, but no substantiation of this limit is referenced.

The CaBER provides a flow field believably analogous to ligament breakup in a spray, or indeed to other industrial applications previously noted, where ligament formation, thinning and breakup dominate the overall behaviour. Further attractions of the CaBER are practical: a measurement is typically comparatively quick and simple to perform, with very little fluid (85µl per measurement in the default geometry), and the commercial instrument is not expensive when compared with analytical shear rheometers, especially considering that it offers unique capability. However, the technique is immature, and the commercial instrument has not sold in sufficient quantities for the manufacturer to be able to justify the cost of developing an improved version (Nijman, 2006). Clasen et al. (2006b) reported difficulties in measurements of model polymer solutions caused by the inaccuracy of the quadratic diameter calibration curve at very low filament diameters. Research at ICI Wilton with industrial fluids which display a variety of complex rheological responses has uncovered a series of issues with the commercial CaBER 1. These can be categorised as mechanical, control/electrical and analysis issues. In this work only technique and analysis development will be considered. There is a rich seam of opportunity for further research and development of the CaBER technique.

7.3 Alternative approaches to extensional rheometry

There are, or have been, other commercial extensional rheometers; the Rheometrics RFX opposed jet rheometer for very low viscosity fluids (now out of production) and polymer melts rheometers from a number of manufacturers for very high viscosities,

which work on the principle of forcing or extruding the sample through a capillary or die; or alternatively stretching the melt through the rollers of a triple roll mill.

The CaBER is not the only possible implementation of the plate separation geometry. If the plates are driven so that they continue to separate at an exponentially increasing rate, the strain rate in the filament will remain constant (Anna et al., 2001, McKinley and Sridhar, 2002, CPG, 2003). In some senses these modern devices are not so different from Trouton's experiments a century ago (Trouton, 1906), except in that Trouton was studying very viscous material and thus had the timescale in which to measure and record the filament diameter manually with a graticule in the eye-piece of a cathetometer telescope. Filament stretching rheometers require a well controlled and exponentially increasing plate separation, so are large and mechanically complex compared with the CaBER, and thus are significantly more costly to construct, house and operate, notwithstanding the lack of commercial availability.

Various other extensional rheometers have been developed. For example, Xing et al. (1999) describes a variation on the spin-line rheometer. Dexter (1996) determines extensional viscosity from the pressure drop across a packed bed. There are many implementations of contraction geometries (e.g. James et al., 1990, Binding and Walters, 1988), the contraction-expansion geometry of Taylor's four roll mill (Lagnado and Leal, 1990), or hyperbolic converging-diverging flows (Janssen et al., 1993). Gupta and Sridhar (1988) and James and Walters (1994) have reviewed experimental methods. However, rather than constructing another instrument, the focus of this research was to study the capability of the CaBER, which is the only commercially available extensional rheometer for low viscosity fluids.

7.4 The state of the art

There were several key experimental studies with model fluids during the development and validation of the CaBER technique (Liang and Mackley, 1994, McKinley and Tripathi, 2000, Anna and McKinley, 2001, Anna et al., 2001). It should be noted that these studies were carried out on instruments constructed by the investigators, before the introduction of the commercial ThermoHaake CaBER 1 instrument. Thus they develop and validate the technique in principle rather than the detail of the implementation in the commercial instrument.

Recently published experimental studies typically still consider the rheological behaviour of relatively simple model systems, and many investigators continue to use instruments they have built themselves, rather than the commercial CaBER 1 instrument. There are several studies with dilute solutions of high molecular weight polymers, exploring variously: the limits of sensitivity of the CaBER instrument, and adherence to and divergence from basic explanatory models such as Zimm theory (Clasen et al., 2006b, Rodd et al., 2005); and also, the formation of "beads on a string" (Oliveira and McKinley, 2005, Clasen et al., 2006a). The behaviour of solutions of flexible, rigid and semi-rigid polymer molecules has been considered, with some demonstrable success in a practical application, relevant to the flat-fan type of atomiser considered in the study reported here (Stelter et al., 2002a, 2002b).

There are only a handful of experimental studies with materials of complexity more akin to real commercial products such as the liquid feed to spray dryer atomisers, or the coatings formulations in the study reported in Chapter 9.

The relaxation times of blends of commercial methyl-hydroxy-ethyl-cellulose solutions have been determined from CaBER measurements (Plog et al., 2005). Hydroxy-ethyl-celluloses are widely used as rheology modifiers in coatings formulations. The relaxation times were shown to correlate with measurements of the molecular weight distributions obtained by other techniques. They also characterised defined blends of polystyrene standards, and showed by moment analysis of the molecular weight distribution, correlation with the methyl-hydroxy-ethyl-cellulose solutions.

Yesilata et al. (2006) have shown that the behaviour in CaBER experiments of wormlike micellar fluids can be accurately predicted by the Giesekus constitutive equation. Quantitative agreement was obtained provided that relaxation time of the solutions in extensional flows was three times lower than in shear. No physical explanation is offered for why this factor of three should arise.

Cooper-White et al. (2002) studied the effect of addition of associative polymer to a dilute polymer solution, concluding that there was a substantial impact on the dynamics of extension, but a gulf between observing the phenomenon and being able to construct formulation guidelines for real commercial systems. The result has more recently been extended to an experimentally validated theory with hydrophobically modified ethylene oxide urethane (HEUR) associative polymers (Tripathi et al., 2006). This might in the

future be a basis for quantitative understanding of the behaviour in extensional flow of HEUR containing formulations such as the materials in the study reported in Chapter 9. However, the behaviour of coatings formulations also containing solid pigment particles is expected to be significantly different again (Buscall, 2006) and it remains to be substantiated that the theory will even qualitatively describe these materials.

Dijkstra et al. (2007) investigated the effect on rheology and sprayability of polymers dispersed in the continuous phase of polyurethane latex adhesives. The storage modulus measured in oscillatory shear showed qualitatively the expected trend with both spray fan length and a qualitative assessment of overspray, although no quantitative correlation is offered. Extensional viscosity measurements were made on a CaBER instrument that had been built at Erlangen-Nürnberg University. This was found not to be capable to making measurements on all the fluids tested, but it is unclear whether the same limitations on measurement range apply to the Haake CaBER 1 also.

Yarin et al. (2004) report that simulants for gelled rocket propellants, the rheology of which followed a power law dependence in shear, could also be described in both shear and elongation by a three dimensional extension of the power law model.

A rheological model for yield stress fluids has been proposed (McKinley, 2005). It remains to be experimentally validated. In an unpublished study at ICI Wilton, it was not found to fit experimental data. Since the rheological response of the studied material was exceedingly complex, it was perhaps an unfairly severe test of an embryonic theory, but it is nonetheless demonstrative that far more work remains to be done before a reliable framework of models is available, upon which to interpret experimental data from fluids of the complexity of commercial product formulations.

The lack of a reliable model for yield stress rheology is especially vexing when considering spray dryer feedstocks. The commercial drive to minimise dryer evaporation load means that particulate suspensions as dryer feedstocks are typically highly concentrated, and yield stress rheology would be expected from a highly concentrated particulate suspension. Theoretical and instrumental development and empirical validation of a yield stress model from CaBER data is a project beyond the scope of this doctoral research project. What is reported in this thesis is a step along that path, with developments to the experimental data analysis, for a fluid which does not conform to any of the published rheological models for the CaBER.

CHAPTER 8 - THE ANALYSIS OF CABER DATA

In this chapter is described the development that has been undertaken of the analysis of CaBER data for a fluid of arbitrary complexity. The discussion begins from the expected behaviour of published rheological model fluids.

The raw data output from the commercial Haake CaBER 1 instrument is a tabulation of filament diameter (as measured by the laser micrometer) against time. The plot of this data is the "*time-diameter curve*". The analysis task is to extract useful rheological insight from this data.

8.1 Behaviour of model fluid cases

The currently available literature models have been usefully summarised by McKinley (2005). In the Newtonian fluid case, the diameter decays linearly with time in the later stages of thinning, once gravitational slump can be neglected. Power law or Bingham plastic rheology destabilises the filament, which is seen as a negative deviation from linear in the time-diameter curve. Elasticity in the fluid will generally progressively retard the thinning of the ligament, which is seen as a positive deviation from linear of the time-diameter curve (although in some cases elastic recoil may decrease the filament stability). A quadratic decay is expected for a second order fluid, the simplest model of finite strain elasticity under flow. It has been shown theoretically for a FENE-P dumbell model visco-elastic fluid, and experimentally validated with polystyrene based Boger fluids, that the filament diameter decays exponentially, limited only by the finite extensibility of polymer chains in solution (Entov and Hinch, 1997, Anna and McKinley, 2001).

8.1.1 The Newtonian case

Only the Newtonian fluid case will be discussed in detail. The reason for this focus is twofold. The Newtonian case is the simplest behaviour, and thus a first step to understanding more complex behaviours. In addition, in the limit any shape of time-diameter curve can be considered to be an infinite sequence of straight lines of differentially short length. In general, real fluids will not correspond perfectly to any of the theoretical models, and no general means has previously been established to transform the time-diameter data into viscosity-strain data, which is shown later to be a

useful method of presentation. The approach proposed in this thesis is that the Newtonian model can be used as a basis for the numerical differentiation of an arbitrary time-diameter curve.

It is important to appreciate that the most successful outcome to be expected from this numerical differentiation approach is a numerical parameter related to transient apparent extensional viscosity. To achieve this would require a true capillary thinning experiment in the CaBER and a material only slightly deviant from Newtonian behaviour. In an experiment with a real material with an arbitrary rheology, the numerical differentiation technique can pragmatically give useful insight, but it is unlikely to advance fundamental understanding. The more extreme the non-Newtonian character of the sample and the further the deviation from a capillary thinning experiment, the less useful it is likely to become, as the underlying assumptions in the simplification are violated. Nonetheless, the utility of the differential timestep analysis approach is demonstrated by the study reported in this thesis.

In the Newtonian model case the extensional viscosity coefficient is obtained simply from the gradient of the time-diameter curve dR_{mid}/dt, with a numerical correction factor for the slight curvature of the filament away from a parallel sided capillary (Renardy, 1995b). McKinley and Tripathi (2000) show analytically and experimentally that the gradient of the time-diameter curve is;

$$\frac{dR_{mid}}{dt} = \frac{(2X-1)}{6}\frac{\sigma}{\eta_s} \qquad \textit{Eqn. 8-1}$$

with the constant X = 0.7127 according to the self-similar solution of Papageorgiou (1995) and σ is the static surface tension, which can be obtained from a separate instrument - for example a DeNoüy ring or plate.

The parameter η_s is confusingly termed an apparent shear viscosity. Although η_s is a viscosity coefficient from a measurement of apparent extensional viscosity, the equation has been cast in such a form that the parameter η_s has numerical magnitude equivalent to the shear viscosity, rather than three times the shear viscosity as would be expected for the extensional viscosity of a Newtonian material. Although it is not made explicit in McKinley and Tripathi (2000), it is likely that it was chosen simply for the convenience of direct comparison of the numerical magnitude of η_s from CaBER data with shear rheometry data in validation experiments. The authors no doubt wanted to

avoid calling the parameter η_s an apparent Newtonian extensional viscosity, as that should be $3\eta_s$. The η_s parameter appears in key papers in the literature, as well as in the commercial CaBER manual and software. However, in order to avoid propagating further confusion by this study, in these analyses only the apparent extensional viscosity will be used, which is numerically three times the magnitude of the η_s parameter;

$$\eta_{app,ext} = 3\eta_s \qquad \textit{Eqn. 8-2}$$

In the Newtonian model case, the extensional viscosity is time invariant. In all other cases in the CaBER experiment, what is measured is a *transient* apparent extensional viscosity $\overline{\eta}_{app,ext}$. The normal expectation is that the viscosity coefficient obtained from CaBER data is a transient apparent extensional viscosity, varying in time, strain, strain rate and total stress state of the sample.

It will be seen from a re-arrangement of the McKinley and Tripathi formula (Eqn. 8-1) that for a Newtonian fluid the apparent extensional viscosity parameter can be estimated from the measured gradient dD_{mid}/dt of an experimental time-diameter curve;

$$\eta_{app,ext} = -\frac{0.4254\sigma}{dD_{mid}/dt} \qquad \textit{Eqn. 8-3}$$

If the fluid were genuinely Newtonian, the numerical value of the extensional viscosity coefficient $\eta_{app,ext}$ obtained from the CaBER experiment should agree quantitatively with three times the shear viscosity obtained by conventional shear rheometry. This was confirmed experimentally by McKinley and Tripathi (2000).

8.2 Behaviour of real fluids in the CaBER experiment

In reality several forces act upon the sample other than the capillary stress, among them inertia, gravity, and uncontrolled viscous and elastic stresses arising from the initial elongation or the loading of the sample into the rheometer. The response of real fluids to the experiment may be far from simple and these other forces may be significant or even dominant over the capillary stress.

Considering once again the initial stretch in the CaBER experiment, a step elongation strain is imposed in as short a time as possible. Both the strain and the strain rate are large. Even if the sample is purely liquid in character the inertial, viscous and

gravitational stresses which develop at this stage will initially overwhelm the capillary stress. However, a key assumption of the CaBER experiment is that the initial stress relaxes away, whilst the capillary stress increases with time and will eventually dominate. The assumption is good provided that the sample is purely viscous at all achievable extension rates and timescales, and the viscosity is not too high. If, however, the sample is visco-elastic, then the terminal relaxation time of the material determines whether or not the initial stresses relax out sufficiently quickly for the CaBER experiment to be measuring capillary thinning. In experiments with real industrial fluids, when the initial stresses have not relaxed out a variety of anomalous behaviours have been observed, as shown in Figure 64. Fluids variously detach from one or other of the plates, or yield in either brittle fracture or ductile failure under the action of the elastic stress developed in the initial step. Many materials pinch off asymmetrically, so that the laser micrometer beam positioned mid-way between the plates does not intersect the narrowest point of the filament and the diameter thus reported cannot be used to quantify the maximum capillary stress. These artefacts are more clearly apparent in video footage of the experiment than from the time-diameter curve. However, the instrument is supplied without a camera, and at the time the study reported in this thesis was conducted, the ICI Wilton CaBER was not fitted with a camera. The analyses in this study are reliant upon careful examination of the time-diameter curve for the identification of data that is invalid for analysis due to artefacts.

Constant surface tension is another assumption in the CaBER experiment. Given the very high rate of creation of liquid-air interfacial area during the CaBER experiment, this is a challengeable assumption for materials with very high surfactant loadings. Any effect on the CaBER experiment of dynamic surface tension has yet to be explored rigorously either theoretically or experimentally.

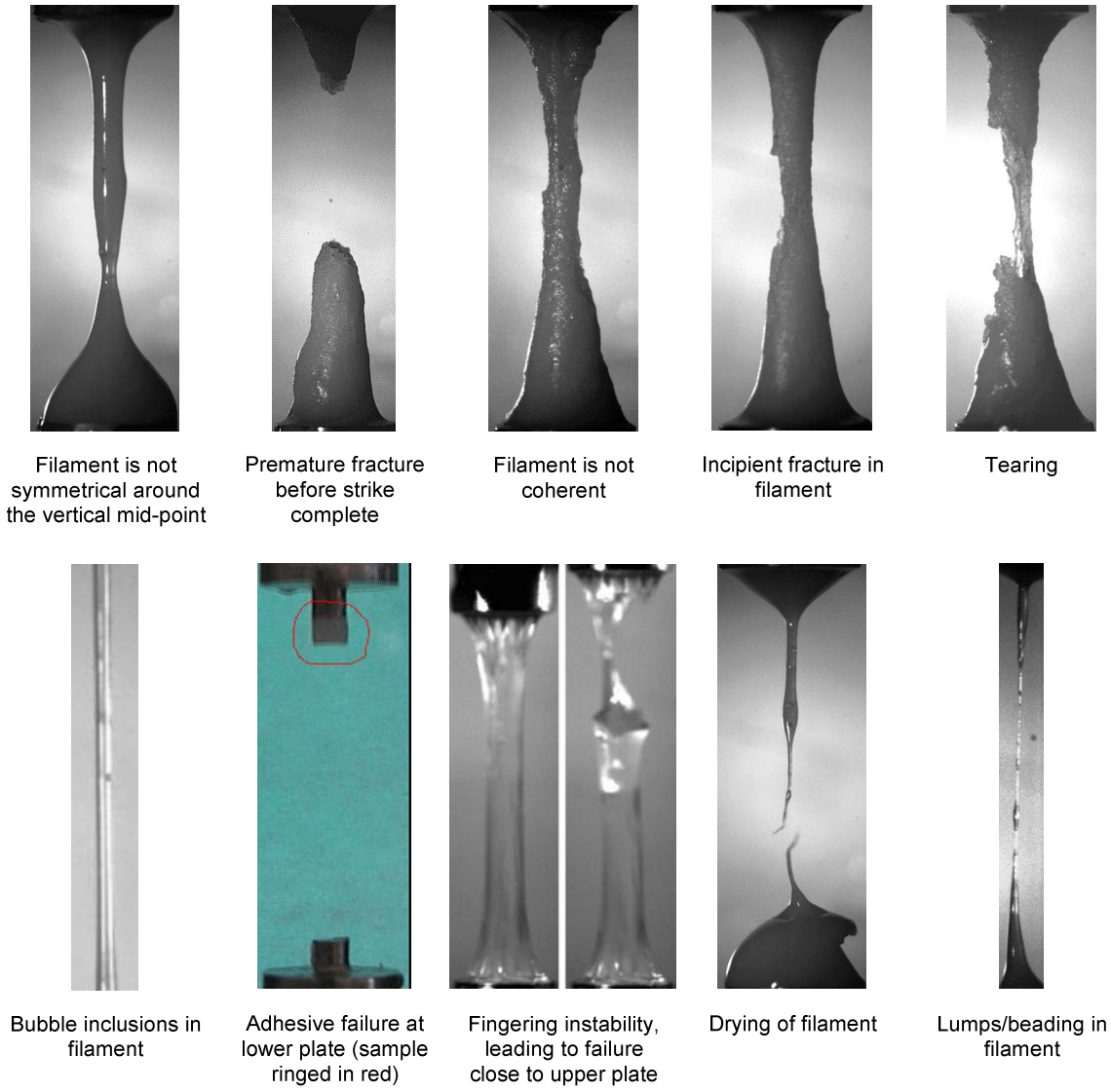

Figure 64: gallery of artefacts in the CaBER experiment (ICI-Phil Threlfall-Holmes)

8.3 Presentation of CaBER data

The native presentation is the time-diameter curve plot. A useful translation method for this curve is proposed in section 8.3.1. However, there are others ways that can be conceived of presenting CaBER data. To take the most sophisticated example in the literature, Petrie (1997) has investigated with theoretical rheology models whether surface plots of transient apparent extensional viscosity against both strain and time could be used to harmonise the measurements from various types of elongational rheometers. He was unable to reach a conclusive verdict, as the deviations from expectation were greatest where the theoretical models are known to be least reliable. The plots had been proposed by others, but exemplified by experimental data covering only a very limited range. It is possible that with more recent elongational rheometer designs that the plot method could now be tested more thoroughly, but no such studies

have been reported. More simply, by analogy with shear rheometry, aspects of material flow behaviour can most clearly be exposed by careful selection of the axes of 2D plots:- stress, strain, shear rate, modulus, etc. The commercial CaBER 1 instrument does not measure sufficient parameters to unlock such fecundity of choices in data presentation as does a shear rheometer, but of particular note is the widely used plot against strain of the Trouton ratio, which is a measure of strain hardening. This Hencky strain - Trouton ratio plot is described in section 8.3.2. In order to create this plot, strain, strain rate and measures of transient apparent extensional viscosity and strain hardening must be derived from the time-diameter data. These transformations are considered in sections 8.3.3 to 8.3.6.

8.3.1 Time re-zeroing of the time-diameter curve

From Eqn. 8-3, it can be seen that a key quantity is the gradient, $dR_{mid}(t) / dt$, and how this gradient changes over the time of the experiment. Hence it is the shape of the curve obtained that gives insight.

It is widely reported in the literature (e.g. McKinley, 2005, Rodd et al., 2005, McKinley and Tripathi, 2000) that the characteristic time to ligament break-up (i.e. the time between the end of the strike and filament failure) can also be used to analyse experimental data. However, experiments with industrial products (both the results reported in this thesis and other unpublished commercial studies) have not typically given repeatable break-up times. The reasons for this discrepancy in findings have yet to be validated, but it is likely to be some combination amongst three; inherent inhomogeneity of the samples on the length scale of the capillary; an artefact of experimental protocols (for example insufficient relaxation time after loading before straining); an artefact of the measurement method (for example, many published studies used home made apparatus rather than the commercial CaBER). As previously noted, the laser beam has a finite thickness. During a breakup event, the calibration may no longer be valid; instead of a parallel sided capillary obscuring the path of the laser beam, there may be a converging neck, or all or part of a drop or drops. Drop formation may precede filament breakup, as in the widely reported "beads-on-a-string" morphology (Clasen et al., 2006a, Oliveira and McKinley, 2005, Bazilevsky et al., 1990b), or more usually, if droplet formation occurs, it follows on from filament rupture. An additional source of variation is the motion control of the linear motor

which drives the strike. Devices built by study authors may record the time of the end of the strike, but the commercial CaBER does not. The time zero in the CaBER output file is at or around the time when the reported diameter begins to drop below the initial plate diameter. This occurs as the upper plate passes through the laser beam, i.e. it is during the transit of the plate, not at the end of the strike. In principle the relative time of the end of the strike could be calculated from the programmed strike profile. In practice this calculation is unreliable. In an unpublished study at ICI Wilton by Dr. Anthony Stickland using high speed photography and image analysis, it was found that the actual strike profiles varied from the intended strike profile in an unpredictable fashion. Thus it is not in general possible to characterise the time to breakup from the laser micrometer signal alone, but only in combination with video footage.

The observation that the time to breakup is not a useful measurable parameter (at least in the commercial CaBER) permits an important transformation to be made to the data. Of primary interest is the shape of the time-diameter curve, and whether the decay curve for one material is more or less rapid than another. That is, it is the gradient and the rate of change of the gradient that is interesting, but the actual position of the curve in time is not important. The rheologist is thus free to choose an arbitrary time zero, and translate the curves along the time axis in order to make comparison between different curves easier. This time-shifting (or time re-zeroing) has been found in this study to be an exceedingly powerful analysis tool, and has been used routinely in the analyses reported here. This analysis technique has not been reported by other authors. The principle is to choose a convenient diameter, and re-define the zero point time to be the time at this diameter. Time-diameter curves can then be translated along the time axis so that they have a common diameter at the new time zero, to enable easier comparison of the shapes of the curves, whether between repeat experiments on the same material or between different materials. In the theoretical analysis for a Newtonian filament, Bond number less than 0.1 is taken to be the criterion for the filament diameter for which gravitational drainage can be considered to have become negligible and the rate of thinning is solely a balance between surface tension and extensional viscosity (McKinley and Tripathi, 2000). The corresponding numerical value of 0.8mm filament diameter is only valid for capillary thinning of a Newtonian fluid, but there are no literature reports of what the diameter should be for other rheological models. In the study reported in the following chapter, 1mm has been used as a pragmatic and convenient zero point time, but it must be appreciated that this is essentially an arbitrary

selection as none of the analyses are truly capillary thinning of a Newtonian fluid, and Bond number of 0.1 is an arbitrary standard.

8.3.2 Hencky Strain - Trouton ratio plot

The Trouton ratio is defined as the ratio of the extensional viscosity to the shear viscosity. From geometrical considerations, for a Newtonian fluid, the uniaxial extensional viscosity is three times the shear viscosity, so the Trouton ratio in this special case is three. So, in a plot from CaBER data of Trouton ratio against a measure of strain, a Newtonian material will plot a straight horizontal line, as the Trouton ratio is always three for any value of strain. The curve for a strain hardening material, where the viscosity increases with increasing strain, will show a positive deviation away from the horizontal, as the viscosity and therefore Trouton ratio increase with increasing strain. The concept is sketched in Figure 65: Figure 71 in Chapter 9 is an example of such a plot from CaBER data for a strain hardening material. It will be seen that the Trouton ratio - Hencky strain plot is useful because strain hardening behaviour is very clearly depicted. It will now be considered how these plot parameters can be calculated from CaBER data.

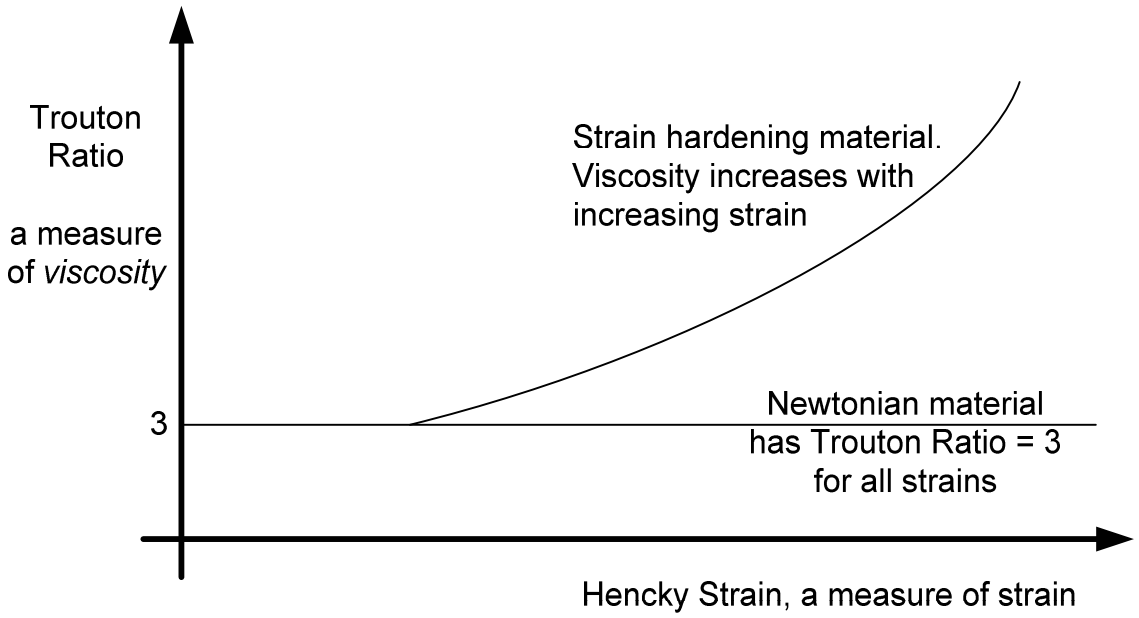

Figure 65: cartoon of the Hencky strain - Trouton ratio plot for Newtonian and strain hardening rheologies

8.3.3 Calculation of Hencky strain from CaBER data

Engineers would normally use the structural engineers' definition of strain, as the change in length of a beam divided by its original length, $\Delta L / L_0$. However, this is a pragmatic simplification for the very small extensions generally encountered in a civil engineering structure. Large extensions would only be encountered if the structure fails, but civil engineering design methods are intended to ensure that structures do not fail, so the implicit assumption of small extensions is perfectly adequate in this context. The problem is that engineering strain is not objective except for infinitesimal strain. On stretching, the strain is $\Delta L / L_0$, but on the reverse compression, the starting position is $L_0 + \Delta L$, so the strain is $-\Delta L / (L_0 + \Delta L)$, that is, the value of strain obtained is lower in magnitude for the same physical deformation. This lack of objective measure is inadequate for the huge extensions in the CaBER experiment. The problem is resolved by defining an infinitesimal strain increment dL / L and integrating from the initial length L_0 to the final length L to get the total strain, or Hencky strain, which is now objective (Eqn. 8-4). In one dimension for an incompressible material, the Hencky strain is *the* strain.

$$\int_{L_0}^{L} \frac{dL}{L} = \left[\ln(L)\right]_{L=L_0}^{L=L} = \ln\left(\frac{L}{L_0}\right) \qquad \textit{Eqn. 8-4}$$

It will be seen that for very small strains, this reduces to the approximation given by the engineering strain;

$$\ln\left(\frac{L_0 + \delta L}{L_0}\right) \approx \frac{\delta L}{L_0} \qquad \textit{Eqn. 8-5}$$

Conservation of sample volume in the CaBER experiment allows the deformation ratio $L(t) / L_0$ to be re-cast in terms of filament diameter, so in practical terms, the Hencky strain *H* is rather straightforward to calculate from CaBER data;

$$H = 2\ln\left(\frac{d_0}{d(t)}\right) \qquad \textit{Eqn. 8-6}$$

where d(t) is the filament mid-point diameter at time t, and d_0 the initial diameter of the sample when it was first loaded, before the imposition of the step strain. Anna and McKinley (2001) define d_0 as the initial diameter of the sample when it was first loaded, but then in an example calculation of the Hencky strain, use the diameter of the filament at the end of the strike. Whichever definition is strictly correct, pragmatically the initial

sample diameter has been used in this study. As noted previously, the time at the end of strike is not recorded by the CaBER instrument, so the diameter at end of strike is not known unless the CaBER data has been synchronised to simultaneous video footage.

A further practical complication, is that the unprocessed CaBER data is a time series of diameter measurements, i.e. the diameter is a dependent variable. In the Hencky strain - Trouton ratio plot, diameter becomes the independent variable. The practical significance is that it is computationally simplest to leave the transformed datasets in the same order, i.e. the first diameter measurement, $d(t_0)$, at t_0, is transformed into the first element of the Hencky strain dataset, and the second diameter measurement, $d(t_1)$ is transformed into the second element of the Hencky strain dataset. Whilst the filament thins over the course of the experiment, there will inevitably be noise in the diameter measurement, so it is not guaranteed that d_{n+1} is smaller than d_n . Consequently the Hencky strain will not monotonically increase as would be desirable in an independent variable, and strange jagged loops can appear if the Hencky strain - Trouton ratio is plotted as a line. Potential solutions are to re-order the dataset in increasing Hencky strain, or to plot the data as points. In the study reported in this thesis, the noise is suppressed as a side effect of the moving average data smoothing in the transient apparent extensional viscosity calculation which is described in section 8.3.5.

8.3.4 Calculating the strain rate from CaBER data

The strain rate $\dot{\varepsilon}$ can be calculated by differentiation of the Hencky strain;

$$\dot{\varepsilon} = \frac{dH}{dt} = 2\frac{d}{dt}\left[\ln\left(\frac{d_0}{d(t)}\right)\right] = 2\frac{1}{\frac{d_0}{d(t)}}\frac{d}{dt}\left[\frac{d_0}{d(t)}\right] = 2\frac{d(t)}{d_0}\left[d_0\frac{-1}{[d(t)]^2}\frac{d}{dt}[d(t)]\right] = -\frac{2}{d(t)}\frac{d}{dt}[d(t)]$$

$$\dot{\varepsilon} = -\frac{2}{d(t)}\frac{d}{dt}[d(t)] \qquad \textit{Eqn. 8-7}$$

Strategies for the numerical differentiation are discussed below

8.3.5 Calculating the transient apparent extensional viscosity from CaBER data

If a fluid conforms reasonably to one of the small selection of rheological models available, then the transient apparent extensional viscosity can be determined from a fit of one or other of the model equations to the experimental time-diameter curve.

However, with industrial non-model fluids, this is found to be the exception rather than the rule. It would be desirable to have a general method to analyse an arbitrary form of time-diameter curve.

The full force balance is (Renardy, 1995a);

$$\underbrace{3\eta_s\left(-\frac{2}{D_m}\frac{dD_m}{dt}\right)}_{\text{Viscous Stress}} = 3\eta_s\dot{\varepsilon} = \underbrace{\frac{4F_Z}{\pi D_m^{\,2}}}_{\text{Tensile Stress}} - \underbrace{\left[\tau_{ZZ}-\tau_{rr}\right]}_{\text{Elastic / Non-Newtonian Stress}} - \underbrace{\frac{2\sigma}{D_m}}_{\text{Capillary Pressure}} \qquad \textit{Eqn. 8-8}$$

As previously introduced, an assumption in the CaBER experiment is that the capillary stress will eventually dominate, so other terms can be neglected and Eqn. 8-8 reduces to;

$$\overline{\eta}_{app,ext} = -\frac{\sigma}{dD_{mid}/dt} \qquad \textit{Eqn. 8-9}$$

In fact recalling Eqn. 8-3 for the Newtonian case, a correction factor is required for the slight curvature of the filament around the mid-point.

The conjecture in this thesis is that a pragmatic approach to analysis of an arbitrary shape of time-diameter curve is to assume that when the filament is fine, contributions to the total stress other than the capillary stress are always sufficiently small to be negligible. That is, the contribution of inertial, gravitational, and uncontrolled viscous and elastic stresses arising from the initial strike or sample loading may be initially large, but diminish over time as these stresses relax, whereas the capillary stress increases, and it is assumed that it eventually dominates, at some time before filament breakage. An arbitrary time-diameter curve can then be considered to be a series of quasi-Newtonian straight lines, and the evolution of the transient apparent extensional viscosity of the fluid over the lifetime of the filament can be calculated from a numerical differentiation of the time-diameter curve;

$$\overline{\eta}_{app,ext} = -\frac{0.4254\sigma}{dD_{mid}(t)/dt} \qquad \textit{Eqn. 8-10}$$

This approach will work best for materials which deviate only slightly from Newtonian behaviour. As the non-Newtonian character of the sample becomes more extreme, the assumption that the other contributions to the total stress are negligible becomes less applicable. An alternative interpretation is that the duration of the experiment for which the capillary stress dominates becomes progressively shorter as the deviations from

Newtonian behaviour increase. Hence the transient apparent extensional viscosity is well estimated by the method for a decreasing portion of the range over which it has been calculated and reported. The method has known limitations, but its utility is demonstrated by the study reported in this thesis.

The proposed method requires a numerical differentiation of the time-diameter tabulated data that is the instrument output. Stepwise calculation of change in diameter over each time increment is not only the simplest strategy to implement, but it has the important advantage of avoiding the imposition of model or fit dependent artefacts upon the data, or unwittingly smoothing out interesting but subtle features of the data. Numerical differentiation is normally noisy, but there is an additional complication in the unmodified commercial CaBER on which the study in this thesis was conducted. A 12-bit data acquisition card is supplied. This gives serious quantisation of the laser micrometer signal (Figure 66). Direct stepwise numerical differentiation gives an unusable noisy trace, as the differential varies from zero on the treads of the steps to extremely large values on the risers. In this study, the first element of data processing has been to apply a repeat data filter. Sequentially repeated diameter data are replaced with a single diameter datum at the average time.

Even following the excision of repeat data, stepwise differentiation has been found to be excessively noisy, and some data smoothing is required. In the study reported here a moving average has been used, where the duration of the average was constant for each group of datasets. The duration was manually adjustable, so by a process of iteration and inspection of results a visually acceptable balance could be struck between excessive noise and oversmoothing.

The study reported here was conducted in 2005. Clasen et al. (2006b) have subsequently shown success by taking logs of the data, another traditional data smoothing strategy, although it is used only as a preparation for a model fit, not for numerical differentiation as proposed here. Model visco-elastic solution were deliberately chosen for that study, and hence a model solution analysis applied (Entov and Hinch, 1997).

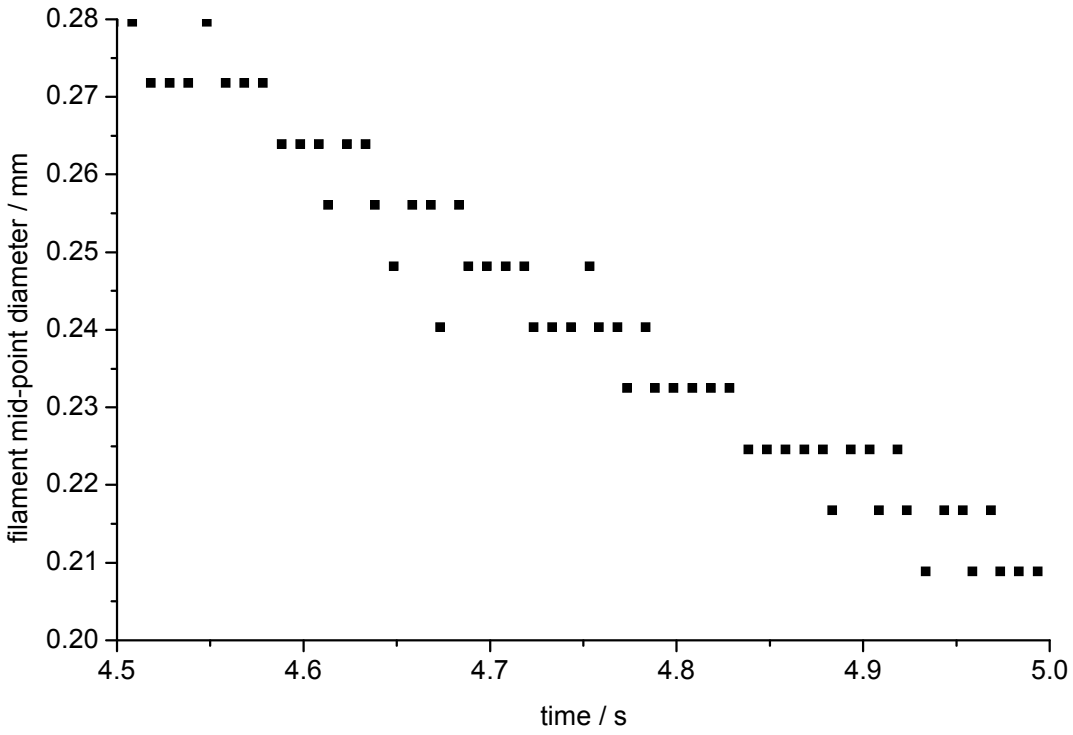

Figure 66: detail of an unprocessed CaBER time-diameter curve showing quantisation due to the 12-bit data acquisition card

8.3.6 Calculating the transient apparent Trouton ratio from CaBER data

The Trouton ratio was defined earlier as the ratio of the extensional viscosity to the shear viscosity. The numerical value is three for uniaxial strain of a Newtonian material from geometrical considerations. The Trouton ratio is thus a measure of excess extensional viscosity over Newtonian expectation. It can alternatively be viewed as an index of strain hardening.

In the literature, the shear viscosity chosen for the transient apparent Trouton ratio is typically the zero shear viscosity (McKinley, 2005). This would appear to be one of the many pragmatic conveniences in reported CaBER analyses. Some of the coatings formulations used in the study reported in Chapter 9 were found to be shear thinning, but strain hardening. The transient apparent Trouton ratio would be underestimated if the zero shear viscosity were used. It would be more satisfactory to choose the shear viscosity η_{shear} at an equivalent deformation rate (Eqn. 8-11). Chan et al. (2007) is the

only literature example where this has been adopted for CaBER analyses. There is a geometry correction factor of √3 in the equivalence of shear rate $\dot{\gamma}$ to strain rate $\dot{\varepsilon}$.

$$\overline{\mathrm{Tr}}(\dot{\varepsilon},t) = \frac{\overline{\eta}_{ext,app}(\dot{\varepsilon},t)}{\eta_{shear}(\dot{\gamma}=\sqrt{3}\dot{\varepsilon})} \qquad \textit{Eqn. 8-11}$$

Where appropriate data is available, the denominator of Eqn. 8-11 can be calculated from a fit to a flow curve obtained from a separate shear rheometry experiment.

8.4 Summary

The derivation of rheological parameters from CaBER time-diameter data has been introduced. Time re-zeroing and numerical differentiation of the time-diameter curve has been proposed as a novel strategy for the analysis of data which does not conform to one of the few published rheological models.

CHAPTER 9 - EXPERIMENTAL MEASUREMENT OF TRANSIENT APPARENT EXTENSIONAL VISCOSITY

In this chapter, the novel analysis method developed in the previous chapter will be applied to an experimental study. This study uses commercial coatings formulations rather than spray dryer feedstocks, as the development by ICI Paints of the "Cuprinol Sprayable" system for spraying Timbercare products provided a good source of comparative sprayable and non-sprayable materials. The industrial application of the materials is immaterial to the demonstration of the method, the important detail is that the fluids exhibited a rheological response in the CaBER experiment that is sufficiently complex that it could not be interpreted using the rheological model fluid cases which have previously been published.

CaBER measurements were performed on seven fluids, four of which were retail fence timbercare products and three were development formulations. To protect commercial confidentiality, they are labelled in this thesis as materials E to M (letters I and L are omitted to avoid confusion with the number 1).

9.1 The expected behaviour of rheology modifier additives

Coatings formulations contain additives to obtain a desirable rheology profile, for example to minimise dripping from a brush during application, or resist sags and runs on the substrate. These additives are often high molecular weight flexible polymers, which characteristically produce strain hardening (Larson, 1998). The enhancement in extensional viscosity over shear viscosity at high strains can be many orders of magnitude. The maximum extension is limited by the polymer chain length, and hence theory predicts that the extensional viscosity will reach a plateau at large strains. This plateau is typically expected to be beyond the range of the commercial CaBER, as discussed later.

The sprayable products contain an associative thickener in place of the high molecular weight polymeric thickeners (Insausti-eci-olaza and Mouzouras, 2005). At rest, the molecules self assemble into a large scale network structure (hence the name "associative"), which gives the product sufficiently high zero shear viscosity to resist sagging and dripping when applied as a coating. But this network is relatively weak,

and is broken up both by high shear deformations and under the strong deformation of extension, so the viscosity drops dramatically.

9.2 Strain and strain rate in the CaBER and in a spray

The Hencky strain and strain rate in the CaBER experiment are determined by the fluid, not selected by the rheologist. The maximum measurable strain is determined by the thinnest resolvable filament. From Figure 66 it can be seen that a single bit on the data acquisition card is equivalent to around 8μm. The maximum measurable strain rate is determined by the measurement frequency. The maximum data acquisition frequency on the commercial CaBER is 30kHz. So for a filament in the default 6mm diameter geometry, the theoretical maximum Hencky strain and strain rate are given by;

$$H = 2\ln\left(\frac{6\text{mm}}{8\mu\text{m}}\right) = 13 \qquad \textit{Eqn. 9-1}$$

$$\dot{\varepsilon} = -\frac{2}{8\mu\text{m}}\frac{8\mu\text{m}}{(1/30000)\text{s}} = 6\text{x}10^4\ /\text{s} \qquad \textit{Eqn. 9-2}$$

These are theoretical maxima. It can be seen from Figure 70 and the plots in Appendix F that the Hencky strain actually obtained in this study was between 3.5 and 9. The strain rate was as low as 10/s for Material G and as high as 1100/s for Material J.

The most basic criterion for sprayability of a fluid from the flat-fan type of atomiser used in this study is that it forms a fan sheet on discharge from the atomiser. The range of strain and strain rate in the fluid during the stretching of this sheet have been estimated from calculation to be of the order of 0 - 4 and 10^5 - 10^3/s respectively. The strain in the CaBER experiment is generally greater, and the strain rate lower, with rather little overlap.

The strain and strain rate during final ligament breakup to drops in the spray are rather harder to estimate or to measure. An attempt was made to measure ligament thinning and breakup to drops directly in the spray. The ligaments are in a frame of reference that is moving rapidly relative to the observer. To measure the rate of thinning requires that the same filament is followed for a period of time. The spray droplets are small, perhaps 50-100μm mean diameter, so the filaments between them are even thinner. To obtain any precision of measurement requires a high magnification lens. Optical

physics constrains that such a lens has a rather small field and depth of view, so it was found that the filaments do not remain either in field or in focus for sufficiently long for a filament thinning measurement to be made. To put it another way, if it was practical to have measured the rate of filament thinning directly in the spray, the abstraction into the filament thinning in the CaBER measurement would have been dispensed with. Instead it is necessary to make the assumption that, since the CaBER time and diameter increments are quantised, but the actual filaments in the spray are both thinner, and thinning continuously, that the strain and strain rate during the final filament breakup in the spray are somewhat larger than is achieved in the CaBER experiment.

Stelter et al. (2002a, 2002b) support the notion that the sprays-relevant measurement is the plateau of constant extensional viscosity expected at high strain rate (coarsely, at full molecular stretching, or fluid restructuring in the case of the associative thickeners). They refer to this as the "Steady Terminal Extensional Viscosity" (STEV).

9.3 Repeated straining as a surrogate for desirably high strain and strain rates

Anomalous behaviour in a single CaBER experiment is frequent, especially for fluids with complex rheology. Experience suggests that good repeatability is indicative that a capillary thinning experiment has really been performed each time, and was largely unaffected by experimental artefacts. Dijkstra et al. (2007) supports the experiential conclusion that it is necessary to make three to five repeats of a CaBER experiment to be confident that the interpretations are valid.

In this study, it was initially noted that the CaBER measurements on some of the test fluids were very non-repeatable. However, if the same sample of fluid was repeatedly stretched, rather than being renewed between each repeat, the time-diameter curves became repeatable. The repeated straining program on the CaBER control software is described by the manufacturer as "batch measurement mode".

On one level, the repeated straining protocol was simply a pragmatic technique in order to obtain a consistent measurement for each material. However, it is instructive to consider why such a protocol should lead to improved repeatability

One possible explanation is chain scission. It is well known that the strain hardening effect in dilute solutions of high molecular weight polymers can be reduced after

excessive strains. This is normally ascribed to polymer chain scission: the flow-induced stress is sufficient to break a backbone bond (Müller et al., 1992). The stress will increase with the chain length: crudely, there are longer lengths of chain to drag in the flow and accumulate stress on the backbone. Hence it is the longest chains which are the most susceptible to scission. These are also the constituents which cause the greatest strain hardening. If chain scission were occurring, the effect of repeated straining should be for strain hardening to decay over time. The extensional viscosity measurement on repeated straining would trend towards a Newtonian response. Chain scission is thus unsatisfactory as an explanation. It can be seen in Figure 77 that there is still significant strain hardening in the samples that have been repeatedly strained.

Materials E and K were the only two samples where the effect of repeated straining was a trend towards a Newtonian response. These two materials have an associative thickener, so chain scission is not a satisfactory explanation. A more credible explanation is that the recovery time for the association network is greater than the time between the repeated strains. A single moderate strain obtained in the CaBER experiment is insufficient to completely disrupt the network. The variation in single strain measurements is probably due to different extents of shear during loading from a pipette, and variable times (and hence extent of recovery) between loading the sample and performing the straining experiment. When the sample is repeatedly strained, the network does not have time to recover fully from each previous strain. Hence, over time, the rheological response becomes more like the behaviour of a fully disrupted network. This is the expected behaviour in the spray, when the fluid is intensely pre-sheared through the nozzle and then subject to very large extensions and rates in the spray. Hence for Materials E and K, which contain an associative thickener, the repeated straining protocol in the CaBER is expected to give an extensional viscosity measurement which is meaningfully representative of the spray, even though the strain and strain rate of a single strain are too low.

The remaining fluids contain a high molecular weight thickener. A reasonable explanation for the improved repeatability from multiple straining is that the molecular alignment from the initial strain has not decayed completely before subsequent strains. Single strains are unrepeatable as there are varying degrees of molecular alignment within the samples, again expected to arise from differences in the shear experienced by the sample loading with a pipette and difference in time lapse from loading to the sample to performing the strain. Subsequent strains all have the same degree of semi-

decayed alignment from previous strains, so the extensional viscosity measurement becomes consistent.

It was initially hoped that the repeated straining would accumulate sufficient molecular pre-alignment for subsequent strains that the "Steady Terminal Extensional Viscosity" (Stelter et al., 2002b) would be approached. Figure 76 does not support such a conclusion.

In this study the CaBER "batch measurement mode" repeated straining protocol has been used as a technique to obtain consistent results. In the case of the associative thickener containing fluids at least, the measurements made in this way are credibly more representative of the fluid behaviour under the much greater extension rates experienced by the fluid during spraying. This has not been reported by others.

9.4 Experimental details of CaBER measurements

In all cases the CaBER default 6mm diameter plates were used, with an initial separation 3mm. The final distance between the plates was empirically chosen to produce a capillary filament with lifetime long enough to allow the rate of reduction in the diameter of the filament to be measured. 8mm was found to give acceptable results. The strike from the initial to the final height was in all cases set as 50ms, with a linear velocity profile.

The number of repeat strains in the "batch measurement mode" was varied for each material. Groups of 20 repeats were performed until the time-diameter curves plotted by the control software were judged to have reached steady state. Hence for most samples 20, 40, 60 or 80 repeats were performed. For Material J only, there were a set of 10 followed by a set of 20.

9.5 The need for software and some degree of automation in analysis

There are a total of almost 400 time-diameter curves to analyse in this study. Even if the "batch measurement mode" had not been used, there would be three to five repeats for each experiment. There are five steps to the analysis of each time-diameter curve. Manual analysis would be slow, tedious, and hence prone to error. The sheer quantity

of data manipulation required for any real study makes at least some degree of automation a pragmatic necessity.

Furthermore, much of the analysis is required simply to plot data in useful formats for interpretation. These plots are useful for the experimenter to determine what experiment to run next. The speed required for such on-line use practically dictates some degree of automation.

9.5.1 The supplied CaBER analysis software

The CaBER Analysis software supplied with the instrument has inadequate capability when compared with the desired list of data processing tasks. It will import only up to 20 datasets, there is inadequate control over what range of data is imported, and the curves cannot be time translated for easier comparison of their gradients. It is possible to select the data range over which a fit can be applied, but the models must be chosen from amongst a short predetermined list. There is no model for associative thickeners. Only one dataset at a time can be fitted, and the fit parameters must be manually saved each time or they are lost when moving onto the next dataset. The analysis software does not calculate the useful derived parameters described in the previous chapter, but relies on these values having been written to columns in the datafile output from the CaBER control software. However, not only is it unclear what calculation the control software is using to derive the parameters, but the columns are not normally fully populated with values. Frequently the columns are totally empty. When values do appear, it is only for the first part of the experiment where the filament is thick and gravitational drainage dominates. Values rarely appear in these columns in the thin filament region where they would be valid. Hence it is not possible to create the desired plots against Hencky strain of transient apparent Trouton ratio and transient apparent extensional viscosity.

The supplied CaBER Analysis software is even more limited for processing the "batch measurement mode" datafiles in this study. These have only time and diameter tabulated data: the derived parameters do not appear even as underpopulated columns. It is possible to import "batch measurement mode data" only into a daughter window, which has no control whatsoever over what is displayed.

9.5.2 Excel VBA macro analysis method

As the CaBER Analysis software was not fit for purpose, a Visual Basic for Applications (VBA) macro to an Excel spreadsheet was written to perform the desired sequence of analysis tasks. The macro code is listed in Appendix E. The tasks performed by the macro are as follows;

1. Redundant data filtering. Filter out invalid data at large filament diameter (where gravity is dominant in determining the thinning rate) and small filament diameter (where artefacts due to e.g. droplet formation confuse the later fitting routines). The maximum and minimum diameter selected for valid data cut points are the same for all data series on each spreadsheet.

2. Re-set time zero to the first valid reading, chosen to be 1mm as previously discussed.

3. Repeat data filtering. As described in section 8.3.5, where diameter values are repeated at sequential times in the list, they are replaced with a single value at the mean time.

4. Smooth the filtered data on a moving average. Averaged over the least number of points, found by manual iteration, to remove gross outlying points (large peaks in the gradient calculation) without excessive smoothing. The number of points in the moving average was the same for all curves for a material, so noise is still apparent in some curves.

5. Apply a stepwise numerical differentiation on the smoothed filtered data and use this to calculate the viscosity.

The calculations for the Hencky strain, Trouton ratio, and the ensemble averages of the batch measurement curves, were performed subsequent to macro execution by spreadsheet cell formulae and manual manipulation of data.

Excel and VBA were selected because it was straightforward to prototype the analysis algorithm using these tools. The disadvantages are that it is not practically scalable: the worksheets are very large (~15 MB), and Excel has a limit to the number of columns in a worksheet. This limit was uncomfortably closely approached for fluid E where 80

repeat strains were performed. VBA is an interpreted, not a compiled language, so the macro is comparatively slow to run. Investigating the effect of changing the smoothing parameter, for example, is undesirably time consuming. A final disadvantage is that it is very user unfriendly. There is little exception handling, and the datasets must be added to the plots manually.

9.5.3 Calculation of transient apparent Trouton ratio

The method of determining the deformation-rate-dependent transient apparent Trouton ratio described in section 8.3.6 requires shear flow curve data, which was not available in this study. The shear rheometry was performed by others. The results were reported at two points for each fluid: shear viscosity at 5000/s, and, for some of the materials, an extrapolation back from low shear measurements to a zero shear viscosity value. In absence of the full flow curve data, the high shear viscosity value has been used to calculate the transient apparent Trouton ratio. The reason for this choice was twofold. The high shear value is more representative of the deformation rates in a spray, as discussed above. The high shear viscosity measurement set was also complete, whereas zero shear measurements were not available for all the test materials. The strain rate in the CaBER experiments was always less than $5000 / \sqrt{3} = 2900$ s, and some of the experiments were at very low strain rates. The use of high shear viscosity may therefore give rise to numerical error in the calculation of transient apparent extensional rheology. However, as the purpose of determining the Trouton ratio was only to compare qualitatively the existence and extent of strain hardening behaviour between materials, the potential numerical error is acceptable.

9.6 Exemplification of analysis method: Material J

The analysis protocol is perhaps most clearly explained by following the analysis for an example material. The single strain experimental data is considered first. The batch measurement mode data is then presented and compared.

It will be seen from inspection of the single strain curves in Figure 67 that the results are far from repeatable. This is most readily apparent in the difference in overall filament lifetime between the repeats, but on closer inspection it can also be seen that the gradient is far from repeatable in the salient sub-millimetre filament diameter region.

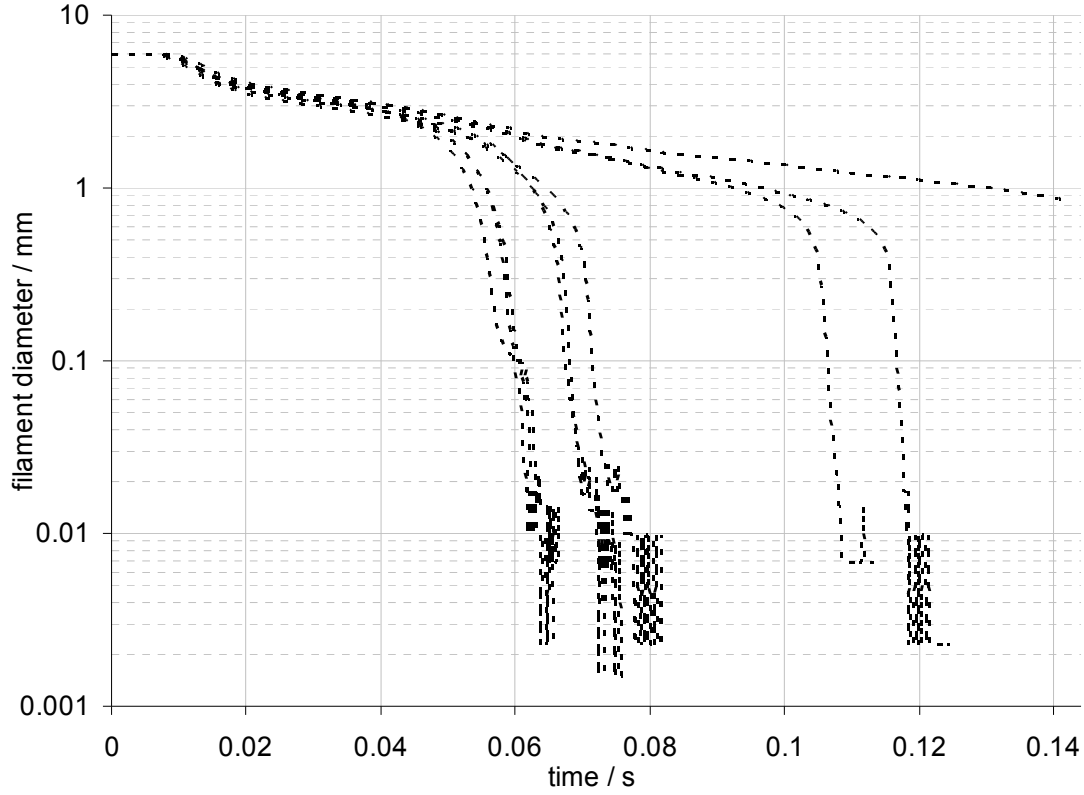

Figure 67: unprocessed CaBER time-diameter curves: material J single strains

The results of the numerical analysis on these data are shown plotted as transient apparent extensional viscosity as a function of strain rate in Figure 68. This means of presentation portrays both qualitative and quantitative differences between the repeat measurements. Four of the curves, shown as continuous lines, show consistently low viscosity at all strains, which indicates approximately Newtonian rheology. Two experiments, shown as continuous lines with square symbols, show the lowest viscosity of all repeats at low strains, but this increases above a Hencky strain of about six. This would suggest visco-elastic extensional strain hardening behaviour. Three of the repeats, shown dotted, show at low strains a transient apparent extensional viscosity that is an order of magnitude greater than the other experiments, but this decays to almost the lowest values at the highest strains measured. This is more similar to the model of power law fluid behaviour.

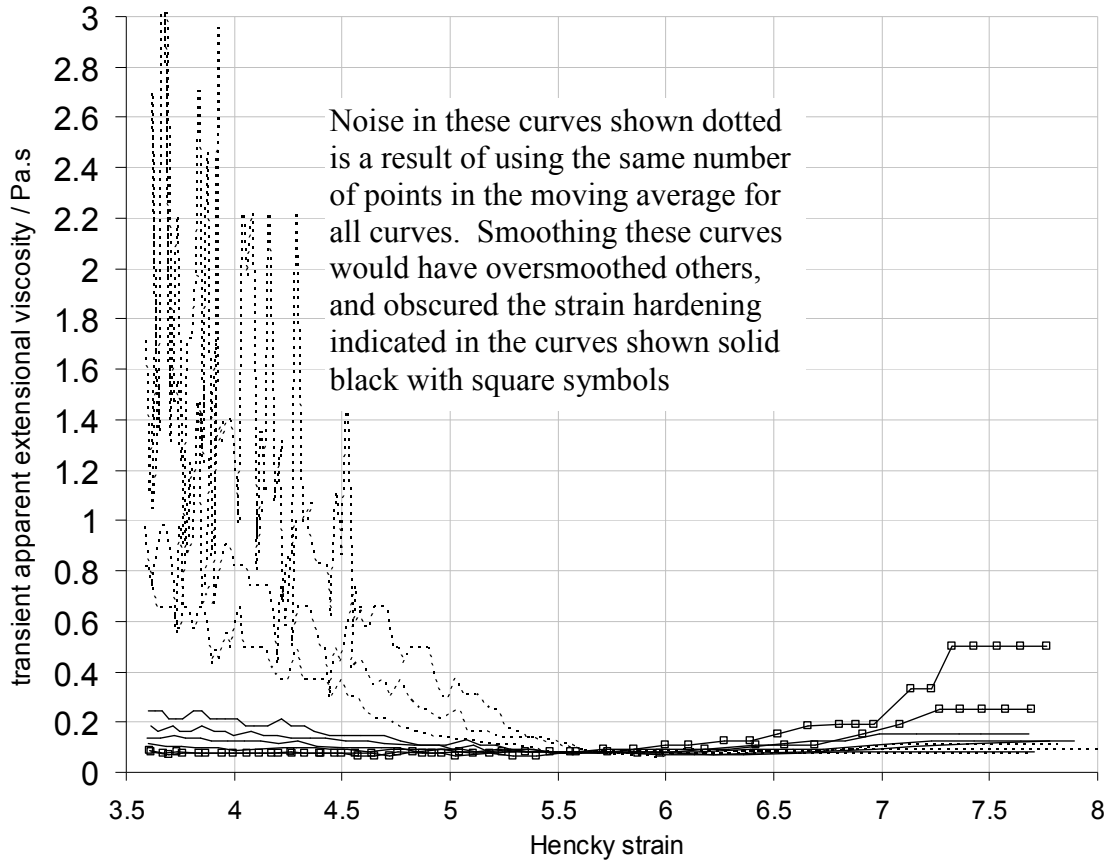

Figure 68: transient apparent extensional viscosity as a function of strain from material J single strain CaBER data

In contrast, in Figure 69 it can be seen that the batch measurement mode data (solid lines) form a mass of very similar shaped curves. There are just two outliers, shown in red. In each case, these two outliers are the first strain of a set of repeated strains. Also in each case, the outliers are similar to one of the single strain time-diameter curves.

The time-diameter curves in Figure 69 suggest that the effect of repeated straining is to move from an erratic to a consistent measurement. This suggestion is supported by the results of the numerical analysis which has been plotted in Figure 70. The datapoints cluster around a trend line. An ensemble average of the data has been calculated and is plotted (heavy black line). Strain hardening is indicated. The first strain in the set (red line) is different. In Figure 69, the first strains from each set are plotted, but only one of these has sub-millimetre data valid for analysis, so there is only one red line in Figure 70.

Also plotted in Figure 70 are dotted horizontal lines which are judged to bound the bulk of the measurements. The dashed horizontal line is mid-way between these bounds.

This range of viscosity values has been used in the analysis in the following chapter. It has been treated as though it were a central tendency and error bound, purely as a means to plot a datum onto the Ohnesorge diagram. It should be understood for the strain hardening materials, however, that this is not to imply that there is a central tendency: the extensional viscosity increases with strain. The simplification of the transient apparent extensional viscosity data into a single central tendency value with error bounds is a more intuitive concept for the materials that exhibit approximately Newtonian rheology.

The summary statistic for the transient apparent extensional viscosity of Material J has been taken to be 0.25 ± 0.2 Pa.s.

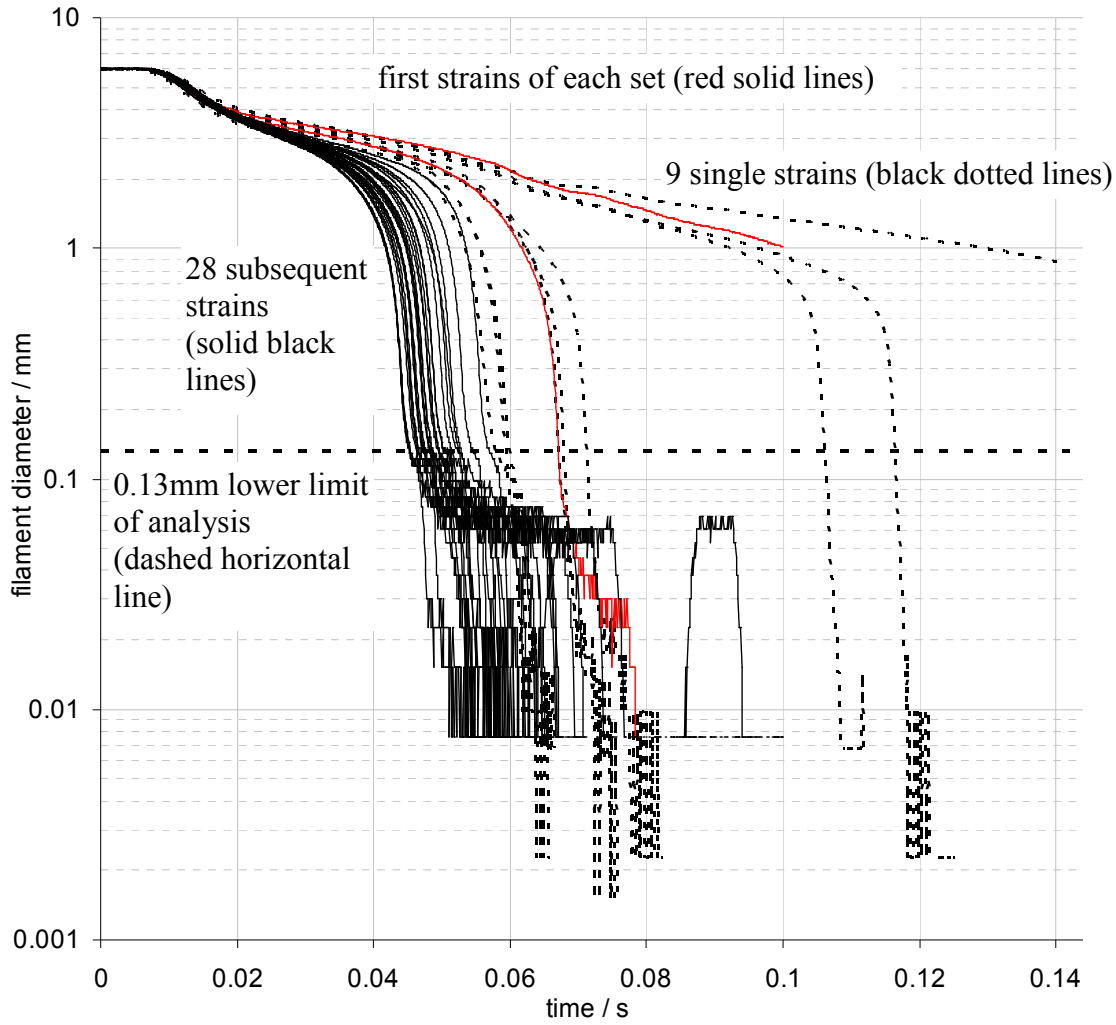

Figure 69: unprocessed CaBER time-diameter curves, material J

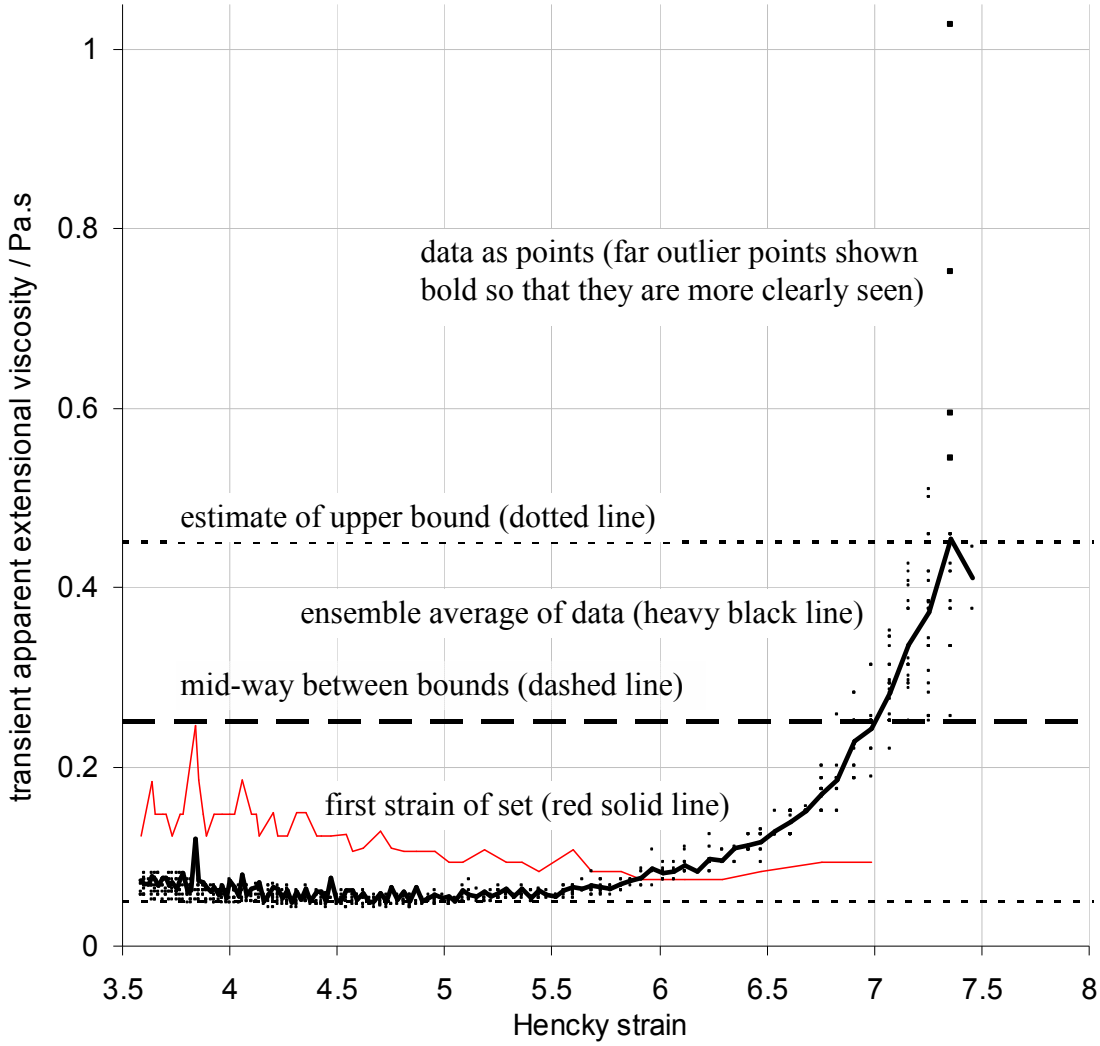

Figure 70: transient apparent extensional viscosity as a function of strain, calculated from material J CaBER batch measurement mode data

A minimum Trouton ratio of three is expected. The consistently lower values indicated in Figure 71 are suggestive of a systematic error. Potential error sources in the CaBER experiment have been discussed previously. The error is not so gross that it detracts from the interpretation as a fluid exhibiting strain hardening behaviour.

The moving average was taken over three readings for Material J. This material was selected for this exemplification discussion partly because the noise was relatively low and features in the data were more clearly apparent. Rather larger averaging sets were required for most of the other materials tested.

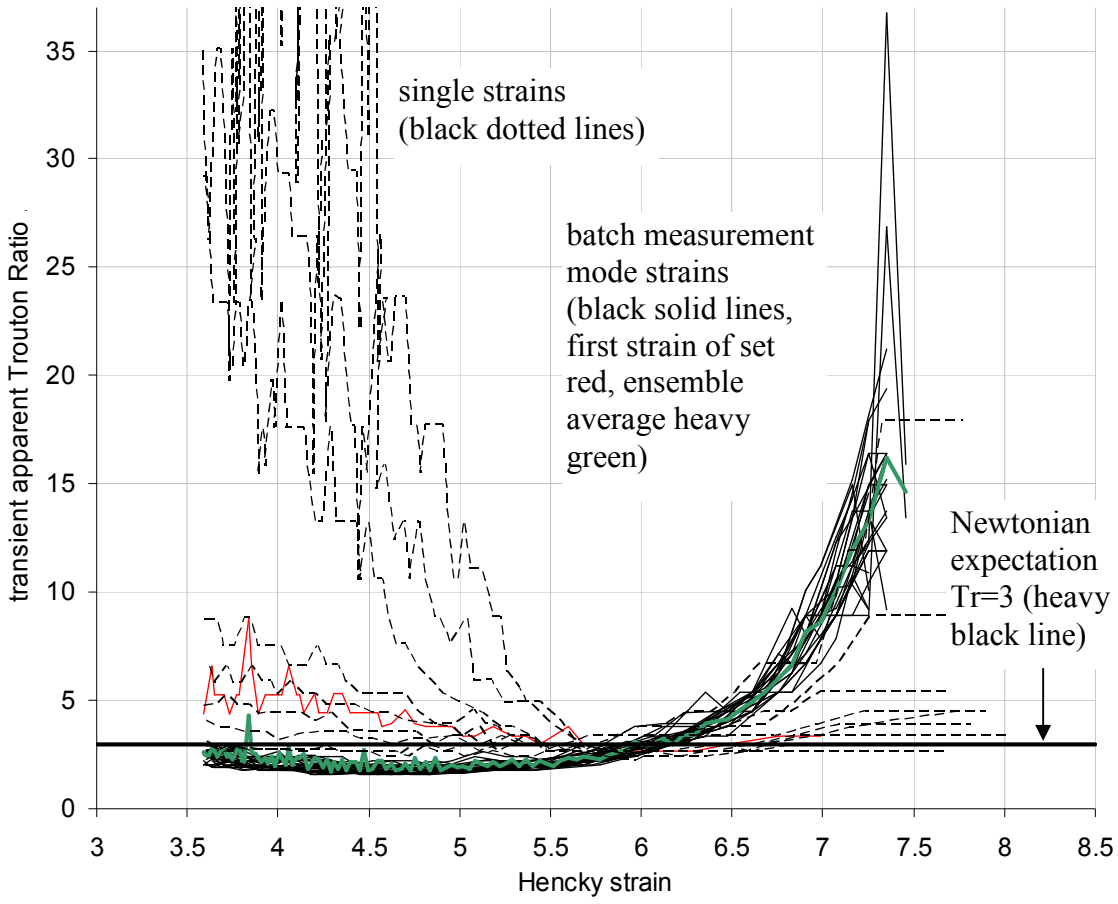

Figure 71: transient apparent Trouton ratio as a function of strain, material J

9.7 Material E results

Material E warrants discussion as this shows the most gradual decay towards steady state.

The time-diameter curves for Material E are plotted in Figure 72. There is a gradual evolution of the curves with repeated straining. The first set of strains, and the first five strains from the second set are shown as red lines. The remainder of the second set of repeats, and the first five strains from the third set also form a group and are depicted blue. The final 35 strains appear to have reached a steady state condition and are shown as black lines. The same pattern is seen in Figure 73 for the trend with repeated straining in transient apparent extensional viscosity as a function of Hencky strain.

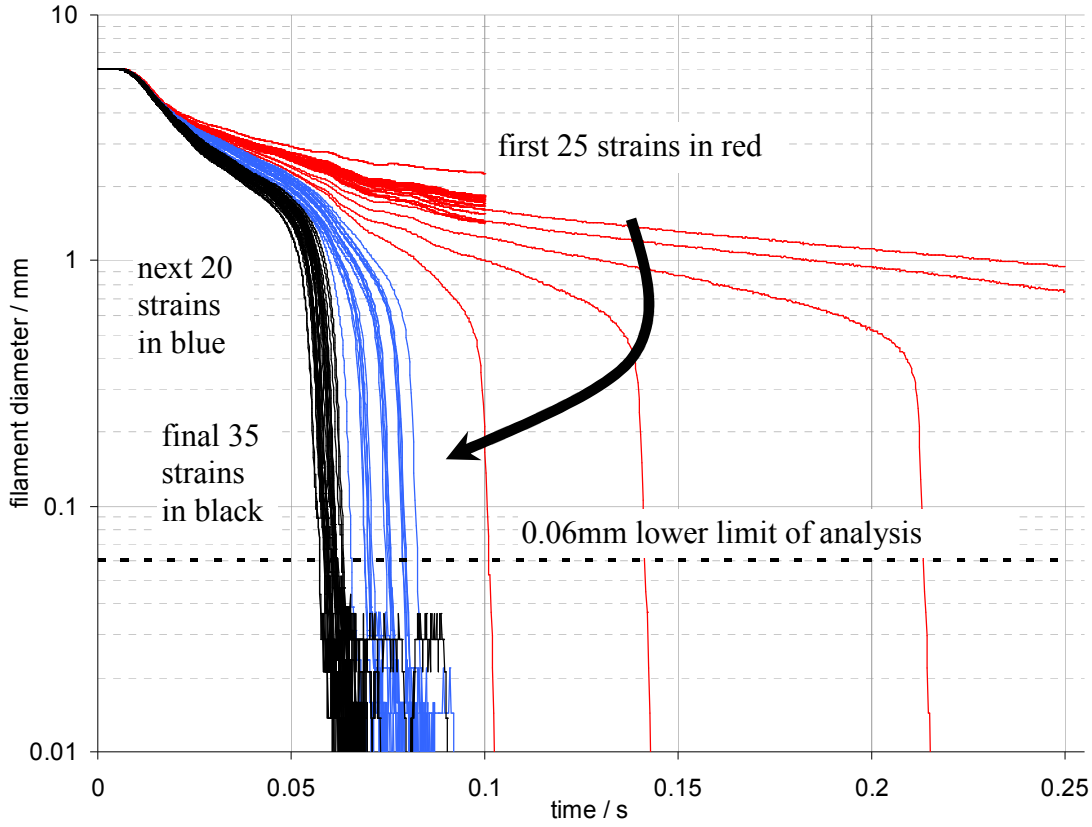

Figure 72: CaBER time-diameter curves for 80 repeated strains of the same sample material E.

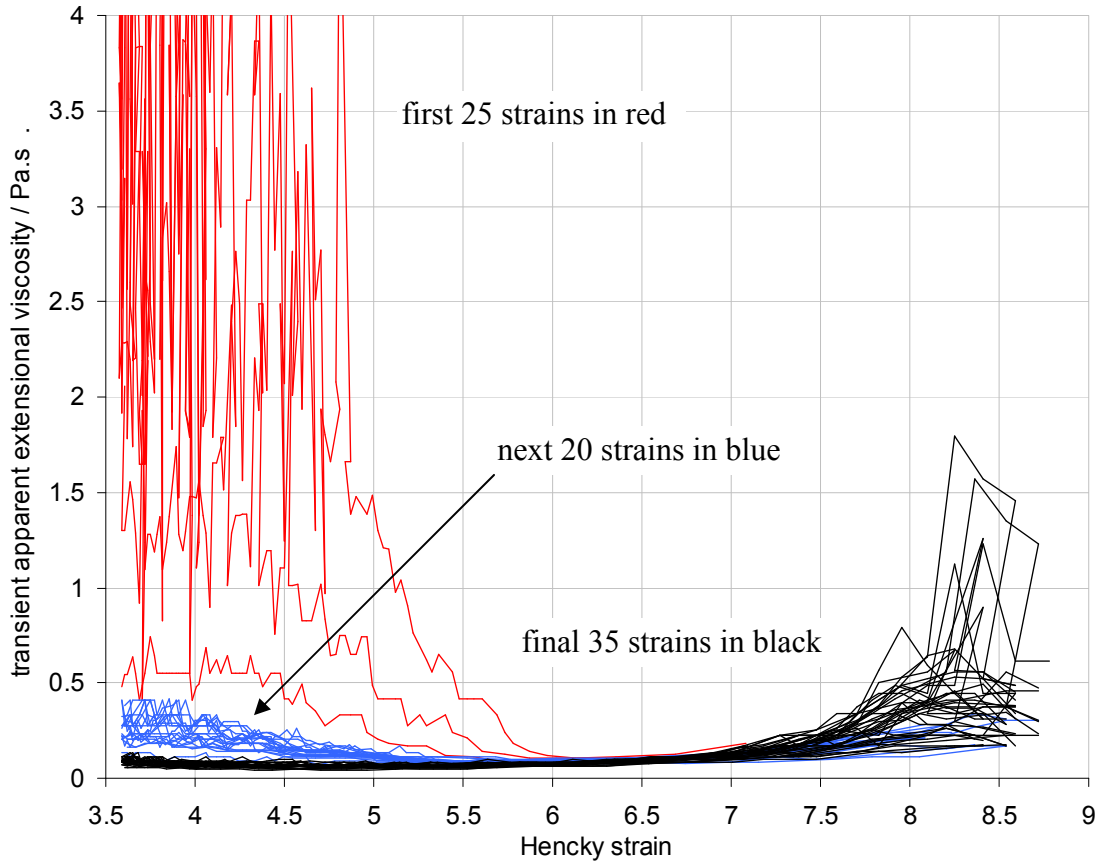

Figure 73: Material E analysed data for repeated strains of the same sample

The ensemble average and the spread of the transient apparent extensional viscosity parameter plotted in Figure 74 have been determined from those final thirty-five strains where a steady-state response appears to have been reached. The summary statistic for the transient apparent extensional viscosity has been taken to be 0.3 ± 0.25 Pa.s. Figure 75 indicates that the behaviour is Newtonian for moderate strains, consistent with the breakdown of the association network of the thickener. There is also a trace of high molecular weight polymer which accounts for the strain hardening at high strain.

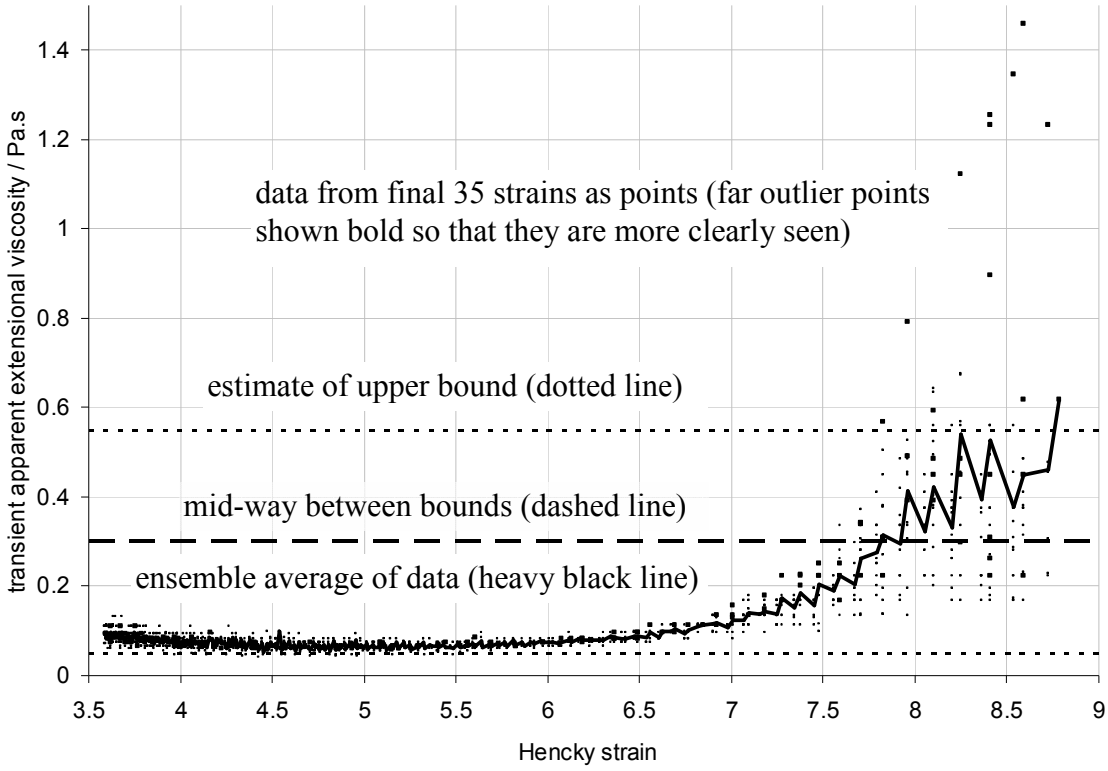

Figure 74: Material E: summary of the magnitude and spread of $\eta_{ext,app}$

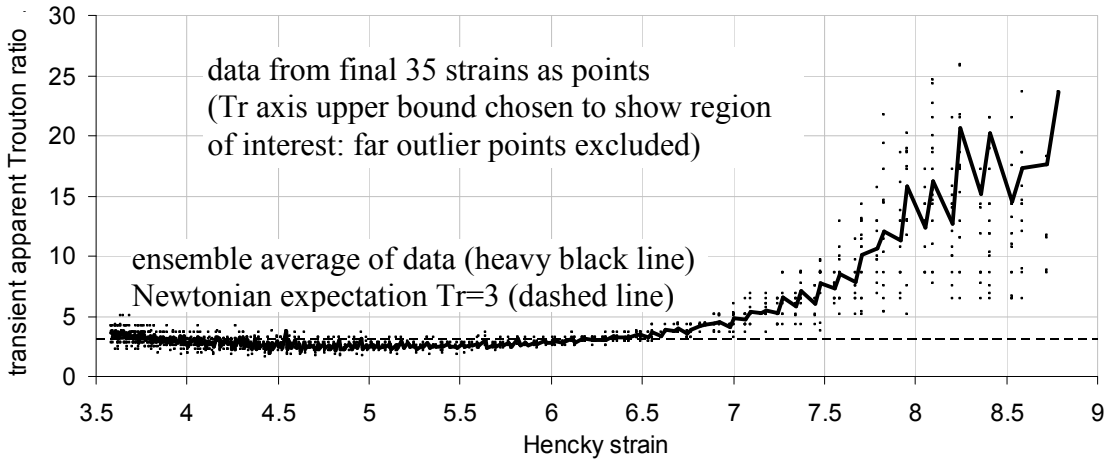

Figure 75: transient apparent Trouton ratio as a function of strain, material E

9.8 Conclusions

The analysis for materials J and E discussed above was repeated for the other materials. The results from these analyses are summarised here, the data are in Appendix F.

The analysis method that was developed in the preceding chapter for an arbitrary CaBER time-diameter curve has successfully been used to determine the transient apparent extensional viscosity parameter for fluids whose response in the CaBER experiment was too complex to successfully have been analysed using any of the rheological models that have so far been published.

Table 6 shows all the data values used in the Ohnesorge diagram plots in the following chapter. This includes the CaBER data measured and reported in this study, and also data for shear viscosity, surface tension and density that was measured for this study by colleagues (Steven and Elliott, 2005).

There is an order of magnitude variation in the measured transient apparent extensional viscosity parameter between the different materials. The spread values are large fractions of the total values, as for all materials the extensional viscosity shows significant fractional variation as a function of strain, as depicted in Figure 76.

In Figure 77 it can be seen from the Trouton ratios elevated over the Newtonian expectation that materials F, G and H show significant strain hardening. The effect is most pronounced for material F, where the onset of strain hardening was at strains too small to be measurable in the CaBER experiment. The strain softening indicated by the dip in curves G and H indicates error in the analysis. Strain softening is exotic and would not be expected for these materials. The most likely explanation is that initial stresses had not fully relaxed by the 1mm diameter taken to be the start of valid data for analysis. A smaller limiting diameter should have been selected, corresponding to a Hencky strain of around 5.5. Material M shows moderate strain hardening. Materials E and J show a Newtonian response until significant strain has developed, and even after onset only show a small degree of strain hardening. The physically meaningless Trouton ratio calculated for material K indicates a systematic error. It was not possible to identify the source of this error.

Material code	Data measured this study		Data measured by Steven & Elliott (2005)		
	$\eta_{ext,\ app}$	Tr_{app}	η_{shear} at 5000/s	surface tension σ	density ρ
	Pa.s	[-]	Pa.s	mN / m	kg/m³
E	0.3 ± 0.25	11 ± 10	0.0261 ± 0.0001	40.0 ± 0.5	1013 ± 5
F	0.7 ± 0.35	100 ± 50	0.0067 ± 0.0001	45.5 ± 0.5	1007 ± 5
G	1.6 ± 0.4	57 ± 14	0.0283 ± 0.0001	46.1 ± 0.5	1013 ± 5
H	1.1 ± 0.5	44 ± 20	0.0251 ± 0.0001	36.9 ± 0.5	1010 ± 5
J	0.25 ± 0.2	9 ± 7	0.0280 ± 0.0001	44.8 ± 0.5	1009 ± 5
K	0.14 ± 0.06	1.1 ± 0.5	0.1300 ± 0.0001	47.4 ± 0.5	1000 ± 5
M	2 ± 1	12 ± 6	0.1730 ± 0.0001	49.1 ± 0.5	1000 ± 5

Table 6: summary statistics for the physical properties for all test fluids.

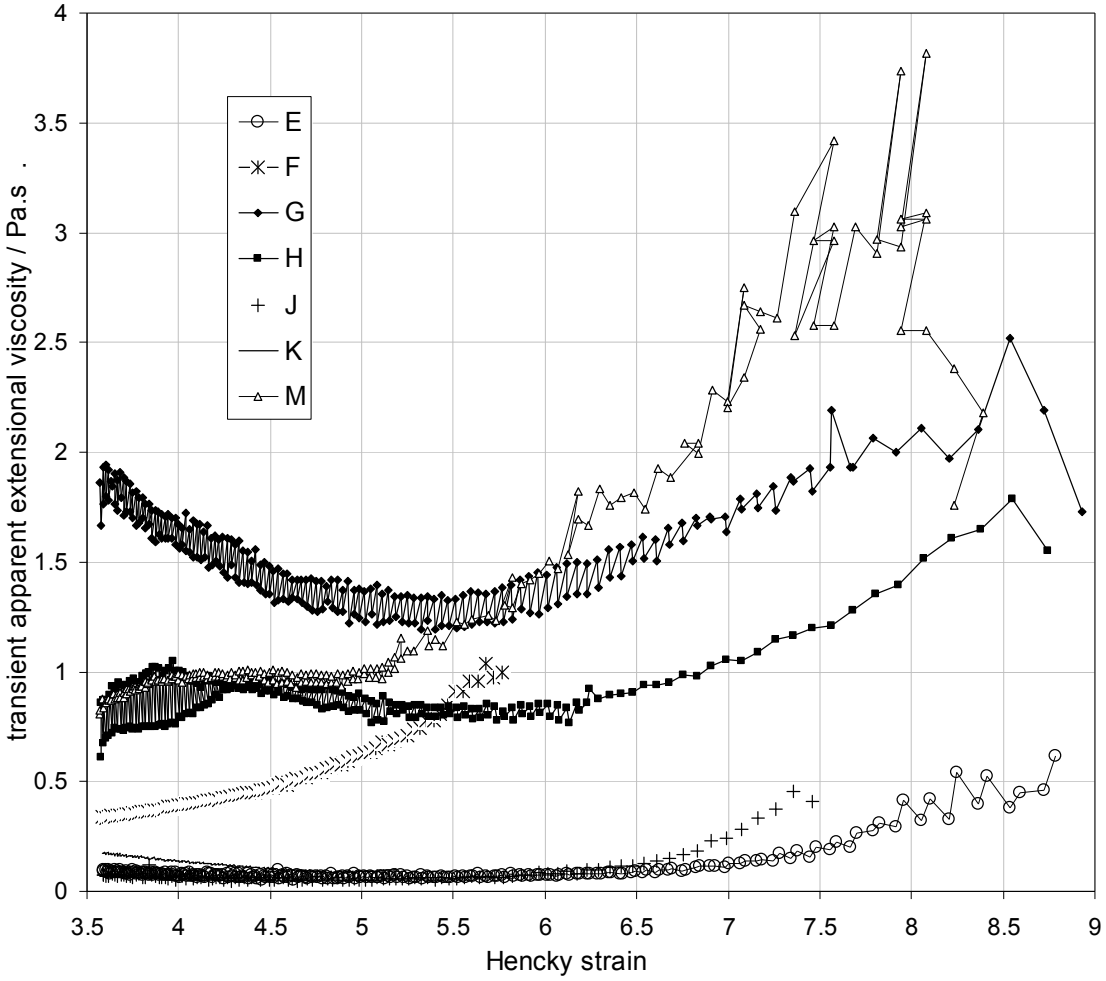

Figure 76: ensemble average of $\overline{\eta}_{app,ext}$ *as a function of strain*

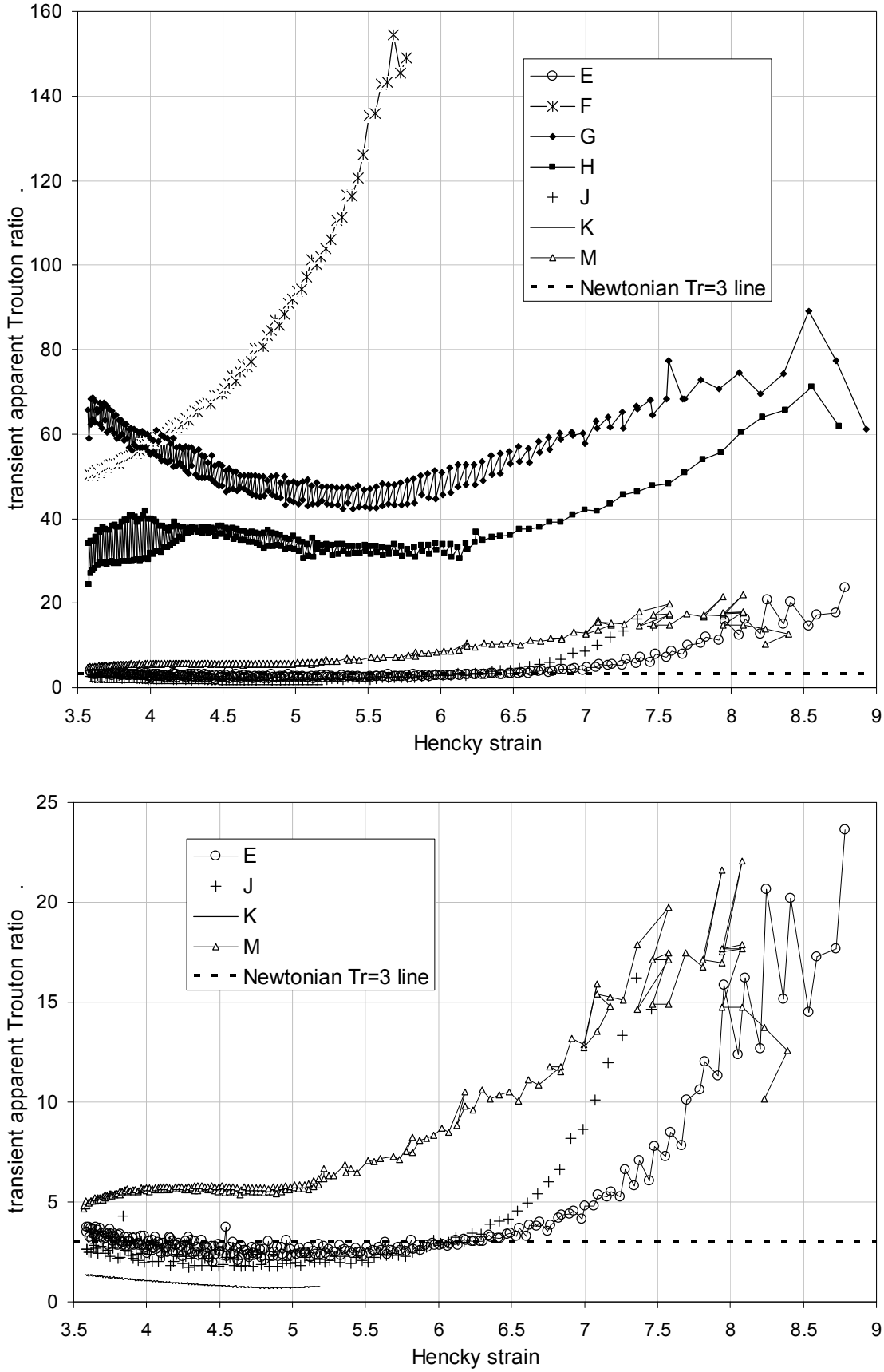

Figure 77: ensemble average of $\overline{\mathrm{Tr}}_{app,ext}$ *as a function of strain. All data (above), expansion of 0 < Tr < 25 (below)*

CHAPTER 10 - THE OHNESORGE DIAGRAM AND PREDICTION OF SPRAYABILITY FROM CaBER DATA

The Ohnesorge diagram (Figure 78) is a map delineating regions of characteristic atomisation phenomena. It is typically referred to in the introductory chapter of spray technology textbooks (Lefebvre, 1989, Bayvel and Orzechowski, 1993), but otherwise neglected. It might reasonably be surmised that workers in the field may find the diagram a helpful visualisation, but not quantitatively of practical use, even if such lack of utility has not been formally acknowledged in the literature.

Surprisingly, in this research it has been found that the Ohnesorge diagram can in fact provide a quantitatively useful guide to spray behaviour, at least for the example case of the fluids in the CaBER study in the previous chapter. Two possible explanations are proposed for the perception that the Ohnesorge diagram is not practically useful. Firstly, the diagram has been incorrectly reproduced by some authors, including the standard textbook (Lefebvre, 1989). Secondly, shear viscosity data are traditionally used in the dimensionless groups which plot onto the diagram, whereas extensional viscosity would be a more appropriate choice of parameter.

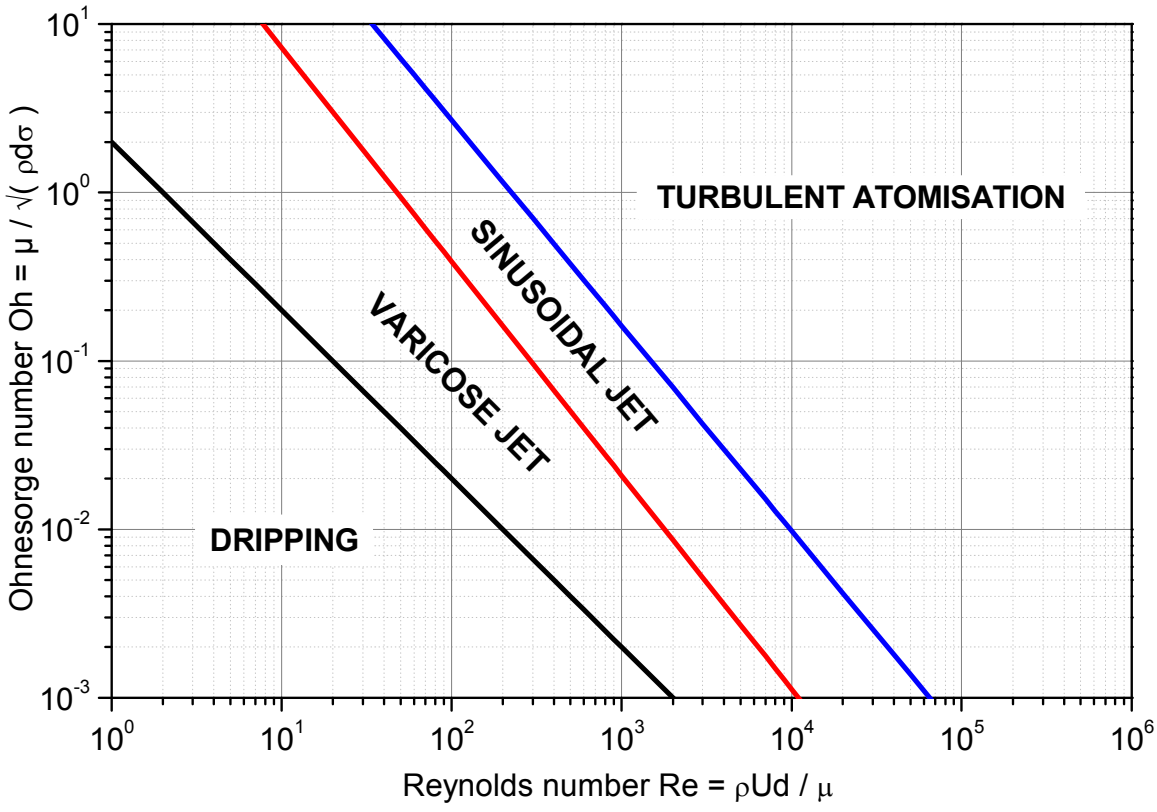

Figure 78: the Ohnesorge jet stability diagram

10.1 The Ohnesorge diagram

Ohnesorge (1936) proposed the diagram which now bears his name. Four distinct regions of behaviour were observed in atomisation experiments;

0	Dripping
I	breakup of a cylindrical laminar jet into drops
II	similar to 2, except that the jet oscillates sinusoidally
III	atomisation

Ohnesorge found that regions I, II and III could be delineated by straight lines on a log-log plot, where the abscissa was the Reynolds number, a ratio of inertial to viscous forces, and the ordinate was a group, now known as the Ohnesorge number, a ratio of viscous to surface tension forces. According to McCarthy and Molloy (1974), the term Ohnesorge number was coined by Miesse (1955), even though the group was in use earlier than Ohnesorge's work. Ohnesorge simply called the group "Kennzahl", characteristic number, and used the notation Z, presumably for Zahl, in the same way that an English speaker might choose N to notate an arbitrary number.

$$Re = \rho U d / \mu$$

$$Z = \sqrt{We} / Re = \mu / \sqrt{(\rho d \sigma)}$$

$$We = \rho U^2 d / \sigma$$

where;

Re	is the Reynolds number
Z	is the Ohnesorge number (alternatively notated Oh)
We	is the Weber number
ρ	is the atomised liquid density
U	is the superficial axial velocity of the liquid jet at the point when it emerges from the nozzle
d	is a characteristic diameter of the nozzle
μ	is the viscosity of the liquid.
σ	is the surface tension of the liquid being atomised

The paper states that the atomisation was into air, so it is the interfacial tension of the liquid with air that is intended.

Experimental data was obtained over a huge parameter space; $2 < Re < 10^4$ and $0.001 < Z < 10$, with water, aniline, gasoil (the fraction of crude oil that is used for diesel and heating oil), glycerine, oil A, oil B (both unspecified) and castor oil.

Experimental temperature is unspecified, but ambient room temperature seems probable from the description of the experiment, and it is improbable that experimental room temperature variation would materially alter the conclusions of the paper. Significantly elevated temperature would have reduced the viscosity of the fluids, but the evidence in the paper suggests that Ohnesorge was a competent and careful experimentalist, so it is reasonable to assume that the viscosity reported was measured at the spraying temperature. The choice of fluids gave a wide range of viscosity, so it anyway seems improbable it would have been necessary to resort to the experimental complexities of raising the temperature of the fluids.

It is not known exactly what oils A and B were, but all the other materials would be expected to have Newtonian rheology, so it is a reasonable inference that they were unexceptional choices, without unusual microstructure, and hence also Newtonian. Ohnesorge uses the word "Zähigskeitsreibung", which roughly translates as "coefficient of stringiness", rather than "viscosität" or "Zähflüssigkeit" which a modern dictionary offers as translations for viscosity, but the description of stringiness should not be taken to mean that Ohnesorge intended extensional viscosity. As discussed in Chapter 7, extensional rheometers for low viscosity fluids are a recent development, so it is highly improbable that Ohnesorge would have had an extensional rheometer, even if it had occurred to him that extensional viscosity would in principle be a more appropriate parameter for the physics of the atomisation process. Finally, a few quantitative checks can be made. Selecting the value $Oh \sim 0.004$ for water sprayed through a 1mm nozzle from Ohnesorge's chart, with the accepted approximate literature values of density 1000 kg/m³ and surface tension 72 mN/m, a viscosity coefficient of ~1.07mPa.s is obtained, which is close to the known value for shear viscosity of water. Similarly for aniline through the 0.7mm nozzle, $Oh \sim 0.025$, with density 1022 kg/m³ and surface tension 43.4 mN/m, viscosity by calculation is 4.4 mPa.s, c.f. 3.7 mPa.s literature value. If extensional viscosity had been used the values would have been three times larger. There is no doubt that shear viscosity is the data that Ohnesorge used and intended.

Ohnesorge (1936) did not propose a transition line between the dripping region 0 and varicose jet region I. A dependency was sought on the dimensionless group r/a , where $a = \sqrt{(\sigma / \rho g)}$ and r is the nozzle radius, but this group was found to vary from 0.01 to 1 between experiments. It can be inferred that Ohnesorge had written a force balance between gravity and surface tension for an incipient drop;

$$\frac{4\pi}{3} r^3 \rho g = 2\pi r \sigma$$

$$r^2 = \frac{3}{2}\frac{\sigma}{\rho g}$$

Eqn. 10-1

These terms might today be more naturally rearranged into the form of a dimensionless Eötvös number. The problems are that this is a static force balance and does not account for the inertia of the flowrate into the developing drop, and also that the radii are not the same - the gravitational force applies to the droplet size, the surface tension to the nozzle radius.

10.2 Extrapolation of the Ohnesorge diagram to flat-fan nozzles

Ohnesorge (1936) does not specify the exact geometry of the nozzle, but the text and the photographs of example jets strongly suggest a simple cylindrical nozzle, with diameter variously 0.5, 0.7, 1.0 and 2.0 mm. This detail is important, because the dimensionless groups characterise the nozzle solely by a diameter, without any modifying shape factors, but it is common knowledge in the atomisation field that the type of nozzle (simple nozzle, pressure swirl etc.) has an influence on the type of atomisation obtained.

The “flat-fan” type of nozzle used in the study reported here is in essence a simple cylindrical pressure nozzle, albeit modified at exit to an ellipse by a “vee” cut perpendicularly across the nozzle exit and with a flow restriction orifice at the entry to the nozzle cap (Figure 79).

It is empirically observed that the "pre-orifice" modifies the droplet size distribution from the nozzle, and smoothes temporal instabilities: the spray is reported to be finer and more even (Insausti-eci-olaza and Mouzouras, 2005). The mechanism of its action is not well established, however. It is postulated that it pre-shears the fluid and thus lowers the effective fluid viscosity in the final exit from the nozzle. It does not appear to modify the point at which a jet becomes a spray, and no separate account of this

internal orifice has been made in the data analysis and plotting onto the Ohnesorge diagram. However, the repeated straining of the fluid in the CaBER experimental protocol described in the previous chapter may serendipitously have produced appropriate data for the pre-sheared case. Thus although the pre-shear nozzle may not have been separately and independently allowed for, it has been accounted for in the aggregate analysis.

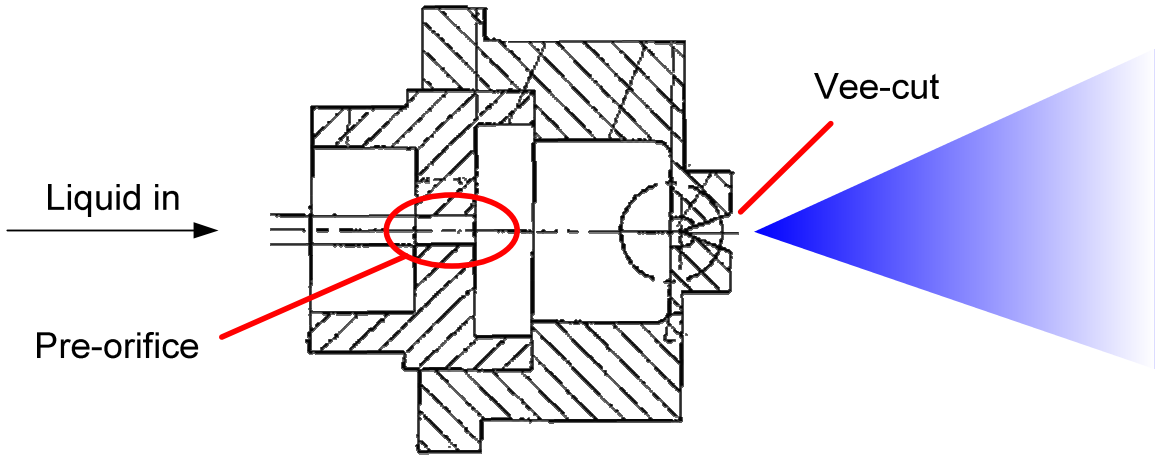

Figure 79: schematic diagram of the type of flat-fan pressure nozzle used (after Insausti-eci-olaza and Mouzouras, 2005)

The vee-cut across the nozzle tip creates the flat-fan shape provided that the liquid momentum is high enough, but it is observed that an approximately cylindrical jet can be obtained from a flat-fan nozzle, if the flowrate is sufficiently low. Hence it is a reasonable initial assumption that an Ohnesorge diagram could be used as an atomisation map. However, it is not clear that the position of the transition lines would be unaltered for a flat-fan nozzle.

10.3 Review of the delineations on the Ohnesorge diagram

A literature review was conducted to establish whether there was any guidance to changes to the transition lines for different nozzle types. A more fundamental issue was uncovered: authors do not agree on the positions of the lines even for the simple cylindrical nozzle.

Reading point values from Ohnesorge's chart (Ohnesorge, 1936), the equation for the transition line from varicose to sinuous breakup has been estimated as;

$$(Re = 7.8, Z = 10),\ (Re = 10{,}950, Z = 0.001),\ \Rightarrow\ Z = 35\ Re^{-1.27} \qquad \textit{Eqn. 10-2}$$

and for the sinuous breakup to secondary atomisation;

$$(Re = 34, Z = 10),\ (Re = 63{,}720, Z = 0.001),\ \Rightarrow\ Z = 741\ Re^{-1.22} \qquad \textit{Eqn. 10-3}$$

Miesse (1955) is the first appearance in an English language journal of the Ohnesorge diagram. It was proposed that, since the lines were straight on a log-log chart, they should follow the form $Z = A\ Re^{-n}$ (where A and n are arbitrary constants). This re-arrangement has been used in this thesis to compare the transitions lines found in the literature.

Miesse's (1955) quantitative result is not useful, however; the diagram in Ohnesorge (1936) was reproduced incorrectly. Miesse's chart has fewer decades on both axes. The most plausible explanation for the transcription error is that Miesse plotted the intercept for Z = 10, at the top of Ohnesorge's chart, onto the top of his chart, at Z = 1. The lines are correct at the base of the chart, where Z = 0.001 on both Ohnesorge and Miesse's charts. Reading point values from the chart, the equation for the line on Miesse's plot intended to be Ohnesorge's varicose to sinuous breakup transition has been estimated as;

$$(Re = 10, Z = 0.7),\ (Re = 10^4, Z = 0.001),\ \Rightarrow\ Z = 6.5\ Re^{-0.95} \qquad \textit{Eqn. 10-4}$$

and for the sinuous breakup to secondary atomisation;

$$(Re = 37, Z = 1),\ (Re = 7x10^4, Z = 0.001),\ \Rightarrow\ Z = 27.3\ Re^{-0.92} \qquad \textit{Eqn. 10-5}$$

Since all Miesse's data was for low values of the Ohnesorge number, the error in the gradients of the transition lines was not apparent. The data covers insufficient range to substantiate Miesse's assumption that the exponent (gradient) of the sinusoidal to turbulent atomisation transition line should be unaltered when translated to the right of the chart to fit new data. Lines with a large range of gradients could validly be plotted through Meisse's data.

Despite the transcription error and the limited data range, Meisse's data does show a transition from sinusoidal breakup to turbulent atomisation that is not consistent with Ohnesorge's data and transition line, and hence at least supports the principle that a change in atomiser type will translate the transition to turbulent atomisation. There is no data regarding other transitions.

McCarthy and Molloy (1974) postulate that reports of uncertainty in the position of the transition between jetting and atomisation could be attributed to differences in the velocity profile and turbulence of the jet as it leaves the nozzle. A thin orifice (axial length short compared to diameter) will have a flat or nearly flat velocity profile, whilst a long nozzle (axial length several diameters) will have a fully developed velocity profile, for example parabolic for laminar flow. Ohnesorge (1936) did not include sufficient detail of his nozzle to be able to reliably estimate the velocity profile. A complication not elaborated by McCarthy and Molloy is that the entry length to develop a velocity profile is dependant on the physical properties of the liquid, especially the viscosity (Dombrowski et al. (1993), cited in Perry and Green, 1997). It is strongly indicated from a critical analysis of the data, that the exit flow varied from effectively completely undeveloped to fully developed over the range of Reynolds numbers in Ohnesorge's experiments. At the high viscosities required for the high Ohnesorge numbers for the Oils A and B and the castor oil, laminar flow fully develops in a very short length, and it would be hard to construct a nozzle mechanically strong enough to resist the required injection pressure (which increases with viscosity), without that nozzle being sufficiently long for laminar flow to fully develop. In contrast, a notable feature is Ohnesorge's datum of a laminar water jet at nozzle Reynolds number around twenty thousand. It seems incredible that such a high Reynolds number could be maintained in a long capillary without turbulent flow developing (and hence precluding a laminar jet issuing). The tip of the nozzle appears to be rounded and much wider than the jet diameter in a photograph in Ohnesorge (1936). It does not look like the tip of a long capillary. A convergent flow into a relatively short nozzle orifice is more probable. Hence a less than fully developed flow profile is to be expected in this case. So, the velocity profile almost certainly did alter over the range of data plotted in the diagram, but it is questionable whether that represents a practical shortcoming or only a theoretical one. It is certainly a possible explanation of variation in literature reports, but in contrast to the nozzle geometries McCarthy and Molloy cite from academic investigations, commercial pressure nozzles are not long capillaries. Change in velocity profile from undeveloped to fully developed over the range of the Ohnesorge diagram is the practical expectation, so does not necessarily represent a shortcoming. The discussion of velocity profile is thought provoking, but it is not necessary to look to any such theoretical complexity to understand why McCarthy and Molloy saw uncertainties in the position of the lines on the Ohnesorge diagram. They reproduced Miesse's (1955) incorrect diagram, although they referenced it directly to Ohnesorge (1936).

The standard atomisation textbook (Lefebvre, 1989) further obfuscates the issue, by once again attributing directly to Ohnesorge (1936) a chart on which the delineations between atomisation region are quantitatively neither those of Ohnesorge nor Miesse (1955) (whose modified delineation is also invoked in the chart). It is suspected to be simply a typesetting error; the lines are positioned identically to the chart attributed to Reitz (1978, cited in Lefebvre, 1989), reproduced on the facing page of Lefebvre's book. Reading values from Lefebvre's chart, (in fact a plot of Reitz's delineations as noted), the equation for the transition line from the varicose to the "first wind induced breakup region" (i.e. varicose to sinusoidal transition by another name) is given by;

$$(Re = 10, Z = 2.8),\ (Re = 10^3, Z = 5.6\text{x}10^{-3}),\ \Rightarrow\ Z = 62.6\ Re^{-1.35} \qquad \textit{Eqn. 10-6}$$

and for the transition from the "second wind induced breakup region" to turbulent atomisation (the sinusoidal to turbulent atomisation transition by another name) as;

$$(Re = 10, Z = 12.52),\ (Re = 10^4, Z = 1.45\text{x}10^{-3}),\ \Rightarrow\ Z = 1650\ Re^{-1.30} \qquad \textit{Eqn. 10-7}$$

Lefebvre (1989) also quotes the result of Grant and Middleman (1966) who proposed $Re = 325\ Oh^{-0.28}$ for the varicose-sinusoidal transition for jets with fully developed parabolic velocity profiles (n.b. not $3.25\ Oh^{-0.28}$ as misquoted by both McCarthy and Molloy (1974) and Lefebvre (1989)). This can be transformed into $Z = 9.35\text{x}10^8\ Re^{-3.57}$ which is unhelpfully dissimilar to all other results. When carefully checked against the data in Grant and Middleman's paper, this may simply be due to correlation to data in a narrow range of $640 < Re < 1500$, $0.09 > Z > 0.004$, compared to the orders of magnitude of Reynolds and Ohnesorge numbers in the data of Ohnesorge (1936).

The Ohnesorge diagram is reproduced substantially correctly in Bayvel and Orzechowski (1993), although the transition lines are actually plotted according to equations which do not quite match the lines in Ohnesorge (1936). The lines are defined by $We = 17400 / \sqrt{Re}$ and $We = 940000 / \sqrt{Re}$, which can be transformed into;

$$Z = \sqrt{17400}\ Re^{-1.25} = 132\ Re^{-1.25} \qquad \textit{Eqn. 10-8}$$

$$Z = \sqrt{940000}\ Re^{-1.25} = 970\ Re^{-1.25} \qquad \textit{Eqn. 10-9}$$

Bayvel and Orzechowski (*ibid.*) describe the regions with different terminology to other authors. The varicose region is characterised by disintegration due to axisymmetric

waves, the sinusoidal region by disintegration due to asymmetric waves, and the turbulent atomisation region by disintegration due to aerodynamic forces. This is more fundamentally correct and consistent terminology than generally used. However, in this thesis the traditional terminology for the regions has been used, because the words "asymmetric" and "axisymmetric" are so similar as to be readily confused.

Bayvel and Orzechowski (*ibid*.) also note that the sinusoidal jet to turbulent atomisation transition has been found to shift parallel to its original position, depending on the magnitude of initial perturbation of the jet. They quote this result from "numerous experiments", and in the context that this comment is made, it is with the implication that these experiments were by a number of other workers, rather than their own experiments, although no references are given. This provides further circumstantial evidence that the position of the transition between sinusoidal jet and turbulent atomisation might alter for a flat-fan nozzle, but again no validatory evidence from experimental data is available.

Bayvel and Orzechowski (*ibid*.) also cite Lyshevskii (1963). This in Russian, so it has not been possible to check the original. Three correlations are quoted in the form;

$$We_i = K_i Lp_i^{m_i} M^{n_i} \qquad \textit{Eqn. 10-10}$$

where K_i, m_i, n_i are a set of empirical constants for each of three transitions, $i \in \{1,2,3\}$, Lp is the Laplace number, $Lp = 1 / Oh^2$, and M is the ratio of the gas to liquid density. The criterion for transition I is linear relationship between jet break-up length and velocity, a criteria for stable varicose jet formation also mentioned by Scheele and Meister (1968b), who note that it may be at order 30% higher velocity than their criteria for incipient jetting. The description of criteria II and III map onto the varicose - sinusoidal and sinusoidal - turbulent atomisation transition lines from other authors. Lyshevskii's equations can be rearranged into the form $Oh = A.Re^{-n}$ to compare the result with that given by other authors, provided that M^{ni} is treated as a constant. This conceit does not seem unreasonable. At least as judged by the translated title of his book offered by Bayvel and Orzechowski's citation, Lyshevskii was concerned with diesel atomisation. Unless he capriciously chose to perform his experiments with fluids much denser than the diesel which interested him, we would expect M, the ratio of gas to liquid density, to vary within a similar and small range to that for the selection of fluids used by Ohnesorge. In the following lines of working, the terms $K_i M^{ni}$ have been grouped together as a new constant term J for convenience;

$$We_i = K_i\left(\frac{Re_i^{\,2}}{We_i}\right)^{m_i} M^{n_i}$$

$$We_i^{\,(1+m_i)} = \left[K_i M^{n_i}\right] Re_i^{2m_i}$$

$$\left[We_i^{\,(1+m_i)}\right]^{\frac{1}{2(1+m_i)}} = J_i^{\frac{1}{2(1+m_i)}}\, Re_i^{\frac{2m_i}{2(1+m_i)}}$$

$$\frac{We_i^{\,1/2}}{Re_i} = J_i^{\frac{1}{2(1+m_i)}}\, Re_i^{\frac{m_i}{(1+m_i)}-1}$$

$$Oh_i = J_i^{\frac{1}{2(1+m_i)}}\, Re_i^{\frac{-1}{(1+m_i)}} = A_i\, Re_i^{-N_i} \qquad \textit{Eqn. 10-11}$$

The values for K_i, m_i, n_i quoted in Bayvel and Orzechowski can then be used to determine the value of the coefficient A_i and the power N_i . The results from this numerical working are shown in Table 7. The density ratio appropriate for water and air is assumed first, and then it is demonstrated for the fluids in the data presented by Ohnesorge (1936), that this does not give rise to an error of more than +30/-15%. Density data has been taken from internet sources - data accuracy is not critical to the conclusion. For the first transition, where there may be an additional 30% error due to the different definitions of jetting velocity, the error might then be as great as 60%, but, to briefly preview the conclusion, the reader will see later from Figure 80, this is still insufficient to account for differences between Lychevskii's first transition line and the data from Ohnesorge.

				Transition i		
i				I	II	III
K_i				10	16.6	266
n_i				-1.08	-1.05	-0.8
m_i				-0.455	-0.302	-0.133
$N_i = {}^1/_{(1+mi)}$				**1.83**	**1.43**	**1.15**
		ρ_{liquid}	$M=\rho_{air}/\rho_{liq}$			
	Castor oil	956	1.3E-3	1359.5	1112.6	209.4
	Glycerine	1258	9.5E-4	1828.7	1484.3	260.9
	Gasoil	870	1.4E-3	1227.9	1007.8	194.2
	Aniline	1024	1.2E-3	1464.2	1195.8	221.3
$M^n i$	Water	998	1.2E-3	1424.1	1164.0	216.8
			max+	28%	28%	20%
			max-	-14%	-13%	-10%
$J_i = K_i . M^n i$				1.4E+4	1.9E+4	5.8E+4
${}^1/_{[2(1+m)]}$				0.92	0.72	0.58
$A_i = J\text{^}({}^1/_{[2(1+mi)]})$				**6465**	**1176**	**557**

Table 7: conversion of Lyshevskii's coefficients to the form $Oh = A.Re^{-N}$ for comparison with the proposed transitions from other authors.

A version of the Ohnesorge diagram used in ICI plots the varicose to sinusoidal jet transition line according to $Z = 148\ Re^{-1.30}$, the sinusoidal jet to turbulent atomisation transition as $Z = 3820\ Re^{-1.40}$, and also has a dripping to varicose jetting transition located at Weber number equal to eight. The sources for this diagram are unrecorded. Lefebvre (1989) derives $We = 8 / C_D$ as the criterion for aerodynamic breakup of a droplet in an airstream, by equating aerodynamic drag to surface tension, but neither this balance nor a drag coefficient of one are intuitively applicable to the incipient jetting case.

The We = 8 criterion at least has the merit of a similar dimensionality to the criterion for incipient jetting in Scheele and Meister (1968a, b), but there the numerical constant is no greater than four, rather than eight. This conclusion is not obvious by inspection of the reference and requires some explanation. It requires that the term $d / (1.24\ V^{1/3})$, the ratio of the nozzle diameter to the diameter of the drop that would form if a jet did not form, is neglected, with justification as follows. The term arises from a consideration of the excess pressure required in the emerging fluid over the continuum to sustain a spherical drop. Scheele and Meister's analysis is general, but focused on liquid-liquid systems. In liquid jetting into gas, this diameter ratio was found to be small in studies cited by Scheele and Meister. The term $d / (1.24\ V^{1/3})$ is non-dimensional, so cannot change the dimensionality of the solution, and is always positive for physically meaningful solutions, so it can only act to reduce the magnitude of the calculated flowrate Q. The value of 1.57 for the coefficient is applicable for a flat velocity profile at the nozzle exit;

$$Q = 1.57\sqrt{\frac{\sigma d^3}{\rho}\left[1 - \frac{d}{1.24V^{\frac{1}{3}}}\right]}$$

$$Q\big|_{max} = 1.57\sqrt{\frac{\sigma d^3}{\rho}}$$

$$\frac{\pi}{4}d^2U = 1.57\sqrt{\frac{\sigma d^3}{\rho}} \qquad \textit{Eqn. 10-12}$$

$$\frac{\rho U^2 d}{\sigma} = \left(\frac{4}{\pi}1.57\right)^2$$

$$We = 3.996$$

Hence a Weber number of four is a well referenced upper limit for the transition from dripping to jetting. This can be rearranged to the form $Z = 2.Re^{-1}$.

All the various literature reported positions of the transitions have been summarised in Table 8 and plotted in Figure 80. There is no evidence in the literature that other authors have made this comparison of the equations for the lines on a like-for-like basis as $Z = A\ Re^{-n}$, even though this arrangement was first applied to this problem over fifty years ago by Miesse (1955).

	Transition line, Oh =		
	Dripping to Varicose	Varicose to Sinusoidal	Sinusoidal to Turbulent atomisation
Ohnesorge (1936)	-	$135\ Re^{-1.27}$	$741\ Re^{-1.22}$
Meisse (1955)	-	-	$100\ Re^{-0.92}$ $Re>10^4$
Meisse's (1955) plot of Ohnesorge (1936)	-	$6.5\ Re^{-0.95}$	$27.3\ Re^{-0.92}$
Reitz (1978) cited in Lefebvre (1989)	-	$62.6\ Re^{-1.35}$	$1650\ Re^{-1.30}$
Grant and Middleman (1966)	-	$9.35x10^8\ Re^{-3.57}$ $640<Re<1500$	-
Ohnesorge (1936) cited in Bayvel and Orzechowski (1993)	-	$132\ Re^{-1.25}$	$970\ Re^{-1.25}$
Lyshevskii (1963) cited in Bayvel and Orzechowski (1993)	$6465\ Re^{-1.83}$	$1176\ Re^{-1.43}$	$557\ Re^{-1.55}$
ICI	$\sqrt{8}\ Re^{-1}$	$148\ Re^{-1.30}$	$3820\ Re^{-1.40}$
Scheele and Meister (1968b)	$2\ Re^{-1}$	-	-

Table 8: summary of literature reports of transition lines on the Ohnesorge diagram.

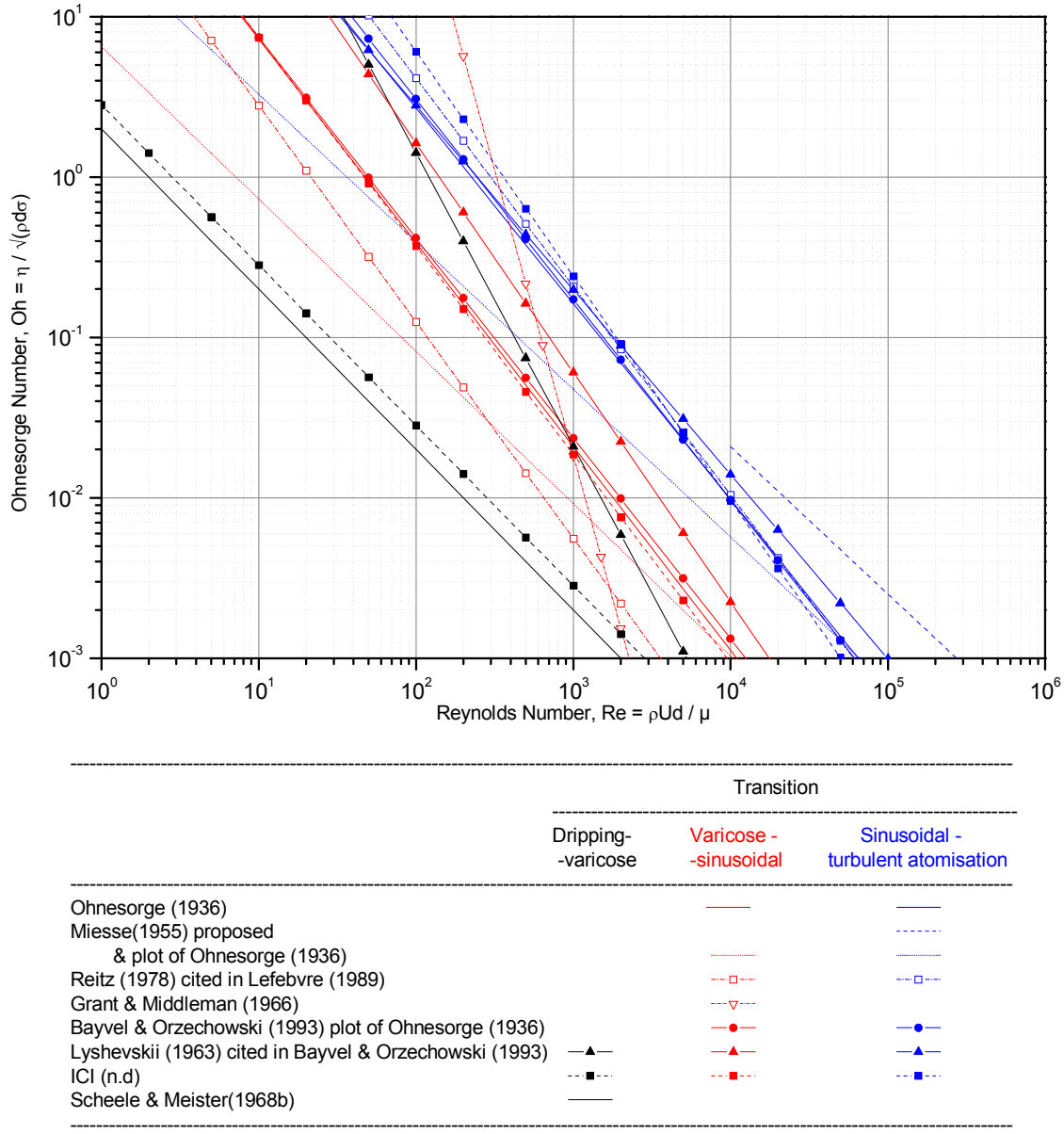

Figure 80: the Ohnesorge jet stability diagram: variations in literature reported positions of transitions.

A number of lines on Figure 80 are readily discarded. Miesse's lines are clearly erroneous due to the transcription error. Grant and Middleman's varicose - sinusoidal transition conflicts grossly with other reports, and is based only on data over a very narrow range of Re and Oh. The ICI dripping-varicose transition line is unreferenced, and conflicts with Scheele and Meister's well referenced transition. The dripping - varicose and varicose - sinusoidal transitions proposed by Lychevskii are physically implausible, as they converge at moderate Ohnesorge number. This is a prediction of flow transition direct from dripping to turbulent atomisation without a region of laminar jetting, at an Ohnesorge number corresponding to the flow of a fluid with a viscosity less than 2 Pa.s through a 1mm diameter orifice.

These deletions leave the plot shown Figure 81, with the data of Ohnesorge overlaid. Frustratingly, only the 70 year old original data of Ohnesorge is available on which to base further selection. This will sort the best fit to the data between the lines proposed in the charts by Ohnesorge, Bayvel and Orzechowski and ICI, as all these claim to be based on Ohnesorge's data. However, both Lefebvre and Bayvel and Orzechowski state that Reitz and Lychevskii respectively used additional data from their own studies when proposing their transition lines. It has not been possible to obtain either original work to critically examine or to use this additional data.

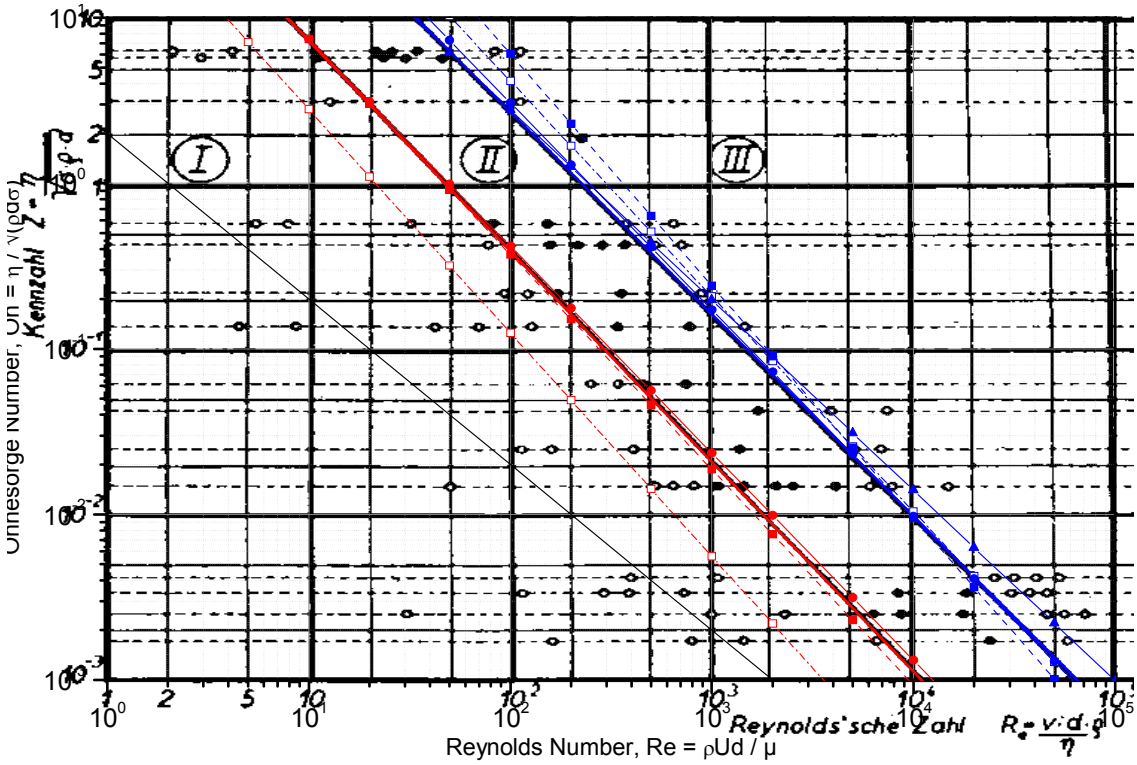

	Transition		
	Dripping- -varicose	Varicose - -sinusoidal	Sinusoidal - turbulent atomisation
Ohnesorge (1936)		——	——
Reitz (1978) cited in Lefebvre (1989)		--□--	--□--
Bayvel & Orzechowski (1993) plot of Ohnesorge (1936)		—●—	—●—
Lyshevskii (1963) cited in Bayvel & Orzechowski (1993)			—▲—
ICI (n.d)		--■--	--■--
Scheele & Meister(1968b)	——		

Figure 81: the Ohnesorge jet stability diagram with selected literature reported flow transitions and the data of Ohnesorge overlaid.

It can be seen from careful examination of Figure 81, that the ICI and the Bayvel and Orzechowski fit to Ohnesorge's varicose-sinusoidal transition line are both not only imperfect fits to that line, but also less good fits to the data. Ohnesorge's line is thus preferred, and can be accurately plotted by the fit proposed in this thesis;

$$Z = 135\ Re^{-1.27} \qquad \textit{Eqn. 10-13}$$

Reitz's proposal for the locus of the varicose-sinusoidal transition is more problematic. When compared to Ohnesorge's line, the gradient is sufficiently similar to preclude abrupt rejection, but the position is in stark disagreement with Ohnesorge's line, and only Lefebvre is available as a secondary source to Reitz's work, without the supporting data. It is a transition within the laminar flow region, so the physical process is expected to be reasonably clearly discernable (c.f. the transition to turbulent atomisation). Reitz's proposed transition line is so grossly conflicting with Ohnesorge's data that the only reasonable conclusion to be drawn is that his definition of "first wind induced breakup" came from observations of phenomena peculiar to his experimental arrangement, at earlier onset than the upper limit of coherent straight sided varicose jets observed other workers. In the absence of supporting data, Reitz's varicose - sinusoidal transition line will be discarded.

Turning to the sinusoidal - turbulent transition lines in Figure 81, the ICI fit to Ohnesorge's line is poor and unreferenced. Bayvel and Orzechowski's fit to this line is acceptable, but it is more closely matched by the fit proposed in this thesis. Bayvel and Orzechowski's line is no better fit to the data, so the better fit to the original work is preferred. Both Reitz and Lychevskii's transition lines are positioned in a close but not identical location to Ohnesorge's transition. They would not be good fits to the transition in Ohnesorge's data. However, in contrast to the varicose-sinusoidal transition, they should not be immediately disregarded for that reason. The disagreement in position of the lines is not large. Considering that the physical process being mapped is a transition to breakup driven by chaotic turbulent instabilities, some dispersion in estimates of this transition might be expected, both due to inherent variability in the process itself, but also in the experimental difficulty in making a definitive and consistent estimate of flow behaviour near to the transition. It is therefore proposed to plot the sinusoidal-turbulent transition according to the fit to Ohnesorge's transition line proposed in this thesis;

$$Z = 741\ Re^{-1.22} \qquad \textit{Eqn. 10-14}$$

but also to plot the transition lines of Reitz and Lychevskii to indicate reasonable variability in estimates of the transition;

$$Z = 1650\ Re^{-1.30}$$

$$Z = 557\ Re^{-1.15} \qquad \textit{Eqn. 10-15}$$

Note that the selected transitions lines are not quite parallel. There is nothing in the original or later works to explain why they should be parallel, although most of the authors quoted seem to have assumed that they should be.

It should also be emphasised that a gradual transition between atomisation regions is more physically realistic than the sharp transitions implied in the diagram.

In conclusion, an acceptable definition has been established for the transition lines for the flow of Newtonian fluids through a simple cylindrical orifice. Whilst no quantitative guidance has been found on appropriate translations of the transition lines for different atomiser types, there is at least support from some authors for the intuition that the lines may in principle need to be so translated. There is no mention of the behaviour of non-Newtonian fluids.

Since neither Ohnesorge (1936) nor others have provided a physical explanation for why the delineations between the regions should lie where they were found to be, further studies would be required to establish the transition lines for a flat-fan nozzle. In the absence of such reports, it is proposed that a reasonable assumption is that the transition from dripping to varicose jet formation would be co-located for both simple cylindrical and flat-fan atomisers, since in the varicose jet region I, the flat-fan nozzle produces a cylindrical jet directly from the orifice without effect of the vee-cut. It is less clear that the transitions to transitional oscillatory behaviour and finally turbulent atomisation would be similarly co-located. As well as the wave instabilities common to the cylindrical jet, breakup of the liquid sheet from a flat-fan atomiser can also be initiated by perforations, especially as the fluid viscosity increases (Lefebvre, 1989).

In the absence of guidance for the flow of fluids with non-Newtonian rheology through a flat-fan nozzle, it was deemed a reasonable approach to plot the experimental data from the study reported in the previous chapter onto a standard Ohnesorge diagram, and examine the result.

10.4 Experimental study data plotted onto the Ohnesorge diagram

In Figure 82 the data co-ordinates of Reynolds and Ohnesorge number have been calculated using the shear viscosity, surface tension and density data in Table 6. Green datapoints are for flowrates and nozzle diameters where a spray fan formed as intended, in experiments run by a colleague at ICI (Steven and Elliott, 2005). Fan spray behaviour is characteristic of the sinusoidal region. The red datapoints are those that failed to spray, but instead formed a jet. This behaviour is characteristic of the varicose region. The data as plotted in Figure 82 do not conform to expectation: the sprayable (green) datapoints are intermingled with the non-sprayable (red) data, and are not separated into two distinct flow regions.

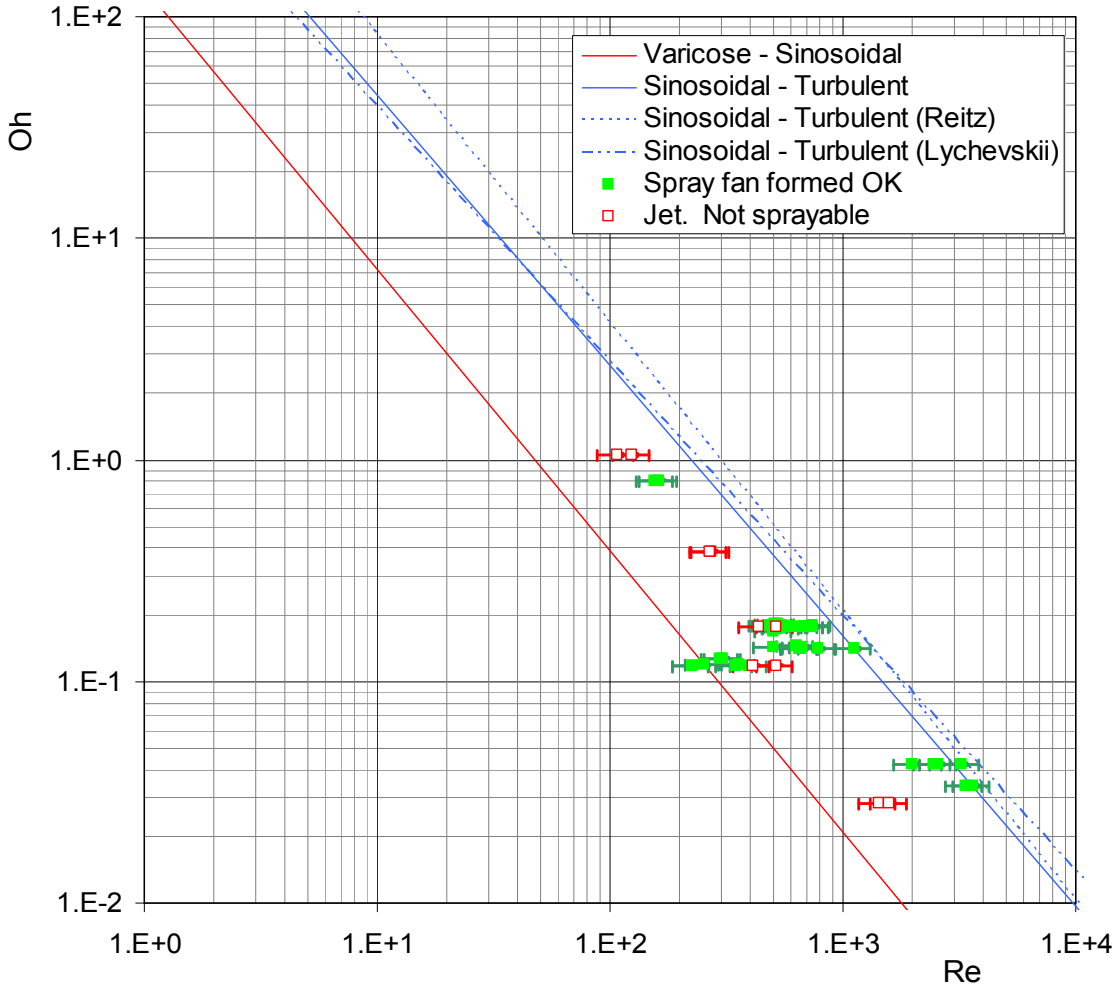

Figure 82: Ohnesorge diagram for study data, using shear viscosity in the dimensionless groups.

Substitutions for the shear viscosity in the dimensionless groups by the transient apparent extensional viscosity measurements from Table 6 can then be made.

The substitution could be made into only one or both dimensionless groups. The substitution of a measure of extensional viscosity in place of shear viscosity into both dimensionless groups is readily justified by qualitative consideration of the physics represented by the numbers, but does require further careful consideration. The Ohnesorge number quantifies the relative magnitude of viscous to surface tension forces. As described in Chapter 7, the balance of extensional viscosity and surface tension is the essence of the filament necking and eventual breakup characterised in the CaBER experiment. The same physical process in the final breakup of fluid filaments to droplets is also where extensional viscosity is expected to dominate in the atomisation mechanism. The Reynolds number quantifies the relative magnitude of inertial to viscous forces. The argument can again be made from the physical process of ligament breakup, that since apparent viscosity in extension will dominate the atomisation behaviour, the apparent extensional viscosity is the correct parameter to use in the Reynolds number. However, the nozzle dimension appears in the Ohnesorge number, and in the Reynolds number the inertia is characterised by the nozzle velocity and diameter. This might suggest that nozzle viscosity (i.e. high shear rate viscosity) should be used in the Reynolds number. Here is argued that it is not the case. The apparent extensional viscosity during filament breakup dominates the atomisation behaviour, so this is the characteristic parameter that should be used.

Rather, the question is posed, why it should be the *nozzle* diameter and velocity that are used, rather than, say, the diameter (or thickness) of the liquid jet (or sheet) and its velocity relative to the surrounding air. It is hypothesised that it is simply a pragmatic convenience, and it is contested that it is defensible. The nozzle diameter and velocity are readily and accurately measurable. In contrast the relative velocity and sheet thickness are hard to measure, and anyway not well defined: both will vary with distance from the nozzle. The physical principle that allows the nozzle diameter and velocity to be used as characteristic parameters is that although atomisation shows stochastic variability, it is not entirely random. The distribution of characteristic thicknesses and relative velocities over time at any distance from the nozzle is deterministic from nozzle conditions, albeit in a relationship sufficiently complex to have eluded investigations so far except in the simplest case of the laminar jet. In the

case of a flat-fan atomiser, it could reasonably be postulated that the Reynolds number should be modified by some corrective factor, a measure of fan angle at nozzle exit, for example, in order to correct the geometry to obtain equivalence on the Ohnesorge diagram to a cylindrical jet. But the same principle applies: nozzle geometry parameters can validly substitute for the spray geometry parameters.

The data plotted in Figure 82 using shear viscosity in the Ohnesorge and Reynolds numbers has been re-plotted in Figure 83, with the shear viscosity replaced by the measurements of transient apparent extensional viscosity obtained from the CaBER study (Table 6). Note that the error bars are now considerably wider because the transient apparent extensional viscosity varied throughout the course of the measurement experiment. The bounds of the range of transient apparent extensional viscosities exhibited by the samples during the experiments have been characterised as error margins about a central magnitude.

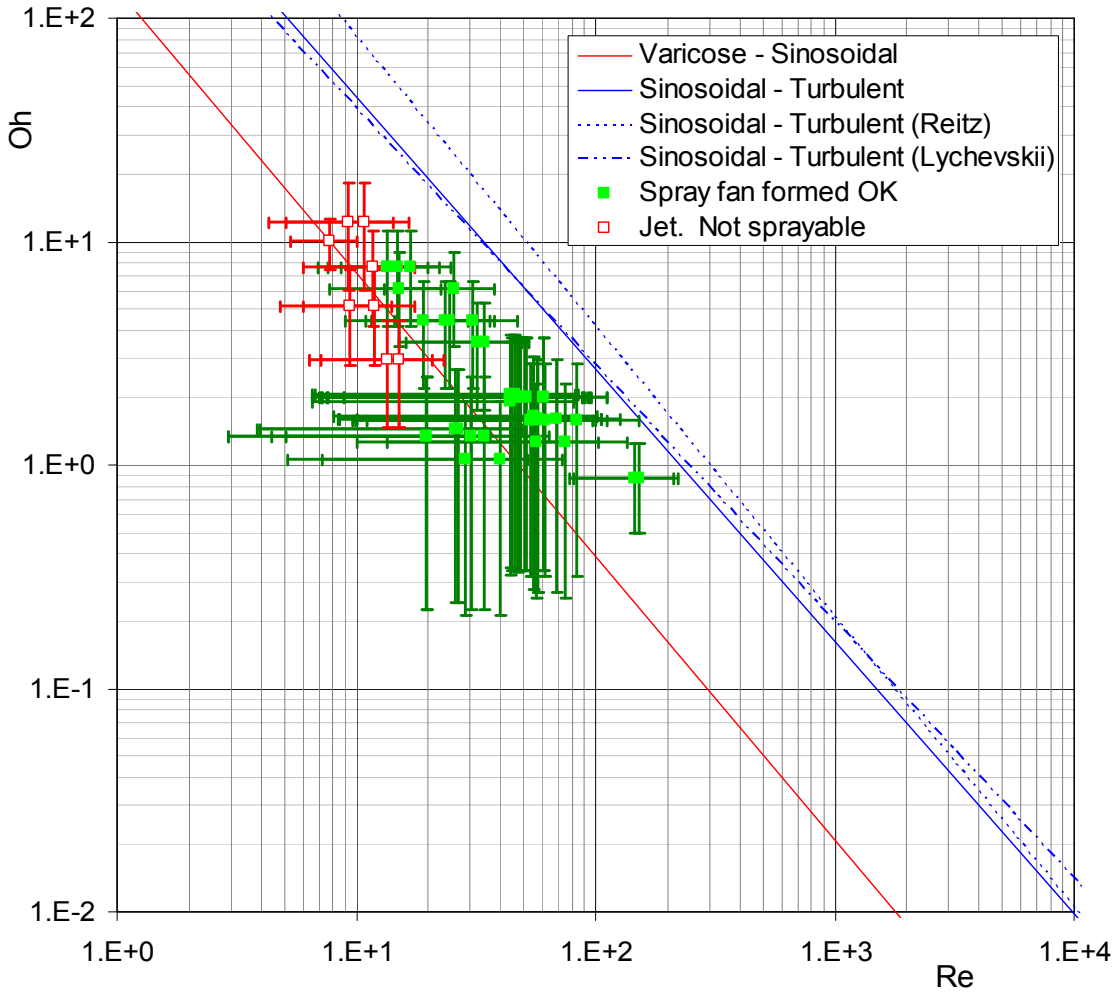

Figure 83: Ohnesorge diagram for study data, using $\overline{\eta}_{app,ext}$ *in both Re and Oh*

The result is most satisfactory. In Figure 82, with shear viscosity data, the green datapoints indicating fan spray formation were intermingled with the red datapoints indicating failure to form a spray. In contrast in Figure 83, with extensional viscosity data, not only are the red and green datapoints almost entirely separated from each other, but within the range shown by the error bars, all the green datapoints fall within the sinusoidal region, as expected for a flat-fan spray, and all the red unsprayable datapoints are in the varicose jet region, which again accords with the experimental finding that they were failing to form a spray fan but rather were jetting.

However, to achieve numerical equivalence on the Ohnesorge diagram after the viscosity parameter substitution into the dimensionless groups, it is expected that the measure of extensional viscosity should be divided by three. This correction has been plotted in Figure 84. The positions of the points change, but the conclusion is unaltered.

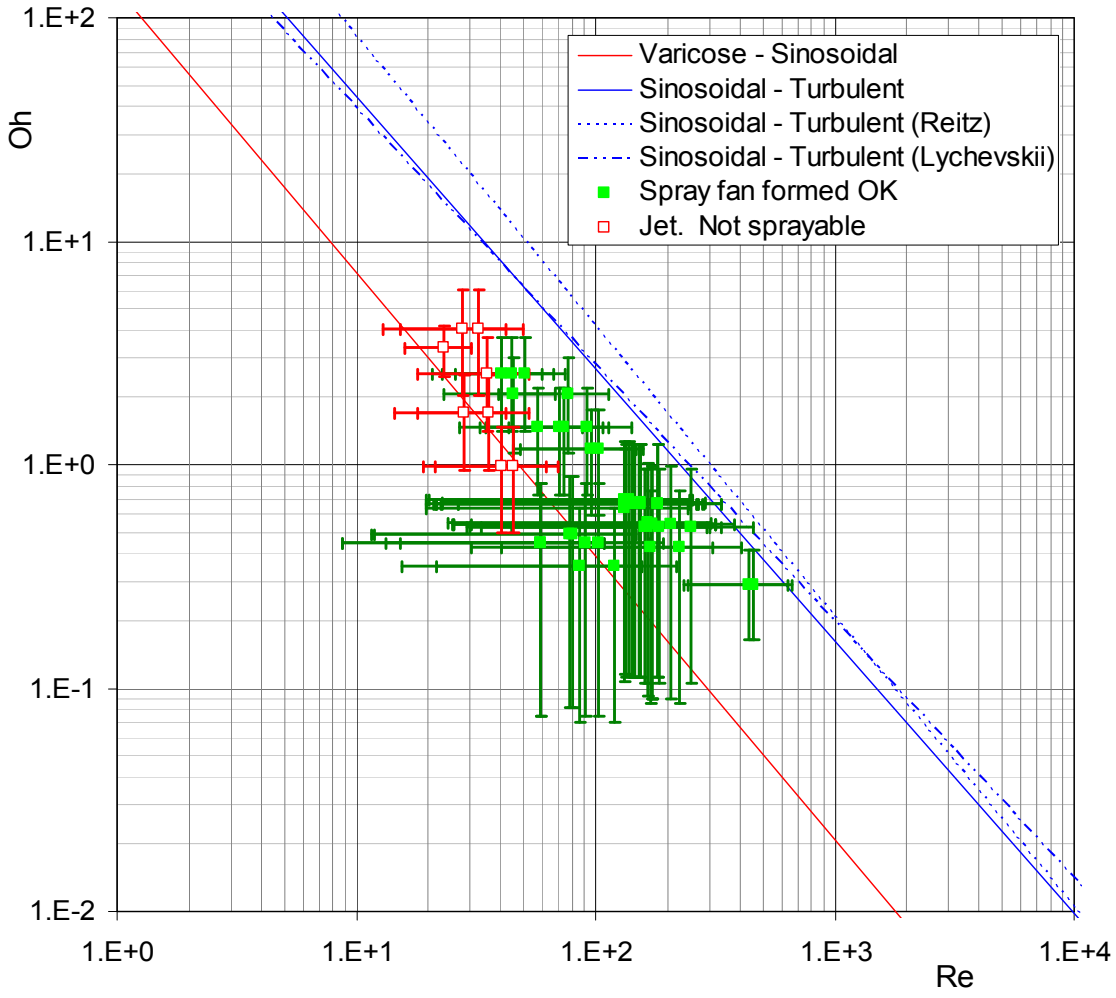

Figure 84: Ohnesorge diagram for study data, using $\overline{\eta}_{app,ext}/3$ *in both Re and Oh*

10.5 Conclusion to the use of CaBER data in the Ohnesorge diagram

This study has successfully demonstrated for the first time the substitution of an extensional viscosity parameter obtained from CaBER experiments in place of the shear viscosity in the dimensionless groups in the Ohnesorge diagram. It has given a preliminary indication that this novel substitution yields quantitatively correct predictions of spray behaviour when the original shear viscosity version does not. This finding has been demonstrated, not for a laboratory model fluid and nozzle, but for real commercial products.

The data separation in figure 83 and figure 84 is not perfect, but it is indicative. It has been discussed earlier that the CaBER instrument, whilst commercially available, is best considered to be a prototype, requiring development both to hardware and measurement data analysis. Additionally, the rheological response of the study materials was complex, requiring innovation in both the experimental protocol and the data analysis. Hence the quantitative accuracy of the CaBER is not well established, and wide error margins were used on the plotted data. Furthermore, it has been established from the sparse literature that the only validation data for the Ohnesorge diagram is for flow of a Newtonian fluid through a simple cylindrical nozzle, and it is reasonable to anticipate that a translation of the boundaries of the regions of characteristic spray behaviour would be required for other nozzle geometries. Any such translations are as yet to be determined.

CHAPTER 11 - CONCLUSION

The research reported in this thesis has met the goal stated in the introduction, to develop models of the spray drying process that could both predict performance and be used to interpret and explain observations in the case where the Acoustic Atomiser was used to produce large particles of film forming materials in a spray dryer.

Assessment of the differences when large particles are dried led to important simplifications to the modelling task. In contrast to much of the recent literature, the computational complexity of 3-D transient CFD simulation was found to be unnecessary. The droplet drying rate was shown to dominate computational models when drying large droplets of film forming materials.

The science is not yet sufficiently developed to be able to predict droplet drying rates from theory, and the drying kinetics must be experimentally determined. A measurement device using the principle of suspension of a single droplet from an electronic ultramicrobalance was chosen from the many techniques described in the literature. A detailed design for such a device has been presented, and the apparatus has been partially realised. The combination of operating range, precision and accuracy of the apparatus design would greatly exceed other devices reported in the literature.

Pending the completion of the new droplet drying kinetics apparatus, it was necessary to find some alternative modelling strategy in order to predict spray drying performance when using the Acoustic Atomiser to create a narrow size distribution of large droplets of film forming materials. In a new approach, it was shown that a simple scaling analysis yielded a prediction of a factor of two increase in mode droplet size, which accords well with experimental observations. A seven-fold decrease in the spread of the residence time distribution was predicted when the Acoustic Atomiser was used in place of a conventional atomiser. This result is consistent with and explains the phenomenological reports that have been made (Fiannaca and Threlfall-Holmes, 2005, Threlfall-Holmes, 2008), that where multiple spray-dried particle morphologies were possible, particles predominantly of a single morphology could be made using an Acoustic Atomiser.

Whilst satisfyingly computationally economical, the analysis is not as general in scope as a well understood computational process model together with accurate drying kinetic

measurement data. The new method requires performance data for an existing process. Hence it is well suited to the case of replacing the atomiser in an existing spray dryer, but cannot make predictions for a novel material or in the design of a new spray dryer.

The scaling model requires a mathematical function to describe the droplet size distribution. The Acoustic Atomiser is novel, so there are no previous reports of a suitable fit function. In this research, it was found that the distribution functions commonly used for sprays are not a good representation of the droplet size distribution from the Acoustic Atomiser. The best representation of the data was obtained using the Stable distribution. This has found practical application in modelling financial data, but there are no previous references to its use to model spray droplet size data. This is undoubtedly partly due to the mathematical complexity. For many practical purposes simple fit functions such as the log-normal are perfectly adequate. Mathematical complexity is not a complete explanation for lack of application to spray size distributions, however. The mathematical complexity of the Stable distribution is no worse than the 4-parameter log-hyperbolic function (4PLH), which has been applied to sprays droplet sizing (Stanton et al., 1998, Xu et al., 1993), and in this research it has been found that the parameter selection of the Stable distribution is more rational than the 4PLH. Indeed, the value of the "alpha" parameter of the Stable distribution was found to be roughly correlated with the viscosity of the liquid feed, tending towards the Gaussian limit of two for low viscosity systems, and towards the Lorentz limit of one as the viscosity increased. This is consistent with behaviour as a simple and damped forced harmonic oscillator respectively. Hence the novel findings reported are not only that the Stable distribution appears to be numerically a good model for the droplet size data from the Acoustic Atomiser, but unusually for a sprays size distribution function, there are indications of some underlying scientific rationale in the choice of parameters.

The reliance of the scaling model on the droplet size distribution created by an atomiser demonstrates the importance of atomisation to the spray drying process. Industrial spray dryer feedstocks are expected to exhibit complex fluid rheology, as they typically contain colloidal dispersions and/or dispersed polymer, and are commonly dewatered close to the rheological limit of sprayability. However, there is no robust theory to predict sprayability. To begin to address this deficit, a study has been reported where a measure of transient apparent extensional viscosity obtained from the Capillary Breakup Extensional Rheometry (CaBER) technique was shown to predict quantitatively,

sprayability using the Ohnesorge diagram. Developments to the technique and the analysis method were required. A repeated straining protocol was required in order to obtain consistent data. A novel analysis method was proposed and exemplified, using the Newtonian model as a basis for the numerical differentiation of an arbitrary time-diameter curve obtained from the CaBER experiment. This allows fluids to be analysed even when they do not exhibit behaviour conforming to one of the limited number of published rheological models. Although the Ohnesorge diagram was first proposed over 70 years ago, this work is the first report of the use of the Ohnesorge diagram to predict quantitatively sprayability for an industrial fluid with complex rheology.

CHAPTER 12 - RECOMMENDATIONS FOR FUTURE WORK

The research reported in this thesis has yielded new insights and contributed to the fields of sprays and spray dryer modelling. However, despite these achievements, there remains much to be done.

The completion and beneficial operation of the ultramicrobalance based drying kinetics apparatus would be a valuable further contribution to the spray drying field.

The scaling model requires performance data from a given product in an existing spray dryer as a basis from which to scale: it does not negate the need for computational process models and accurate drying kinetic measurement data in order to make predictions for new products or dryers when the existing process data is not available. It has been observed that there is broad similarity in the pattern of large scale recirculation flows within a spray dryer obtained from the models reported by independent research groups (Liang and King, 1991, Sano, 1993, Kievet et al., 1997, Schwartzbach, 2000, Lebarbier et al., 2001, Huang et al., 2003, Lo, 2005). For the specific case of large droplets which fall in a well defined shower trajectory, it would seem plausible to use these results to create an assumed steady state model of the flow field contours with considerably better representation of the time-temperature history of the droplets than a 1-D model, but with little more computational effort

The use of the Stable distribution as a physically meaningful model for spray droplet size is deserving of further study to investigate its wider relevance to modelling spray size distributions.

The analysis method that was proposed for an arbitrary CaBER time-diameter curve would benefit from further theoretical and experimental validation.

It would be useful to validate the extensional viscosity substitution in the Ohnesorge diagram using the flow through a simple cylindrical nozzle of simple model strain hardening fluids. Furthermore by reference to the conceptual visco-elasto-capillary balance diagram in McKinley's review paper (McKinley, 2005), for visco-elastic fluids it is anticipated that the Ohnesorge diagram should be extensible to a third dimension in the Weissenberg number. Also helpful would be careful experimental studies of the effect of nozzle geometry on the position of the transition lines on the Ohnesorge

diagram. A final useful study would consider the sprayability of non-model fluids with a range of non-Newtonian rheological responses to strain, in a selection of nozzle geometries. A successful conclusion of such a study would be at least an empirical robustly validated predictive model for sprayability.

APPENDIX A - ACOUSTIC ATOMISER SIZE DISTRIBUTION DATA

A.1 Water from a single laminar jet vibrated at resonance, measured by PDA

Data measured on a now obsolete AEA PD Lisatek PDA, with only 5000 counts per acquisition - half what would now normally be accepted for a valid PDA measurement to make sure that there were sufficient counts in peripheral size bins. The sizing bins are undesirably wide compared to distribution width.

Normal (i.e. $\alpha = 2$ in Stable distribution) and log-normal fits for Water are shown Figure 38 of main text.

Nozzle A	
diam µm	CumVol %
22.17	0
28.62	0.01
35.06	1.23
41.50	42.07
47.94	84.92
54.39	92.64
60.83	93.76
67.27	93.83
73.72	93.83
80.16	93.83
86.60	93.96
93.05	93.96
99.49	93.96
105.93	93.96
112.38	93.96
118.82	93.96
125.26	93.96
131.71	93.96
138.15	93.96
144.59	93.96
151.03	93.96
157.48	93.96
163.92	93.96
170.36	93.96
176.81	93.96
183.25	93.96
189.69	93.96
196.14	93.96
202.58	93.96
209.02	93.96
215.47	96.04
221.91	96.04
228.35	96.04
234.80	96.04
241.24	96.04
247.68	96.04
254.13	96.04
260.57	96.04
267.01	100.00

Nozzle B	
diam µm	CumVol %
244.32	0.00
256.27	0.01
268.22	10.51
280.17	84.37
292.13	99.89
304.08	100.00

A.2 Material A. Sieve size data from production spray-solidification

Data is percent of weight under size as transcribed from plant logs. Expressed to 0.1% precision. In principle error bars could be plotted as with other sieve data (see subsequent sections of this appendix). Those are frequently 100g total expressed to 0.1g, so the error bars would be of the same order for the individual days samples in datasets A. However with datasets A the fit is to the ensemble average, where the error is reduced by the square root of the number of readings - i.e. the error bar is reduced by a factor of about three for Dataset A1 and five for Datasets A2 and A3. By inspection the error bars even in the tails on the DSP plot will be insignificant.

The plant logs record occasional process changes and disturbances that changed the size distribution, and hence these data have been excluded from the analysed datasets.

A.2.1 Dataset A1

sieve size	% weight under size						
µm	sample 2	sample 3	sample 4	sample 5	sample 6	sample 7	sample 8
5600	100.0	100.0	100.0	100.0	99.8	100.0	100.0
4750	99.8	99.8	99.3	99.8	99.4	100.0	99.9
4000	97.7	97.3	96.9	96.5	97.5	98.0	98.4
3650	95.1	94.5	93.6	93.3	94.3	95.9	96.1
2800	70.5	68.5	65.5	61.7	66.4	69.8	74.8
2400	22.8	20.5	20.4	20.9	21.3	25.5	42.4
2000	6.9	5.1	4.9	4.0	5.5	7.2	14.9
1680	4.9	3.4	3.0	2.1	3.7	4.9	4.8
1200	2.6	1.7	1.7	0.8	2.1	2.9	2.8
850	1.2	0.6	0.8	0.2	1.0	1.3	1.5
420	0.1	0.0	0.1	0.1	0.1	0.2	0.1
0	0.0	0.0	0.0	0.0	0.0	0.0	0.0

60 te/hr production plant trial

Log-normal fits for Dataset A1 are shown Figure 26 of main text.

Stable fits (next page) performed on the ensemble average data of 7 samples. Dsp limits have been set for (number of sieves per sizing)* √(number of sizings) = 12* √ 7 = 32 points.

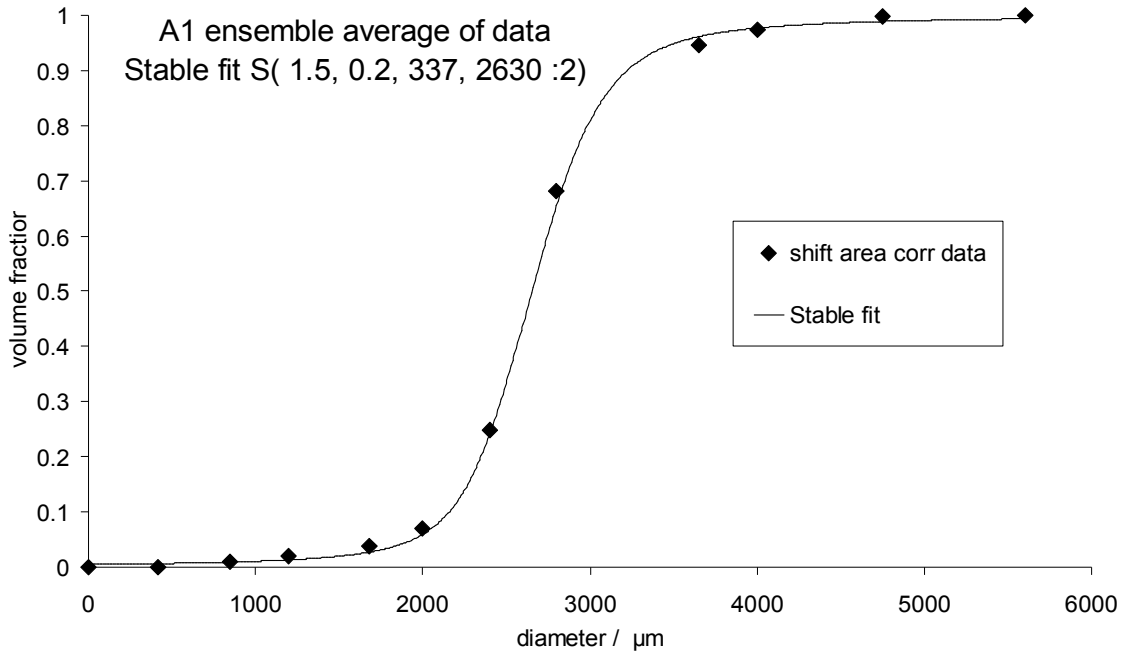

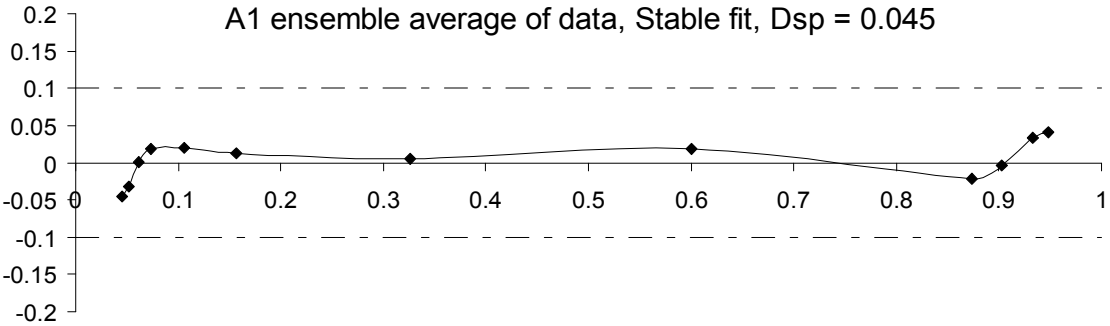

A.2.2 Datasets A2 and A3

70-80 te/hr production plant daily QC checks covering one month for each dataset.

The assumption that the different day's records are samples from the same population is much less defensible for datasets A2 and A3 than for A1 or B. There is one extreme outlier in A3 in particular which in hindsight could reasonably be rejected. However, one dataset amongst 27 does not much skew the ensemble average.

Data tables for A2 and A3 are on the next page, followed by log-normal and then Stable fits. The Stable fits are performed only on the ensemble average data. Dsp limits have been set for (number of sieves per sizing)* √(number of sizings) = 11* √ 29 = 59 points for A2 and 12 * √ 29 = 62 points for A3. The Stable distribution is in each case a better fit to the data.

Dataset A2:

sieve size	% weight retained on sieve by day no. in month																												
µm	1	2	3	4	5	6	8	9	10	11	12	13	14	15	16	17	18	19	20	21	22	23	24	25	26	27	28	29	30
4750	0	0	0	0	0	0.3	0.2	0	0	0.1	0	0	0	0	0	0	0	0	0	0	0	0	0	0	0	0	0	0	0
4000	0.2	0.2	0.4	0.2	0.6	1.3	1.8	0.1	1.4	0.9	0.2	0.3	0.3	0.4	0.3	0.4	0.3	0.3	0.3	0.1	0.1	0.3	0.2	0.1	0.1	0.2	0.4	0.1	0.3
3350	4.2	4.7	5.3	2.9	6.9	9.7	14.3	7.8	13.5	9.5	7.6	4.3	3.7	7.2	5.1	4.9	5.3	8.2	5.3	2.2	2.9	3.4	3.1	2.8	2.5	2.8	6.1	2.6	4.8
2800	40.1	37.9	43.7	21.6	23.4	29.8	37.2	27.6	30.1	32.9	28.9	19	17.6	28.4	25.8	28.3	24.8	17.6	28.3	14.8	15.6	17.9	17.4	14.4	12.5	12.3	28.4	14.8	21.3
2360	99	89.4	87.4	93.8	57.3	76.8	88.5	92.5	84.3	80	81.4	90.8	88.9	89.5	88.9	89.1	89.7	90.8	91	96.2	95.4	89.7	92.6	77.9	51.6	49.8	88.7	71.2	90.2
2000	99.6	99.6	89.9	99.4	99.3	99	99.3	99.5	99.2	99.5	99.6	98.3	97.3	99.6	99.6	99.5	99.4	99.6	99.5	99.8	99.6	99.2	99.3	99.6	99.7	99.6	99.3	99.3	99.4
1700	99.7	99.7	99.2	99.8	99.7	99.9	99.7	99.7	99.7	99.7	99.9	99.6	99.2	99.8	99.8	99.7	99.7	99.8	99.7	99.9	99.8	99.7	99.7	99.8	99.8	99.7	99.8	99.6	99.8
1400	99.9	99.8	99.6	99.9	99.9	100	99.9	99.8	99.9	99.9	100	99.9	99.7	99.9	99.9	99.9	99.9	99.9	99.9	99.9	99.9	99.9	99.9	99.9	99.9	99.9	99.9	99.8	99.9
1000	100	100	99.9	100	100	100	100	100	100	100	100	100	99.9	100	100	100	100	100	100	100	100	100	100	100	100	100	100	100	100
500	100	100	100	100	100	100	100	100	100	100	100	100	100	100	100	100	100	100	100	100	100	100	100	100	100	100	100	100	100
0	100	100	100	100	100	100	100	100	100	100	100	100	100	100	100	100	100	100	100	100	100	100	100	100	100	100	100	100	100

Dataset A3:

sieve size	% weight retained on sieve by day no. in month																												
µm	1	2	3	4	5	6	7	8	11	12	13	14	15	16	17	19	20	21	22	23	24	25	26	28	29	30	31		
4750	1.7	0.6	0.3	0.4	0.5	0.7	0.4	0.9	0.3	0.3	0.6	0.3	0.6	0.1	0.1	0.5	0.3	0.6	0.6	0.5	0.4	0.4	0.4	0.3	0.4	0.2	0.3		
4000	8.1	2.8	1.3	1.9	2.4	2.4	2.3	2.9	2.3	2.6	2.6	3	3.9	3.6	2.7	3.1	2.4	3.8	4.3	2.4	3.1	2.9	1.9	2.9	2.2	2.5	3		
3350	27.4	12.3	6.7	8	9.1	10.1	10.6	9.3	13.8	11.3	12.6	13.6	17.3	17.3	13.8	14	11.2	16.4	16.7	10.3	12.8	13.1	10.1	13.6	12.3	13.1	15.1		
2800	58.1	35.3	24	25.3	26.7	31.9	31.4	26.4	34.9	27.7	31	31.3	38.6	39.7	33	34.4	31.1	35.9	37	30.6	33.2	35	30	34.6	33.9	32.6	34.9		
2360	92.2	81.1	70.9	75.6	82.5	84.5	78.5	78.5	87.5	87.2	88.9	90.5	90.5	89.2	88.1	89.6	87.7	92.5	87.6	85.3	87	86.9	85.2	89.9	87.9	85.4	86		
2000	99	95.5	94.3	94.9	95.9	95.5	95.5	94.5	96.2	96.5	96.9	97.9	92.6	97	96.3	97.1	97.1	97.7	96.3	97.6	97	95.9	96.5	97.2	95.2	96	97		
1700	99.9	98	98.4	98.5	98.9	98.6	98.5	98.3	97.5	98.5	98.9	99.2	98.7	98.9	98.4	98.9	99.1	99.2	98.7	99.2	99.3	98	98.8	98.9	97.9	97.9	98.1		
1400	100	99.3	99.8	99.8	99.8	99.6	99.5	99.7	99.1	99.5	99.6	99.8	99.7	99.8	99.2	99.7	99.7	99.7	99.7	99.8	99.8	99.4	99.7	99.5	99.4	99.5	99.7		
1180	100	99.8	99.9	99.9	99.9	99.7	99.6	99.8	99.8	99.8	99.8	99.9	99.8	99.9	99.5	99.8	99.8	99.8	99.8	99.9	99.9	99.8	99.9	99.8	99.7	99.8	99.9		
1000	100	99.9	100	100	100	100	100	99.9	100	100	100	100	100	100	99.8	99.9	99.9	99.9	99.9	100	100	100	100	100	100	100	100		
500	100	100	100	100	100	100	100	100	100	100	100	100	100	100	100	100	100	100	100	100	100	100	100	100	100	100	100		
0	100	100	100	100	100	100	100	100	100	100	100	100	100	100	100	100	100	100	100	100	100	100	100	100	100	100	100		

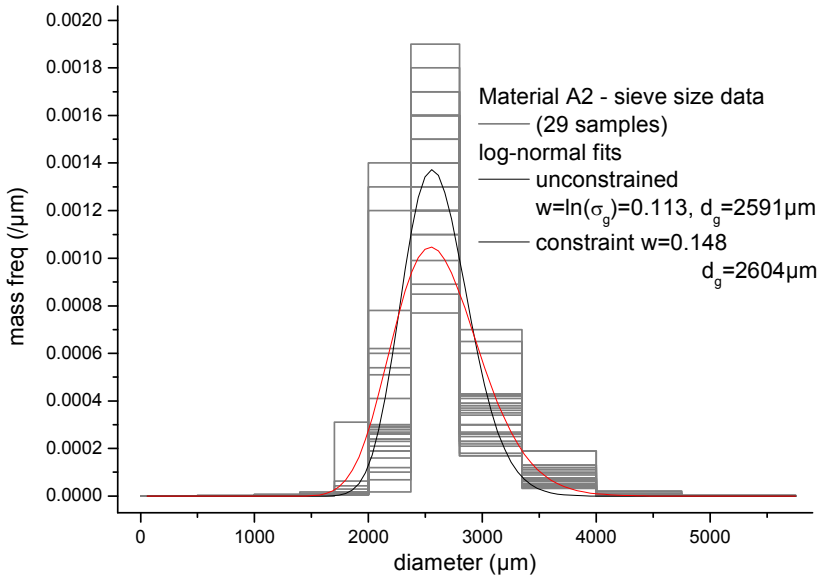
mass freq (/µm)
diameter (µm)
Material A2 - sieve size data
(29 samples)
log-normal fits
unconstrained
w=ln(σg)=0.113, dg=2591µm
constraint w=0.148
dg=2604µm

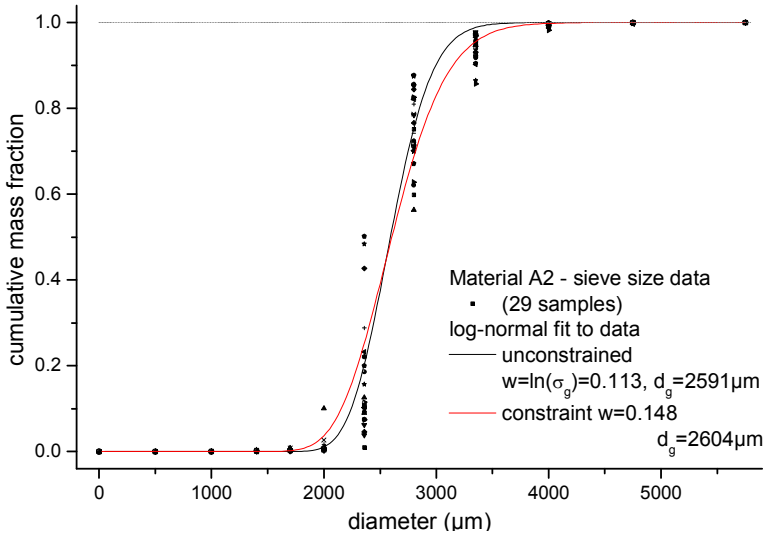
cumulative mass fraction
diameter (µm)
Material A2 - sieve size data
(29 samples)
log-normal fit to data
unconstrained
w=ln(σg)=0.113, dg=2591µm
constraint w=0.148
dg=2604µm

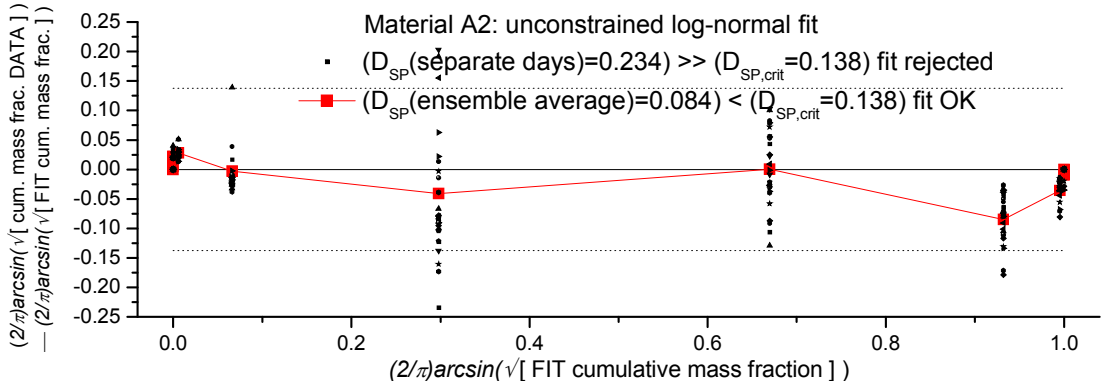
Material A2: unconstrained log-normal fit
(DSP(separate days)=0.234) >> (DSP,crit=0.138) fit rejected
(DSP(ensemble average)=0.084) < (DSP,crit=0.138) fit OK
(2/π)arcsin(√[cum. mass frac. DATA]) — (2/π)arcsin(√[FIT cum. mass frac.])
(2/π)arcsin(√[FIT cumulative mass fraction])

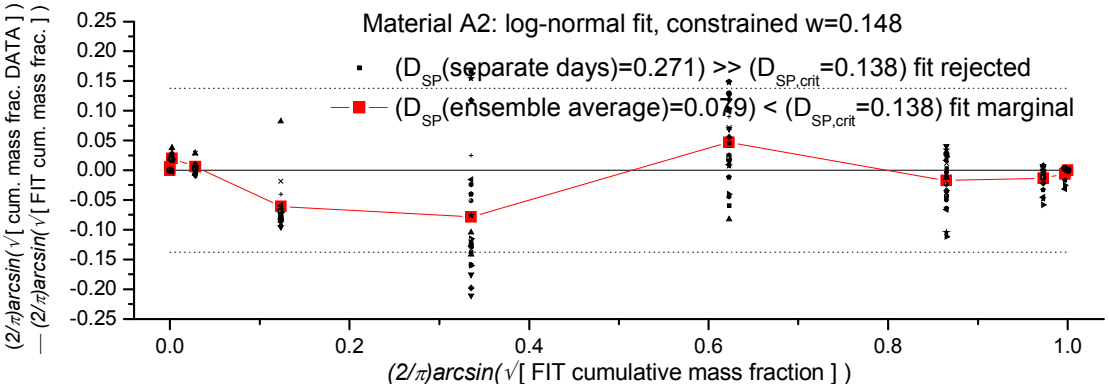
Material A2: log-normal fit, constrained w=0.148
(DSP(separate days)=0.271) >> (DSP,crit=0.138) fit rejected
(DSP(ensemble average)=0.079) < (DSP,crit=0.138) fit marginal
(2/π)arcsin(√[cum. mass frac. DATA]) — (2/π)arcsin(√[FIT cum. mass frac.])
(2/π)arcsin(√[FIT cumulative mass fraction])

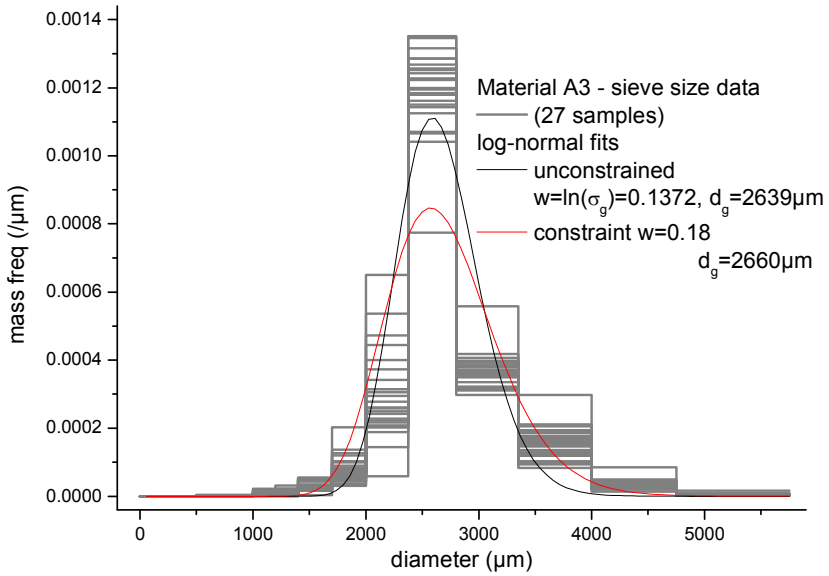
Material A3 - sieve size data
(27 samples)
log-normal fits
unconstrained
w=ln(σg)=0.1372, dg=2639μm
constraint w=0.18
dg=2660μm
mass freq (/μm)
diameter (μm)

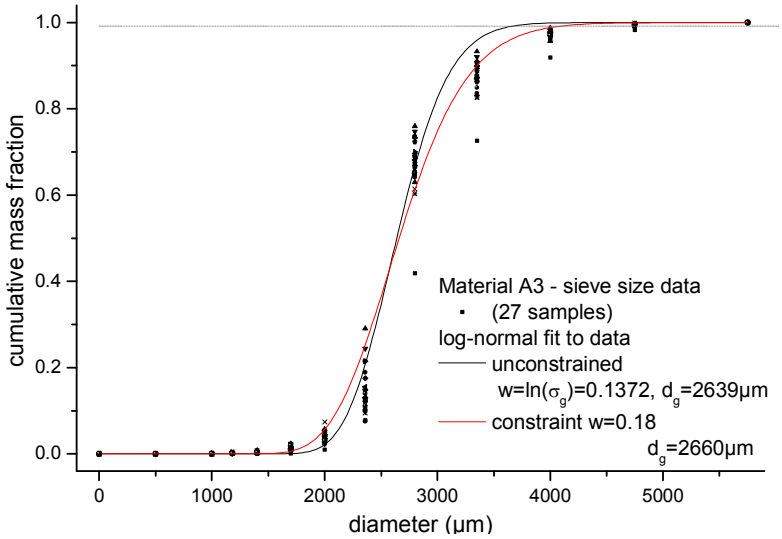
Material A3 - sieve size data
(27 samples)
log-normal fit to data
unconstrained
w=ln(σg)=0.1372, dg=2639μm
constraint w=0.18
dg=2660μm
cumulative mass fraction
diameter (μm)

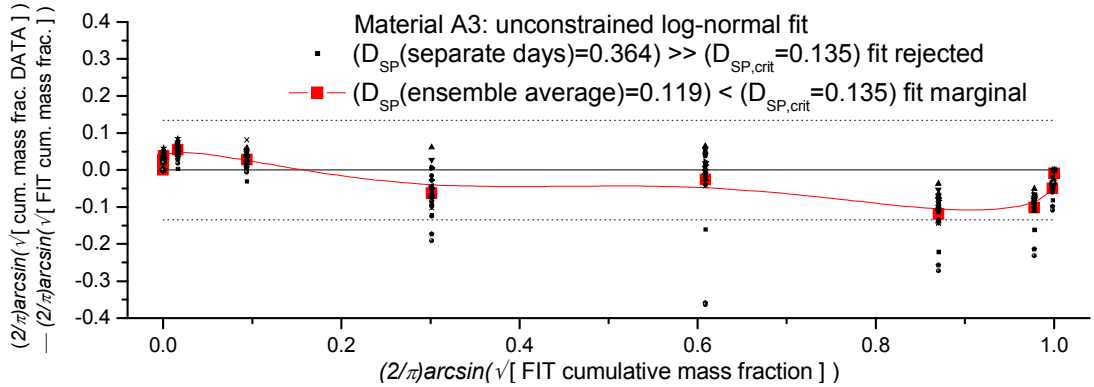
Material A3: unconstrained log-normal fit
(DSP(separate days)=0.364) >> (DSP,crit=0.135) fit rejected
(DSP(ensemble average)=0.119) < (DSP,crit=0.135) fit marginal
(2/π)arcsin(√[cum. mass frac. DATA]) — (2/π)arcsin(√[FIT cum. mass frac.])
(2/π)arcsin(√[FIT cumulative mass fraction])

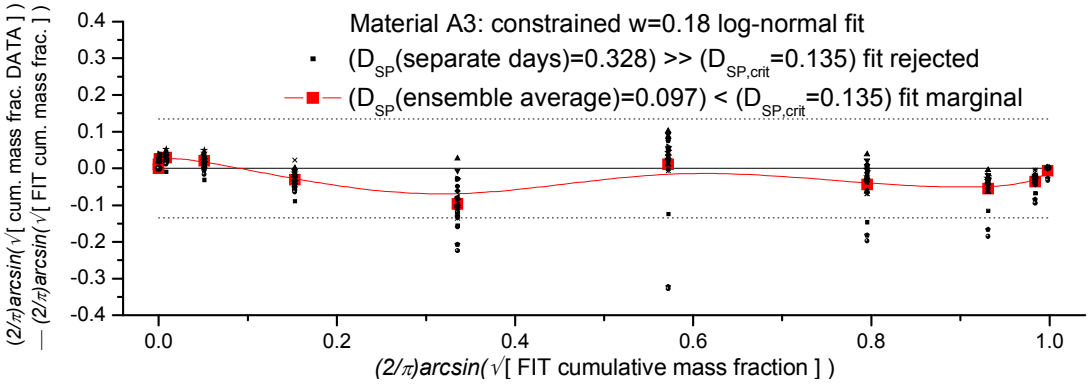
Material A3: constrained w=0.18 log-normal fit
(DSP(separate days)=0.328) >> (DSP,crit=0.135) fit rejected
(DSP(ensemble average)=0.097) < (DSP,crit=0.135) fit marginal
(2/π)arcsin(√[cum. mass frac. DATA]) — (2/π)arcsin(√[FIT cum. mass frac.])
(2/π)arcsin(√[FIT cumulative mass fraction])

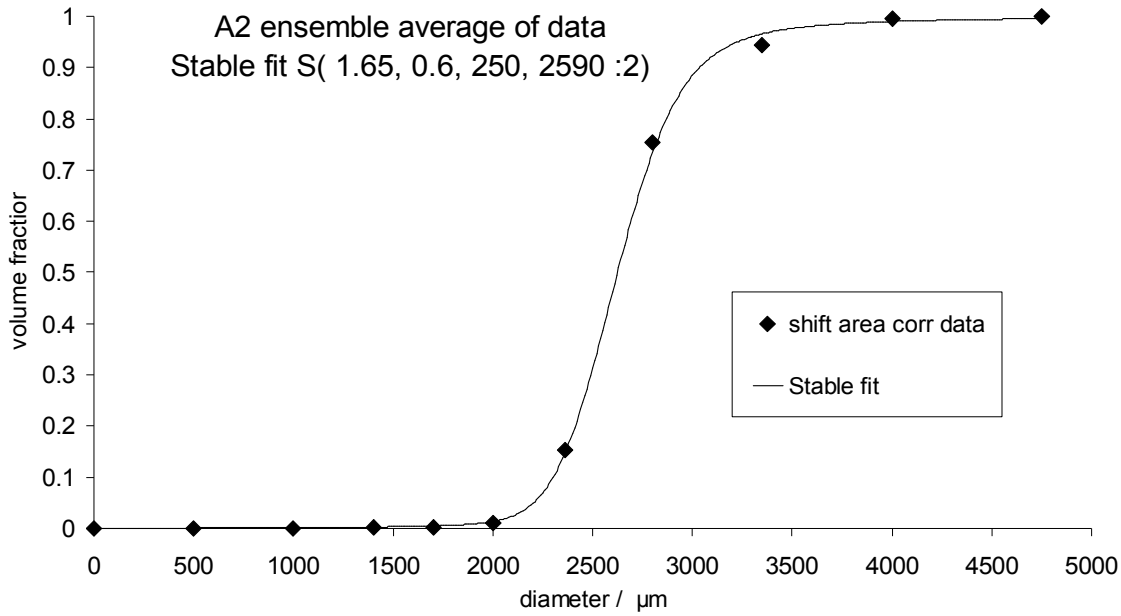
A2 ensemble average of data
Stable fit S(1.65, 0.6, 250, 2590 :2)
volume fractior
diameter / µm
shift area corr data
Stable fit

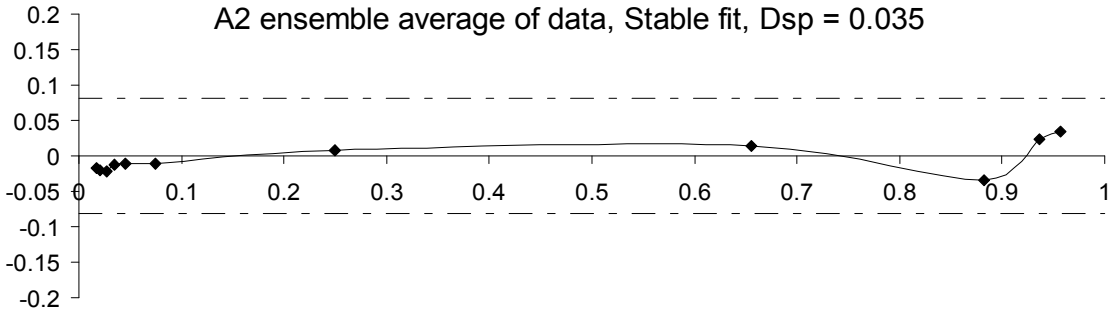
A2 ensemble average of data, Stable fit, Dsp = 0.035

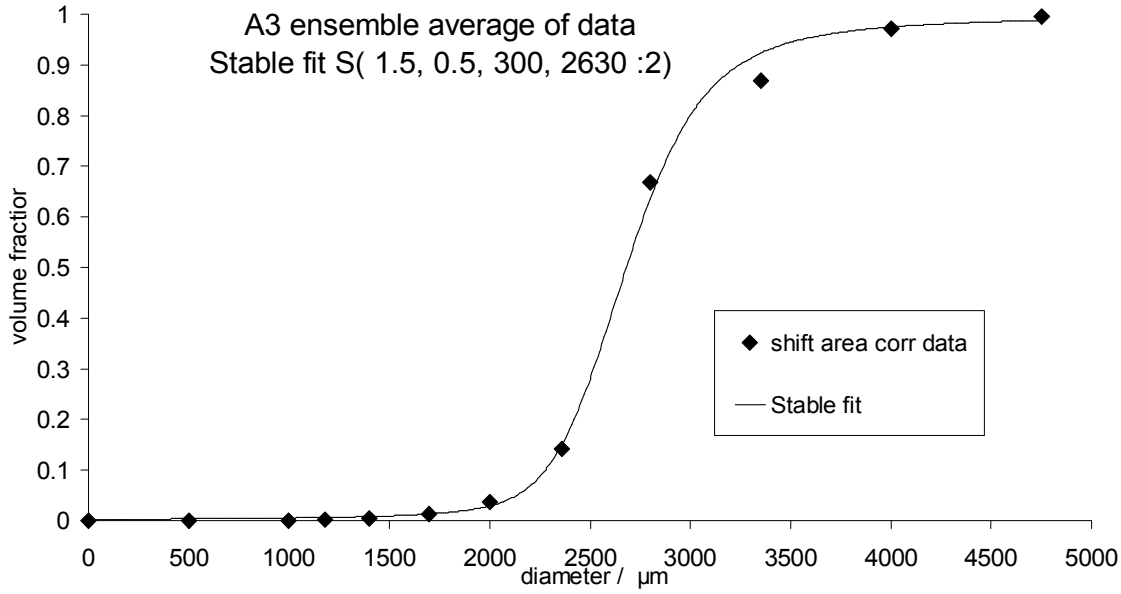
A3 ensemble average of data
Stable fit S(1.5, 0.5, 300, 2630 :2)
volume fractior
diameter / µm
shift area corr data
Stable fit

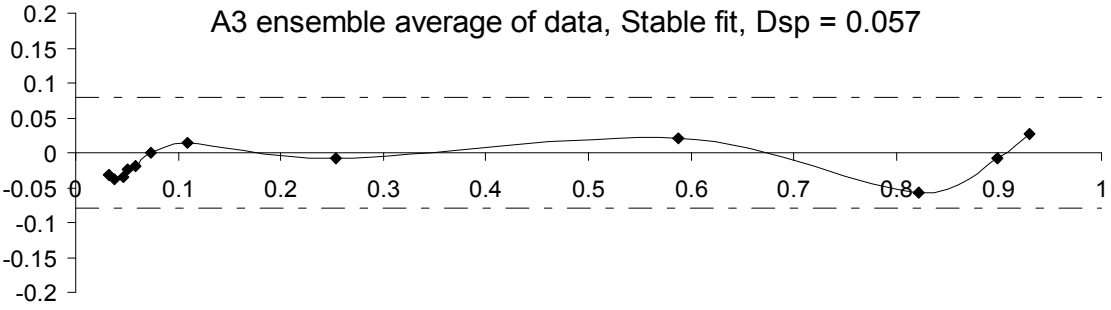
A3 ensemble average of data, Stable fit, Dsp = 0.057

A.3 Material B. Sieve size data for spray-cooled product

Dataset B. 5 kg/hr experimental tower

sieve size	mass on sieve /g	
µm	sample 1	sample 2
850	2.6	2.2
710	8.8	8.4
600	177.5	135.9
500	304.7	289.2
425	108.6	110.7
355	16.9	13.7
250	3.9	3.4
106	0.3	0.3
0	0.1	0.2

Log-normal fits for Material B are shown Figure 25 of main text.

Stable fits (below) performed on the ensemble average data of both samples. Dsp limits set for (number of sieves per sizing)* √(number of sizings) = 9* √ 2 = 13 points.

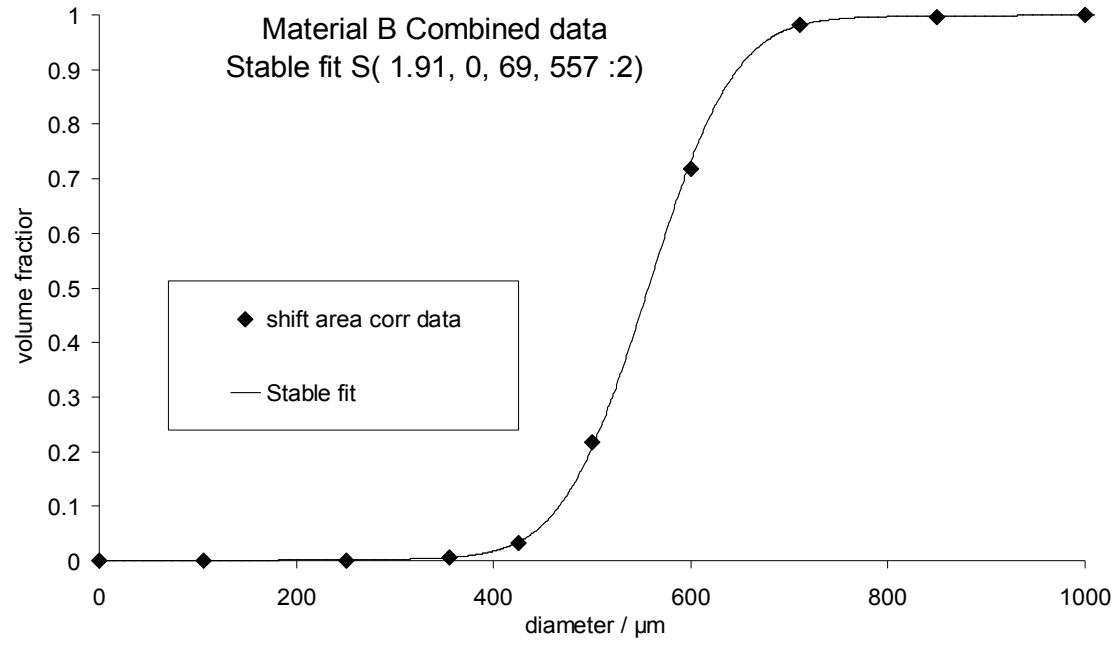

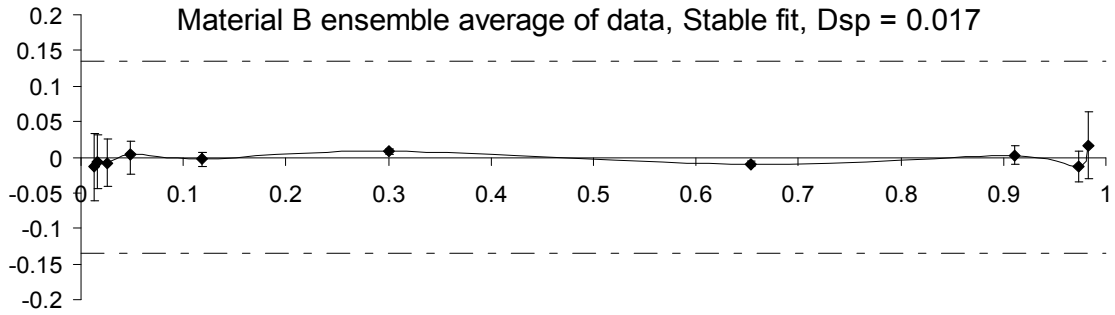

A.4 Material C. Laminar jets at resonance, measured by PDA

C1	
diam	CumVol
µm	%
233.74	0.00
247.14	0.02
260.55	0.15
273.95	1.43
287.35	40.90
300.75	76.18
314.15	95.70
327.55	99.61
340.96	99.76
354.36	99.86
367.76	99.90
381.16	99.90
394.56	99.94
407.97	100.00

C2				
diam				
µm			%	
30.58				
33.04			0.00	
35.50			0.01	
37.96		0.00	0.02	0.00
40.42	0.00	0.27	0.27	0.39
42.88	1.36	16.30	37.64	40.16
45.33	73.52	90.19	91.74	96.44
47.79	90.72	97.84	97.97	99.29
50.25	93.63	98.45	98.80	99.40
52.71	94.94	98.73	99.17	99.44
55.17	97.30	98.95	99.32	99.47
57.63	98.47	99.11	99.54	99.47
60.08	98.67	99.35	99.68	99.57
62.54	98.78	99.40	99.85	99.63
65.00	98.78	99.46	99.85	99.69
67.46	99.07	99.46	99.92	99.69
69.92	99.07	99.46	100.00	99.69
72.38	99.07	99.46		99.69
74.83	99.07	99.46		99.69
77.29	99.29	99.56		99.69
79.75	99.29	99.67		99.69
82.21	99.29	99.67		99.69
84.67	99.29	99.67		99.69
87.13	99.60	99.67		99.99
89.58	99.60	99.83		99.99
92.04	99.60	99.99		99.99
94.50	99.99	99.99		99.99
96.96	99.99	99.99		99.99
99.42	99.99	99.99		99.99
101.88	99.99	99.99		99.99
104.33	99.99	99.99		99.99
106.79	99.99	99.99		99.99
109.25	99.99	99.99		99.99
111.71	99.99	99.99		99.99
114.17	99.99	99.99		99.99
116.63	99.99	99.99		99.99
119.08	99.99	99.99		99.99
121.54	99.99	99.99		99.99
124.00	99.99	99.99		99.99

Normal (i.e. $\alpha = 2$ in Stable distribution) and log-normal fits for Datasets C1 and C2 are shown Figure 39 of main text.

Datasets C3 and C4 are from a chart (next page) comparing the size distribution of a production Acoustic Atomiser (line 3, dataset C3) to the rotary atomiser that it replaced (line 1, dataset C4). Line 2 refers to another novel atomiser design that was tested, but is not discussed in this work. The ICI internal report indicates that these lines were

drawn from PDA measured data, but the original instrument data tables are no longer available. The chart has been digitised using an Origin add-in tool where the user manually clicks on points on the graph. The precision of the digitisation is thus limited by the accuracy to which the cursor is placed. It can also be observed by careful examination of the chart, that the hand-sketched curve is not entirely smooth. Hence the points on the digitised dataset are rather noisy.

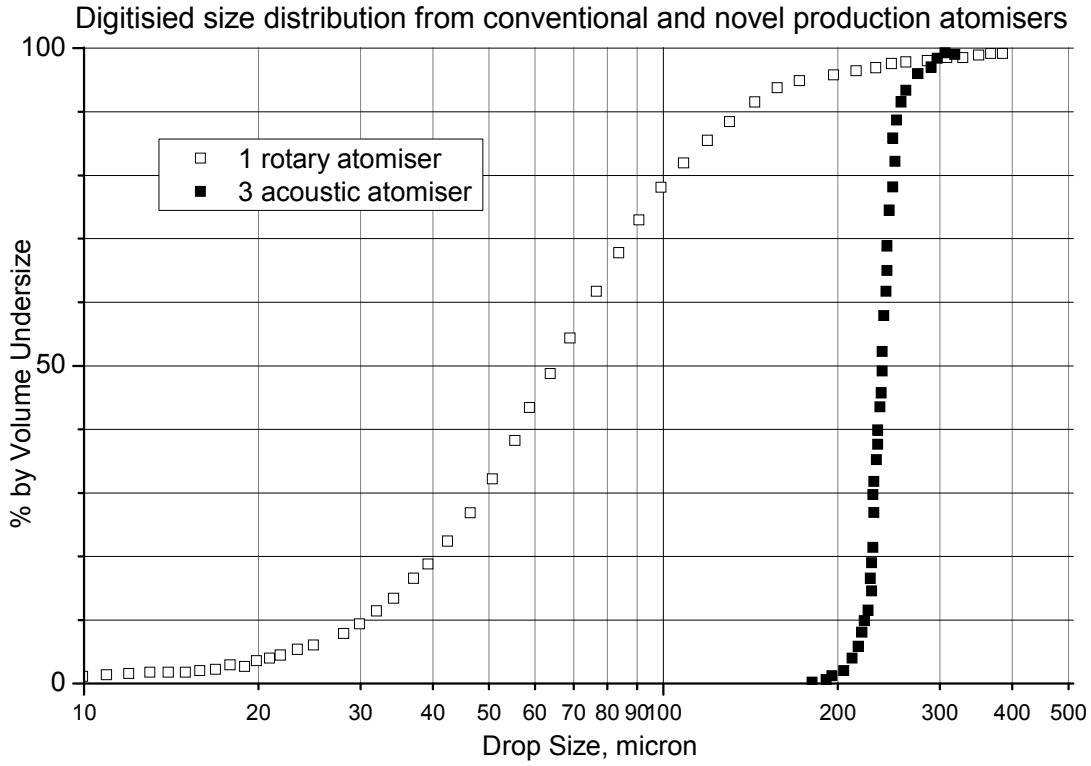

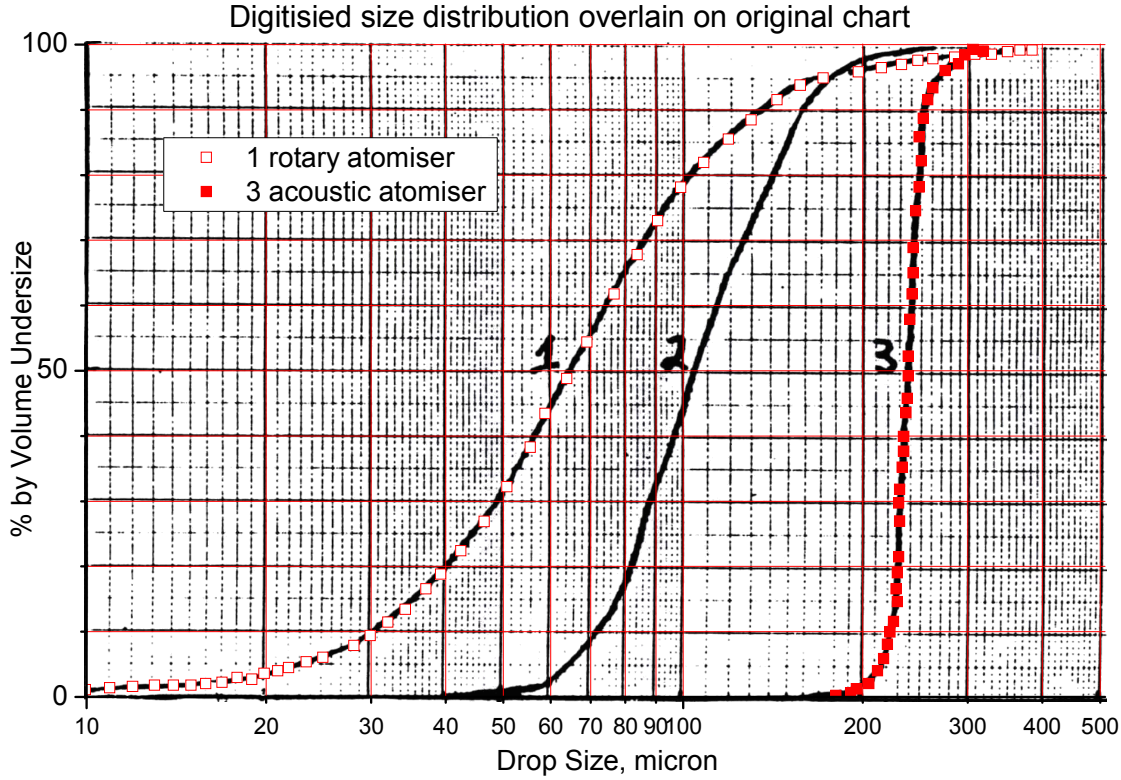

To estimate an appropriate value for the 95% confidence limits on the DSP chart, an estimate of the number of points in the original dataset is needed. The bin size in the AEA Lisatek PDA was fixed with the choice of lens focal length, which in turn was determined by the measurable size range. Since the size range of dataset C3 is similar to C1, it seems reasonable to assume that the bin size was also 13.4 µm, and hence the digitised size range of dataset C3 must have covered 10 size bins. Thus the 95% confidence limits plotted on the DSP chart (below) for dataset C3 are set for 10 readings.

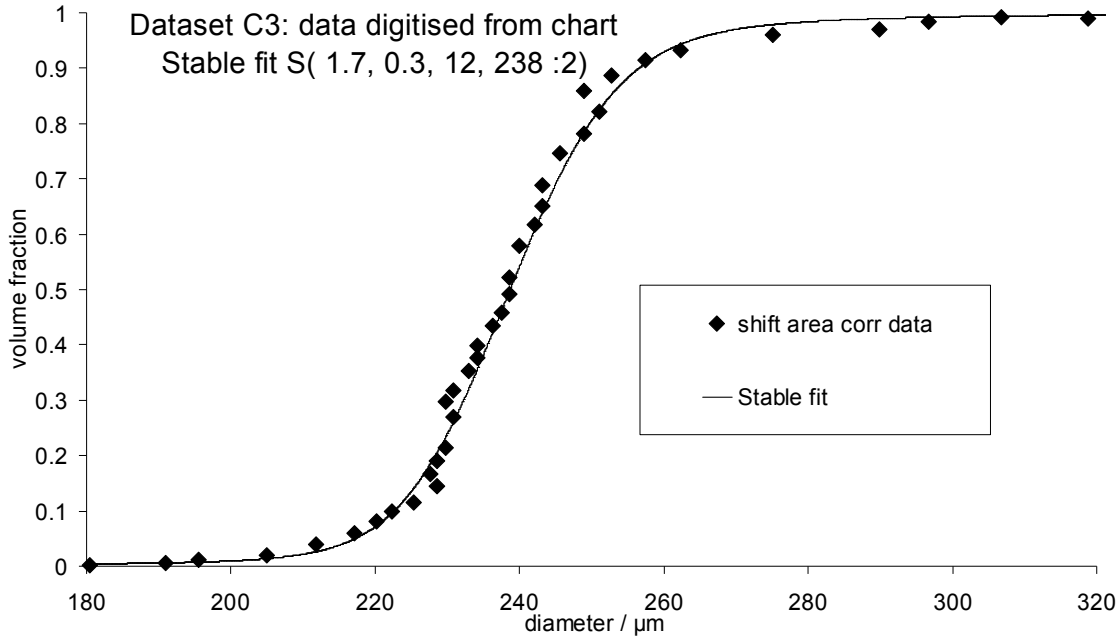

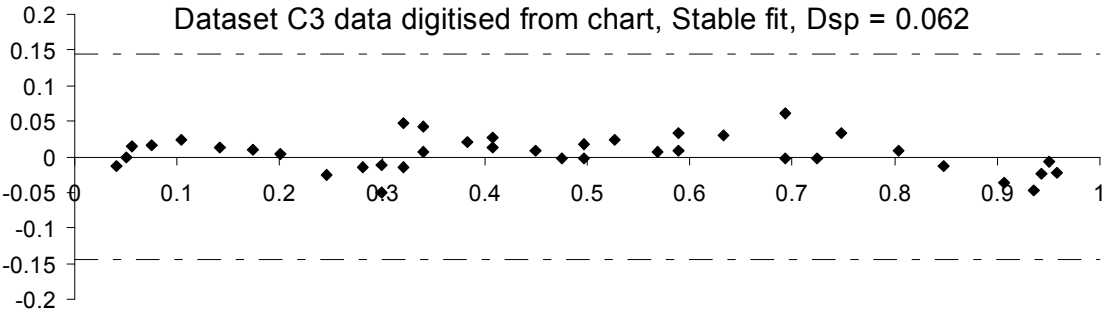

The rotary atomiser dataset C4 has been fitted to a log-normal distribution (next page). Sizing bins are again assumed to be 13.4µm width, hence 30 bins cover the data range, with 95% confidence limits on the DSP chart set accordingly.

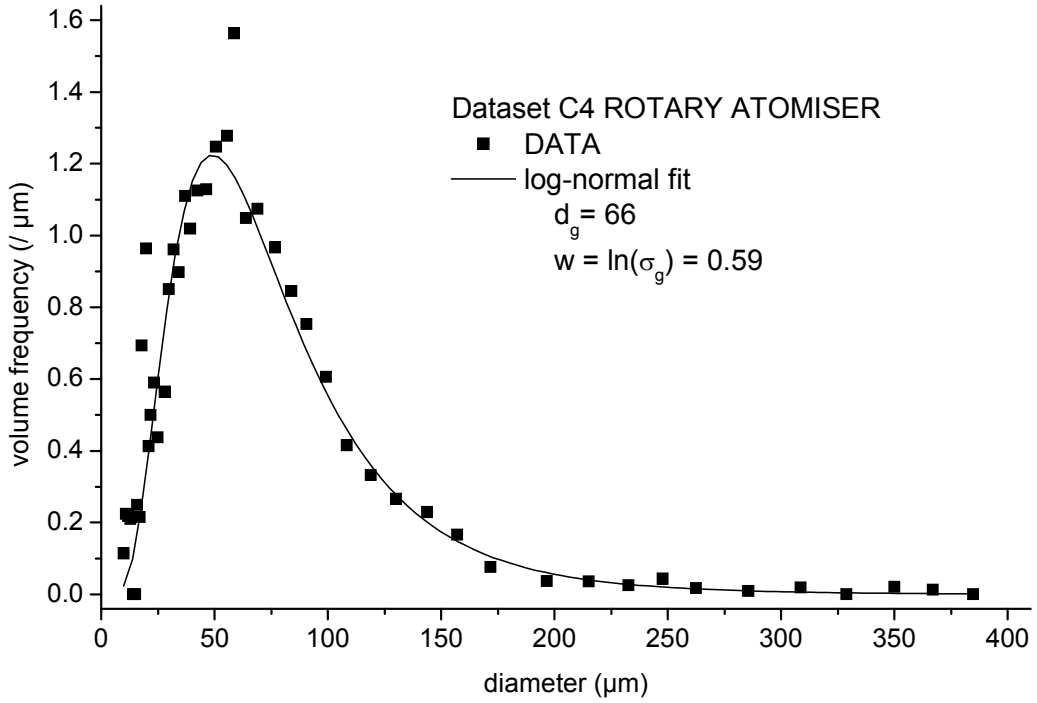
Dataset C4 ROTARY ATOMISER
DATA
log-normal fit
d_g = 66
w = ln(σ_g) = 0.59
volume frequency (/ µm)
diameter (µm)

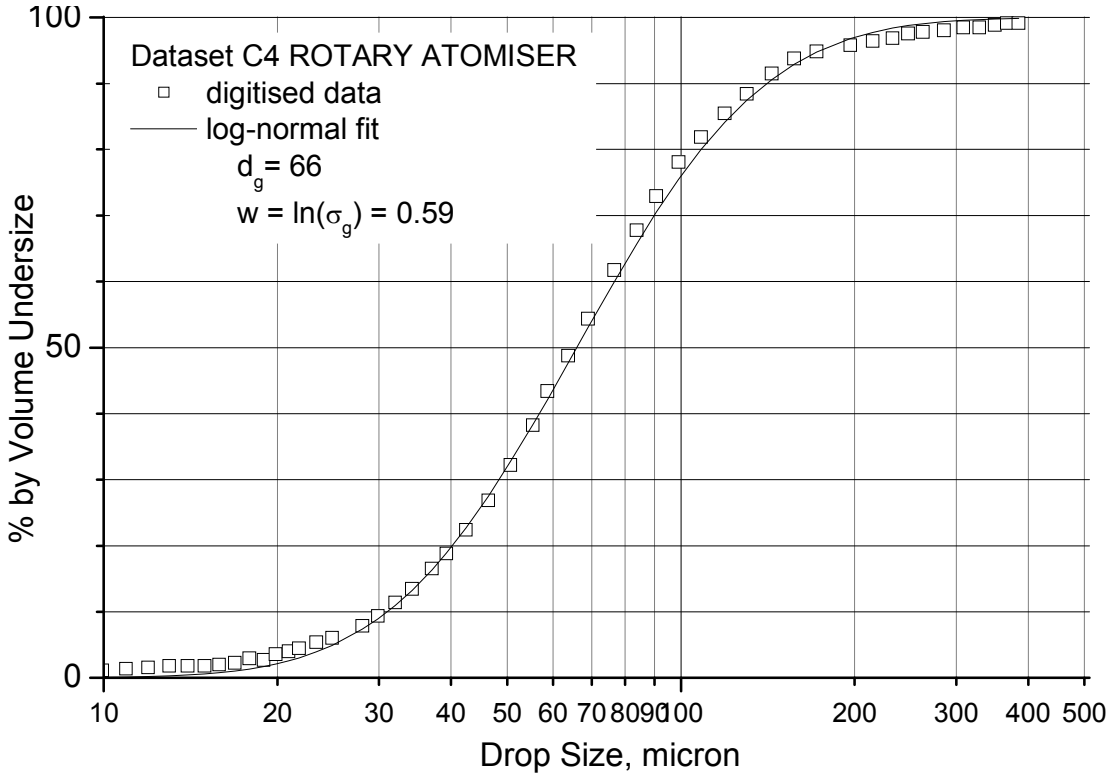
Dataset C4 ROTARY ATOMISER
digitised data
log-normal fit
d_g = 66
w = ln(σ_g) = 0.59
% by Volume Undersize
Drop Size, micron

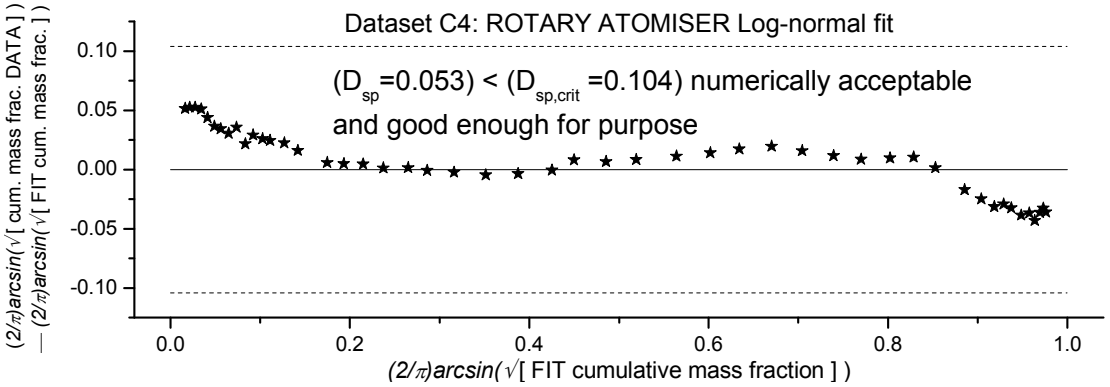
Dataset C4: ROTARY ATOMISER Log-normal fit
(D_sp=0.053) < (D_sp,crit =0.104) numerically acceptable
and good enough for purpose
(2/π)arcsin(√[cum. mass frac. DATA])
— (2/π)arcsin(√[FIT cum. mass frac.])
(2/π)arcsin(√[FIT cumulative mass fraction])

A.5 Material D. Spray-dried powder product, measured by sieve sizing

Data collected during the Acoustic Atomiser development programme at ICI Wilton. The purpose was to roughly assess the size and width of the distribution. It is immediately apparent from inspection of the data tables that there are insufficient sieves in most cases for an analytical sieve sizing, and the sizes have not been chosen to carefully define the shape of the peak, but rather to roughly quantity relative amount of agglomerates, primary peak, and fines. The research focus at this stage of the programme was mechanical reliability of the atomiser and product morphology. Sieve sizing is time consuming and requires a reasonable quantity of powder, so was not performed routinely, but only for a selection of experiments.

Data has been recorded as mass on sieve in grams, to 0.1g or 0.5g precision. The accuracy cannot be better than the precision, so error bars for ±0.1g or ±0.5g can be plotted on the DSP chart (error is insignificant on the cumulative chart, but significant in the tails on the DSP chart, as this plot magnifies the tails). It should be emphasised that these represent the *least* possible error in the data. Given the purpose and circumstance of the data collection, careful analytical experimental methodology is not the expectation: the actual error will be greater. However it is not possible to reliably estimate this actual greater error.

Given the likely low reliability of these sieve data, they are best considered as consistency checks against the other data sources.

A.5.1 Material D1

Sieve size µm	mass retained g D1.17a 150µm	Sieve size µm	Mass retained on sieve g D1.17b 150µm	D1.23 120µm	D1.25 150µm	D1.26 150µm	D1.28 120µm	D1.30 120µm
0	0	0	0	0.24	0	0	0.1	0
90	0.6	150	0	3.6	1.2	0.2	2.2	4.6
180	5.5	250	20.6	71.3	22.4	21.2	59.2	70.6
250	146.6	500	79.4	24.7	75.4	76.4	38.4	26
355	256.2	1250	0	0	0	0	0	0
500	31.2							
600	35.7							

Two independent sieve sizings were made for experiment D17. The large discrepancy between them emphasises the low reliability of these sieve-sizing datasets. The selection of sieve sizes in Dataset D1.17a gives the most definition of the peak. The unexpectedly large fraction on the largest sieve may indicate some agglomeration. The nozzle sizes were either 120 or 150µm as indicated in the table header. These sieve sizing data may not be very accurate, but the pattern of relative fractions between the 250 and 500µm sieves is at least consistent with the expectation of larger size particles from the larger nozzles.

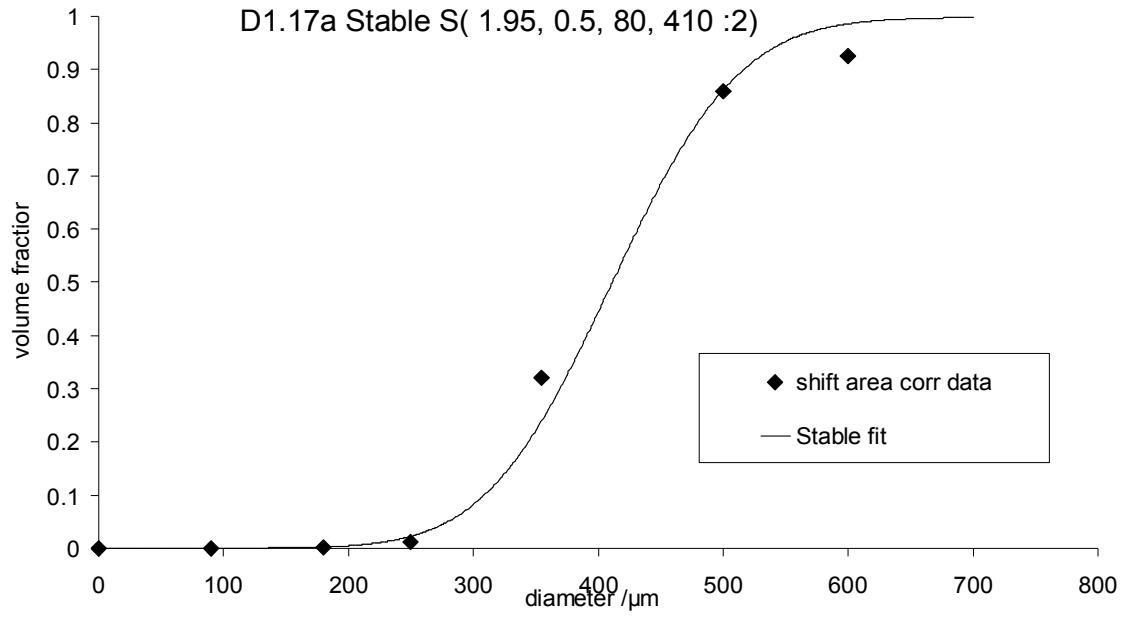

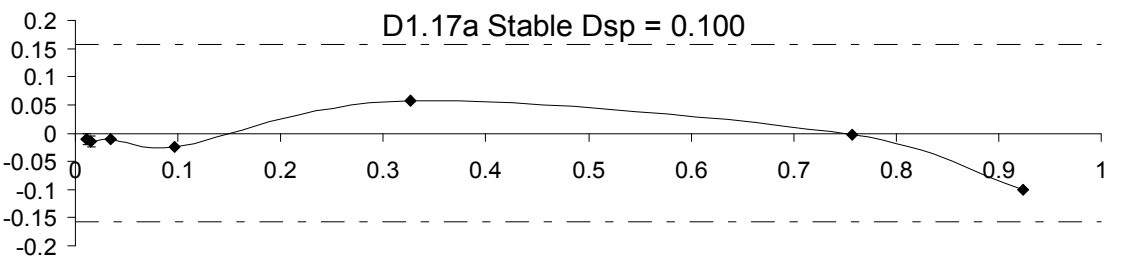

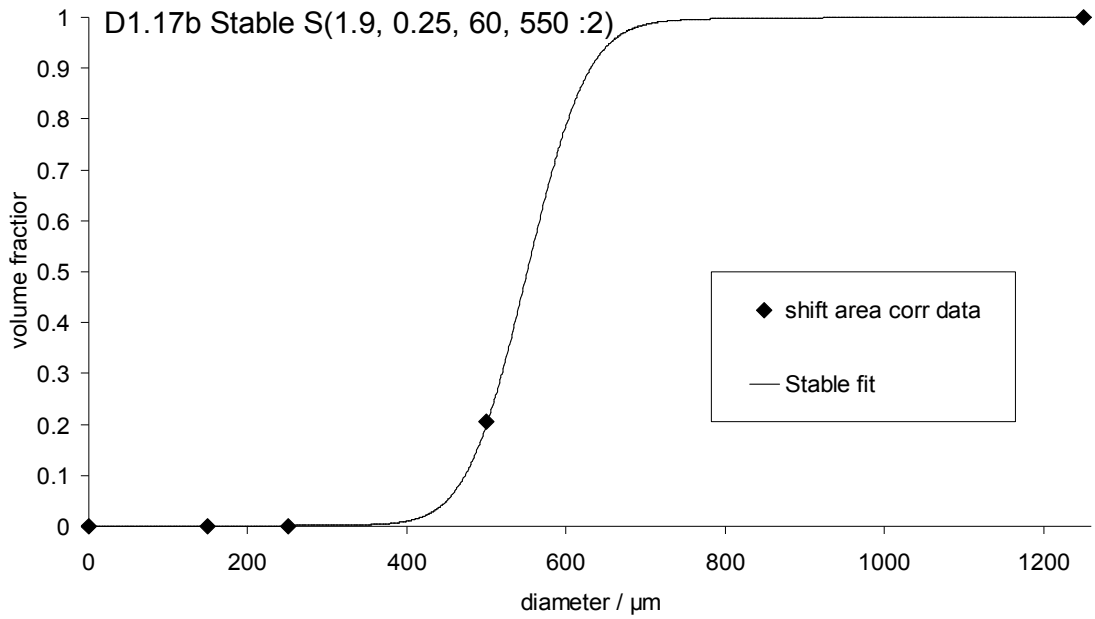
D1.17b Stable S(1.9, 0.25, 60, 550 :2)
volume fractior
diameter / µm
shift area corr data
Stable fit

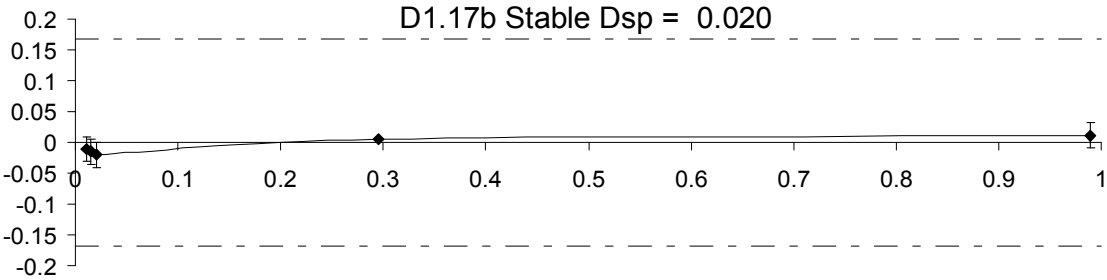
D1.17b Stable Dsp = 0.020

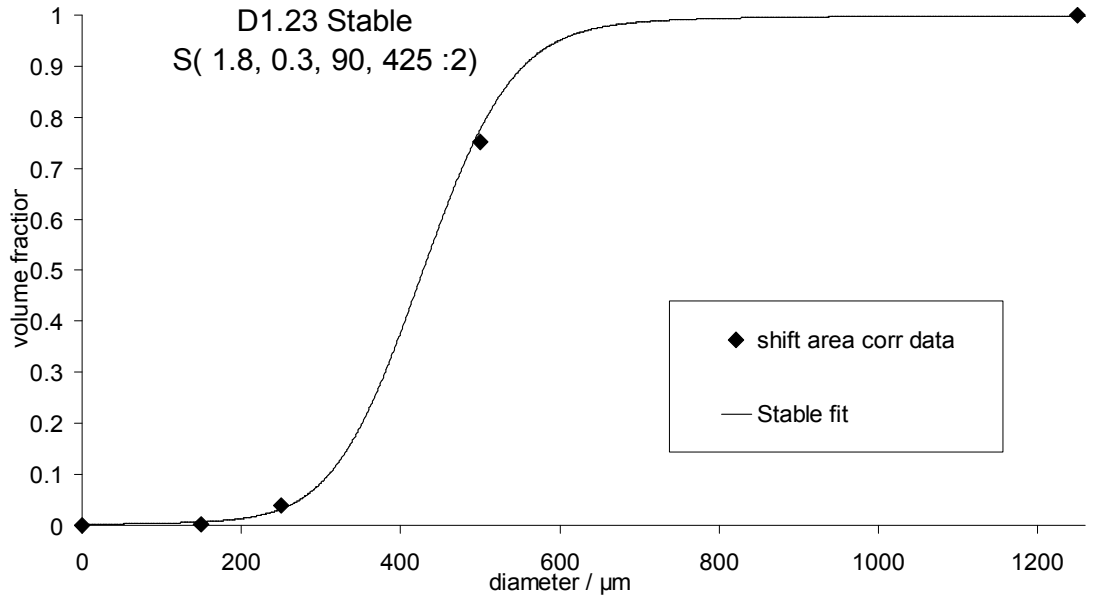
D1.23 Stable
S(1.8, 0.3, 90, 425 :2)
volume fractior
diameter / µm
shift area corr data
Stable fit

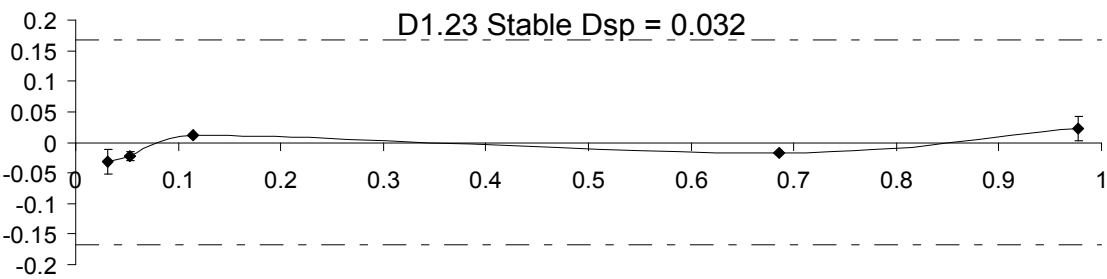
D1.23 Stable Dsp = 0.032

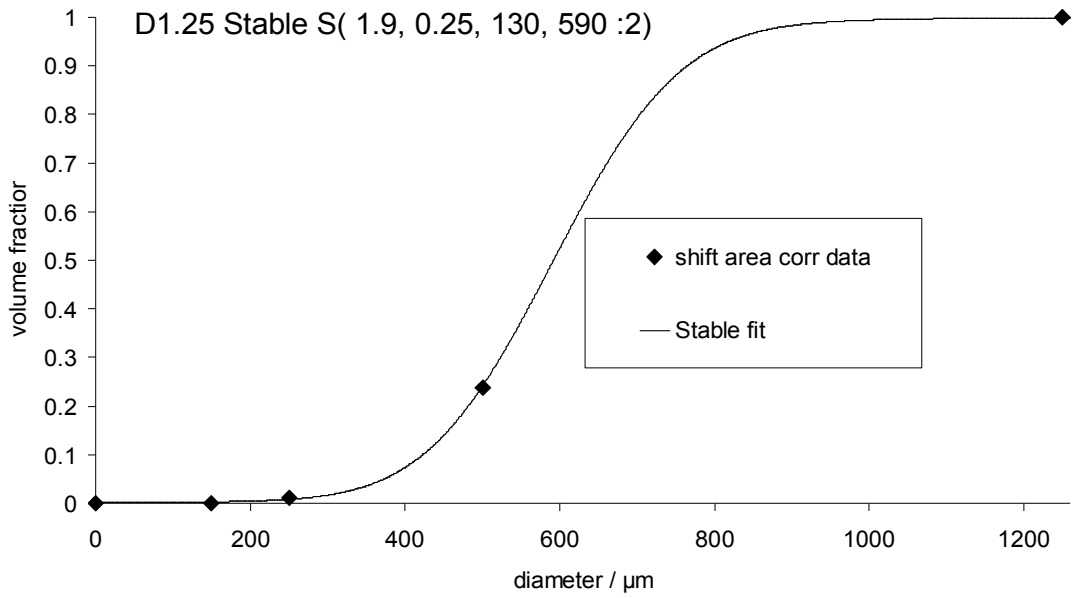
D1.25 Stable S(1.9, 0.25, 130, 590 :2)
volume fractior
diameter / µm
shift area corr data
Stable fit

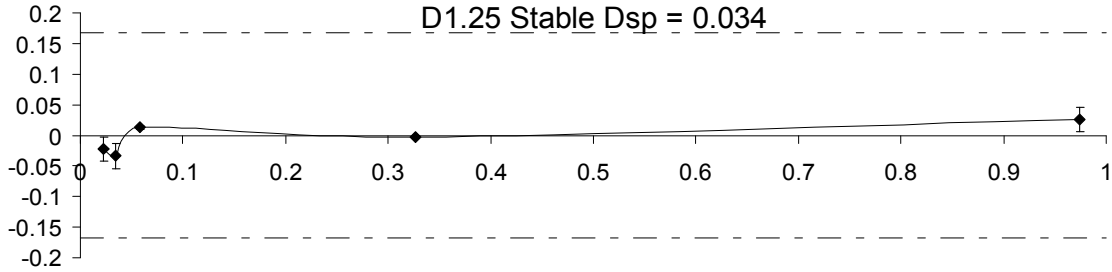
D1.25 Stable Dsp = 0.034

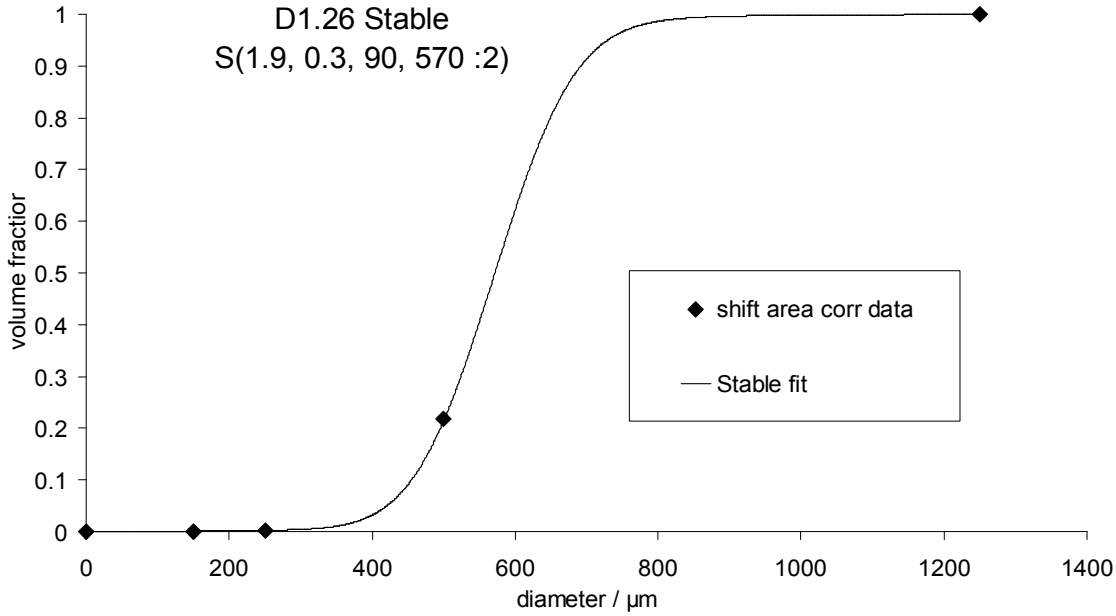
D1.26 Stable
S(1.9, 0.3, 90, 570 :2)
volume fractior
diameter / µm
shift area corr data
Stable fit

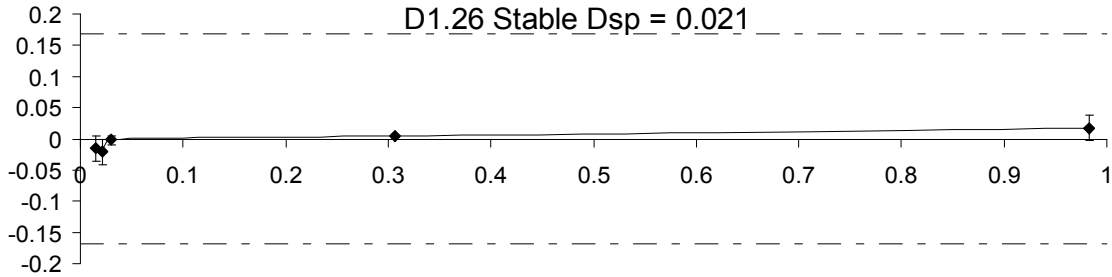
D1.26 Stable Dsp = 0.021

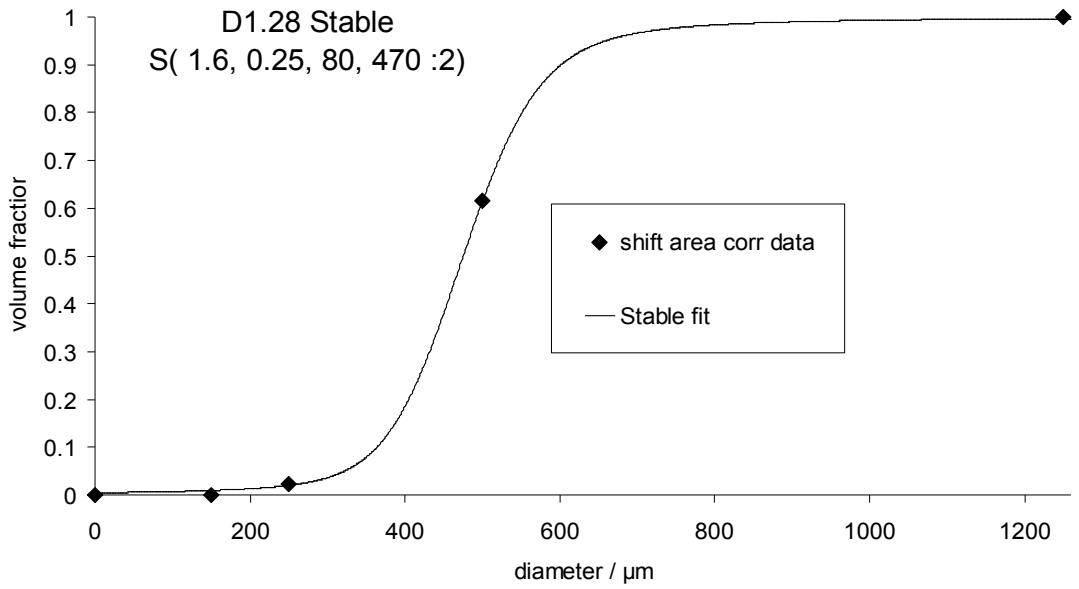
D1.28 Stable
S(1.6, 0.25, 80, 470 :2)
volume fractior
diameter / µm
shift area corr data
Stable fit

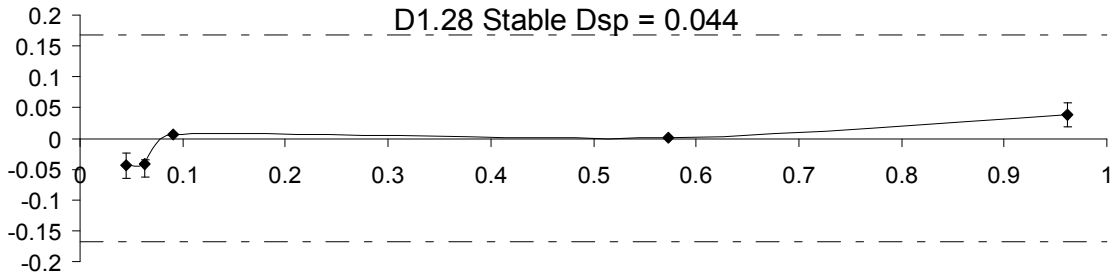
D1.28 Stable Dsp = 0.044

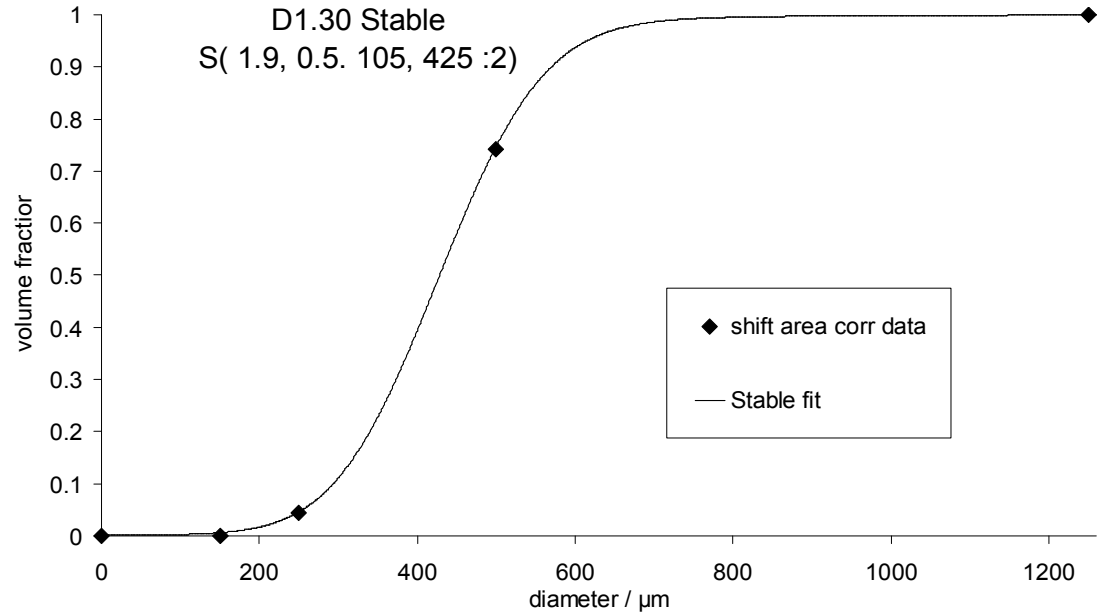
D1.30 Stable
S(1.9, 0.5. 105, 425 :2)
volume fractior
diameter / µm
shift area corr data
Stable fit

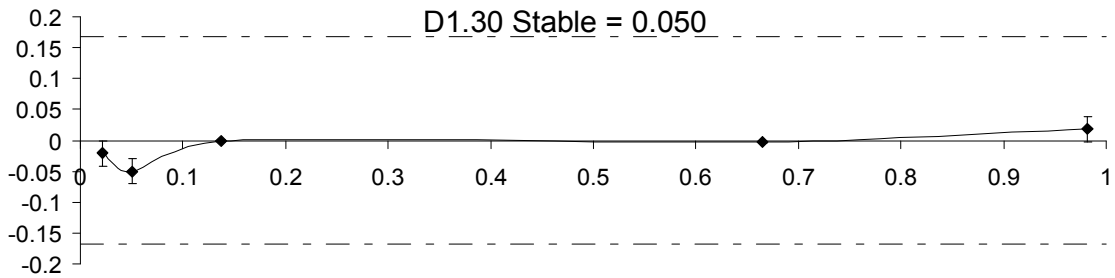
D1.30 Stable = 0.050

A.5.2 Material D8

Sieve size µm	Mass retained on sieve g
	D8.14 rotary
30	3
90	11.5
125	13
150	15
180	20.5
212	28.5
300	13.5
355	8
425	0
500	0

There is a single set of sieve sizing data for a rotary atomiser comparison experiment, which has been fitted with a log-normal distribution.

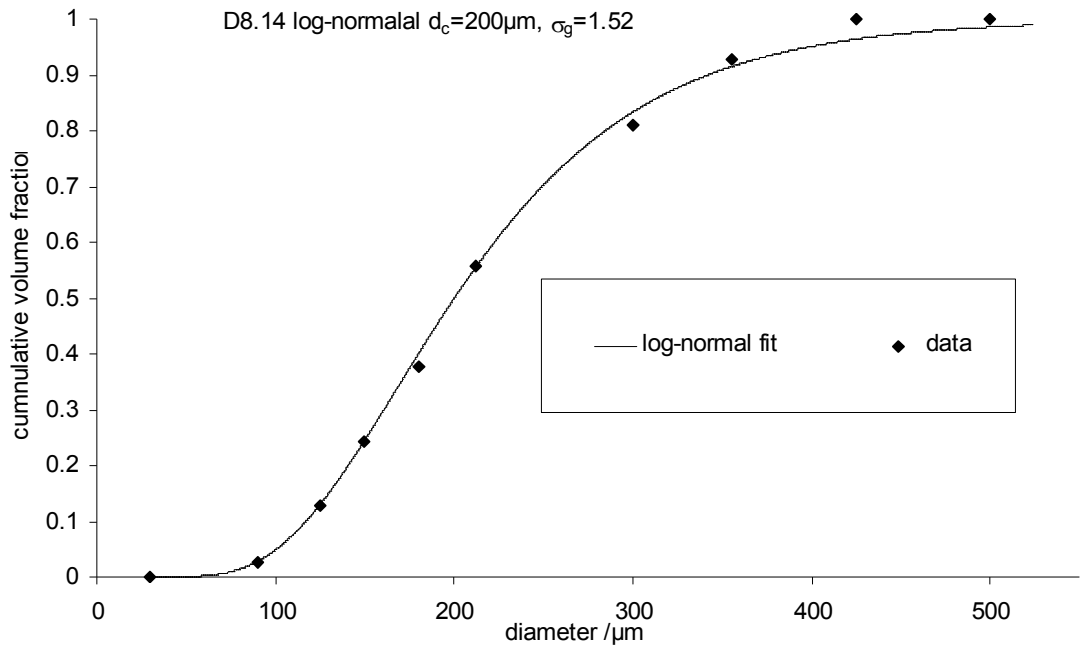

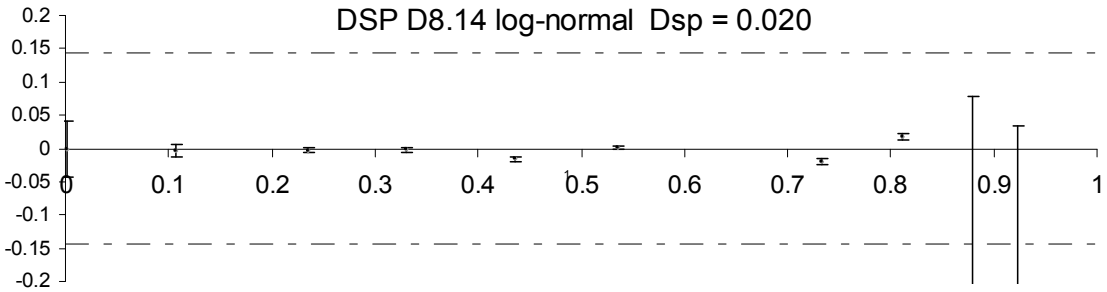

A.5.3 Material D10

Sieve size µm	Mass retained on sieve g		
	D10.3 rotary	D10.5 150µm	D10.6 120µm
0	0		0
106	0.32	0	0
125	1	0	
150	2	0	0.34
180	5	0.3	
212	6	1	7
250	14.8	5	16.3
300	8	10	18.5
350		17	1.9
355	5.25		
400		10	1.1
425	2	4	1.75
450		3	1.69

These datasets are a bit messy and difficult to interpret in isolation. However, the material was rather similar in composition to D11, except in the presence of an encapsulated surfactant rather than an oil, and it was found that similar Stable parameters were overall the most satisfactory fit to datasets D10.5 and D10.6.

An acceptable fit is obtained for $S(\alpha, \beta, \gamma, \delta ;2) = S(2, 0, 61, 375 ; 2)$ for D10.5 and $S(2, 0, 43, 300 ;2)$ for D10.6. Numerically superior fits could be obtained for other combinations of (α, β) for either dataset taken in isolation, but (α, β) should be the same for experiments with the same material but with a different nozzle size. Note that the β parameter is irrelevant in the special Gaussian case of $\alpha = 2$. Note also that an almost as acceptable fit could be obtained for identical $(\alpha, \beta) = (1.9, 0.25)$ as used for D11.

If the 400µm sieve fraction in D10.5 had been just a couple of grams less, the fit would appear markedly improved. A variation in a single sieve fraction strongly suggests either experimental error or an artefact due to a few agglomerated lumps for example.

Similarly the unexpectedly large 425 and 450µm sieve fractions for D10.6 suggests agglomeration, although it is unusual for more agglomeration to be evident for the experiment with smaller nozzles. Normally in these experiments agglomeration was

associated with the larger particles and is postulated to be due to less complete drying and hence sticky particle surfaces at the base of the spray dryer.

In each case delta is the same multiple (2.5) of the nozzle diameter. The ratio of the droplet size to the nozzle size should be constant for the same material at optimum frequency. In principle it is possible within a limited window to change the frequency (and hence the droplet size) away from the optimum, with insignificant detriment to the uniformity of droplet size. However, it was found that in practice this window becomes narrower for more viscous and especially for non-Newtonian materials. Normally a greater influence on the final particle size is morphological changes during drying. In this case SEM showed that the powder was substantially the same morphology in each case. Hence an approximation to a constant multiplier between the nozzle size and the distribution mode is the expectation. Whilst it is probably serendipitous that the agreement in these two datasets is so close, it is additional support for the Stable distribution as a good model for the size distribution data.

The rotary atomiser data D10.3 are well fitted by S(1.9, 0.25, 70, 280 ; 2). It is a surprise that the Stable distribution is a good model to the rotary data - there is neither physical explanation or prior experience to show that it should be. It is also incredibly narrow for a rotary atomiser distribution, with a incredibly large mean size. Rather close in fact to the D10.6 experiment with 120µm nozzles. A rotary atomiser comparative experiment was certainly performed, from which a powder sample is still available. Whilst it is now far too agglomerated to perform a meaningful new size distribution (starch is hydroscopic and the material was made 7 years ago), it is by inspection quite clearly much finer than the corresponding Acoustic Atomiser samples. Overall the most credible explanation is experimental error, and that the size distribution recorded for rotary atomisation experiment D10.3 is in fact the size distribution from Acoustic Atomiser experiment D10.1

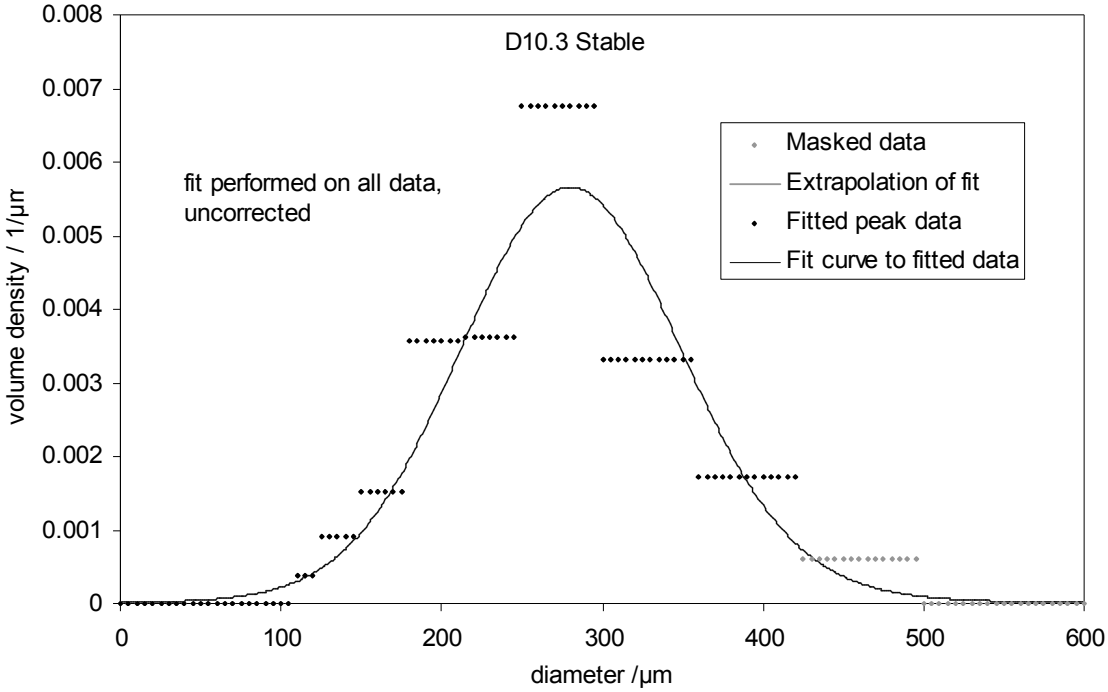
D10.3 Stable
fit performed on all data,
uncorrected
Masked data
Extrapolation of fit
Fitted peak data
Fit curve to fitted data
volume density / 1/µm
diameter /µm
0.008
0.007
0.006
0.005
0.004
0.003
0.002
0.001
0
0
100
200
300
400
500
600

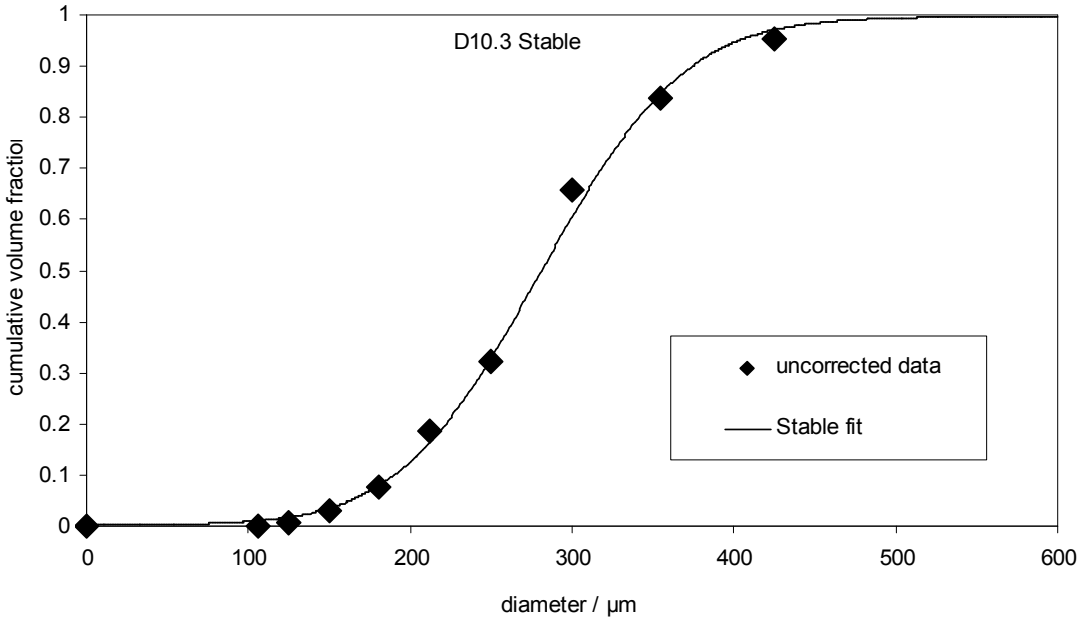
D10.3 Stable
uncorrected data
Stable fit
cumulative volume fractio
diameter / µm
1
0.9
0.8
0.7
0.6
0.5
0.4
0.3
0.2
0.1
0
0
100
200
300
400
500
600

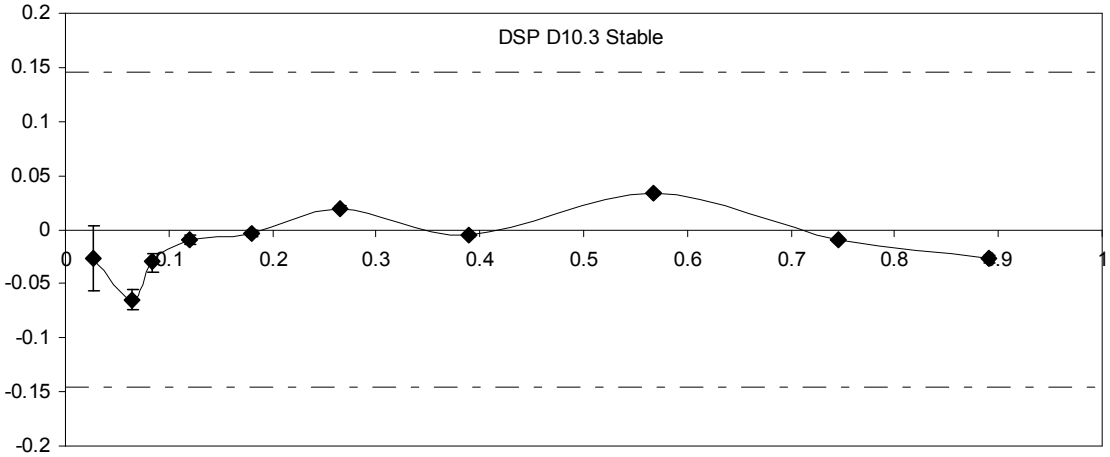
DSP D10.3 Stable
0.2
0.15
0.1
0.05
0
-0.05
-0.1
-0.15
-0.2
0
0.1
0.2
0.3
0.4
0.5
0.6
0.7
0.8
0.9
1

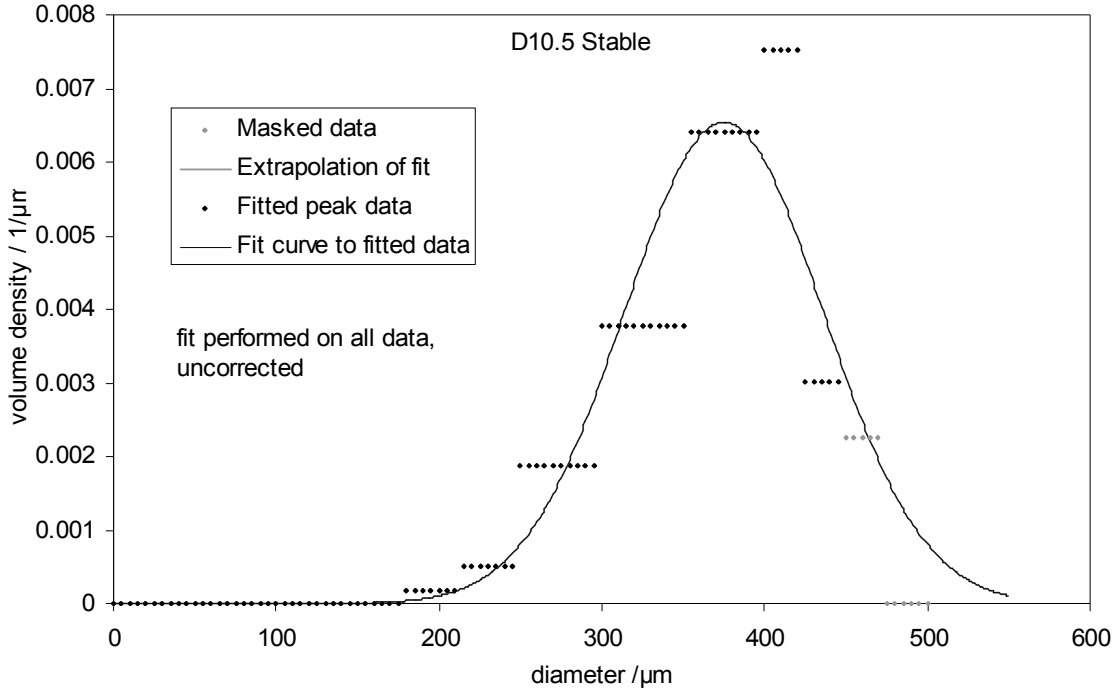
D10.5 Stable
Masked data
Extrapolation of fit
Fitted peak data
Fit curve to fitted data
fit performed on all data, uncorrected
volume density / 1/µm
diameter /µm
0.008
0.007
0.006
0.005
0.004
0.003
0.002
0.001
0
0
100
200
300
400
500
600

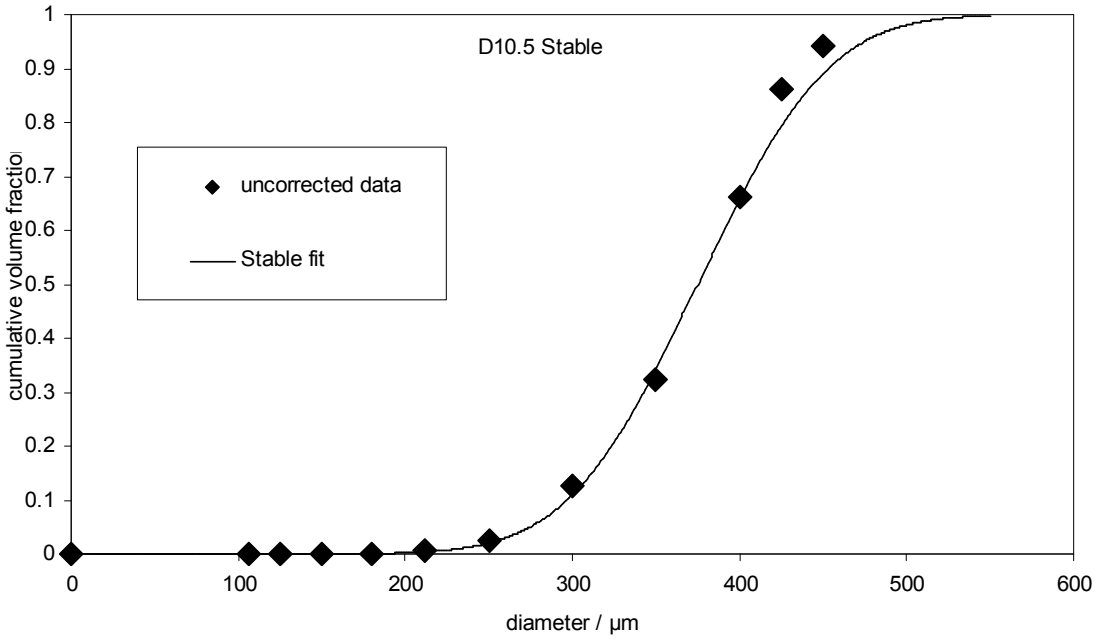
D10.5 Stable
uncorrected data
Stable fit
cumulative volume fractio
diameter / µm
1
0.9
0.8
0.7
0.6
0.5
0.4
0.3
0.2
0.1
0
0
100
200
300
400
500
600

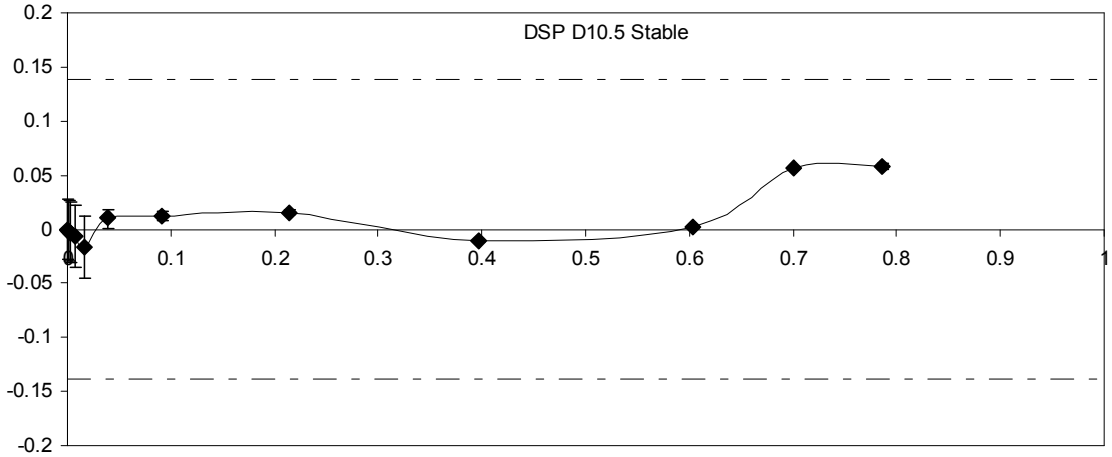
DSP D10.5 Stable
0.2
0.15
0.1
0.05
0
-0.05
-0.1
-0.15
-0.2
0.1
0.2
0.3
0.4
0.5
0.6
0.7
0.8
0.9
1

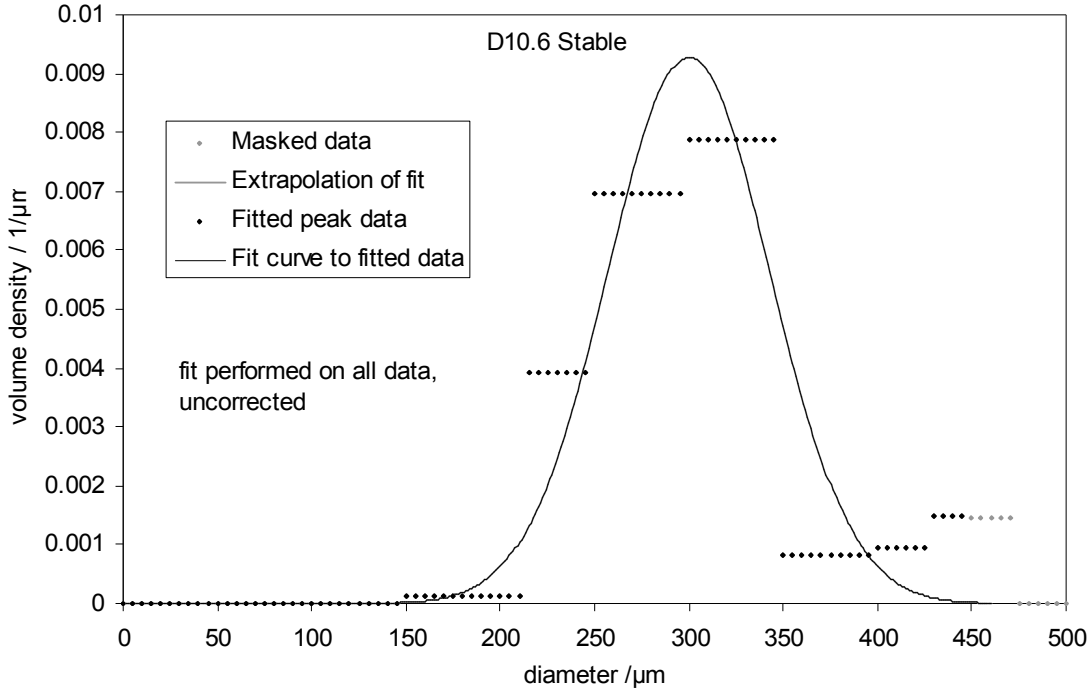
D10.6 Stable
Masked data
Extrapolation of fit
Fitted peak data
Fit curve to fitted data
fit performed on all data, uncorrected
volume density / 1/µm
diameter /µm
0.01
0.009
0.008
0.007
0.006
0.005
0.004
0.003
0.002
0.001
0
0 50 100 150 200 250 300 350 400 450 500

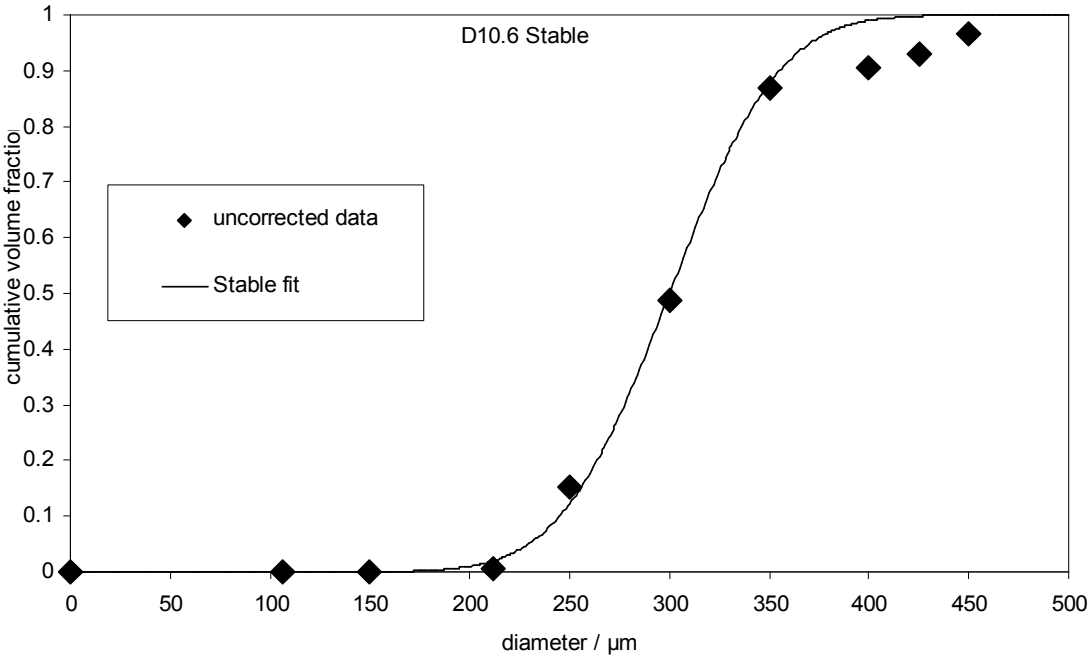
D10.6 Stable
uncorrected data
Stable fit
cumulative volume fractio
diameter / µm
1
0.9
0.8
0.7
0.6
0.5
0.4
0.3
0.2
0.1
0
0 50 100 150 200 250 300 350 400 450 500

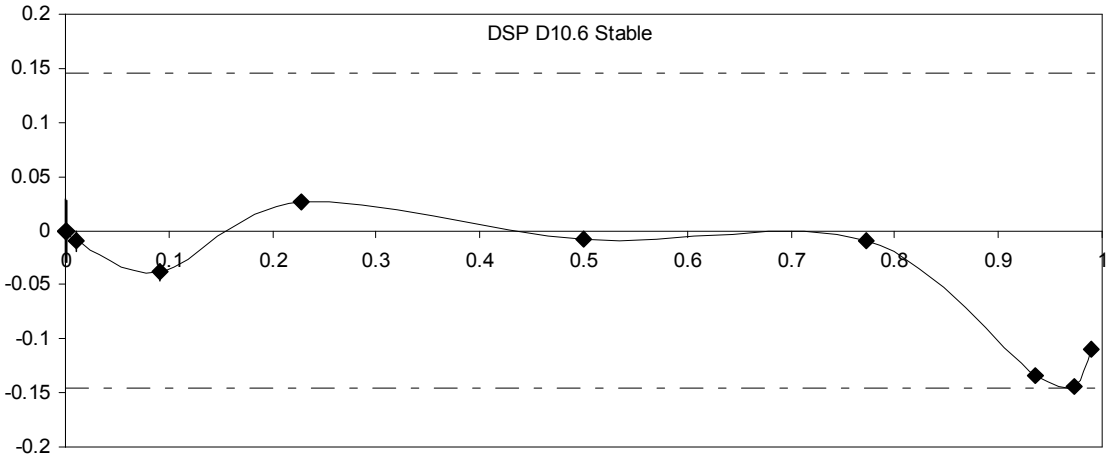
DSP D10.6 Stable
0.2
0.15
0.1
0.05
0
-0.05
-0.1
-0.15
-0.2
0 0.1 0.2 0.3 0.4 0.5 0.6 0.7 0.8 0.9 1

A.5.4 Material D11

Sieve size µm	Mass retained on sieve g	
	D11.3 120µm	D11.4 120µm
63	0	
75		0
90		0
106	0	0
125	1.1	0.1
150	3.7	0.8
180	15.4	1.2
212	37	4.9
250	6.5	10
300		18
355		7
425		1.4
500		2.8
600		1
800		0

In many experiments during mechanical development of the atomiser, the outlet cone of the spray dryer was wetted by dripping nozzles and no powder could be recovered from the main tower. The size distribution D11.3 is from powder collected from the cyclone. The size distribution looks rather curious at first sight, but using the data and fit peak area matching functionality built into the spreadsheet, it looks like the truncated lower portion of the size distribution of the powder obtained from the main tower in repeat experiment D11.4.

Both datasets have been fitted with $S(\alpha, \beta, \gamma, \delta : 2) = S(1.9, 0.25, 62, 318 : 2)$. The surprisingly large 500µm sieve fraction in dataset D11.4 suggests some agglomeration, to which phenomenon is ascribed the relatively poor fit above 355µm.

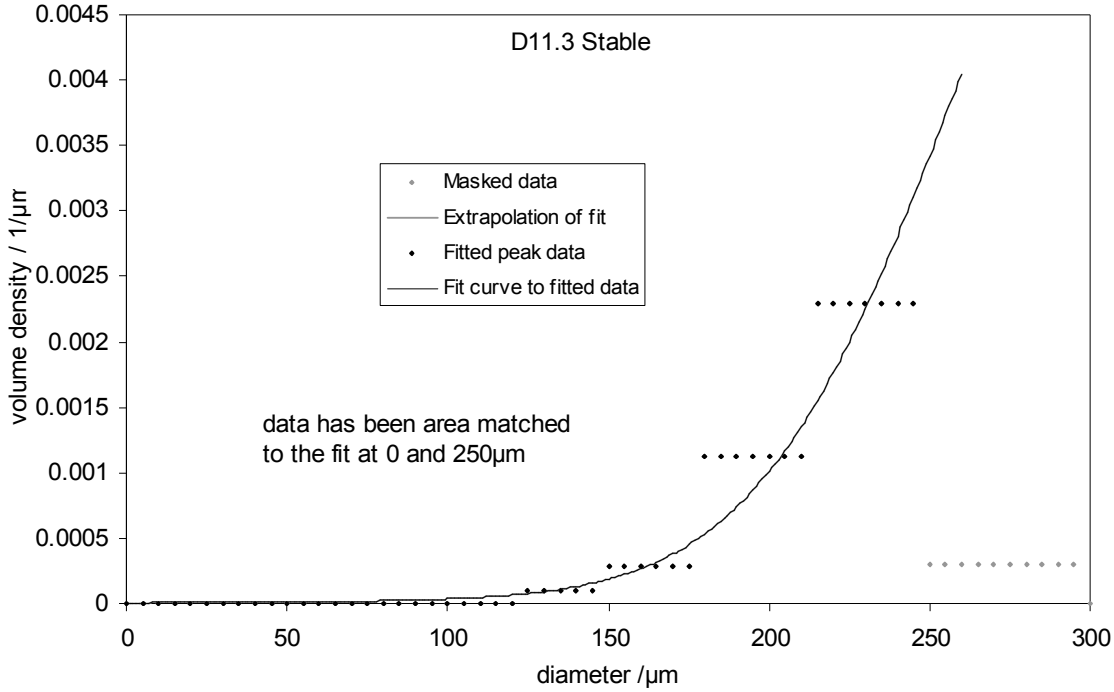
D11.3 Stable
Masked data
Extrapolation of fit
Fitted peak data
Fit curve to fitted data
data has been area matched
to the fit at 0 and 250µm
volume density / 1/µm
diameter /µm
0.0045
0.004
0.0035
0.003
0.0025
0.002
0.0015
0.001
0.0005
0
0
50
100
150
200
250
300

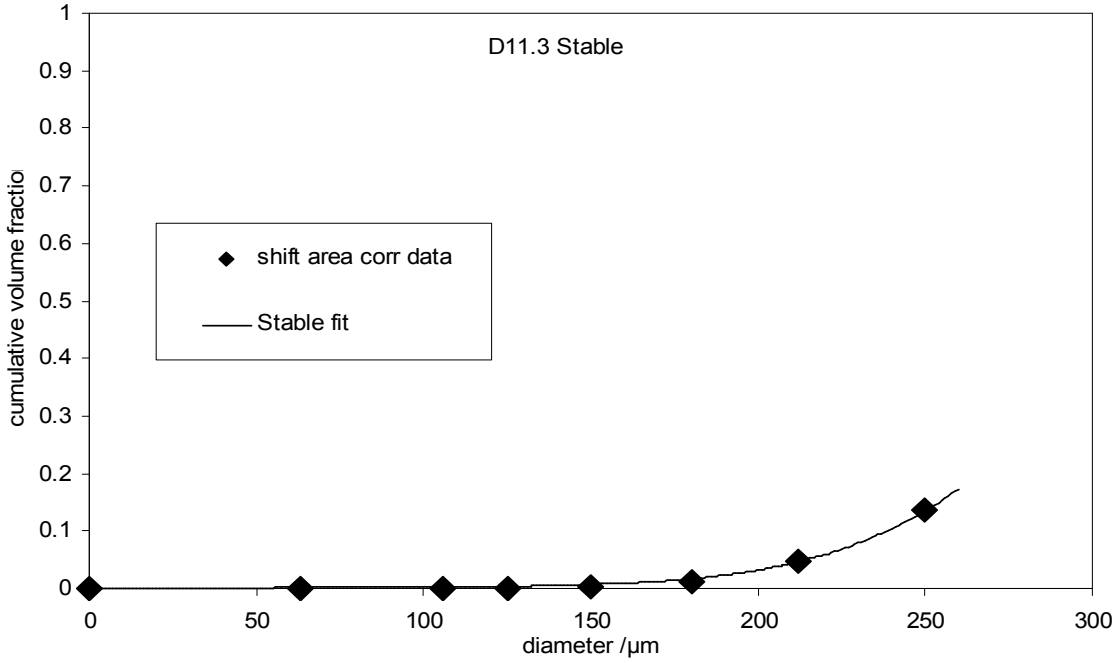
D11.3 Stable
shift area corr data
Stable fit
cumulative volume fractio
diameter /µm
1
0.9
0.8
0.7
0.6
0.5
0.4
0.3
0.2
0.1
0
0
50
100
150
200
250
300

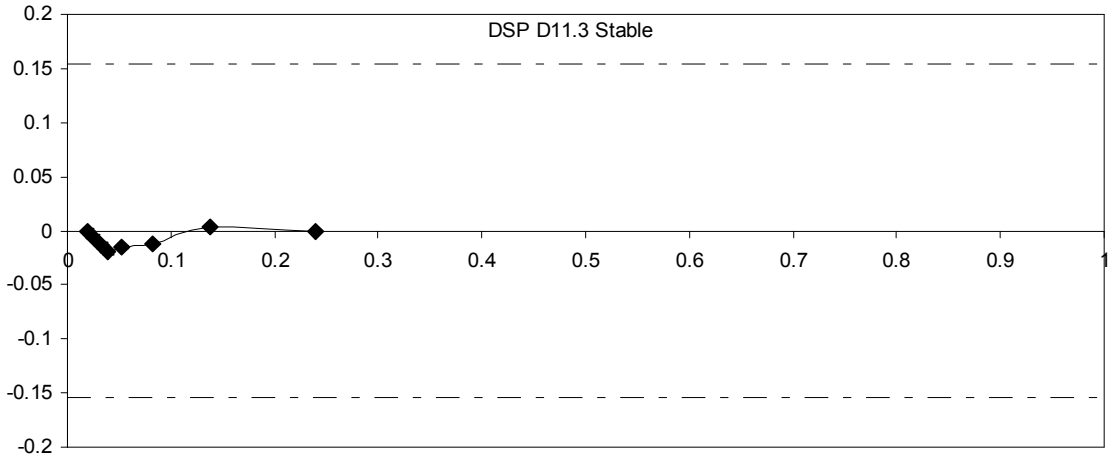
DSP D11.3 Stable
0.2
0.15
0.1
0.05
0
-0.05
-0.1
-0.15
-0.2
0
0.1
0.2
0.3
0.4
0.5
0.6
0.7
0.8
0.9
1

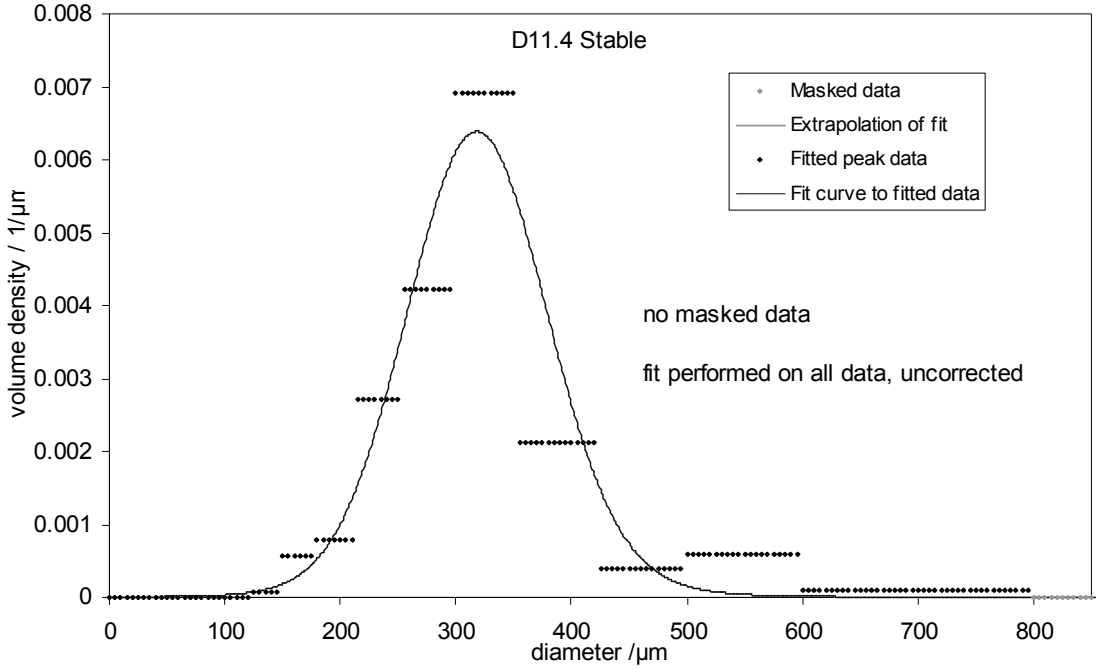
D11.4 Stable
Masked data
Extrapolation of fit
Fitted peak data
Fit curve to fitted data
no masked data
fit performed on all data, uncorrected
volume density / 1/µm
diameter /µm
0.008
0.007
0.006
0.005
0.004
0.003
0.002
0.001
0
0
100
200
300
400
500
600
700
800

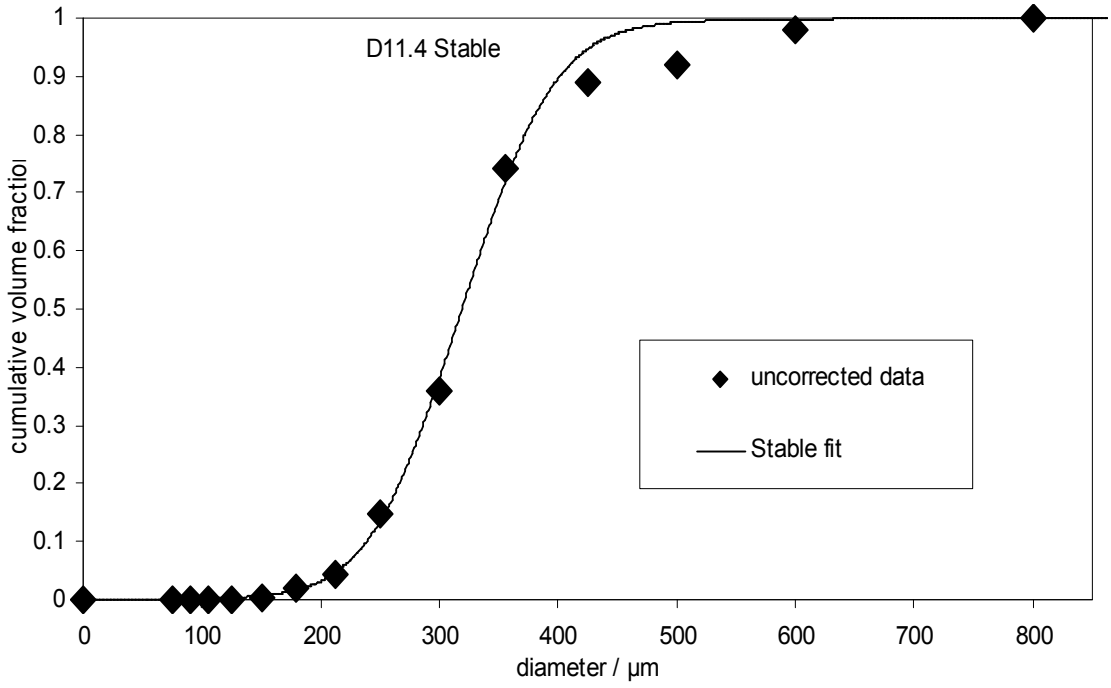
D11.4 Stable
uncorrected data
Stable fit
cumulative volume fractio
diameter / µm
1
0.9
0.8
0.7
0.6
0.5
0.4
0.3
0.2
0.1
0
0
100
200
300
400
500
600
700
800

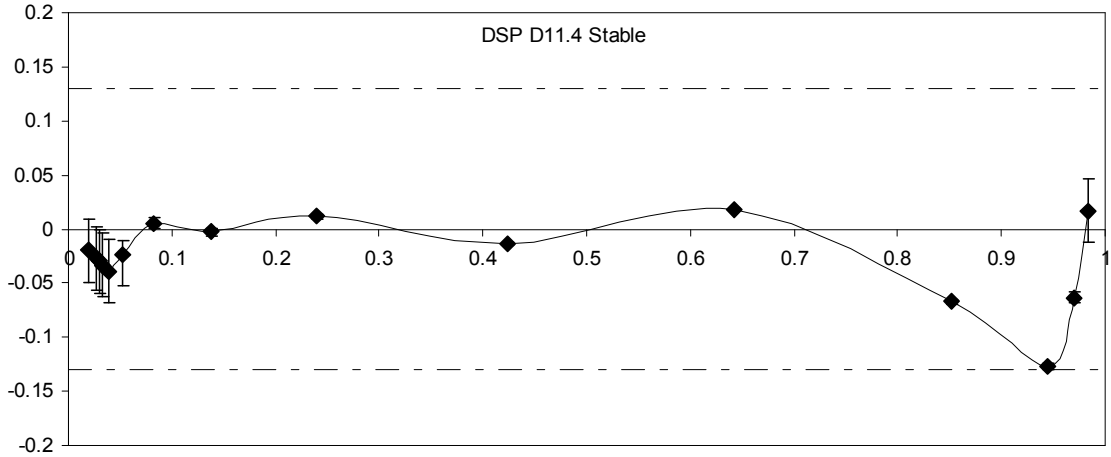
DSP D11.4 Stable
0.2
0.15
0.1
0.05
0
-0.05
-0.1
-0.15
-0.2
0
0.1
0.2
0.3
0.4
0.5
0.6
0.7
0.8
0.9
1

A.6 Material D. Spray-dried powder product, measured by image analysis

The circularity parameter plotted for the Visisize data is the ratio of the perimeter of an area-equivalent circle, to the measured perimeter, i.e. $2\sqrt{(\pi A)} / P$

All Visisize datasets have just over 10,000 particle counts (normally considered sufficient for validity) with the exception of D3.9, D7.5a and D8.11a which only have 5340, 4516 and 1614 counts respectively.

A.6.1 Material D3

Dataset D3.8 is one of the few Visisize measurements that were repeated. The Stable distribution fit parameters are satisfactorily similar between the two repeats. The primary and secondary peaks are rather closely spaced, with a relatively large volume fraction in the secondary peak. This would be an unusual signature for satellite droplets. A more likely explanation is one or more incorrectly sized nozzles in the sprayplate.

Dataset D3.9 is the only dataset for Material D3 with no indication of a secondary peak. It was the experiment with the least solids concentration in the liquid feed, and hence also the lowest viscosity. Lower viscosity is correlated with a wider window for resonant jet breakup, and hence a greater probability that all jets will be breaking up uniformly without satellite droplet formation, even with the same manufacturing tolerance between nozzles as in the other experiments.

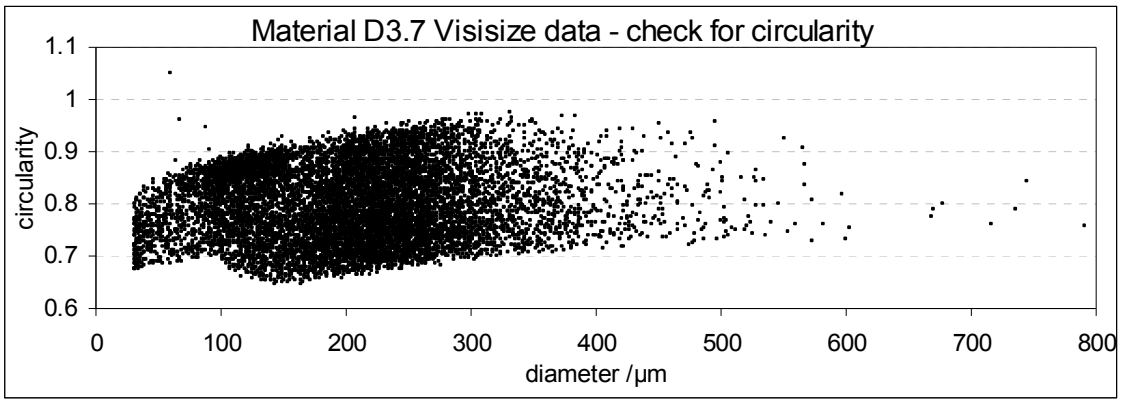
Material D3.7 Visisize data - check for circularity
circularity
1.1
1
0.9
0.8
0.7
0.6
0
100
200
300
400
500
600
700
800
diameter /µm

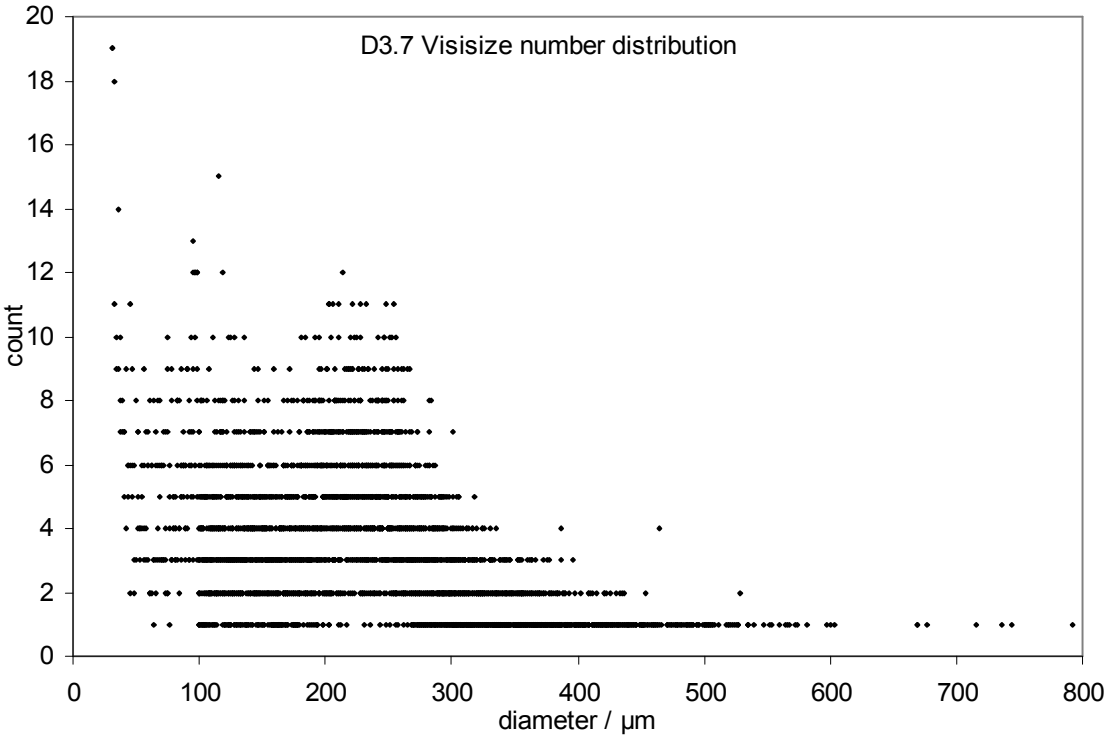
D3.7 Visisize number distribution
count
20
18
16
14
12
10
8
6
4
2
0
0
100
200
300
400
500
600
700
800
diameter / µm

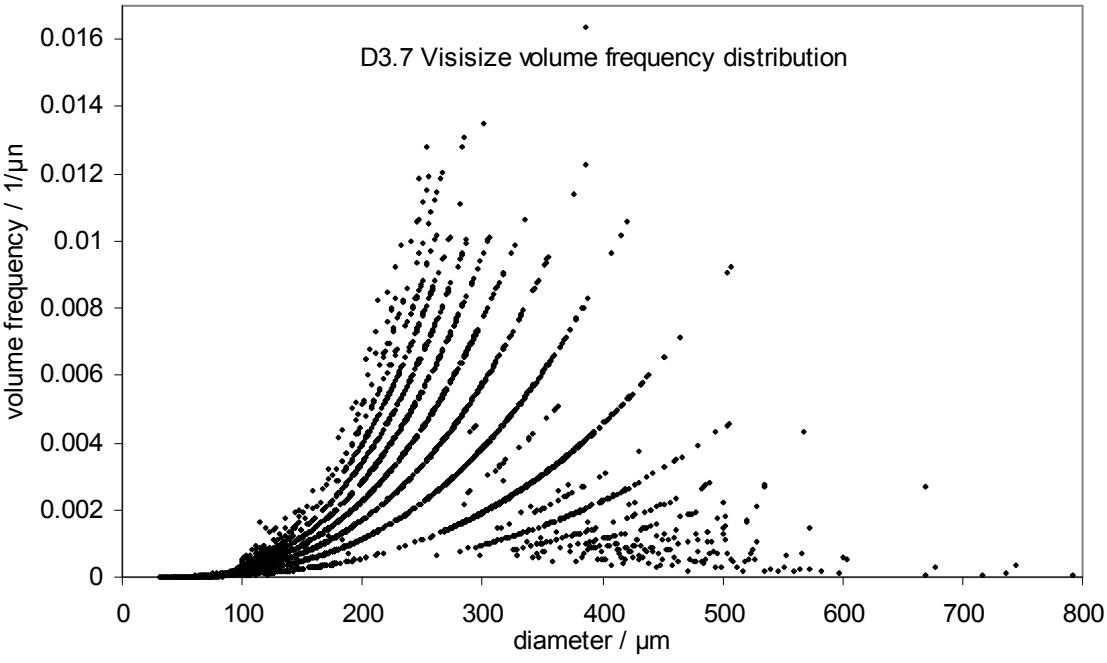
D3.7 Visisize volume frequency distribution
volume frequency / 1/µn
0.016
0.014
0.012
0.01
0.008
0.006
0.004
0.002
0
0
100
200
300
400
500
600
700
800
diameter / µm

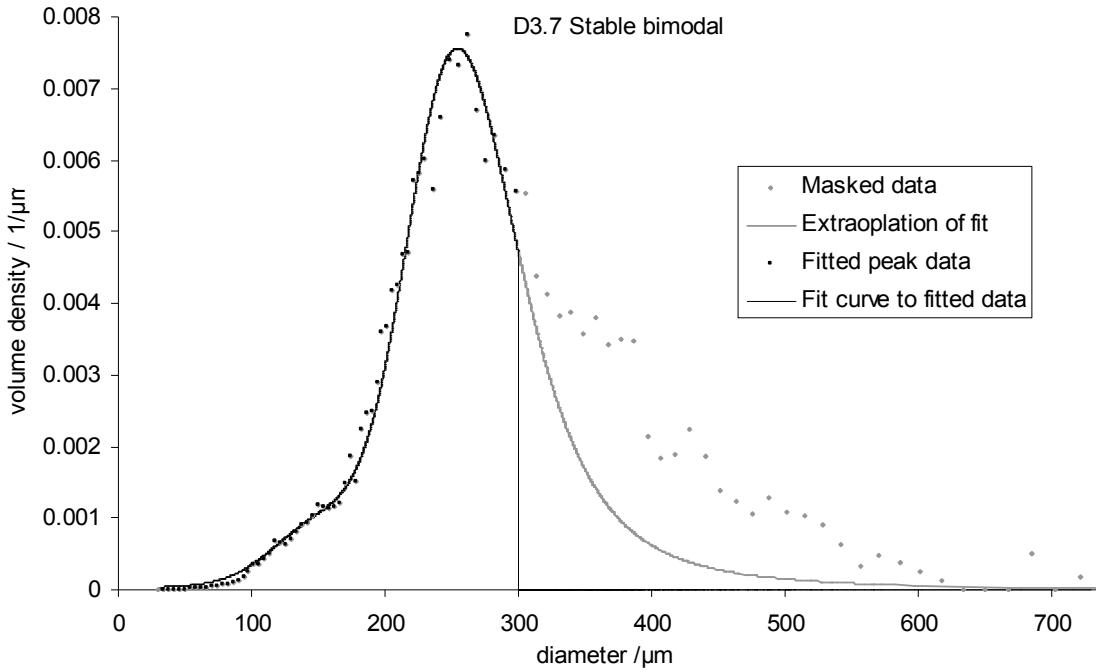

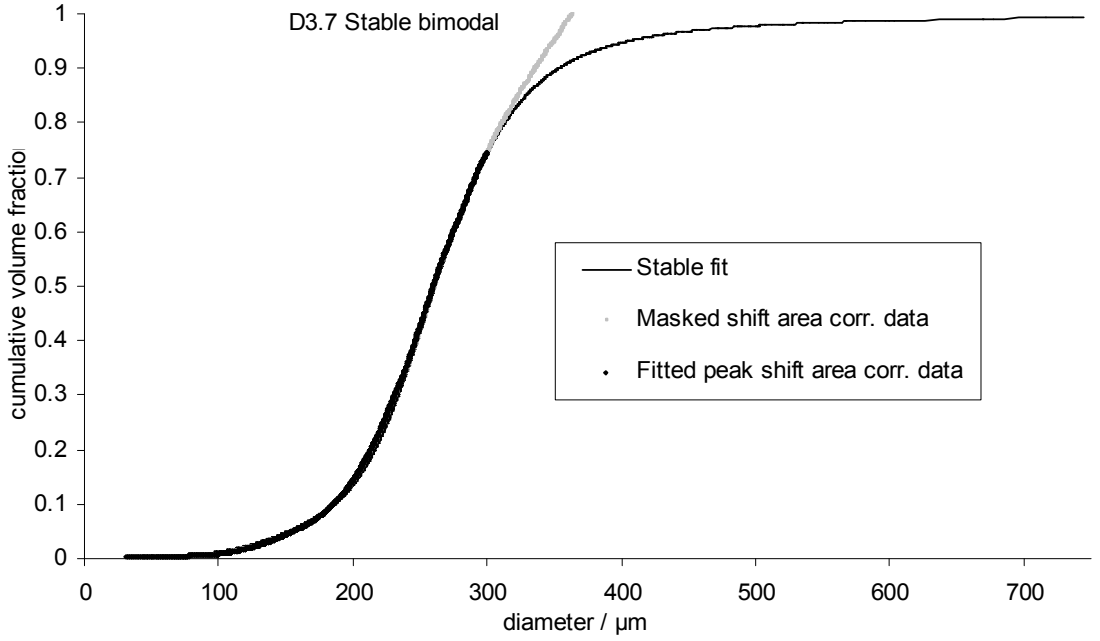

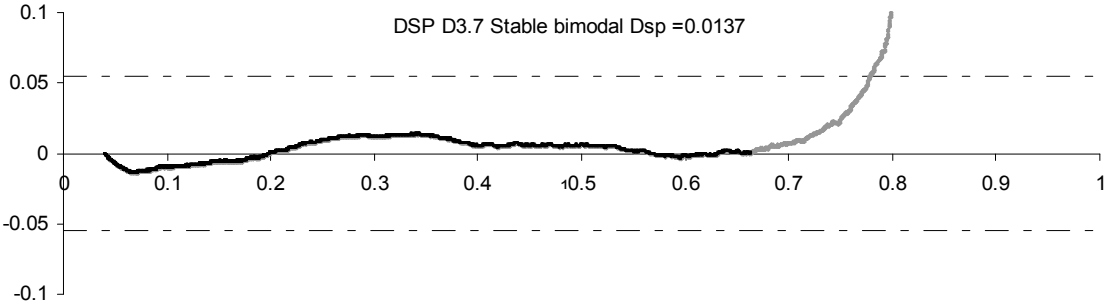

peak		Parameters of the Stable distribution			
D3.7	%vol	α	β	γ	δ
1°	90	1.49	0.72	45	255.1
2°	10				155

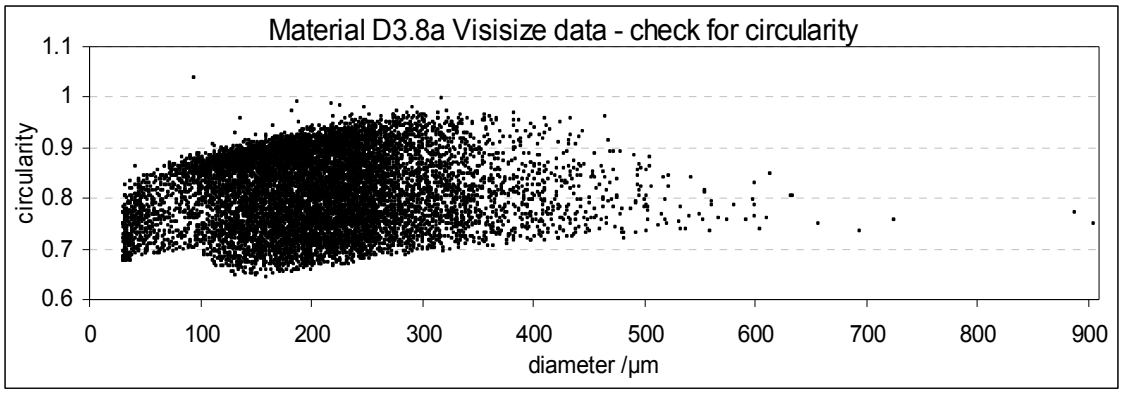
Material D3.8a Visisize data - check for circularity
circularity
1.1
1
0.9
0.8
0.7
0.6
0
100
200
300
400
500
600
700
800
900
diameter /µm

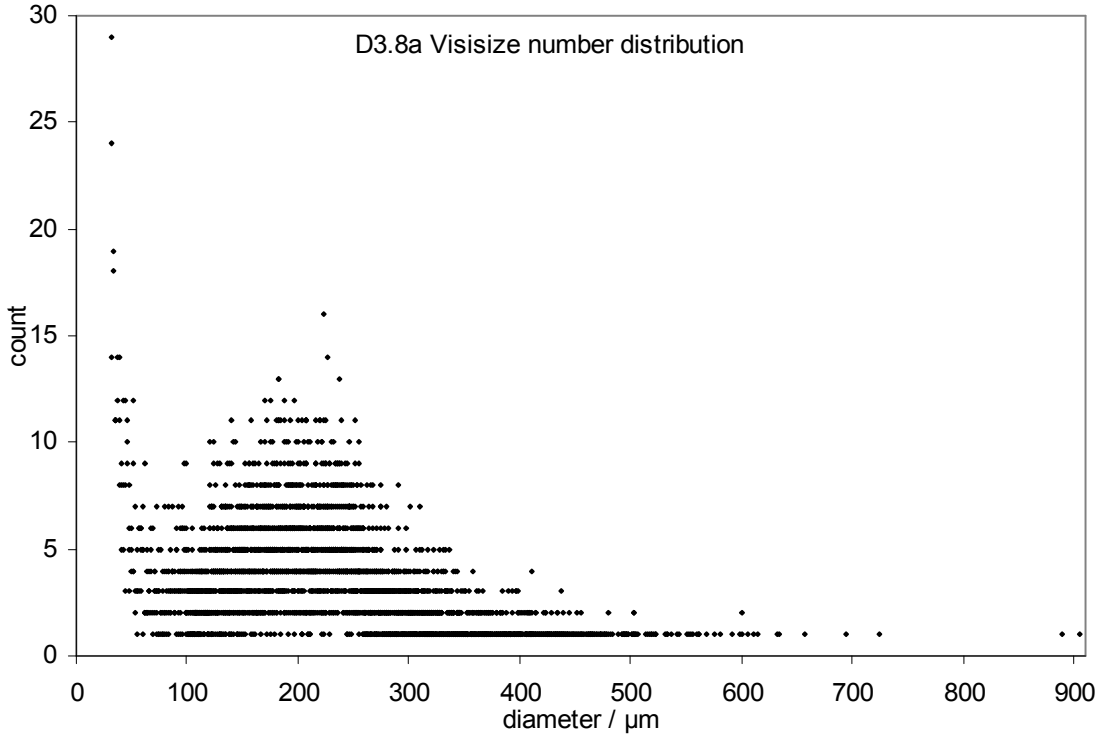
D3.8a Visisize number distribution
count
30
25
20
15
10
5
0
0
100
200
300
400
500
600
700
800
900
diameter / µm

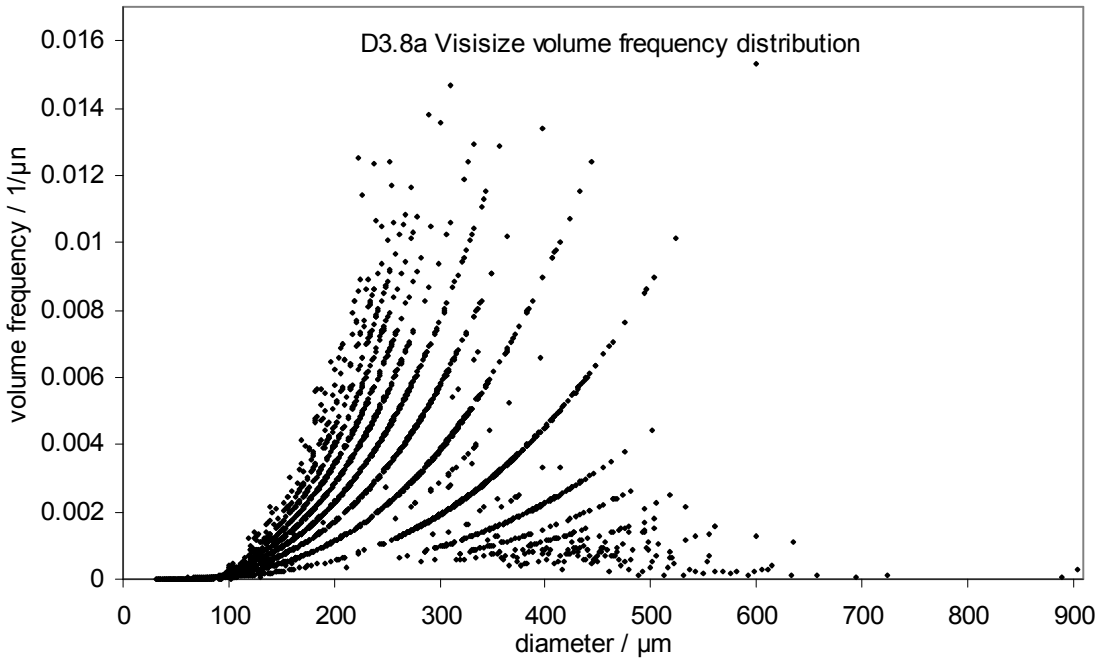
D3.8a Visisize volume frequency distribution
volume frequency / 1/µn
0.016
0.014
0.012
0.01
0.008
0.006
0.004
0.002
0
0
100
200
300
400
500
600
700
800
900
diameter / µm

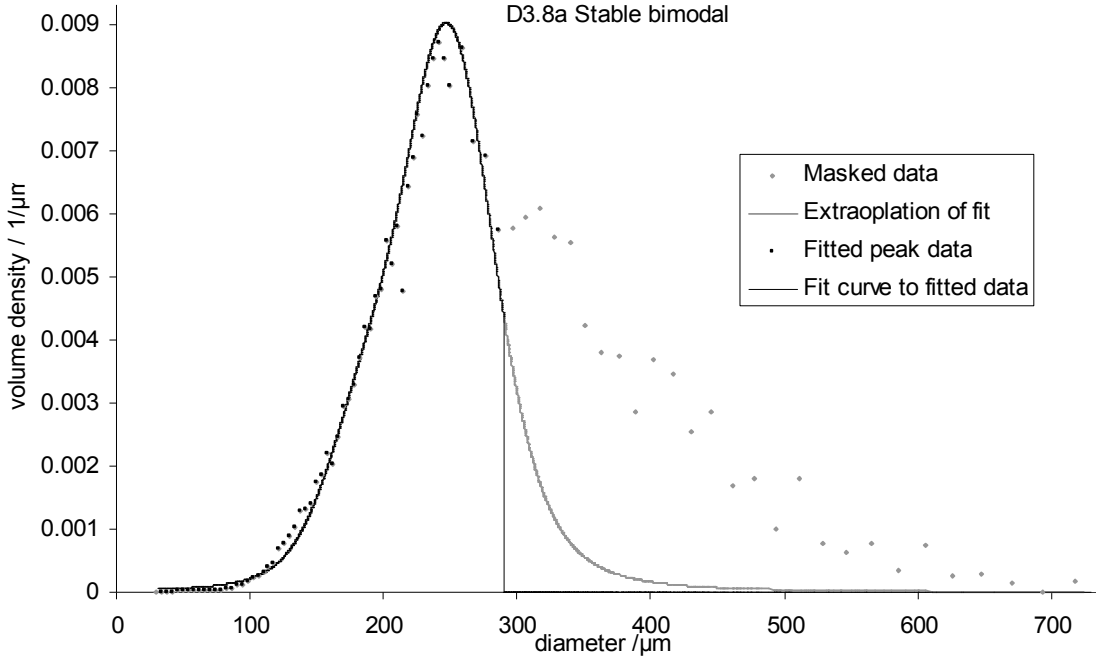

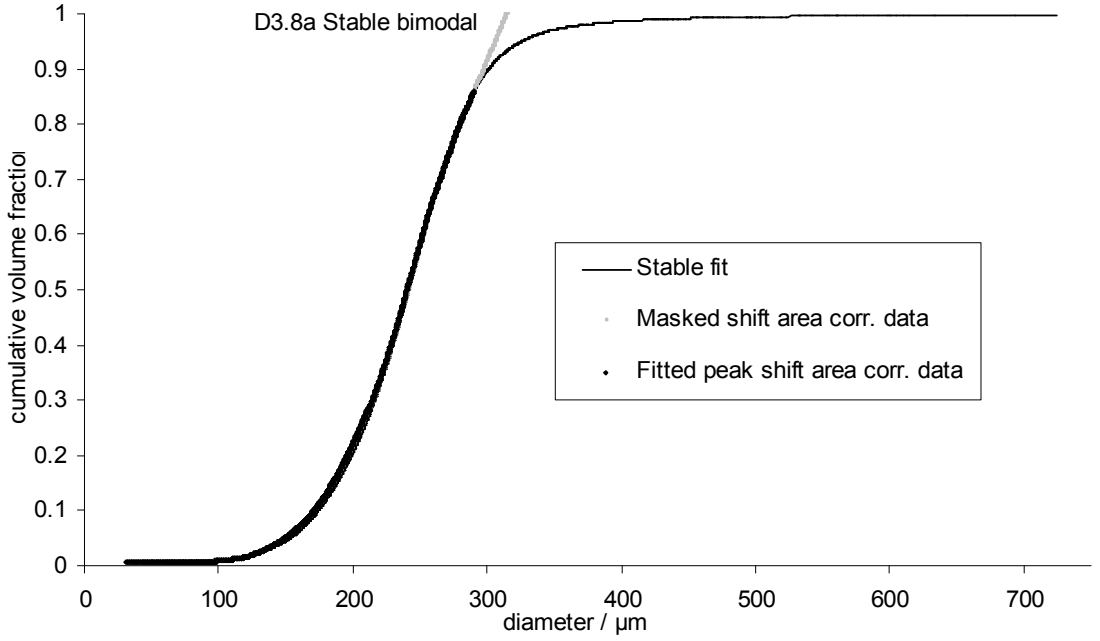

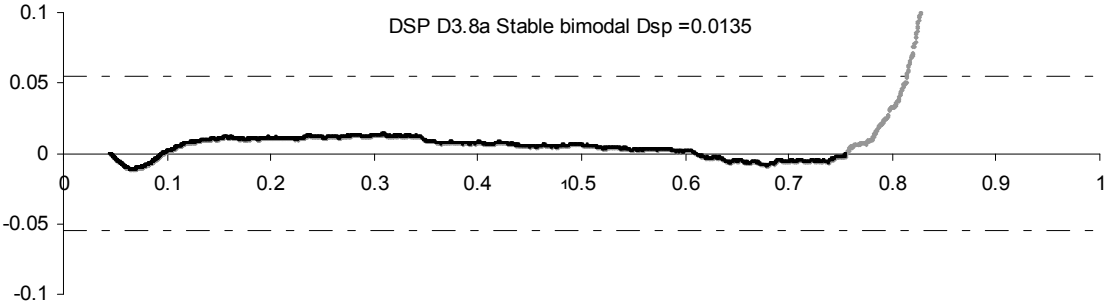

peak		Parameters of the Stable distribution			
D3.8a	%vol	α	β	γ	δ
1°	76	1.6	0.25	35	250
2°	24				190

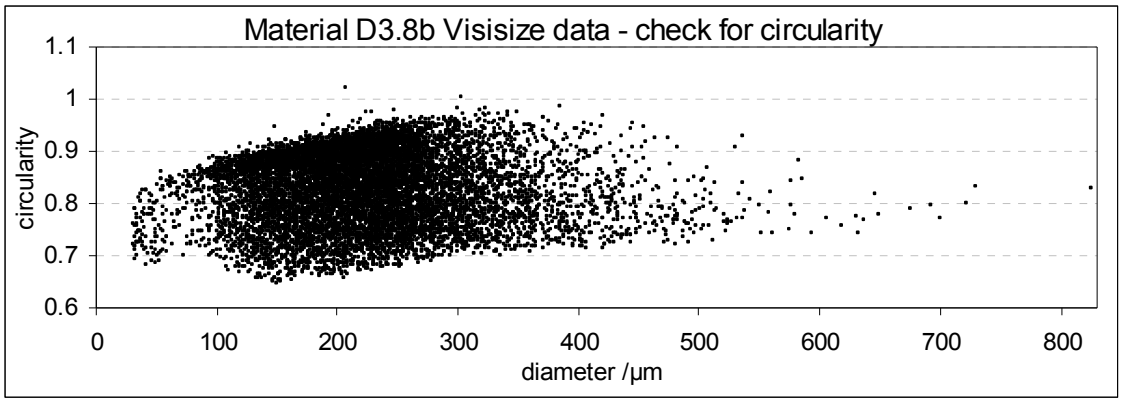
Material D3.8b Visisize data - check for circularity
circularity
1.1
1
0.9
0.8
0.7
0.6
0
100
200
300
400
500
600
700
800
diameter /µm

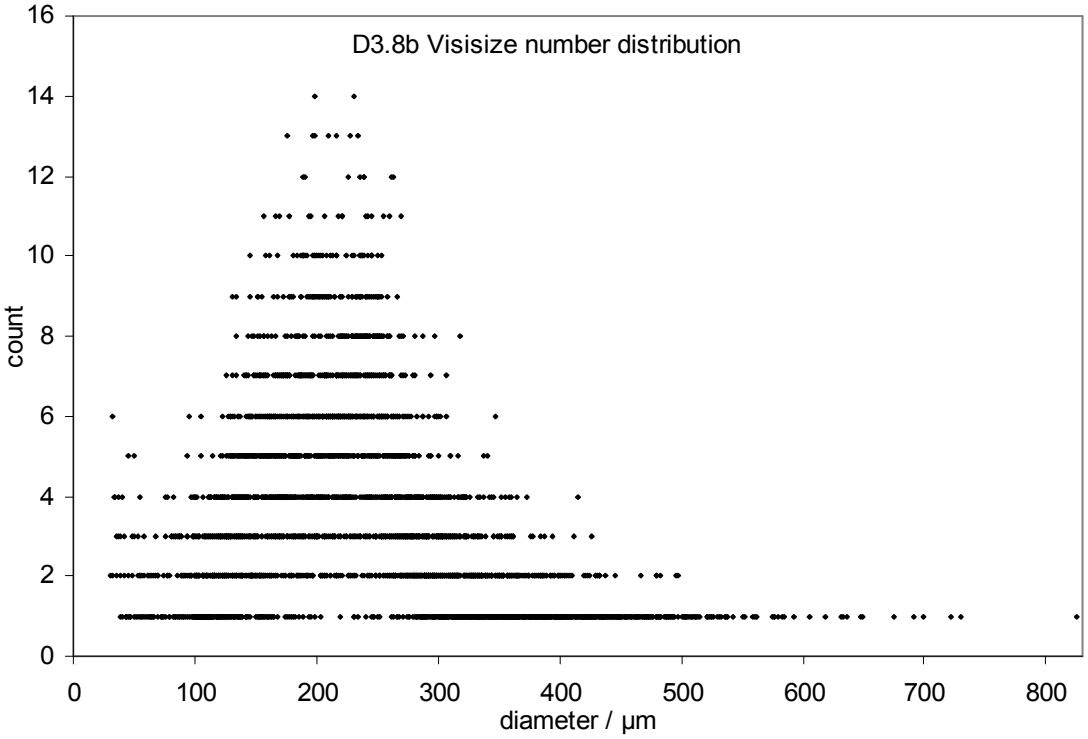
D3.8b Visisize number distribution
count
16
14
12
10
8
6
4
2
0
0
100
200
300
400
500
600
700
800
diameter / µm

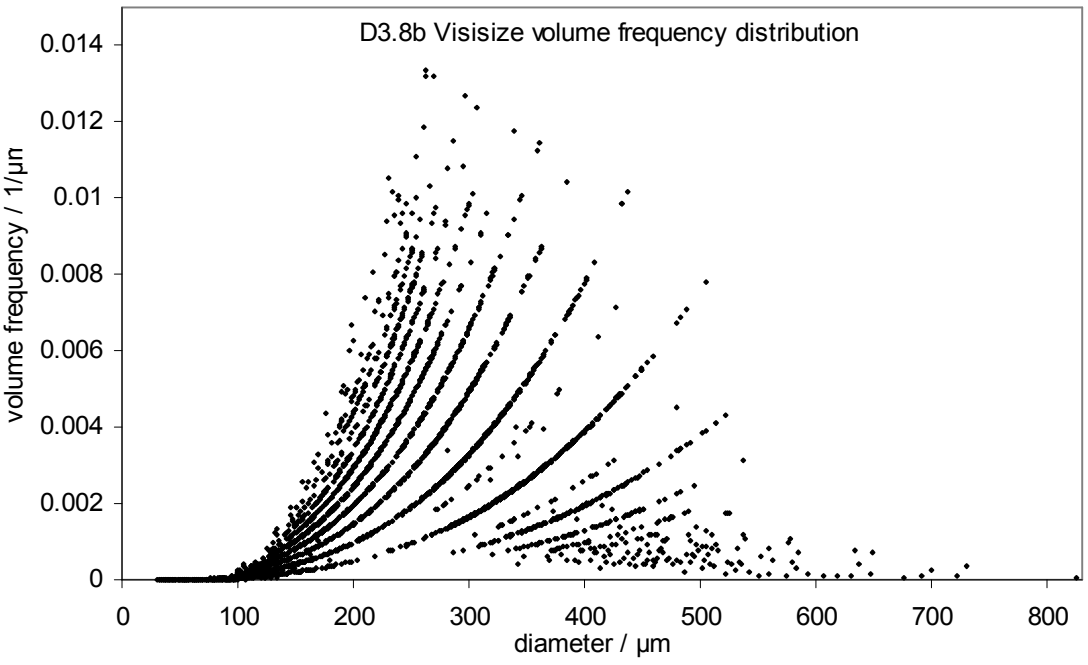
D3.8b Visisize volume frequency distribution
volume frequency / 1/µn
0.014
0.012
0.01
0.008
0.006
0.004
0.002
0
0
100
200
300
400
500
600
700
800
diameter / µm

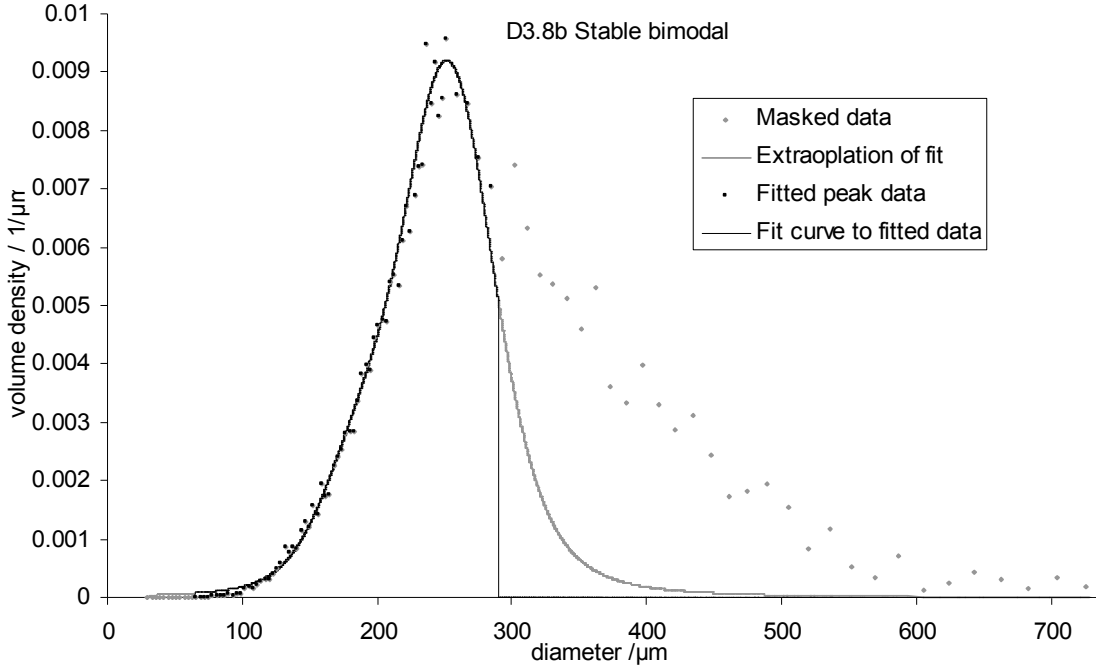

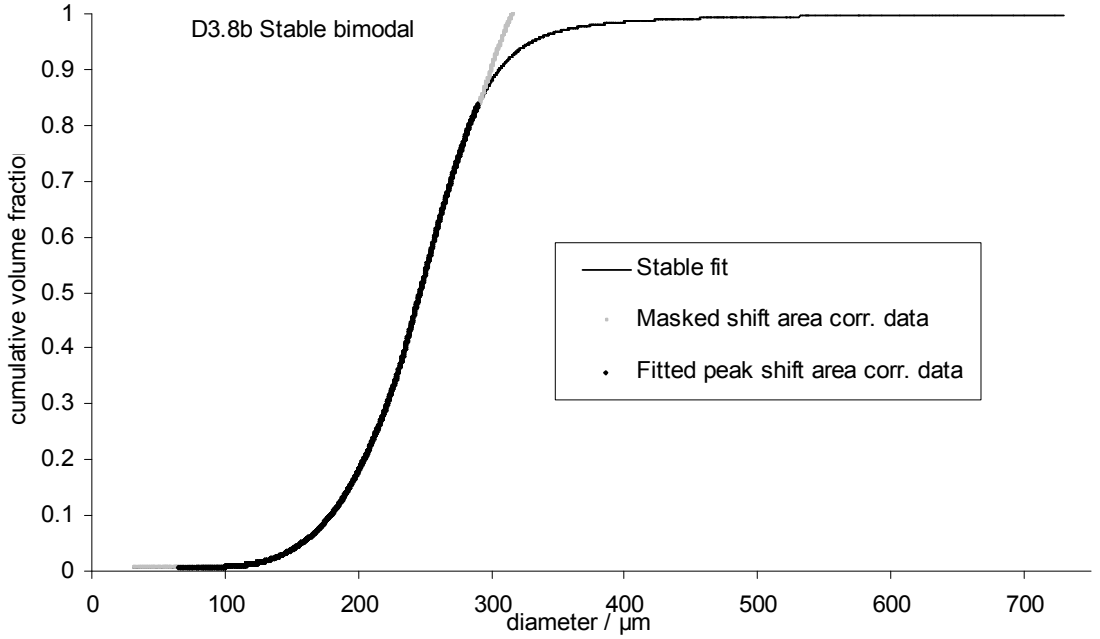

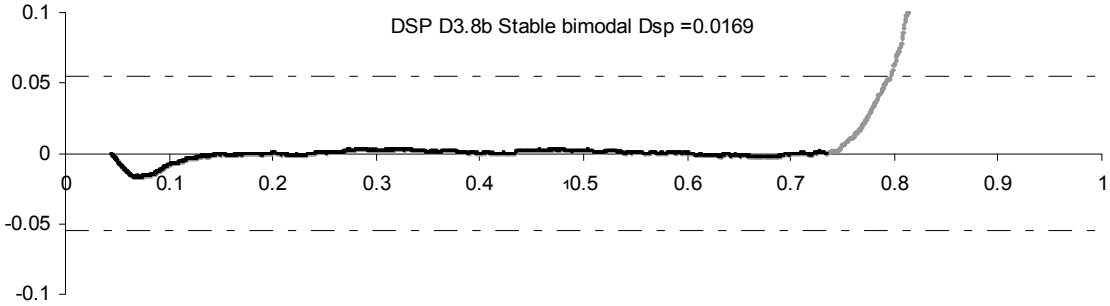

peak		Parameters of the Stable distribution			
D3.8b	%vol	α	β	γ	δ
1°	79	1.6	0.25	35	254
2°	21				192

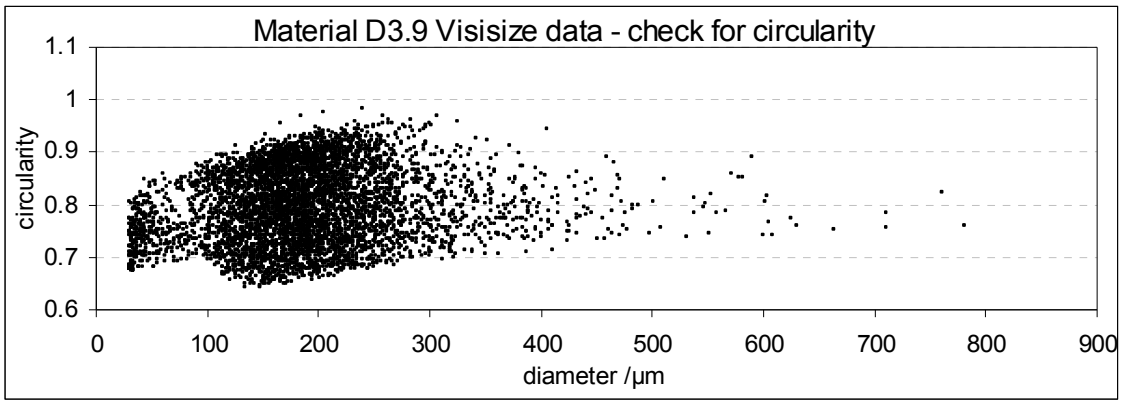
Material D3.9 Visisize data - check for circularity
circularity
1.1
1
0.9
0.8
0.7
0.6
0
100
200
300
400
500
600
700
800
900
diameter /µm

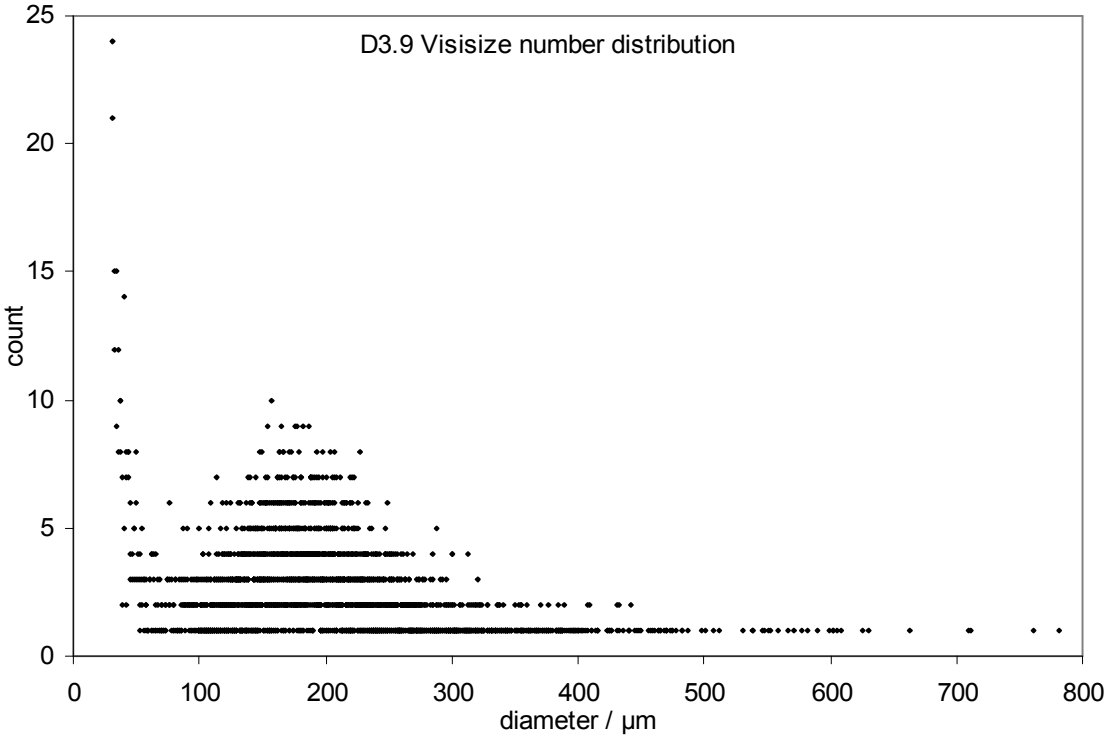
D3.9 Visisize number distribution
count
25
20
15
10
5
0
0
100
200
300
400
500
600
700
800
diameter / µm

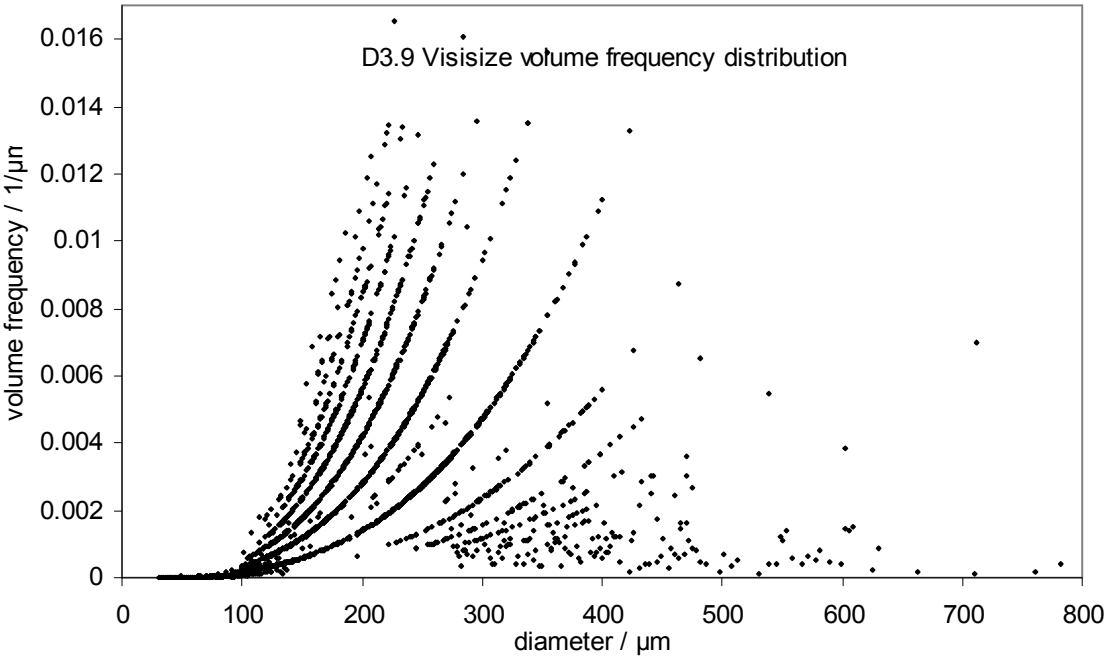
D3.9 Visisize volume frequency distribution
volume frequency / 1/µm
0.016
0.014
0.012
0.01
0.008
0.006
0.004
0.002
0
0
100
200
300
400
500
600
700
800
diameter / µm

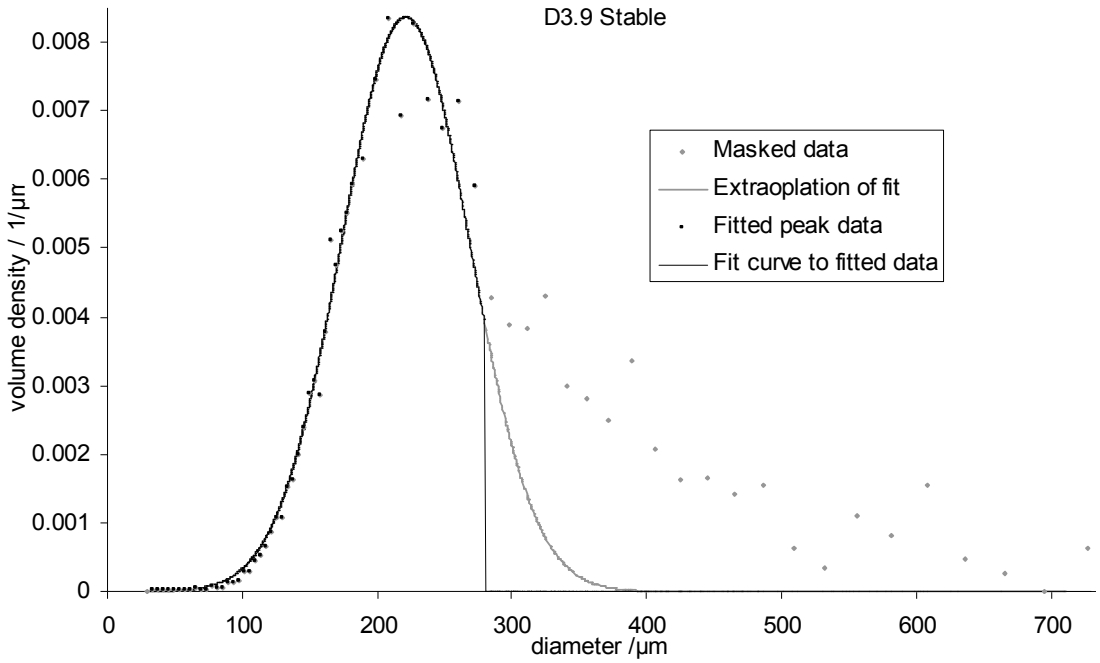

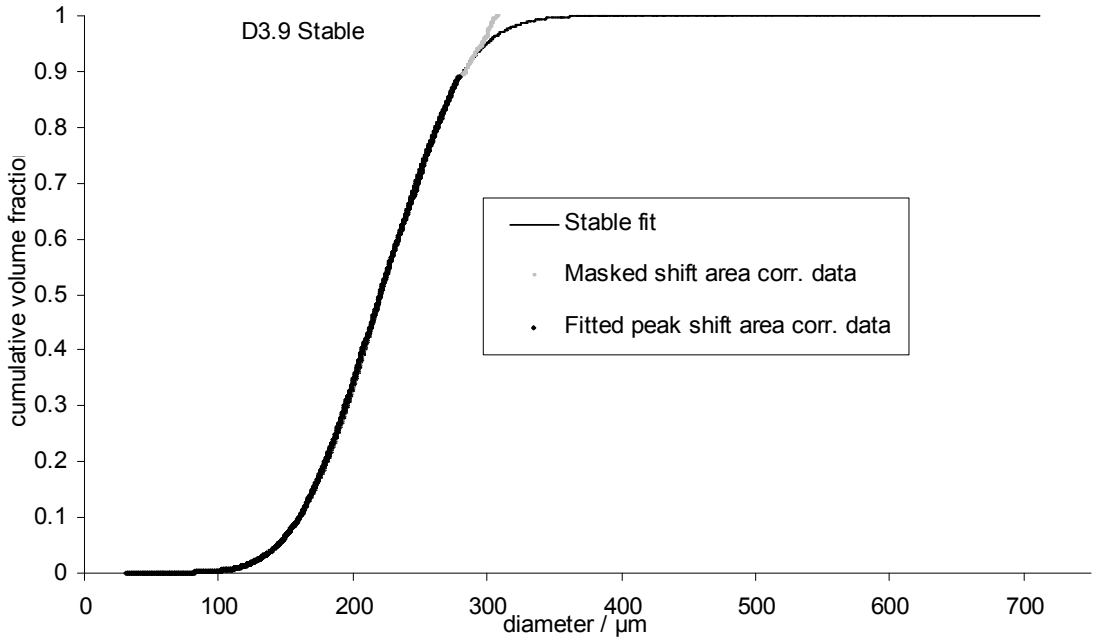

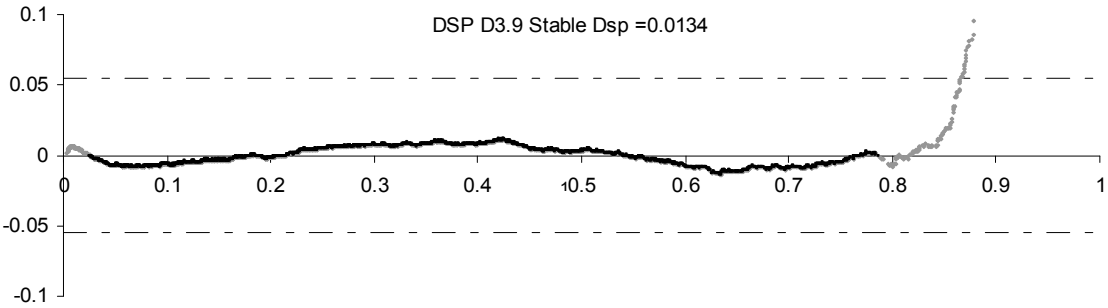

peak	Parameters of the Stable distribution			
D3.9	α	β	γ	δ
1°	2	0.11	47.7	221

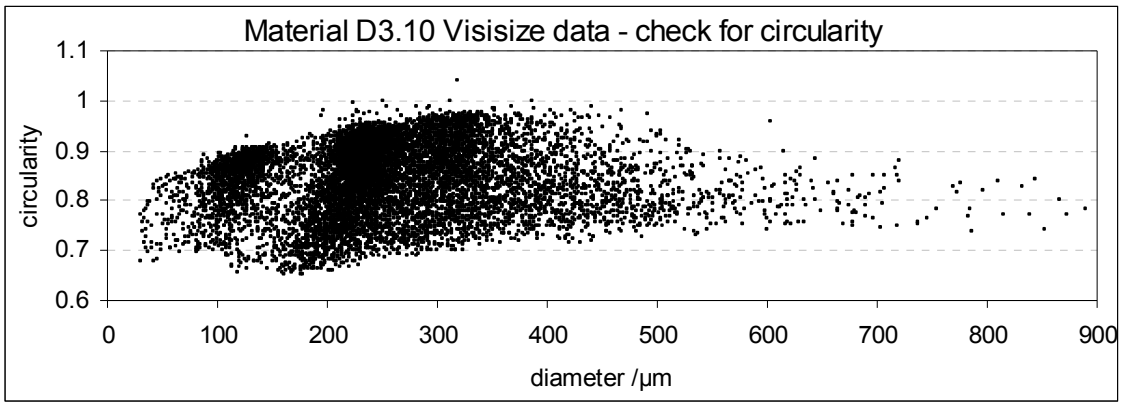
Material D3.10 Visisize data - check for circularity
circularity
1.1
1
0.9
0.8
0.7
0.6
0
100
200
300
400
500
600
700
800
900
diameter /µm

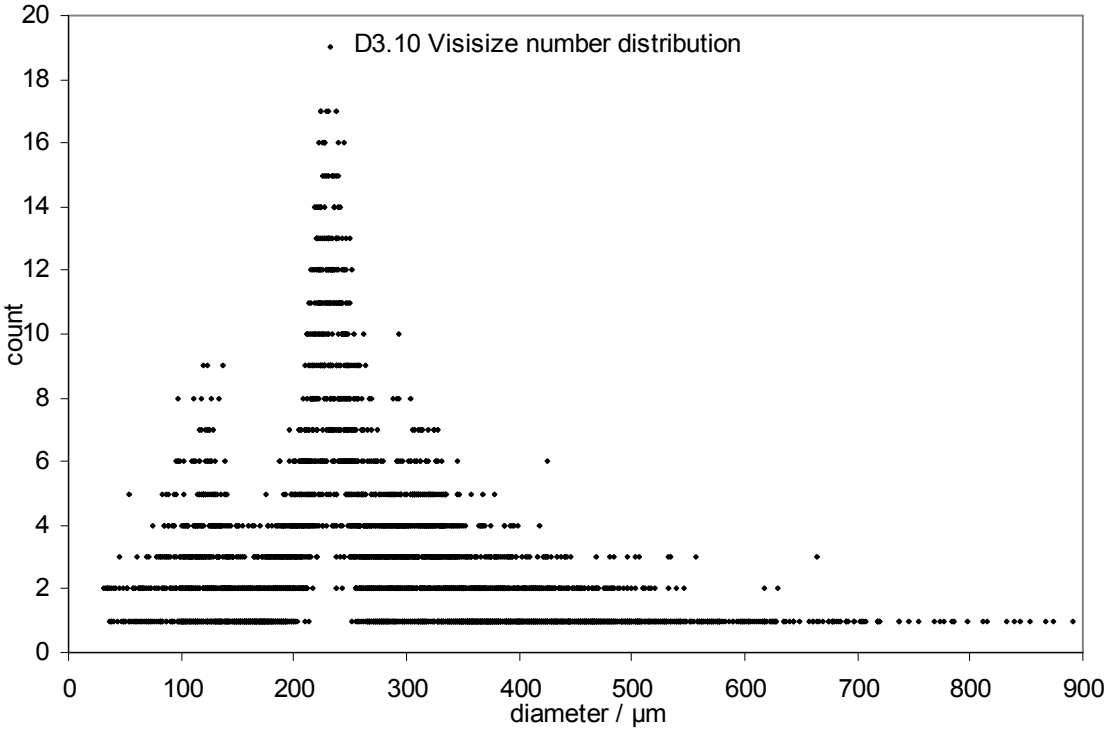
D3.10 Visisize number distribution
count
20
18
16
14
12
10
8
6
4
2
0
0
100
200
300
400
500
600
700
800
900
diameter / µm

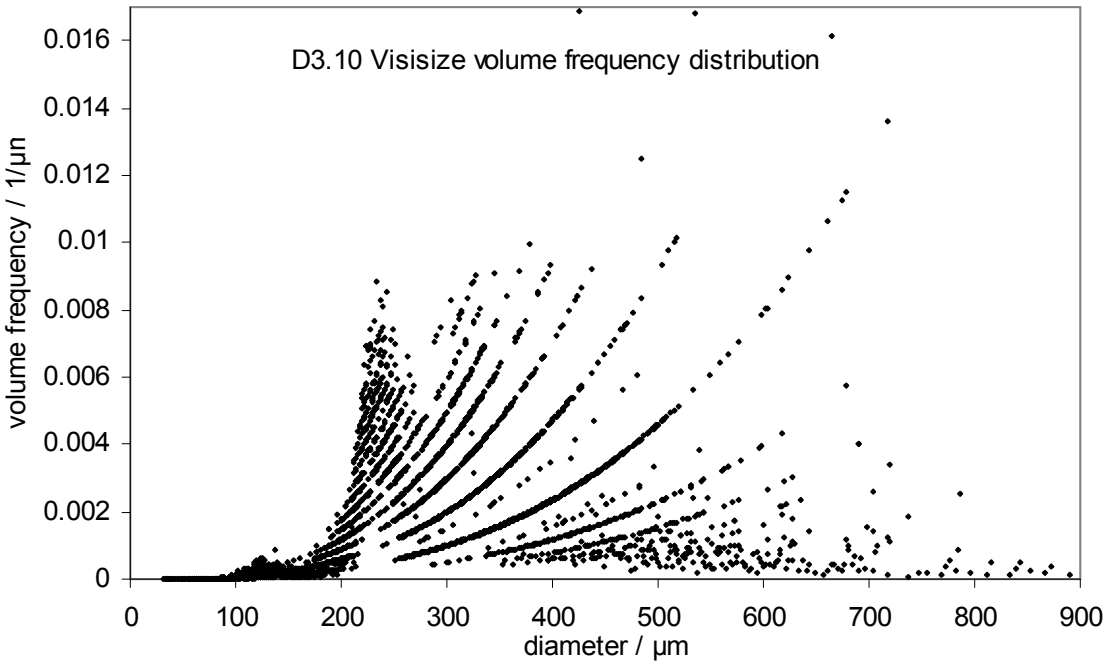
D3.10 Visisize volume frequency distribution
volume frequency / 1/µn
0.016
0.014
0.012
0.01
0.008
0.006
0.004
0.002
0
0
100
200
300
400
500
600
700
800
900
diameter / µm

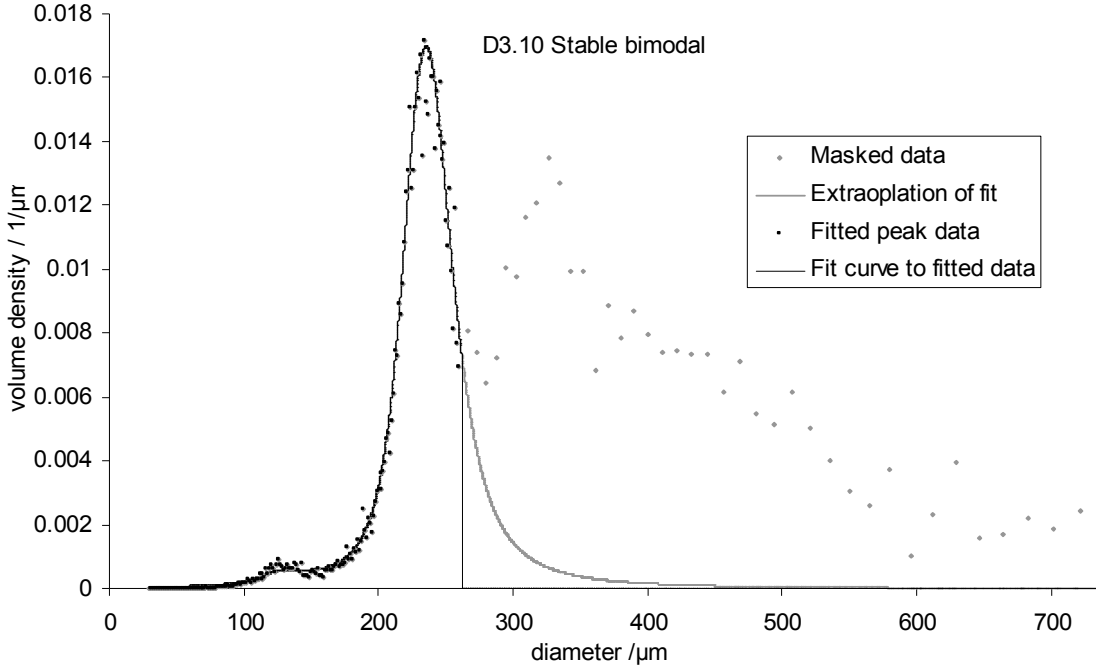

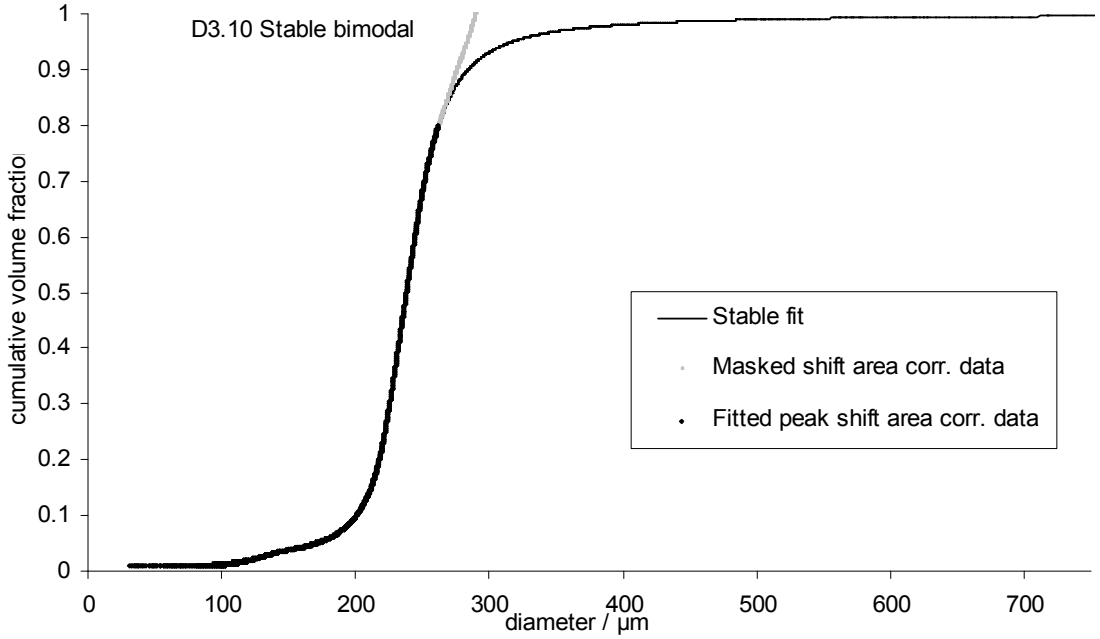

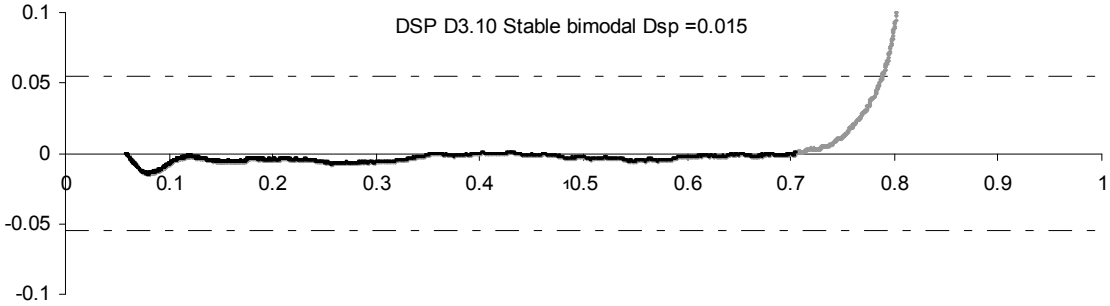

peak D3.10	%vol	Parameters of the Stable distribution α	β	γ	δ
1°	98	1.27	0.25	20.5	235.4
2°	2				129.4

A.6.2 Material D4

Fits for dataset D4.15 are in the main text.

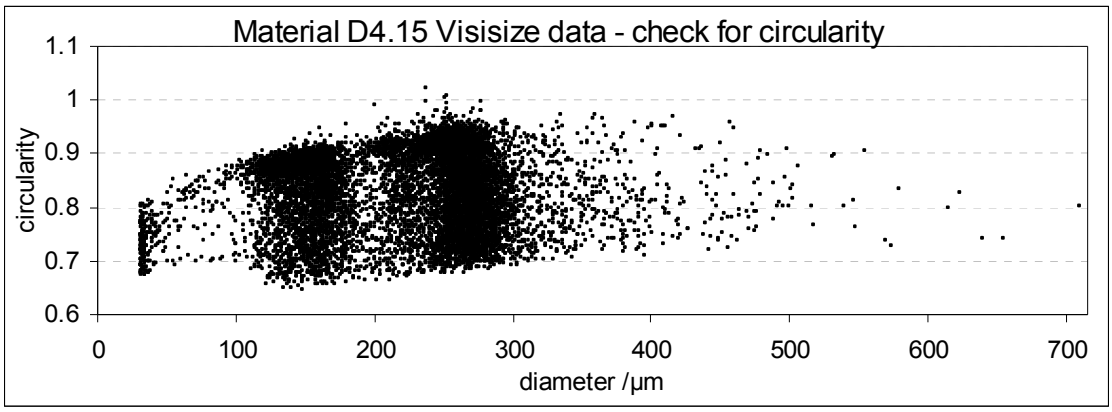
Material D4.15 Visisize data - check for circularity
circularity
1.1
1
0.9
0.8
0.7
0.6
0
100
200
300
400
500
600
700
diameter /µm

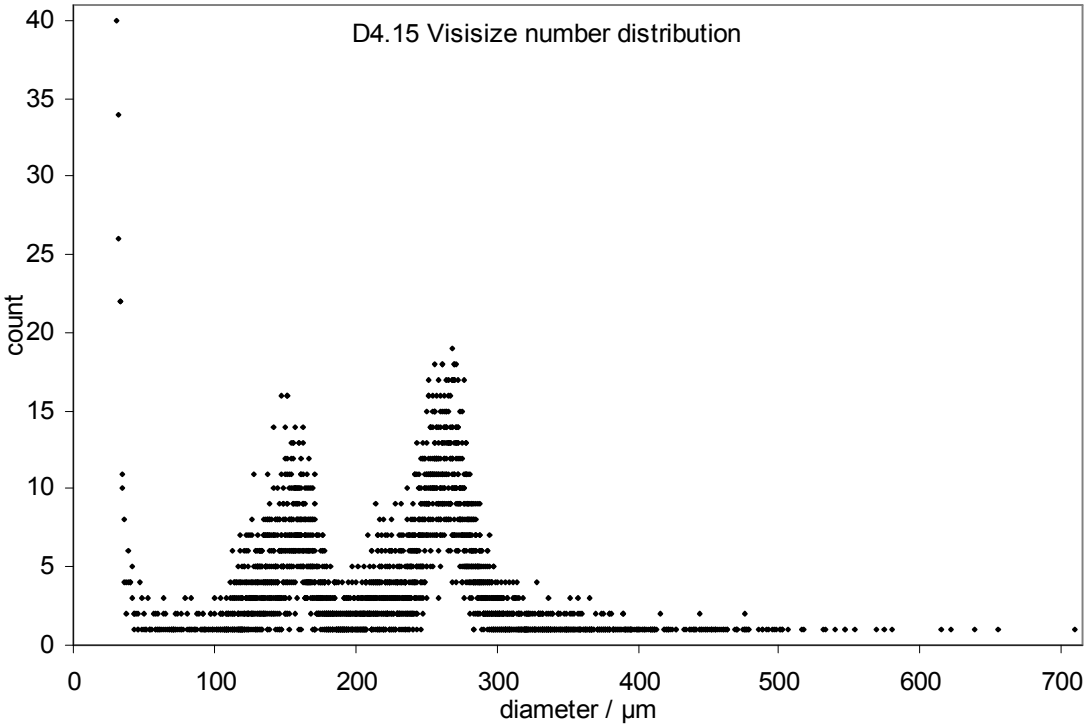
D4.15 Visisize number distribution
count
40
35
30
25
20
15
10
5
0
0
100
200
300
400
500
600
700
diameter / µm

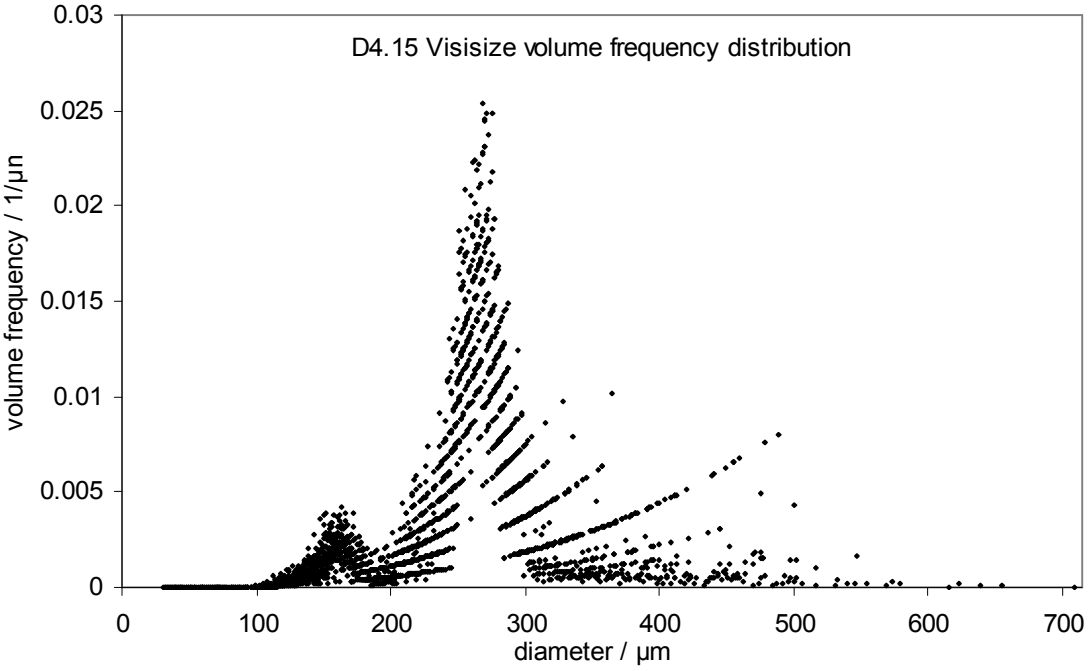
D4.15 Visisize volume frequency distribution
volume frequency / 1/µn
0.03
0.025
0.02
0.015
0.01
0.005
0
0
100
200
300
400
500
600
700
diameter / µm

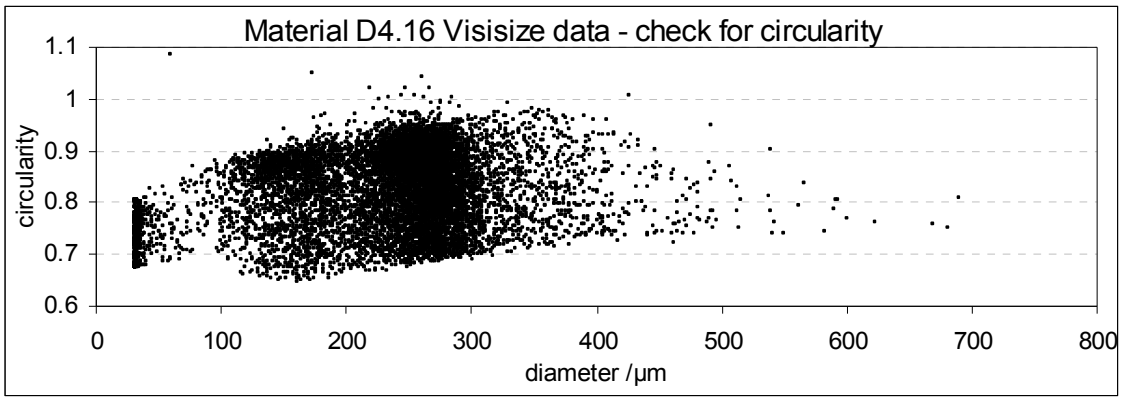
Material D4.16 Visisize data - check for circularity
circularity
1.1
1
0.9
0.8
0.7
0.6
0
100
200
300
400
500
600
700
800
diameter /µm

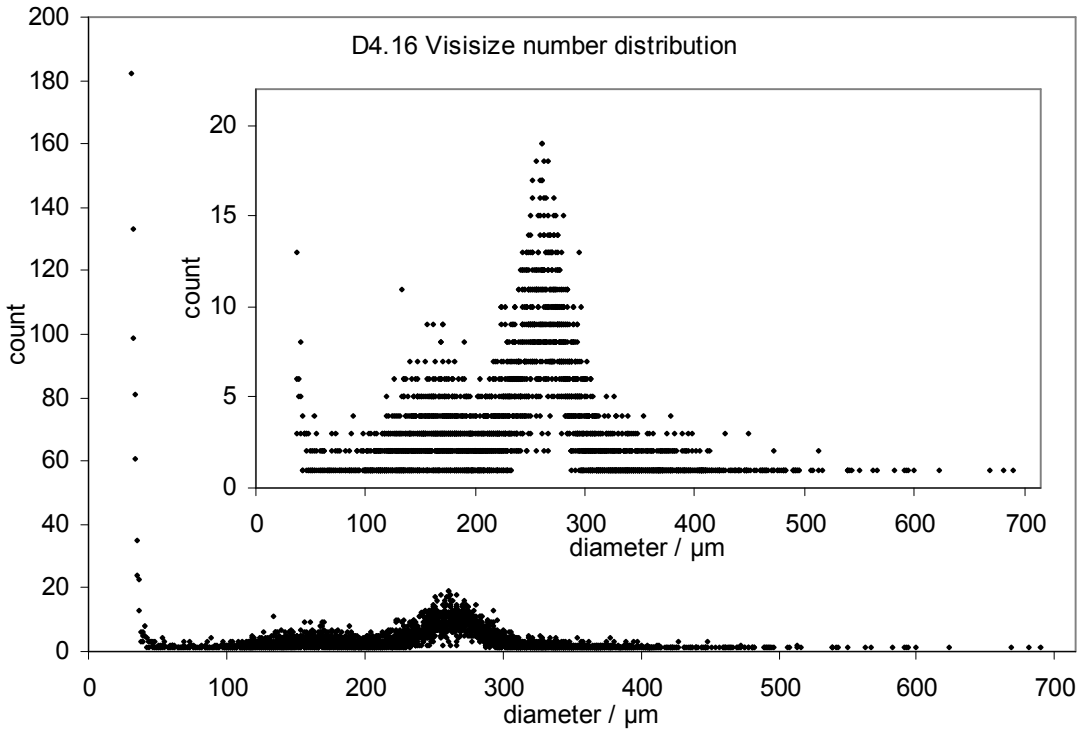
D4.16 Visisize number distribution
count
200
180
160
140
120
100
80
60
40
20
0
count
20
15
10
5
0
0
100
200
300
400
500
600
700
diameter / µm
0
100
200
300
400
500
600
700
diameter / µm

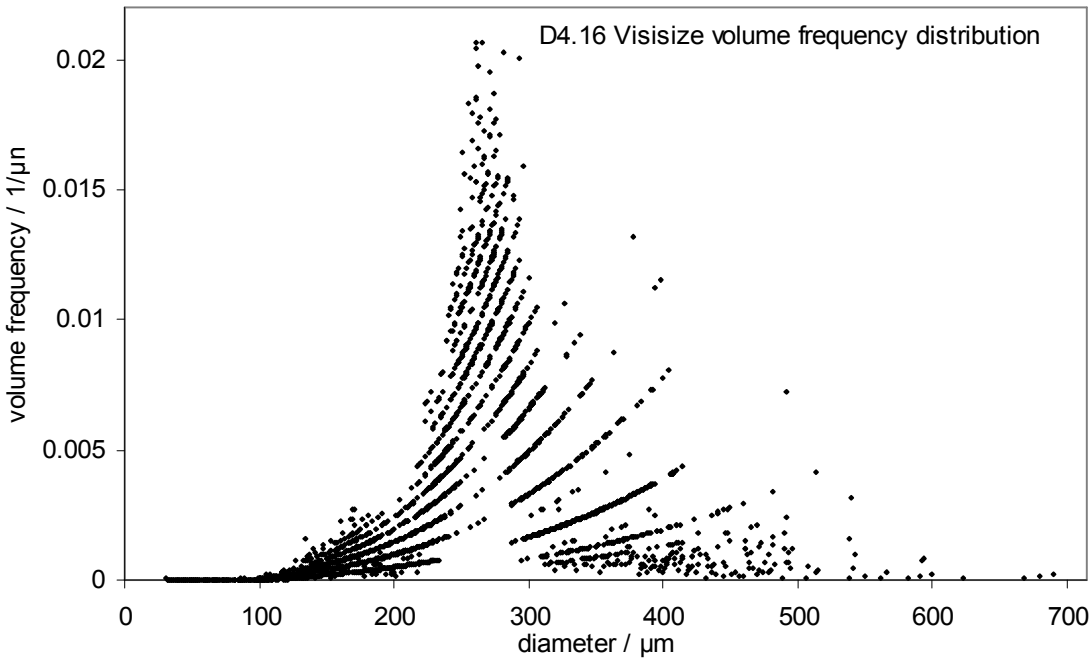
D4.16 Visisize volume frequency distribution
volume frequency / 1/µn
0.02
0.015
0.01
0.005
0
0
100
200
300
400
500
600
700
diameter / µm

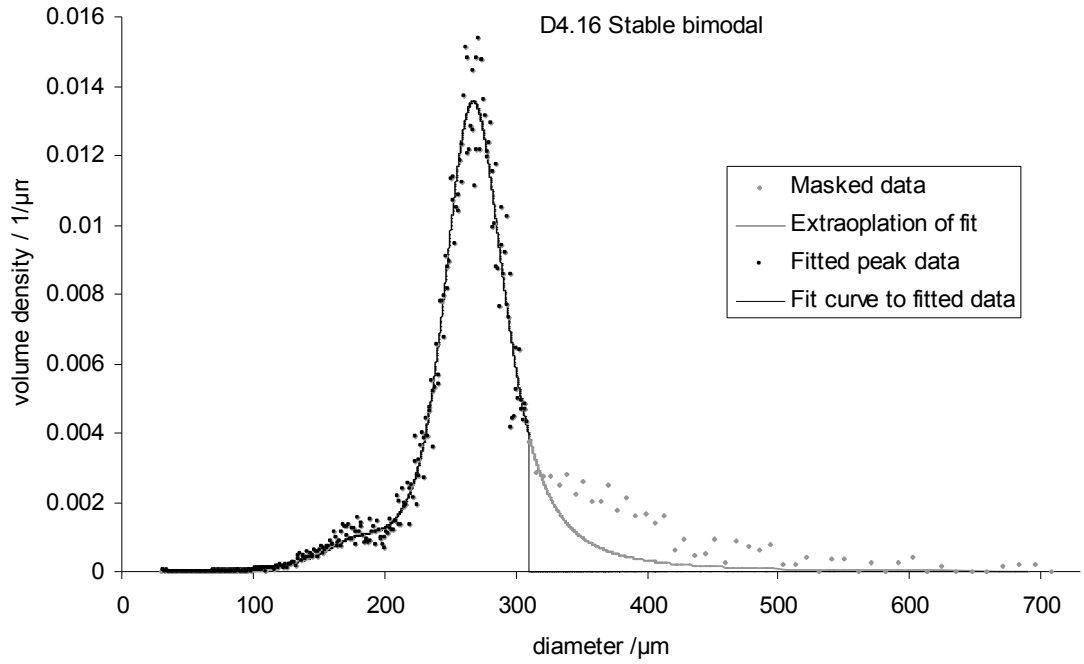

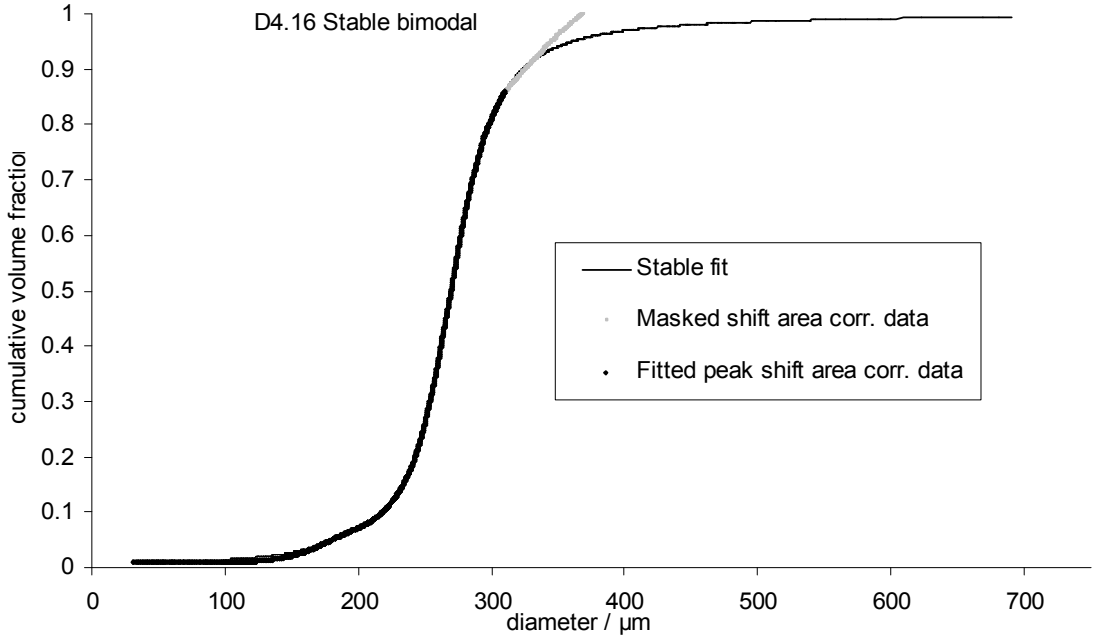

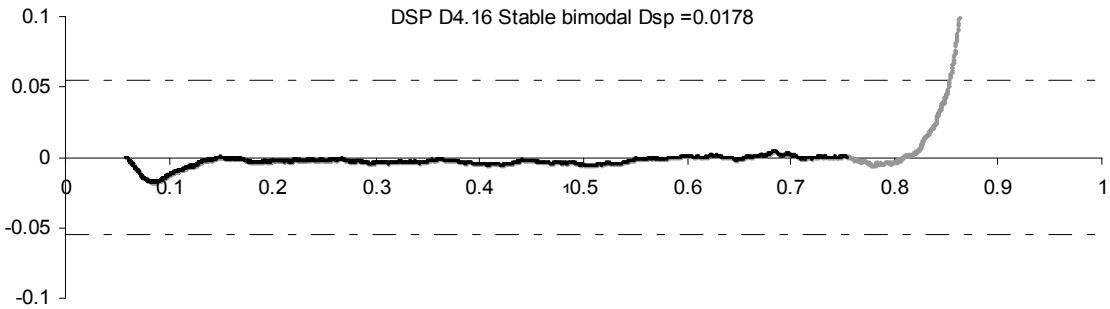

peak D4.16	%vol	Parameters of the Stable distribution α	β	γ	δ
1°	96	1.3	0.225	25.45	267.47
2°	4				176.81

A.6.3 Material D7

D7.1 and D7.2a are rejected as the data are too non-circular. It is unclear from the records of either the spray drying or the measurement experiments what was so different about these two datasets.

Stable fits for dataset D7.3a are in the main text.

Datasets D7.5 and D7.6 each have 2 repeats of the Visisize measurement. In each case the "b" measurements, repeat measurements made a couple of weeks after the original, have a much greater tail of large sizes. This may indicate some agglomeration during storage of an imperfectly dry powder. The large tail gives a much greater Dv90 for the raw data and hence a much higher PDI - almost 50% greater in both cases. As the raw data is intrinsically wider in the "b" repeats, the agreement between the fitted Stable parameters for datasets D7.5 and D7.6 "a" and "b" repeats is less good than between the Stable parameters for the repeated Visisize measurements on dataset D3.8. However, the Stable parameters are still reasonably similar between the "a" and "b" repeats, and the fit acts as a filter on the large size tail, so the PDI for the fitted primary peak is only around 20% greater in the "b" measurements than in the "a" measurements.

Unusually, D7.7 cannot be fitted satisfactorily for $\gamma_2 = \gamma_1$, but only for $\gamma_2/\gamma_1 = \delta_2/\delta_1$. In dataset D7.9, two peaks can be observed, of about equal size and closely spaced. The secondary peak is too large volume fraction to be accounted for by satellite droplet formation. Error on the hole size is a more credible explanation, although it is initially surprising that an approximately equal number of two sizes of orifice should have been fitted to the sprayplate. However, re-examining the other D7 datasets in light of this analysis of D7.7 and D7.9, shows the same pattern of unusually closely spaced peaks and large volume fraction of the secondary peak. The overall most plausible explanation is of a poor batch of orifices, or two sizes of orifice having been mixed up, with a varying number of each orifice size being fitted to the sprayplate for each experiment.

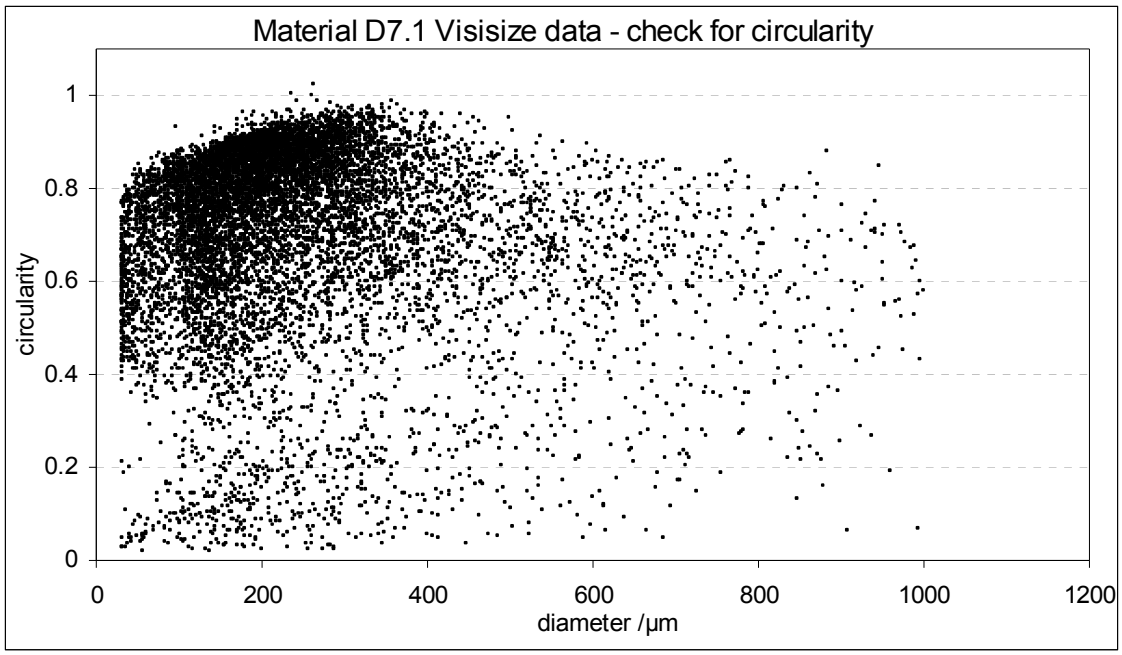
Material D7.1 Visisize data - check for circularity
circularity
diameter /µm
0
0.2
0.4
0.6
0.8
1
0
200
400
600
800
1000
1200

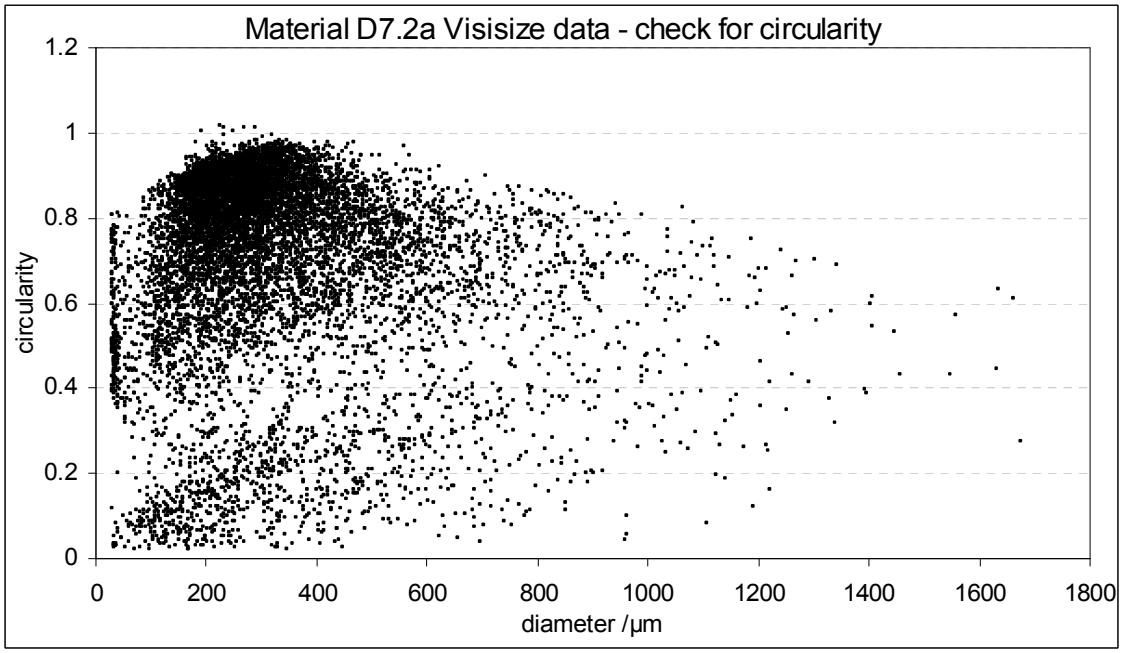
Material D7.2a Visisize data - check for circularity
circularity
diameter /µm
0
0.2
0.4
0.6
0.8
1
1.2
0
200
400
600
800
1000
1200
1400
1600
1800

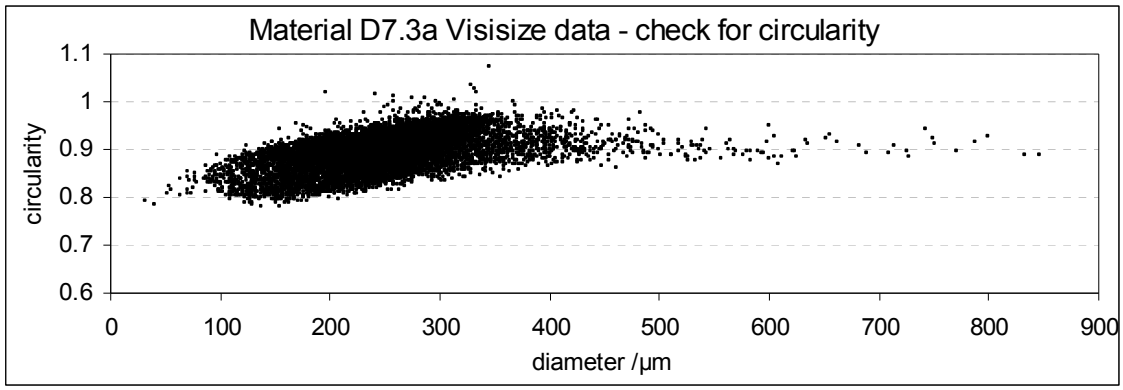
Material D7.3a Visisize data - check for circularity
circularity
1.1
1
0.9
0.8
0.7
0.6
0
100
200
300
400
500
600
700
800
900
diameter /µm

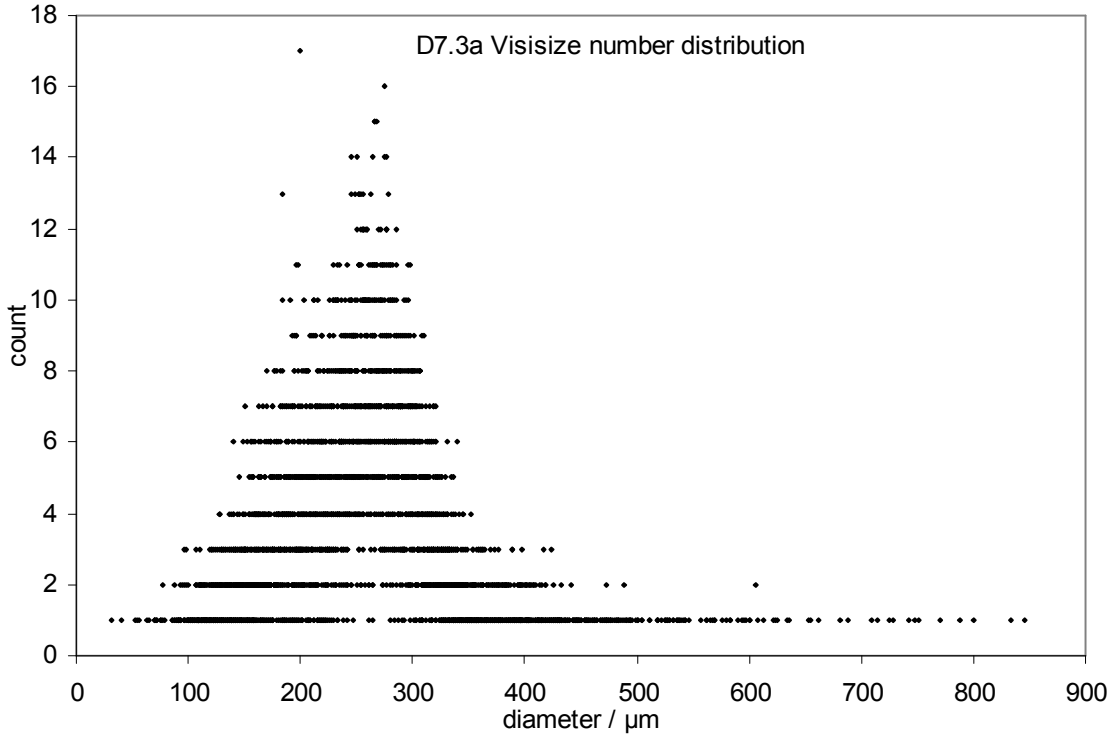
D7.3a Visisize number distribution
count
18
16
14
12
10
8
6
4
2
0
0
100
200
300
400
500
600
700
800
900
diameter / µm

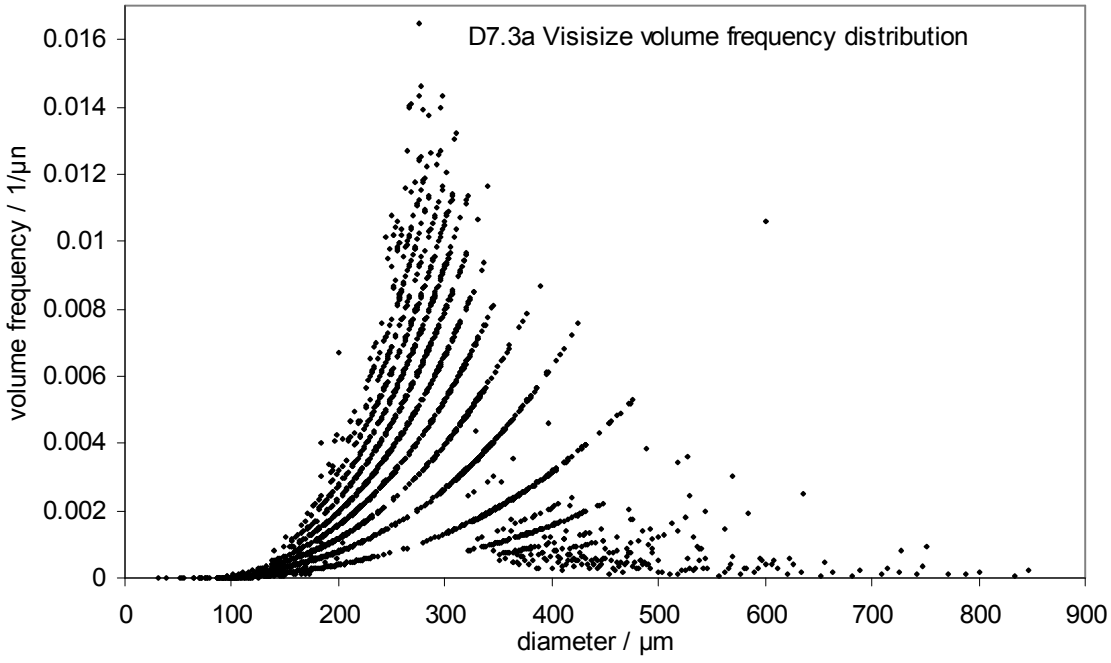
D7.3a Visisize volume frequency distribution
volume frequency / 1/µn
0.016
0.014
0.012
0.01
0.008
0.006
0.004
0.002
0
0
100
200
300
400
500
600
700
800
900
diameter / µm

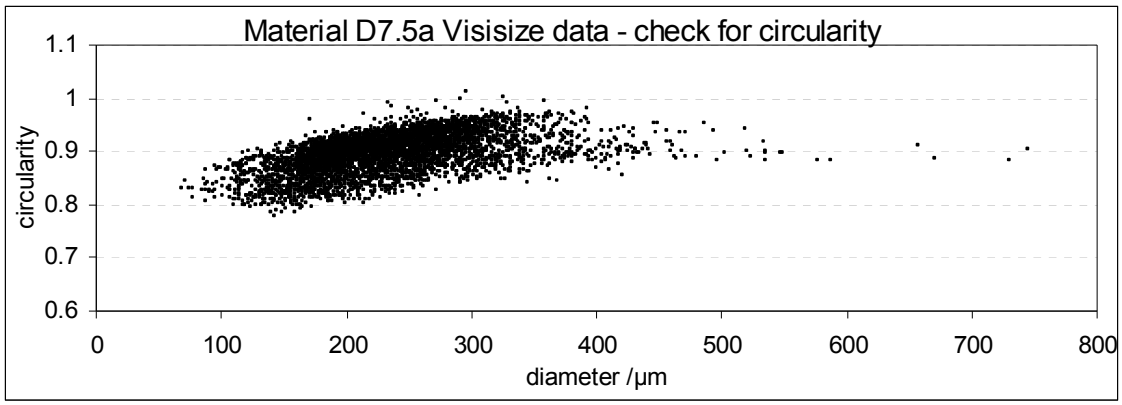
Material D7.5a Visisize data - check for circularity
circularity
1.1
1
0.9
0.8
0.7
0.6
0
100
200
300
400
500
600
700
800
diameter /µm

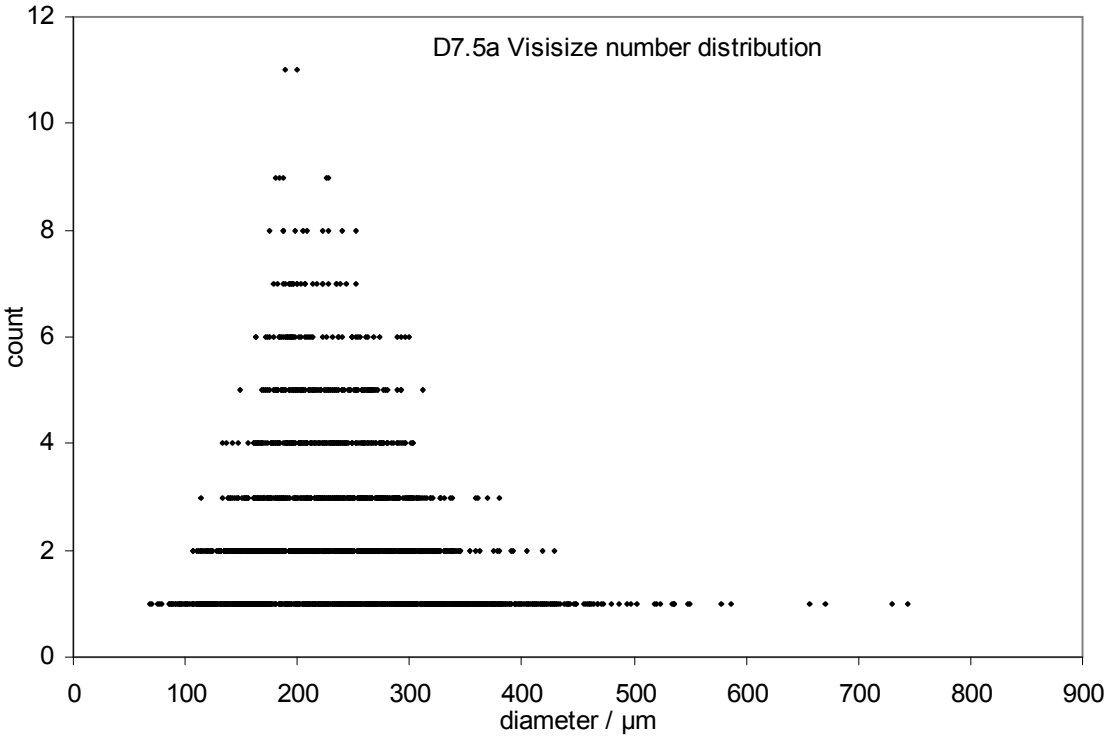
D7.5a Visisize number distribution
count
12
10
8
6
4
2
0
0
100
200
300
400
500
600
700
800
900
diameter / µm

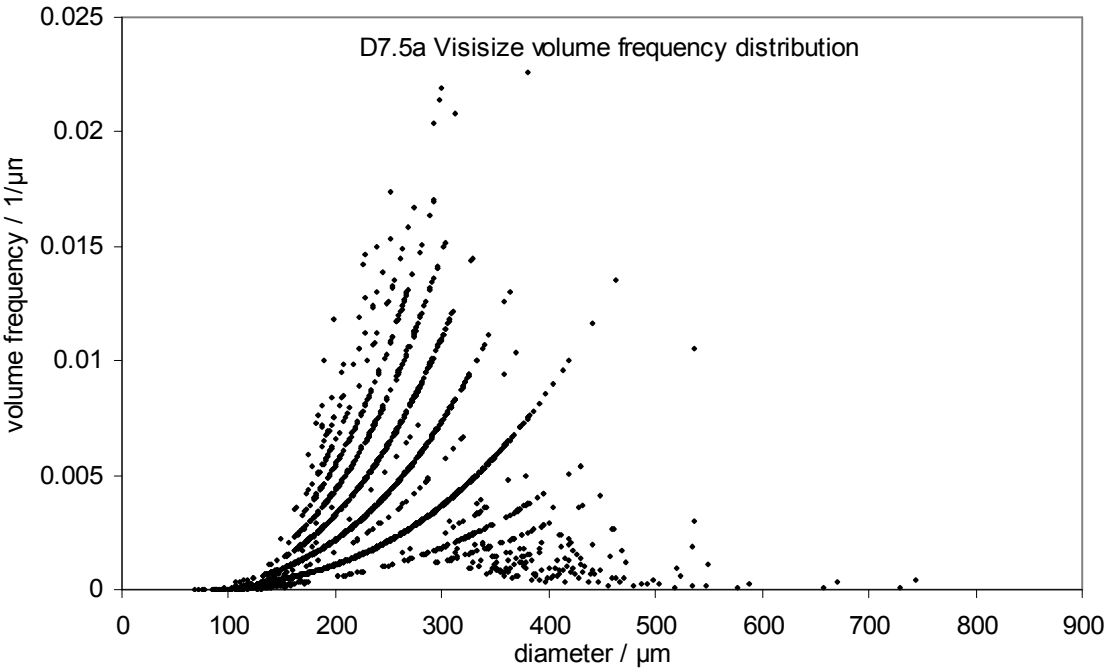
D7.5a Visisize volume frequency distribution
volume frequency / 1/µn
0.025
0.02
0.015
0.01
0.005
0
0
100
200
300
400
500
600
700
800
900
diameter / µm

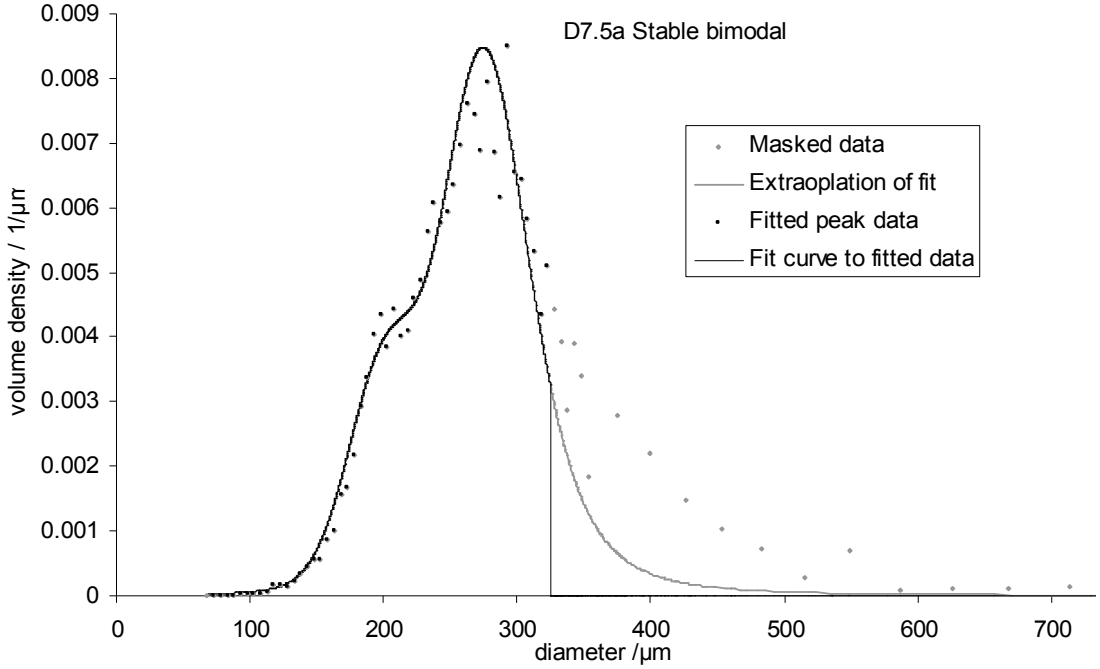

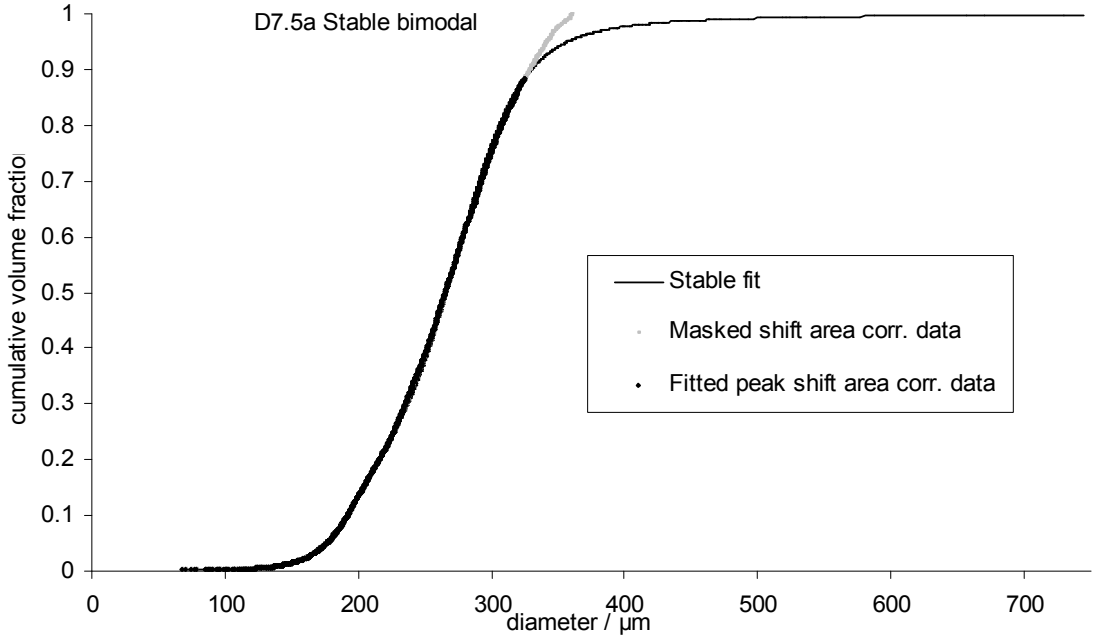

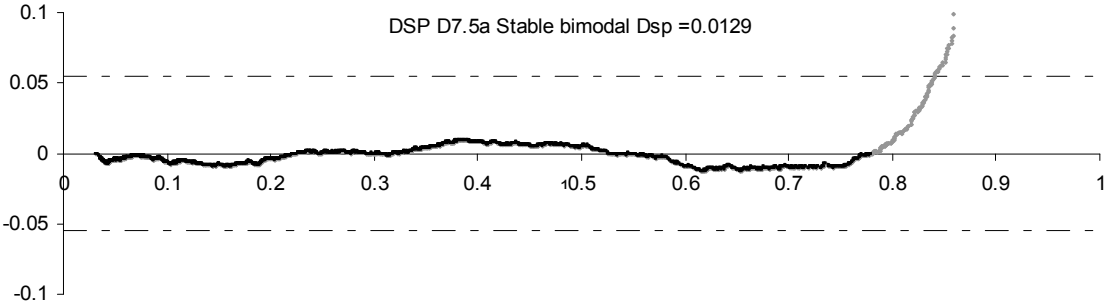

peak		Parameters of the Stable distribution			
D7.5a	%vol	α	β	γ	δ
1°	68	1.6	0.65	33	277
2°	32				204

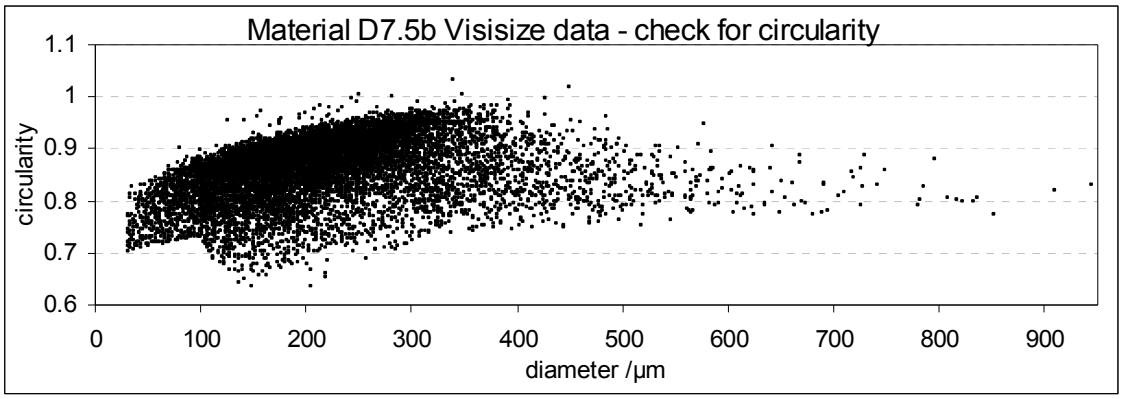
Material D7.5b Visisize data - check for circularity
circularity
1.1
1
0.9
0.8
0.7
0.6
0
100
200
300
400
500
600
700
800
900
diameter /µm

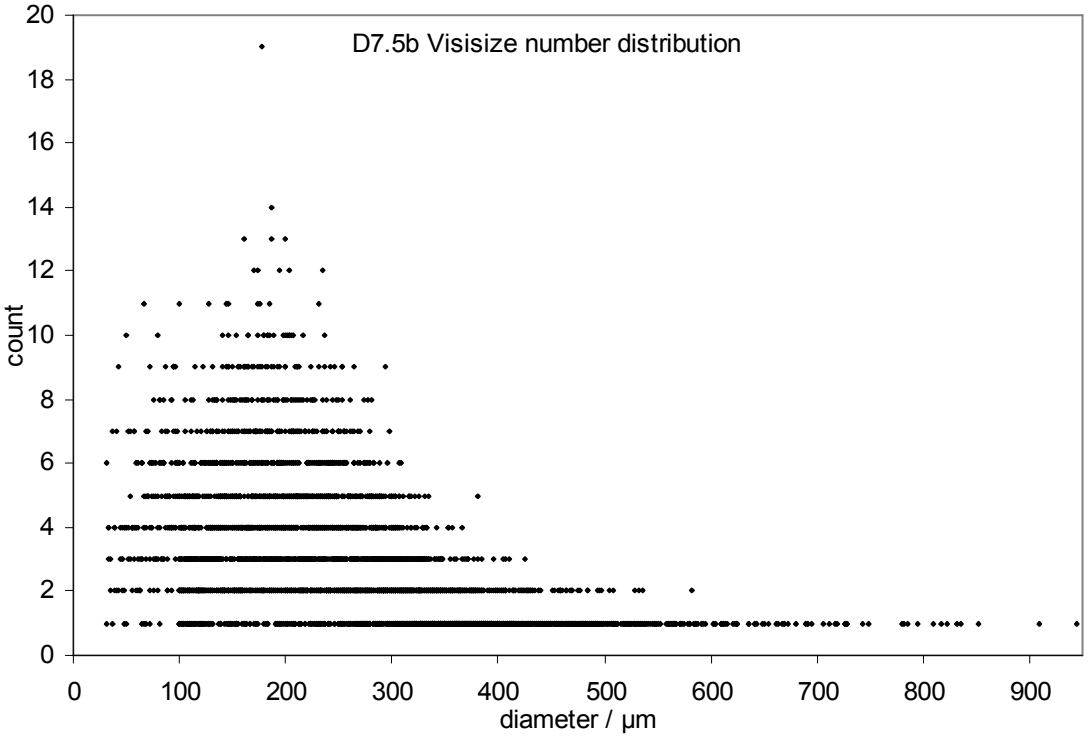
D7.5b Visisize number distribution
count
20
18
16
14
12
10
8
6
4
2
0
0
100
200
300
400
500
600
700
800
900
diameter / µm

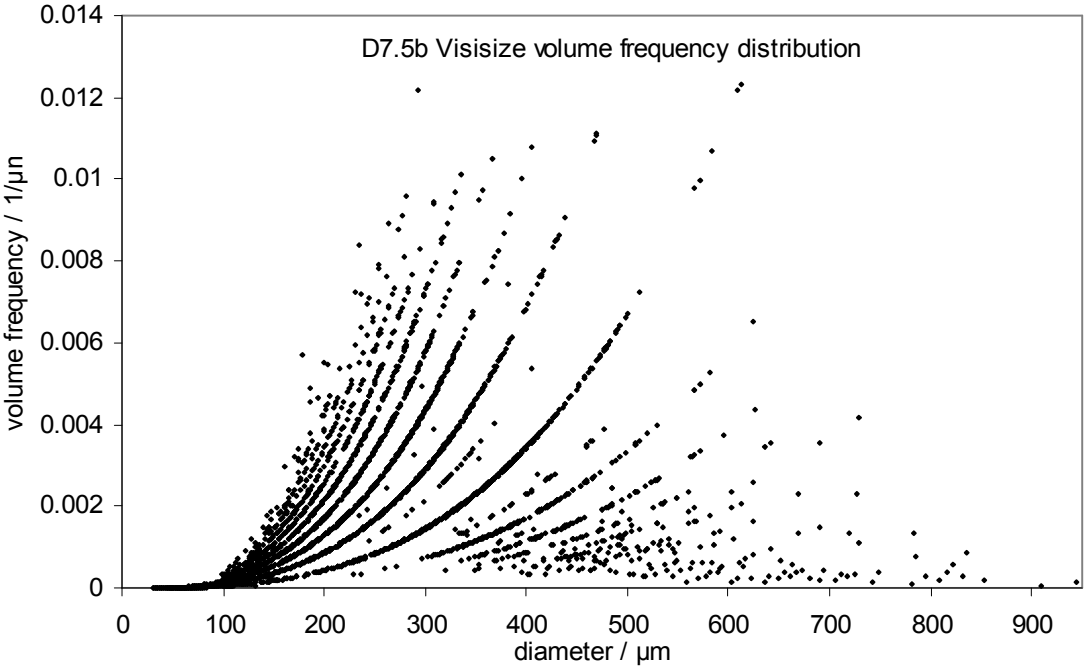
D7.5b Visisize volume frequency distribution
volume frequency / 1/µn
0.014
0.012
0.01
0.008
0.006
0.004
0.002
0
0
100
200
300
400
500
600
700
800
900
diameter / µm

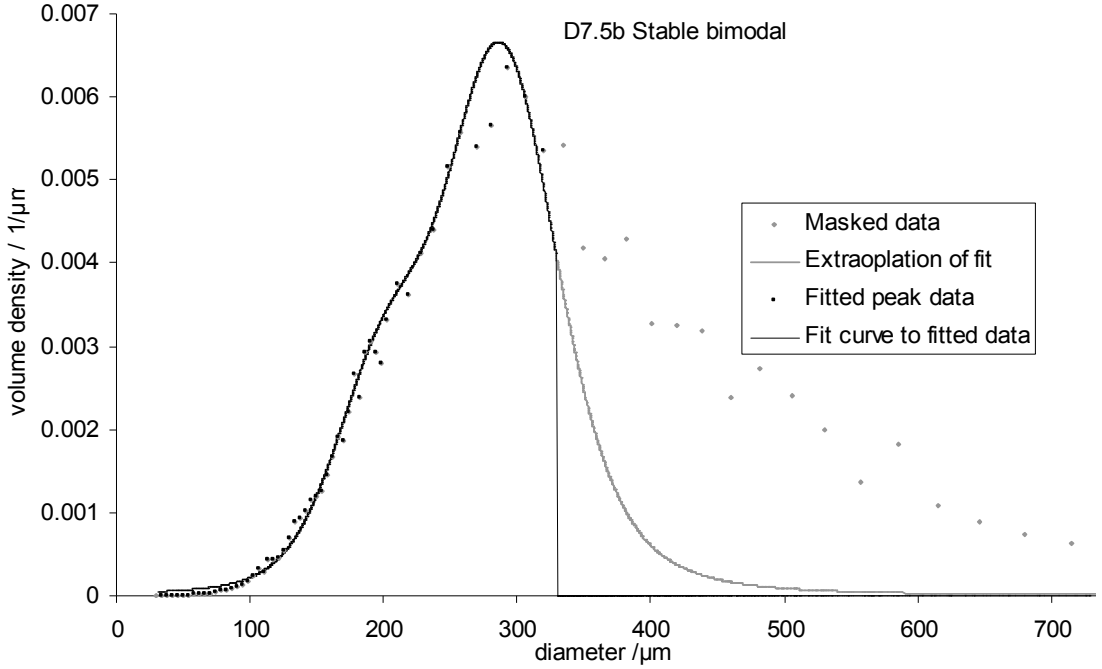

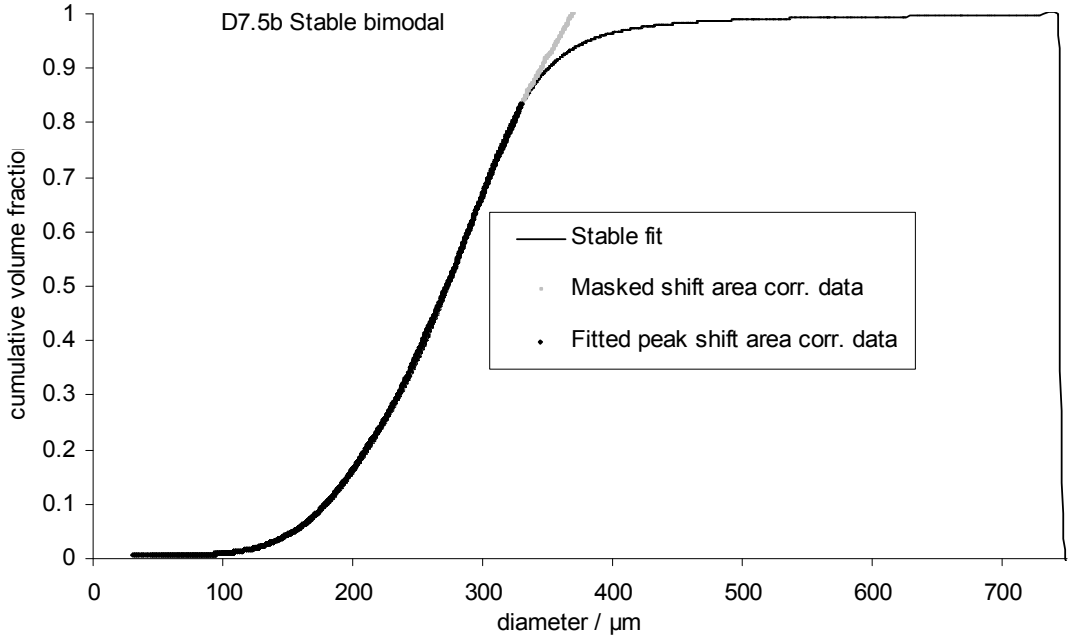

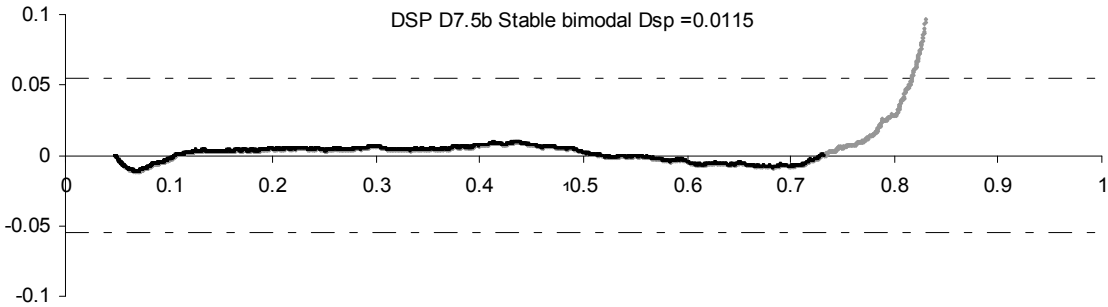

peak		Parameters of the Stable distribution			
D7.5b	%vol	α	β	γ	δ
1°	69	1.6	0.3	43	290
2°	31				204

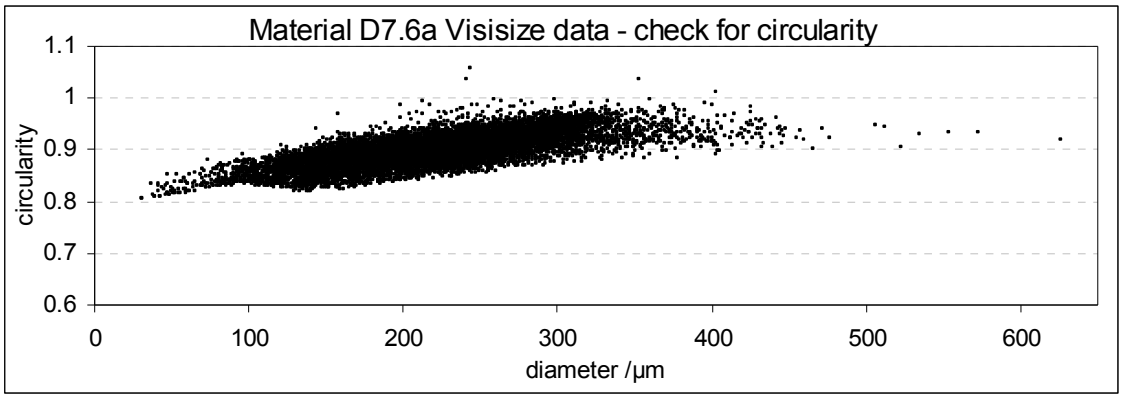
Material D7.6a Visisize data - check for circularity
circularity
1.1
1
0.9
0.8
0.7
0.6
0
100
200
300
400
500
600
diameter /µm

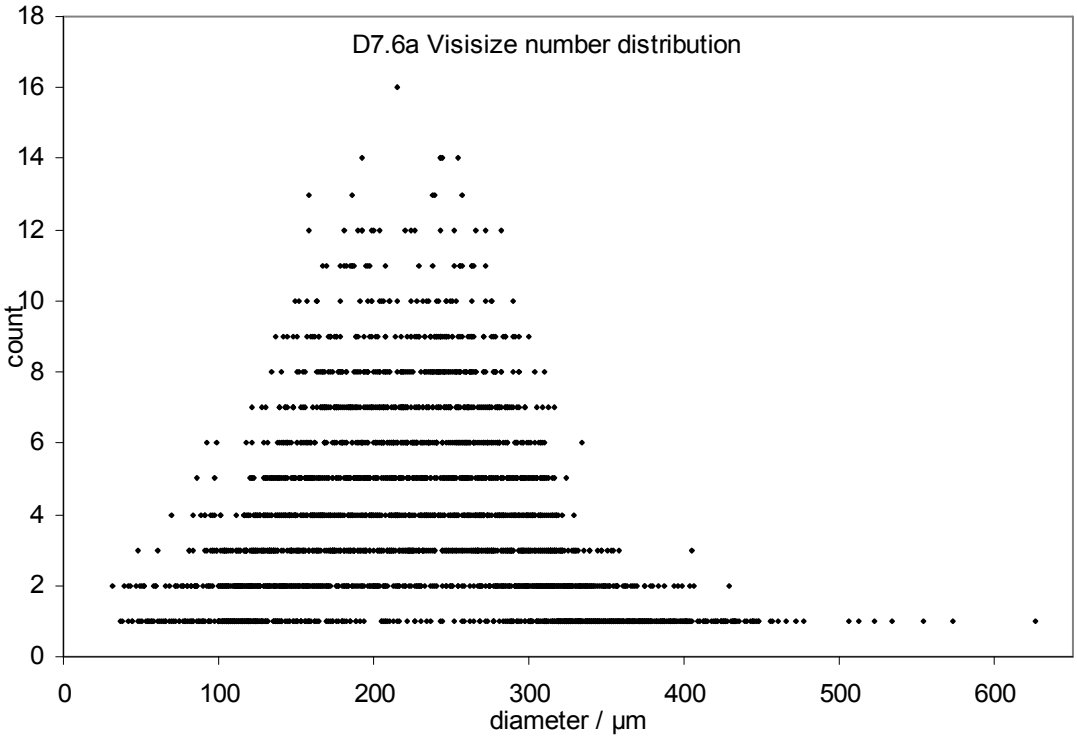
D7.6a Visisize number distribution
count
18
16
14
12
10
8
6
4
2
0
0
100
200
300
400
500
600
diameter / µm

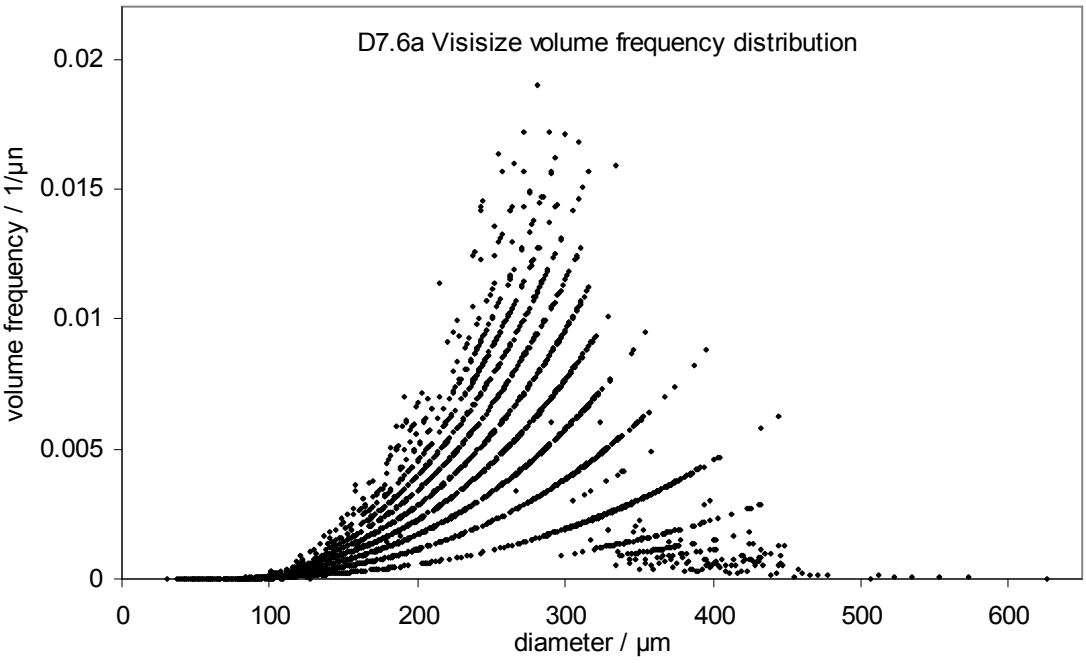
D7.6a Visisize volume frequency distribution
volume frequency / 1/µn
0.02
0.015
0.01
0.005
0
0
100
200
300
400
500
600
diameter / µm

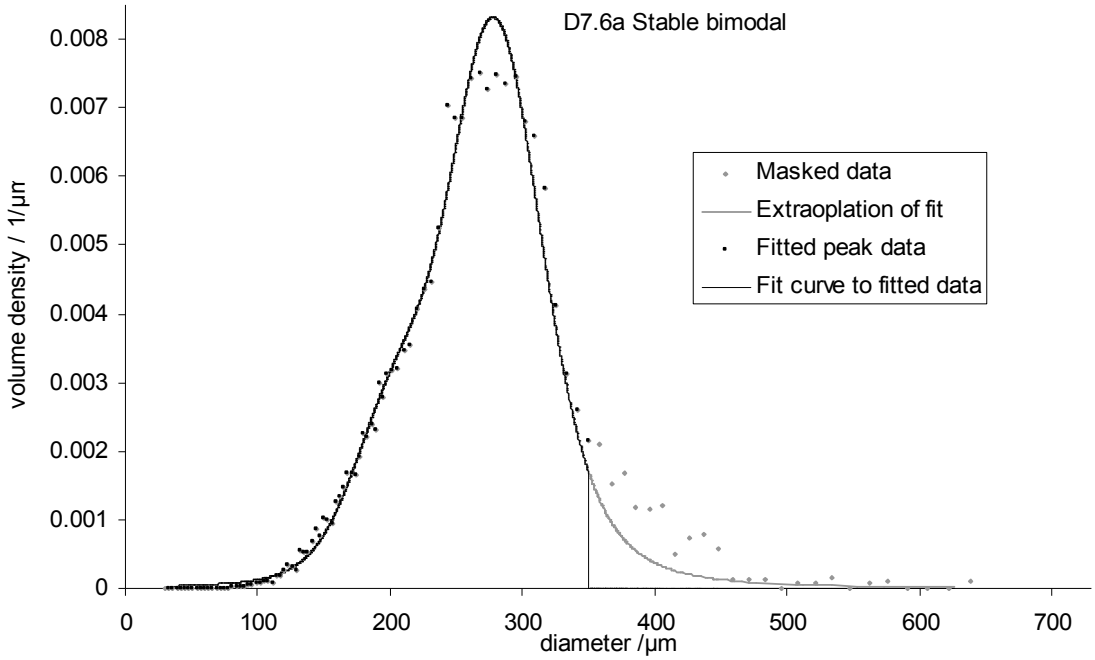

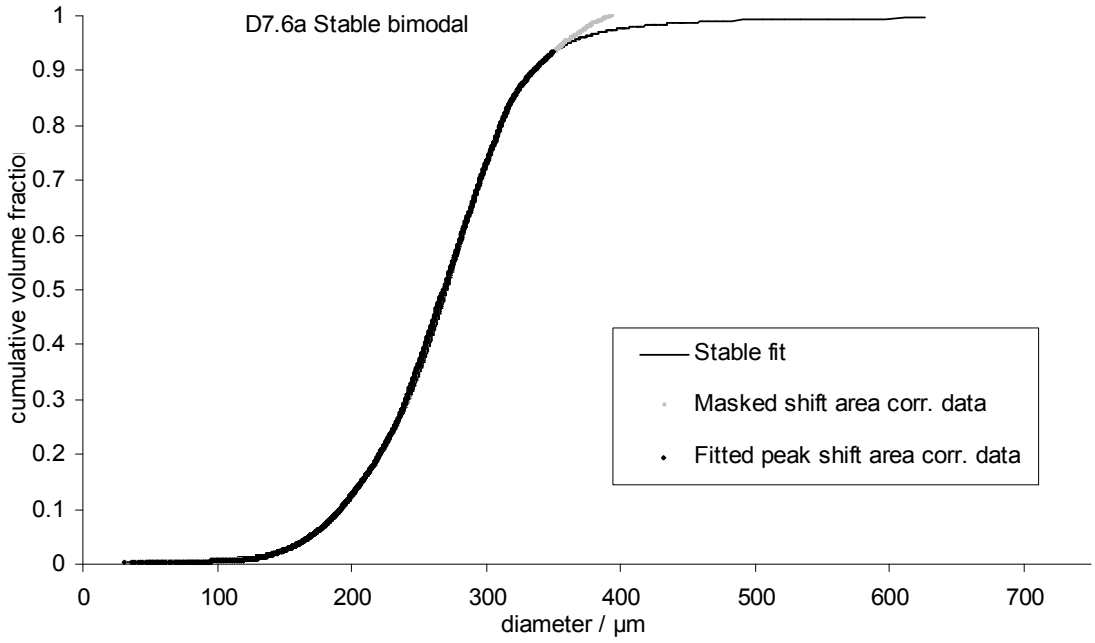

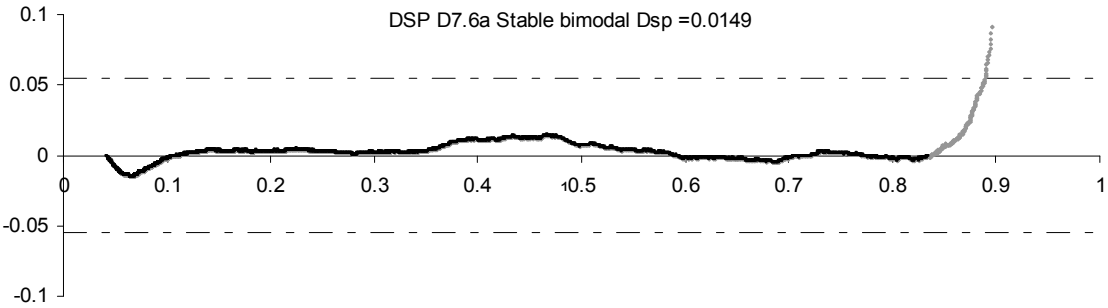

peak		Parameters of the Stable distribution			
D7.6a	%vol	α	β	γ	δ
1°	76	1.6	0.3	37	280
2°	24				206

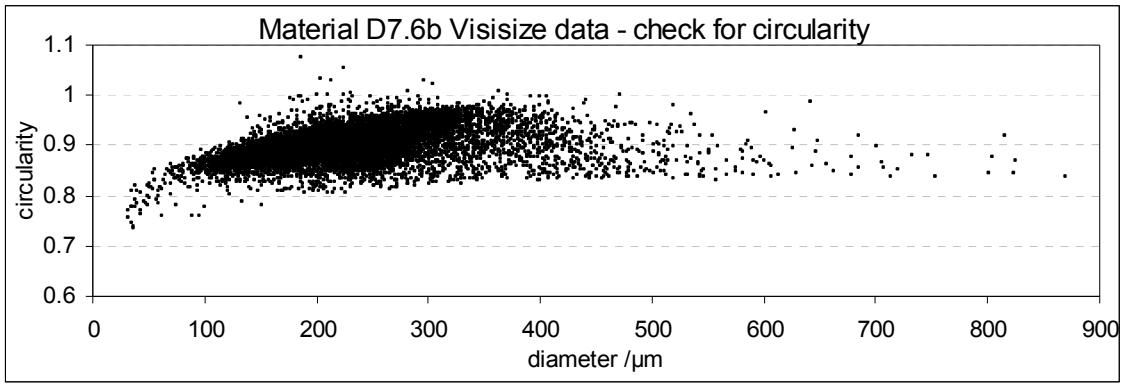
Material D7.6b Visisize data - check for circularity
circularity
1.1
1
0.9
0.8
0.7
0.6
0
100
200
300
400
500
600
700
800
900
diameter /µm

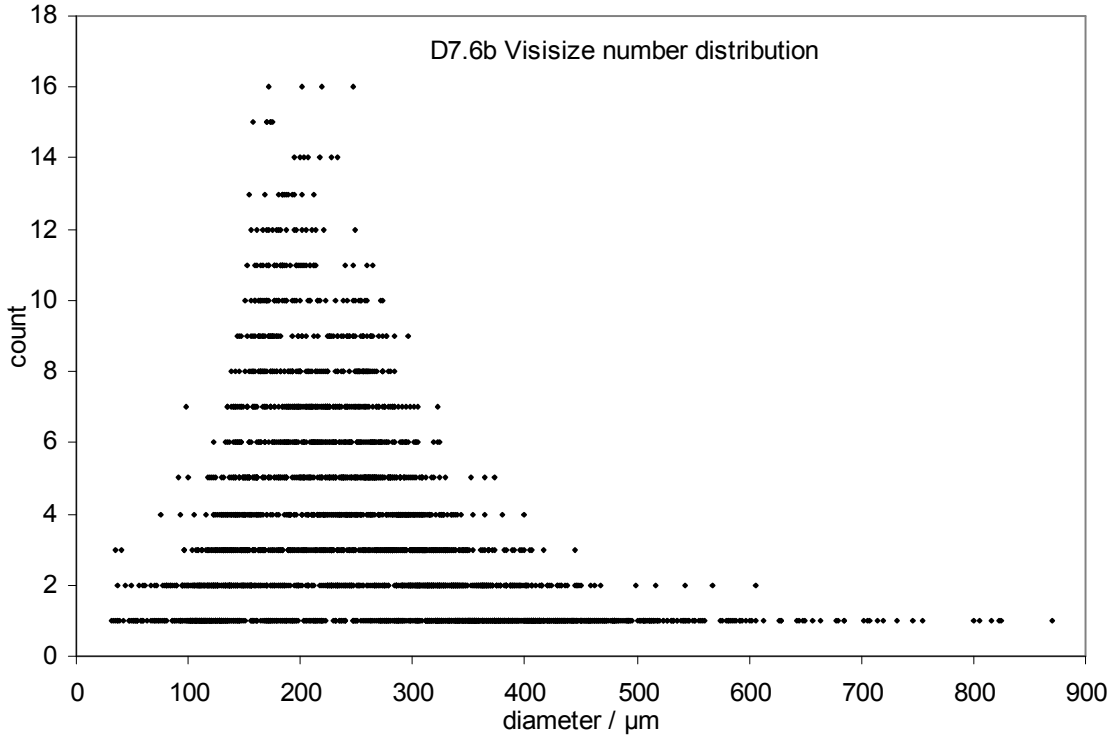
D7.6b Visisize number distribution
count
18
16
14
12
10
8
6
4
2
0
0
100
200
300
400
500
600
700
800
900
diameter / µm

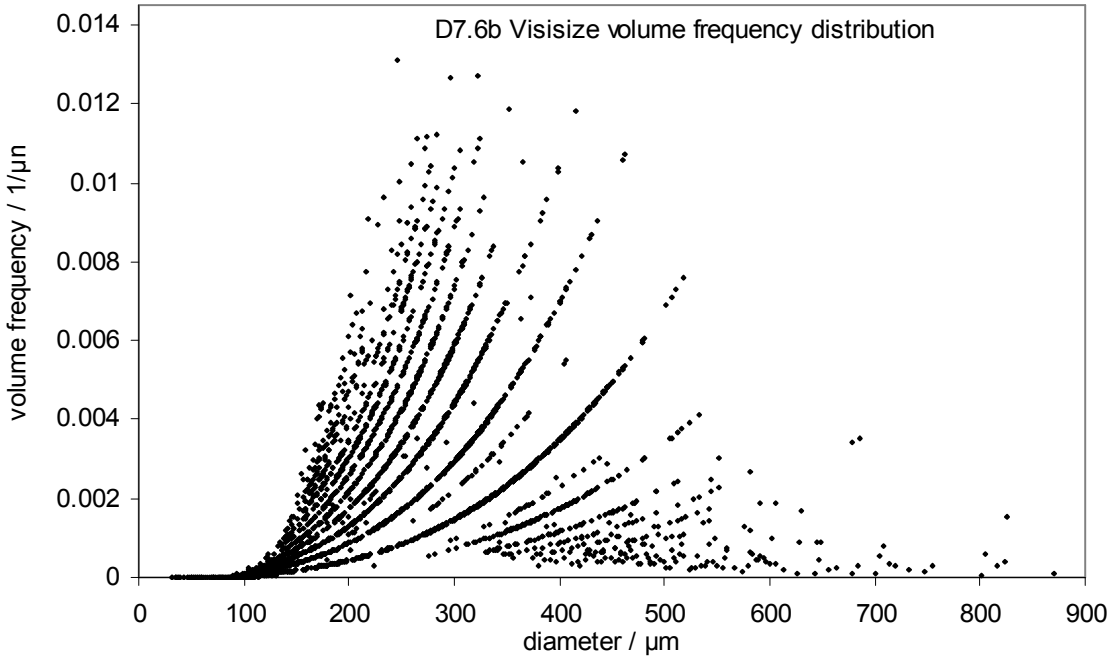
D7.6b Visisize volume frequency distribution
volume frequency / 1/µn
0.014
0.012
0.01
0.008
0.006
0.004
0.002
0
0
100
200
300
400
500
600
700
800
900
diameter / µm

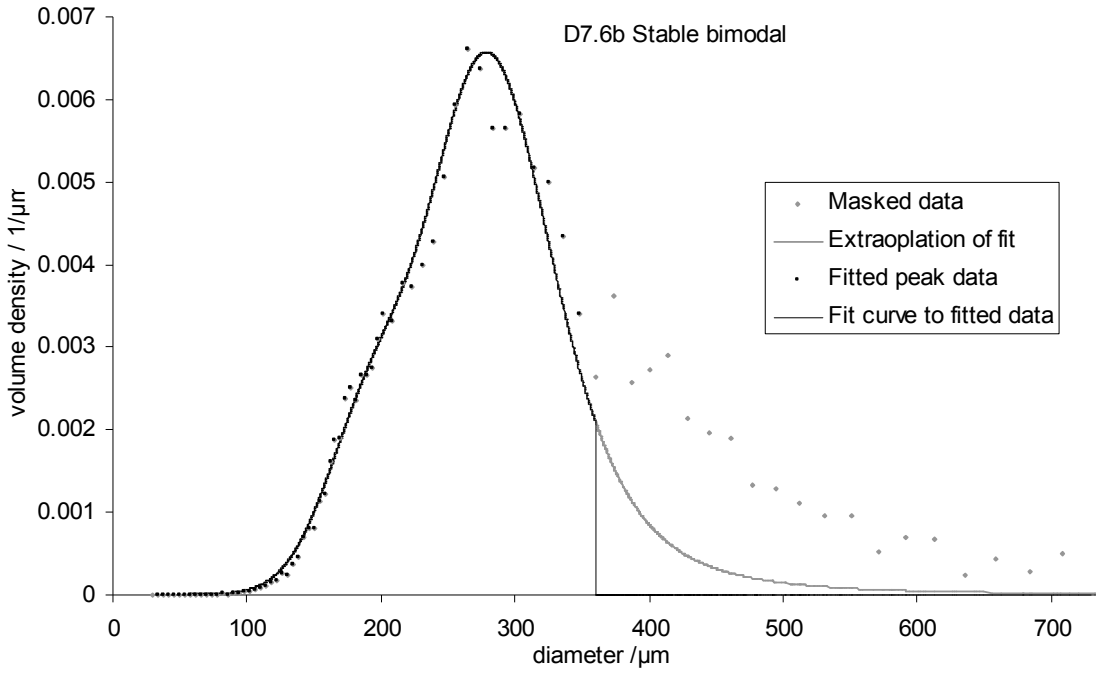

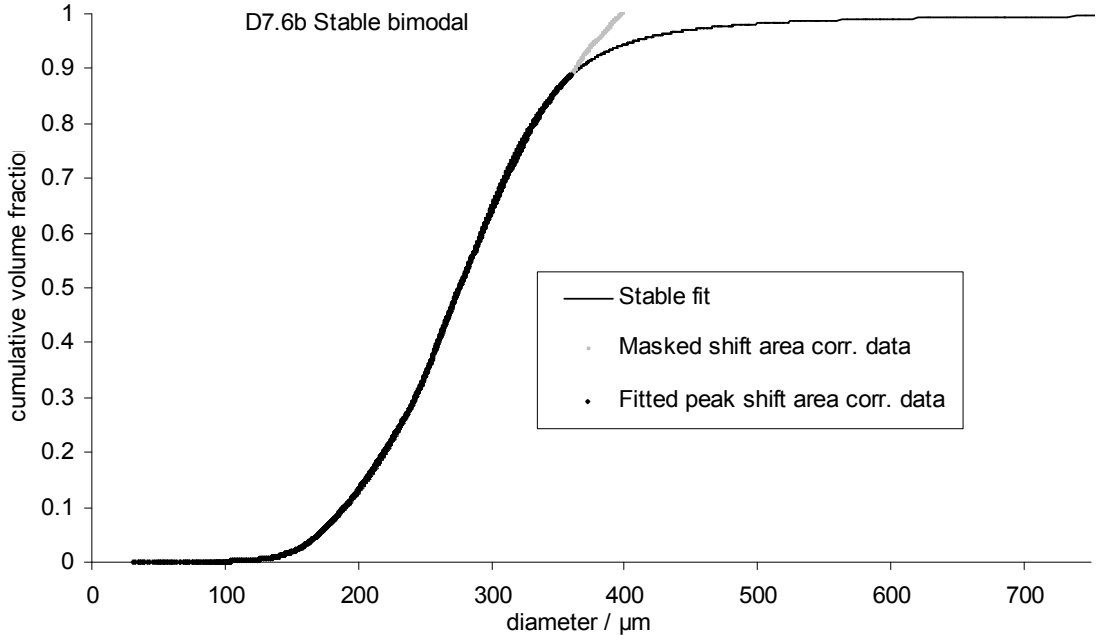

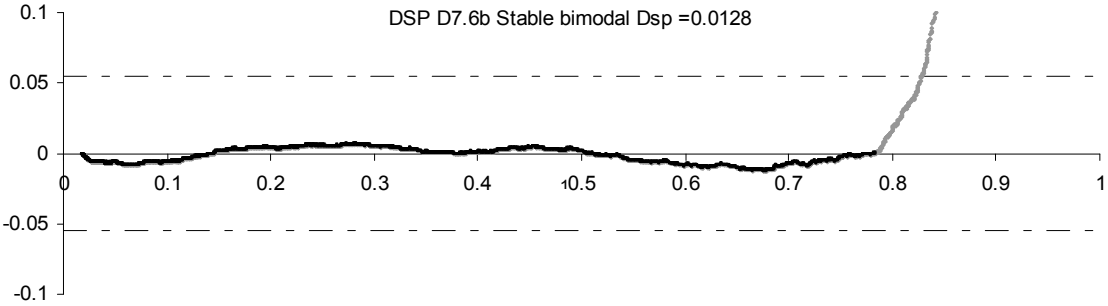

peak		Parameters of the Stable distribution			
D7.6b	%vol	α	β	γ	δ
1°	68	1.6	0.9	45	285
2°	32				205

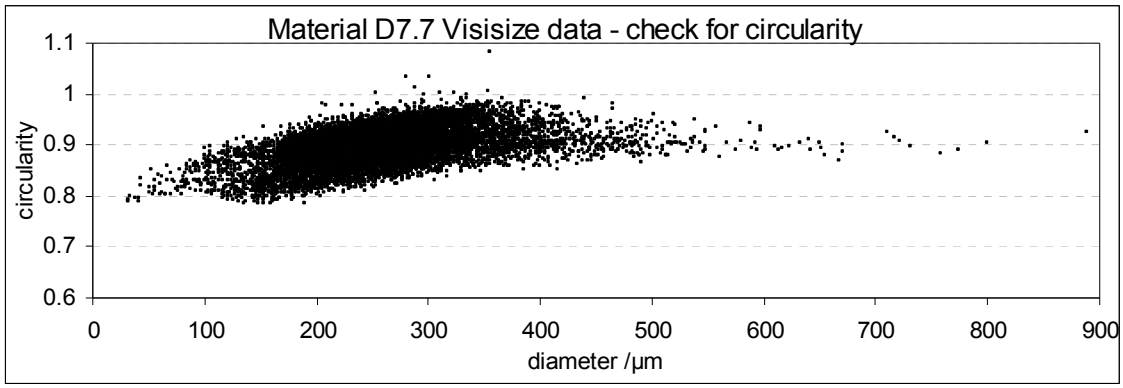
Material D7.7 Visisize data - check for circularity
circularity
1.1
1
0.9
0.8
0.7
0.6
0
100
200
300
400
500
600
700
800
900
diameter /µm

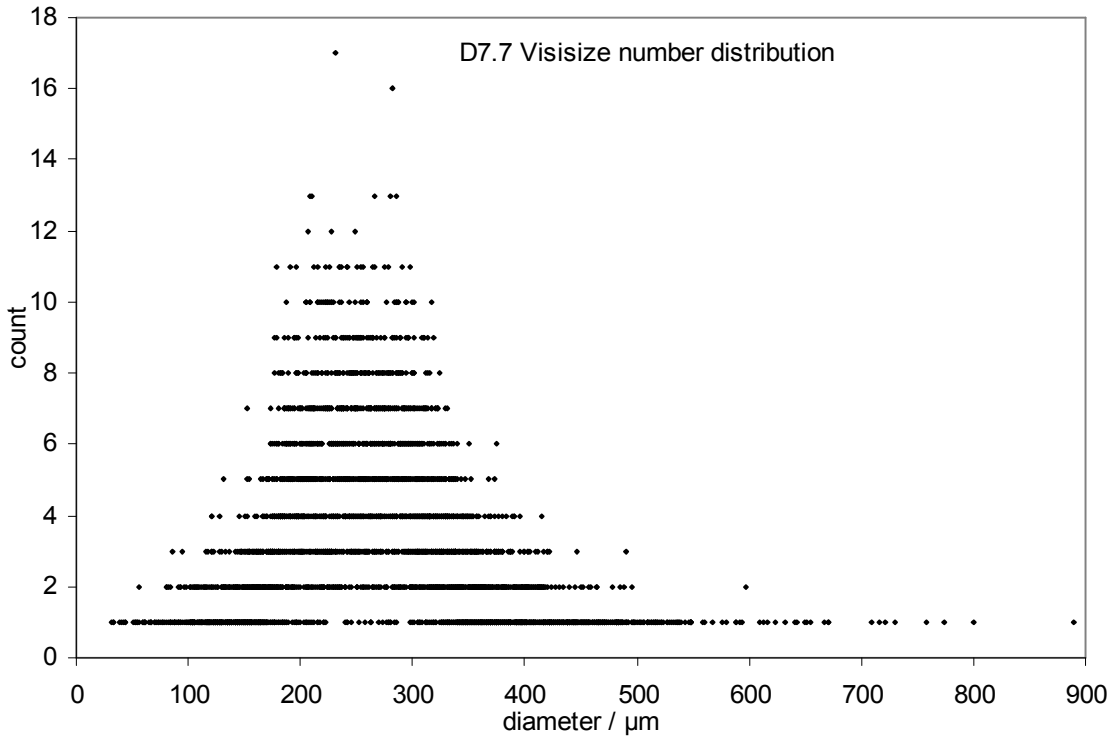
D7.7 Visisize number distribution
count
18
16
14
12
10
8
6
4
2
0
0
100
200
300
400
500
600
700
800
900
diameter / µm

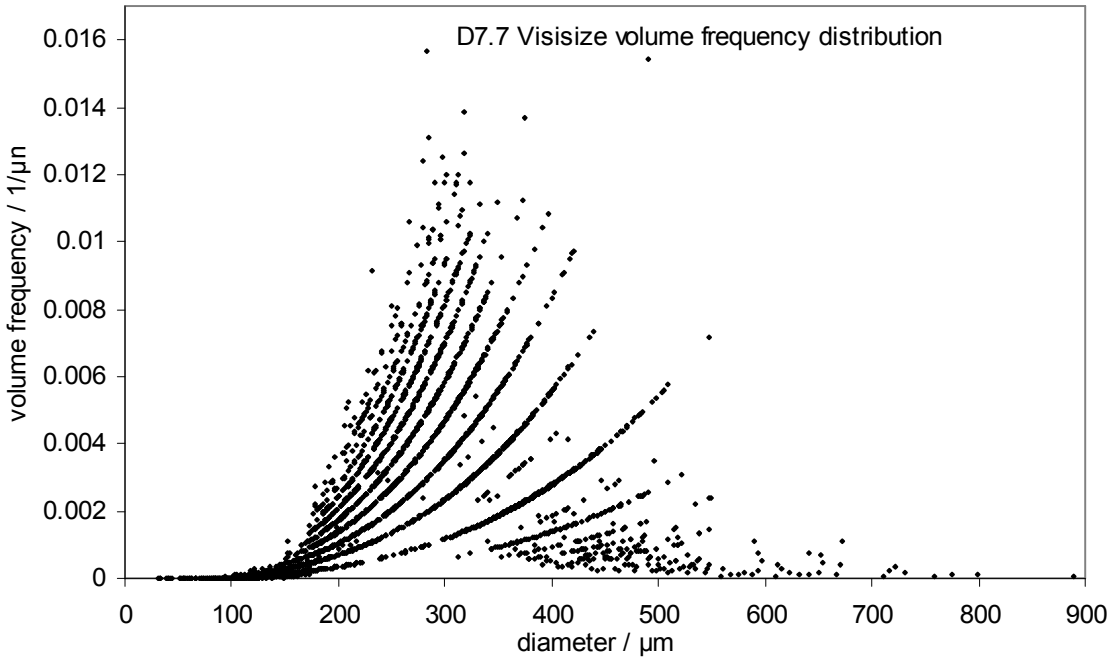
D7.7 Visisize volume frequency distribution
volume frequency / 1/µn
0.016
0.014
0.012
0.01
0.008
0.006
0.004
0.002
0
0
100
200
300
400
500
600
700
800
900
diameter / µm

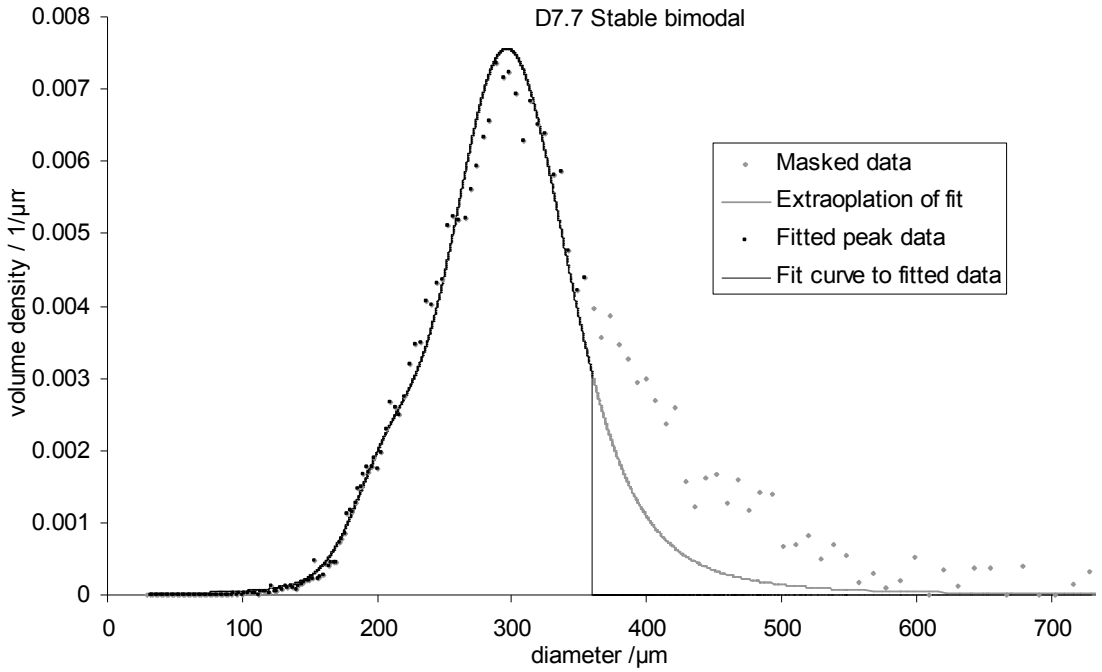

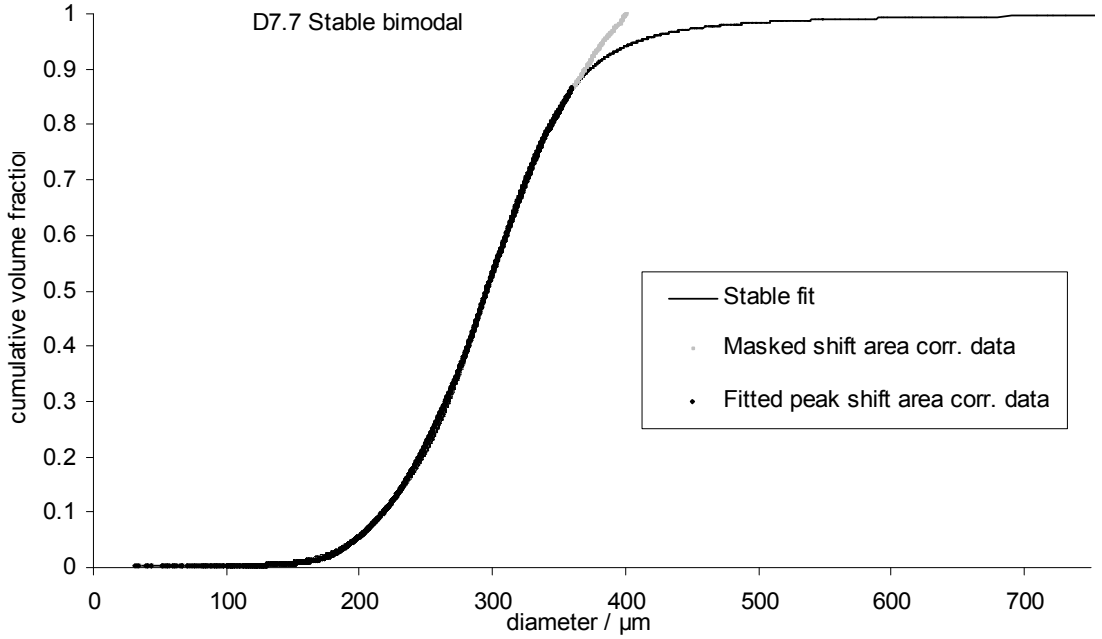

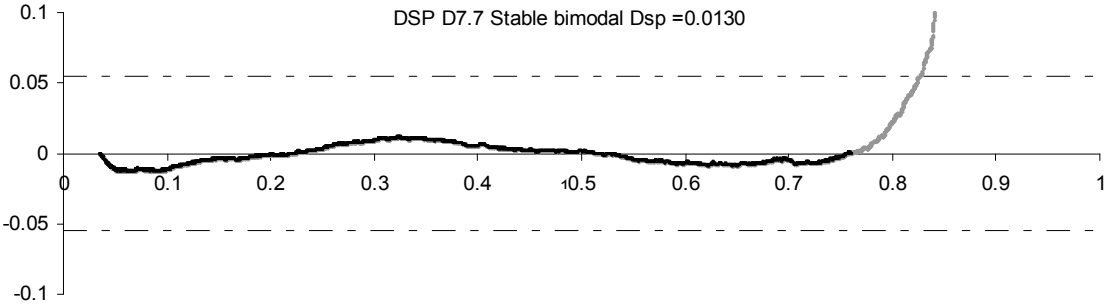

peak		Parameters of the Stable distribution			
D7.7	%vol	α	β	γ	δ
1°	88	1.6	0.5	45	297
2°	12			30	210

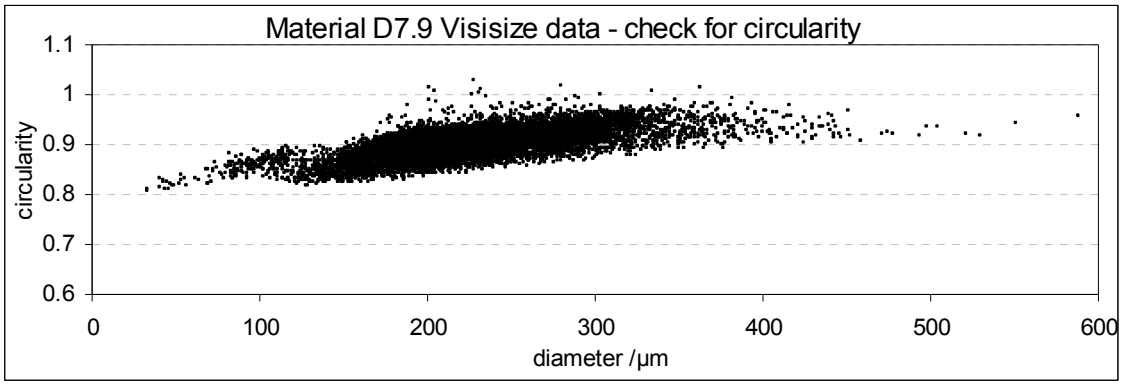
Material D7.9 Visisize data - check for circularity
circularity
1.1
1
0.9
0.8
0.7
0.6
0
100
200
300
400
500
600
diameter /µm

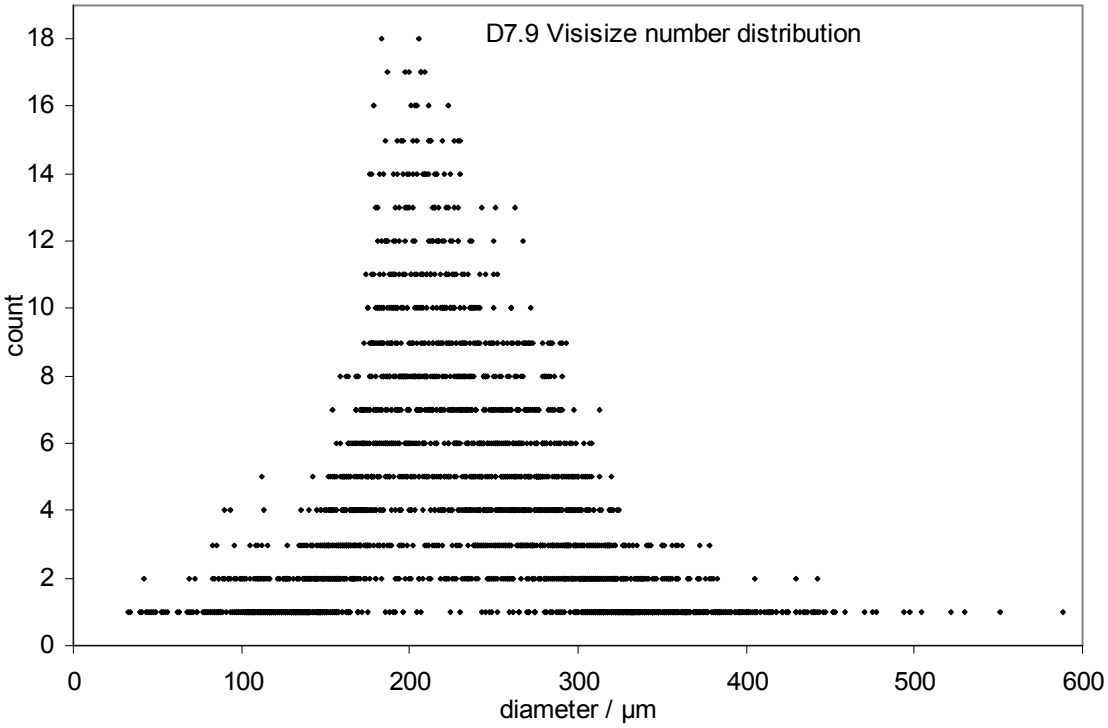
D7.9 Visisize number distribution
count
18
16
14
12
10
8
6
4
2
0
0
100
200
300
400
500
600
diameter / µm

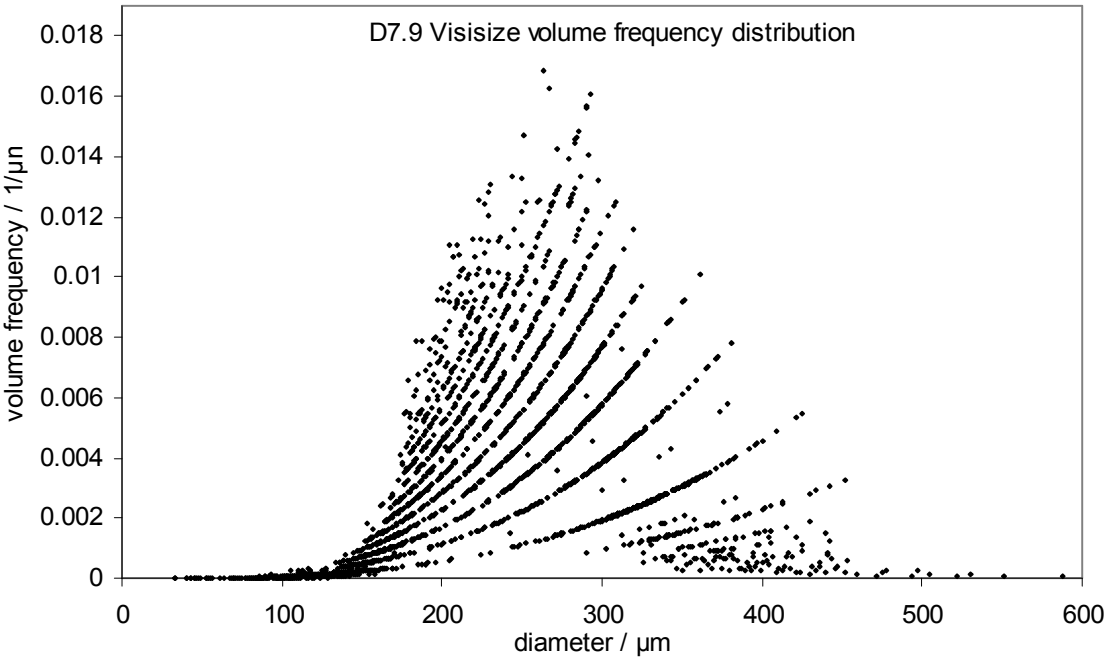
D7.9 Visisize volume frequency distribution
volume frequency / 1/µn
0.018
0.016
0.014
0.012
0.01
0.008
0.006
0.004
0.002
0
0
100
200
300
400
500
600
diameter / µm

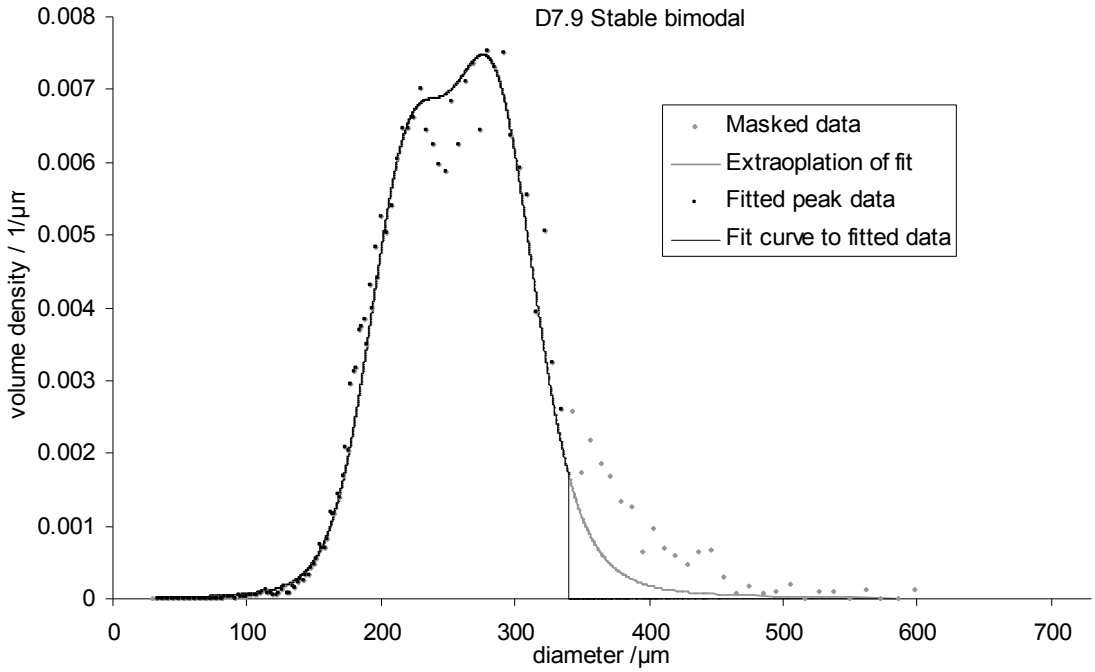

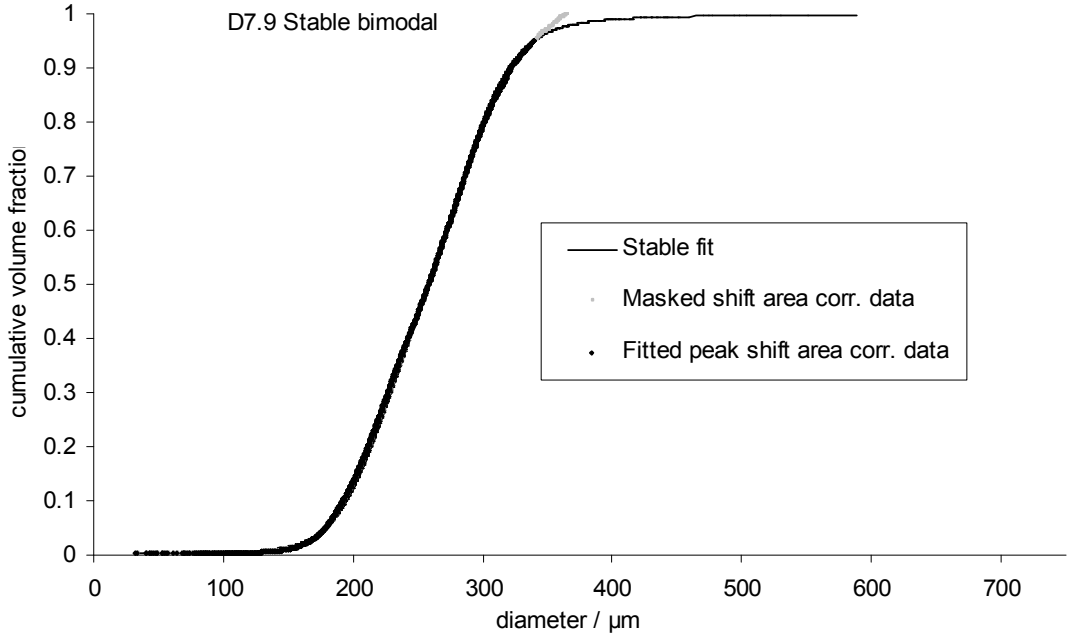

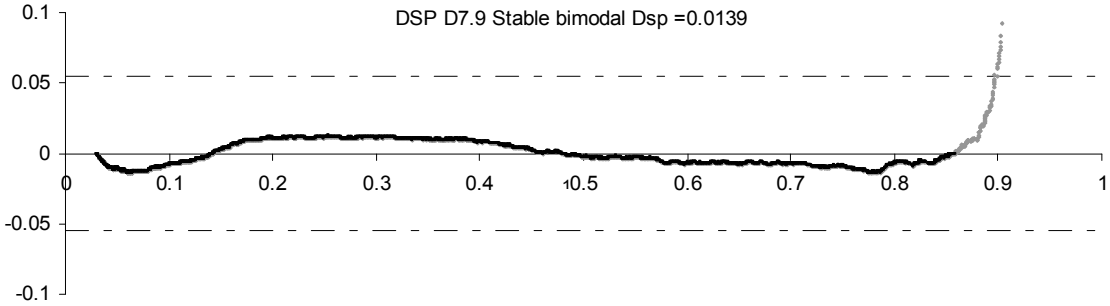

peak		Parameters of the Stable distribution			
D7.7	%vol	α	β	γ	δ
1°	52	1.7	0.3	32	285
2°	48				221

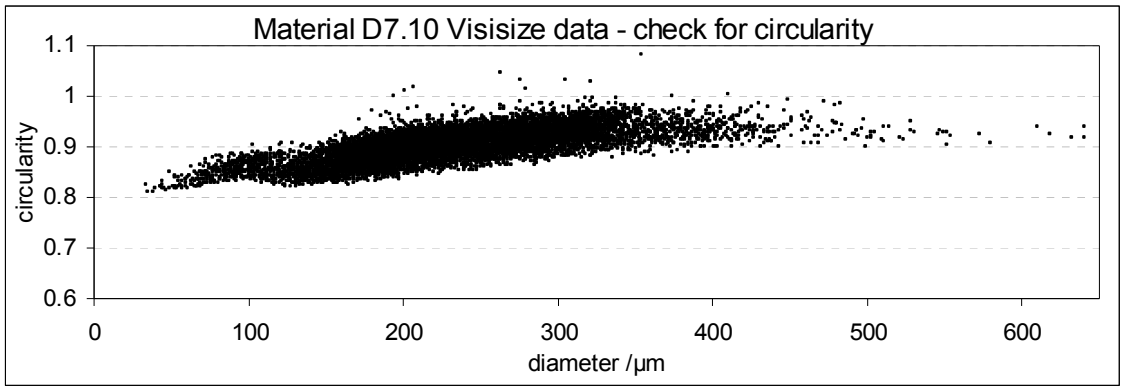
Material D7.10 Visisize data - check for circularity
circularity
1.1
1
0.9
0.8
0.7
0.6
0
100
200
300
400
500
600
diameter /µm

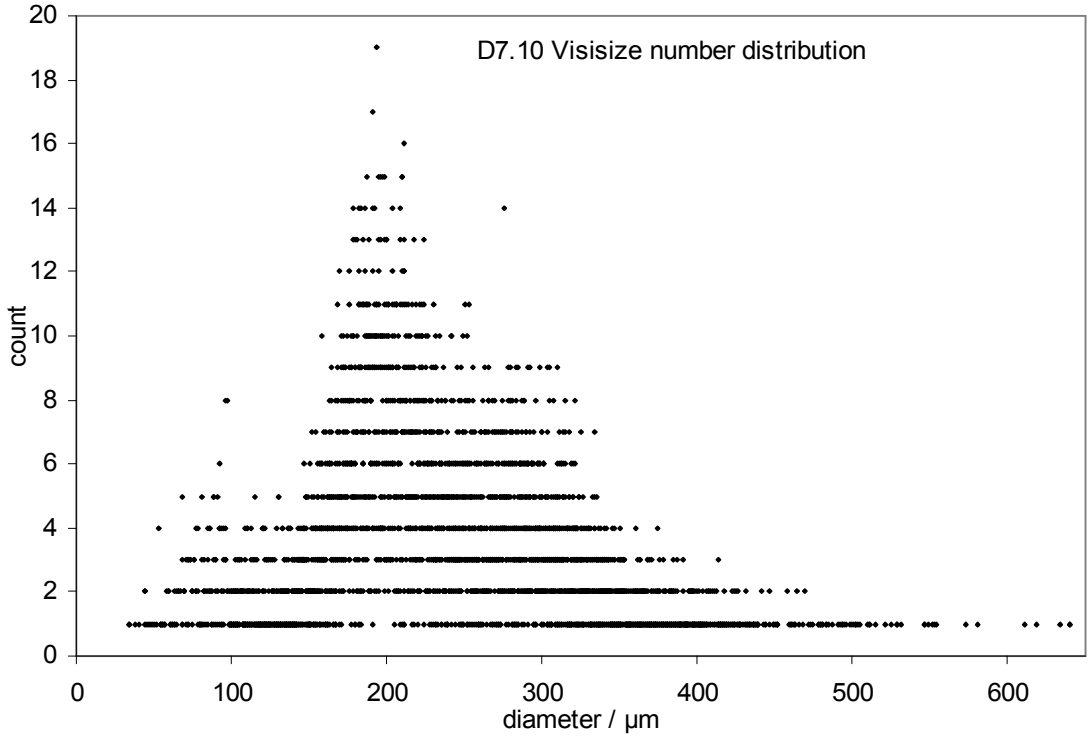
D7.10 Visisize number distribution
count
20
18
16
14
12
10
8
6
4
2
0
0
100
200
300
400
500
600
diameter / µm

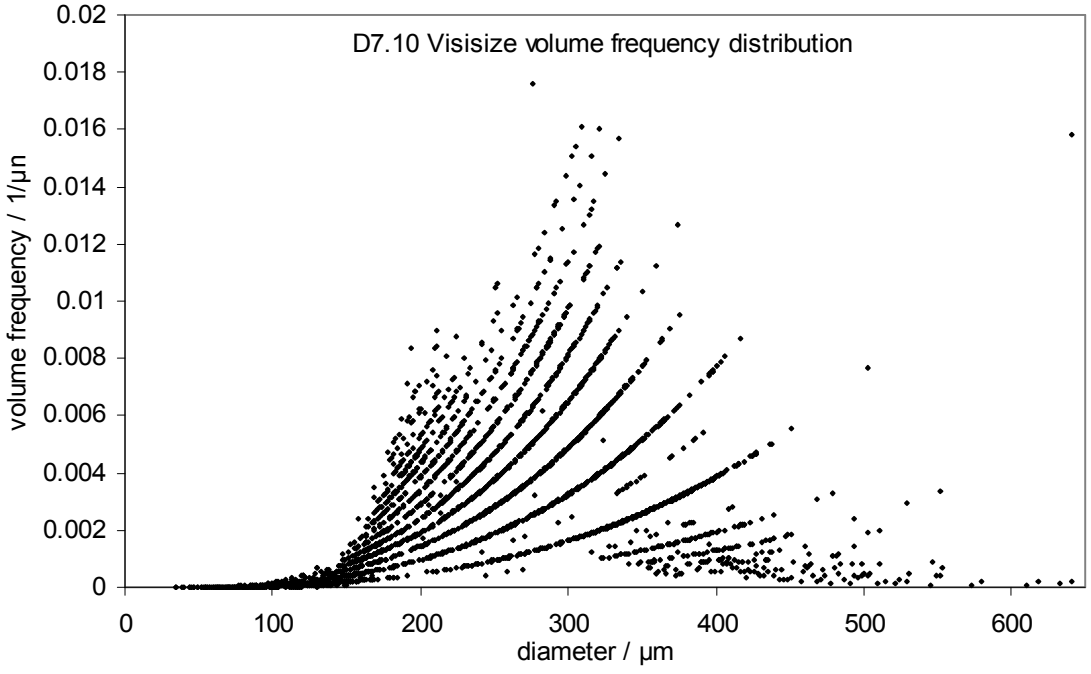
D7.10 Visisize volume frequency distribution
volume frequency / 1/µn
0.02
0.018
0.016
0.014
0.012
0.01
0.008
0.006
0.004
0.002
0
0
100
200
300
400
500
600
diameter / µm

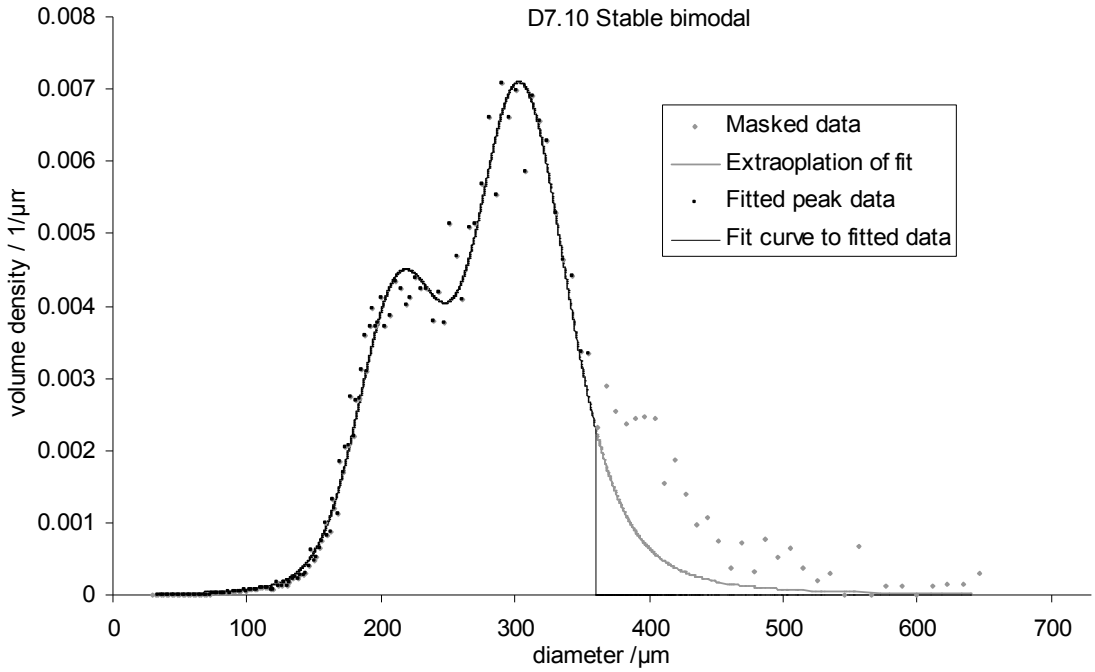

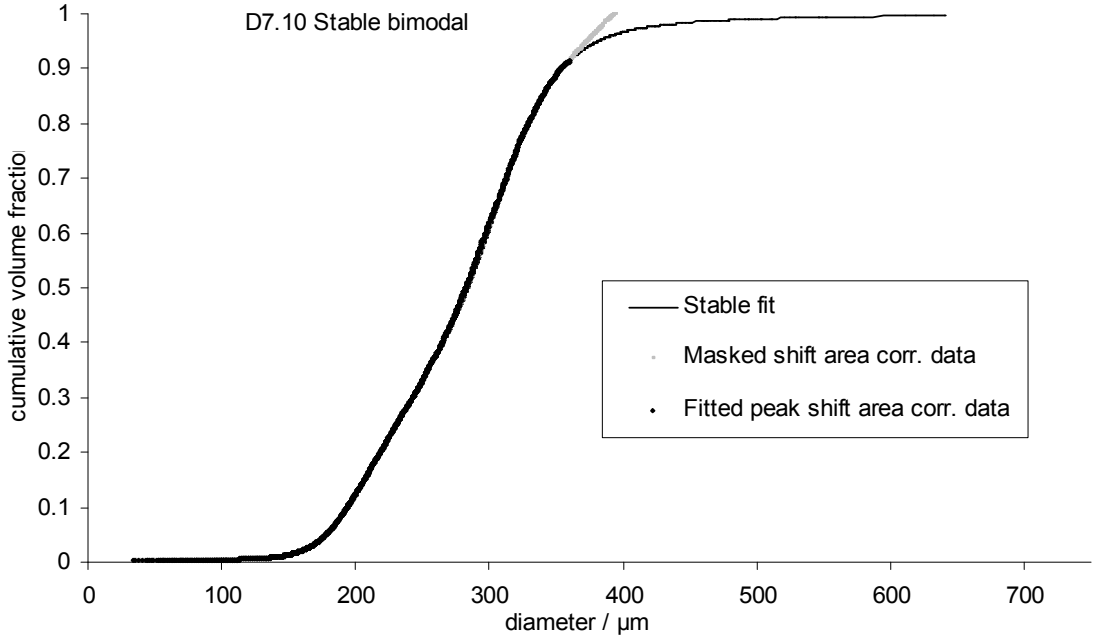

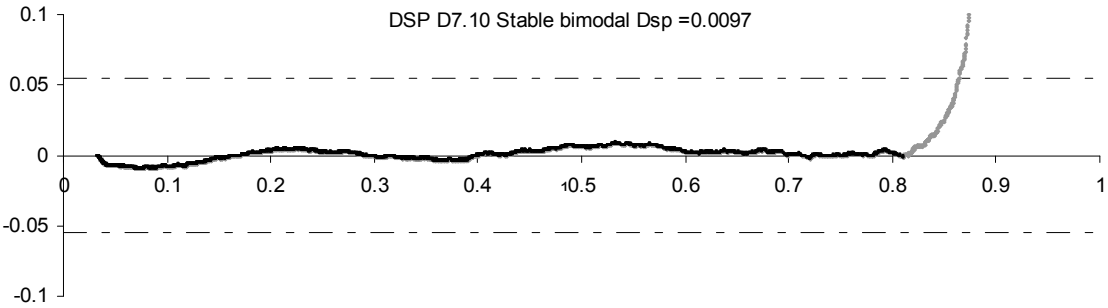

peak D7.10	%vol	Parameters of the Stable distribution α	β	γ	δ
1°	61	1.6	0.5	35	305
2°	39				215

Dataset D7.17 is from a rotary atomiser comparison experiment. The raw data volume distribution indicates that there was some agglomeration, but both the number distribution and the histogram indicate that it was relatively unimportant. Hence a unimodal fit is acceptable. A log-normal distribution has been used and fits well. A lower bound of 45μm has been used, eliminating the tail of surprisingly high count near to the limit of the instrument resolution, which is believed to be an artefact. Emphasising the unimportance of agglomeration to this dataset, it can be seen in the graphs there is very little difference in the best fit width parameter whether or not the large size data is included or excluded.

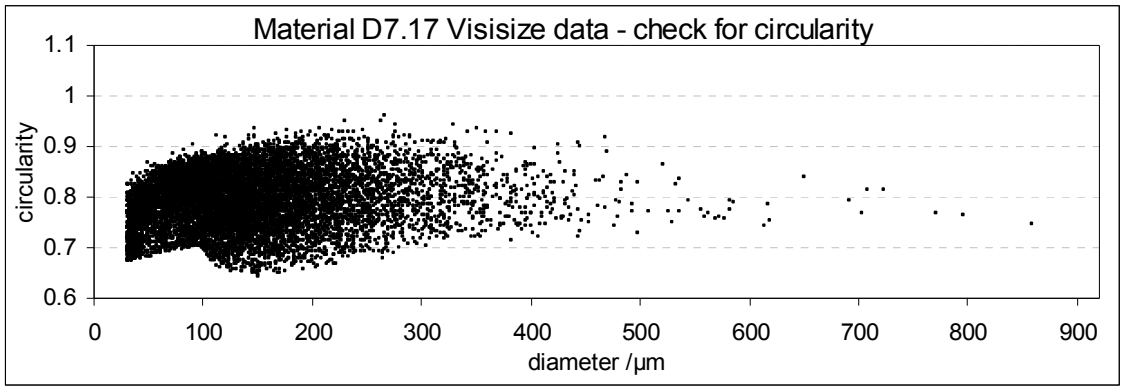
Material D7.17 Visisize data - check for circularity
circularity
1.1
1
0.9
0.8
0.7
0.6
0
100
200
300
400
500
600
700
800
900
diameter /µm

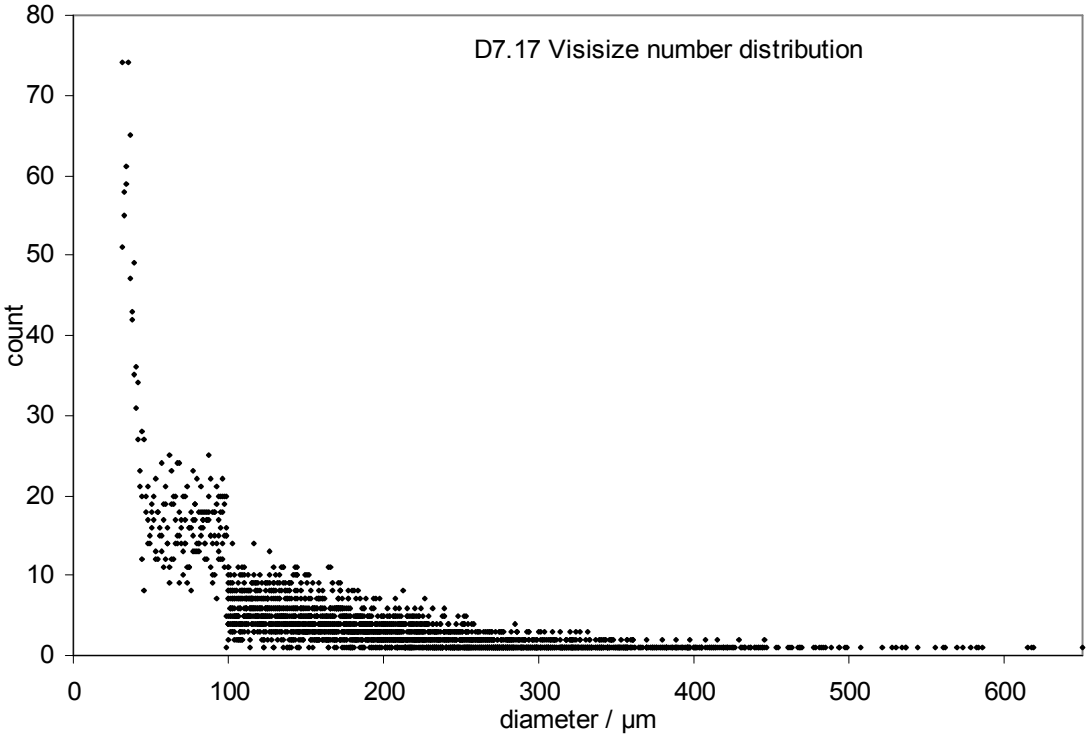
D7.17 Visisize number distribution
count
80
70
60
50
40
30
20
10
0
0
100
200
300
400
500
600
diameter / µm

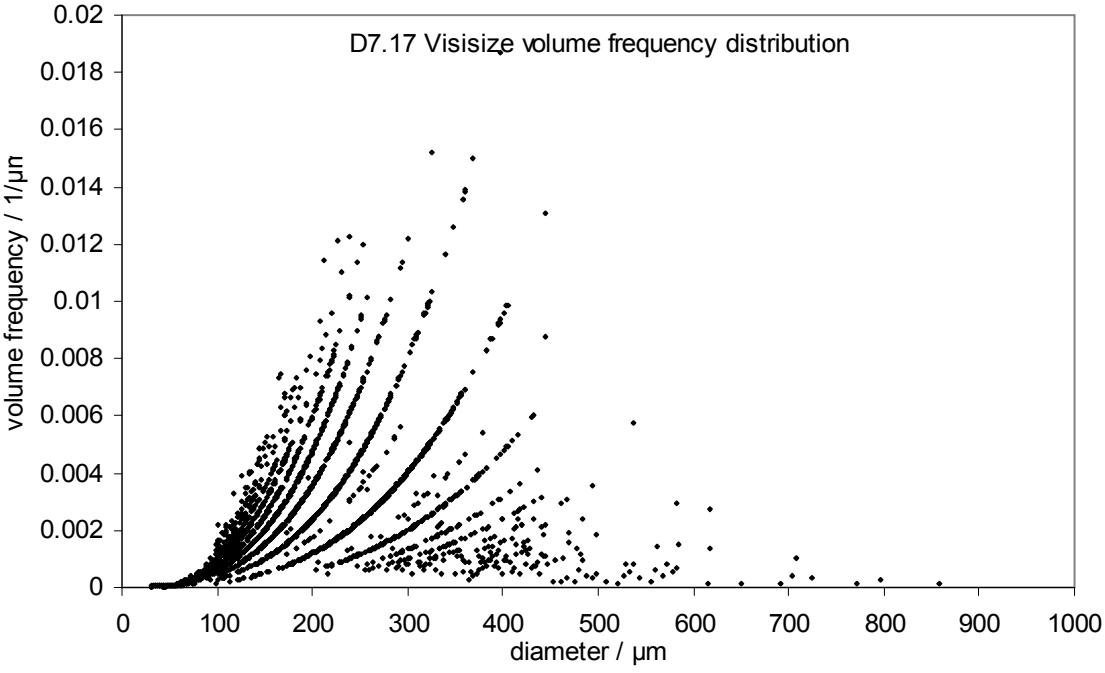
D7.17 Visisize volume frequency distribution
volume frequency / 1/µm
0.02
0.018
0.016
0.014
0.012
0.01
0.008
0.006
0.004
0.002
0
0
100
200
300
400
500
600
700
800
900
1000
diameter / µm

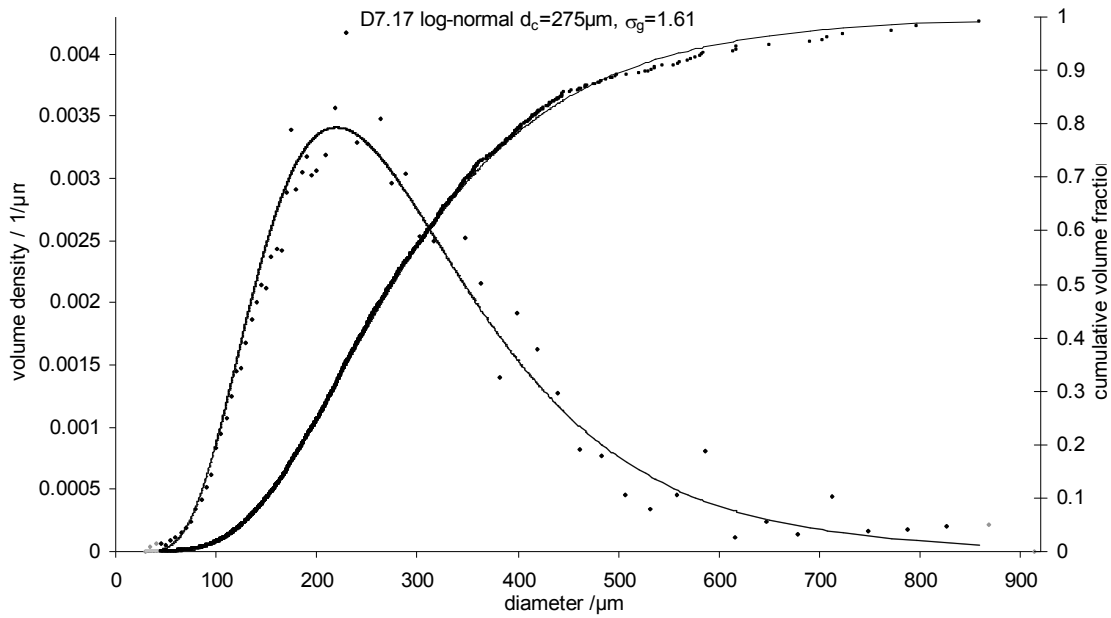
D7.17 log-normal d_c=275µm, σ_g=1.61
volume density / 1/µm
cumulative volume fractio
diameter /µm
0
0.0005
0.001
0.0015
0.002
0.0025
0.003
0.0035
0.004
0.1
0.2
0.3
0.4
0.5
0.6
0.7
0.8
0.9
100
200
300
400
500
600
700
800
900

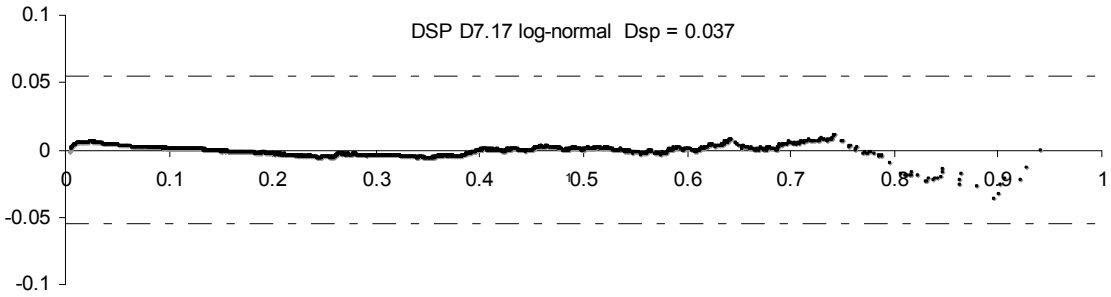
DSP D7.17 log-normal Dsp = 0.037
0.1
0.05
0
-0.05
-0.1
0.1
0.2
0.3
0.4
0.5
0.6
0.7
0.8
0.9
1

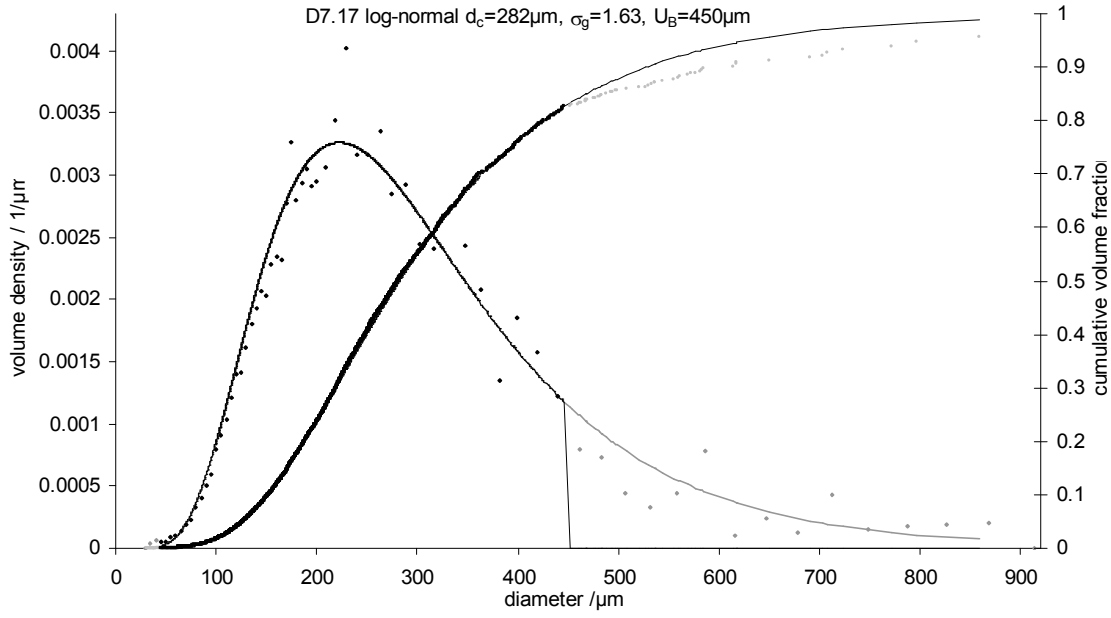
D7.17 log-normal d_c=282µm, σ_g=1.63, U_B=450µm
volume density / 1/µm
cumulative volume fractio
diameter /µm
0
0.0005
0.001
0.0015
0.002
0.0025
0.003
0.0035
0.004
0.1
0.2
0.3
0.4
0.5
0.6
0.7
0.8
0.9
100
200
300
400
500
600
700
800
900

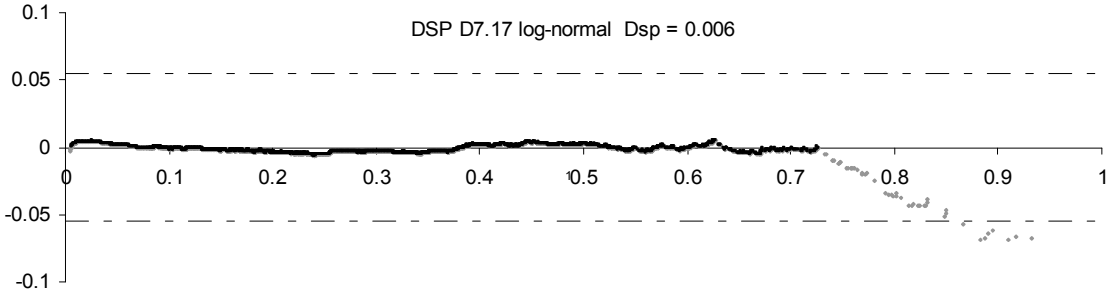
DSP D7.17 log-normal Dsp = 0.006
0.1
0.05
0
-0.05
-0.1
0.1
0.2
0.3
0.4
0.5
0.6
0.7
0.8
0.9
1

A.6.4 Material D8

Datasets D8 are particularly noisy. Both the number and the volume frequency distributions suggest that there are a number of overlapping peaks. Nonetheless, reasonable Stable bimodal fits to the data have been obtained. It is possible to fit all four datasets with the same set of Stable parameters $S(\alpha, \beta, \gamma, \delta_1, \delta_2 : 2) = S(1.3, 0.3, 40, 330, 190 : 2)$ and the same volume ratio between the peaks $(v_1:v_2) = (71:29)$. However, the fits are more convincing with the parameters shown in the plots in the next few pages. The similar position of the peaks in all the datasets is surprising, as the experimental log records that D8.11 and D8.12 used a smaller orifice size than D8.9 and D8.10.

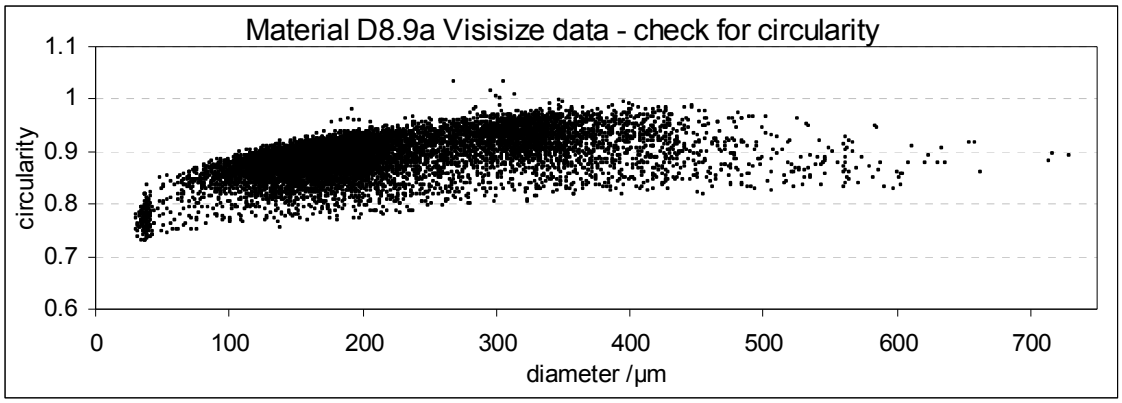
Material D8.9a Visisize data - check for circularity
circularity
1.1
1
0.9
0.8
0.7
0.6
0
100
200
300
400
500
600
700
diameter /µm

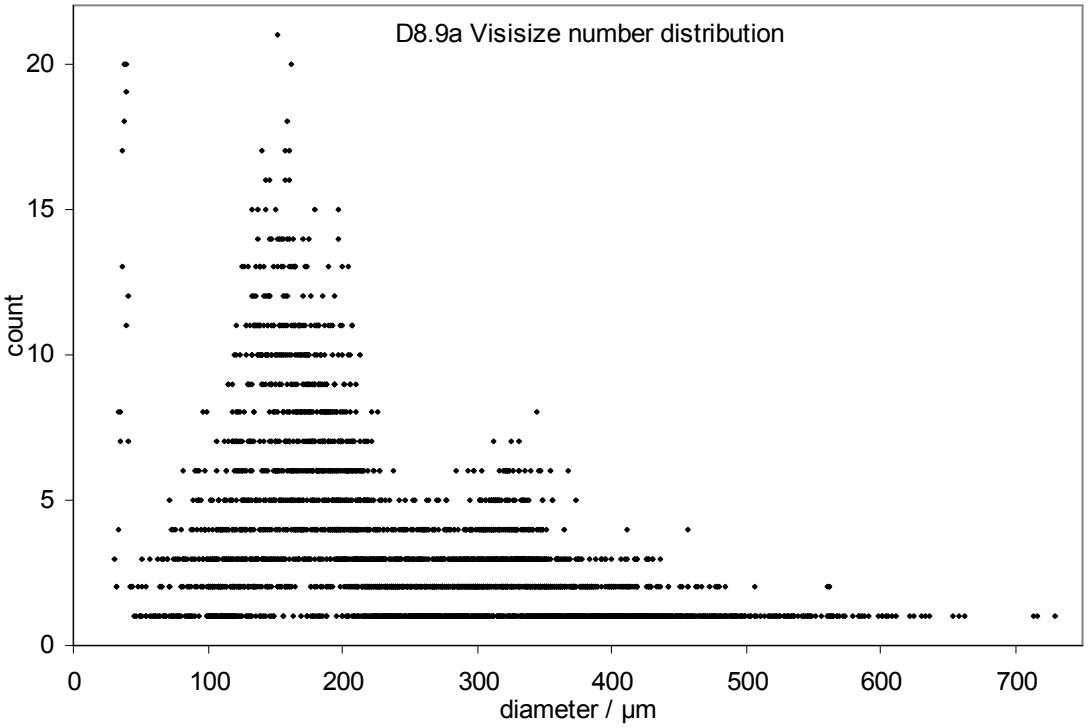
D8.9a Visisize number distribution
count
20
15
10
5
0
0
100
200
300
400
500
600
700
diameter / µm

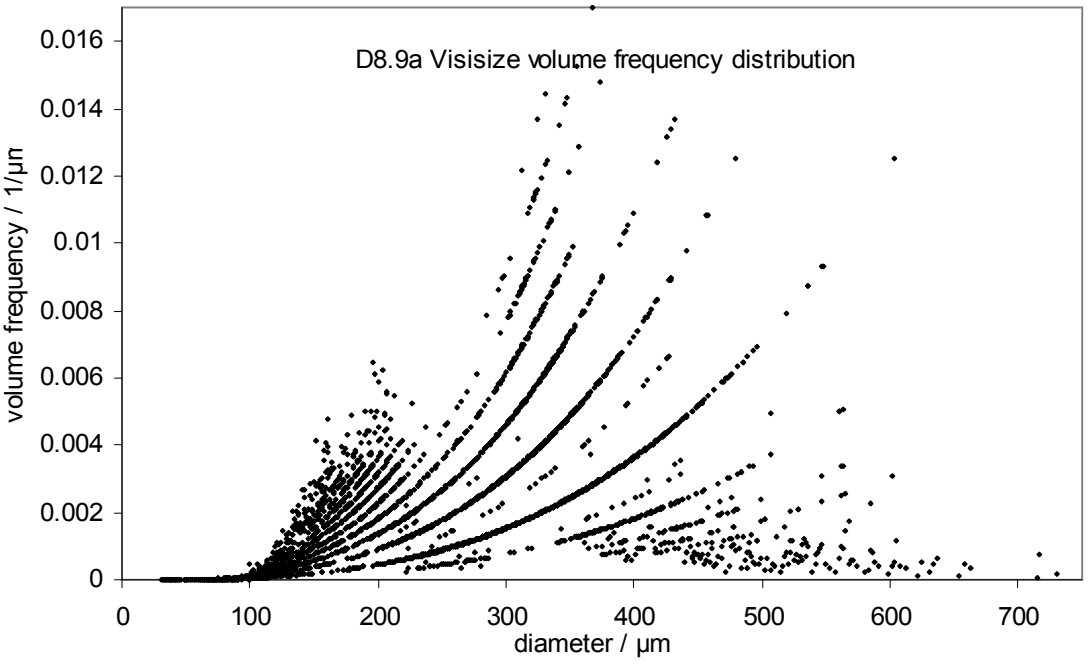
D8.9a Visisize volume frequency distribution
volume frequency / 1/µm
0.016
0.014
0.012
0.01
0.008
0.006
0.004
0.002
0
0
100
200
300
400
500
600
700
diameter / µm

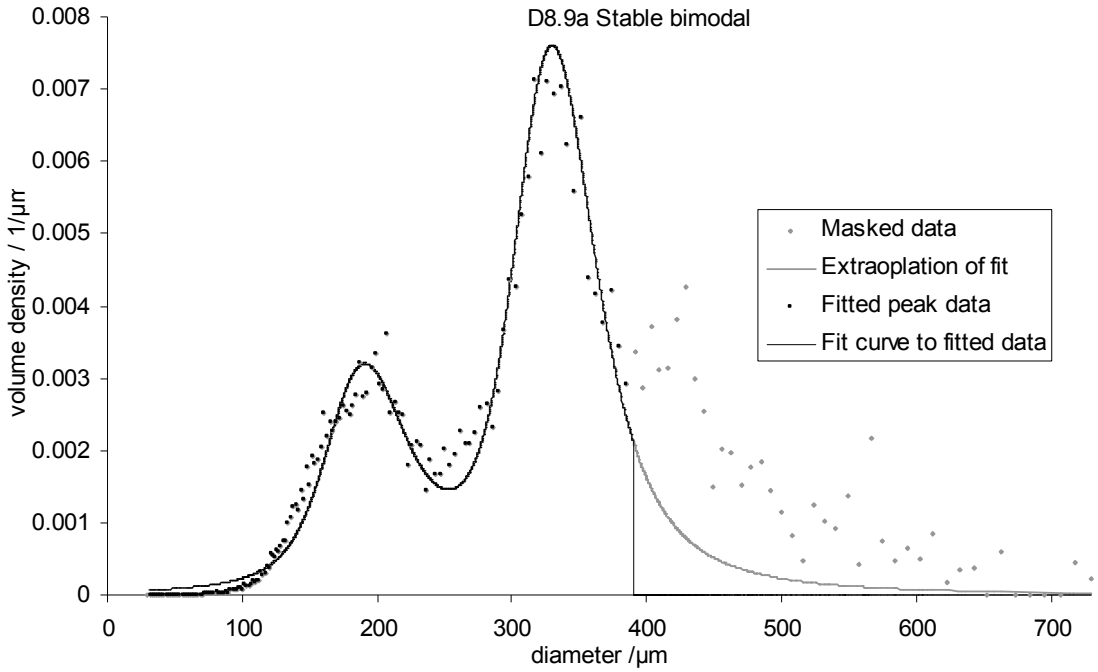

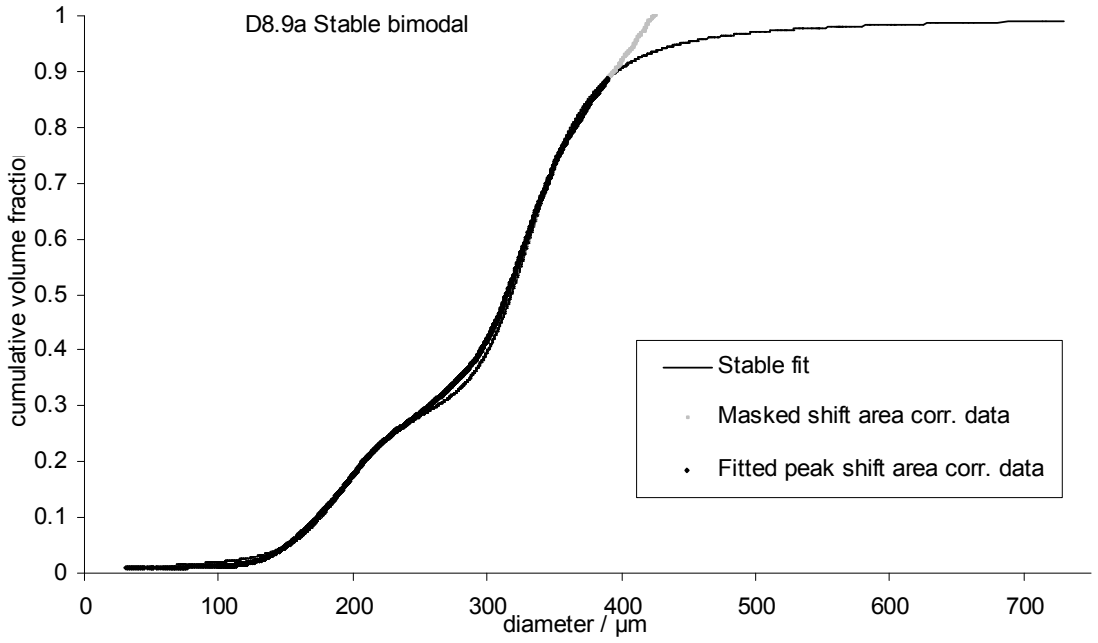

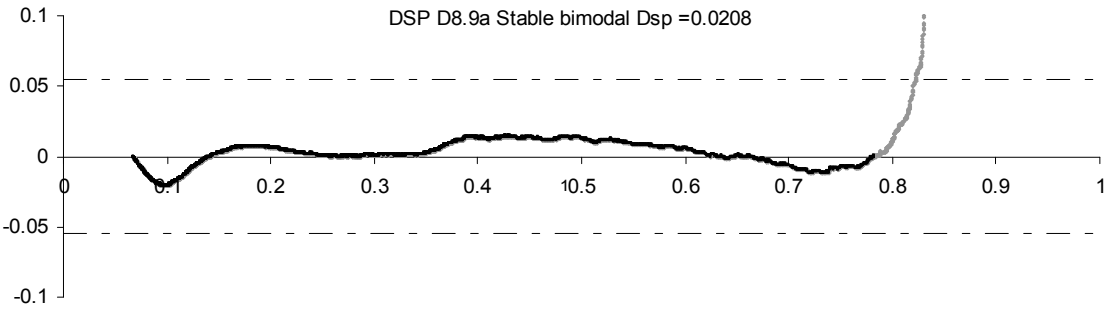

peak		Parameters of the Stable distribution			
D8.9a	%vol	α	β	γ	δ
1°	71	1.3	0.3	34	330
2°	29				190

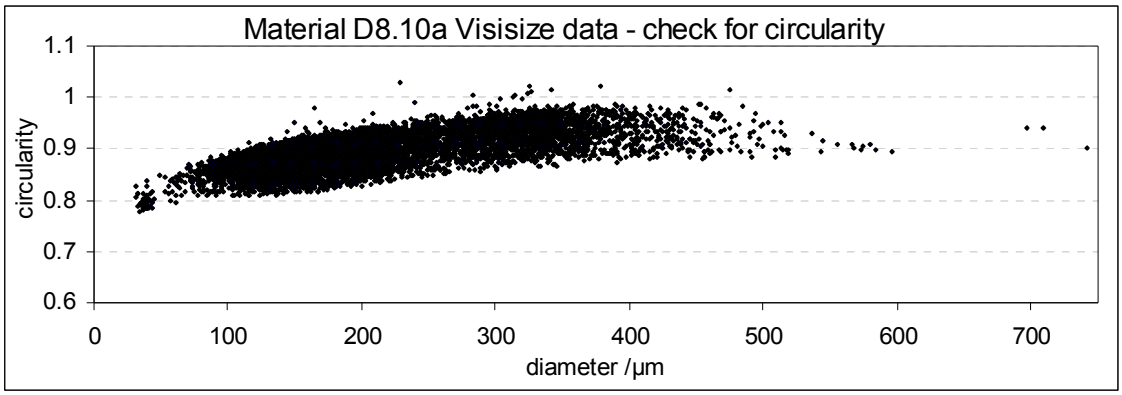
Material D8.10a Visisize data - check for circularity
circularity
1.1
1
0.9
0.8
0.7
0.6
0
100
200
300
400
500
600
700
diameter /µm

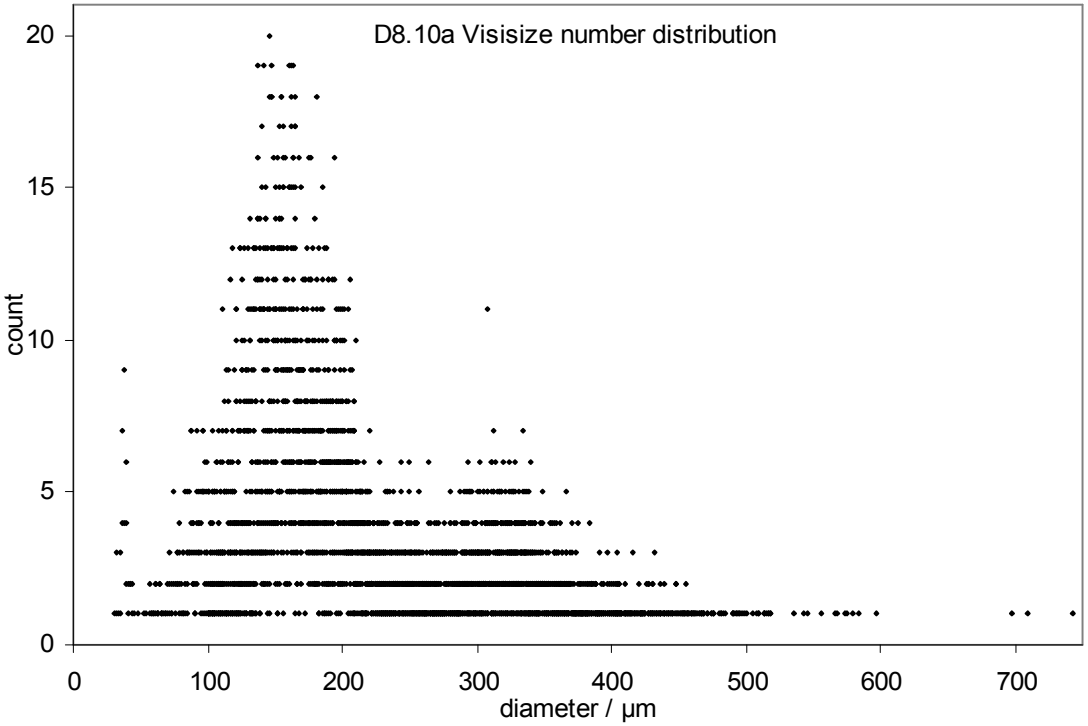
D8.10a Visisize number distribution
count
20
15
10
5
0
0
100
200
300
400
500
600
700
diameter / µm

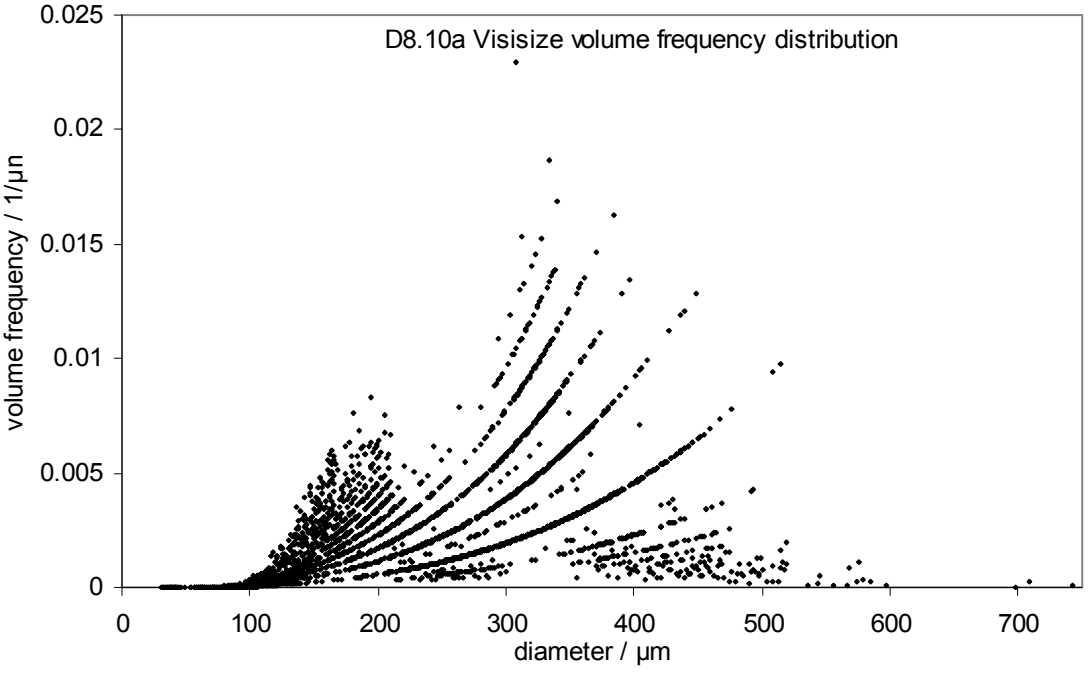
D8.10a Visisize volume frequency distribution
volume frequency / 1/µn
0.025
0.02
0.015
0.01
0.005
0
0
100
200
300
400
500
600
700
diameter / µm

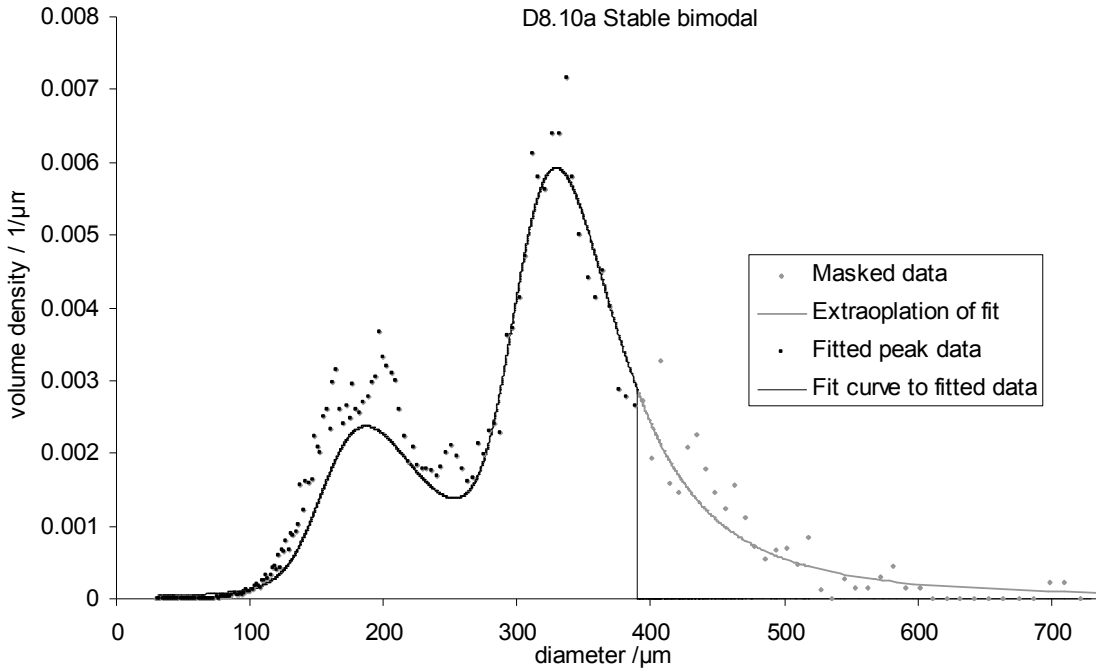

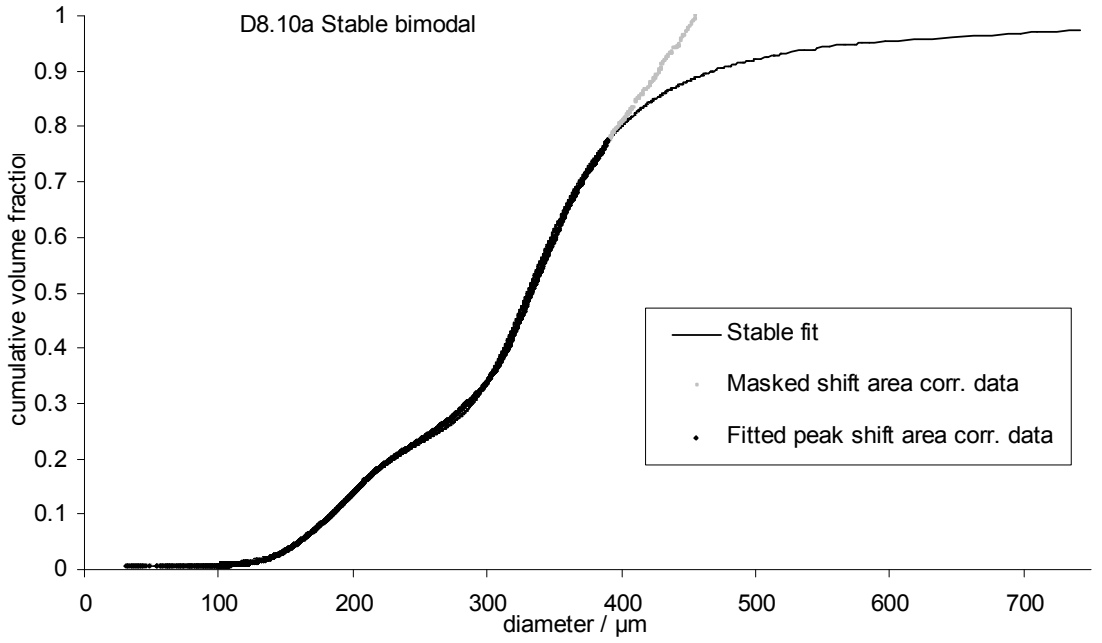

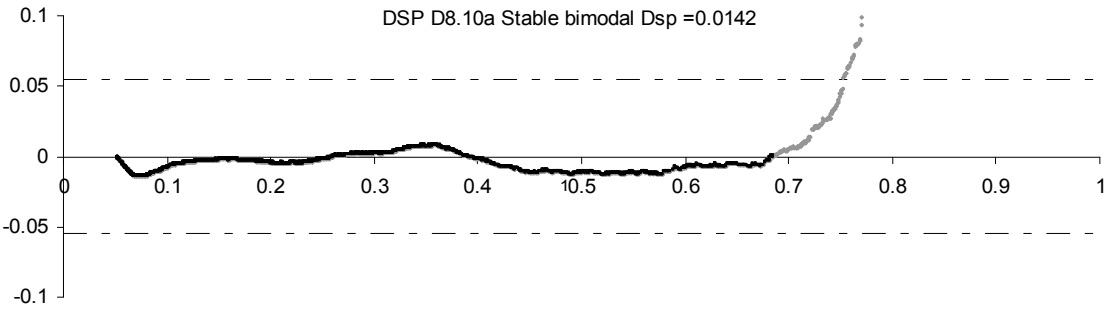

peak		Parameters of the Stable distribution			
D8.10a	%vol	α	β	γ	δ
1°	71	1.2	0.75	42	330
2°	29				186

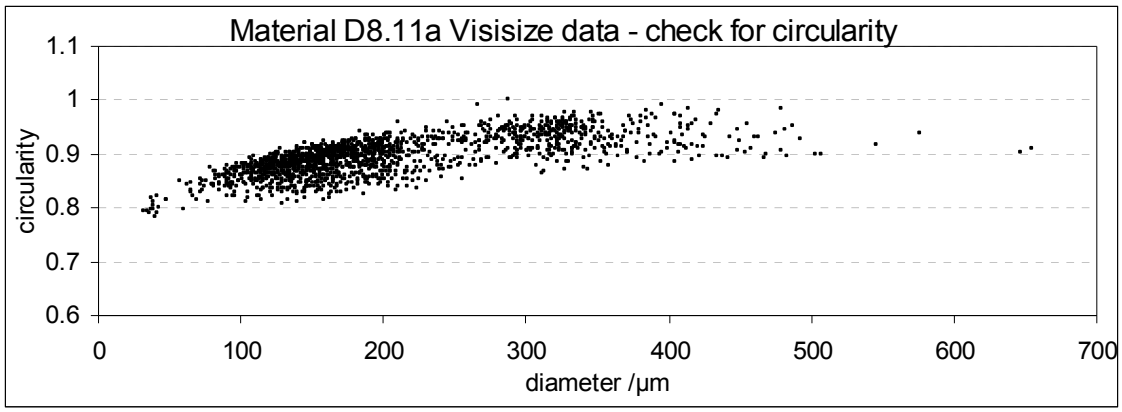
Material D8.11a Visisize data - check for circularity
circularity
1.1
1
0.9
0.8
0.7
0.6
0
100
200
300
400
500
600
700
diameter /µm

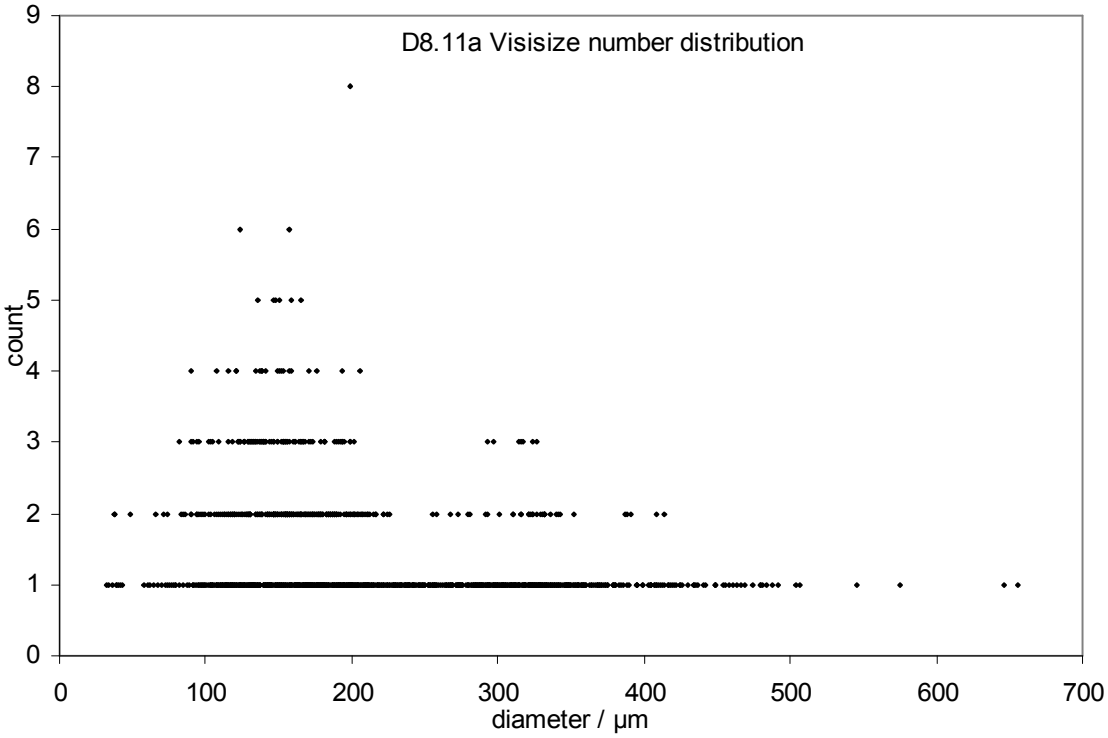
D8.11a Visisize number distribution
count
9
8
7
6
5
4
3
2
1
0
0
100
200
300
400
500
600
700
diameter / µm

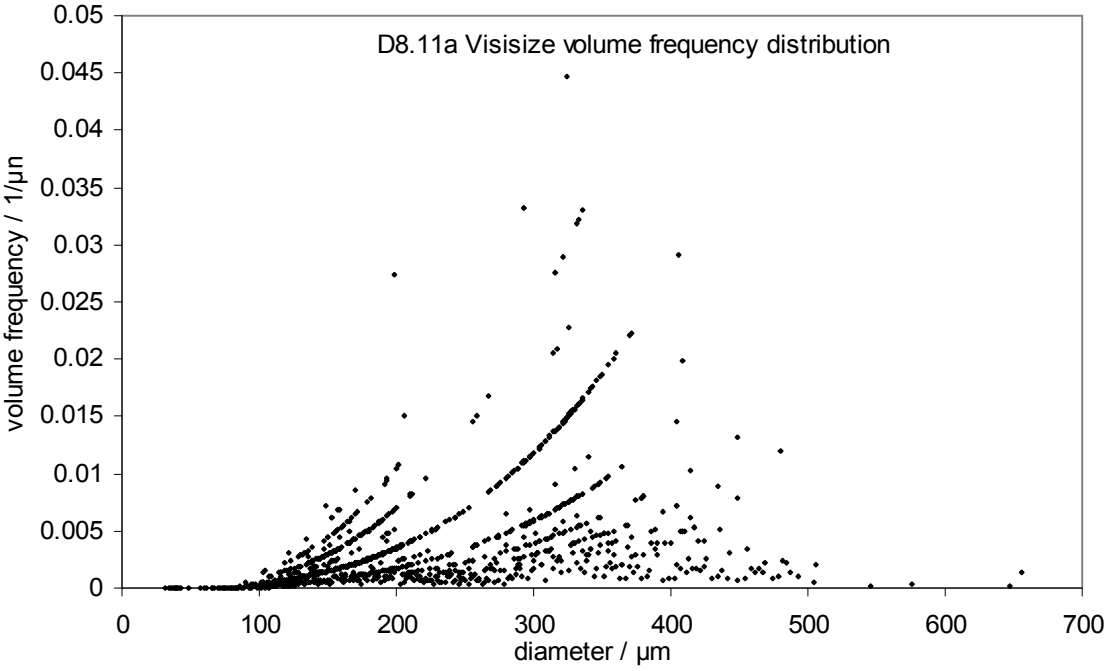
D8.11a Visisize volume frequency distribution
volume frequency / 1/µn
0.05
0.045
0.04
0.035
0.03
0.025
0.02
0.015
0.01
0.005
0
0
100
200
300
400
500
600
700
diameter / µm

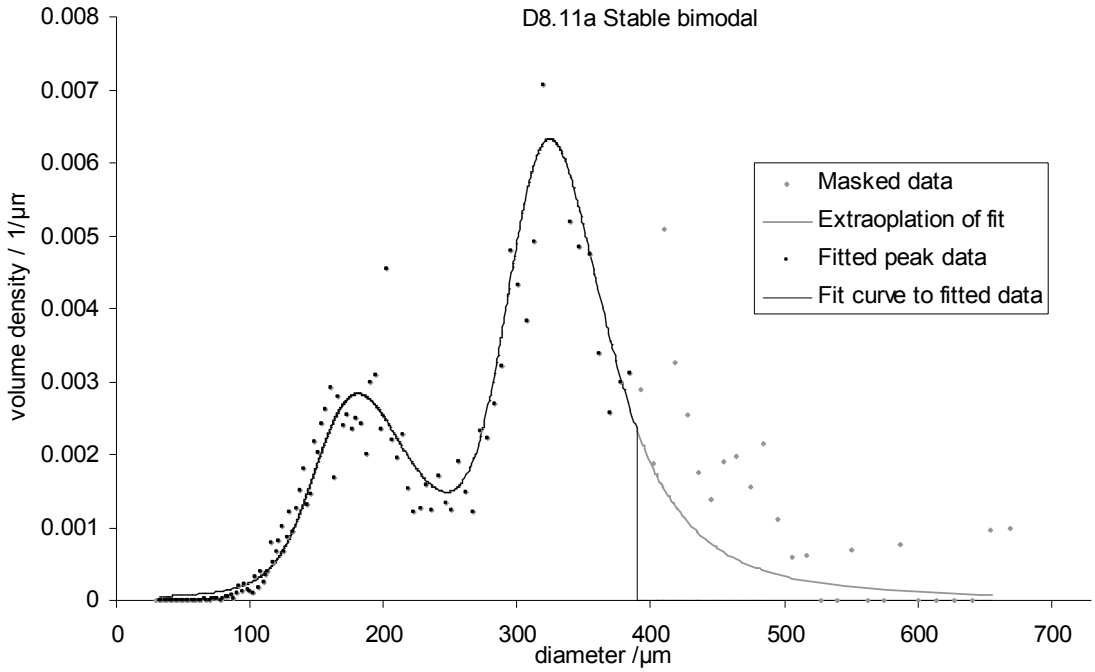

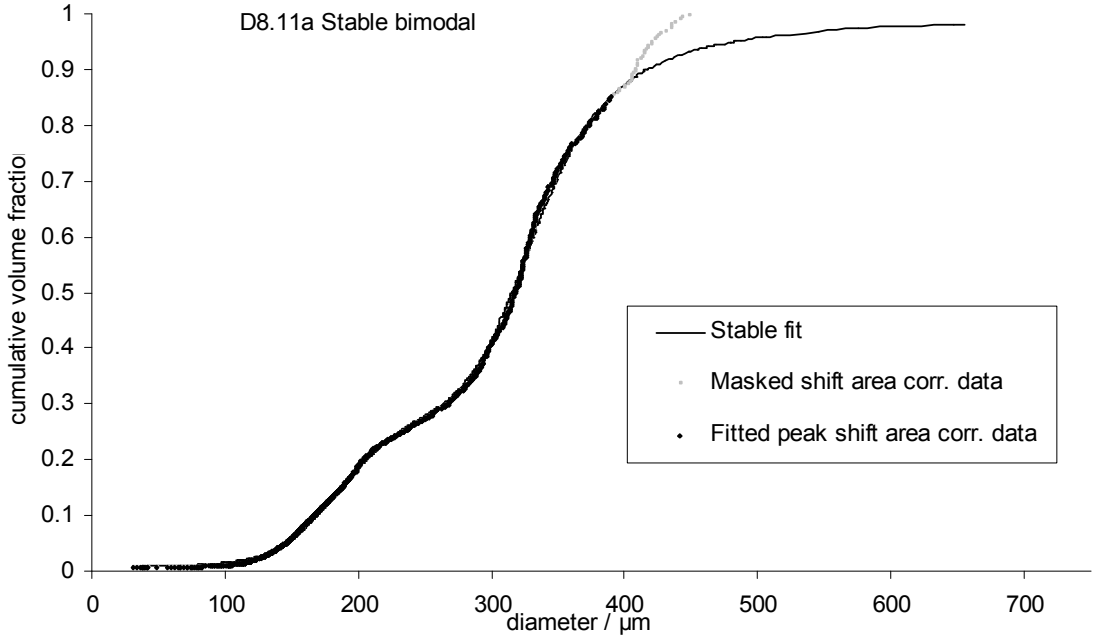

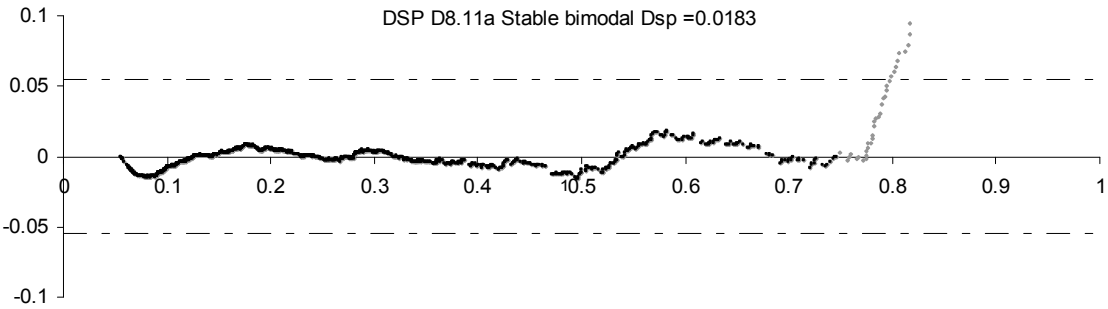

peak		Parameters of the Stable distribution			
D8.11a	%vol	α	β	γ	δ
1°	69	1.32	0.6	40	325
2°	31				180

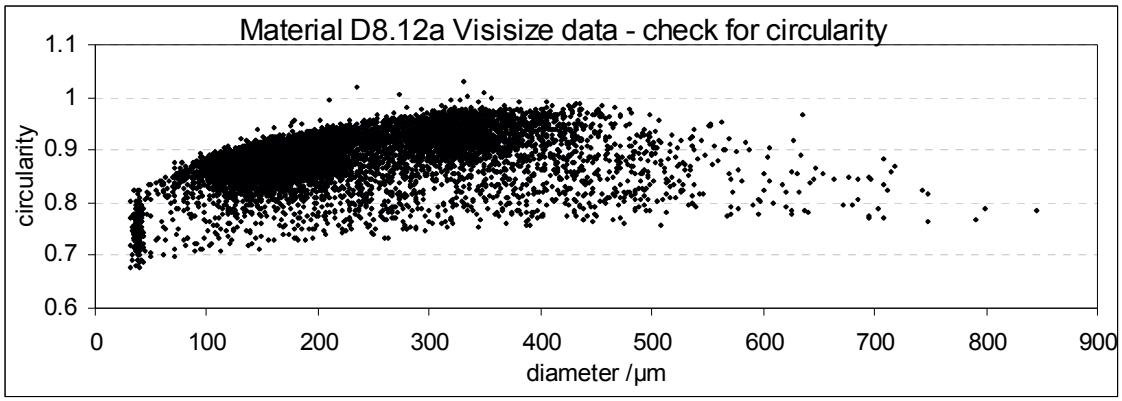
Material D8.12a Visisize data - check for circularity
circularity
1.1
1
0.9
0.8
0.7
0.6
0
100
200
300
400
500
600
700
800
900
diameter /µm

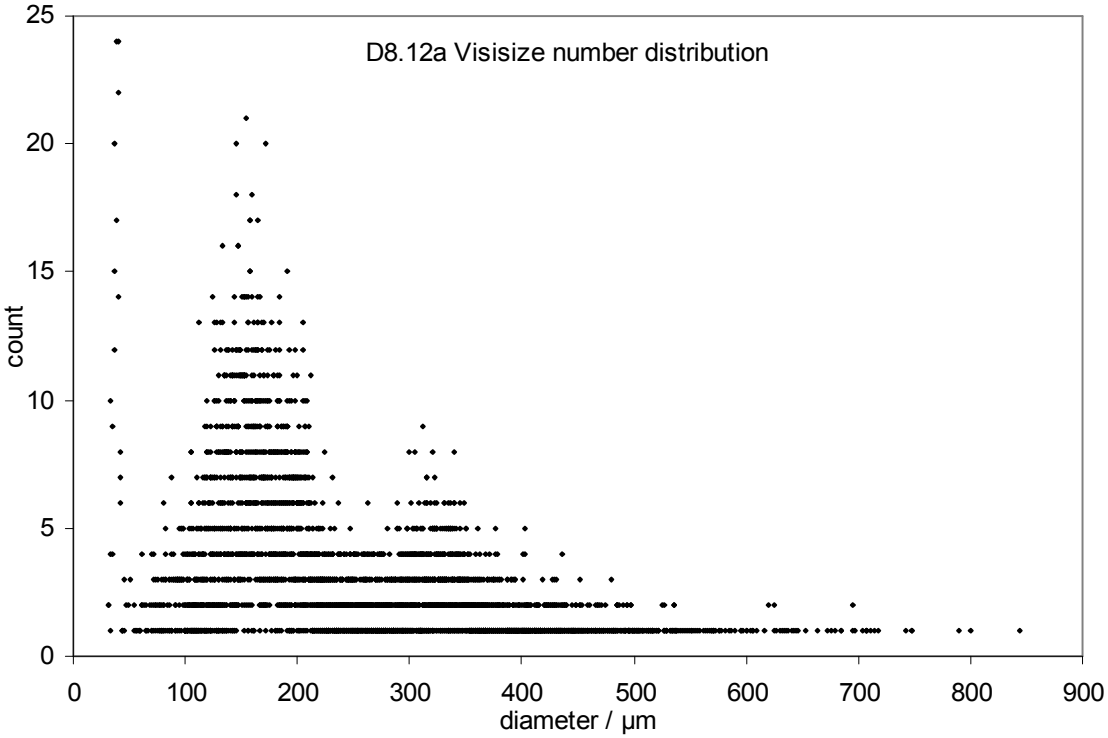
D8.12a Visisize number distribution
count
25
20
15
10
5
0
0
100
200
300
400
500
600
700
800
900
diameter / µm

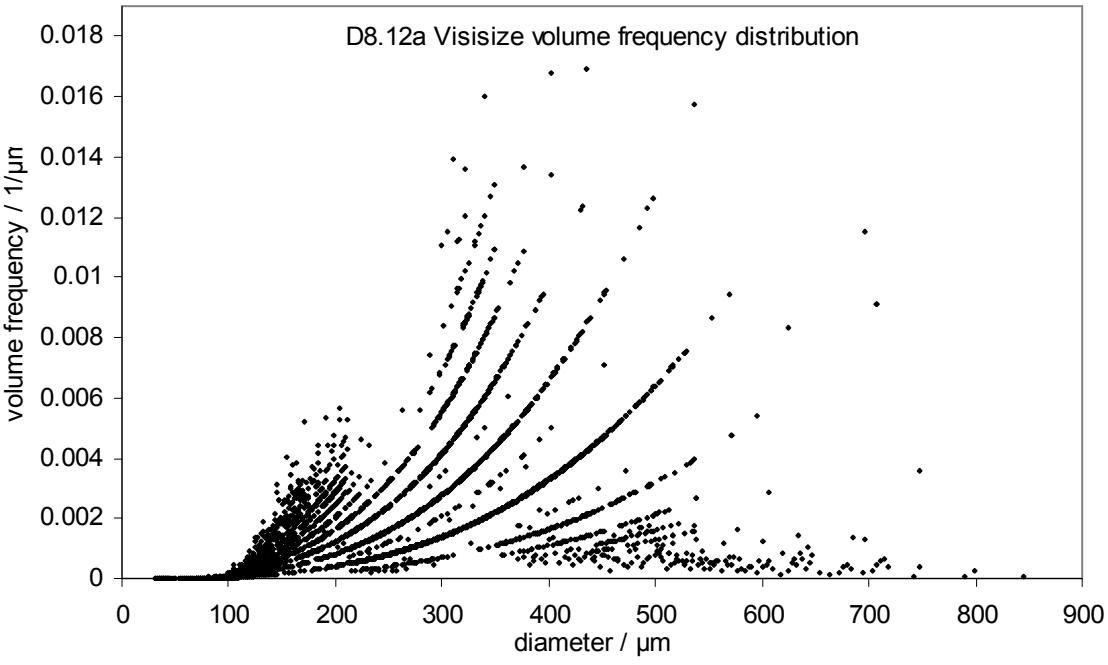
D8.12a Visisize volume frequency distribution
volume frequency / 1/µn
0.018
0.016
0.014
0.012
0.01
0.008
0.006
0.004
0.002
0
0
100
200
300
400
500
600
700
800
900
diameter / µm

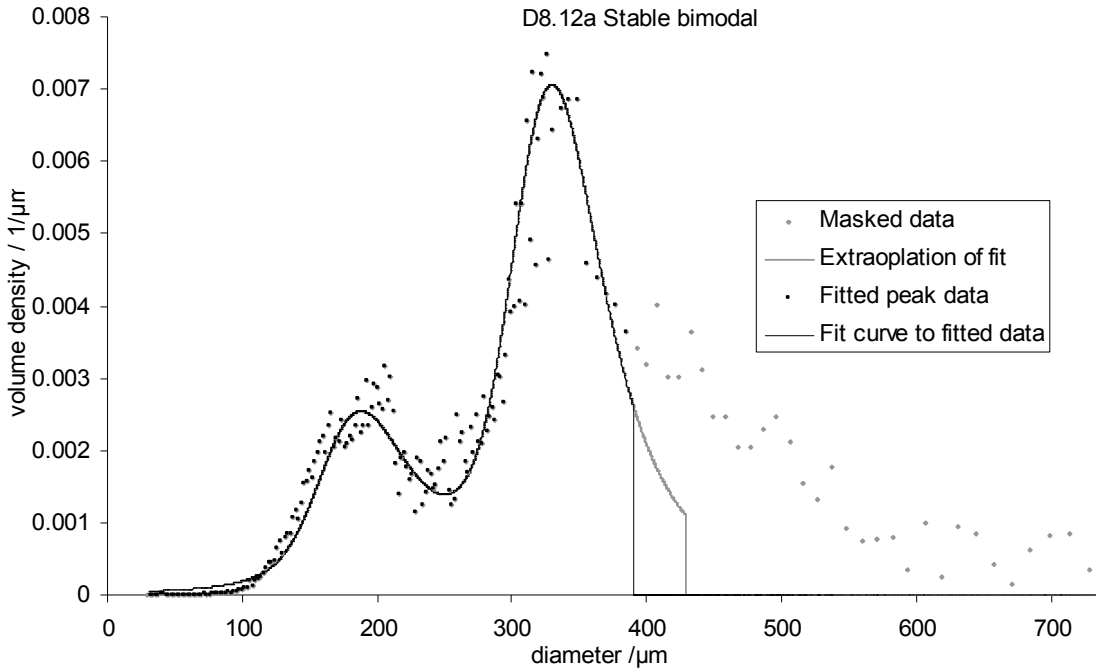

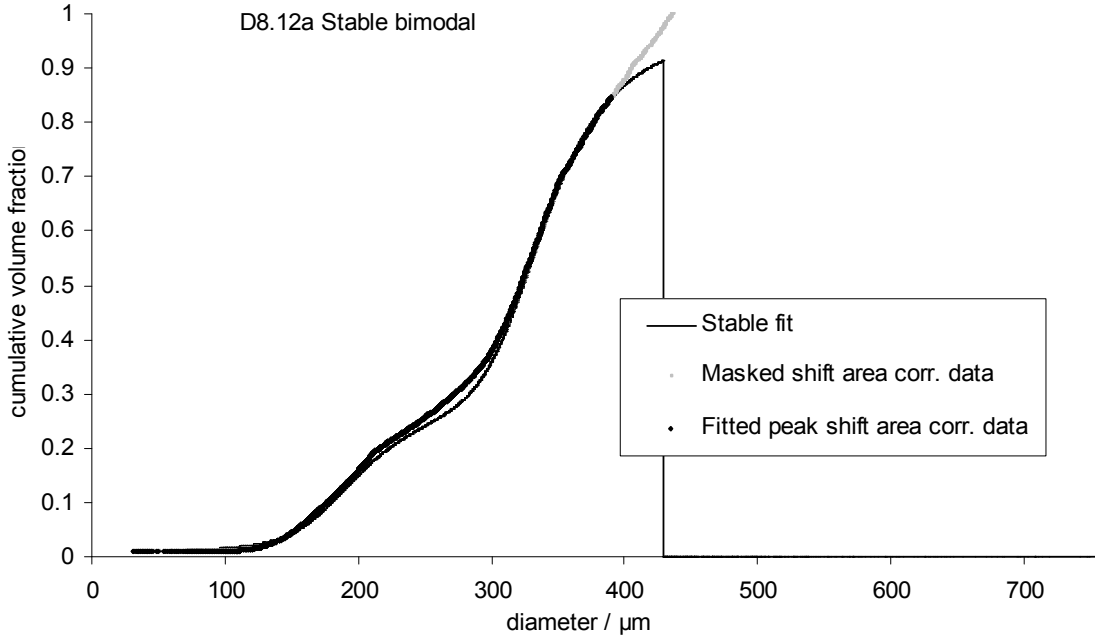

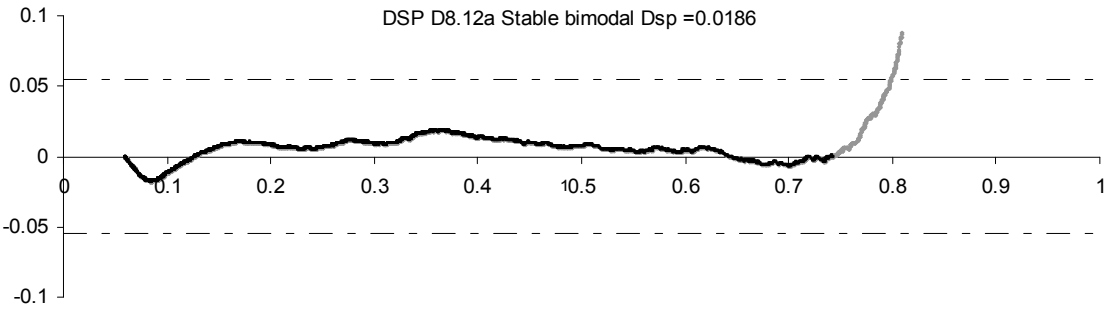

peak		Parameters of the Stable distribution			
D8.12a	%vol	α	β	γ	δ
1°	74	1.3	0.5	38	330
2°	26				187

APPENDIX B: PROCEDURE TO RE-NORMALISE DSD DATA

Datasets with secondary peaks due to satellite droplet formation and agglomeration (sections 5.2.1 and 5.2.2 respectively) can be considered to be the superposition of three DSDs as shown in the sketch Figure 85.

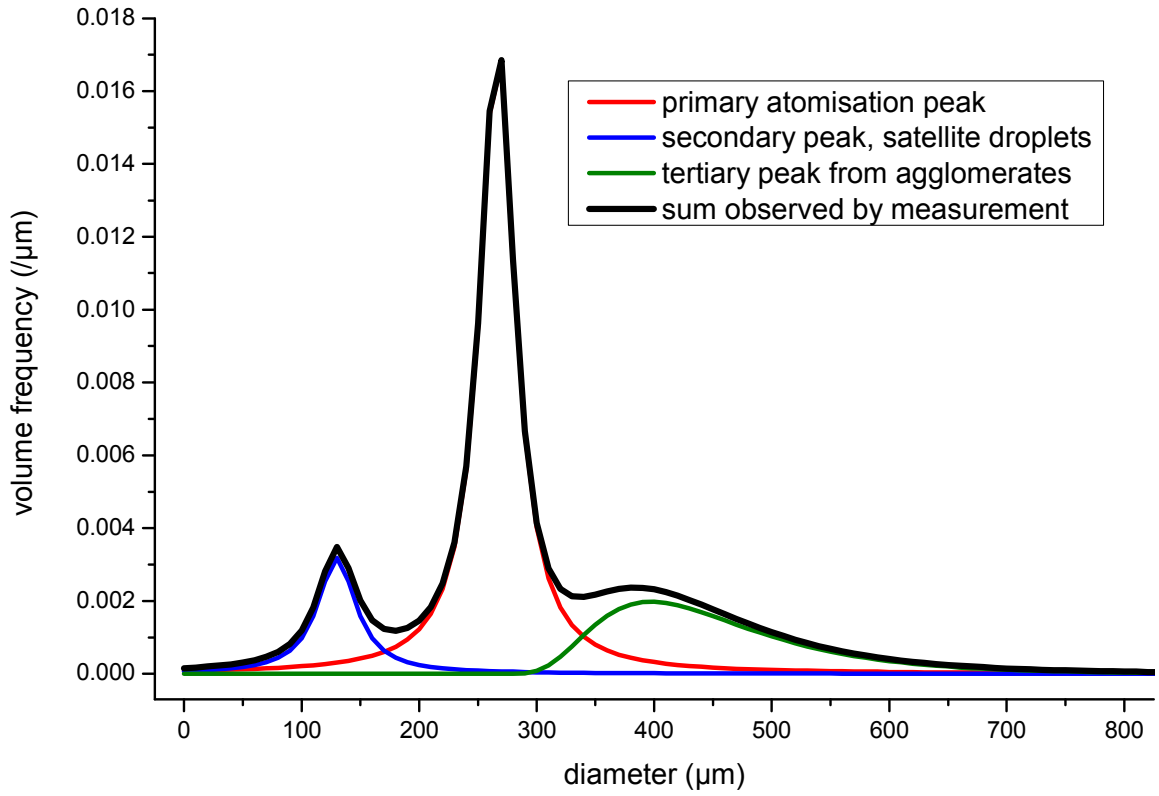

Figure 85: sketch superposition of DSDs from primary atomisation, satellite formation and agglomeration

The task in Chapter 5 is to fit a function to that primary peak. However, neither the equation or the parameters of the distribution function are known *a priori*. For preliminary screening, i.e. selecting a shortlist of likely candidate functions, it is most efficient (quickest) to simply fit a normalised distribution function to the normalised data. Functions with the wrong shape can be discarded, but a good fit to the peak cannot be obtained whilst insisting that both data and fit are normalised, even though a significant fraction of the data volume distribution is contained in secondary peaks.

Typically the superposed DSDs have overlapping tails as indicated in Figure 85. The secondary peaks cannot be eliminated by inspection of clear separation between the peaks (except for some of the PDA datasets). It is, however, possible to select by eye a range of the volume density distribution which (good enough to a first approximation)

only contains particles from the primary peak. This is a simple observation from the data that is available, it will not be true for an arbitrary measurement of droplet size data. However, if a clear primary peak could not be discerned by eye, that size distribution would not be a good exemplar of the Acoustic Atomiser size distribution, and it would not be necessary to find a fit function to it. This range of data of the primary peak is the range of data that the fit is applied to. The lower bound diameter d_L and the upper bound diameter d_U, are shown in Figure 86. The selection of these bounds is a subjective judgement.

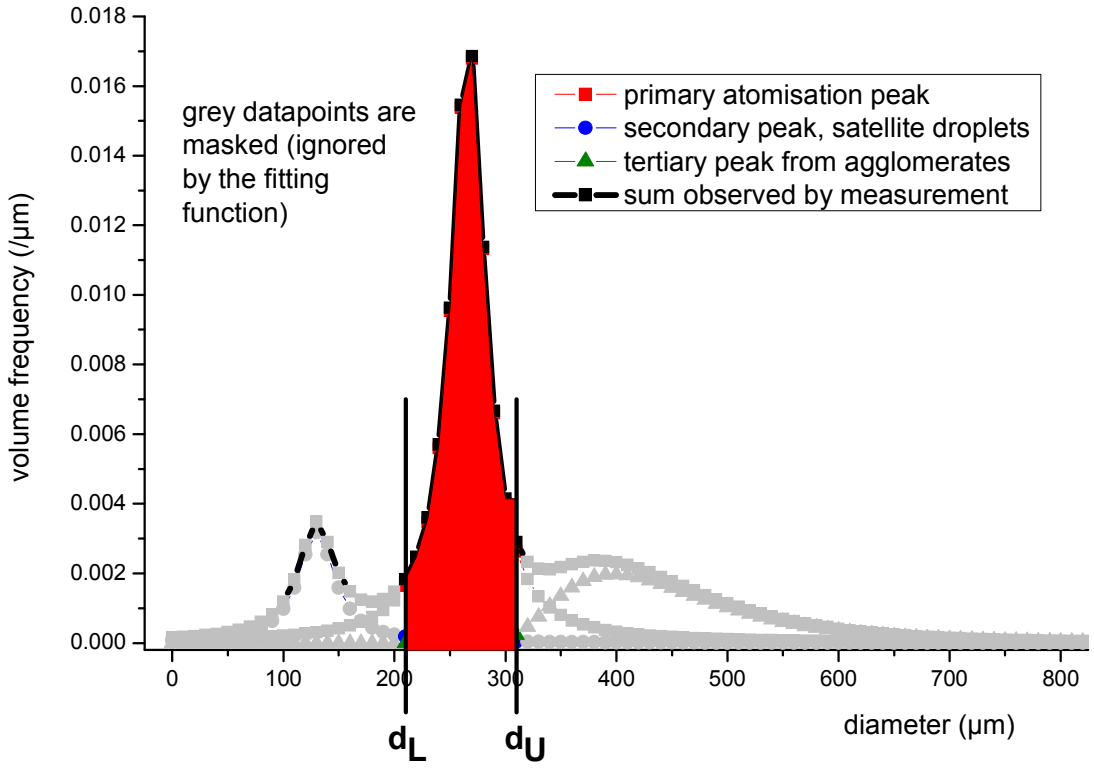

Figure 86:selection of primary peak for fitting theoretical distribution

A normalised fit function is the goal, so the normalised data volume density distribution is scaled by a factor x (where $x \geq 1$), so that the area under the curve in the primary peak range between d_L and d_U is the same in both the data and the fit function. The total cumulative volume of the scaled data is now greater than 1. It is equal to the scale factor x. The excess volume (x - 1) is the volume in the secondary peaks of the measured data that is in excess of the expectation value according to the fit function.

$$x = \frac{\int_{d_L}^{d_U} w_{normalised\_fit}(d).dd}{\int_{d_L}^{d_U} w_{normalised\_data}(d).dd} = \frac{W(d_U) - W(d_U)\big|_{normalised\_fit}}{W(d_U) - W(d_U)\big|_{normalised\_data}} \qquad \text{Eqn B.1}$$

It will be immediately apparent that this procedure is distribution-dependent, and will be iterative. Iteration by manual direct substitution of estimates of x is found to be both robust and rapidly convergent.

A correction is required to the DSP goodness of fit plot. The cumulative volume fraction of the entire dataset is no longer normalised. In order to judge goodness-of-fit, the origin of the data cumulative volume fraction sum is set at d_L, rather than at zero. The cumulative volume fraction of the data at d_L is set to be equal to the cumulative volume fraction of the fit at d_L. The cumulative sum is then performed from d_L for both lower and higher diameters. The cumulative volume fraction for small diameters will become negative and the stabilized probability $(2 / \pi) \sin^{-1}[\sqrt{W(d)}]$ will become complex and hence unplottable. However, the purpose of the test is goodness-of-fit to the peak. It is not to be expected that a good fit would be obtained of a unimodal theoretical distribution function to secondary peaks in the tails of the data. It should also be noted that since $W_{data}(d_L) = W_{fit}(d_L)$ has been fixed, and by definition of the re-normalisation procedure (eqn B.1), $W_{data}(d_U) = W_{fit}(d_U)$ is also fixed. Hence a perfect fit will be indicated on the DSP plot at these two fixed points. Overall positive or negative displacement of the line (as seen in the uncorrected DSP plots when skew is indicated) is not possible. Goodness-of-fit is indicated only by the divergence of the data from the perfect fit line for the intermediate points plotted between d_L and d_U.

APPENDIX C: CRITICAL D_{SP} FOR LARGE n

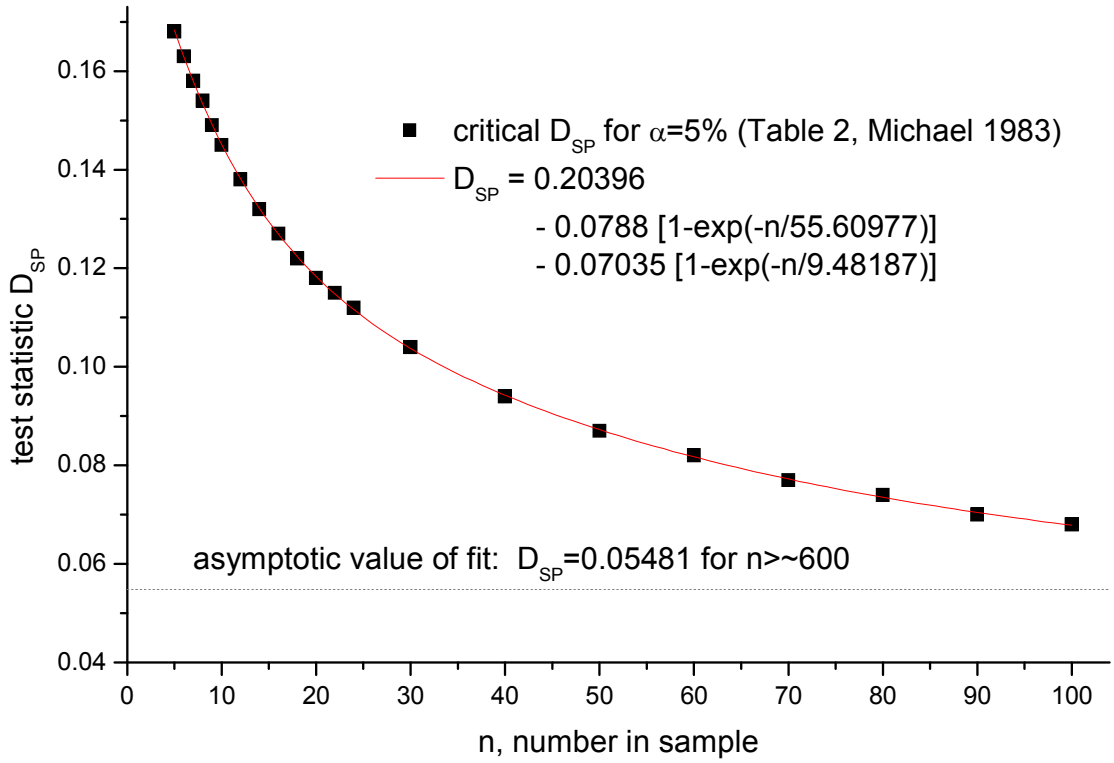

Michael, 1983		Curve fit			ε|data-fit|
n	D_{SP} α=0.05	n	D_{SP}	to 3d.p	
5	0.168	5	0.1683535	0.168	0
6	0.163	6	0.1629141	0.163	0
7	0.158	7	0.1579135	0.158	0
8	0.154	8	0.1533097	0.153	0.001
9	0.149	9	0.1490649	0.149	0
10	0.145	10	0.1451449	0.145	0
12	0.138	12	0.1381595	0.138	0
14	0.132	14	0.1321424	0.132	0
16	0.127	16	0.1269221	0.127	0
18	0.122	18	0.1223595	0.122	0
20	0.118	20	0.1183414	0.118	0
22	0.115	22	0.1147754	0.115	0
24	0.112	24	0.1115868	0.112	0
30	0.104	30	0.1037277	0.104	0
40	0.094	40	0.0942285	0.094	0
50	0.087	50	0.0872365	0.087	0
60	0.082	60	0.081724	0.082	0
70	0.077	70	0.0772332	0.077	0
80	0.074	80	0.0735214	0.074	0
90	0.07	90	0.0704344	0.07	0
100	0.068	100	0.0678603	0.068	0
		200	0.0569707		
		300	0.0551678		
		500	0.0548198		
		600	0.0548116		
		1000	0.05481		
		3000	0.05481		

APPENDIX D: EXCEL VBA MACRO TO FIT STABLE DISTRIBUTIONS TO DROPLET SIZE DATA

The use of this method is described in sections 5.3.8 and 5.4. The macros used for bimodal distributions are not shown, they simply added additional worksheets pages and parameters γ_1, γ_2, δ_1, δ_2 rather than just δ and γ, and had calling routines to fit one or other curve separately as well as a routine to fit both together.

Spreadsheet screendump following page.

Named ranges called by the macro are:

Name	Cell range
alpha	O2
beta	P2
gamma	Q2
delta	R2
DSP	AA23 when minimising against $\Sigma(\Delta sp)$ AA25 when minimising against D_{sp}
ItAlpha	O3
ItBeta	P3
ItDelta	R3
ItGamma	Q3
ItFine	L7
lbound	L3
ubound	L4

where the prefix "It" is a contraction of Iterate

D.1 Macro code in worksheet

```
Private Sub RunStableButton_Click()

    ModuleRunStable.WorkingFileName = ActiveWorkbook.Name
    SingleStableRun
    Range("alpha").Activate

End Sub


Private Sub IterateStableButton_Click()

    ModuleRunStable.WorkingFileName = ActiveWorkbook.Name
    IterateStable
    Range("alpha").Activate

End Sub
```

D.2 Macro code in ModuleRunStable

```
Option Explicit
Public WorkingFileName As String
Public Stable_completed_normally As Boolean
Dim alpha, beta, gamma, delta, L_bound, U_bound As Variant
Dim ItAlpha, ItBeta, ItGamma, ItDelta As Variant
Dim Input_data_written_normally As Boolean


Sub SingleStableRun()
    alpha = Range("alpha")
    beta = Range("beta")
    gamma = Range("gamma")
    delta = Range("delta")
    L_bound = Range("lbound")
    U_bound = Range("ubound")
    RunStable
End Sub ' InitialStableRun


Sub IterateStable()
Dim DSP1, DSP2, i As Variant
Dim Dummy As Variant

    alpha = Range("alpha")
    beta = Range("beta")
    gamma = Range("gamma")
    delta = Range("delta")
    L_bound = Range("lbound")
    U_bound = Range("ubound")
    ItAlpha = Range("ItAlpha") ' flag to iterate each parameter
    ItBeta = Range("ItBeta")
    ItGamma = Range("ItGamma")
    ItDelta = Range("ItDelta")
    i = Range("ItFine") ' multiplier on fineness of parameter increments in iteration

    If ItAlpha = 1 Then
        DSP1 = 1
        DSP2 = DSP1
        Do Until DSP2 > DSP1
            DSP1 = Range("DSP")
            RunStable
            DSP2 = Range("DSP")
            alpha = alpha + 0.1*i
            Dummy = DoEvents
            If alpha > 2 Then Exit Do
        Loop
        alpha = alpha - 0.2*i

        DSP1 = 1
        DSP2 = DSP1
        Do Until DSP2 > DSP1
            DSP1 = Range("DSP")
```

```
            RunStable
            DSP2 = Range("DSP")
            alpha = alpha - 0.1*i
            Dummy = DoEvents
            If alpha < 0.4 Then Exit Do
        Loop
        alpha = alpha + 0.2*i
        RunStable
    End If 'ItAlpha

    If ItBeta = 1 Then
        DSP1 = 1
        DSP2 = DSP1
        Do Until DSP2 > DSP1
            DSP1 = Range("DSP")
            RunStable
            DSP2 = Range("DSP")
            beta = beta + 0.1*i
            Dummy = DoEvents
            If beta > 1 Then Exit Do
        Loop
        beta = beta - 0.2*i

        DSP1 = 1
        DSP2 = DSP1
        Do Until DSP2 > DSP1
            DSP1 = Range("DSP")
            RunStable
            DSP2 = Range("DSP")
            beta = beta - 0.1*i
            Dummy = DoEvents
            If beta < -1 Then Exit Do
        Loop
        beta = beta + 0.2*i
        RunStable
    End If 'ItBeta

    If ItGamma = 1 Then
        DSP1 = 1
        DSP2 = DSP1
        Do Until DSP2 > DSP1
            DSP1 = Range("DSP")
            RunStable
            DSP2 = Range("DSP")
            gamma = gamma + 1*i
            Dummy = DoEvents
        Loop
        gamma = gamma - 2*i

        DSP1 = 1
        DSP2 = DSP1
        Do Until DSP2 > DSP1
            DSP1 = Range("DSP")
            RunStable
            DSP2 = Range("DSP")
            gamma = gamma - 1*i
            Dummy = DoEvents
        Loop
        gamma = gamma + 2*i
        RunStable
    End If 'ItGamma

    If ItDelta = 1 Then
        DSP1 = 1
        DSP2 = DSP1
        Do Until DSP2 > DSP1
            DSP1 = Range("DSP")
            RunStable
            DSP2 = Range("DSP")
            delta = delta + 1*i
            Dummy = DoEvents
        Loop
        delta = delta - 2*i

        DSP1 = 1
        DSP2 = DSP1
        Do Until DSP2 > DSP1
            DSP1 = Range("DSP")
            RunStable
            DSP2 = Range("DSP")
```

```
            delta = delta - 1*i
            Dummy = DoEvents
        Loop
        delta = delta + 2*i
        RunStable
    End If 'ItDelta

End Sub


Sub RunStable()
' Runs John Nolan's FORTRAN "Stablec.exe"
'   once for density calc with "pdfip.dat" input file
'   again for cumulative calc with "cdfip.dat" input file
' VB "Shell" command doesn't parse DOS pipes correctly. Command line
'     stablec < pdfip.dat
'   written as single line DOS batch file stblpdf.bat
'   (and equivalently for cdf)
Dim ResultsCheck, ResponseCheck
Dim OriginalDir As Variant
Dim fs
On Error GoTo ErrorHandler

    Stable_completed_normally = False
    Input_data_written_normally = False
    OriginalDir = CurDir
    ChDrive "c:"
    ChDir "c:\Program Files\Stable"
    Call WriteStableInputFiles
    If Not Input_data_written_normally Then Err.Raise vbObjectError + 2002

' VB Shell command runs concurrently, code checks that "StableC.exe" has
' written "stable.out" results file before continuing
' also check for excessive elapsed time- suggests excecution problem
    Set fs = CreateObject("Scripting.FileSystemObject")
    ResponseCheck = Now
    Shell ("stblpdf.bat")
    Do Until fs.FileExists("stable.out")
    'loop until results file is written
      'if 60 seconds elapsed assume problem with StableC.exe.
      'First guess stable.out open in Excel, try closing and reset
      'if not the case, attempting to close stable.out flags error,
      'errorhandler displays dialog box warning
        If Now > (ResponseCheck + 3*0.00023) Then    '0.00023=20secs; 1=24hours
            Windows("stable.out").Close
            ResponseCheck = Now
            Shell ("stblpdf.bat")
        End If
    Loop
    Do Until FileLen("stable.out") > 2000   ' Stablec.exe first creates file, then
                                            ' populates it.  This checks length is
                                            ' greater than 2K  (i.e. some data
                                            ' written) before proceeding
    If Now > (ResponseCheck + 3*0.00023) Then
       Windows("stable.out").Close
            ResponseCheck = Now
            Shell ("stblpdf.bat")
        End If
    Loop


    Call ReadStablepdf  'read "stable.out" into Excel

    ResponseCheck = Now
    Shell ("stblcdf.bat")
    Do Until fs.FileExists("stable.out")
        If Now > (ResponseCheck + 3*0.00023) Then
            Windows("stable.out").Close
            ResponseCheck = Now
            Shell ("stblcdf.bat")
        End If
    Loop
    Do Until FileLen("stable.out") > 2000
        If Now > (ResponseCheck + 3*0.00023) Then
            Windows("stable.out").Close
            ResponseCheck = Now
            Shell ("stblcdf.bat")
        End If
    Loop
```

```
    Call ReadStablecdf

'tidy up - return to calling directory, set success flag
    ChDir OriginalDir
    Stable_completed_normally = True
    Exit Sub

ErrorHandler:
    Select Case Err.Number
        Case 9
            Fatal_Calculation_error_2.Show
        Case 2002
            Fatal_input_error_2.Show
        Case Else
            Fatal_Calculation_error_3.Show
    End Select
    ChDir OriginalDir
    Stable_completed_normally = False
    Exit Sub
End Sub 'RunStable()


Private Sub WriteStableInputFiles()
'NB Print #file1, alpha, alpha, 0
'doesn't work, Excel prefixes a space to each line when
'outputting variables, crashes Stablec.exe
Dim file1 As Integer
Dim a, b, g, d, lb, ub

On Error GoTo ErrorHandler

    a = CStr(alpha)
    b = CStr(beta)
    g = CStr(gamma)
    d = CStr(delta)
    lb = CStr(L_bound)
    ub = CStr(U_bound)

    file1 = FreeFile
    Open "pdfip.dat" For Output As #file1
    Print #file1, "1"           'pdf calculation
    Print #file1, "2"           '2 parameterisation
    Print #file1, a, a, "0"     'first alpha, last alpha, stepsize
    Print #file1, b, b, "0"     'first beta, last beta, stepsize
    Print #file1, lb, ub, "0.1" 'first x, last x, x stepsize"
    Print #file1, g, d          'gamma, delta
    Print #file1, "2"           'output to "stable.out" file
    Close #file1

    file1 = FreeFile
    Open "cdfip.dat" For Output As #file1
    Print #file1, "2"           'cdf calculation
    Print #file1, "2"
    Print #file1, a, a, "0"
    Print #file1, b, b, "0"
    Print #file1, lb, ub, "0.1"
    Print #file1, g, d
    Print #file1, "2"
    Close #file1

    Input_data_written_normally = True
    Exit Sub

ErrorHandler:
    Input_data_written_normally = False
    Exit Sub
End Sub 'WriteStableInputFiles


Sub ReadStablepdf()
    Workbooks.OpenText Filename:= _
        "stable.out", _
        Origin:=xlMSDOS, StartRow:=1, DataType:=xlDelimited, TextQualifier:= _
        xlDoubleQuote, ConsecutiveDelimiter:=True, Tab:=True, Semicolon:=False, _
        Comma:=False, Space:=True, Other:=False, FieldInfo:=Array(Array(1, 1), _
        Array(2, 1), Array(3, 1), Array(4, 1), Array(5, 1), Array(6, 1), Array(7, 1)), _
        TrailingMinusNumbers:=True
    Columns("B:I").Select
    Selection.Copy
```

```
    Windows(WorkingFileName).Activate
    Columns("B:I").Select
    ActiveSheet.Paste
    ' clear clipboard and close
    Application.CutCopyMode = False
    Windows("stable.out").Close
    Kill "stable.out"  ' must delete stable.out:successive runs appended not overwritten
End Sub 'ReadStablepdf


Sub ReadStablecdf()
    Workbooks.OpenText Filename:= _
        "stable.out", _
        Origin:=xlMSDOS, StartRow:=1, DataType:=xlDelimited, TextQualifier:= _
        xlDoubleQuote, ConsecutiveDelimiter:=True, Tab:=True, Semicolon:=False, _
        Comma:=False, Space:=True, Other:=False, FieldInfo:=Array(Array(1, 1), _
        Array(2, 1), Array(3, 1), Array(4, 1), Array(5, 1), Array(6, 1), Array(7, 1)), _
        TrailingMinusNumbers:=True
    Columns("B:I").Select
    Selection.Copy

    Windows(WorkingFileName).Activate
    Columns("AH:AO").Select
    ActiveSheet.Paste
    ' clear clipboard and close
    Application.CutCopyMode = False
    Windows("stable.out").Close
'    Windows("stable.out").Activate
'    ActiveWindow.Close
    Kill "stable.out"
End Sub 'ReadStablecdf
```

APPENDIX E: EXCEL VBA MACRO TO PROCESS CaBER DATA

```
Option Explicit
Sub CaBERDataSort()
Dim i, j, k As Integer
Dim NumInMovingAve As Integer
Dim RepeatFlag, EndFlag As Boolean
Dim Sigma As Double
Dim Column1, Column2, Column3, Column4, FirstRow, LastRow, FirstFittingRow,
LastFittingRow As Integer
Dim FirstSortedDataRow, LastSortedDataRow, DataNumber, FirstHsappRow, LastHsappRow,
MaxRows As Integer
Dim TimeReZero, OldValue, NewValue, RepStartTime, RepEndTime, TimeValue, d1, d2, t1, t2,
hsapp, HsappMean, HsappSD, SigFigs As Double
Dim DataTitle As Variant
'-------------------------------------------------------------
    k = 7  'counter for row in B4 to write to
    Sigma = Worksheets("batch").Cells(34, 3).Value     'surface tension
    NumInMovingAve = Range("NumInMovingAverage").Value
    Worksheets("B4").Range("B7:D200").ClearContents
'process batch data first
    Sheets("batch").Select
    Range("$b$4").Select
    EndFlag = False
    Do Until EndFlag
        Application.Calculation = xlCalculationManual
        Column1 = ActiveCell.Column
        Column2 = Column1 + 1
        FirstRow = Cells(5, Column1).Value
        LastRow = Cells(7, Column1).Value
        FirstFittingRow = Cells(5, Column2).Value
        LastFittingRow = Cells(7, Column2).Value
        Worksheets("B2").Range(Worksheets("b2").Cells(FirstRow, Column1),
                               Worksheets("b2").Cells(LastRow, Column2)).ClearContents
        Sheets("B3").Range(Worksheets("B3").Cells(FirstRow, Column1),
                               Worksheets("b3").Cells(LastRow, Column2)).ClearContents
        TimeReZero = Cells(FirstFittingRow, Column1).Value
        j = FirstRow    'counter for row number on B2 to write to
        RepeatFlag = False
        If (LastFittingRow > FirstFittingRow) Then
            For i = FirstFittingRow To LastFittingRow
                OldValue = Worksheets("B2").Cells(j-1, Column2).Value
                NewValue = Worksheets("batch").Cells(i, Column2).Value
                If (NewValue = OldValue) Then
                    RepeatFlag = True
                    If (i = LastFittingRow) Then
                       RepStartTime = Worksheets("B2").Cells(j-1, Column1).Value
                       RepEndTime=Worksheets("batch").Cells(i,Column1).Value-TimeReZero
                       TimeValue = (RepEndTime + RepStartTime) / 2
                       Worksheets("B2").Cells(j-1, Column1).Value = TimeValue
                    End If
                Else
                    If RepeatFlag Then
                       RepStartTime = Worksheets("B2").Cells(j-1, Column1).Value
                       RepEndTime=Worksheets("batch").Cells(i-1,Column1).Value-TimeReZero
                       TimeValue = (RepEndTime + RepStartTime) / 2
                       Worksheets("B2").Cells(j-1, Column1).Value = TimeValue
                       RepeatFlag = False
                    End If
                    TimeValue = Worksheets("batch").Cells(i, Column1).Value - TimeReZero
                    Worksheets("B2").Cells(j, Column1).Value = TimeValue
                    Worksheets("B2").Cells(j, Column2).Value = NewValue
                    j = j+1
                End If
            Next
        End If
'now convert sorted data into extensional viscosity.  Moving average used.
'If this would cause divide-by-zero error, use point values only
        Application.CalculateFullRebuild
                            'need to calculate sheet to count sorted data rows correctly
        Application.Calculation = xlCalculationAutomatic
        FirstSortedDataRow = Worksheets("B2").Cells(5, Column1).Value
        LastSortedDataRow = Worksheets("B2").Cells(7, Column1).Value
        j = FirstSortedDataRow    'counter for row number on B3 to write to
        If (LastSortedDataRow > FirstSortedDataRow) Then
            For i = FirstSortedDataRow To LastSortedDataRow - NumInMovingAve
                d1=Application.WorksheetFunction.Average(Range(Worksheets("B2").Cells(i,
```

```
                    Column2), Worksheets("B2").Cells(i+NumInMovingAve-1, Column2)))
                d2=Application.WorksheetFunction.Average(Range(Worksheets("B2").Cells(i
                       +1, Column2), Worksheets("B2").Cells(i+NumInMovingAve, Column2)))
                If (d1 = d2) Then
                    d1 = Worksheets("B2").Cells(i, Column2).Value
                    d2 = Worksheets("B2").Cells(i+1, Column2).Value
                    t1 = Worksheets("B2").Cells(i, Column1).Value
                    t2 = Worksheets("B2").Cells(i+1, Column1).Value
                Else
                t1=Application.WorksheetFunction.Average(Range(Worksheets("B2").Cells(i,
                          Column1), Worksheets("B2").Cells(i+NumInMovingAve-1, Column1)))
                t2=Application.WorksheetFunction.Average(Range(Worksheets("B2").Cells(i
                       +1, Column1), Worksheets("B2").Cells(i+NumInMovingAve, Column1)))
                End If
                hsapp = 0.4254*Sigma*(t2-t1) / (d1-d2)
                If (hsapp > 0) Then
                    Worksheets("B3").Cells(j, Column2).Value = hsapp
                    DataNumber = j-FirstSortedDataRow+1
                    Worksheets("B3").Cells(j, Column1).Value = DataNumber
                    j = j+1
                End If
            Next
        End If
'then move to the next series of data
        Sheets("batch").Select
        Worksheets("batch").Cells(4, Column1+2).Select
        If (ActiveCell.Value <> Worksheets("batch").Cells(4, Column1).Value) Then
                                                                          EndFlag = True
    Loop
    Range("$a$1").Select

'then process the SINGLE MEASUREMENT data
'{*this code not shown: identical to batch but on worksheet page "single" *}

    Range("$a$1").Select
End Sub
```

APPENDIX F: CaBER DATA

For each material apart from E and J which are in the main text, plots are shown for time-diameter curves, both unprocessed and the data selected as valid for analysis, and then on the following page, plots against Hencky strain of each of transient apparent Trouton ratio and transient apparent extensional viscosity.

As the full shear rheometry flow curve data was not available, the plots against strain rate are less interesting in this study. Only the plots for the materials with greatest and least strain rate are shown below.

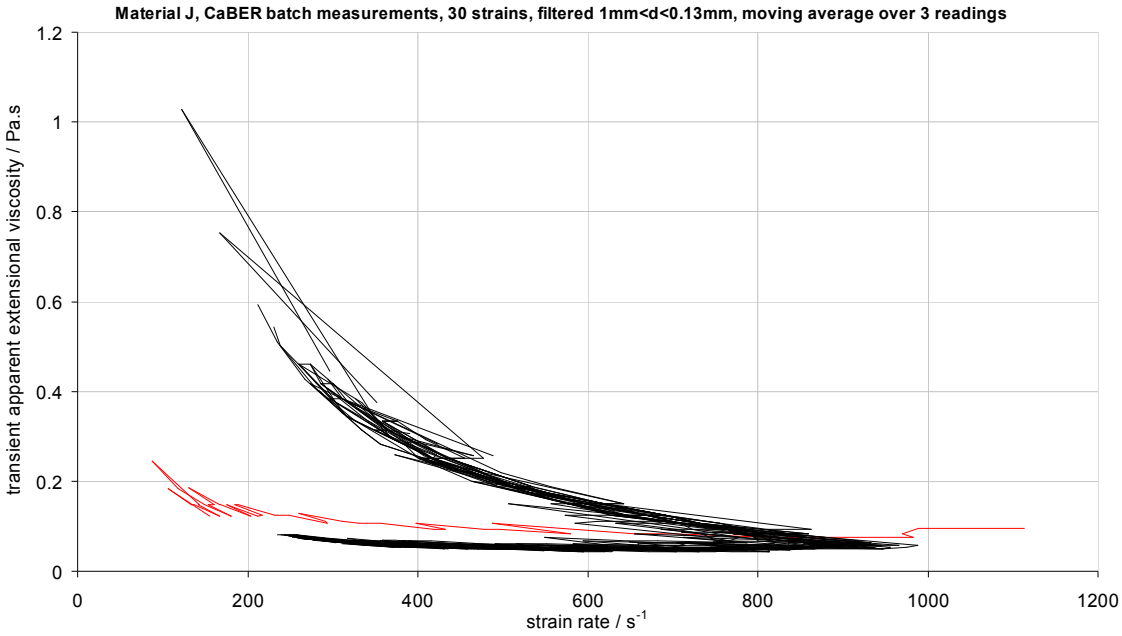

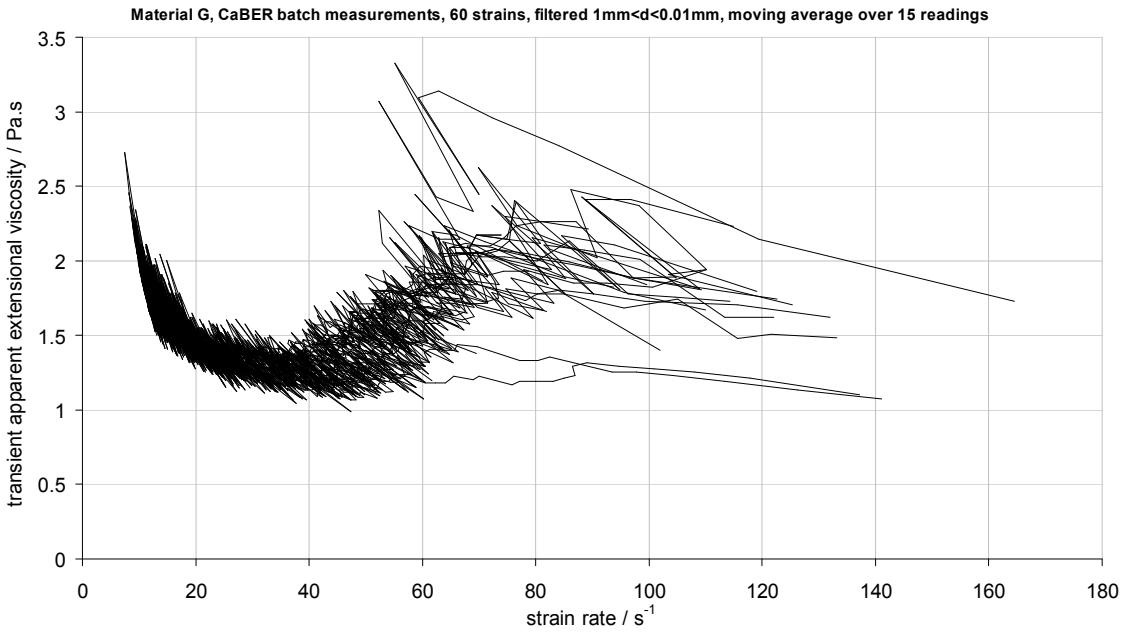

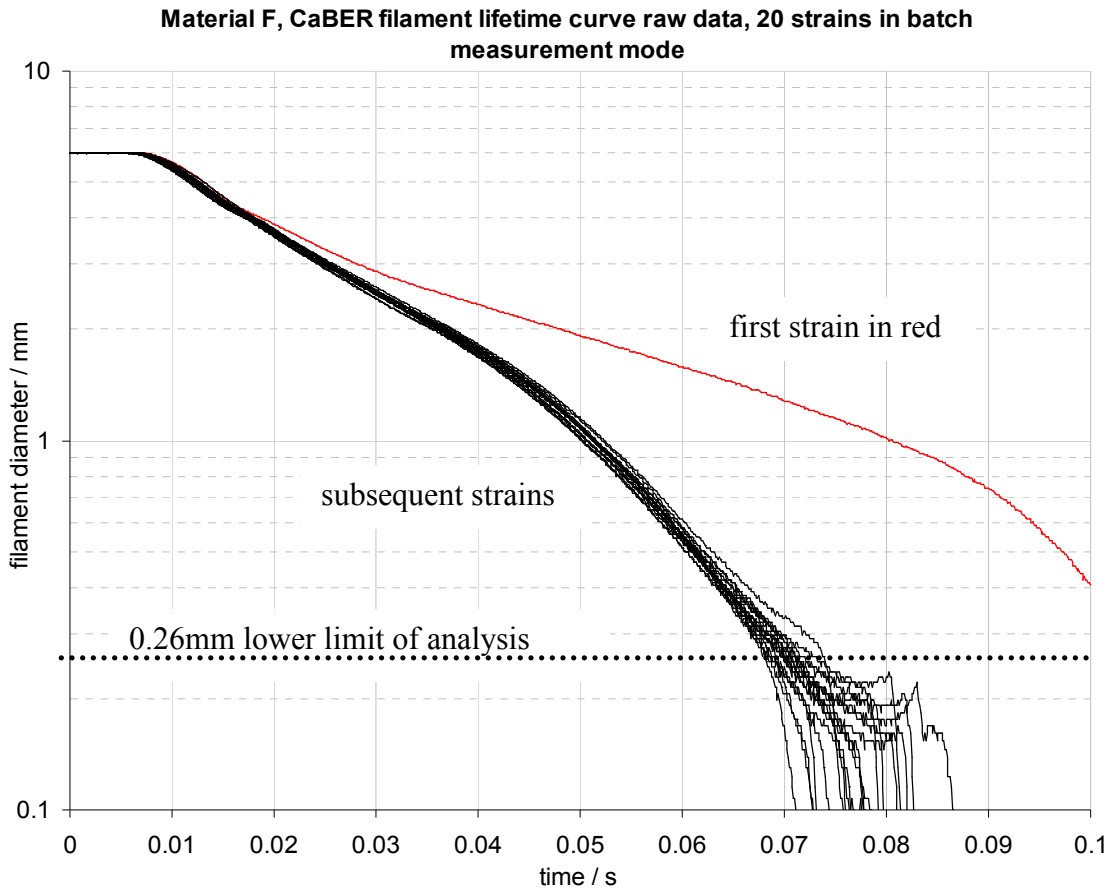
Material F, CaBER filament lifetime curve raw data, 20 strains in batch measurement mode
filament diameter / mm
10
1
0.1
first strain in red
subsequent strains
0.26mm lower limit of analysis
0
0.01
0.02
0.03
0.04
0.05
0.06
0.07
0.08
0.09
0.1
time / s

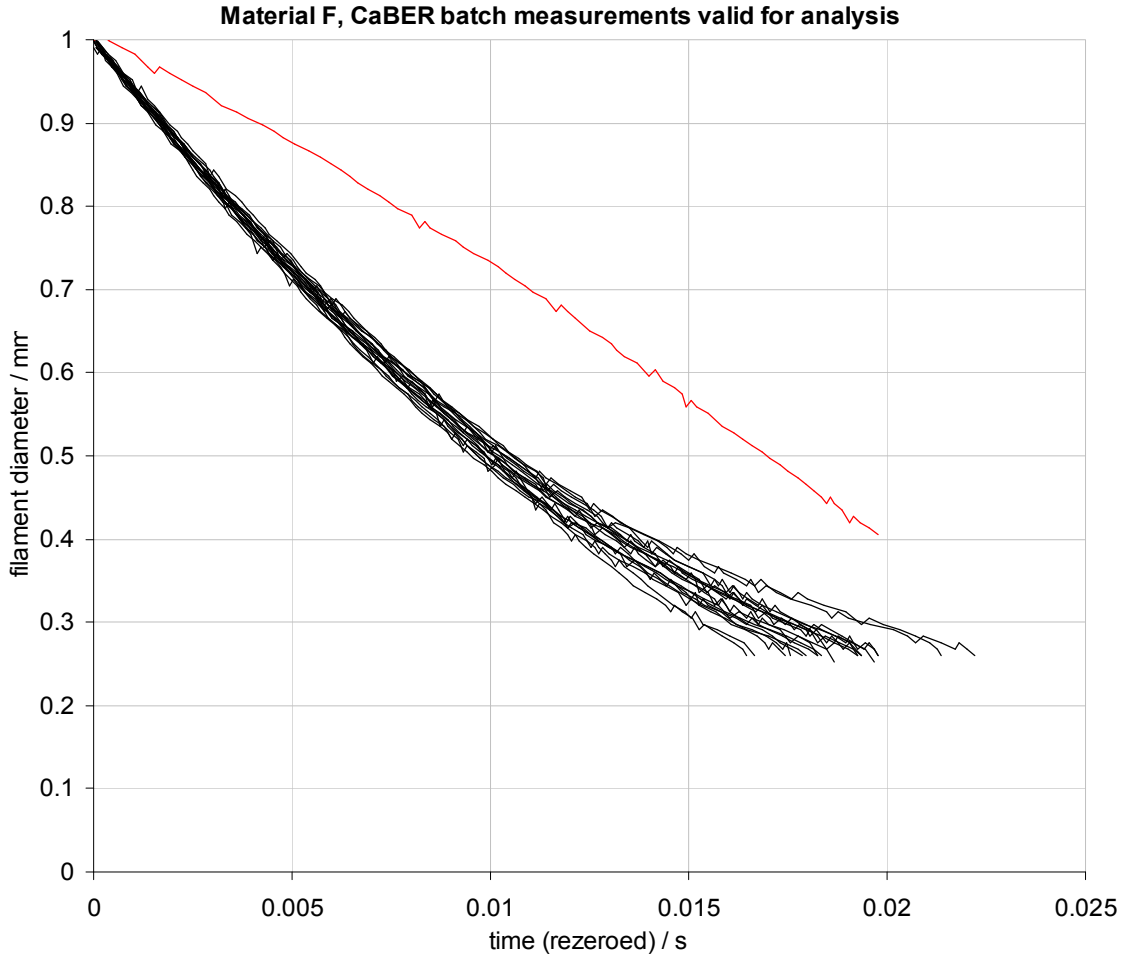
Material F, CaBER batch measurements valid for analysis
filament diameter / mm
1
0.9
0.8
0.7
0.6
0.5
0.4
0.3
0.2
0.1
0
0
0.005
0.01
0.015
0.02
0.025
time (rezeroed) / s

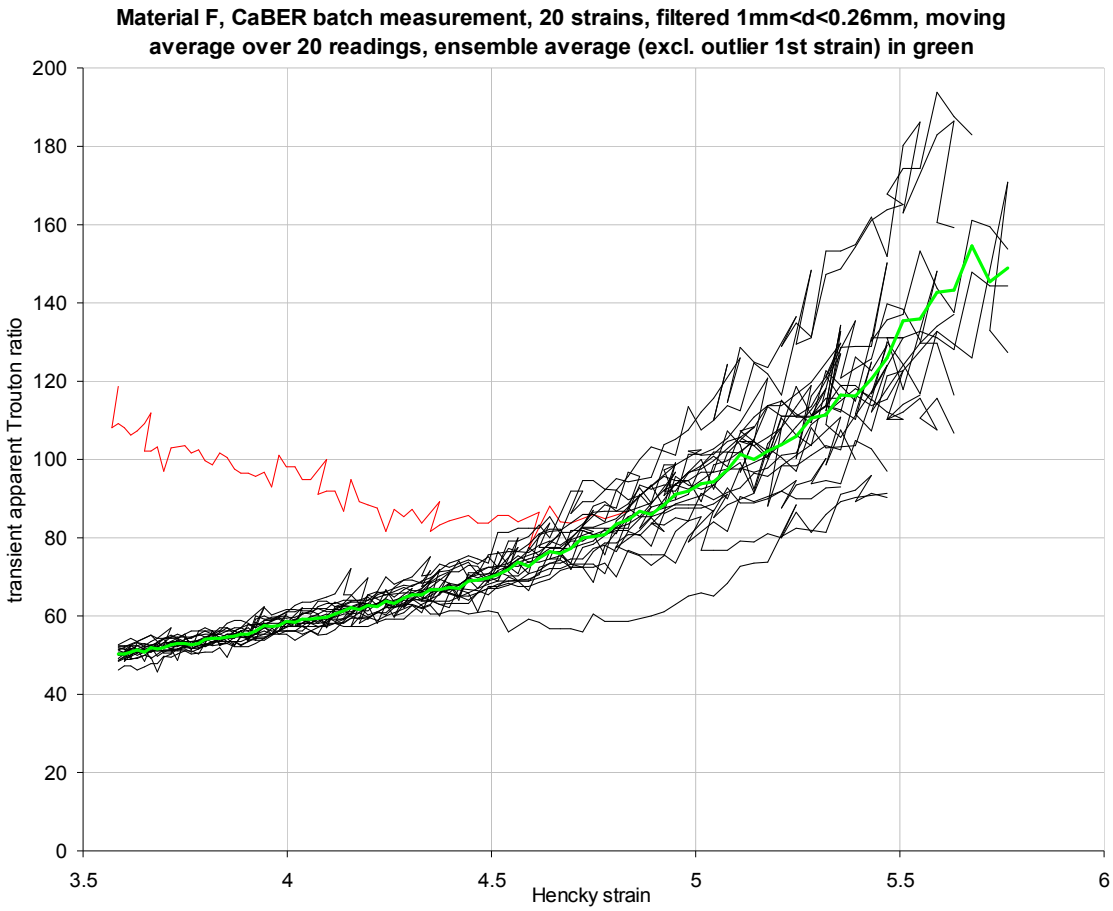

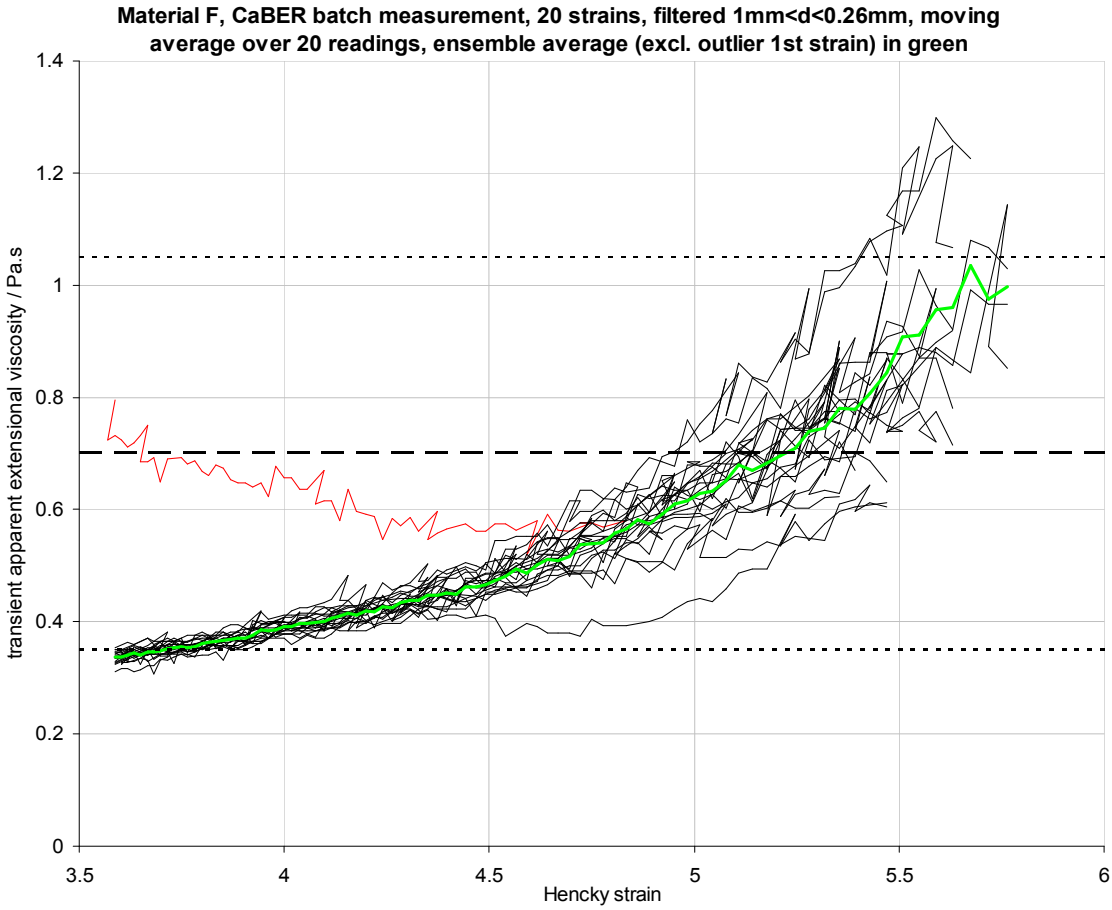

Material F, transient apparent extensional viscosity taken to be 0.7 ± 0.35 Pa.s

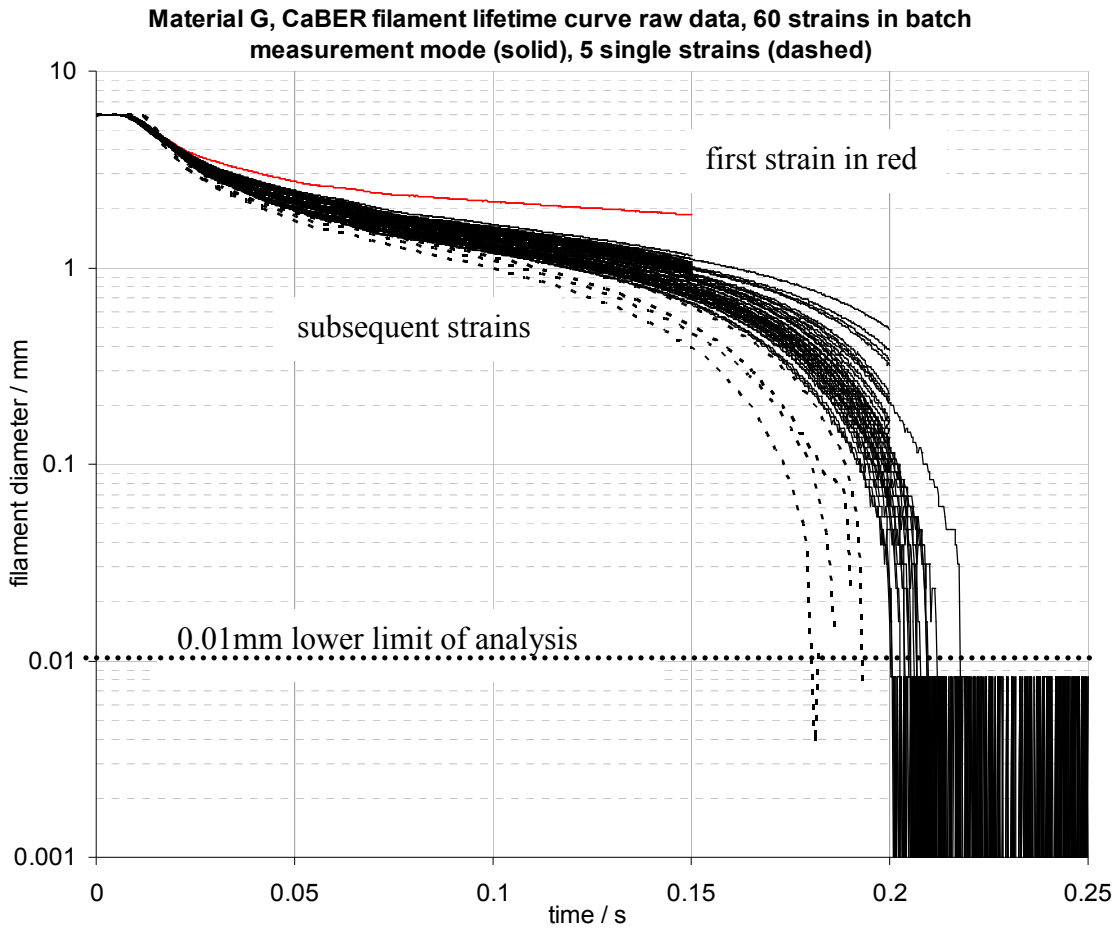
Material G, CaBER filament lifetime curve raw data, 60 strains in batch measurement mode (solid), 5 single strains (dashed)
first strain in red
subsequent strains
0.01mm lower limit of analysis
filament diameter / mm
time / s
10
1
0.1
0.01
0.001
0
0.05
0.1
0.15
0.2
0.25

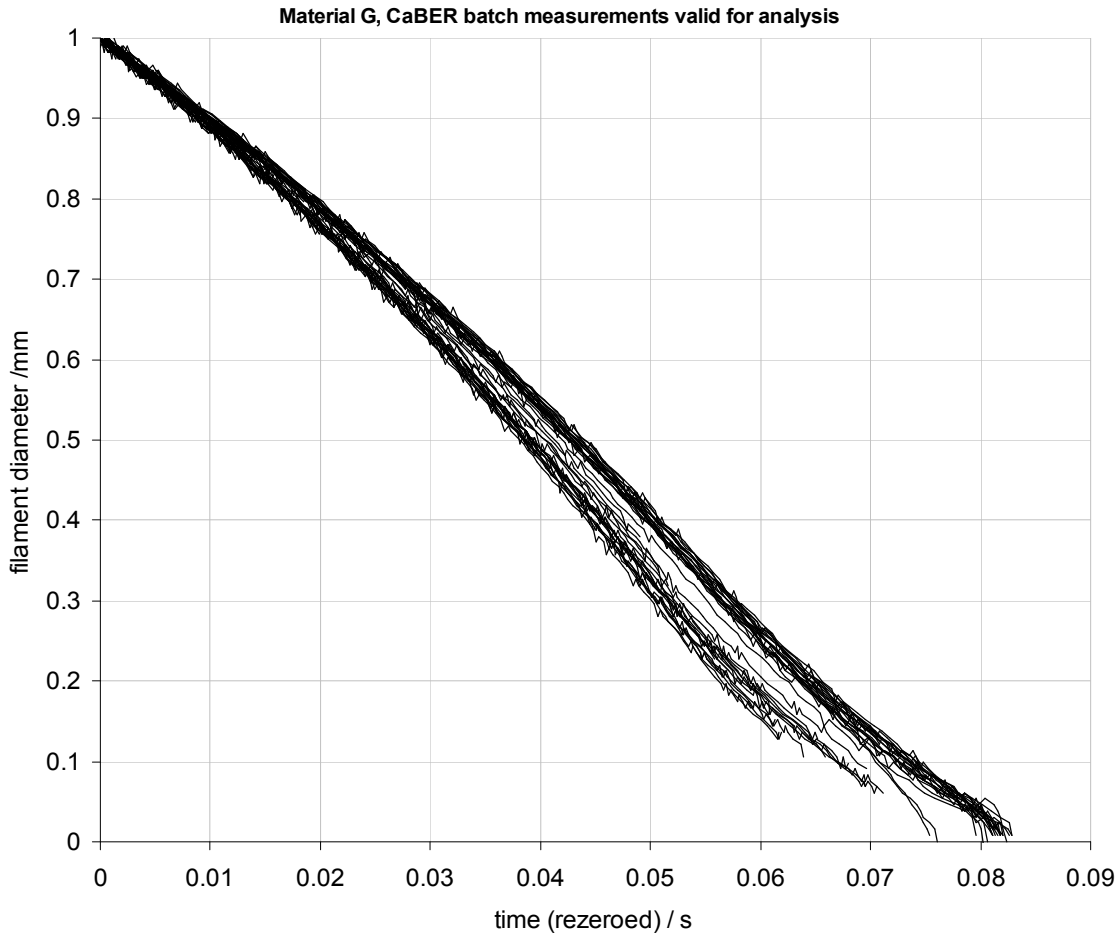
Material G, CaBER batch measurements valid for analysis
filament diameter /mm
time (rezeroed) / s
1
0.9
0.8
0.7
0.6
0.5
0.4
0.3
0.2
0.1
0
0
0.01
0.02
0.03
0.04
0.05
0.06
0.07
0.08
0.09

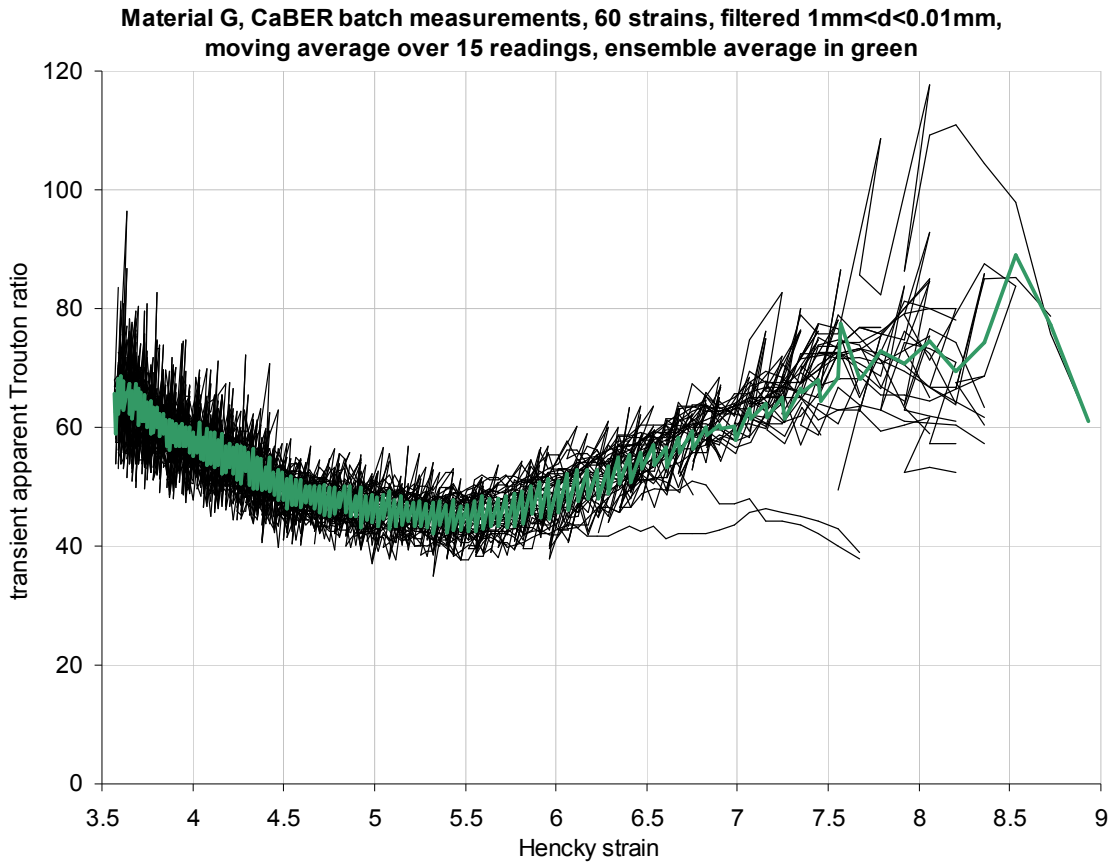

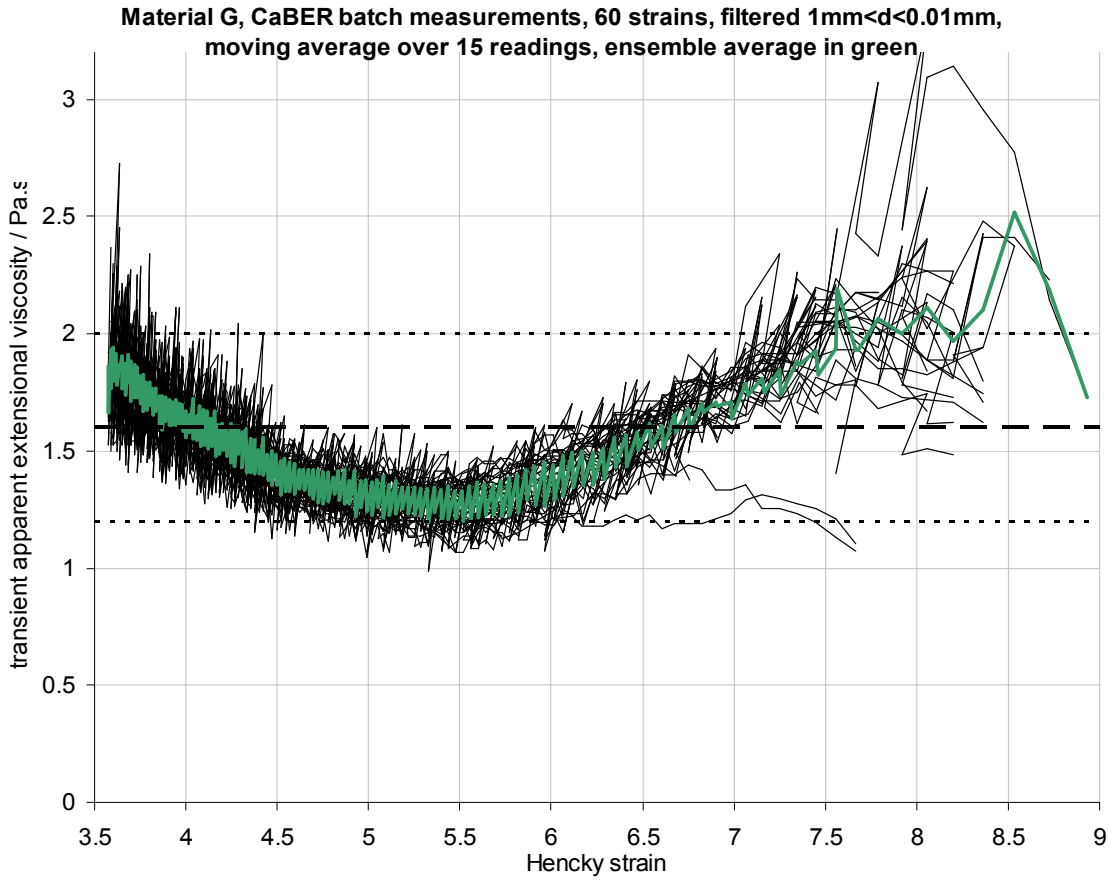

Material G, transient apparent extensional viscosity taken to be 1.6 ± 0.4 Pa.s (single strain values were similar, plots not shown)

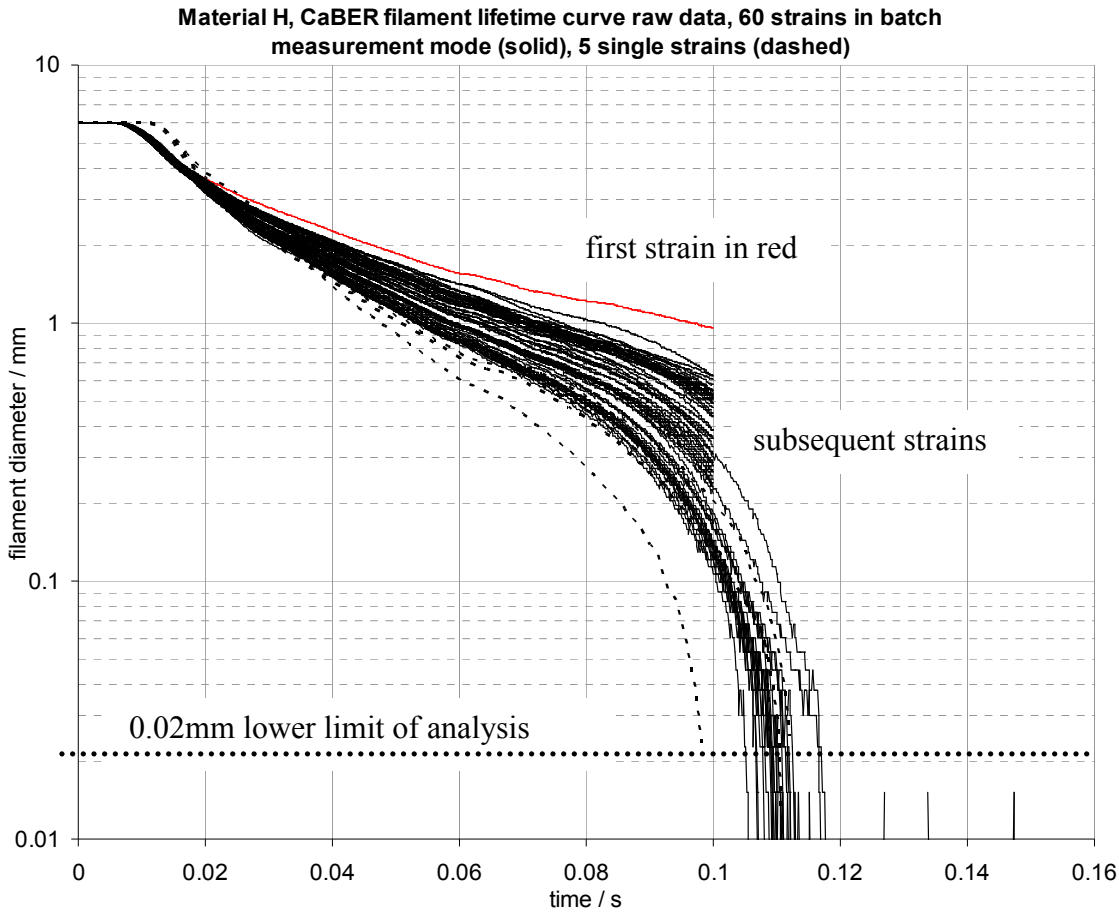
Material H, CaBER filament lifetime curve raw data, 60 strains in batch measurement mode (solid), 5 single strains (dashed)
first strain in red
subsequent strains
0.02mm lower limit of analysis
filament diameter / mm
time / s
10
1
0.1
0.01
0
0.02
0.04
0.06
0.08
0.1
0.12
0.14
0.16

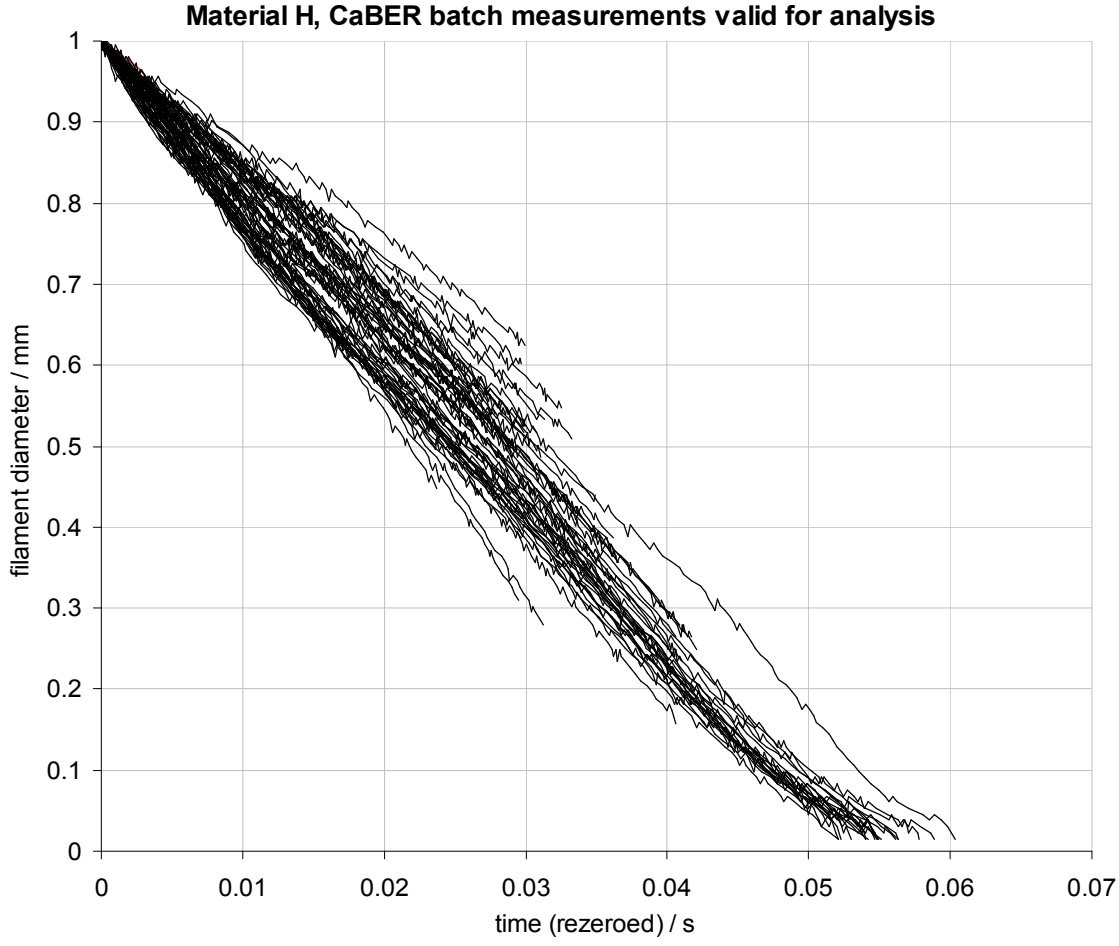
Material H, CaBER batch measurements valid for analysis
filament diameter / mm
time (rezeroed) / s
1
0.9
0.8
0.7
0.6
0.5
0.4
0.3
0.2
0.1
0
0
0.01
0.02
0.03
0.04
0.05
0.06
0.07

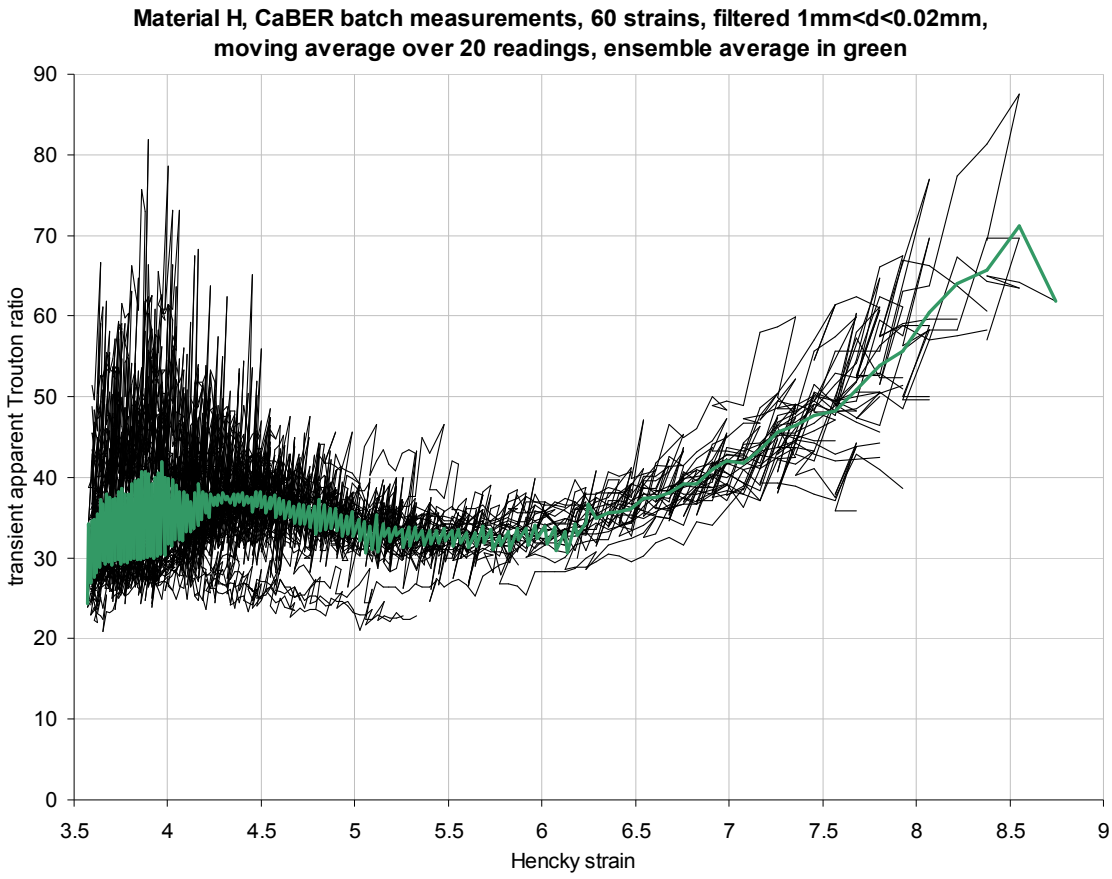

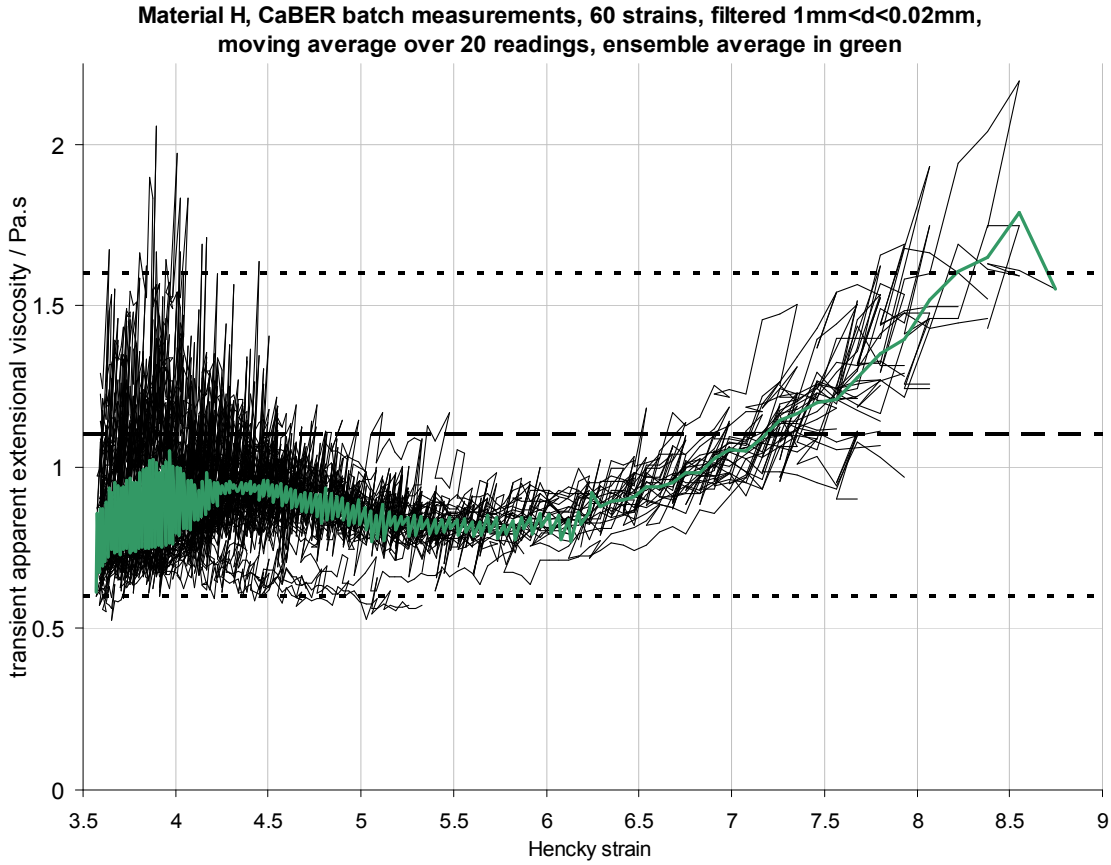

Material H, transient apparent extensional viscosity taken to be 1.1 ± 0.5 Pa.s (single strain values were similar, plots not shown)

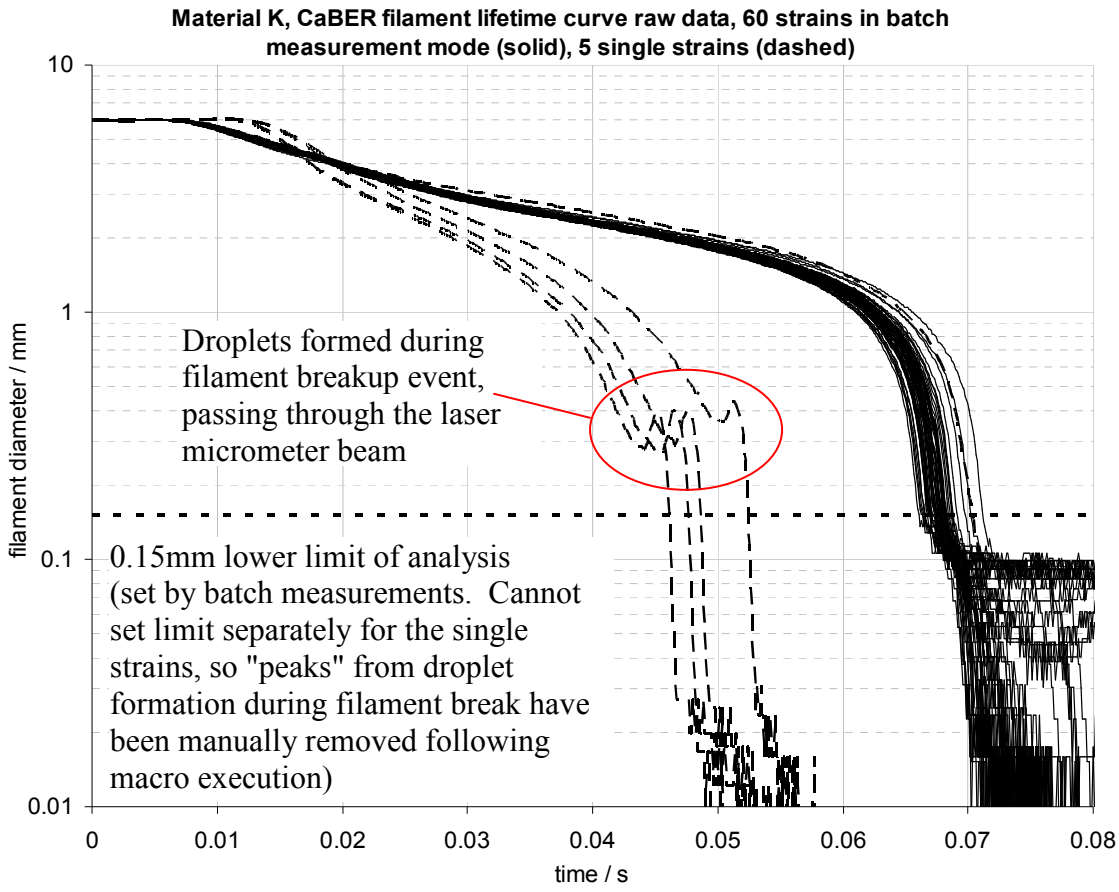
Material K, CaBER filament lifetime curve raw data, 60 strains in batch measurement mode (solid), 5 single strains (dashed)
filament diameter / mm
time / s
Droplets formed during filament breakup event, passing through the laser micrometer beam
0.15mm lower limit of analysis (set by batch measurements. Cannot set limit separately for the single strains, so "peaks" from droplet formation during filament break have been manually removed following macro execution)

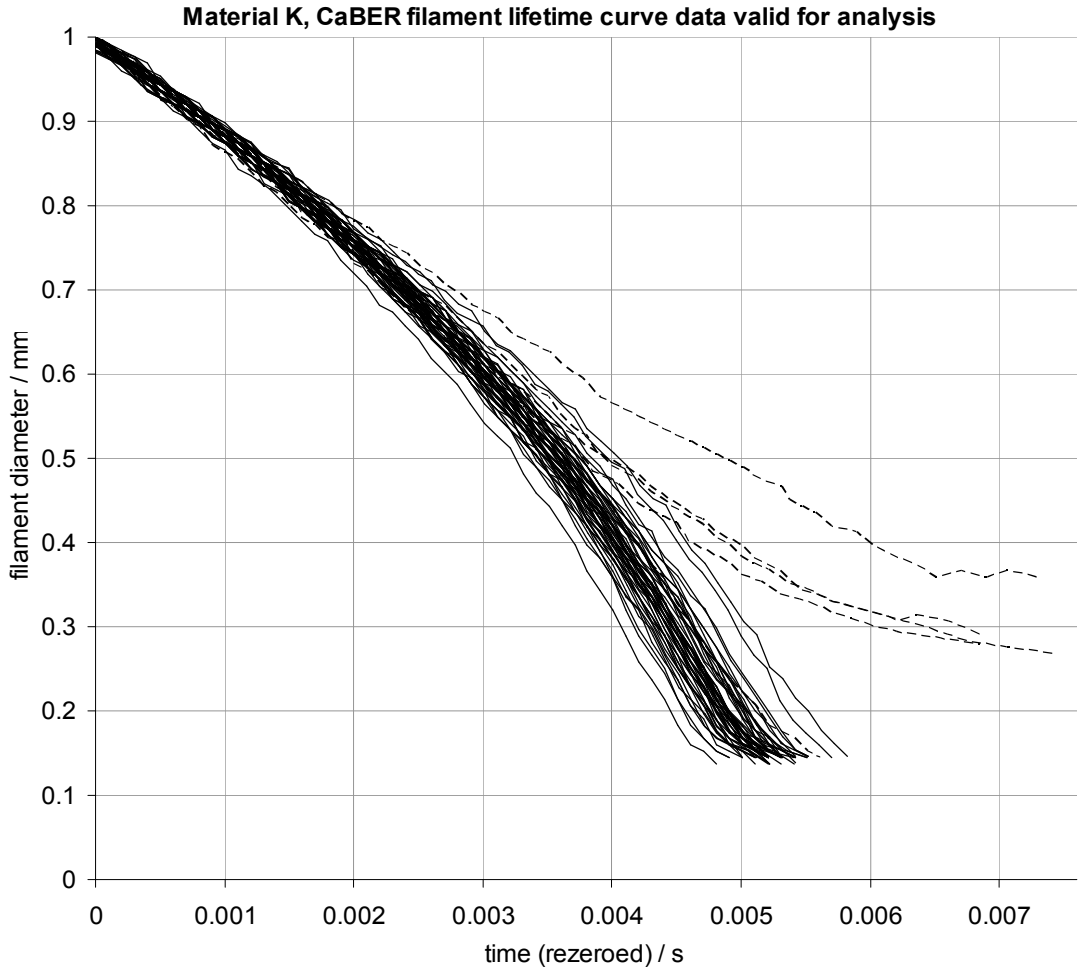
Material K, CaBER filament lifetime curve data valid for analysis
filament diameter / mm
time (rezeroed) / s

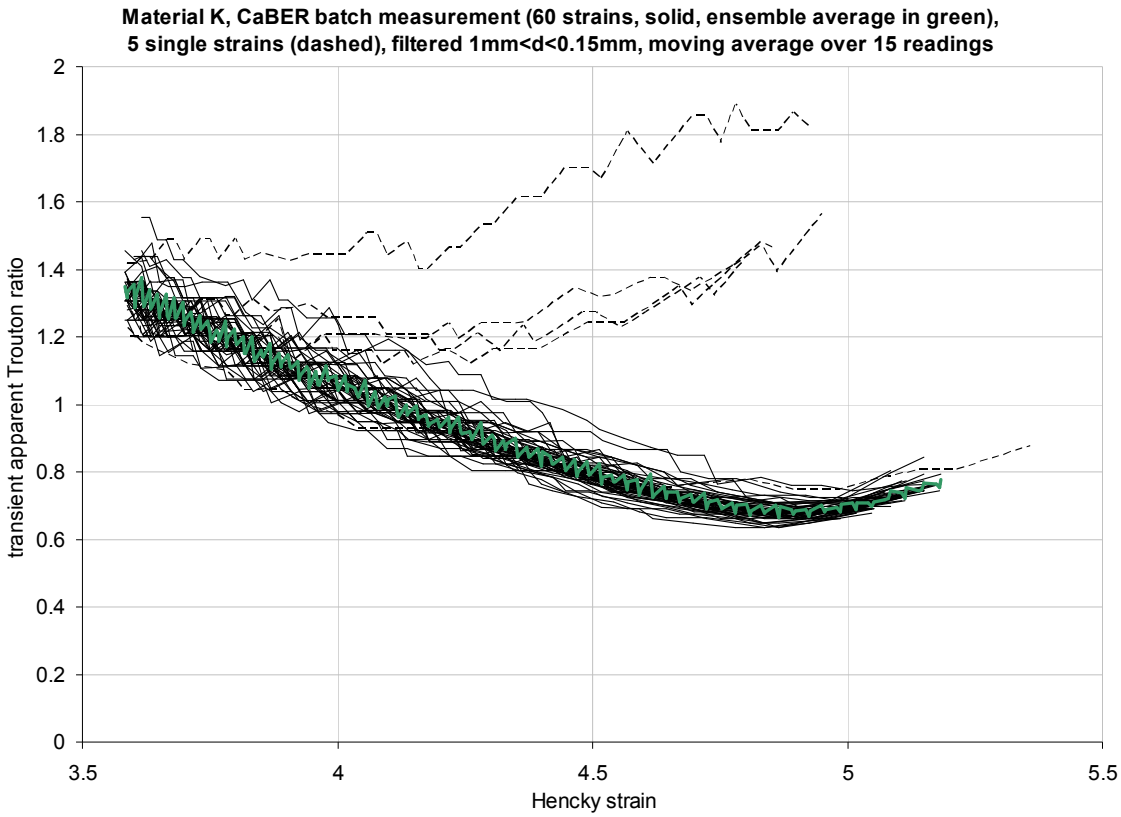

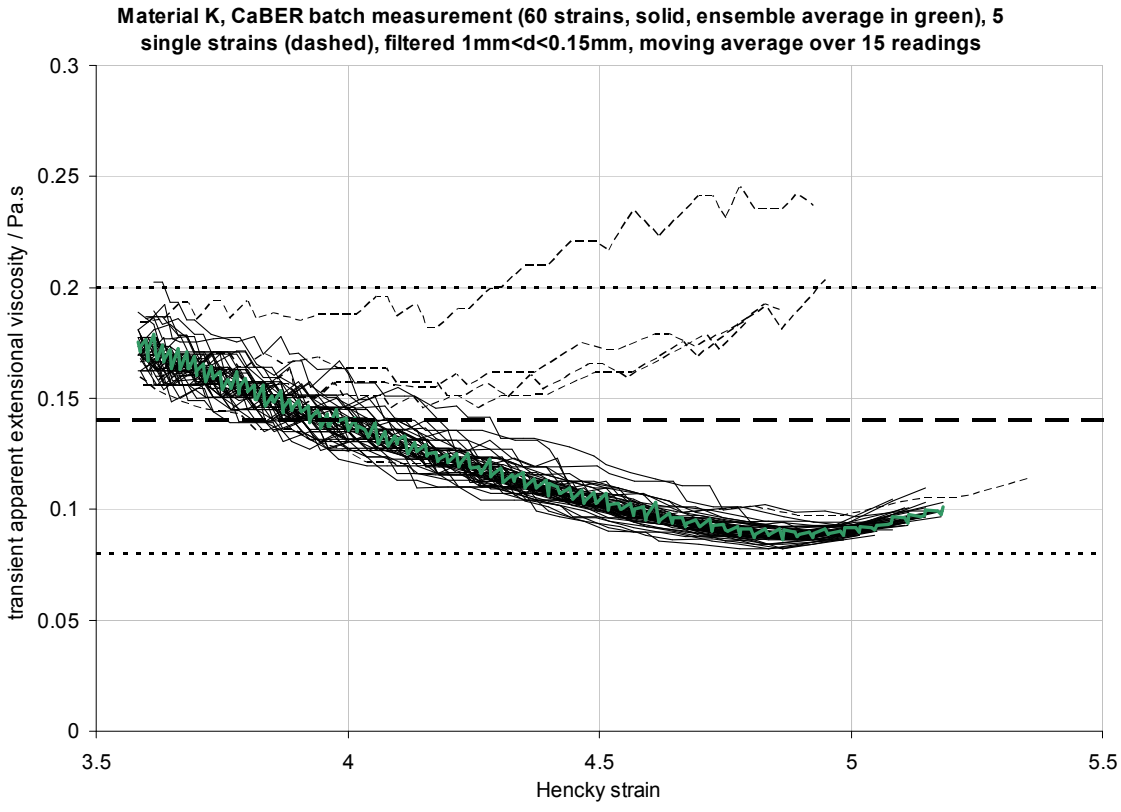

Trouton ratio less than three is not physically meaningful. Potential error sources in the Trouton ratio calculation are discussed in the main text.

Material K transient apparent extensional viscosity taken to be 0.14 ± 0.06 Pa.s

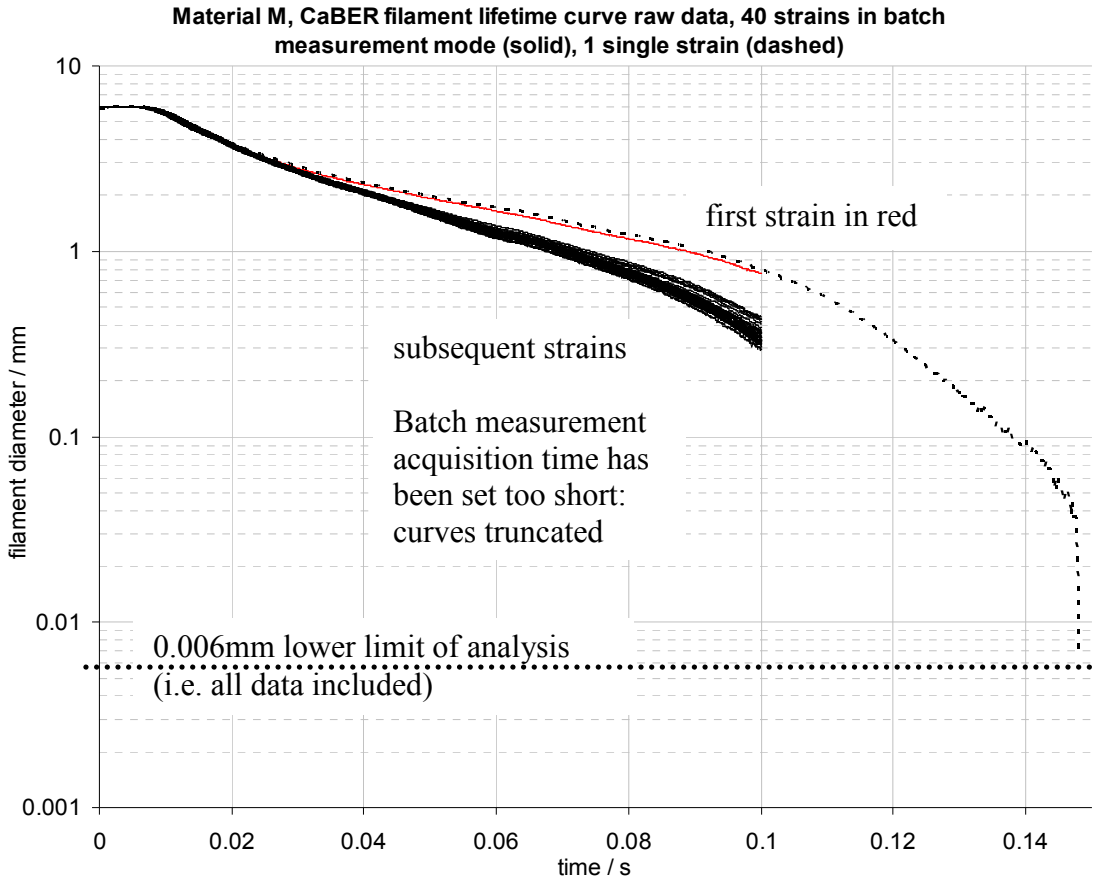
Material M, CaBER filament lifetime curve raw data, 40 strains in batch measurement mode (solid), 1 single strain (dashed)
filament diameter / mm
time / s
first strain in red
subsequent strains
Batch measurement acquisition time has been set too short: curves truncated
0.006mm lower limit of analysis
(i.e. all data included)
10
1
0.1
0.01
0.001
0
0.02
0.04
0.06
0.08
0.1
0.12
0.14

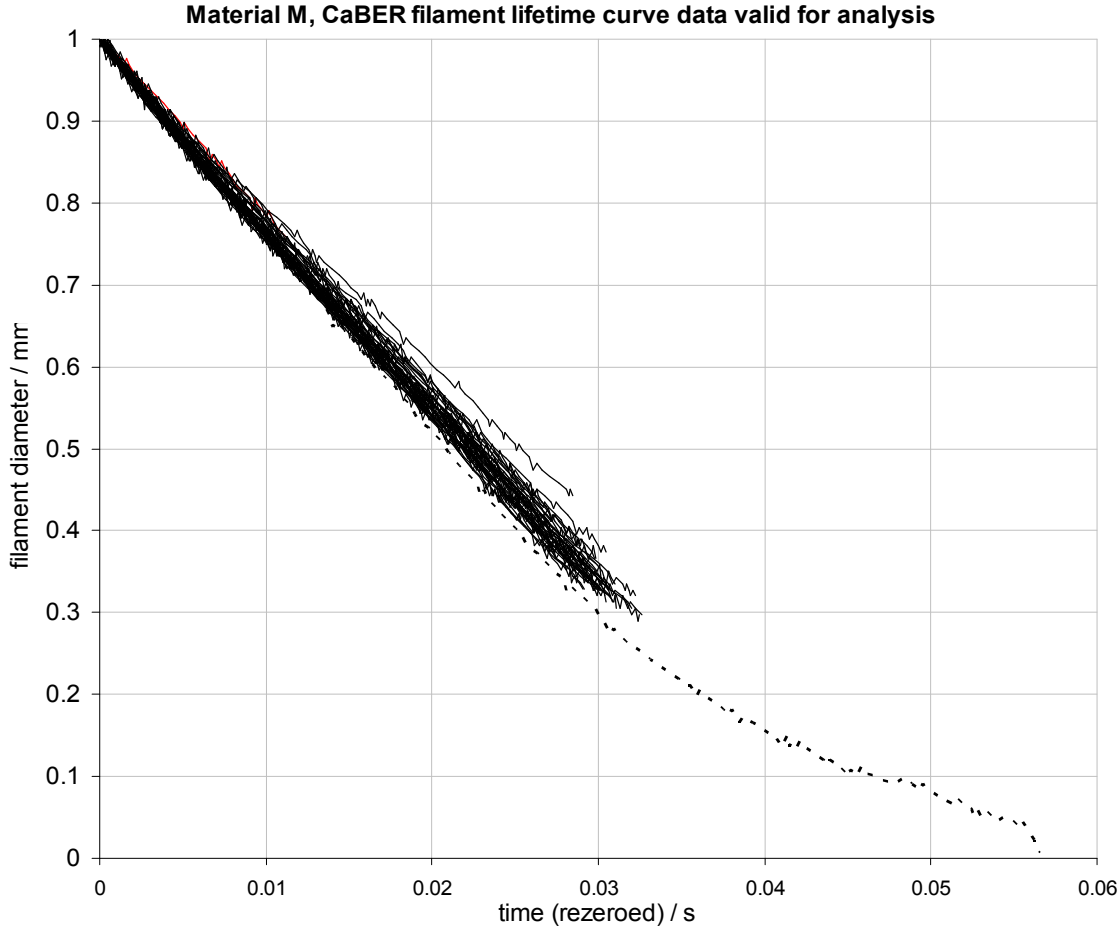
Material M, CaBER filament lifetime curve data valid for analysis
filament diameter / mm
time (rezeroed) / s
1
0.9
0.8
0.7
0.6
0.5
0.4
0.3
0.2
0.1
0
0.01
0.02
0.03
0.04
0.05
0.06

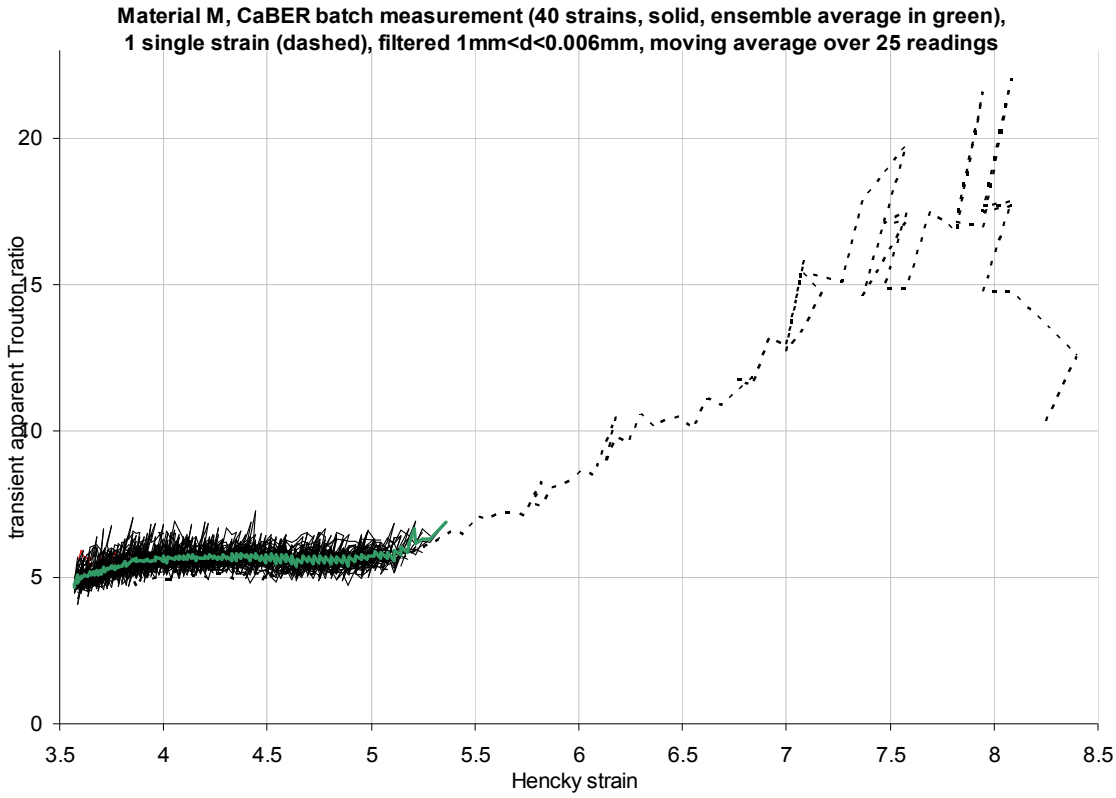

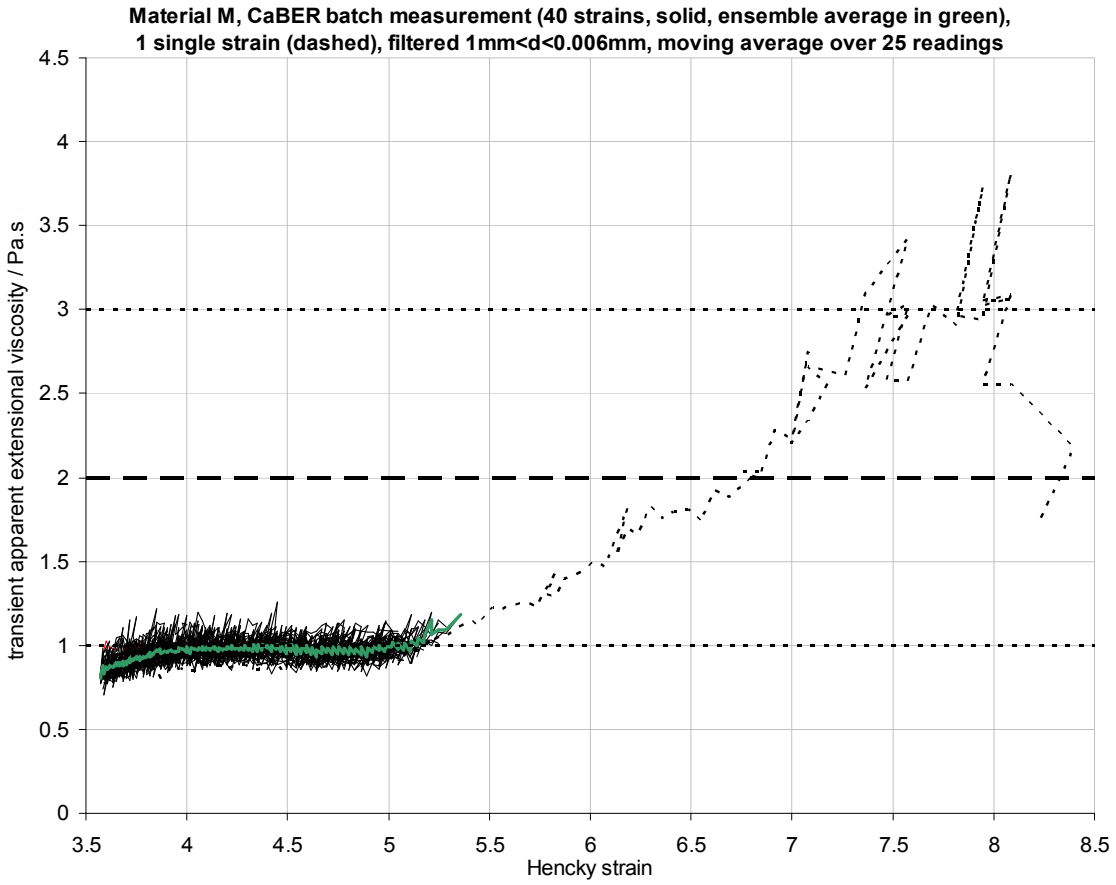

Material M, transient apparent extensional viscosity taken to be 2 ± 1 Pa.s (from single strain value: batch measurements look similar at low strain, but measurement was truncated due to insufficient acquisition time set).

REFERENCES

AKBAR, S. (1988) The drying of droplets in free-flight. PhD thesis**,** Dept. Chem. Engg. & Applied Chem., Aston University.

ALASSAR, R. S. & BADR, H. M. (2007) Heat convection from a sphere placed in a fluctuating free stream. *AIChE J.,* 53(7)**,** 1670-1677.

ALEXANDER, K. & KING, C. J. (1985) Factors governing surface morphology of spray-dried amorphous substances. *Drying Technology,* 3(3)**,** 321-348.

ALI, H. H., MUMFORD, C. J., JEFFREYS, G. V. & BAINS, G. S. (1988) A study of evaporation from, and drying of, single droplets. IN MUJUMDAR, A. S. & ROQUES, M. A. (Eds.) *Proc. 6th Intl. Drying Symposium (IDS'88).* Versailles, France, September 1988. 463-470 (378-385 in Drying'89 - published version of Proc.).

ANNA, S. & MCKINLEY, G. H. (2001) Elasto-capillary thinning and breakup of model elastic liquids. *J. Rheology,* 45(1)**,** 115 - 138.

ANNA, S., MCKINLEY, G. H., NGUYEN, D. A., SRIDHAR, T., MULLER, S. J., HUANG, J. & JAMES, D. F. (2001) An interlaboratory comparison of measurements from filament-stretching rheometers using common test fluids. *J. Rheology,* 45(1)**,** 83-114.

AUDU, T. O. K. & JEFFREYS, G. V. (1975) The drying of drops of particulate slurries. *Chem. Engg. Res. Des., Trans. IChemE Part A,* 53**,** 165-172.

BAKER, C. G. J. & MCKENZIE, K. A. (2002) Energy consumption of industrial spray dryers. IN CAO, C. W., PAN, Y. K., LIU, X. D. & QU, Y. X. (Eds.) *Drying 2002 - Proc. 13th Intl. Drying Symposium (IDS 2002).* Beijing, China, 27-30 August 2002. Vol A, 645-652.

BAKER, C. G. J. & MCKENZIE, K. A. (2005) Energy consumption of industrial spray dryers. *Drying Technology,* 23(1&2)**,** 365-386.

BARLOW, J. B., RAE, W. H., JR. & POPE, A. (1999) *Low-speed wind tunnel testing,* 3rd Ed., pp. 61-123 Wiley-Interscience, New York.

BARTELS, J. (2006) Spray drying in the dairy industry. IN VERSCHUEREN, M. (Ed.) *Designing, optimising and controlling spray drying processes.* NIZO, Ede, The Netherlands, 21-22 Sept 2006.

BAYER AG, IMPERIAL COLLEGE OF SCIENCE TECHNOLOGY AND MEDICINE LONDON, CENTRE NATIONAL DE LA RECHERCHE SCIENTIFIQUE ROUEN, NATIONAL TECHNICAL UNIVERSITY OF ATHENS, CRANFIELD UNIVERSITY SCHOOL OF MECHANICAL ENGINEERING & NIRO A/S SOEBORG DENMARK Energy Efficient, Intensified Spray Drying. *Joule III Program.* Project JOE3-CT97-0086 (DG 12 - WSMN), January 1998-January 2001.

BAYVEL, L. & ORZECHOWSKI, Z. (1993) *Liquid Atomisation*, pp. 63-68, Taylor and Francis, Washington, DC.

BAZILEVSKY, A. V., ENTOV, V. M. & ROZHKOV, A. N. (1990a) Liquid filament microrheometer and some of its applications. IN OLIVER, D. R. (Ed.) *Third European Rheology Conference.* 41-43.

BAZILEVSKY, A. V., ENTOV, V. M., ROZHKOV, A. N. & YARIN, A. L. (1990b) Polymeric jets beads-on-string breakup and related phenomena. IN OLIVER, D. R. (Ed.) *Third European Rheology Conference.* 44-46.

BEARD, K. V. & PRUPPACHER, H. R. (1971) A wind tunnel investigation of the rate of evaporation of small water drops falling at terminal velocity in air. *J. Atmospheric Sciences,* 28**,** 1455-1464.

BINDING, D. M. & WALTERS, K. (1988) On the use of flow through a contraction in estimating the extensional viscosity of mobile polymer solutions. *J. Non-Newtonian Fluid Mech.,* 30(2-3)**,** 233-250.

BIRCHAL, V. S. & PASSOS, M. L. (2005) Modeling and simulation of milk emulsion drying in spray dryers. *Brazilian Journal of Chemical Engineering,* 22(2)**,** 293.

BOUSFIELD, D. W., KEUNINGS, R., MARRUCCI, G. & DENN, M. M. (1986) Nonlinear analysis of the surface tension driven breakup of viscoelastic filaments. *J. Non-Newtonian Fluid Mech.,* 21(1)**,** 79-97.

BRADSHAW, P. & PANKHURST, R. C. (1964) The design of low-speed wind tunnels. *Progress in Aeronautical Science,* 5**,** 1-59.

BRENN, G., HELPIOE, T. & DURST, F. (1997) New apparatus for the production of monodisperse sprays at high flow rates. *Chem. Engg. Sci.,* 52(2)**,** 237-244.

BUSCALL, R. (2006) *pers. comm.*

BÜTTIKER, R. (1981) Mechanism of particle formation during drying of free-falling drops containing solids. *Ger. Chem. Engg.,* 4**,** 298-304.

CHAN, P. S.-K., CHEN, J., ETTELAIE, R., LAW, Z., ALEVISOPOULOS, S., DAY, E. & SMITH, S. (2007) Study of the shear and extensional rheology of casein, waxy maize starch and their mixtures. *Food Hydrocolloids,* 21(5-6)**,** 716-725.

CHARLESWORTH, D. H. & MARSHALL, W. R. (1960) Evaporation from drops containing dissolved solids. *AIChE J.,* 6(1)**,** 9-23.

CHEN, X. D. (2002) Heat-mass transport and micro-structural aspects of the drying of single droplets containing food solids/solute - recent developments. IN CAO, C. W., PAN, Y. K., LIU, X. D. & QU, Y. X. (Eds.) *Drying 2002 - Proc. 13th Intl. Drying Symposium (IDS 2002).* Beijing, China, 27-30 August 2002. Vol A, 88-95.

CHEN, X. D. & LIN, S. X. Q. (2005) Air drying of milk droplet under constant and time-dependent conditions. *AIChE Journal,* 51(6)**,** 1790 - 1799.

CHEONG, H. W., JEFFREYS, G. V. & MUMFORD, C. J. (1986) A receding interface model for the drying of slurry droplets. *AIChE J.,* 32(8)**,** 1334-1346.

CHIOU, D. & LANGRISH, T. A. G. (2008) A comparison of crystallisation approaches in spray drying. *Journal of Food Engineering,* 88(2)**,** 177-185.

CHUCHOTTAWORN, P., FUJINAMI, A. & ASANO, K. (1984) Experimental study of evaporation of a volatile pendant drop under high mass flux conditions. *J. Chem. Engg. Japan,* 17(1)**,** 7-13.

CLASEN, C., EGGERS, J., FONTELOS, M. A., LI, J. & MCKINLEY, G. H. (2006a) The beads-on-string structure of viscoelastic threads. *J. Fluid Mech.,* 556**,** 283 - 308.

CLASEN, C., PLOG, J. P., KULICKE, W. M., OWENS, M., MACOSKO, C., SCRIVEN, L. E., VERANI, M. & MCKINLEY, G. H. (2006b) How dilute are dilute solutions in extensional flows? *J. Rheology,* 50(6)**,** 849-881.

CLIFT, R., GRACE, J. R. & WEBER, M. E. (1978) *Bubbles, Drops and Particles*, pp. 69ff, 103, 331, Academic Press, New York.

COMBLOUX (1990) Proceedings of an International Conference on Extensional Flow, held at Combloux, France, 20–23 March 1989. *J. Non-Newtonian Fluid Mech.,* 35(1-2)**,** 85–470.

COOPER-WHITE, J. J., CROOKS, R. C., CHOCKALINGAM, K. & BOGER, D. V. (2002) Dynamics of polymer-surfactant complexes: Elongational properties and drop impact behavior. *Ind. Engg. Chem. Res.,* 41(25)**,** 6443-6459.

CPG (2003) The basics of filament stretching rheometry. Cambridge Polymer Group.

CROSBY, E. J. & MARSHALL, W. R. (1957) Experimental spray dryer for product development studies. *Chem. Engg. Progress,* 53(7)**,** 347-352.

CROWE, C. T., P., S. M. & STOCK, D. E. (1977) Particle-source in cell (PSI-cell) model for gas-droplet flows. *J. Fluids Engg.,* 99(2)**,** 325-332.

DEXTER, R. W. (1996) Measurement of extensional viscosity of polymer solutions and its effects on atomization from a spray nozzle. *Atomization and Sprays,* 6**,** 167-191.

DICKINSON, D. R. & MARSHALL, W. R. (1968) The rates of evaporation of sprays. *AIChE J.,* 14(4)**,** 541-552.

DIJKSTRA, D. J., KIYOMOTO, Y., ABE, K., TANI, T. & UMEMOTO, S. (2007) The Relationship between Rheological Properties and Spraying Behavior of Polymer Dispersions. *Macromolecular Symposia,* 249-250(1)**,** 647-653.

DLOUGHY, J. & GAUVIN, W. H. (1960) Heat and mass transfer in spray drying. *AIChE J.,* 6(1)**,** 29-34.

DOLINSKY, A. A. (2001) High temperature spray drying. *Drying Technology,* 19(5)**,** 785-806.

DOMBROWSKI, N. & JOHNS, W. R. (1963) The aerodynamic instability and disintegration of viscous liquid sheets. *Chem. Engg. Sci.,* 18**,** 203-214.

DRANSFIELD, P. & DAVIS, D. C. (1985) Stable floating drops of liquid. *Trans. ASME,* 107**,** 530-533.

DUFFIE, J. A. & MARSHALL, W. R. (1953a) Factors Influencing the properties of spray-dried materials Part I. *Chem. Engg. Progress,* 49(8)**,** 417-423.

DUFFIE, J. A. & MARSHALL, W. R. (1953b) Factors Influencing the properties of spray-dried materials Part II. *Chem. Engg. Progress,* 49(9)**,** 480-486.

ECKERT, W. T., MORT, K. W. & JOPE, J. (1976) Aerodynamic design guidelines and computer program for estimation of subsonic wind tunnel performance. TN D-8243, NASA Ames Research Center.

EIA/JEDEC (1999) Integrated circuit thermal test method environmental conditions - forced convection (moving air). Standard JESD51-6, Electronic Industries Alliance / JEDEC Solid State Technology Association.

EL-SAYED, T. M., WALLACK, D. A. & KING, C. J. (1990) Changes in particle morphology during drying of drops of carbohydrate solutions and food liquids. 1. Effect of composition and drying conditions. *Ind. Engg. Chem. Res.,* 29(12)**,** 2346-2354.

ENTOV, V. M. & HINCH, E. J. (1997) Effect of a spectrum of relaxation times on the capillary thinning of a filament of elastic fluid. *J. Non-Newtonian Fluid Mech.,* 72**,** 31-53.

ETSU (1996) Spray Drying. *Carbon Trust Good Practice Guide no. 185.* UK Gov't Energy Efficiency Best Practice Programme.

ETZEL, M. R. & KING, C. J. (1984) Loss of volatile trace organics during spray drying. *Ind. Engg. Chem. Proc. Des. Dev.,* 23(4)**,** 705 - 710;.

FANO, G. (1908) Contributo allo studio dei corpi filanti (Contribution to the study of thread-forming materials), . *Archivio di Fisiologia,* 5**,** 365–370.

FARID, M. (2003) A new approach to modelling of single droplet drying. *Chem. Engg. Sci.,* 58(13)**,** 2985-2993.

FIANNACA, C. & THRELFALL-HOLMES, P. (2005) *Particulate Materials*. Patent WO 2005/058473,

FLETCHER, D. F., GUO, B., HARVIE, D. J. E., LANGRISH, T. A. G., NIJDAM, J. J. & WILLIAMS, J. (2006) What is important in the simulation of spray dryer performance and how do current CFD models perform? *Applied Mathematical Modelling,* 30(11)**,** 1281-1292.

FLICK, D., LENOIR, P. & GILBERT, H. (1988) The drying of free-falling droplets of concentrated skim-milk. IN MUJUMDAR, A. S. & ROQUES, M. A. (Eds.)

Proc. 6th Intl. Drying Symposium (IDS'88). Versailles, France, September 1988. 471-477 (NB: does not appear in Drying'89 - published version of Proc.).

FLORES-MARTÍNEZ, H., OSORIO-REVILLA, G. & GALLARDO-VALÁZQUEZ, T. (2004) Optimal spray-drier encapsulation process of orange oil. IN SILVA, M. A. & ROCHA, S. C. S. (Eds.) *Drying 2004 - Proc. 14th Intl. Drying Symposium (IDS2004).* Sao Paulo, Brazil, 22-25 August 2004. Vol A, 621-627.

FREY, D. D. & KING, C. J. (1986a) Effects of surfactants on mass transfer during spray drying. *AIChE J.,* 32(3)**,** 437-443.

FREY, D. D. & KING, C. J. (1986b) Experimental and theoretical investigation of foam-spray drying. 2. Experimental investigation of volatiles loss during foam-spray drying. *Ind. Engg. Chem. Fund.,* 25(4)**,** 730-735.

FUCHS, N. A. (1959) *Evaporation and droplet growth in gaseous media*, pp. 20, 40, 45, Pergamon Press, London.

FYHR, C. & KEMP, I. C. (1998) Comparison of different drying kinetics models for single particles. *Drying Technology,* 16(7)**,** 1339-1369.

GAUVIN, W. H. & KATTA, S. (1976) Basic concepts of spray dryer design. *AIChE Journal,* 22(4)**,** 713-724.

GLUCKERT, F. A. (1962) A theoretical correlation of spray-dryer performance. *AIChE J.,* 8(4)**,** 460-466.

GRANT, R. P. & MIDDLEMANN, S. (1966) Newtonian jet stability. *AIChE J.,* 12(4)**,** 669-678.

GREENWALD, C. G. & KING, C. J. (1981) The effects of design and operating conditions on particle morphology for spray-dried foods. *J. Food Proc. Engg.,* 4**,** 171-187.

GREENWALD, C. G. & KING, C. J. (1982) The mechanism of particle expansion in spray drying of foods. *AIChE Symposium Series,* 78(218)**,** 101-110.

GROENEWOLD, C., MÖSER, C., GROENEWOLD, H. & TSOTSAS, E. (2000) Determination of single-particle drying kinetics in an acoustic levitator. IN KERKHOF, P. J. A. M., COUMANS, W. J. & MOOIWEER, G. D. (Eds.) *Drying 2000 - Proc. 12th Intl. Drying Symposium (IDS2000).* Noordwijkerhout, The Netherlands, 28-31 August 2000. Vol 08A, Paper no. 58.

GROENEWOLD, C., MÖSER, C., GROENEWOLD, H. & TSOTSAS, E. (2002) Determination of single-particle drying kinetics in an acoustic levitator. *Chemical Engineering Journal,* 86(1-2)**,** 217-222.

GUPTA, R. K. & SRIDHAR, T. E. (1988) Elongational Rheometers. IN COLLYER, A. A. & CLEGG, D. W. (Eds.) *Rheological Measurement.* Elsevier Applied Science, London.

HAIRE, G. & KALDAS, A. (1989) The acoustic levitated drop set-up commissioning report. *ICI internal report.* Unpublished.

HALL, C. W. (1992) Dimensionless numbers and groups for drying. *Drying Technology,* 10(4)**,** 1081-1095.

HAN, R. J., MOSS, O. R. & WONG, B. A. (1996) Derivation and application of an analytical solution of the mass transfer equation to the case of forced convective flow around a cylindrical and a spherical particles with fluid surface properties. *J. Aerosol Science,* 27(2)**,** 235-247.

HANDSCOMB, C. S., KRAFT, M. & BAYLY, A. E. (2009) A new model for the drying of droplets containing suspended solids. *Chem. Engg. Sci.,* 64(4)**,** 628-637.

HARVIE, D. J. E., LANGRISH, T. A. G. & FLETCHER, D. F. (2001) Numerical Simulations of Gas Flow Patterns Within a Tall-Form Spray Dryer. *Chem. Engg. Res. Des., Trans. IChemE Part A,* 79(3)**,** 235-248.

HASATANI, M. & ITAYA, Y. (1996) Drying-induced strain and stress: a review. *Drying Technology,* 14(5)**,** 1011-1040.

HASSAN, H. M. & MUMFORD, C. J. (1996) Mechanisms of Drying of Skin-Forming Materials; the Significance of Skin Formation and a Comparison Between Three Types of Material. *Drying Technology,* 14(7)**,** 1763 - 1777.

HASSAN, H. M., SAYED, A. A. & MUMFORD, C. J. (1996a) Volatiles Retention in the Drying of Skin Forming Materials PART 2: Natural Materials. *Drying Technology,* 14(3)**,** 565 - 579.

HASSAN, H. M., SAYED, A. A. & MUMFORD, C. J. (1996b) Volatiles Retention in the Drying of Skin Forming Materials PART 3: Heat-Sensitive Materials. *Drying Technology,* 14(3)**,** 581 - 593.

HECHT, J. P. (1999) Influence of the development of drop morphology on drying rates and loss rates of volatile components during drying. Doctor of Philosophy**,** Chemical Engineering, University of California at Berkeley.

HECHT, J. P. (2002) *pers. comm.*

HECHT, J. P. & KING, C. J. (2000a) Spray drying: Influence of the development of drop morphology on drying rates and loss rates of volatile substances. 1. single-drop drying. *Ind. Engg. Chem. Res.,* 39(6)**,** 1756-1765.

HECHT, J. P. & KING, C. J. (2000b) Spray drying: Influence of the development of drop morphology on drying rates and loss rates of volatile substances. 2. Modeling. *Ind. Engg. Chem. Res.,* 39(6)**,** 1766-1774.

HERRING, W. H. & MARSHALL, W. R. (1955) Performance of vaned-disk atomizers. *AIChE J.,* 1(2)**,** 200-209.

HIRSCHMANN, C., FYHR, C., TSOTSAS, E. & KEMP, I. C. (1998) Comparison of two basic methods for measuring drying curves: thin layer studies and drying channel. *Drying '98 - Proc. 11th International Drying Symposium.* Halkidiki, Greece, August 19-22, 1998. Vol A, 224-231.

HORTIG, H. P. (1970) Zur auslegung von sprühtürmen (The design of spraytowers). *Chemie Ing. Tech.,* 42(6)**,** 390-396.

HUANG, L., KUMAR, K. & MUJUMDAR, A. S. (2003) A parametric study of the gas flow patterns and drying performance of co-current spray dryer: results of a computational fluid dynamics study. *Drying Technology,* 21(6)**,** 957-978.

HUANG, L., KUMAR, K. & MUJUMDAR, A. S. (2004) Computational fluid dynamic simulation of droplet drying in a spray dryer. IN SILVA, M. A. & ROCHA, S. C. S. (Eds.) *Drying 2004 - Proc. 14th Intl. Drying Symposium (IDS2004).* Sao Paulo, Brazil, 22-25 August 2004. Vol A, 326-332.

HULL, G. (n.d.; 1988?) The single drop dryer. *ICI internal memo.* Unpublished.

HUNIK, J. H. & TRAMPER, J. (1993) Large-scale production of κ-carrageenan droplets for gel-bead production: theoretical and practical limitations of size and production rate. *Biotechnology Progress,* 9(2)**,** 186-192.

HUNTINGTON, D. H. (2004) The Influence of the Spray Drying Process on Product Properties. *Drying Technology,* 22(6)**,** 1261 - 1287.

INSAUSTI-ECI-OLAZA, S. & MOUZOURAS, R. (2005) *Airless spray-coating of a surface with a viscous aqueous architectural coating composition*. Patent WO 2006/015869,

IRANI, R. R. & CALLIS, C. F. (1963) *Particle Size: Measurement, Interpretation and Application*, pp. 39-45, Wiley, New York.

JAMES, D. F., CHANDLER, G. M. & ARMOUR, S. J. (1990) A converging channel rheometer for the measurement of extensional viscosity. *J. Non-Newtonian Fluid Mech.,* 35(1-2)**,** 421 - 443.

JAMES, D. F. & WALTERS, K. (1994) A critical appraisal of available methods for the measurement of extensional properties of mobile systems. IN COLLYER, A. A. (Ed.) *Techniques of Rheological Measurement.* Elsevier, New York.

JANSSEN, J. M. H., PETERS, G. W. M. & MEIJER, H. E. H. (1993) An opposed jets device for studying the breakup of dispersed liquid drops. *Chem. Engg. Sci.,* 48(2)**,** 255-265.

JONES, S. J. R. & SMITH, W. (1962) Mass transfer from solids freely suspended in an air stream. IN ROTTENBURG, P. A. (Ed.) *Proc. symp. interaction between fluids and particles.* Third Congress Eur. Fed. Chem. Engg., London, 20-22 June 1962. 190-196.

JØRGENSEN, K., JENSEN, A. D., SLOTH, J., DAM-JOHANSEN, K. & BACH, P. (2006) Comments to "Analysis of constant rate period of spray drying of slurry" by Liang et al., 2001. *Chem. Engg. Sci.,* 61(6)**,** 2096-2100.

KATTA, S. & GAUVIN, W. H. (1975) Some fundamental aspects of spray drying. *AIChE Journal,* 21(1)**,** 143-152.

KEEY, R. B. (1972) *Drying:Principles and Practice*, pp. 1,3,22ff,185ff, Pergamon, Oxford.

KEMP, I. C., FYHR, B. C., LAURENT, S., ROQUES, M. A., GROENEWOLD, C. E., TSOTSAS, E., SERENO, A. A., BONAZZI, C. B., BIMBENET, J.-J. & KIND, M. (2001) Methods for processing experimental drying kinetics data. *Drying Technology,* 19(1)**,** 15 - 34.

KIECKBUSCH, T. G. & KING, C. J. (1980) Volatiles Loss during atomization in spray drying. *AIChE J.,* 26(5)**,** 718-725.

KIEVET, F. G. (1997) Modelling Quality in Spray Drying. PhD thesis**,** Chemical Engineering, Technische Universiteit Eindhoven.

KIEVET, F. G. & KERKHOF, P. J. A. M. (1995) Measurements of particle residence time distributions in a co-current spray tower. *Drying Technology,* 13(5-7)**,** 1241-1248.

KIEVET, F. G., VAN RAAIJ, J., DE MOOR, P. P. E. A. & KERKHOF, P. J. A. M. (1997) Measurement and Modelling of the Air Flow in a Pilot-Plant Spray Dryer. *Chem. Engg. Res. Des., Trans. IChemE Part A,* 75(3)**,** 321-328.

KOHOUT, M., GROF, Z. & ŠTĚPÁNEK, F. (2006) Pore-scale modelling and tomographic visualisation of drying in granular media. *J. Colloid and Interface Sci.,* 299(1)**,** 342-351.

KRAFT, M. (2007) Modelling across the length scales. *Procter & Gamble particle modelling meeting.* Cambridge, UK, 14 February 2007.

KRÖGER, B. & SCHULTE, G. (2000) Einfluß der Strömungsverhältnisse auf die Tropfenverteilung in einem Sprühtrocknerturm (Influence of the flow conditions on the droplet distribution in a spray drying tower). *ACHEMA 2000.* Frankfurt, 22-27 May 2000.

KUMAR, A. & HARTLAND, S. (1999) Correlations for the Prediction of Mass Transfer Coefficients in Single Drop Systems and Liquid-Liquid Extraction Columns. *Chem. Engg. Res. Des., Trans. IChemE Part A,* 77(5)**,** 372-384.

KWAPINSKI, W. & TSOTSAS, E. (2004) Experimental determination of single-particle kinetics and equilibria for convective drying, desorption or adsorption by a magnetic suspension balance. IN SILVA, M. A. & ROCHA, S. C. S. (Eds.) *Drying 2004 - Proc. 14th Intl. Drying Symposium (IDS2004).* Sao Paulo, Brazil, 22-25 August 2004. Vol B, 1419-1426.

LAGNADO, R. R. & LEAL, L. G. (1990) Visualization of three-dimensional flow in a four-roll mill. *Experiments in Fluids,* V9(1)**,** 25-32.

LANGRISH, T. A. G. (2007) New engineered particles from spray dryers: research needs in spray drying. *Drying Technology,* 25(6)**,** 971 - 983.

LANGRISH, T. A. G., BAHU, R. E. & REAY, D. (1991) Drying kinetics of particles from thin layer drying experiments. *Chem. Engg. Res. Des., Trans. IChemE Part A,* 69**,** 417-424.

LANGRISH, T. A. G. & KOCKEL, T. K. (2001) The assessment of a characteristic drying curve for milk powder for use in computational fluid dynamics modelling. *Chemical Engineering Journal,* 84(1)**,** 69-74.

LANGRISH, T. A. G., MARQUEZ, N. & KOTA, K. (2006) An investigation and quantitative assessment of particle shape in milk powders from a laboratory-scale spray dryer. *Drying Technology,* 24(12)**,** 1619 - 1630.

LANGRISH, T. A. G., OAKLEY, D. E., KEEY, R. B., BAHU, R. E. & HUTCHINSON, C. A. (1993) Time-dependent flow patterns in spray dryers. *Chem. Engg. Res. Des., Trans. IChemE Part A,* 71**,** 355-360.

LARSON, R. G. (1998) *The structure and rheology of complex fluids*, p. 140, Oxford University Press.

LEBARBIER, C., KOCKEL, T. K., FLETCHER, D. F. & LANGRISH, T. A. G. (2001) Experimental Measurement and numerical simulation of the effect of swirl on flow stability in spray dryers. *Chem. Engg. Res. Des., Trans. IChemE Part A,* 79(3)**,** 260 - 268.

LEE, C. P., ANILKUMAR, A. V. & WANG, T. G. (1991) Static shape and instability of an acoustically levitated liquid drop. *Physics of Fluids A,* 3(11)**,** 2497-2515.

LEFEBVRE, A. H. (1989) *Atomization and sprays*, pp. 31, 42-45, 52, 85-89, Hemisphere Publishing Corp, New York.

LI, X. & ZBICINSKI, I. (2005) A Sensitivity Study on CFD Modeling of Cocurrent Spray-Drying Process. *Drying Technology,* 23(8)**,** 1681 - 1691.

LIANG, B. & KING, C. J. (1991) Factors influencing flow patterns, temperature fields and consequent drying rates in spray drying. *Drying Technology,* 9(1)**,** 1 - 25.

LIANG, H., SHINOHARA, K., MINOSHIMA, H. & MATSUSHIMA, K. (2001) Analysis of constant rate drying period of spray drying of slurry. *Chem. Engg. Sci.,* 56(6)**,** 2205-2213.

LIANG, R. F. & MACKLEY, M. R. (1994) Rheological Characterization of the Time and Strain Dependence for Polyisobutylene Solutions. *J. Non-Newtonian Fluid Mech.,* 52(3)**,** 387-405.

LIN, J.-C. & GENTRY, J. W. (1999a) Spray drying droplet morphology: experimental investigation. *J. Aerosol Science,* 30(Supplement 1)**,** 319-320.

LIN, J.-C. & GENTRY, J. W. (1999b) Spray drying droplet morphology: Theoretical model. *J. Aerosol Science,* 30(Supplement 1)**,** 545-546.

LIN, J.-C., ZHANG, H.-J. & GENTRY, J. W. (2000) Spray drying droplet morphology: Formation of shell. *J. Aerosol Science,* 31(Supplement 1)**,** 797-798.

LIN, S. X. Q. & CHEN, X. D. (2002) Improving the Glass-Filament Method for Accurate Measurement of Drying Kinetics of Liquid Droplets. *Chem. Engg. Res. Des., Trans. IChemE Part A,* 80(4)**,** 401-410.

LIN, S. X. Q. & CHEN, X. D. (2005) Prediction of air-drying of milk droplet under relatively high humidity using the reaction engineering approach. *Drying Technology,* 23(7)**,** 1395.

LIN, S. X. Q. & CHEN, X. D. (2007) The reaction engineering approach to modelling the cream and whey protein concentrate droplet drying. *Chemical Engineering and Processing,* 46(5)**,** 437-443.

LLOYD, E. (1984) *Handbook of applicable mathematics, Volume VI part B: Statistics*, pp. 606-611, Wiley-Interscience, Chichester.

LO, S. (2005) ES Spraydry V1.0 Product description. IN VERSCHUEREN, M. (Ed.) *Designing, optimising and controlling spray drying processes.* NIZO, Ede, The Netherlands, 22 Sept 2005.

LUIKOV, A. V. (1967) *Heat and mass transfer in capillary-porous bodies*, p. 199, Pergamon Press, London.

LYSHEVSKII, A. S. (1963) *Processes of Fuel Atomization in Diesel Nozzles*, Mashgiz, Moscow.

MANDAL, A., JOG, M. A., XUE, J. & IBRAHIM, A. A. (2008) Flow of power-law fluids in simplex atomizers. *Intl. J. Heat & Fluid Flow,* In Press, Corrected Proof.

MASTERS, K. (1991) *Spray Drying Handbook,* 5th Ed., pp. 4, 9, 121, 167, 195-196, 207-209, 271, 345-352, 598, Longman, England.

MASTERS, K. (2004) Current Market-Driven Spray Drying Development Activities. *Drying Technology,* 22(6)**,** 1351 - 1370.

MATSUMOTO, S., BELCHER, D. W. & CROSBY, E. J. (1985) Rotary atomizers: performance understanding and prediction. *ICLASS-85; Proceedings of the Third International Conference on Liquid Atomisation and Spray Systems.* The Institute of Energy, London, July 8-10, 1985. 1A/1/1 - 1A/1/21.

MCCARTHY, M. J. & MOLLOY, N. A. (1974) Review of stability of liquid jets and the influence of nozzle design. *Chemical Engineering Journal,* 7(1)**,** 1-20.

MCKINLEY, G. H. (2005) Visco-elasto-capillary thinning and break-up of complex fluids. *Rheology Reviews***,** 48.

MCKINLEY, G. H. & SRIDHAR, T. (2002) Filament - stretching rheometry of complex fluids. *Ann. Rev. Fluid Mech.,* 34**,** 375-415.

MCKINLEY, G. H. & TRIPATHI, A. (2000) How to extract the Newtonian viscosity from capillary breakup measurements in a filament rheometer. *J. Rheology,* 44(3)**,** 653.

MCLAUGHLIN, M. P. (1999) A compendium of probability distributions. *Regress + software documentation Appendix A.*

MCMINN, W. A. M. & MAGEE, T. R. A. (1996) Moisture transport in starch gels during convective drying. *Trans. IChemE PartC: Food and Bioproducts Processing,* 74**,** 3-12.

MEERDINK, G. & VAN'T RIET, K. (1994) Drying Kinetics of Free Falling Droplets IN RUDOLPH, V. & KEEY, R. B. (Eds.) *DRYING '94 - Proc. 9th Intl. Drying Symp. (IDS'94).* Gold Coast, Australia, 1-4 August 1994. Vol A, 383-390.

MEERDINK, G. & VAN'T RIET, K. (1995) Prediction of product quality during spray drying. *Food and Bioproducts Processing,* 73**,** 165-170.

MEHTA, R. D. & BRADSHAW, P. (1979) Design rules for small low speed wind tunnels. *The aeronautical journal of the Royal Aeronautical Society,* November 1979**,** 443-449.

MICHAEL, J. R. (1983) The stabilized probability plot. *Biometrika,* 70**,** 11-17.

MIESSE, C. C. (1955) Correlation of experimental data on the disintegration of liquid jets. *Ind. & Engg. Chem.,* 47(9)**,** 1690-1701.

MINOSHIMA, H. (2006) Reply to the Comment by K. Jorgensen et al. to "Analysis of constant rate period of spray drying of slurry". *Chem. Engg. Sci.,* 61(6)**,** 2101-2102.

MITRA, S. K., BRINKMANN, J. & PRUPPACHER, H. R. (1992) A wind tunnel study on the drop-to-particle conversion *J. Aerosol Science,* 23(3)**,** 245-256.

MIURA, K., MIURA, T. & OHTANI, S. (1977) Heat and mass transfer to and from droplets. *AIChE Symposium Series,* 73(95)**,** 163-164.

MIURA, T. & OHTANI, S. (1980) Heat transfer characteristics in a concurrent spray dryer. *Heat Transfer - Japanese Research,* 79**,** 20-29.

MOOR, S. S. & KING, C. J. (1998) Visualization of Spray Dynamics in a Pilot Spray Dryer by Laser-Initiated Fluorescence. *Ind. Engg. Chem. Res.,* 37(2)**,** 561 - 568.

MORIMOTO, M., CHUCHOTTAWORN, P. & ASANO, K. (1985) Measurements and simulation of an evaporating drop. *ICLASS-85; Proceedings of the Third International Conference on Liquid Atomisation and Spray Systems.* Imperial College, London, July 8-10, 1985. VIB/5/1-VIB/5/8.

MORSE, H. W. (1910) On evaporation from the surface of a solid sphere. *Proc. Am. Acad. Sci.,* 45**,** 363-367.

MUGELE, R. A. & EVANS, H. D. (1951) Droplet size distribution in sprays. *Ind. & Engg. Chem.,* 43(6)**,** 1317-1324.

MUJUMDAR, A. S. (1995) *Handbook of Industrial Drying,* 2nd Ed., Marcel Dekkar, New York.

MUJUMDAR, A. S. (2004) Role of IDS in promoting innovation and global R&D effort in drying technologies. IN SILVA, M. A. & ROCHA, S. C. S. (Eds.) *Drying 2004 - Proc. 14th Intl. Drying Symposium (IDS2004).* Sao Paulo, Brazil, 22-25 August 2004. Vol A, 101-118.

MÜLLER, A. J., ODELL, J. A. & CARRINGTON, S. (1992) Degradation of semidilute polymer solutions in elongational flows. *Polymer,* 33(12)**,** 2598-2604.

NAWAZ, S. (1997) Characterisation of the drop tube. *ICI internal report.* Unpublished.

NEGIZ, A., LAGERGREN, E. S. & CINAR, A. (1995) Mathematical models of cocurrent spray drying. *Ind. Engg. Chem. Res.,* 34(10)**,** 3289-3302.

NEŠIĆ, S. & VODNIK, J. (1991) Kinetics of droplet evaporation. *Chem. Engg. Sci.,* 46(2)**,** 527-537.

NIJDAM, J. J., GUO, B., FLETCHER, D. F. & LANGRISH, T. A. G. (2004) Challenges of simulating droplet coalescence within a spray. *Drying Technology,* 22(6)**,** 1463 - 1488.

NIJDAM, J. J., GUO, B., FLETCHER, D. F. & LANGRISH, T. A. G. (2006) Validation of the Lagrangian approach for predicting turbulent dispersion and evaporation of droplets within a spray. *Drying Technology,* 24(11)**,** 1373 - 1379.

NIJMAN, J. (2006) *pers. comm.*

NIRO (1999) Spray Drying. *(manufacturer's sales literature).*

NOLAN, J. P. (1997) Numerical calculation of stable densities and distribution functions. *Commun. Statist. - Stochastic Models,* 13(4)**,** 759-774.

NOLAN, J. P. (1998) Parameterizations and modes of stable distributions. *Statistics and Probability Letters,* 38**,** 187-195.

NOLAN, J. P. (2009) *Stable distributions - models for heavy tailed data*, Birkhäuser, Boston.

NONHEBEL, G. & MOSS, A. A. H. (1971) *Drying of solids in the chemical industry*, p. 3, Butterworths, London.

O'BRIEN, S. B. G. (1991) On the shape of small sessile and pendant drops by singular perturbation techniques. *J. Fluid Mech.,* 233**,** 519-537.

OAKLEY, D. E. (1997) Produce uniform particles by spray drying. *Chem. Engg. Progress,* 93**,** 48 - 54.

OAKLEY, D. E. (2004) Spray Dryer Modeling in Theory and Practice. *Drying Technology,* 22(6)**,** 1371 - 1402.

OCONE, R. & ASTARITA, G. (1991) Two conceptual problems in heat and mass transfer to arrays of particles. *Unpublished*.

OHNESORGE, W. (1936) Die bildung von tropfen an dusen und die auflosung flussiger strahlen. *Zeitschr Angewandte Mathematik und Mechanik,* 16(5)**,** 355-358.

OHSAKA, K. & TRINH, E. H. (1989) Melting and solidification of acoustically levitated drop. *J. Crystal Growth,* 96**,** 973-978.

OLIVEIRA, M. S. N. & MCKINLEY, G. H. (2005) Iterated stretching and multiple beads-on-a-string phenomena in dilute solutions of highly extensible flexible polymers. *Physics of Fluids,* 17(7)**,** 071704.

OLIVER, R., FAIRCLOUGH, A. R. N., ANTONINI, A. M., MUNRO, R. J. & LIPSCOMBE, L. W. (1994) *Production of particulate materials*. Patent WO9420204,

OLIVER, R. & LLOYD-JONES, G. N. (1993) *Controlled break-up of liquid jets*. Patent EP0320153,

OTENG-ATTAKORA, G. & MUMFORD, C. J. (1994a) Evaporation from droplets in free-flight: effects of skin-forming materials. *The 1994 IChemE Research Event.* 477-479.

OTENG-ATTAKORA, G. & MUMFORD, C. J. (1994b) Mechanism of drop oscillations. IN RUDOLPH, V. & KEEY, R. B. (Eds.) *DRYING '94 - Proc. 9th Intl. Drying Symp. (IDS'94).* Gold Coast, Australia, 1-4 August 1994. Vol A, 375-382.

OZMEN, L. & LANGRISH, T. A. G. (2003) A study of the limitations to spray dryer outlet performance. *Drying Technology,* 21(5)**,** 895-917.

PALENCIA, C., NAVA, J., HERMAN, E., RODRIGUEZ-JIMENES, G. C. & GARCIA-ALVARADO, M. A. (2002) Spray-drying dynamic modeling with a mechanistic model. *Drying Technology,* 20(3)**,** 569-586.

PAPADAKIS, S. E. & KING, C. J. (1988a) Air temperature and humidity profiles in spray drying. 1. Features predicted by the particle source in cell model. *Ind. Engg. Chem. Res.,* 27(11)**,** 2111-2116.

PAPADAKIS, S. E. & KING, C. J. (1988b) Air temperature and humidity profiles in spray drying. 2. Experimental measurements. *Ind. Engg. Chem. Res.,* 27(11)**,** 2116-2123.

PAPAGEORGIOU, D. T. (1995) On the breakup of viscous liquid threads. *Physics of Fluids,* 7(7)**,** 1529-1544.

PATEL, K. C. & CHEN, X. D. (2005) Prediction of spray-dried product quality using two simple drying kinetics models. *Journal of Food Process Engineering,* 28(6)**,** 567 - 594.

PATEL, K. C., CHEN, X. D. & KAR, S. (2005) The temperature uniformity during air drying of a colloidal liquid droplet. *Drying Technology,* 23(12)**,** 2337 - 2367.

PATEL, K. C., CHEN, X. D., LIN, S. X. Q. & ADHIKARI, B. (2009) A composite reaction engineering approach to drying of aqueous droplets containing sucrose, maltodextrin (DE6) and their mixtures. *AIChE Journal,* 55(1)**,** 217-231.

PEI, D. C. T., NARASIMHAN, C. & GAUVIN, W. H. (1962) Evaporation from drops and particles in high-temperature surroundings. IN ROTTENBURG, P. A. (Ed.) *Proc. symp. interaction between fluids and particles.* Third Congress Eur. Fed. Chem. Engg., London, 20-22 June 1962. 243-249.

PEMBERTON, S. T. & KEEY, R. B. (1980) Evaluating the performance of spray dryers in the dairy industry. *J. Separation Process Technology,* 1(3)**,** 42-46.

PERRÉ, P. & MAY, B. K. (2001) A numerical drying model that accounts for the coupling between transfers and solid mechanics. Case of highly deformable products. *Drying Technology,* 19(8)**,** 1629 - 1643.

PERRY, R. H. & GREEN, D. W. (1997) *Perry's chemical engineering handbook,* 7th Ed., pp. 6-11, McGraw-Hill.

PETRIE, C. J. S. (1978) *Elongational flows: aspects of the behaviour of model elasticoviscous fluids*, Pitman, London.

PETRIE, C. J. S. (1997) Three-dimensional presentation of extensional flow data. *J. Non-Newtonian Fluid Mech.,* 70(3)**,** 205 - 218.

PETRIE, C. J. S. (2006a) Extensional viscosity: A critical discussion. *J. Non-Newtonian Fluid Mech.,* 137(1-3)**,** 15 - 23.
PETRIE, C. J. S. (2006b) One hundred years of extensional flow. *J. Non-Newtonian Fluid Mech.,* 137(1-3)**,** 1 -14.
PÍSECKÝ, J. (1983) New generation of spray dryers for milk products. *Dairy Industries International,* 48(4)**,** 21-24.
PLOG, J. P., KULICKE, W. M. & CLASEN, C. (2005) Influence of the molar mass distribution on the elongational behaviour of polymer solutions in capillary breakup. *Applied Rheology,* 15(1)**,** 28-37.
POLLARD, J. H. (1977) *A handbook of numerical and statistical techniques*, pp. 151-155, CUP, Cambridge.
RÄDERER, M., BESSON, A. & SOMMER, K. (2002) A thin film dryer approach for the determination of water diffusion coefficients in viscous products. *Chemical Engineering Journal,* 86(1-2)**,** 185-191.
RANZ, W. E. & MARSHALL, W. R. (1952a) Evaporation from Drops Part I. *Chem. Engg. Progress,* 48(3)**,** 141-146.
RANZ, W. E. & MARSHALL, W. R. (1952b) Evaporation from Drops Part II. *Chem. Engg. Progress,* 48(4)**,** 173-180.
RAYLEIGH (1878) On the instability of jets. *Proc. London Math. Soc.,* 10**,** 4-13.
RAYLEIGH (1879) On the capillary phenomena of jets. *Proc. Royal Society,* 29**,** 71-97.
RÉ, M. I. (1998) Microencapsulation by spray drying. *Drying Technology,* 16(6)**,** 1195 - 1236.
RENARDY, M. (1995a) A numerical study of the asymptotic evolution and breakup of Newtonian and viscoelastic jets. *J. Non-Newtonian Fluid Mech.,* 59(2-3)**,** 267-282.
RENARDY, M. (1995b) A numerical study of the asymptotic evolution and breakup of Newtonian and viscoelastic jets. *Journal of Non-Newtonian Fluid Mechanics,* 59(2-3)**,** 267-282.
RODD, L. E., SCOTT, T. P., COOPER-WHITE, J. J. & MCKINLEY, G. H. (2005) Capillary break-up rheometry of low-viscosity elastic fluids. *Applied Rheology,* 15(1)**,** 12 -27.
ROOS, Y. H. (2002) Importance of glass transition and water activity to spray drying and stability of dairy powders. *Lait,* 82**,** 475-484.
ROUTH, A. F. & RUSSEL, W. B. (1998) Horizontal drying fronts during solvent evaporation from latex films. *AIChE J.,* 44(9)**,** 2088-2098.
RULKENS, W. H. & THIJSSEN, H. A. (1972) The retention of organic volatiles in drying aqueous carbohydrates solutions. *J. Food Technology,* 7**,** 186-191.
SALMAN, H. & SOTERIOU, M. (2004) Lagrangian simulation of evaporating droplet sprays. *Physics of Fluids,* 16(12)**,** 4601-4622.
SANO, Y. (1993) Gas flow behaviour in spray dryer. *Drying Technology,* 11(4)**,** 697 - 718.
SANO, Y. & KEEY, R. B. (1982) The drying of a spherical particle containing colliodal material into a hollow sphere. *Chem. Engg. Sci.,* 37(6)**,** 881-889.
SAYED, A. A., HASSAN, H. M. & MUMFORD, C. J. (1996) Volatiles Retention in the Drying of Skin Forming Materials PART 1: Materials Which Gelatinise at Moderately High Temperatures. *Drying Technology,* 14(3)**,** 529 - 563.
SCHEELE, G. F. & MEISTER, B. J. (1968a) Drop formation at low velocities in liquid-liquid systems: part 1. prediction of drop volume. *AIChE J.,* 14(1)**,** 9-15.
SCHEELE, G. F. & MEISTER, B. J. (1968b) Drop formation at low velocities in liquid-liquid systems: part 2. prediction of jetting velocity. *AIChE J.,* 14(1)**,** 15-19.

SCHRÖDER, T. & WALZEL, P. (1998) Design of laminar operating rotary atomizers under consideration of the detachment geometry. *Chemical Engineering & Technology,* 21(4)**,** 349-354.
SCHUCK, P. (2002) Spray drying of dairy products: state of the art. *Lait,* 82**,** 375-382.
SCHWARTZBACH, C. (2000) Simulations of spray drying by CFD. *ACHEMA 2000.* Frankfurt, Germany, 22-27 May 2000.
SEYDEL, P., BLOMER, J. & BERTLING, J. (2006) Modeling particle formation at spray drying using population balances. *Drying Technology,* 24(2)**,** 137-146.
SJENITZER, F. (1962) The evaporation of a liquid spray injected into a stream of gas. *Chem. Engg. Sci.,* 17**,** 309-322.
SLOTH, J., KIIL, S., JENSEN, A. D., ANDERSEN, S. K., JØRGENSEN, K., SCHIFFTER, H. & LEE, G. (2006) Model based analysis of the drying of a single solution droplet in an ultrasonic levitator. *Chem. Engg. Sci.,* 61(8)**,** 2701-2709.
SOMMERFELD, M. & QIU, H. H. (1998) Experimental studies of spray evaporation in turbulent flow. *International Journal of Heat and Fluid Flow,* 19(1)**,** 10.
SOUTHWELL, D. B. & LANGRISH, T. A. G. (2000) Observations of flow patterns in a spray dryer. *Drying Technology,* 18(3)**,** 661 - 685.
SOUTHWELL, D. B. & LANGRISH, T. A. G. (2001) The Effect of Swirl on Flow Stability in Spray Dryers. *Chem. Engg. Res. Des., Trans. IChemE Part A,* 79(3)**,** 222-234.
SOUTHWELL, D. B., LANGRISH, T. A. G. & FLETCHER, D. F. (2001) Use of computational fluid dynamics techniques to assess design alternatives for the plenum chamber of a small spray dryer. *Drying Technology,* 19(2)**,** 257-268.
STAFFORD, R. A., FAUROUX, O. & GLASS, D. H. (1997) Flow visualisation and instantaneous velocity measurements of spray dryer gas and spray flows using particle imaging velocimetry. *Drying Technology,* 15(6)**,** 1661 - 1671.
STANTON, D. W., SENECAL, P. K., HUNG, C. C., RUTLAND, C. J. & REITZ, R. D. (1998) Methodology for model discrimination and criticism for liquid atomization data. *Atomization and Sprays,* 8**,** 363-392.
STEIN, W. A. (1973) Berechnung der verdampfung von flüssigkeit aus feuchten produkten im sprühturm (Calculation of evaporation of liquids from moist products in spray towers). *Verfahrenstechnik,* 7(9)**,** 262-265.
STELTER, M., BRENN, G. & DURST, F. (2002a) The influence of viscoelastic fluid properties on spray formation from flat-fan and pressure-swirl atomizers. *Atomization and Sprays,* 12(1-3)**,** 299-327.
STELTER, M., BRENN, G., YARIN, A. L., SINGH, R. P. & DURST, F. (2002b) Investigation of the elongational behavior of polymer solutions by means of an elongational rheometer. *J. Rheology,* 46(2)**,** 507 - 527.
ŠTĚPÁNEK, F. (2008) Contact drying research developments: Pore-scale modelling and visualisation. *Solids Drying in Theory & Practice.* University College London, 2 April 2008.
STEVEN, F. & ELLIOTT, D. (2005) ICI internal communication. *pers. comm.*
STRAATSMA, J., VAN HOUWELINGEN, G., STEENBERGEN, A. E. & DE JONG, P. (1999a) Spray drying of food products: 1. Simulation model. *Journal of Food Engineering,* 42(2)**,** 67-72.
STRAATSMA, J., VAN HOUWELINGEN, G., STEENBERGEN, A. E. & DE JONG, P. (1999b) Spray drying of food products: 2. Prediction of insolubility index. *Journal of Food Engineering,* 42(2)**,** 73-77.
SUNKEL, J. M. & KING, C. J. (1993) Influence of the development of particle morphology on rates of loss of volatile solutes during drying of drops. *Ind. Engg. Chem. Res.,* 32(10)**,** 2357-2364.

SUZUKI, M., KEEY, R. B. & MAEDA, S. (1977) On the characteristic drying curve. *AIChE Symposium Series,* 73(163)**,** 47-56.

TANIGUCHI, I. & ASANO, K. (1994) Evaporation of an aqueous salt solution drop in dry air during crystallization of salt. *ICLASS-94.* Rouen, France, July 1994. 859-866.

TANIGUCHI, I., HUZIMORI, Y., MAEDA, N. & ASANO, K. (1999) Evaporation of water from alumina slurry drop containing dissolved poly(vinyl alcohol). *J. Chem. Engg. Japan,* 32(4)**,** 449-455.

TANIGUCHI, I., KURIYAMA., T. & ASANO, K. (1991) Simultaneous measurement of drag coefficients and mass transfer of a chain of uniform volatile drops. *J. Chem. Engg. Japan,* 24(2)**,** 232-237.

TANNO, S., FUKAI, J., MIURA, T., OHTANI, S., DAIKOKU, M. & AOKI, H. (1988) Heat and mass transfer on a droplet of 200-300µm diameter. *ICLASS-88; 4th Intl. Conf. Liquid Atomization and Spray Systems.* Sendai, Japan, 22-24 August, 1988.

THERMOHAAKE (2003) Instruction Manual Haake CaBER 1. 1.2 ed. Karlsruhe, ThermoHaake.

THRELFALL-HOLMES, P. (2008) Acoustic atomisation in spray drying. *Solids drying in theory and practice.* IChemE Particle Technology Subject Group Meeting, UCL, 2 April 2008.

THRELFALL-HOLMES, P. & OCONE, R. (2005) Spray drying kinetics measurement apparatus. *7th World Congress of Chemical Engineering.* Glasgow, 10-14 July 2005.

TOEI, R. & FURUTA, T. (1982) Drying of a droplet in a non-supported state. *AIChE Symposium Series,* 78(218)**,** 111-117.

TRIPATHI, A., TAM, K. C. & MCKINLEY, G. H. (2006) Rheology and dynamics of associative polymers in shear and extension: theory and experiments. *Macromolecules,* 39**,** 1981-1999.

TROMMELEN, A. M. & CROSBY, E. J. (1970) Evaporation and drying of drops in superheated vapours. *AIChE J.,* 16(5)**,** 857-867.

TROUTON, F. T. (1906) On the Coefficient of Viscous Traction and Its Relation to that of Viscosity. *Proceedings of the Royal Society of London. Series A, Containing Papers of a Mathematical and Physical Character (1905-1934),* 77(519)**,** 426 - 440.

TRUONG, H. T., PHAM, Q. T. & KEEY, R. B. (1983) Evaporation in a cocurrent spray dryer with a pneumatic nozzle. *J. Separ. Proc. Technol.,* 4(2)**,** 11-19.

TRUONG, V., BHANDARI, B. R. & HOWES, T. (2005) Optimization of co-current spray drying process of sugar-rich foods. Part I-Moisture and glass transition temperature profile during drying. *Journal of Food Engineering,* 71(1)**,** 55-65.

TSAPIS, N., DUFRESNE, E. R., SINHA, S. S., RIERA, C. S., HUTCHINSON, J. W., MAHADEVAN, L. & WEITZ, D. A. (2005) Onset of Buckling in Drying Droplets of Colloidal Suspensions. *Physical Review Letters,* 94(1)**,** 018302-4.

VAN DYCKE, F. (2006) Spray drying in the pharmaceutical industry. IN VERSCHUEREN, M. (Ed.) *Designing, optimising and controlling spray drying processes.* NIZO, Ede, The Netherlands, 21-22 Sept 2006.

VEHRING, R., FOSS, W. R. & LECHUGA-BALLESTEROS, D. (2007) Particle formation in spray drying. *J. Aerosol Science,* 38(7)**,** 728-746.

VENTURELLI, P. A. & CULICK, F. E. C. (2003) *Method and apparatus for optical acoustic molding*. Patent US 2003/0154790 A1,

VERDERBER, P. A. & KING, C. J. (1992) Measurement of instantaneous rates of loss of volatile compounds during drying of drops. *Drying Technology,* 10(4)**,** 875-891.

VERDURMEN, R. E. M., MENN, P., RITZERT, J., BLEI, S., NHUMAIO, G. C. S., SØRENSEN, T. S., GUNSING, M., STRAATSMA, J., VERSCHUEREN, M., SIBEIJN, M., SCHULTE, G., FRITSCHING, U., BAUCKHAGE, K., TROPEA, C., SOMMERFELD, M., WATKINS, A. P., YULE, A. J. & SCHØNFELDT, H. (2004) Simulation of Agglomeration in Spray Drying Installations: The EDECAD Project. *Drying Technology,* 22(6)**,** 1403 - 1461.

VERSCHUEREN, M. (2005) State of the art and future opportunities. IN VERSCHUEREN, M. (Ed.) *Designing, optimising and controlling spray drying processes.* NIZO, Ede, The Netherlands, 22 Sept 2005.

VUATAZ, G. (2002) The phase diagram of milk: a new tool for optimising the drying process. *Lait,* 82**,** 485-500.

WALLACK, D. A., EL-SAYED, T. M. & KING, C. J. (1990) Changes in particle morphology during drying of drops of carbohydrate solutions and food liquids. 2. Effects of drying rate. *Ind. Engg. Chem. Res.,* 29(12)**,** 2354-2357.

WALTON, D. E. (2000) The morphology of spray-dried particles a qualitative view. *Drying Technology,* 18(9)**,** 1943-1986.

WALTON, D. E. (2004) The Evaporation of Water Droplets. A Single Droplet Drying Experiment. *Drying Technology,* 22(3)**,** 431-456.

WALTON, D. E. & MUMFORD, C. J. (1999) The morphology of spray-dried particles. The effect of process variables upon the morphology of spray-dried particles. *Chem. Engg. Res. Des., Trans. IChemE Part A,* 77**,** 442-460.

WALZEL, P. (1990) Zerstäuben von Flüssigkeiten (Atomizing of liquids). *Chemie Ing. Tech.,* 62(12)**,** 983-994.

WATSON, R. (2001) Single droplet drying studies. *ICI internal report.* Unpublished.

WELANDER, P. & VINCENT, T. L. (2001) Select the right spray nozzle. *Chem. Engg. Progress,* 97**,** 75-79.

WERNER, S. R. L., EDMONDS, R. L., JONES, J. R., BRONLUND, J. E. & PATERSON, A. H. J. (2008) Single droplet drying: Transition from the effective diffusion model to a modified receding interface model. *Powder Technology,* 179(3)**,** 184-189.

WINBORNE, D. A., NORDINE, P. C., ROSNER, D. E. & MARLEY, N. F. (1976) Aerodynamic levitation technique for containerless high temperature studies on liquid and solid samples. *Metallurgical Trans. B,* 7B**,** 711-713.

WU, W. D., PATEL, K. C., ROGERS, S. & CHEN, X. D. (2007) Monodisperse Droplet Generators as Potential Atomizers for Spray Drying Technology. *Drying Technology,* 25(12)**,** 1907 - 1916.

XING, L.-L., GLASS, J. E. & FERNANDO, R. H. (1999) Parameters influencing the spray behavior of waterborne coatings. *J. Coatings Technology,* 71(890)**,** 37-50.

XU, T.-H., DURST, F. & TROPEA, C. (1993) The three-parameter log-hyperbolic distribution and its application to particle sizing. *Atomization and Sprays,* 3**,** 109-124.

YAMAMOTO, S. & SANO, Y. (1992) Drying of enzymes: enzyme retention during drying of a single droplet. *Chem. Engg. Sci.,* 47(1)**,** 177-183.

YAMAMOTO, S. & SANO, Y. (1995) Drying of carbohydrate and protein solutions. *Drying Technology,* 13(1&2)**,** 29-41.

YARIN, A. L., BRENN, G., KASTNER, O., RENSINK, D. & TROPEA, C. (1999) Evaporation of acoustically levitated droplets. *J. Fluid Mech.,* 399**,** 151-204.

YARIN, A. L., ZUSSMAN, E., THERON, A., RAHIMI, S., SOBE, Z. & HASAN, D. (2004) Elongational behavior of gelled propellant simulants. *J. Rheology,* 48(1)**,** 101-116.

YESILATA, B., CLASEN, C. & MCKINLEY, G. H. (2006) Nonlinear shear and extensional flow dynamics of wormlike surfactant solutions. *J. Non-Newtonian Fluid Mech.,* 133(2-3)**,** 73-90.

YUEN, M. C. & CHEN, L. W. (1978) Heat-transfer measurements of evaporating liquid droplets. *Intl. J. Heat Mass Transfer,* 21**,** 537-542.

ZAKARIAN, J. A. & KING, C. J. (1982) Volatiles loss in the nozzle zone during spray drying of emulsions. *Ind. Engg. Chem. Proc. Des. Dev.,* 21(1)**,** 107 - 113.

ZBICINSKI, I., DELAG, A., STRUMILLO, C. & ADAMIEC, J. (2002) Advanced experimental analysis of drying kinetics in spray drying. *Chemical Engineering Journal,* 86(1-2)**,** 207-216.

ZBICINSKI, I. & LI, X. (2002) An investigation of error sources in CFD modelling of a co-current spray dryer. IN CAO, C. W., PAN, Y. K., LIU, X. D. & QU, Y. X. (Eds.) *Drying 2002 - Proc. 13th Intl. Drying Symposium (IDS 2002).* Beijing, China, 27-30 August 2002. Vol A, 415-423.